University of Alberta
Department of Civil &
Environmental Engineering

Structural Engineering Report No. 294

Shear in Steel Fiber Reinforced Concrete Members without Stirrups

by

Abdoladel Shoaib,

Adam S. Lubell

and

Vivek S. Bindiganavile

June, 2012

Abstract

Hooked end steel fibers were included between 0~1% by volume to provide enhanced shear resistance to three different types of steel fiber reinforced concrete (SFRC) namely, a regular concrete mix, a lightweight aggregate mix and a high strength mix. The test results at the material scale showed a substantial increase in the shear strength of regular and high strength concrete, but only limited enhancement in the case of the lightweight aggregate concrete. The steel fibers were most efficient in enhancing the post-peak shear performance in the regular concrete, where the cracks progressed around the coarse aggregate. The fractured surface of the specimens revealed that in the lightweight and high strength mixes, cleavage was through the aggregates.

A total of 18 structural SFRC specimens were designed and constructed to capture the behavior of shear-critical SFRC members. The specimens contained longitudinal reinforcement but no stirrups, and utilized different mixes with 1% fiber content selected from the material scale testing phase. The specimens varied in overall height from 308 to 1000 *mm* with constant shear span to effective depth ratio of 3. The normalized shear stress at failure decreased with an increase in the specimen total depth, indicating that a size effect exists for SFRC specimens without stirrups. However, adding steel fibers into the concrete matrix considerably enhanced the shear capacity compared to the *ACI 318-08* and *CSA A23.3-04* predictions for RC members without steel fibers.

An analytical shear capacity model was developed based on mechanical principles and empirical measurements of crack geometry observed in the current study for both normal weight and lightweight SFRC members without stirrups. The analytical model was then further simplified to be suitable for use in design. For validation, shear capacity predictions were examined for a large database and gave reliable and accurate predictions. The prediction quality of the proposed design model was also compared against published SFRC shear models from other researchers. Among the SFRC shear models studied, the proposed design model was the most accurate model in prediction quality and relatively the least sensitive model to different common design variables.

Acknowledgements

Financial support for this study provided by the Cement Association of Canada, Lehigh Inland Heidelberg Cement (Canada) and the Natural Sciences and Engineering Research Council (Canada) is gratefully acknowledged. Support through materials donations was also provided by Bekaert, BASF, and EPCOR.

Table of Contents

List of Tables

List of Figures

List of Notations

A	Effective tension area equivalent to twice of the area extending from extreme tensile fiber to the centroid of longitudinal reinforcement (mm^2)
A_f	Area under load-deflection diagram of flexural test (*ASTM C1609*) from deflection 0 to L/150 (N.mm)
A_v	Area under direct shear load-deflection curve from deflection 0 to $\delta_s=h/m$ (N.mm)
A_s	Area of longitudinal steel reinforcement (mm^2)
a/d	Shear-span to depth ratio
a_g	Maximum aggregate size (mm)
b	Specimen width (mm)
b_w	Web width (mm)
c	Compression zone depth (mm)
C	Resultant compression force in the compression zone (N)
C_M	Crack mouth opening displacement (mm)
$C_{M,0.5}$	Crack mouth opening displacement for SFRC with V_f=0.5% (mm)
$C_{M,1}$	Crack mouth opening displacement for SFRC with V_f=1% (mm)

C_W	Shear crack width at level of longitudinal reinforcement (mm)
C_{Wmax}	Maximum shear crack width at level of longitudinal reinforcement at $P=P_{max}$ (mm)
D_L	Dead load (N/m^2)
d	Effective depth of specimen (mm)
d_c	Distance from extreme tension fiber to the center of the closest longitudinal bar (mm)
d_f	Bond factor accounting for the fiber's shape
D_f	Fiber diameter (mm)
d_v	Effective shear depth (= 0.9d) (mm)
e	Arch action factor
E_c	Modulus of elasticity of concrete (MPa)
E_s	Young's modulus for steel (MPa)
F	Fiber factor
f_1	Dead load factor
f_2	Live load factor
f_{ac}	Compression strength resulted from accelerated boiling water test method curing (MPa)

f'_c	Cylinder compressive strength of concrete (MPa)
f_{c7}	Cylinder compressive strength of concrete after 7 days regular curing (MPa)
f_{c28}	Estimated cylinder compressive strength of concrete at 28-days (MPa)
f_{cuf}	Cube strength of steel fiber reinforced concrete (MPa)
f_r	Modulus of rupture (MPa)
$f_{r,\ plain}$	Modulus of rupture for plain concrete (MPa)
$f_{r,\ SFRC}$	Modulus of rupture for steel fiber reinforced concrete (MPa)
f_s	Tensile stress in longitudinal steel reinforcement (MPa)
f'_t	Cylinder splitting strength of concrete (MPa)
f_{spfc}	Computed value for split-cylinder strength of normal weight SFRC (MPa)
$f_{spfc,l}$	Computed value for split-cylinder strength of lightweight SFRC (MPa)
f_v	Peak direct shear stress (MPa)
f_{vh}	Direct shear strength for high strength SFRC (MPa)
f_{vl}	Direct shear strength for lightweight SFRC (MPa)
f_{vn}	Direct shear strength for normal strength SFRC (MPa)

$f_{v0,h}$ Direct shear strength for high strength plain concrete (MPa)

$f_{v0,l}$ Direct shear strength for lightweight plain concrete (MPa)

$f_{v0,n}$ Direct shear strength for normal strength plain concrete (MPa)

$f_{v,\ plain}$ Peak direct shear stress for plain concrete (MPa)

$f_{v,\ SFRC}$ Peak direct shear stress for steel fiber reinforced concrete (MPa)

f_y Yielding stress for longitudinal steel reinforcement (MPa)

h Height of specimen (mm)

L Specimen span, center to center of supports (mm)

L_c Distance of interception point of critical shear crack with the longitudinal steel from mid-span (mm)

L_f Fiber length (mm)

L_f/D_f Fiber aspect ratio

L_L Live load (N/m^2)

M Bending moment (N.mm)

M_{ACI} Nominal flexural capacity according to *ACI 318-08* (N.mm)

M_{max} Maximum bending moment (N.mm)

m	An arbitrary number that determine the maximum direct shear deflection as h/m
P	Applied load at mid-span (N)
P_{peak}	Peak load in direct shear test (N)
P_{max}	Maximum applied load at mid-span (N)
R	Nominal ultimate capacity
R_1	The normalized uniform fiber tensile stress and a size effect term based on member total depth for the proposed analytical shear capacity model
S	Average diagonal cracks spacing at mid-depth level (mm)
S_L	Service load (N/m^2)
s_x	Average crack spacing ($=d_v=0.9d$)(mm)
s_{xe}	Effective crack spacing accounting for aggregate size (mm)
T	Resultant tension force in the tension zone of the section (N)
$T_{c,plain}$	Compressive toughness factor for plain concrete mix without fibers (N/mm^2)
$T_{c,SFRC}$	Compressive toughness factor for steel fiber reinforced concrete (N/mm^2)
T_{150}^{D}	Flexural toughness factor according to *ASTM C1609-05* (N/mm^2)

T_f Flexural toughness factor (N/mm^2)

T_{fh} Flexural toughness factor for high strength concrete (N/mm^2)

T_{fl} Flexural toughness factor for lightweight concrete (N/mm^2)

T_{fn} Flexural toughness factor for normal strength concrete (N/mm^2)

$T_{f,plain}$ Flexural toughness factor for plain concrete mix without fibers (N/mm^2)

$T_{f,SFRC}$ Flexural toughness factor for steel fiber reinforced concrete (N/mm^2)

$T_{s,m}$ Shear toughness factor up to direct shear displacement $\delta_s = h/m$ (N/mm^2)

$T_{sh,m}$ Shear toughness factor for high strength concrete up to direct shear displacement $\delta_s = h/m$ (N/mm^2)

$T_{sl,m}$ Shear toughness factor for lightweight concrete up to direct shear displacement $\delta_s = h/m$ (N/mm^2)

$T_{sn,m}$ Shear toughness factor for normal strength concrete up to direct shear displacement $\delta_s = h/m$ (N/mm^2)

$T_{s,plain}$ Shear toughness factor for plain concrete mix without fibers up to shear displacement $\delta_s = h/25$ (N/mm^2)

$T_{s,SFRC}$ Shear toughness factor for steel fiber reinforced concrete up to shear displacement $\delta_s = h/25$ (N/mm^2)

V Shear force (N)

V_{ACI} Shear force capacity of RC members according to *ACI 318-08* (N)

V_c Shear force capacity of RC members (N)

V_{cc} Shear force resistance from compressive concrete zone (N)

V_{CSA} Shear force capacity of RC members according to *CSA A23.3-04* (N)

$V_{CSA,f}$ Shear force capacity of SFRC members according to a modified *CSA A23.3-04* shear model (N)

V_{model} Shear force capacity calculated based on shear prediction model (N)

V_f Volume fraction of fibers expressed in percentage in text but in decimals for calculations (Example: 1% in text = 0.01 in calculations)

V_{frc} Shear force capacity of SFRC members without stirrups (N)

V_{frc1} Shear force capacity of normal weight SFRC members without stirrups based on the proposed analytical model in this study (N)

V_{frc2} Shear force capacity of normal weight SFRC members without stirrups based on the simplified design model in this study (N)

V_{ft} Shear force resistance from vertical component of fibers tensile force (N)

v_{ft} Ultimate shear stress from vertical component of fibers tensile stress (MPa)

V_{ft1} Shear force resistance from vertical component of fibers tensile force for *Khuntia et al.* (1999) shear model (N)

V_{ft2} Shear force resistance from vertical component of fibers tensile force for *Yakoub* (2011) shear model (N)

V_{lfrc1} Shear force capacity of lightweight SFRC members without stirrups based on the proposed analytical model in this study (N)

V_{lfrc2} Shear force capacity of lightweight SFRC members without stirrups based on the simplified design model in this study (N)

V_{test} Failure shear force during test at shear critical section (N)

v_{ci} Transmitted shear stress across a crack in MCFT (MPa)

v_u Ultimate shear stress (MPa)

v_{u1} Ultimate shear stress based on *Sharma* (1986) shear model (MPa)

v_{u2} Ultimate shear stress based on *Narayanan and Darwish* (1987) shear model (MPa)

v_{u3} Ultimate shear stress based on *Ashour et al.* (1992) model (modified *Zsutty* (1968) model (MPa)

v_{u4} Ultimate shear stress based on *Ashour et al.* (1992) model (modified *ACI 318* model) (MPa)

v_{u5} Ultimate shear stress based on *Khuntia et al.* (1999) shear model (MPa)

v_{u6} Ultimate shear stress based on *Kwak et al.* (2002) shear model (MPa)

v_{u7} Ultimate shear stress based on *Dinh* (2009) shear model (MPa)

v_{u8} Ultimate shear stress based on *Kang and Kim* (2010) shear model (modified *Ashour et al.* 1992) (MPa)

v_{u9} Ultimate shear stress based on *Kang and Kim* (2010) shear model (modified *Kwak et al.* 2002) (MPa)

v_{u10} Ultimate shear stress based on *Yakoub* (2011) shear model (MPa)

w Crack width in MCFT (mm)

z Crack control factor (N/mm)

σ_f Tensile stress representing steel fibers along flexural crack of SFRC prism in bending test (*ASTM C1609-05*) (MPa)

σ_{f0} Tensile stress representing steel fibers along diagonal shear crack of SFRC members for *Dinh* (2009) shear model (MPa)

σ_{f1} Tensile stress representing steel fibers along diagonal shear crack of SFRC members based on C_{Wmax} and for steel fibers with L_f/D_f=55 (MPa)

σ_{f2} Modified σ_{f1} to include the size effect factor R_1 (MPa)

σ_{f3} Modified σ_{f2} for steel fibers with aspect ratio L_f/D_f different than 55 (MPa)

σ_{f4} Modified σ_{f3} based on a constant steel fiber's aspect ratio L_f/D_f=60 (MPa)

σ_{cu} Ultimate uniform compressive stress for *Bresler and Pister*(1958) model

α_{frc} Size effect term for SFRC

α_1	A parameter to determine the magnitude of uniform compressive stress as $\alpha_1 f'_c$ for the compressive stress block
β	A parameter which includes so-called strain effect and size effect terms for RC members
β_{test}	Normalized shear stress for SFRC from test
β_1	A parameter to determine the depth of compressive stress block as $a=\beta_1 c$
γ	Concrete density (kg/m^3)
λ	Concrete density factor
λ_1	Ratio of live-to-dead loads L_L / D_L
δ	Deflection at mid-span (mm)
δ_q	Deflection at quarter-point (mm)
δ_{max}	Maximum deflection of *L/150* in flexural test (*ASTM C1609-05*) (mm)
δ_s	Maximum deflection of *h/m* in direct shear test (*JSCE-G 553-1999*) (mm)
ε_s	Steel strain
$\varepsilon_{s,test}$	Strain obtained from strain gauges on the steel bars at the critical section at the ultimate state before shear failure

ε_x	Average axial strain at mid-depth of member (= ½ of the tensile strain in longitudinal reinforcement)
ε'_c	Strain at peak compressive stress
ζ	Strain effect term
η	Recommended fiber contribution factor
θ	Idealized angle of critical shear crack (degree)
φ	Resistance factor
ρ	Longitudinal reinforcement ratio
τ	Average fiber matrix interfacial bond stress (N/mm^2)
τ_{cu}	Ultimate shear stress in uncracked concrete compression zone (N/mm^2)

List of Abbreviations

CMOD	Crack mouth opening displacement
CTF	Compressive toughness factor
COV	Coefficient of variation
DIC	Digital image correlation
FTF	Flexural toughness factor
HRWR	Higher range water reducer
HSC	High strength concrete
LWC	Lightweight concrete
NSC	Normal strength concrete
RC	Reinforced concrete
SFRC	Steel fiber reinforced concrete
STF	Shear toughness factor
SLS	Serviceability limit state

1. Introduction

1.1 Background

Past studies have shown that the addition of steel fibers into the concrete matrix will enhance the shear strength and ductility in reinforced concrete (RC) members (e.g. *Batson et al.* 1972, *Narayanan and Darwish* 1987). Steel fibers increase shear resistance by providing post-cracking diagonal tension resistance across the crack surfaces. They also control crack spacing, similar to the effect of stirrups, and this leads to reduced crack widths and an increase in shear resistance through aggregate interlock (e.g. *Kwak et al.* 2002, *Parra-Montesinos* 2006). The use of steel fibers to enhance the shear response is particularly attractive in high strength concrete (*Wafa and Ashour* 1992) and lightweight concrete (*Balaguru and Foden* 1996), where the brittleness and suddenness of matrix failure is more pronounced compared to normal strength concrete. Several researchers have studied the shear performance of steel fiber reinforced concrete (SFRC) beams with normal and high strength matrices (e.g. *Narayanan and Darwish* 1987, *Ashour et al.* 1992, *Kwak et al.* 2002); however, the influence of steel fibers on shear strength of beams with lightweight aggregate has not been established, and very limited work on lightweight concrete with fibers has been reported (*Swamy et al.* 1993, *Kim and Kang* 2010). Furthermore, there is insufficient knowledge about the relationships between SFRC mix-design and member performance in shear critical conditions. To understand the role of steel fibers in the shear response of structural concrete, the compressive and flexural response of SFRC must also be examined in conjunction with its shear response. In particular this exercise can lead to a rational comparison of the strength and toughness enhancement due to fibers across different types of concrete.

Meanwhile, previous research has established a size effect in the shear strength of RC members without transverse web reinforcement and without fibers, where the

shear resistance decreases with an increase in the member depth or a decrease in the aggregate size (e.g. *Kani* 1967, *Shioya et al.* 1989, *Collins and Kuchma* 1999, *Lubell et al.* 2004). Research has also shown that the shear stress at failure decreases in members constructed with high strength concrete, due to the fracture of aggregates and therefore the reduction in aggregate interlock at the crack faces (*Angelakos et al.* 2001, *Lubell et al.* 2004). Several researchers have examined shear in SFRC members without stirrups; however, most specimens in these member-scale investigations had effective depths less than *300 mm*, preventing assessment of size effect in SFRC members without stirrups (*Parra-Montesinos* 2006, *Kwak et al.* 2002). Therefore, there is a need for more tests on larger size slender SFRC members to verify the size effect in shear associated with member depth or aggregate size in the presence of fibers. Furthermore, the ability of fibers to mitigate the decrease in shear capacity associated with the use of lightweight aggregate or high strength concrete and the combined effects of aggregate type or concrete strength with member size needs to be investigated. In each case, the use of fibers in place of minimum web reinforcement may lead to simpler construction practices and more economical structures.

In previous research (e.g. *Narayanan and Darwish* 1987, *Ashour et al.* 1992, *Kwak et al.* 2002), several analytical models were proposed for prediction of shear strength of SFRC members without stirrups, but there has not yet been a specific recognized model for SFRC members established beyond the existing shear models for RC members in the design codes. Most of these proposed models for SFRC members were empirically derived from regression analysis of test data and they were therefore dependent on the specimen population used for the analysis. A more rational mechanics-based approach is required to predict the shear strength of SFRC members, which can directly correlate the data from material and structural responses.

1.2 Research Significance

In this research, the constitutive response of concrete with/without fibers in compression, flexure, and direct shear was characterized to understand the ability of fibers to enhance the strength and ductility of different types of concrete namely, normal strength concrete, high strength concrete, and lightweight aggregate concrete. This exercise provided valuable knowledge required later for establishing the relationships between SFRC mix-design and member performance in shear critical conditions. The shear response of 18 large-scale SFRC members without stirrups having total height of h=300 *mm*, 600 *mm*, 1000 *mm* and utilizing normal strength, high strength, and lightweight SFRC was investigated. This unique investigation allowed verification of the size effect in shear associated with member depth or aggregate size in the presence of fibers over a scaling factor of about 3.7 along with the influences of concrete compressive strength and aggregate density. A new mechanics-based shear model was developed for SFRC members without stirrups which offers significant improvements over prior empirical models. The proposed shear model in this research correlates the material and structural responses and directly considers the influences of certain parameters.

1.3 Research Methodology

According to the objectives of this research (Section 1.2), the project was defined in three principal tasks:

Task 1: Mix-development and characterization of mechanical properties of mixes

The initial focus of the research was directed towards the development and characterization of suitable SFRC mixes, in collaboration with local concrete

suppliers: 9 mix-designs in total including normal strength, high strength and lightweight aggregate concrete. Mix parameters included: volume-fraction of hooked end steel fibers (0%, 0.5% and 1%), aggregate type (normal and lightweight) and compressive strength of concrete. The regular and lightweight concrete were cast to similar compressive strength, whereas the high strength concrete was 2.5 times as strong. Where possible, locally produced constituent materials were utilized. Characterization of mechanical properties of the mixes was completed by relevant standardized test protocols. At the material scale, the mechanical properties of SFRC were examined through compression, flexure (indirect tension), and direct shear tests, to quantitatively understand the ability of fibers to enhance the strength and/or mitigate the post-cracking brittleness in concrete.

Task 2: Evaluation of shear response of large-scale SFRC members without stirrups

Using selected mixes from task one, 18 specimens containing normal strength, high strength and lightweight SFRC were constructed to evaluate the size effect in shear. These structural specimens, representative of large-scale slender beams or slabs, contained longitudinal reinforcement, steel fibers and no web reinforcement. All specimens were tested under monotonically-increasing loading in 3-point bending. Constant width of 300 *mm* and shear-span to depth ratio of about 3 were considered for all specimens. Geometrically scaled specimens with a total depth of *h=300, 600, and 1000 mm* allowed assessment of size effect over a scaling factor of about 3.7. In each test, crack width and pattern, load, deflection, and strains in the longitudinal reinforcement and on the specimen surface were measured and recorded all the way to the failure.

Task 3: Development of analytical and design shear models

The data from material and structural responses in tasks 1 and 2 were analyzed to develop a mechanics-based analytical model for shear strength of slender SFRC members without stirrups. Then, the analytical shear model was further simplified to be used as a design model. For validation, both models were examined for a filtered test database assembled from previous research and the current study. The accuracy of the proposed shear design model was compared against seven published SFRC models from other researchers. Meanwhile, the analytical and design shear models in the current study were compared against *ACI 318-08* and *CSA A23.3-04* shear models for RC members without stirrups and without fibers.

1.4 Organization

This report has nine chapters and two appendices. In the second chapter, the literature for mechanical properties of SFRC in compression, flexure, pullout, and direct shear is reviewed. Previous research on shear strength of SFRC structural members without stirrups is discussed along with the influence of different parameters on shear strength such as fiber content, longitudinal reinforcement ratio, shear-span to depth ratio, depth size, concrete compressive strength, member width, and aggregate type or size. The previous research on shear modeling of SFRC members as well as existing models for RC members without fibers is also discussed in Chapter 2.

Chapter 3 reports the mix design development and the experimental methods to characterize the mechanical properties of normal strength, high strength and lightweight concrete with and without fibers. The relevant standardized test protocols for compression (*ASTM C39-05*), flexure (*ASTM C1609-05 & JSCE-G 552-1999*) and direct shear (*JSCE-G 553-1999*) are explained. The material test results are analyzed and discussed in Chapter 4. The correlation between flexural

and shear toughness for different mixes is also studied. The flexural test data for SFRC prisms is employed to derive a relationship between the equivalent uniform tensile stress along a crack versus the crack mouth opening displacement (CMOD).

The experimental program related to testing SFRC structural-scale specimens is discussed in Chapter 5. Details of specimen configurations, instrumentation and test procedure are provided. The test results for shear strength, load-deflection response, load-steel strain response, load-crack width relationships, failure mode, and crack development in the normal and high strength SFRC specimens are reported and analyzed in Chapter 6. The effect of different parameters on the shear strength such as longitudinal reinforcement ratio and depth size effect are also investigated in Chapter 6.

In Chapter 7, an analytical model based on mechanics principles and the data from material and structural tests is developed to predict the shear strength of normal weight slender SFRC members containing hooked end steel fibers. A simplified shear model is also presented. The analytical and simplified models are validated for a filtered test database including 56 specimens from previous research and the current study. The proposed shear models are also compared against published SFRC models from *Sharma* (1986), *Narayanan and Darwish* (1987), *Ashour et al.* (1992), *Khuntia et al.* (1999), *Kwak et al.* (2002), *Dinh* (2009), and *Yakoub* (2011).

For structural lightweight SFRC specimens, the test results and related analytical modeling are presented in Chapter 8. The shear strength, crack development, failure mode, load-deflection response, load-steel strain response, and load-crack width relationships for structural lightweight SFRC specimens are investigated. The influences of member depth and longitudinal reinforcement ratio on the shear strength of lightweight SFRC specimens are also studied. Based on the test results

for lightweight SFRC members, the shear models from Chapter 7 are modified to account for the concrete density.

Conclusions from this project are summarized in Chapter 9. Based on test results, discussions and conclusions in this study, some recommendations are given. Further investigations on the shear behavior of SFRC members beyond the scope of this project are also recommended in Chapter 9.

Appendix *A* reports the detailed test results for material-scale specimens discussed in Chapters 3 and 4. These results include the responses of normal strength, high strength and lightweight specimens with and without fibers under compression, flexure and direct shear loadings. Appendix *B* presents the details of test results for structural-scale specimens discussed in Chapters 5 and 6. For each structural-scale specimen, the details of instrumentation, load-deflection responses at mid-span and quarter-span, load-steel strain responses for strain gauges, and the crack development before and after failure are presented.

2. Literature Review

In this chapter, the relevant literature for mechanical properties of steel fiber reinforced concrete (SFRC) in compression, flexure, pullout, and direct shear is reviewed. Previous research on shear strength of SFRC structural members without stirrups is also discussed along with the influence of different parameters on shear strength. The shear modeling of SFRC members from previous research as well as existing shear models for RC members without fibers is reviewed.

2.1 Mechanical Properties of SFRC

2.1.1 Compressive Strength of SFRC

Adding steel fibers to the plain concrete does not change the pre-peak compressive strength of concrete considerably (e.g. *Fanella and Naaman* 1985, *Wafa and Ashour* 1992, *Balaguru and Foden* 1996). *Fanella and Naaman* (1985) reported that adding straight steel fibers with aspect ratio L_f/D_f =47~100 and length L_f=19~25 *mm* to mortar at a volume fraction V_f up to 3% increased the compressive strength between 0 and 15% compared to that of plain mortar without fibers. A *4.6%* increase in the compressive strength was observed by *Wafa and Ashour* (1992) for high strength concrete with f'_c=94 *MPa* and including up to V_f= 1.5% hooked end steel fibers with L_f/D_f =75 and L_f=60 *mm*. For lightweight concrete including expanded shale aggregates, *Balaguru and Foden* (1996) reported an increase of approximately 20% in compressive strength for SFRC including V_f= 1.1% hooked end steel fibers (L_f/D_f =75~100, L_f=50~60 *mm*) compared to plain lightweight concrete without fibers. Meanwhile, a small increase in the strain at peak stress ε'_c was observed for SFRC compared to concrete without fibers, especially when hooked end steel fibers were used (e.g. *Soroushian and Bayasi* 1991).

Previous research has shown that steel fibers substantially increase the post-peak ductility and energy absorption capacity of concrete in compression (e.g. *Fanella and Naaman* 1985, *Soroushian and Bayasi* 1991, *Ezeldin and Balaguru* 1992). *Soroushian and Bayasi* (1991) used different types of steel fibers with similar aspect ratio L_f/D_f =57~60 (L_f =30~50 *mm*) and at constant volume fraction of V_f= 2%. Their test results indicated that hooked end steel fibers were more effective than straight or crimped fibers in enhancing the energy absorption capacity of SFRC under compressive stresses (Figure 2-1). *Wafa and Ashour* (1992) tested high strength SFRC containing hooked end steel fibers (L_f/D_f =75, L_f=60 *mm*) with different volume fractions, and reported that increasing V_f from 0 to 1.5% substantially increased the ductility as described by the area under the descending portion of the stress-strain curve (Figure 2-2). A similar trend was also observed by *Balaguru and Foden* (1996) for lightweight concrete including V_f =0~1.1% hooked end steel fibers (L_f/D_f =75~100, L_f=50~60 *mm*).

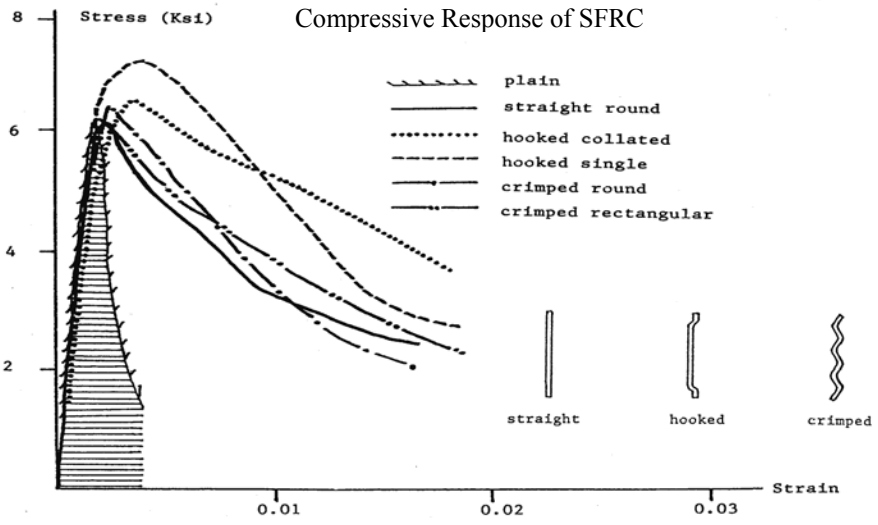

Figure 2-1: Compressive stress-strain response of SFRC with different types of steel fibers (Adapted from *Soroushian and Bayasi* 1991).

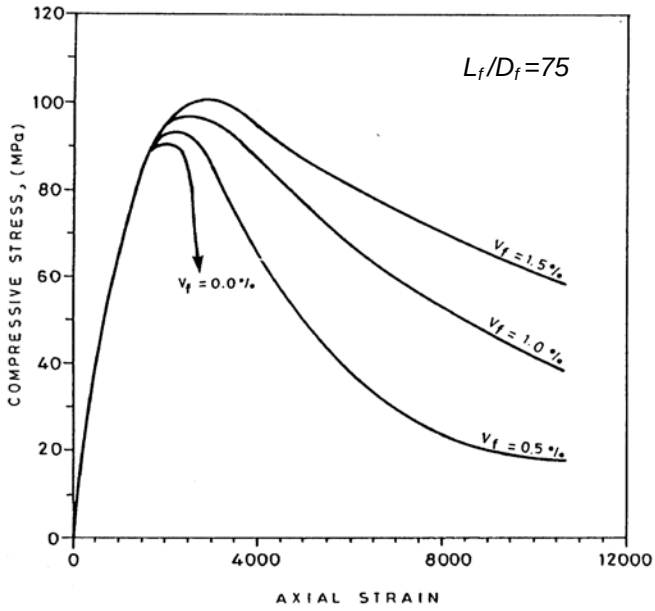

Figure 2-2: Compressive response of high strength SFRC with different volume fractions of hooked end steel fibers (adapted from *Wafa and Ashour* 1992).

2.1.2 Flexural Response of SFRC

Several researchers have studied the flexural response of SFRC (e.g. *Soroushian and Bayasi* 1991, *Balaguru et al.* 1992, *Wafa and Ashour* 1992, *Balaguru and Foden* 1996). *Balaguru et al.* (1992) performed flexural tests on normal (f'_c=27 *MPa*) and high strength (f'_c=81 *MPa*) SFRC with hooked end fibers (L_f/D_f =60~100, L_f=30~60 *mm*), and indicated that fiber content of V_f = 0.75% for normal strength and V_f =1.1% for high strength SFRC provided significant ductility compared to the corresponding plain matrices (Figure 2-3). However, the results showed only a small additional increase in ductility of the normal and high strength SFRC when the fiber content increased beyond 0.75% and 1.1%, respectively. Figure (2-3a) shows a deflection hardening for normal strength SFRC with $V_f \geq$ 1.1%. However, *Balaguru et al.* (1992) reported that for high strength SFRC, the post-peak strength decreased at a higher rate compared to the normal strength SFRC, indicating a more brittle post-peak failure pattern (Figure

2-3b). *Wafa and Ashour* (1992) investigated the flexural resistance of high strength SFRC (f'_c=94 *MPa*), and concluded that addition of 1.5% by volume of hooked end steel fibers (L_f/D_f =75, L_f=60 *mm*) resulted in an increase of 67% in the modulus of rupture compared to that of a plain matrix. *Balaguru and Foden* (1996) observed that adding hooked end steel fibers (L_f/D_f =75~100, L_f=50~60 *mm*) up to V_f =1.1% into plain lightweight concrete resulted in more than a 100% increase in the modulus of rupture. They also reported that the toughness of lightweight SFRC was higher than that of plain lightweight concrete.

Soroushian and Bayasi (1991) studied SFRC specimens with different types of steel fibers (L_f =30~50 *mm*) but containing similar fiber volume fraction of V_f = 2% and L_f/D_f =57~60. They reported that hooked end fibers generated flexural strengths and energy absorption capacities which were higher than those generated by straight or crimped fibers. Similarly, *Balaguru et al.* (1992) reported a higher toughness for SFRC including hooked end steel fibers (L_f/D_f =60~100, L_f=30~60 *mm*) compared to SFRC with other type of fibers. Moreover, *Balaguru et al.* (1992) concluded that for mixes with hooked end steel fibers, increasing the length of fibers from 30 *mm* to 50 *mm* (even with similar diameter of D_f=0.5 *mm*) did not affect the SFRC energy absorption capacity significantly.

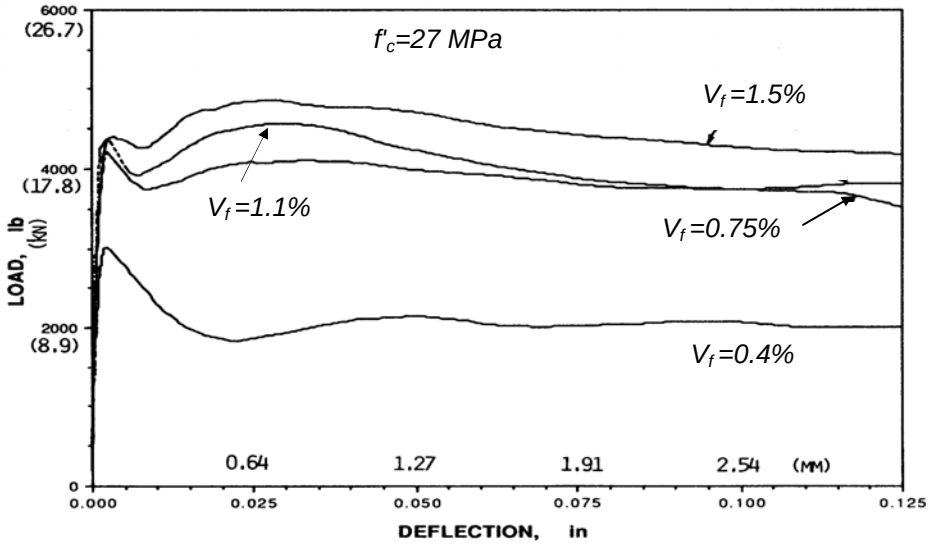

(a)

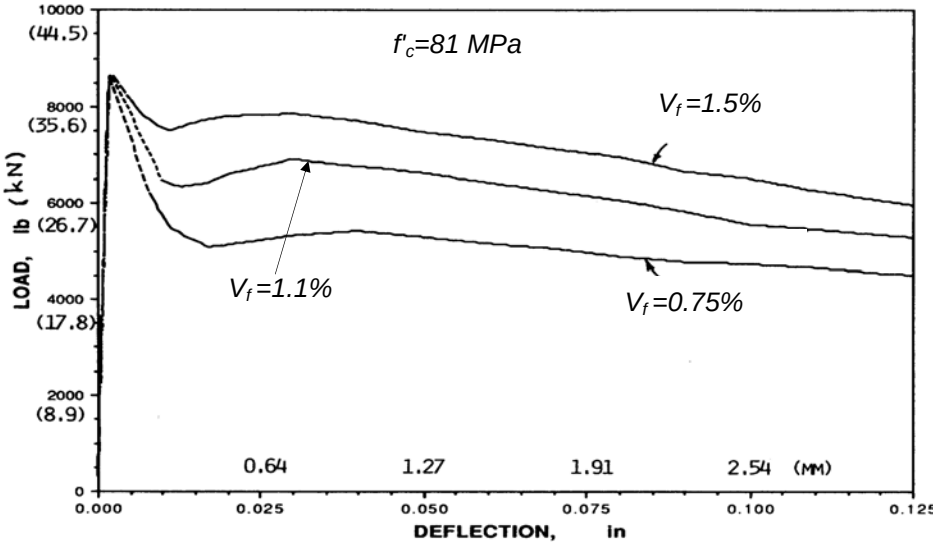

(b)

Figure 2-3: Flexural load-deflection curves for a) normal strength SFRC; b) high strength SFRC (adapted from *Balaguru et al.* 1992).

Fiber-Matrix Bond and Pullout Resistance

Research on post-crack flexural strength of SFRC indicated that steel fibers tend to pull out of the matrix after cracking. For the case of a high strength concrete matrix, a brittle response caused by fiber fracture might also be observed. These observations have been the motivation for several studies on the pullout resistance of single fibers embedded in cement-based matrices (e.g. *Hughes and Fattuhi* 1975, *Gray and Johnston 1984*, *Naaman and Najm* 1991, *Banthia and Trottier* 1994). These researchers reported that the pullout resistance of a single fiber is influenced by several parameters including the inclination of the fiber with respect to the pullout loading direction, the embedment length of fiber into the matrix, the fiber geometry, and the strength of the matrix. However, the influence of aggregate type or density on the pullout resistance of a single fiber has not been adequately studied.

Naaman and Najm (1991) performed pullout tests on smooth and hooked end steel fibers embedded in cement matrices with strengths ranging from 35 *MPa* to 59 *MPa*. They reported that hooked end steel fibers had higher resistance to pullout compared to smooth fibers, mainly due to the mechanical contribution of the end hooks to the overall pullout mechanism (Figure 2-4a). The pullout work for hooked end fibers, defined as the area under the load-slip curve, was typically four times larger than the pullout work for smooth fibers. *Naaman and Najm* (1991) also observed that increasing the embedment length of hooked end steel fibers did not significantly affect the load-slip response of fibers, because the equivalent bond strength was mainly provided by the end hooks. As shown in Figure (2-4b), an increase in the matrix strength leads to an increase in the bond between fibers and matrix. For hooked end steel fibers, when the cement matrix strength increased from 35 *MPa* to 59 *MPa*, the bond stress at the peak load, measured as the peak load divided by the embedded surface area of fiber, showed a 75 % increase from 4.32 *MPa* to 7.55 *MPa*.

Banthia and Trottier (1994) studied the bond-slip response of three types of fibers embedded in concrete matrices with 10 *mm* aggregate size and different compressive strengths. The fibers were embedded 30 mm into the concrete matrix with inclination of $\theta = 0^o \sim 60^o$ with respect to the loading direction (Figure 2-5). For hooked end steel fibers aligned in the loading direction $\theta = 0^o$, *Banthia and Trottier* (1994) observed that increasing the concrete strength from 40 *MPa* to 85 *MPa* resulted in only 9% increase in the bond stress at the peak load (from 3.63 *MPa* to 3.94 *MPa*). The slip at peak load was 1.55 *mm* and 1.19 *mm* for normal strength (40 *MPa*) and high strength (85 *MPa*) matrices, respectively. Also, they observed a brittle response for the case of high strength concrete matrix, caused generally by premature matrix splitting or fiber fracture.

The number of fibers bridging a flexural crack can be highly variable, mainly due to the random alignment of fibers in the SFRC mix. As a result, the post-crack flexural response for SFRC can also be highly variable. For example, both *Balaguru et al.* (1992) and *Banthia and Trottier* (1995) reported that the post-crack flexural response of SFRC had coefficient of variation (COV) of more than 20%. *Balaguru et al.* (1992) also noted that doubling the fiber content of a mix does not increase the post-cracking residual strength proportionally, in spite of the fact that this change would proportionally increase the number of fibers crossing the cracked section.

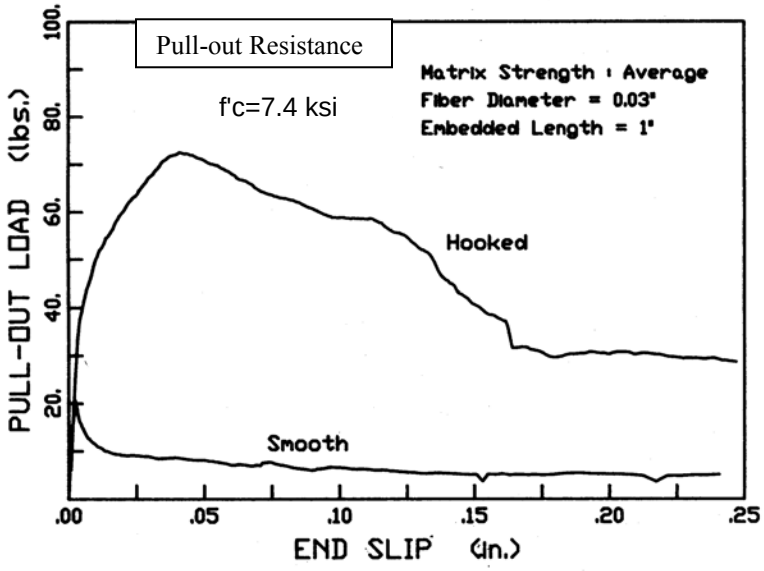

(a)

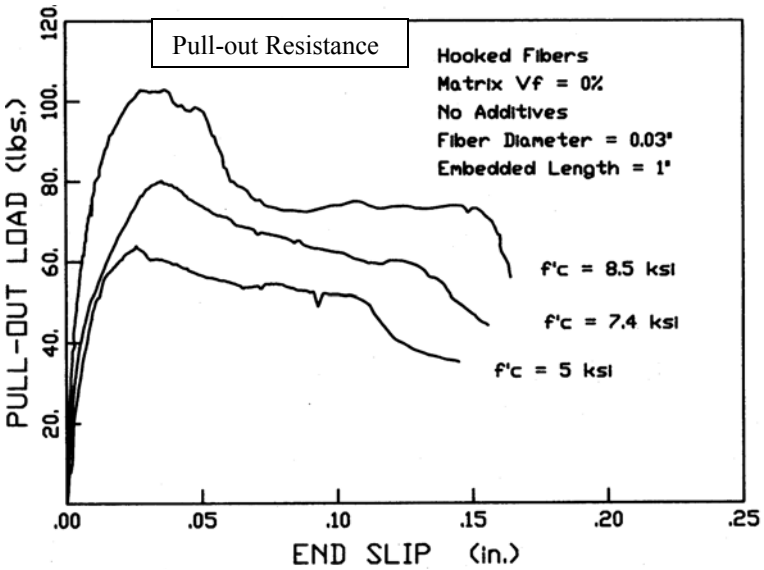

(b)

Figure 2-4: Pullout resistance of steel fibers in cement matrix. a) Influence of fiber shape; b) Influence of matrix compressive strength (adapted from *Naaman and Najm* 1991).

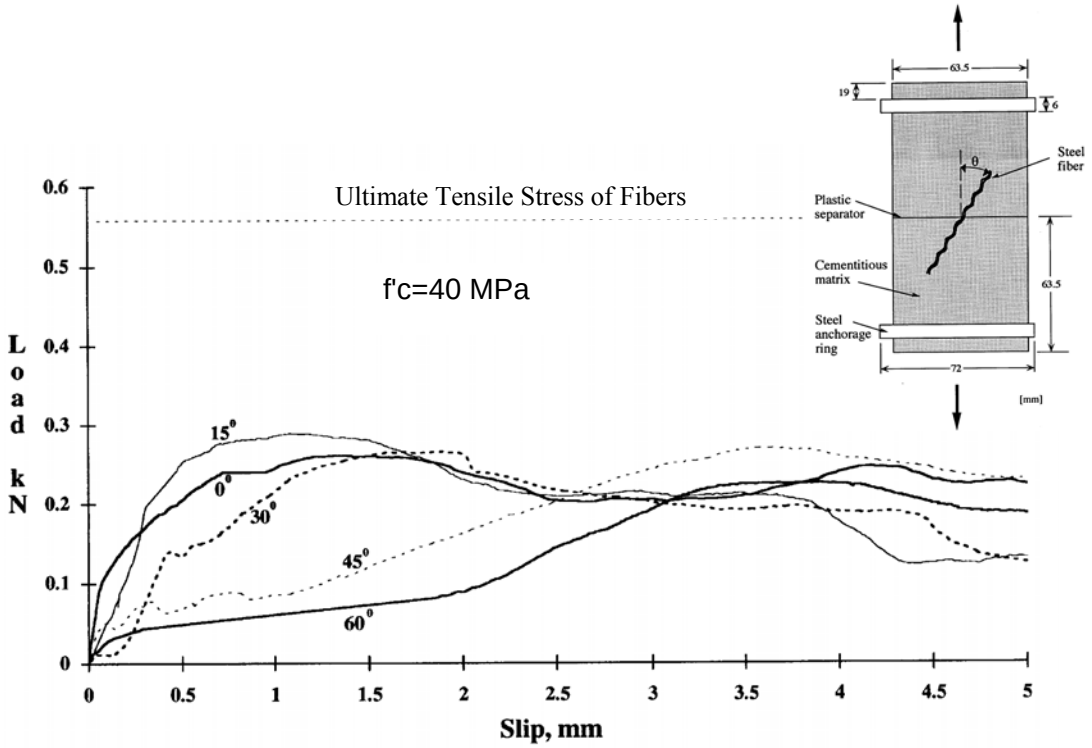

(a)

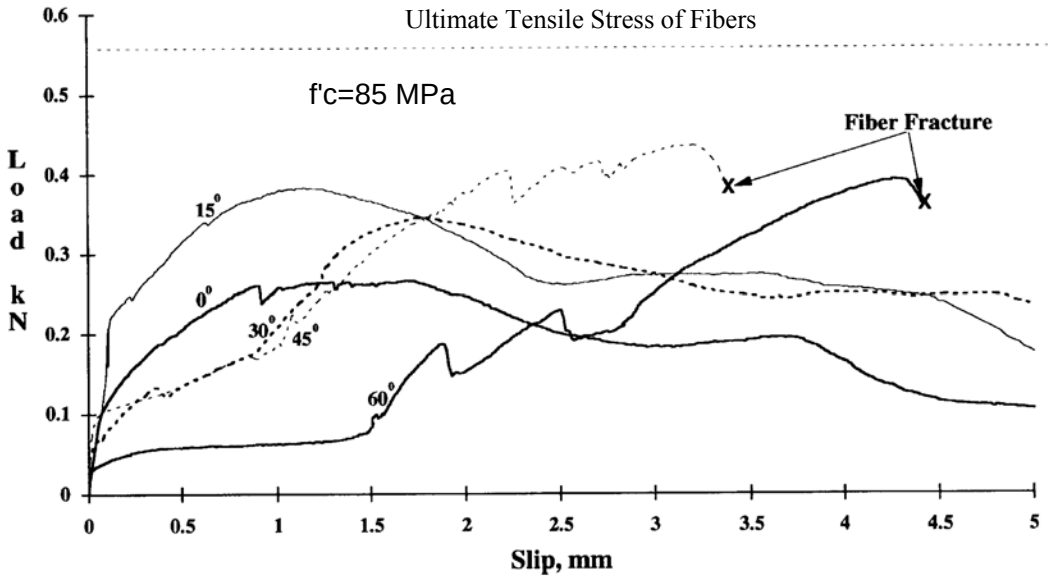

(b)

Figure 2-5: Bond-slip curves for hooked end steel fibers at various inclinations a) Normal strength concrete matrix; b) High strength concrete matrix (adapted from *Banthia and Trottier* 1994).

Dinh (2009) used an analytical model and flexural test data for SFRC prisms to derive a relationship between an equivalent uniform stress along flexural crack versus crack mouth opening displacement (CMOD), C_M. Similar to *Armelin and Banthia* (1997), a single flexural crack was assumed by *Dinh* (2009) for SFRC prisms exhibiting deflection softening behavior. Accordingly, the behavior of SFRC prism after cracking was modeled as two rigid blocks rotating with respect to each other (Figure 2-6). Based on the measured mid-span deflection δ data and the geometry, the CMOD, C_M, was estimated as:

$$C_M = \frac{2\delta(h-c)}{l-a} \tag{2-1}$$

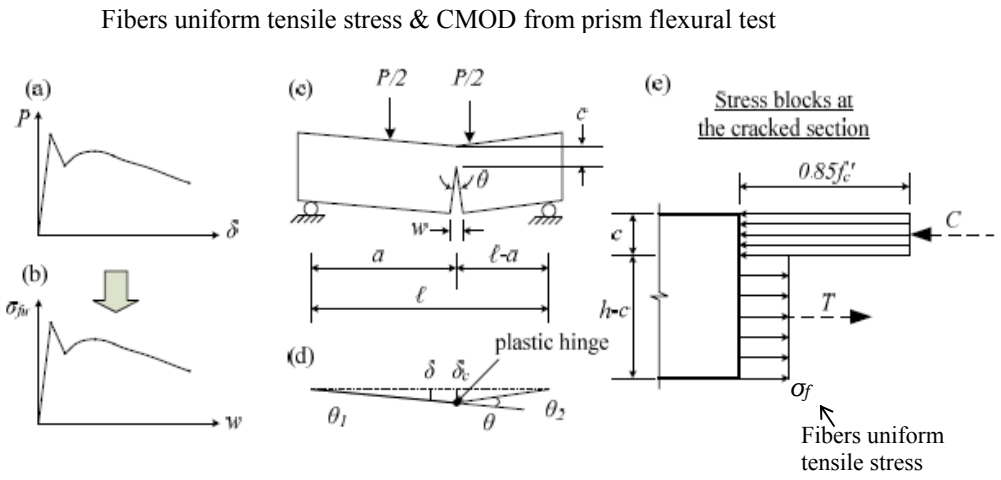

Figure 2-6: Derivation of relationship between uniform tensile stress versus CMOD (adapted from *Dinh* 2009).

To determine c, a uniform compressive stress of $0.85f'_c$ was assumed in the compression zone regardless of the prism deflection. This assumption was inaccurate over a wide range of deflections; however, according to *Dinh* (2009), this assumption had a negligible effect on the determination of the average tensile stress σ_f, since c represented a very small percentage of the total prism depth.

From equilibrium of forces in the section (Figure 2-6e), c and σ_f were calculated as follows:

$$c = \frac{2M}{0.85 f_c' bh} \tag{2-2a}$$

$$\sigma_f = \frac{2M}{bh(h-c)} \tag{2-2b}$$

where M is the applied moment from the flexural test at the cracked section. The relationship between the equivalent uniform tensile stress σ_f from Equation (2-2b) versus CMOD, C_M from Equation (2-1) were then illustrated for SFRC specimens from material flexural tests. A sample of this relationship is shown in Figure (2-7) for SFRC with $f'_c = 45\ MPa$ and including hooked end steel fibers at $V_f = 1.5\%$.

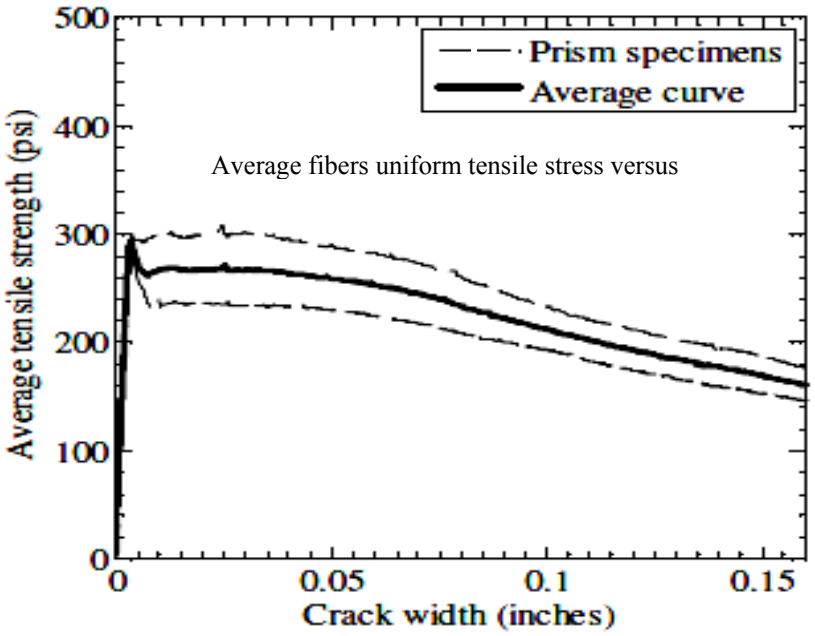

Figure 2-7: Average tensile stress versus CMOD (*Dinh* 2009)

2.1.4 Direct Shear Strength of SFRC

There is currently no standardized test method in North America to evaluate the material properties of cement based composites loaded in direct shear. A summary of experimental methods to characterize the direct shear response of concrete is described by *Xu and Reinhardt* (2005) and illustrated in Figure (2-8). According to *Xu and Reinhardt* (2005), all these methods except case (a) result in a mode of failure which is not a pure shear mode. Due to eccentric loading or deformation during testing, a tensile mode is also present in these testing arrangements. The shear strength of concrete subjected to combined compression and shear loading (*Bresler and Pister* 1958) is discussed in Section (2.3.1).

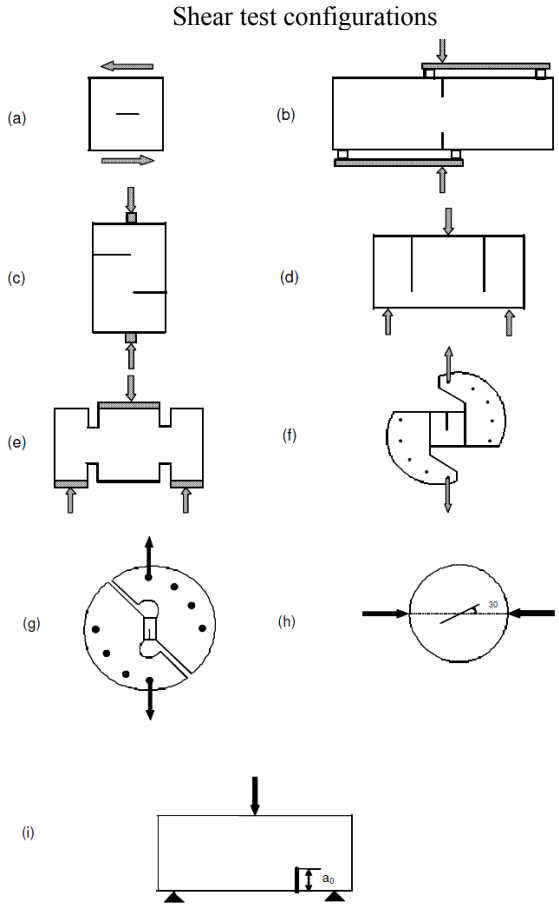

Figure 2-8: Different shear mode testing configurations (adapted from *Xu and Reinhardt 2005*).

A Z-shaped specimen was employed by *Valle and Buyukozturk* (1993) to study the push-off response of normal strength (f'_c=26~34 *MPa*) and high strength (f'_c=62~80 *MPa*) structural concrete reinforced with 1% volume fraction of steel or polypropylene fibers (Figure 2-9). They noticed that the increase in normalized shear stress $\tau/\sqrt{f'_c}$ due to steel fibers (crimped-end, L_f/D_f =60, L_f=30 *mm*) was more pronounced for the high strength matrix (60%) compared to that of the normal strength matrix (36%). However, as shown in Figure (2-9) the difference between the peak normalized shear stresses for normal and high strength SFRC was insignificant.

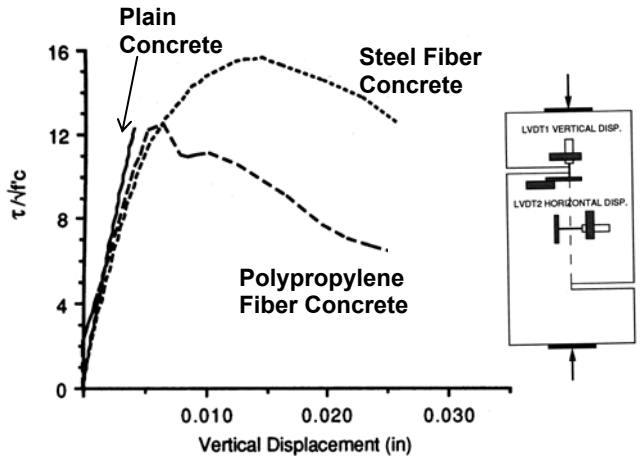

(a)

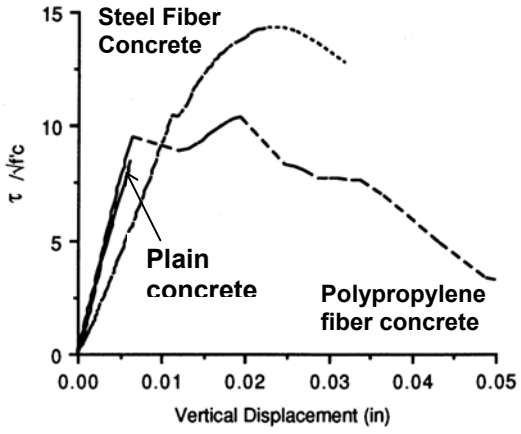

(b)

Figure 2-9: Normalized direct shear stress versus vertical displacement for a) normal strength matrix; b) high strength matrix (adapted from *Valle and Buyukozturk* 1993).

Using a similar push-off specimen configuration, *Khaloo and Kim* (1997) reported that addition of hooked end steel fibers (V_f =0.5~1.5%, L_f/D_f =29~58, L_f=16~32 *mm*) to plain concrete with different compressive strengths ranging from 28 to 72 *MPa*, resulted in enhancement in shear strength, ductility, and toughness. Similar to *Valle and Buyukozturk* (1993), they observed that the improvement in shear strength for higher strength concrete was larger than that obtained for lower strength concrete. This was mainly attributed to the higher bond strength between fibers and high-strength concrete matrix.

From the point of view of modeling the material response in direct shear, it is desirable that the test method and specimen preparation remain simple. In this context, the Japan Society of Civil Engineers has proposed a standard test method wherein the stress field in the region of the crack remains substantially that of pure shear (*JSCE-G 553-1999*) (Figure 2-10). Using a modified version of this test method, *Mirsayah and Banthia* (2002) reported that addition of crimped or flattened ends steel fibers (L_f/D_f =50, L_f=50 *mm*) up to V_f =1% improved the shear strength and toughness of normal strength concrete (f'_c=47 *MPa*). *Higashiyama and Banthia* (2008) tested normal strength SFRC (f'_c=41~47 *MPa*) and lightweight SFRC (f'_c=21~25 *MPa*), and indicated that improvement in post-crack flexural and shear strength due to crimped steel fibers (V_f =0.5~1%, L_f/D_f =33~56, L_f=38~63 *mm*) was higher for normal strength concrete compared to lightweight concrete. However, they did not isolate the role of the aggregate type and matrix strength that may significantly affect the shear response of SFRC.

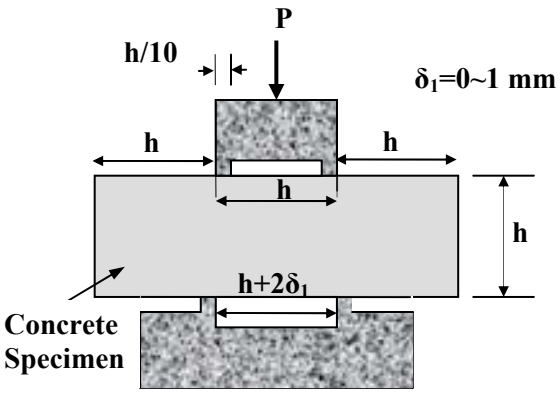

Figure 2-10: Direct shear test configuration according to *JSCE-G 53-1999*.

2.1.5 SFRC under Multi-axial Loading

Vecchio and Collins (1986) studied the stress-strain relationships for cracked concrete by testing reinforced concrete (RC) panels loaded in shear combined with axial stress. They observed that even after formation of diagonal cracks, tensile stresses were still present in the concrete between the cracks. These tensile stresses combined with shear stresses on the crack faces influenced the shear resistance of the cracked concrete. Based on equilibrium and compatibility relationships, as well as the test results for stress-strain relationships, *Vecchio and Collins* (1986) developed an analytical model called the modified compression field theory (MCFT). This model was able to estimate the load-deformation response of RC elements subjected to in-plane shear and normal stresses. Moreover, in the MCFT, *Vecchio and Collins* (1986) suggested a basic relationship which relates the transmitted shear stress across a crack v_{ci} to the crack width w, the maximum aggregate size a_g, and the concrete strength f'_c. A widely accepted simplification to this relationship had the following form in equivalent metric notation:

$$v_{ci} = \frac{0.18\sqrt{f_c'}}{0.31 + \frac{24w}{a_g + 16}} \quad (2\text{-}3)$$

Available studies on the behavior of SFRC subjected to in-plane shear and normal stresses are scarce. *Susetyo et al.* (2011) tested reinforced SFRC panels under in-plane pure shear but without presence of normal stresses. They observed that SFRC panels exhibited ductile behavior, additional shear strength, and superior crack control characteristics compared to the conventional RC panels. *Chern et al.* (1992) conducted an experimental program to study the strength and deformational behavior of SFRC cylinders subjected to triaxial compression loading. They reported that the enhancements in tensile strength and ductility due to use of steel fibers increased considerably with an increase in the confining pressure. This was attributed to the increase of interfacial bond strength caused by confining pressure on the fibers.

2.1.6 Toughness of SFRC

In order to understand the role of steel fibers on the behavior of SFRC, the post-crack response of the composite must be characterized. *Khaloo and Kim* (1997) defined a shear toughness parameter equal to the area under the stress-displacement response, to describe the influence of hooked steel fibers in concrete under shear. Similarly, *Barragan et al.* (2006) evaluated the shear toughness using the area under load-slip curve obtained in the push-off test. However, very few studies offer size-independent shear toughness parameters (*Higashiyama and Banthia 2008*). It is also unclear how these toughness parameters respond to changes in the compressive strength of matrix, aggregate type, and fiber content. At the ultimate state, the critical shear section of a structural SFRC member might be subjected to shear, flexure, and compression (in the uncracked compression region) simultaneously. Therefore, there is a need to evaluate and compare the

post-crack energy dissipative ability of steel fibers when concrete is subjected to compression, flexure or shear.

Section (4.4) in Chapter 4 of this report provides further information on toughness factors and seeks to answer the questions raised above.

2.2 Shear Response of SFRC Members without Stirrups

Previous research indicated that the shear resistance of slender RC members with $a/d > 2.5$ can be predicted based on a sectional shear model (e.g. *Zsutty* 1968, *Kani et al.* 1979). Some early sectional models for the shear strength of RC members without stirrups, assumed that all the shear force was carried by the uncracked concrete compression zone (e.g. *Bresler and Pister* 1958). Later, other researchers showed that in order to maintain beam action at a cross-section, shear stresses must be transferred across diagonal cracks by aggregate interlock (*Fenwick and Paulay* 1968, *Kani et al.* 1979, *Walraven* 1981, *Vecchio* and *Collins* 1986). These researchers reported that a considerable portion of vertical shear is carried by the aggregate interlock mechanism V_{ag}, and the remaining shear resistance is carried through the compression block V_{cb} and by dowel action of the longitudinal reinforcement V_d (Figure 2-11a). The influencing parameters on the shear strength of RC members without stirrups included member effective depth d, shear-span to effective depth ratio a/d, longitudinal reinforcement ratio ρ, compressive strength f'_c , aggregate size and type, and member width.

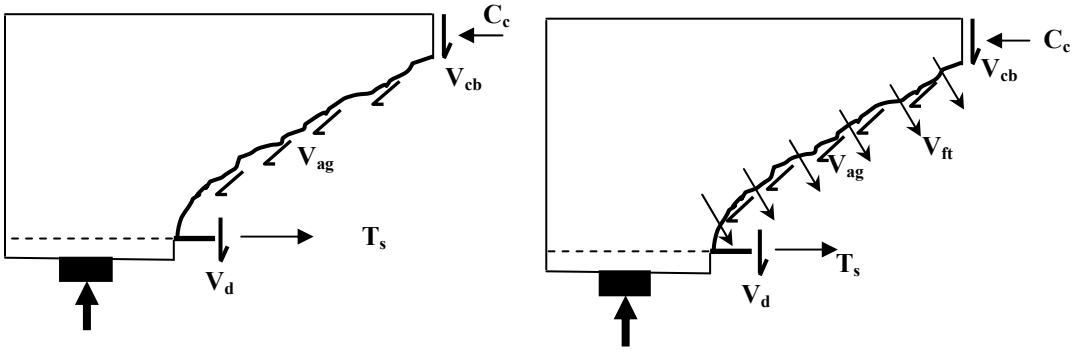

(a) (b)

Figure 2-11: The shear force components across a flexural-shear crack in a) RC members without stirrups b) SFRC members without stirrups

Steel fibers increase shear resistance by providing post-cracking diagonal tension resistance across the crack surfaces V_{ft} (Figure 2-11b) in addition to the other three mechanisms of aggregate interlock V_{ag}, shearing in the compression block V_{cb}, and dowel action of the longitudinal reinforcement V_d (*ACI 544-88*). This resistance by the fibers is called crack-bridging stress. The shear response of SFRC members without stirrups has been studied by several researchers (e.g. *Batson et al.* 1972, *Narayanan and Darwish* 1987, *Ashour et al.* 1992 and *Kwak et al.* 2002). Similar to the role of stirrups in RC members, addition of steel fibers generally enhances the shear strength, decreases the crack spacing, increases deformation capacity, and alters a brittle failure mode to a ductile one for SFRC members without stirrups (e.g. *Narayanan and Darwish* 1987, *Kwak et al.* 2002). However, the extent of the fiber influence on the shear response of SFRC members is related to several parameters including fiber content V_f, member effective depth d, shear-span to effective depth ratio a/d, longitudinal reinforcement ratio ρ, compressive strength f'_c , aggregate size and type, and member width.

2.2.1 Effect of Fiber Volume Fraction V_f

Dinh (2009) tested SFRC members containing 0.75%, 1% and 1.5% hooked end steel fiber with L_f/D_f=55 ~ 80. Using hooked steel fibers in a volume fraction $V_f \geq 0.75\%$ led to at least 100% increase in the shear strength of SFRC members compared to similar RC members without fibers. However, *Dinh* (2009) reported only a relatively small additional increase in shear strength when the fiber volume fraction was increased beyond 1%. *Mansur et al.* (1986), *Ashour et al.* (1992), and *Kwak et al.* (2002) also tested SFRC members containing different volume fractions of hooked end steel fibers with aspect ratio L_f/D_f = 60~75. These studies showed that using steel fibers between 0.5% to 1.5% volume fraction generally improved the shear strength, but the extent of this improvement was highly related to the other parameters such as a/d (see Section 2.2.2).

The influence of steel fibers on shear strength of lightweight aggregate concrete has not been established, and very limited work on lightweight concrete with fibers has been reported. *Swamy et al.* (1993) tested lightweight SFRC beams ($\gamma \approx 1800\ kg/m^3$) with I-shaped cross sections, and reported that the improvement in ultimate shear strength was dependent upon the shear-span to depth ratio a/d (Section 2.2.2) and the longitudinal reinforcement ratio ρ (Section 2.2.4). They showed that for V_f =1% the ultimate shear strength increased by 60% to 210% compared to equivalent beams without steel fibers. *Kang & Kim* (2009) reported that addition of V_f =0.5% and V_f =0.75% steel fibers increased the shear strength by about 25% and 45%, respectively, compared to similar members without fibers.

Narayanan and Darwish (1987) reported that steel fibers reduced the spacing of diagonal cracks to 20% of those in companion RC members without fibers. This observation was attributed to a more uniform redistribution of stresses in SFRC members compared to similar RC members. *Kwak et al.* (2002) reported about 38% decrease in crack spacing, when steel fibers at V_f =0.5% ~ 0.75% were added to RC members without stirrups. *Dinh* (2009) observed that RC members without stirrups exhibit a single diagonal crack followed by a brittle shear failure whereas SFRC members with V_f =0.75% ~ 1.5% exhibited multiple inclined cracks followed by widening of at least one dominant crack before shear failure. *Dinh* (2009) reported that an increase in effective depth of SFRC members from d=375*mm* to d=610 *mm* resulted in larger absolute crack spacing, but the average horizontal crack spacing for all members was approximately constant as a fraction of d, at $\sim 0.4d$. These studies indicated that using a moderate volume fraction of steel fibers reduced the spacing of diagonal cracks in SFRC members compared to similar RC members without fibers.

Figure (2-12) shows the curves for mid-height diagonal crack width versus load for three identical specimens tested by *Minelli and Plizzari* (2006). The main

difference between these specimens was in the fiber content V_f. While the maximum crack width for the RC specimen (V_f =0%) was only about 0.3 *mm*, the SFRC specimens with V_f =0.4% and V_f =0.6% had maximum crack widths of 2 *mm* and 3 *mm* prior to failure, respectively. This difference in maximum crack widths was attributed to the bridging action of fibers across the adjacent crack surfaces in SFRC specimens (*Minelli and Plizzari* 2006). According to these researchers, the crack widening in SFRC members prior to shear failure provides some visual warning about impending failure. Meanwhile, *Dinh et al.* (2010) observed that SFRC members without stirrups start to show deflection-softening behavior when the diagonal crack widths reach approximately 5% of the fiber length L_f.

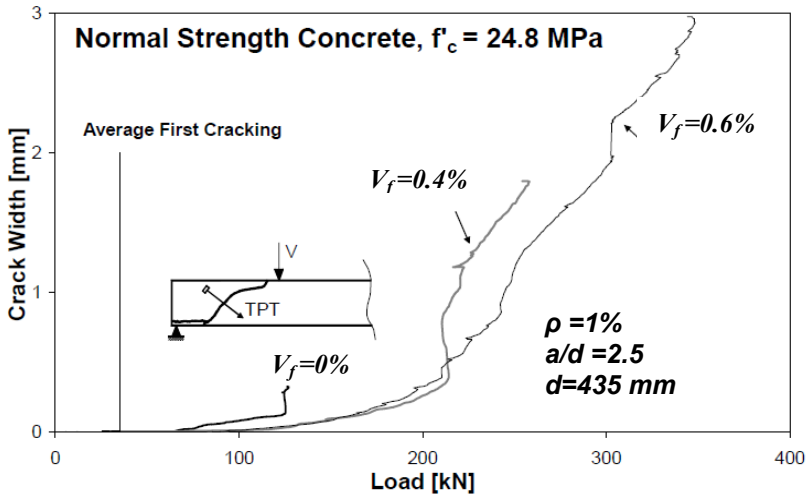

Figure 2-12: Load-crack width curve (TPT: Potentiometric transducer placed at the mid-height with a 40^o inclination to the longitudinal axis for crack width measurement) (adapted from *Minelli and Plizzari* 2006).

2.2.2 Effect of shear-span to depth ratio *a/d*

Several researchers have investigated the effect of shear-span to effective depth ratio *a/d* (e.g., *Mansur et al.* 1986; *Ashour et al.* 1992, *Kwak et al.* 2002) on the

shear strength of SFRC members without stirrups. A graphical summary of previous experimental results is provided in Figure (2-13).

As shown in Figure (2-13), the shear stress at failure for SFRC members with *a/d* < *2.5* was generally higher compared to that of members with *a/d* > *2.5*. This increase in the shear resistance was mainly due to the arch action, also seen in RC members with *a/d* < 2.5 (e.g. *Zsutty* 1968, *Kani et al.* 1979). In RC members with *a/d* < 2.5, the vertical component of a compressive strut between the loading point and support increases the shear capacity. *Narayanan and Darwish* (1987) reported that the arch action due to decrease in *a/d* became larger when a higher volume fraction of steel fibers was employed.

On the other hand, for members with *a/d* > *2.5* (Figure 2-13), an increase in *a/d* resulted in a small decrease in the shear strength (*Shin et al.* 1994, *Kwak et al.* 2002). In the same context, and for a constant fiber content, *Batson et al.* (1972) noted a higher rate of increase in shear strength for members with *a/d<3* compared to members with *a/d>3*. The critical value of *a/d=2.5* to distinguish between short and slender SFRC members is comparable to *a/d=2.5* for RC members, seen as a transition point between the beam action and arch action (*Zsutty* 1968, *Kani et al.* 1979).

Influence of *a/d* on normalized shear stress

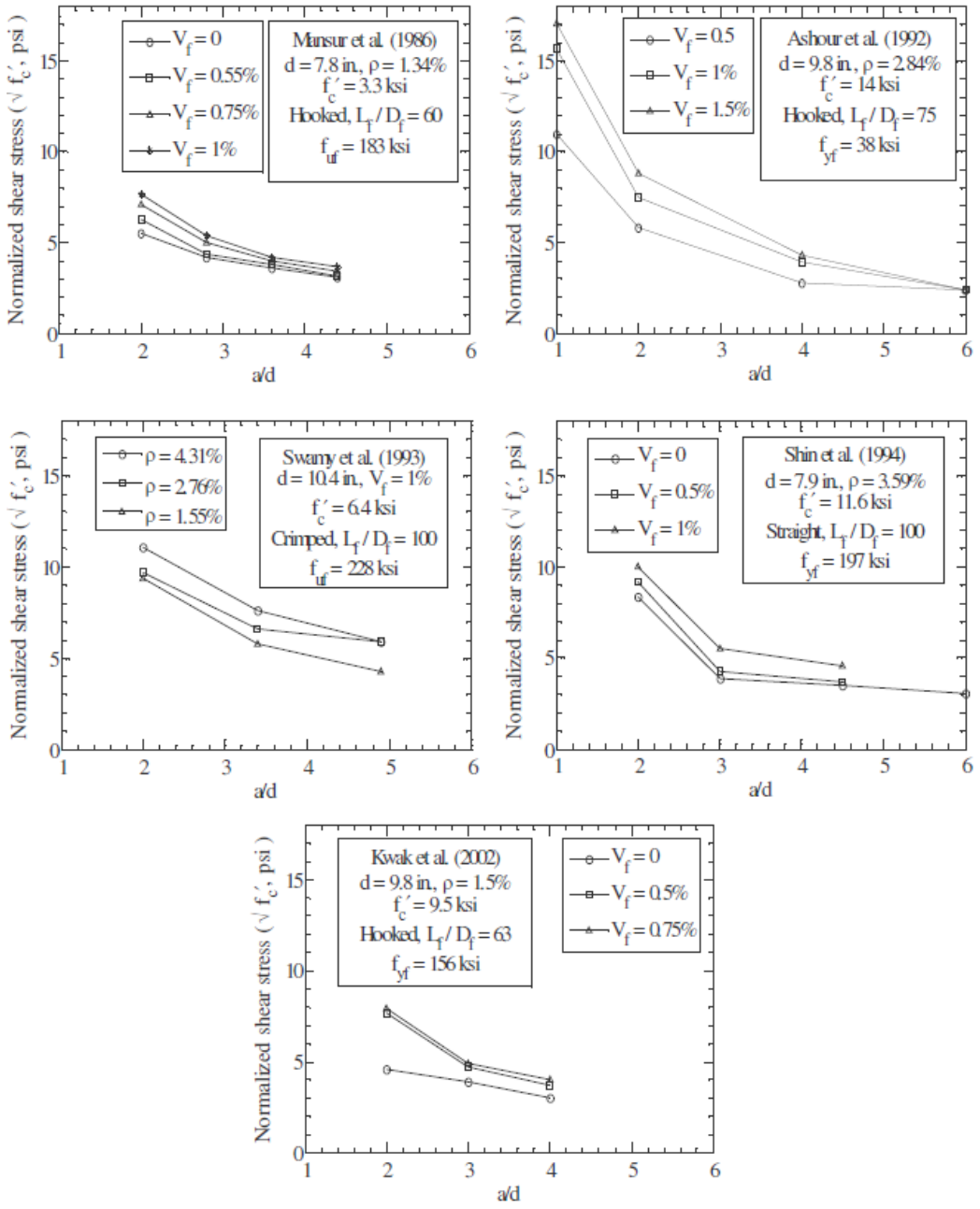

Figure 2-13: Effect of shear-span to effective depth ratio *a/d* on the shear strength of SFRC members without stirrups from previous researchers (adapted from *Dinh 2009*).

2.2.3 Effect of member depth size

Previous research has identified a size effect in the shear strength of RC members without stirrups, where the shear stress at failure decreases with an increase in the member depth (e.g. *Kani* 1967, *Shioya et al.* 1989, *Collins and Kuchma* 1999, *Lubell et al.* 2004). Different approaches have been proposed to account for the size effect such as fracture mechanics approach (*Bazant and Sun* 1987) and aggregate interlock approach (*Collins and Kuchma* 1999, *Sherwood et al.* 2007). The focus of the current research is on the aggregate interlock models.

According to aggregate interlock models (*Vecchio* and *Collins* 1986, *Walraven* 1981), the size effect in shear for RC members without stirrups can be captured by considering the decreased ability of wide cracks to transmit shear stress. There is almost a direct relationship between crack widths and both the tensile strain in the reinforcement and the spacing between cracks for RC members without fibers (*Sherwood et al.* 2007). *Shioya et al.* (1989) have shown that the spacing of cracks at the mid-height of the web of a reinforced concrete member without stirrups is about *0.5h*. Thus, doubling the member depth will double the crack width at mid-depth, if the strain in the longitudinal steel is kept the same. When the crack widths increase, the aggregate interlock decreases. Hence, the shear stress at failure in large members is lower than in small members.

Shioya et al. (1989) studied the size effect in shear through an experimental program. Figure (2-14) summarizes the main results of this study. The shear stress at failure decreases both as the member depth increases and as the maximum aggregate size decreases. When the effective depth increases from *d=203 mm* (*8 in.*) to *d=2007 mm* (*79 in.*), the shear stress at failure decreases by about 64%.

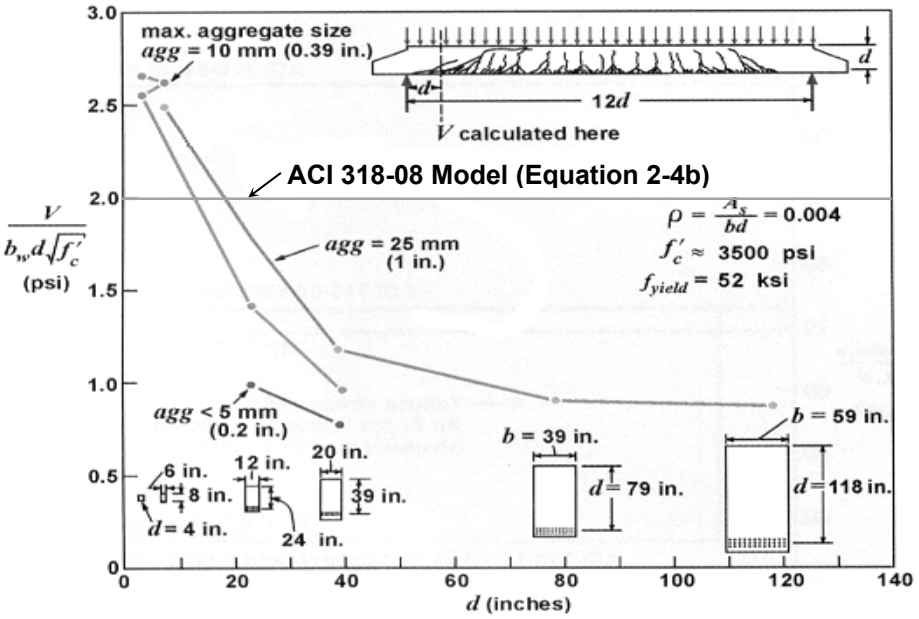

Figure 2-14: Influence of member depth and maximum aggregate size on the normalized shear stress at failure from tests performed by *Shioya et al.* 1989 and *Shioya* 1989 (figure adapted from *Lubell et al.* 2004).

While previous tests on shear critical RC members have considered a wide range for parameter *d*, the SFRC members considered in prior research mostly had effective depths less than 300 *mm* (*Parra-Montesinos* 2006). Some researchers have studied slender SFRC members ($a/d \geq 2.5$) with effective depth $300mm < d \leq 610mm$ (e.g. *Schantz* 1993, *Noghabai* 2000, *Rosenbusch and Teutsch* 2002, *Dinh* 2009). *Rosenbusch and Teutsch* (2002) reported that an increase in effective depth from *260 mm* to *540 mm*, with other parameters kept almost the same, resulted in a 26% decrease in the average shear strength. However, the shear stress at failure did not decrease significantly for specimens with *d=460 mm* compared to specimens with *d=260 mm*. *Kwak et al.* (2002) compared the shear strength of small size SFRC members from different researchers, mostly with $d \leq 300\ mm$, and did not observe a significant size effect on the shear strength.

More tests on large size members especially with $d > 600\ mm$ are necessary to establish a better understanding about the shear behaviour of SFRC members

without stirrups. Meanwhile, there is a need for testing both large size and small size members to investigate the size effect on the shear strength of SFRC members, especially when a scaling factor greater than 2 is applied.

2.2.4 Effect of longitudinal reinforcement ratio ρ

The effect of longitudinal reinforcement ratio ρ on the shear strength of SFRC members without stirrups was investigated by several researchers. Most of the SFRC members tested in previous research included $\rho \geq 1\%$. *Li et al.* (1992) tested SFRC members with $\rho = 1.1\%$, 2.2% and 3.3%, and concluded that a higher longitudinal reinforcement ratio resulted in a higher shear stress at failure because of increased dowel action and reduced crack width. However, the increase in shear strength was relatively small between $\rho = 2.2\%$ and $\rho = 3.3\%$. *Dinh* (2009) and *Ashour et al.* (1992) reported that the primary effect of longitudinal reinforcement ratio was on member ductility. Flexural steel yielding was mostly observed in specimens with lower reinforcement ratios, whereas no yielding prior to failure occurred in specimens with higher reinforcement ratio. *Narayanan and Darwish* 1997 noted that the dowel resistance of longitudinal reinforcement increased when the fiber content increased. They concluded that steel fibers improve the tensile strength of concrete in the splitting plane along the reinforcing bars.

2.2.5 Effect of compressive strength f'_c

Kwak et al. (2002) studied SFRC specimens with different concrete compressive strength f'_c, and concluded that an increase in SFRC compressive strength leads to an increase in member shear strength. They indicated that for identical SFRC slender members, when the concrete strength was doubled (from 31 to 65 *MPa*) the shear strength increased by 23%. *Narayanan and Darwish* (1987) noted that

using higher compressive strength concrete resulted in a steady rate of increase in ultimate shear strength of SFRC members. They observed that for a higher volume fraction of steel fibers, the rate of increase in shear strength due to increasing of compressive strength was higher. *Minelli and Plizzari* (2006) observed that for shear critical RC members without fibers, increasing the compressive strength of concrete from 25 *MPa* to 60 *MPa* resulted in much more brittle shear failure; however, for SFRC members, a similar increase in compressive strength did not result in more brittleness in shear failure. Note that the shear failure of SFRC specimens was generally reported as less brittle and sometimes ductile compared to that of similar RC members with identical compressive strength (*Narayanan and Darwish* 1987, *Ashour et al.* 1992, *Minelli and Plizzari* 2006). Research has also shown that the shear stress at failure decreases in RC members without fibers constructed with high strength concrete ($f'_c > 70$ *MPa*) due to the fracture of aggregates and therefore the reduction in aggregate interlock at the crack faces (e.g. *Angelakos et al.* 2001, *Lubell et al.* 2004).

2.2.6 Effect of aggregate size and type

A decrease in the maximum aggregate size or cleavage of more aggregates crossing the crack plane, reduces the crack surface roughness and therefore decreases the shear stress carried by the aggregate interlock (e.g. *Shioya et al.* 1989, *Sherwood et al.* 2007). *Shioya et al.* (1989), showed that for identical RC members without stirrups and without fibers, decreases in maximum aggregate size from 25 *mm* to 10 *mm* and 5 *mm* resulted in decreases in the shear stress at failure by 21% and 37%, respectively (Figure 2-14). *Kang and Kim* (2009) reported that for identical SFRC members without stirrups, the shear capacity of lightweight SFRC members was slightly lower than that of normal weight SFRC members. Previous researchers mostly used small aggregate size (~10 *mm*) in their SFRC specimens (e.g. *Mansur et al.* 1986, *Ashour et al.* 1992, *Dinh et al.*

2010); however, for SFRC members without stirrups, further research is needed to understand the effect of aggregate size and type on the shear strength.

2.2.7 Effect of member width

Kani et al. (1979) studied pairs of RC specimens without stirrups and without fibers in which the main variable was the specimens width. The width of wider specimens was four times of that for narrower specimens (*b=600 mm* and *b=150 mm*). For shear-span to depth ratios $3 \leq a/d \leq 6$, *Kani et al.* (1979) observed that the average shear failure load for wider specimens was about four times of that for narrower specimens. In other words, the width of specimen does not change the shear stress at failure if the specimen details are uniform across the width. These observations were confirmed later by other researchers e.g. *Lubell et al.* (2004) and *Sherwood et al.* (2007). The data from previous research on SFRC specimens without stirrups indicate that most researchers used a constant width for their specimens (*Parra-Montesinos* 2006).

2.2.8 Effect of Fiber Type

The influence of fiber type on the mechanical properties of SFRC was discussed in Section (2.1). However, the data from previous research on the shear strength of structural SFRC specimens without stirrups show that most of researchers used a single type of steel fibers (straight, crimped or hooked) in their specimens with a fiber tensile strength ranged between 1000 and 1240 *MPa*, $45 \leq L_f/D_f \leq 100$, and $25mm \leq L_f \leq 60$ *mm* (*Parra-Montesinos* 2006, *Yakoub* 2011). *Batson et al.* (1972) investigated the shear strength of SFRC specimens including straight or crimped steel fibers, but they could not draw a clear conclusion about the influence of steel fiber type due to the differences in the size of fibers. Therefore, more research is

needed to directly establish the effect of fiber type on the shear strength of SFRC members without stirrrups.

2.3 Shear Capacity Prediction Models

In this section, first the recognized shear models from *ACI 318-08* and *CSA A23.3-04* for RC members without stirrups and without fibers are explained. Then, a shear model from *Bresler and Pister* (1958) based on contribution of shearing in the compression block of RC members is reviewed.

There is as yet no recognized code model to predict the shear strength of SFRC members without stirrups. However, several researchers have proposed prediction models for shear strength of SFRC members. In Section (2.3.2), ten shear capacity models for SFRC members without stirrups from previous researchers are reviewed.

2.3.1 Shear Models for RC Members without Stirrups

ACI 318-08 Shear Model

The basic equation in *ACI 318-08* for the shear resistance of a reinforced concrete member without stirrups was empirically derived from a series of experimental works on slender beams (*a/d >2.5*) with effective depth ranging from 254 mm to 375mm (*ACI-ASCE Committee 326*, 1962). The *ACI Committee 318* equation for shear strength using equivalent metric notation is:

$$V_{ACI} = \lambda(0.16\sqrt{f_c'} + 17\rho\frac{Vd}{M})b\ d \le 0.29\sqrt{f_c'}b\ d \qquad (2\text{-}4a)$$

or, simply:

$$V_{ACI} = 0.167\ \lambda\ \sqrt{f_c'}\ b\,d \qquad (2\text{-}4b)$$

The density factor λ is equal to 1, 0.85 and 0.75 for normal density, semi-low-density, and low-density concrete, respectively. In Clause (8.6.1) of *ACI 318-08*, a semi-low-density concrete is defined as a concrete which may include natural sand and lightweight coarse aggregates, but the density ranges for low-density and semi-low-density concretes are not indicated. According to *MacGregor et al. (2006)*, concretes with $\gamma \leq 1850\ kg/m^3$ and $1850\ kg/m^3 < \gamma \leq 2150\ kg/m^3$ can be considered as low-density and semi-low-density concretes, respectively.

Due to the limited size range of the members studied, the empirically derived *ACI 318* expression was not able to capture the size effect in shear. Therefore, Equation (2-4) can be seriously non-conservative for large size members without stirrups (*Kani* 1967, *Collins and Kuchma* 1999, *Lubell et al.* 2004). Figure (2-14) indicates that *ACI 318* estimation for shear capacity of members with $d > 500\ mm$ is clearly higher than the measured shear strengths obtained from the tests by *Shioya et al.* (1989). The shear strength of the beam with $d = 2000\ mm$ was only about 45% of that predicted by Equation (2-4b).

To mitigate the non-conservative nature of this equation for the shear strength of large concrete beams, *ACI 318* requires that a minimum area of stirrups be used if the factored shear force exceeds $0.5\varphi V_c$ (*Collins and Kuchma* 1999). However, slabs and footings which can often be very thick and lightly reinforced were excluded from this provision for minimum shear reinforcement. Based on Clause (11.4.6) of *ACI 318-08*, and as an exception, when $0.5\varphi V_c < V_u \leq \varphi V_c$ and $f'_c \leq 41\ MPa$ the minimum stirrups requirement can be waived for SFRC members with overall depth $h \leq 610\ mm$ meeting certain material performance standards for post-cracking residual strength. In other words, *ACI 318-08* accepts that steel fibers can enhance the shear capacity of such members to at least φV_c, but *ACI 318-08* does not modify the basic shear model for SFRC members. According to Clause (5.6.6.2) of *ACI 318-08*, the SFRC mixes must include an equivalent fiber content of $V_f \geq 0.75\%$ and satisfy specific performance criteria to be acceptable as a replacement for minimum shear reinforcement. To meet these performance

criteria, the material flexural strengths (*ASTM C1609*) at midspan deflections of 1/300 and 1/150 of the span length must be greater than or equal to 90% and 75% of the first-peak flexural strength, respectively.

For the *ACI 318-08* shear model, the critical section in shear for a simple span member subjected to a concentrated load and its own weight is considered at a distance of *d* from the support edge.

CSA A23.3-04 Shear Model

The *CSA A23.3-04* standard incorporates shear design provisions for concrete structures based on a simplified version of the Modified Compression Field Theory (MCFT) (*Bentz et al.* 2006, *Vecchio and Collins* 1986). The *CSA A23.3* equation for shear strength is:

$$V_{CSA} = \lambda \beta \sqrt{f_c'}\, b d_v \tag{2-5}$$

where $\sqrt{f_c'} \leq 8$ and the effective shear depth d_v can be taken as $0.9d$. The density factor λ is equal to 1, 0.85 and 0.75 for normal density, semi-low-density and low-density concrete, respectively. According to Clause (8.6.5) of *CSA A23.3-04*, a semi-low-density concrete is defined as a concrete which may include natural sand and lightweight coarse aggregates; however, the density ranges for low-density and semi-low-density concretes are not indicated. According to *MacGregor et al.* (2006), concretes with $\gamma \leq 1850$ *kg/m*^{3} and 1850 *kg/m*^{3} $< \gamma \leq$ *2150 kg/m*^{3} can be considered as low-density and semi-low-density concretes, respectively.

Within this model, *CSA A23.3-04* considers the shear capacity as a function of the crack widths, which are, in turn, related to the member depth and the average axial strain in the member. Furthermore, the shear capacity is related to the roughness of the diagonal shear cracks which is influenced by the aggregate size for normal strength concrete with $f'_c < 70\ MPa$. These factors are reflected in parameter β, which includes so-called strain effect and size effect terms through parameters ε_x and s_{xe}:

$$\beta = \frac{0.40}{(1+1500\varepsilon_x)} \cdot \frac{1300}{(1000+s_{xe})} \tag{2-6}$$

For members without significant axial load or prestressing, the longitudinal strain ε_x at a cross-section is conservatively assumed as 1/2 the strain in the longitudinal tensile reinforcing steel through the relationship:

$$\varepsilon_x = \frac{M/d_v + V}{2E_s A_s} \leq 0.003 \tag{2-7}$$

To account for the size effect on shear strength, an equivalent crack spacing factor s_{xe} is used:

$$s_{xe} = \frac{35 s_x}{(15+a_g)} \tag{2-8}$$

where, a_g is the maximum aggregate size and s_x can be taken as d_v. For members made of high strength concrete with $f'_c \geq 70\ MPa$, since the cracks pass through the aggregates, maximum size of the aggregate does not influence aggregate interlock capacity, and a_g is taken equal to zero (*CSA A23.3-04*, *Angelakos et al.* 2001). The maximum aggregate size a_g can be reduced linearly to zero as f'_c increases from 60 *MPa* to 70 *MPa* (*CSA A23.3-04*, *Lubell et al.* 2004).

The critical section in shear for a simple span member subjected to a concentrated load and its own weight may be assumed at about $d_v=0.9d$ from the point load, where the imposed bending moment and shear are both considerable. At this critical section, ½ of the strain in the longitudinal reinforcement (ε_x from Equation 2-7) reaches a high level and therefore Equations (2-6) & (2-5) give lower estimates of shear strength for V_{CSA}.

Equations (2-5) to (2-8) show that *CSA A23.3-04* accounts for the size effect and strain effect in shear for RC members without stirrups and without fibers. However, *CSA A23.3-04* does not elaborate in the size and strain effects for RC members without web reinforcement but containing moderate volume-fraction of steel fibers. The shear model in the Canadian Highway Bridge Design Code (*CSA S6-06*) is similar to the *CSA A23.3-04* shear model. According to Section 16 of *CSA S6-06*, randomly distributed fiber reinforcement is permitted in deck slabs, barrier walls, and surfacing of stressed log bridges for the control of cracks that develop in concrete during its early life; however, *CSA S6-06* ignores the influence of steel fibers on the shear strength.

Bresler and Pister **Shear Model**

Bresler and Pister (1958) first tested material-scale tubular specimens made of plain concrete (21 $MPa \le f'_c \le 41$ MPa) under combined axial compression and torsion. Using the experimental data and a regression analysis, they derived a failure criterion for concrete under combined normal compressive stress and shear stress. This failure criterion had the following form in equivalent metric notation:

$$\frac{\tau_{cu}}{f'_c} = 0.1\sqrt{0.62 + 7.86\left(\frac{\sigma_{cu}}{f'_c}\right) - 8.46\left(\frac{\sigma_{cu}}{f'_c}\right)^2} \qquad (2\text{-}9)$$

where σ_{cu} and τ_{cu} are the ultimate uniform compressive stress and shear stress, respectively. According to Equation (2-9), for pure compression (τ_{cu}=0) the ultimate compression stress is equal to f'_c, while for pure shear (σ_{cu}=0) the ultimate shear stress is $0.08f'_c$. The maximum shear stress τ_{cu}=0.156 f'_c can be obtained when the compressive stress is σ_{cu}=0.4f'_c. As discussed in Section (2.1.5), *Vecchio and Collins* (1986) related the transmitted shear stress across a crack to the crack width, the maximum aggregate size, and the concrete compressive strength in RC panels subjected to in-plane shear and normal stresses.

The failure criterion (Equation 2-9) was then employed by *Bresler and Pister* (1958) to predict the shear strength of RC members without stirrups and without fibers. They assumed that the aggregate interlock and dowel action of longitudinal reinforcement are negligible, and therefore the entire shear strength was provided by the shearing in the compression zone (Figure 2-15). Accordingly, *Bresler and Pister* (1958) assumed that shear failure occurs due to destruction of the compression zone. In the *Bresler and Pister* (1958) shear model, the location of the critical section in shear is not indicated. However, the critical shear crack for a simple span member subjected to a concentrated load and its own weight may be assumed to start at about *d* from the point load, and reaches the uncracked compression zone under the point load. A uniform compressive stress at shear failure, acting on the whole compression zone depth *c* was considered. This uniform compressive stress was adapted from *Hognestad et al.* (1955), as follows:

$$\sigma_{cu} = \frac{3900 + 50.7 f_c^{'}}{3200 + 144.9 f_c^{'}} f_c^{'} \qquad (MPa) \qquad (2\text{-}10)$$

Hognestad et al. (1955) obtained the uniform compressive stress (Equation 2-10) from equilibrium of forces in the section and assuming that longitudinal reinforcement yields. By limiting the reinforcement ratio to the range of $1\% \leq \rho \leq$

2%, *Bresler and Pister* (1958) adapted the assumption of reinforcement yielding in the shear critical section. They applied the compressive stress from Equation (2-10) into the failure criterion (Equation 2-9) to calculate the ultimate shear stress at failure. *Bresler and Pister* (1958) reported that the calculated shear strength correlated well with test data of RC specimens without stirrups. For 21 specimens with 21 $MPa \leq f'_c \leq 41$ MPa, d=262 mm~272 mm, and $1\% \leq \rho \leq 2\%$, they reported an average of V_{test}/V_{model}=1.13 with COV=16%.

Bresler and Pister Model

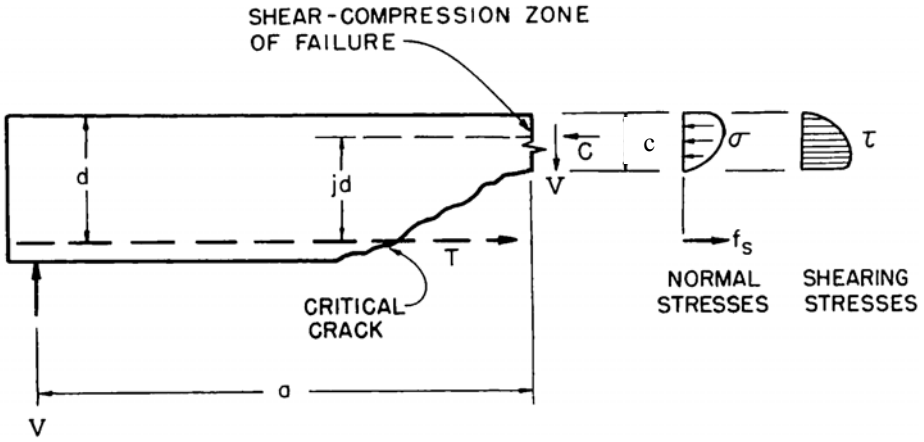

Figure 2-15: Normal and shear stresses in compression zone at shear failure (adapted from *Bresler and Pister* 1958).

2.3.2 Shear Models for SFRC Members without Stirrups

***Sharma* (1986)**

A simple empirical model was proposed by *Sharma* (1986) to predict the ultimate shear stress of SFRC members without stirrups:

$$v_{u1} = \frac{2}{3} f_t^{'} (d/a)^{0.25} \tag{2-11}$$

where, $f_t^{'}$ is the cylinder splitting tensile strength. According to *Sharma* (1986), in absence of splitting test results, the splitting strength $f_t^{'} = 0.79\sqrt{f_c^{'}}$ (in *MPa*) can be used in Equation (2-11). *Sharma* (1986) compared capacity predictions using Equation (2-11) against an assembled database of 41 specimens, and reported a reasonable estimation for the shear strength of SFRC members without stirrups (V_{test}/V_{model}=1.03 with *COV*=7.6 %). This equation, while easy and simple to use, does not explicitly take into consideration the effects of important factors such as fiber content or longitudinal reinforcement ratio (see Section 2.2). *Kwak et al.* (2002) validated the Equation (2-11) against 139 SFRC specimens with different *a/d* ratios, and reported an average V_{test}/V_{model}=1.26 with *COV*=37%. They concluded that this model estimation is conservative for $a/d < 2.5$ and non-conservative for $a/d > 4$ (Figure 2-16).

In the *Sharma* (1986) shear model, the location of the critical section in shear for a simple span member subjected to a concentrated load and its own weight is not indicated; however, the critical section in shear for this case may be assumed at a distance of *d* from the point load.

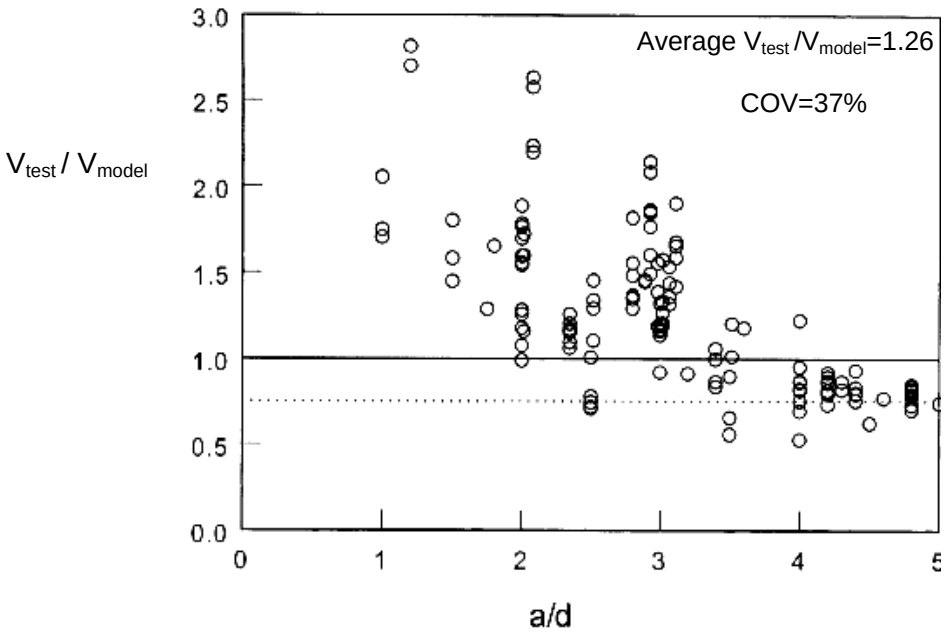

Figure 2-16: Sensitivity of *Sharma*'s Equation (2-11) to *a/d* (adapted from *Kwak et al.* 2002).

***Narayanan and Darwish* (1987)**

An empirical model was proposed by *Narayanan and Darwish* (1987) which includes three terms to account for the split-cylinder strength, dowel action, and tensile stress due to steel fibers along the diagonal shear crack, respectively:

$$v_{u2} = e(0.24 f_{spfc} + 80\rho\frac{d}{a}) + \sigma_f \qquad (MPa) \qquad (2\text{-}12)$$

The factor *e* accounts for the arch action, and is equal to 1.0 for $a/d > 2.8$, and $2.8d/a$ for $a/d \leq 2.8$. Based on a regression analysis, the split-cylinder strength f_{spfc} is calculated as follows:

$$f_{spfc} = \frac{f_{cuf}}{20 - \sqrt{F}} + 0.7 + \sqrt{F} \qquad (MPa) \qquad (2\text{-}13)$$

f_{cuf} is the cube compressive strength, and the fiber factor *F* is defined as:

$$F = \frac{L_f}{D_f} V_f d_f \tag{2-14}$$

The bond factor d_f accounts for the fiber geometry and is equal to 0.50 for round fibers, 0.75 for crimped fibers, and 1.00 for indented fibers.

The third term in Equation (2-12), σ_f accounts for the fiber pullout strength along a 45^o diagonal crack with a vertical projection equal to the distance between the center of reinforcement to the lower tip of the compression zone:

$$\sigma_f = 0.41 \tau F \tag{2-15}$$

The fiber-matrix bond stress τ is equal to 4.15 *MPa*, as proposed by *Swamy et al.* (1974).

Kwak et al. (2002) validated the Equation (2-12) against 139 SFRC specimens (Figure 2-17). According to *Kwak et al.* (2002), this model gives reliable and conservative estimates, since it directly considers some of the important factors affecting shear strength, and employs the regression analysis of only shear critical specimens (Figure 2-17). However, in Equation (2-12), *Narayanan and Darwish* (1987) do not specify the contribution of the compression zone and neglect the effect of aggregate interlock on the shear strength of SFRC members without stirrups.

The location of the critical section in shear for a simple span member subjected to a concentrated load and its own weight is not indicated in the *Narayanan and Darwish* (1987) shear model; however, the critical section in shear for this case may be assumed at a distance of *d* from the point load.

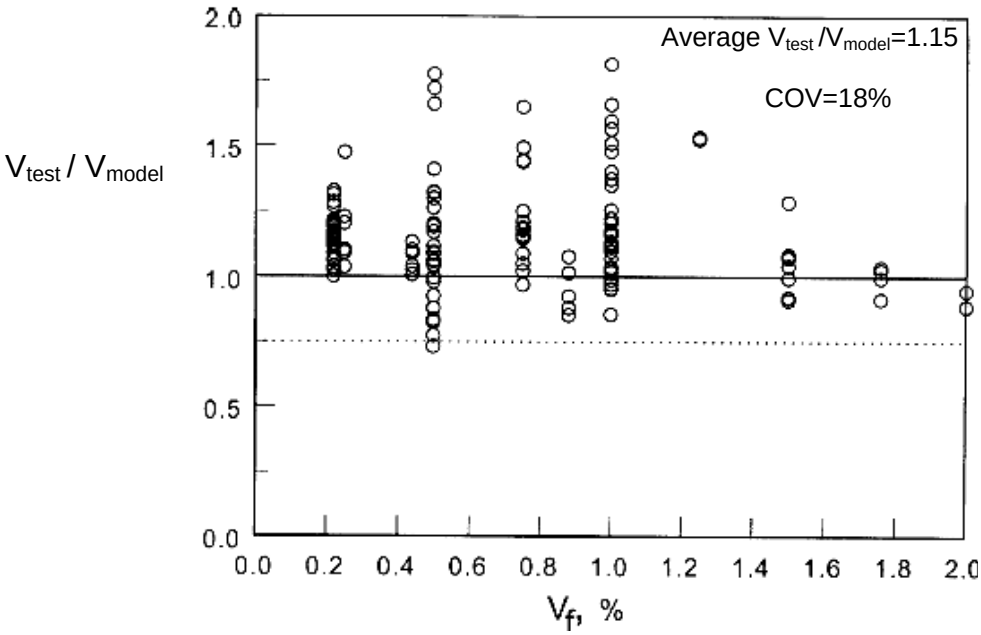

Figure 2-17: Shear strength prediction using *Narayanan and Darwish* (1987) Equation (2-12) (adapted from *Kwak et al.* 2002).

Ashour et al. (1992)

Based on their test results for high strength SFRC members and regression analysis, *Ashour et al.* (1992) modified the *Zsutty* (1968) model for shear in plain RC members to account for the steel fibers by including the fiber factor *F*:

$$v_{u3} = (2.11\sqrt[3]{f_c'} + 7F)\sqrt[3]{\rho\frac{d}{a}} \quad (MPa) \text{ for } a/d \geq 2.5 \tag{2-16a}$$

$$v_{u3} = \left[(2.11\sqrt[3]{f_c'} + 7F)\sqrt[3]{\rho\frac{d}{a}}\right]\frac{2.5d}{a} + \sigma_f\left(2.5 - \frac{a}{d}\right)$$

$$(MPa) \text{ for } a/d < 2.5 \tag{2-16b}$$

The parameters σ_f and F are the same parameters used for *Narayanan and Darwish* (1987) model. In addition to Equation (2-16), *Ashour et al.* (1992) proposed another expression for prediction of shear strength by incorporating the

fiber factor *F* into *ACI Committee 318* equation. This expression has the following form:

$$v_{u4} = (0.7\sqrt{f_c'} + 7F)\frac{d}{a} + 17.2\rho\frac{d}{a} \qquad (MPa) \qquad (2\text{-}17)$$

Ashour et al. (1992) reported that these equations gave good estimations for their 18 tested specimens except those with low reinforcement ratios (ρ=0.37%) which failed in flexure; however, no statistical analysis of prediction quality was given. Also, *Kwak et al.* (2002) reported that the Equations (2-16) and (2-17) give less accurate predictions compared to the *Narayanan and Darwish* (1987) evaluation. Comparing Equations (2-16) and (2-17) against test results of 139 specimens, *Kwak et al.* (2002) indicated average V_{test}/V_{model} ratios equal to 1.27 (*COV*=19%) and 1.12 (*COV*=21%), respectively.

In the *Ashour et al.* (1992) shear models, the location of the critical section in shear for a simple span member subjected to a concentrated load and its own weight is not indicated; however, the critical section in shear for this case may be assumed at a distance of *d* from the point load.

***Khuntia et al.* (1999)**

A uniform tensile stress for the fiber contribution was applied by *Khuntia et al.* (1999) along a 45^o diagonal crack with a vertical projection equal to *0.9d* (Figure 2-18). The location of the critical section in shear for a simple span member subjected to a concentrated load and its own weight is not indicated in the *Khuntia et al.* (1999) shear model; however, the critical section in shear for this case may be assumed at a distance of *d* from the point load. The uniform tensile stress was calculated as:

$$\sigma_f = 0.41\tau F \tag{2-18}$$

where, the fiber-matrix bond stress τ is equal to $0.68\sqrt{f_c'}$ and the fiber factor F can be obtained from Equation (2-14). The fiber geometry factor d_f in Equation (2-14) is taken equal to 1 for hooked end steel fibers.

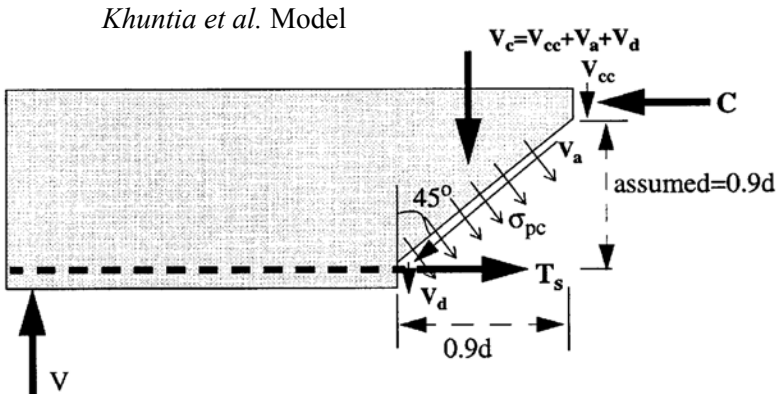

Figure 2-18: Contribution of steel fibers to the shear resistance of SFRC members without stirrups (adapted from *Khuntia et al.* 1999).

Therefore, the contribution of steel fibers to the shear strength can be expressed as below:

$$V_{ft1} = 0.41 \times 0.68\sqrt{f_c'}Fb \times 0.9d = 0.25\sqrt{f_c'}Fbd \tag{2-19}$$

As shown in Figure (2-18), the total contribution of the compression region, aggregate interlock, and dowel action is shown as V_c. This shear strength for slender RC members ($a/d \geq 2.5$) without stirrups and without fibers is calculated as $V_c = 0.167\sqrt{f_c'}bd$ in accordance to *ACI Committee 318* (see Equation 2-4). However, *Khuntia et al.* (1999) incorporated an arch action factor e from *Zsutty* (1968) into *ACI 318* equation for short RC members with $a/d < 2.5$. Therefore, the total ultimate shear stress for SFRC members without stirrups can be written as:

$$v_{u5} = (0.167e + 0.25F)\sqrt{f_c'} \tag{2-20}$$

where, the arch action factor e = 1 for $a/d \geq 2.5$ and e =2.5 d/a <3 for $a/d < 2.5$.

Khuntia et al. (1999) compared Equation (2-20) against published results for 68 specimens having a wide range of configurations, and showed that the model gives conservative predictions with relatively large scatter for SFRC members without stirrups (average V_{test}/V_{model}=1.51, *COV*=37%).

***Kwak et al.* (2002)**

Kwak et al. (2002) modified the *Zsutty* (1968) equation to account for the split-cylinder tensile strength and the contribution of fibers to the shear strength of SFRC members without stirrups:

$$v_{u6} = 3.7e(f_{spfc})^{2/3}\left(\rho\frac{d}{a}\right)^{1/3} + 0.8\sigma_f \qquad (MPa) \tag{2-21}$$

where, e is equal to 1 for $a/d \geq 3.4$ and $3.4d/a$ for a/d <3.4. The split-cylinder tensile strength f_{spfc} is calculated from Equation (2-13), as explained for the *Narayanan and Darwish* (1987) model. *Kwak et al.* (2002) compared Equation (2-21) against 139 specimens and reported an average V_{test}/V_{model}=1.00 with *COV*=15%.

In the *Kwak et al.* (2002) shear model, the location of the critical section in shear for a simple span member subjected to a concentrated load and its own weight is

not indicated; however, the critical section in shear for this case may be assumed at a distance of *d* from the point load.

***Dinh* (2009)**

In the model proposed by *Dinh* (2009), the aggregate interlock was neglected or considered as supplementary to the fibers tensile stress along a 40^o diagonal shear crack with respect to the member longitudinal axis. The diagonal shear crack had a vertical projection equal to the distance between the center of reinforcement to the lower tip of the compression zone. For a simple span member subjected to a concentrated load and its own weight, the compression zone was located at the edge of the loading plate. The dowel action was assumed to be negligible. Accordingly, the shear strength was defined as the sum of the shear force across the compression region based on *Bresler and Pister* (1958) model (Section 2.3.1) and the shear force due to the fiber tension along the diagonal crack. The predicted ultimate shear stress had the following form:

$$v_{u7} = 0.11\beta_1 f_c^{'}\frac{c}{d} + \sigma_{f0}(1-\frac{c}{d})\cot 40^o \qquad (MPa) \qquad (2\text{-}22)$$

where, $f'_c \leq 55\ MPa$ and the compressive zone height c is calculated from Equation (2-23). However, even for members with $\rho > 2\%$, *Dinh* (2009) considered a limit of $\rho = 2\%$ for calculation of c from Equation (2-23).

$$c = \frac{A_s f_y}{0.85\beta_1 f_c^{'}} \qquad (mm) \qquad (2\text{-}23)$$

According to *Dinh* (2009), the uniform tensile stress due to fibers σ_{f0} is obtained from an empirical formula which was based on unpublished data of material flexural tests (*ASTM C1609*) conducted at the University of Michigan:

$$\sigma_{f0} = 2.76(\frac{L_f}{D_f})\sqrt{0.0075V_f} \qquad (MPa) \tag{2-24}$$

The parameter β_1 was calculated according to *ACI 318-08* as follows:

$$\beta_1 = \begin{cases} 0.85 & \text{for } f'_c \leq 28\ MPa \\ 1.05\text{-}0.007 f'_c \geq 0.65 & \text{for } f'_c > 28\ MPa \end{cases} \tag{2-25}$$

Equation (2-22) was validated against a filtered data set including 56 slender specimens with $a/d \geq 2.5$, $f'_c \leq 55\ MPa$, and containing at least 0.5% volume fraction of hooked end steel fibers. The results showed that Equation (2-22) gives good predictions of shear capacity with an average V_{test}/V_{model}=1.18 and *COV*=17%. However, more than 50% of specimens in the data set included $\rho > 2\%$, but the extra influence of longitudinal reinforcement ratio beyond 2% on the compression zone depth was neglected (Equation 2-23). Meanwhile, the Equation (2-24) for tensile stress of fibers σ_f, did not explicitly account for the matrix strength which plays an important role in the pullout strength of steel fibers (*Naaman and Najm* 1991).

Kang and Kim (2010)

Kang and Kim (2010) modified *Ashour et al.* (1992) and *Kwak et al.* (2002) models to predict the shear capacity of lightweight SFRC specimens without stirrups. In order to account for the weakness and brittleness of lightweight aggregates, *Kang and Kim* (2010) replaced the cylinder compressive strength f'_c with a term $\lambda^2 f'_c$ in both *Ashour et al.* (1992)(modified *Zsutty* 1968) and *Kwak et al.* (2002) models. The density factor $\lambda = 0.75$ was selected for lightweight concrete ($\gamma = 1800\ kg/m^3$) in accordance with *ACI 318-08*. The modified *Ashour*

et al. (1992) model for ultimate shear stress of lightweight SFRC had the following form:

$$v_{u8} = (2.11\sqrt[3]{\lambda^2 f_c'} + 7F)\left(\rho\frac{d}{a}\right)^{0.333} \quad (MPa) \text{ for } a/d \geq 2.5 \tag{2-26a}$$

$$v_{u8} = [\,(2.11\sqrt[3]{\lambda^2 f_c'} + 7F)(\rho\frac{d}{a})^{0.333}\,]\frac{2.5d}{a} + \sigma_f(\,2.5 - \frac{a}{d}\,) \quad (MPa) \text{ for } a/d < 2.5 \tag{2-26b}$$

Similarly, the modified *Kwak et al.* (2002) model for lightweight SFRC members was expressed as:

$$v_{u9} = 3.7e(f_{spfc,l})^{2/3}\left(\rho\frac{d}{a}\right)^{1/3} + 0.8\sigma_f \quad (MPa) \tag{2-27}$$

where,

$$f_{spfc,l} = \frac{\lambda^2 f_{cuf}}{20 - \sqrt{F}} + 0.7 + \sqrt{F} \quad (MPa) \tag{2-28}$$

The cube compressive strength f_{cuf} was taken equal to $1.2f'_c$. Other parameters in Equations (2-27) and (2-28) are the same as described earlier for the *Kwak et al.* (2002) model.

In the *Kang and Kim* (2010) shear models, the location of the critical section in shear for a simple span member subjected to a concentrated load and its own weight is not indicated; however, the critical section in shear for this case may be assumed at a distance of *d* from the point load.

Kang and Kim (2010) compared Equations (2-26) and (2-27) against the test results of 15 lightweight SFRC specimens from *Kang and Kim* (2009) and *Swamy*

et al. (1993). They reported an average V_{test}/V_{model} equal to 1.33 (*COV*=11%) and 1.30 (*COV*=19%) for Equations (2-26) and (2-27), respectively.

***Yakoub* (2011)**

By taking into account the fiber bond characteristics, fiber geometry and shear span to effective depth ratio *a/d* of the member, *Yakoub* (2011) developed an equation to calculate steel fiber contribution to the ultimate shear stress of SFRC members:

$$V_{ft2} = 0.405\frac{L_f}{D_f}V_f R_g \frac{d}{a}\sqrt{f_c'} \qquad \text{for } a/d \le 2.5 \qquad \text{(2-29a)}$$

$$V_{ft2} = 0.162\frac{L_f}{D_f}V_f R_g \sqrt{f_c'} \qquad \text{for } a/d \ge 2.5 \qquad \text{(2-29b)}$$

where the fiber geometry factor R_g is equal to 1, 0.83, and 0.91 for hooked end, crimped and round fibers, respectively. Then, *Yakoub* (2011) assumed that for prediction of ultimate shear stress of SFRC members, steel fiber contribution from Equation (2-29) can be added to the *CSA A23.3-04* shear stress model from Equation (2-5) for normal weight RC members without fibers. By rearranging and taking into account the average value of parameter β for a large data base of tests used in regression analysis, the ultimate shear stress of SFRC members was calculated as:

$$v_{u10} = 2.5\beta\sqrt{f_c'}\left(1 + 0.7V_f\frac{L_f}{D_f}R_g\right)\frac{d}{a} \qquad (MPa) \quad \text{for } a/d \le 2.5 \qquad \text{(2-30a)}$$

$$v_{u10} = \beta\sqrt{f_c'}\left(1 + 0.7V_f\frac{L_f}{D_f}R_g\right) \qquad (MPa) \quad \text{for } a/d \ge 2.5 \qquad \text{(2-30b)}$$

The location of the critical section in shear for a simple span member subjected to a concentrated load and its own weight is not indicated in the *Yakoub* (2011) shear

model; however, the critical section in shear for this case may be assumed at a distance of *d* from the point load.

Yakoub (2011) compared the Equation (2-30) against published results for 103 SFRC specimens including hooked end steel fibers, and showed that Equation (2-30) gives conservative predictions for ultimate shear strength of SFRC members (average V_{test}/V_{model}=1.43 with *COV*=19%).

3. Mechanical Properties of SFRC: Experimental Program

In this chapter the mix design development for normal strength, high strength and lightweight concrete with and without fibers is discussed. The experimental methods and relevant standardized test protocols to characterize the mechanical properties of mix designs in compression (*ASTM C39-05*), flexure (*ASTM C1609-05 & JSCE-G 552-1999*) and direct shear (*JSCE-G 553-1999*) are also explained.

3.1 Mix Development

The mix designs for three types of plain concrete were developed:

- Normal strength, normal weight concrete (NSC)
- Normal strength, lightweight concrete (LWC)
- High strength, normal weight concrete (HSC)

For each matrix, several trial mixes were developed. Selection of target mixes was based on consideration of the following factors:

1) *Compressive strength*

Two different compressive strengths were considered:

i) f'_c*=30-40 MPa* for both the regular normal strength concrete and lightweight concrete

ii) f'_c*=80-90 MPa* for high strength concrete

A similar compressive strength f'_c=*30-40 MPa* was selected for both NSC and LWC, to enable study of the influence of aggregate type on the mechanical properties of concrete largely separate from any additional influence of f'_c. Meanwhile, for HSC, a higher compressive strength with target f'_c=*80-90 MPa* allowed studying the effect of compressive strength on the constitutive response of normal weight concrete. The range of f'_c=*80-90 MPa* for HSC was selected to provide more than two times stronger concrete compared to NSC and to exceed the limit $f'_c \approx$*70 MPa* where aggregate fracture is known to influence the shear resistance of plain RC beams (*Angelakos et al.* 2001, *Lubell et al.* 2004). Note that as described in Section (4.1), some mixes had f'_c exceeding *100 MPa*.

2) *Density*

Two different densities were targeted for concrete with f'_c=*30-40 MPa*:

i) Normal weight concrete with a density of about *2400 kg/m*^{3}

ii) Lightweight aggregate concrete with a density less than 2000 *kg/m*^{3}

In addition to the normal weight concrete (*2400 kg/m*^{3}), a semi-low-density concrete with γ=*1900~2000 kg/m*^{3} including locally available lightweight aggregates was selected to study the influence of aggregate type and density on the mechanical properties of mix designs.

3) *Workability*

Since adding steel fibers to the RC matrix would reduce the workability (*Johnston 1974*), a minimum slump of *100mm* for plain concrete was targeted to provide adequate workability after addition of steel fibers (*slump > 50 mm*).

4) *Proximity of aggregates source*

Locally available aggregates were utilized for all mix designs. The properties of these aggregates are shown in Table (3-1). The lightweight concrete included angular expanded clay with maximum particle size of 10 *mm* and crushed bottom ash with maximum particle size of 4.75 *mm* as coarse and fine aggregates, respectively. In order to keep the maximum aggregate size as a constant parameter, most of the normal density trial mixes were designed to also include angular pea gravel with maximum size of 10 *mm*. Natural river sand with maximum particle size of 4.75 *mm* was used as fine aggregate for the normal weight concrete.

Table 3-1: Properties of the Aggregates

Aggregate		**Max. Particle Size (mm)**	**Bulk Density (kg/m^3)**	**Moisture Content (%)**	**Absorption (%)**
Normal weight Aggregates	Pea Gravel	10	2500	0.1	1.32
		20	2500	0.1	1.32
	River Sand	4.75	2700	0.4	1.46
Lightweight Aggregates	Expanded Clay	10	1770	0.7	10
	Bottom Ash	4.75	1360	10.9	20.3

As described in Section (2.1), hooked end steel fibers better improved the mechanical responses of plain concrete compared to the other types of steel fibers, mainly due to the mechanical contribution of end hooks. Therefore, hooked end steel fibers type *ZP305* (see Section 3.3) were used to produce the SFRC mixes in the current study.

3.1.1 Mixing Procedure

A portable drum mixer with 75 *liters* capacity was employed for concrete mixing in this phase of the project. The drum mixer was rinsed with water and completely drained before each mixing. First, the dry material including cement or cementitious material (cement + silica fume + fly ash), fine and coarse aggregates, and steel fibers (in the case of SFRC mixes) were mixed together and then the water or (water + super plasticizer + air entraining admixture) was added. In the case of high strength concrete, the retarder was added to the mix near the end of the mixing process (see Section 3.1.3). For lightweight concrete, the total material was divided into three or four parts and mixed in sequence (see Section 3.1.4). The total time of mixing was about 8~10 minutes for normal weight concrete and 12~15 minutes for lightweight concrete. All aggregates were in a wet condition with moisture contents shown in Table (3-1). To cast the concrete samples, the concrete was placed in the molds in 2 or 3 layers and compacted by using a vibrating table with frequency of 60 to 90 *Hz*. For regular curing, the specimens were demolded 24 hours after casting, and were placed in a controlled environment chamber (humidity = 100%; temperature = 23 ± 2 °C).

3.1.2 Regular Normal Strength Concrete (NSC)

For regular normal strength concrete, eight trial mixes were produced (Table 3-2). No supplementary cementitious material (e.g. silica fume and fly ash) or admixtures such as super plasticizer were added to the trial mixes. The main variable in the trial mixes *N1*, *N2*, and *N4* was the water to cement ratio *w/c*. The material proportions for trial mixes *N2* and *N3* were identical, but the maximum aggregate size was different. For trial mixes *N5*, *N6*, *N7*, and *N8*, the cement quantity was lower compared to *N1*, *N2*, *N3*, and *N4*. With reference to the trial

mix *N5*, the main variables in the trial mixes *N6*, *N7*, and *N8* were fine aggregate quantity, maximum aggregate size, and steel fiber content, respectively.

Note that in Table (3-2), the required water for absorption (Table 3-1) is also included in the water to cement ratio *w/c*.

Table 3-2: Trial mixes for regular normal strength concrete (NSC)

Trial Mix	***N1***	***N2***	***N3***	***N4***	***N5***	***N6***	***N7***	***N8***
Target Strength (MPa)	30-40	30-40	30-40	30-40	30-40	30-40	30-40	30-40
Max. Agg. Size (mm)	10	10	20	10	10	10	20	10
Material proportions per 1 m^3								
Cement-General Use type (kg)	460	460	460	460	391	390	391	391
Silica Fume-Dry compacted Rheomac SF100 (kg)	----	----	----	----	----	----	----	----
Fly Ash-type CI (kg)	----	----	----	----	----	----	----	----
Fine Agg.-Sand (kg)	841	841	841	841	655	714	655	655
Coarse Agg.-Pea Gravel (kg)	682	682	682	682	993	990	993	993
w/c	0.45	0.5	0.5	0.55	0.6	0.6	0.6	0.6
HRWR-Glenium 3030 (l)	----	----	----	----	----	----	----	----
Retarder-Pozolith 122R (ml)	----	----	----	----	----	----	----	----
Air Admixture-MB-AE 90 (ml)	----	----	----	----	----	----	----	----
Hooked Steel Fibers-Dramix ZP305 (kg)	----	----	----	----	----	----	----	40
Measured Slump (mm)	90	130	190	200	180	180	200	130
Dry hardened Concrete Density (kg/m^3)	2410	2405	2405	2395	2390	2390	2385	2390
Accelerated Method								
28.5 hours strength (MPa)	26.9	24.6	22.9	20.2	15.7	15.7	12.9	----
Estimated 28 days strength* (MPa)	48.3	45.2	42.9	39.3	32.6	33.2	29.5	----
7 days hot water curing strength (MPa)	38	36	32	----	----	----	----	----
Regular curing strength (MPa)								
Measured 3 days	----	----	----	----	----	----	----	----
Measured 7 days	----	38	----	34	22	26	20	24
Estimated 28-days strength*	---	43.3	---	40.0	30.1	33.4	28.5	31.8
Measured 28 days	46.8	43.1	42.3	41.1	32.5	33	30.2	31.8

* According to Equation (3-1) from *Malhotra and Zoldners (1969)*

** According to Equation (3-2)

3.1.3 High Strength Concrete (HSC)

As a starting point for trial mixes of high strength concrete, some available data from previous research (*Kosmatka et al.* 2002) were used. Then, the material proportions were modified to be applicable for the commercially available admixtures and to meet the target strength and workability. In total, four trial mixes were produced for high strength concrete (Table 3-3). In order to increase the strength without reducing the workability of cementitious paste, silica fume (*dry compacted-Rheomac SF100*) and fly ash (*type CI*) were used in two trial mixes, as partial replacement for general use (*GU*) cement. Silica fume and fly ash were dry-mixed with the cement at the beginning of the mixing process. Note that in Table (3-3), *w/c* is the ratio of total weight of water including the required water for absorption (Table 3-1) to the total weight of cementitious material.

A high range water reducer-HRWR (*Glenium 3030*) and a retarder (*Pozzolith 122R*) were added into the concrete mixture to reduce the water content and improve the workability. Also, adding a very small amount of air-entraining admixture (*MB-AE 90*) improved the workability without reducing the concrete strength. The super plasticizer and air admixture were mixed into the water at the beginning of the mixing process, but the retarder was added to the concrete mixture at the end of mixing to provide enough time for casting the samples. However, in order to have a reasonable workability, the casting and finishing time for the fresh high strength concrete should not take longer than 20-30 minutes.

Table 3-3: Trial mixes for high strength concrete (HSC)

Trial Mix	*H1*	*H2*	*H3*	*H4*
Target Strength (MPa)	80-90	80-90	80-90	80-90
Max. Agg. Size (mm)	10	10	10	10
Material proportions per 1 m^3				
Cement-General Use type (kg)	564	564	327	500
Silica Fume-Dry compacted Rheomac SF100 (kg)	------	------	27	40
Fly Ash-type CI (kg)	------	------	87	20
Fine Agg.-Sand (kg)	647	640	734	640
Coarse Agg.-Pea Gravel (kg)	1068	1055	1107	1055
w/c	0.28	0.32	0.37	0.31
HRWR-Glenium 3030 (l)	11.61	11.61	9.52	11.61
Retarder- Pozolith 122R (ml)	1040	1040	------	1040
Air Admixture- MB-AE 90 (ml)	220	220	170	220
Hooked Steel Fibers-Dramix ZP305 (kg)	------	------	------	------
Measured Slump (mm)	140	190	200	200
Dry Concrete Density (kg/m^3)	2445	2440	2425	2450
Accelerated Method				
28.5 hours strength (MPa)	------	48.2	------	57.1
Estimated 28 days strength (MPa)*	------	76.9	------	88.9
Regular curing strength (MPa)				
Measured 3 days	66	58	34.5	58.2
Measured 7 days	76.9	67.2	44	68
*Estimated 28-days strength***	75.2	67.2	48.2	67.9
Measured 28 days	86	76	60	90

*According to Equation (3-1) from *Malhotra and Zoldners (1969)*
** According to Equation (3-2)

3.1.4 Lightweight Concrete

For the structural lightweight concrete, a lightweight expanded clay coarse aggregate was obtained from a local supplier. Meanwhile, crushed bottom ash was used as the fine aggregate and was sourced from a coal-fed thermal power plant near Edmonton (Figure 3-1). The water absorption of the bottom ash and expanded clay were much higher than that of river sand and pea gravel used in the normal weight mixes (Table 3-1). This fact was taken into consideration during the mix design and proportioning the required water. In Table (3-4), *w/c* is the ratio of the total weight of water including the required water for absorption to the total weight of cementitious material. Silica fume was added to the lightweight mixes to achieve the desired compressive strength. For lightweight concrete, nine trial mixes were investigated (Table 3-4). The main variables in these nine trial mixes were *w/c* and/or super plasticizer quantity. For trial mixes *L3* and *L4*, while the mix proportions for cement, silica fume, and aggregates were slightly different, the main variable was the amount of retarder used in the mix. Furthermore, in trial mixes *L8* and *L9*, the type and/or amount of fine aggregates were also different compared to the other trial mixes.

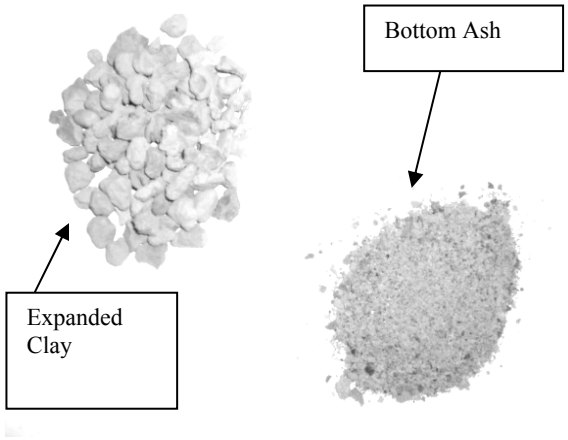

Figure 3-1: Coarse and fine lightweight aggregates

From the trial mixes, it was observed that for the same measured slump, the workability of the lightweight concrete was qualitatively superior to that of normal aggregate concrete. Adding more water to increase the workability (or slump) resulted in a weaker strength; therefore, an HRWR (*Glenium 3030*) was used for the lightweight concrete mixes to achieve the desired slump with less added water. However, in contrast to the normal aggregate concrete, using the HRWR beyond 8.5 l/m^3 caused a weaker lightweight concrete even with a considerably reduced *w/c* ratio. It was observed that using a maximum of 7 l/m^3 super plasticizer along with adjustment of the *w/c* ratio resulted in acceptable mixes in terms of strength and workability. Also, adding a very small amount of air-entraining admixture helped to improve the workability without decreasing the concrete strength. The super plasticizer and air-entraining admixture were mixed into the water at the beginning of the mixing process.

The bottom ash retained a considerable amount of water on its surface beyond what was required for absorption. This would reduce the amount of water available for chemical reaction with the cement, and might result in a qualitatively dry concrete without any slump. Mixing the dry materials together first, including the cement, silica fume, bottom ash, expanded clay and steel fibers (in case of SFRC), and then adding the water to the dry mix helped to avoid the dryness of the mix. Furthermore, the total material for lightweight concrete (dry materials and water) were divided into three or four parts, and each part was added and mixed based on the procedure explained above in sequence (i.e. dry material part 1, water part 1, dry material part 2, water part 2,…). The approximate mixing time for each part of dry materials or water was 2~3 minutes.

Table 3-4: Trial mixes for lightweight concrete (LWC)

Trial Mix	*L1*	*L2*	*L3*	*L4*	*L5*	*L6*	*L7*	*L8*	*L9*
Target Strength (MPa)	30	30	30	30	30	30	30	30	30
Max. Agg. Size (mm)	10	10	10	10	10	10	10	10	10
Material proportions per 1 m^3									
Cement-General Use type (kg)	394	394	394	410	394	394	412	430	394
Silica Fume-Dry Compacted Rheomac SF100 (kg)	28	28	39.4	35	28	28	32	37	28
Fly Ash-type CI (kg)	------	------	------	------	------	------	------	------	------
Fine Agg.-Bottom Ash (kg)	412	412	509	478	412	412	378	333	585 Sand
Coarse Agg.-Expanded Clay (kg)	713	713	531	572	713	713	749	766	802
w/c (Mixing water+ Absorption)	0.49 + 0.25	0.47 + 0.25	0.37 + 0.22	0.37 + 0.22	0.42 + 0.25	0.43 + 0.25	0.45 + 0.23	0.51 + 0.22	0.40 + 0.19
HRWR-Glenium 3030 (l)	------	7.0	12.0	12.0	12.5	15.7	8.5	------	10.0
Retarder- Pozolith 122R (ml)	------	------	1000	------	------	------	------	------	------
Air Admixture- MB-AE 90 (ml)	175	175	175	175	------	------	------	------	------
Hooked Steel Fibers-Dramix ZP305 (kg)	------	------	------	------	------	------	------	------	------
Measured Slump (mm)	0	120	50	50	0	50	90	50	200
Dry Concrete Density (kg/m^3)	1930	1920	1820	1820	1920	1920	1910	1930	1960
Accelerated Method									
28.5 hours strength (MPa)	17.3	19.3	17	12.9	21.2	13.1	24.4	19.9	17.5
Estimated 28-days strength (MPa)*	34.7	37.2	34.3	29	39.7	29.3	43.8	38	34.9
Regular curing strength (MPa)-Humidity room									
Measured 7 days strength	23	22.8	14	10	15.4	10.2	22.1	24.7	21.4
*Estimated 28-days strength***	31.0	30.8	23.6	20.3	24.7	20.5	30.2	32.4	29.6
Measured 28 days strength	31.4	31.2	23.4	20.5	25	20.7	31.7	32.9	26.5

* According to Equation (3-1) from *Malhotra and Zoldners (1969)*

** According to Equation (3-2)

3.2 Accelerated Method for Estimating 28-Day Compressive Strength

The boiling water test method based on *CSA A23.2-00* was employed as an accelerated test method to estimate the 28-day cylinder compressive strength. According to this method, 23 hours (+/-0.25 hour) after casting, the samples in plastic molds were placed in a boiling water tank with 98^{o}C or higher temperature for a period of 3.5 hours (+/-0.25 hour). Then, the samples were removed from the hot water tank, demolded and allowed to cool under the ambient laboratory condition of 23^{o}C (+/-2 ^{o}C) for 1 hour before being tested under compression. The total time between casting and testing did not exceed 28.5 hours.

Malhotra and Zoldners (1969) proposed an equation to estimate the 28-day compressive strength from the accelerated curing strength:

$$f_{c28} = 12.43 + 1.286 f_{ac} \quad (MPa) \tag{3-1}$$

where f_{ac} (MPa) is the compression strength resulted from the accelerated boiling water test method and f_{c28} is the estimated 28-day compressive strength.

Based on the results from trial mixes in this study, Equation (3-1) gives good estimations with less than 5% error for the 28-day compressive strength of moist cured normal density concrete having either normal strength (Table 3-2) or high strength (Table 3-3). However, using the same relationship for the lightweight concrete resulted in 11% to 59% error in estimation of the 28-day compressive strength (see Table 3-4). Figure (3-2) also shows that for lightweight trial mixes in this study, a linear estimation can not accurately estimate the 28-day strength based on the accelerated method results. Instead, Figure (3-3) shows a good linear correlation between the strength of one week regular curing f_{c7} and the 28-day strength:

$$f_{c28} = 12.1 + 0.82 f_{c7} \qquad (MPa) \tag{3-2}$$

Equation (3-2) can also accurately estimate the 28-day compressive strength of normal density concrete with normal strength (Table 3-2) with less than 7% error. However, Equation (3-2) gives inaccurate estimations with 12% to 25% error for the compressive strength of normal density concrete with high strength (Table 3-3).

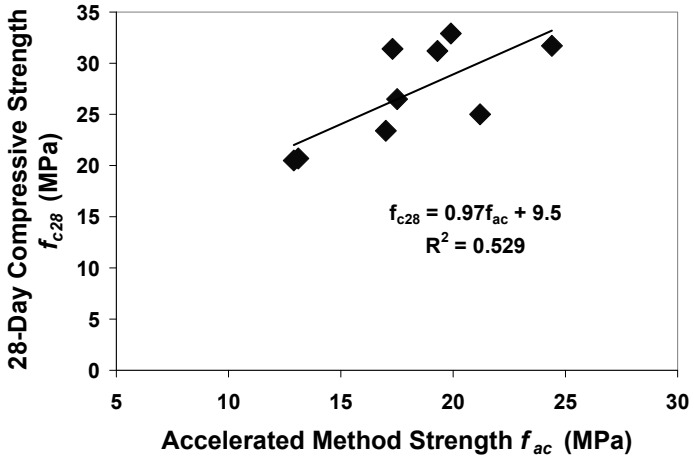

Figure 3-2: Correlation between 28-day compressive strength and accelerated method strength for lightweight concrete trial mixes in this study.

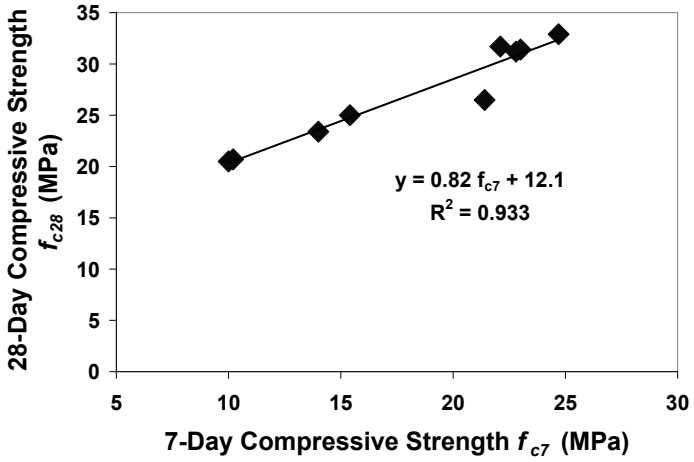

Figure 3-3: Correlation between 28-day and 7-day compressive strengths for lightweight trial mixes in this study.

3.3 Selected mix compositions for SFRC

From the trial mixes described in Section 3.1, three matrices were selected to further evaluate the mechanical properties of normal strength, high strength and lightweight SFRC. The selected mixes included maximum aggregate size of 10 *mm*, and achieved the target strength and workability indicated in Section 3.1:

- Trial mix *N5* for regular normal strength concrete (Table 3-2)
- Trial mix *H4* for high strength concrete (Table 3-3)
- Trial mix *L2* for lightweight concrete (Table 3-4)

For each matrix composition, hooked end steel fibers (type *Dramix ZP305*) shown in Figure (3-4) were included. The steel fibers had aspect ratio $L_f/D_f = 55$, $L_f = 30$ *mm*, and yielding strength of 1100 *MPa*. Three different volume fractions of fibers 0%, 0.5% and 1% were used for each matrix composition, resulting in 9 mixes in all. The summary of SFRC mix designs and designations are shown in Table (3-5).

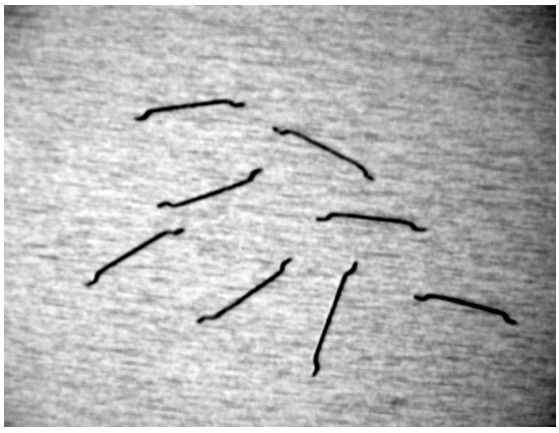

Figure 3-4: Hooked end steel fibers *ZP305*

Table 3-5: SFRC mix design per 1 m^3 and designation

	Normal Strength mixes (NSC)			***Lightweight mixes (LWC)***			***High Strength mixes (HSC)***		
Cement-General Use type (kg)	391			394			500		
Silica Fume-Dry Compacted Rheomac SF100 (kg)	-----			28			40		
Fly Ash-type CI (kg)	-----			-----			20		
Fine Aggregate (kg)	655 (Sand)			412 (Bottom Ash)			640 (Sand)		
Coarse Aggregate (kg)	993 (Pea Gravel)			713 (Expanded Clay)			1055 (Pea Gravel)		
w/c	0.6			0.72			0.31		
HRWR-Glenium 3030 (ml)	-----			7000			11610		
Retarder- Pozolith 122R (ml)	-----			-----			1040		
Air Admixture- MB-AE 90 (ml)	-----			175			220		
Mix Designation	***N-0***	***N-0.5***	***N-1***	***L-0***	***L-0.5***	***L-1***	***H-0***	***H-0.5***	***H-1***
Hooked Steel Fibers-Dramix ZP305 (kg)	0	40	80	0	40	80	0	40	80

3.4 Test Methods for Mechanical Properties

All mechanical property tests in this study were performed using two universal testing frames (MTS) with 1000 *kN* and 2600 *kN* capacities. Three cylinders (100 *mm* x 200 *mm*) and three prisms (100 *mm* x 100 *mm* x 400 *mm*) were cast per each mix to be tested in compression and flexure, respectively. Three prisms (100 *mm* x 100 *mm* x 400 *mm*) per mix were also cast for direct shear tests. To cast the concrete samples, the concrete was placed in the molds in 2 or 3 layers and compacted by using a vibrating table with frequency of 60 to 90 *Hz*. In each case, the specimens were demolded 24 hour after casting, and were placed in a controlled environment chamber (humidity = 100%; temperature = 23 ± 2 °C) for further 12 to 21 weeks before tests. It was assumed that the compressive strength

of concrete specimens remained largely constant after reaching the age of 12 weeks (e.g. *Kosmatka et al.* 2002)

3.4.1 Compression Test

Quasi-static loading was applied at the rate of 0.2 to 0.3 *MPa/s* according to *ASTM C39-05*. Three cylindrical specimens (100 *mm* x 200 *mm*) per mix were tested. The axial displacement of the cylindrical specimen was obtained from the travel in the loading platens which was recorded by the *MTS-2600* test machine shown in Figure (3-5). This was used to compute the average axial strain of each cylinder. Note that all the cylinders were end-ground prior to testing.

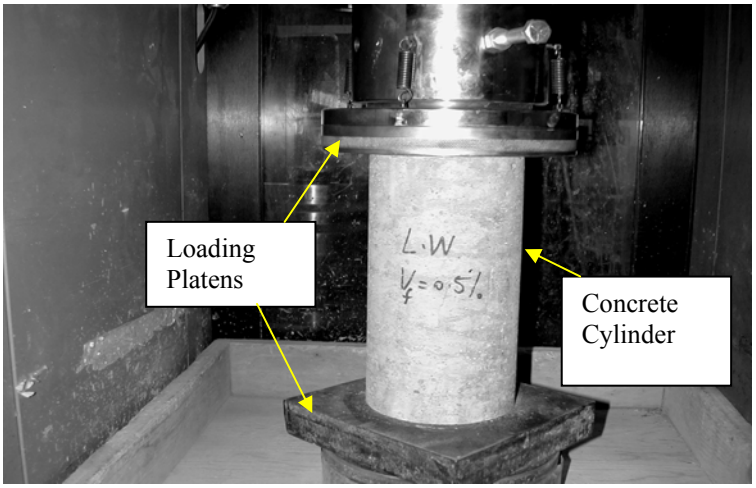

Figure 3-5: Test set-up for compression test

3.4.2 Flexural Test

The flexural response was evaluated according to *ASTM C1609-05* under third point loading in the *MTS-1000* test machine (Figure 3-6). Three prisms (100 *mm* x

100 *mm* x 400 *mm*) per mix were tested. Noting that the crack often deviates from the expected path in the middle of the span, a 25mm-deep notch was sawn on the tension face at mid-span (Figure 3-7). This notch predefined the crack plane and imposed a flexural failure at the prescribed location. Two Linear Variable Displacement Transducers (LVDTs) were attached to a yoke as described in *JSCE-G 552-1999* to obtain the mid-span deflection relative to the specimen mid-height. Displacement-controlled loading at a rate of 0.05 *mm/min* was applied until the mid-span deflection reached 1/150 of the clear span.

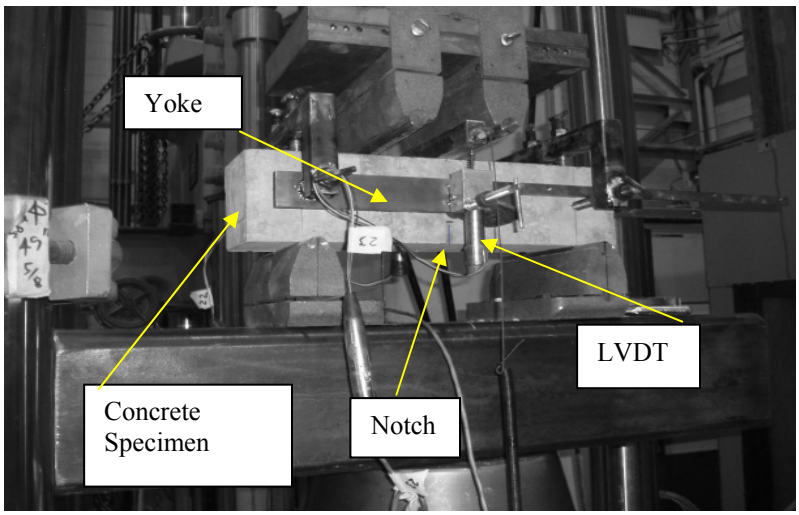

Figure 3-6: Test set-up for flexural test

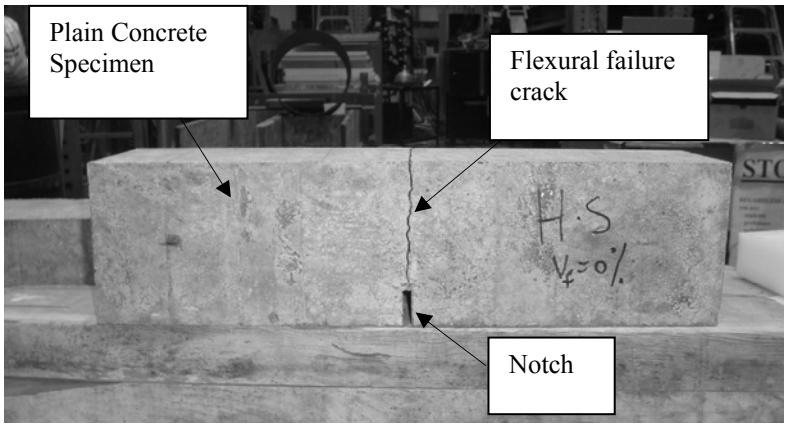

Figure 3-7: A notched specimen failed in flexure

3.4.3 Direct shear test

Direct shear tests were performed based on a modified version of the *JSCE-G 553-1999* standard (Section 2.1.4) using the *MTS-1000* test machine. Three prisms (100 *mm* x 100 *mm* x 400 *mm*) per mix were tested. As shown in Figure (3-8), the shear load was applied by a loading block with two knife edges 100 *mm* apart. A second rigid block under the specimen supported the beam by means of two knife edges separated by 105 *mm*. This left a 2.5 *mm* wide gap between the loading and the supporting knife edges that was subjected to a concentrated shear stress, with the shear failure plane expected to occur here. However, *Mirsayah and Banthia* (2002) showed that the failure plane often deviates from the expected location making the results invalid for evaluation in direct shear. To impose the shear failure in the prescribed plane, a 25 *mm* deep notch was sawn all around the specimen in the region of the gap (Figures 3-9 and 3-10).

Displacement-controlled loading was applied continuously at a rate of 0.01 *mm/s* as an equivalent rate for 0.075 *MPa/s* as per *JSCE-G 553-1999*. Data from two LVDTs attached to the sides of the specimens at the mid-span was further analyzed to obtain the shear displacement, defined here as the linear displacement of the central block as it pushed away from the adjacent sections of the prismatic specimen (Figure 3-10).

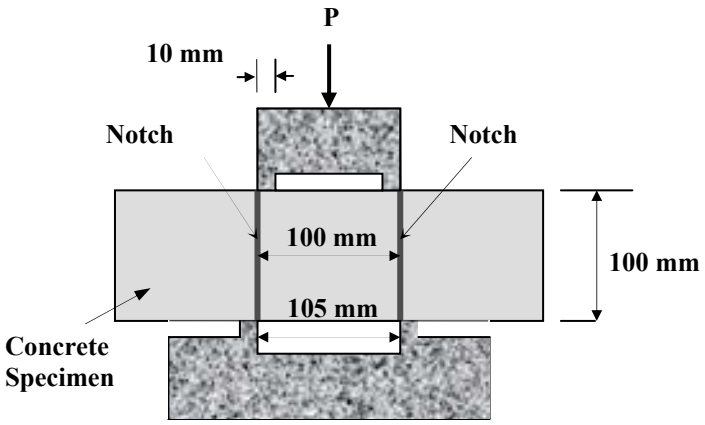

Figure 3-8: Schematic of the Direct Shear Test

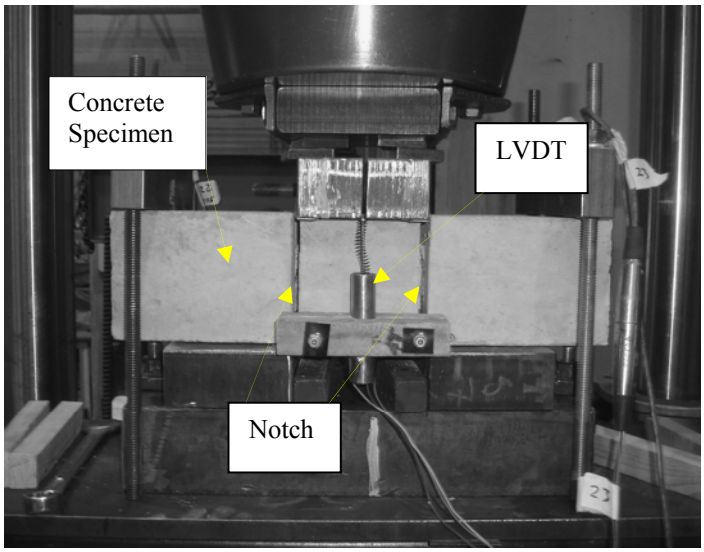

Figure 3-9: Direct shear test in progress

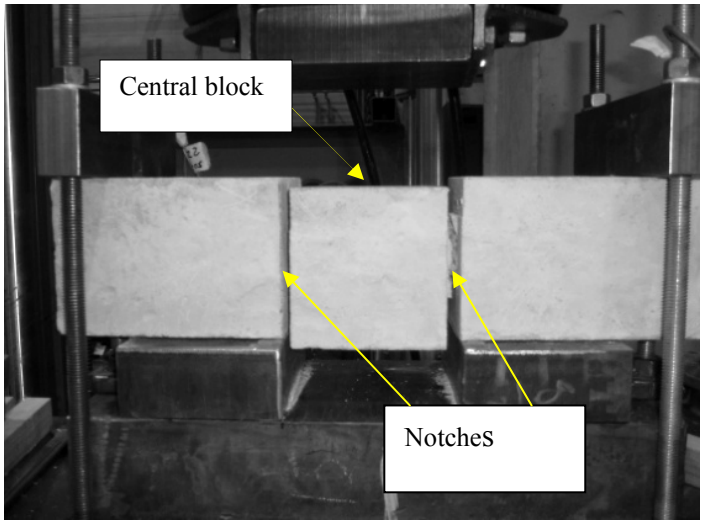

Figure 3-10: Displacement of central block of specimen in direct shear failure

4. Mechanical Properties of Concrete with/without Steel Fibers: Results and Discussion

In this chapter, the material test results for compression, flexure, and direct shear responses of regular normal strength concrete (NSC), high strength concrete (HSC), and lightweight concrete (LWC) with and without fibers are analyzed and discussed. The correlation between flexural and shear toughness for different mixes is also studied. The flexural test data for SFRC prisms is employed to derive a relationship between a uniform tensile stress along a flexural crack versus the crack mouth opening displacement (CMOD).

4.1 Compressive Strength

Figure (4-1) and Table (4-1) show the compressive response of the mixes studied in this testing program. Note that each graph in Figure (4-1) as well as strengths and toughness factors shown in Table (4-1) represent the average of three replicate tests performed for each mix. The detailed results of tests can be found in Appendix A.

As expected, within a given type of concrete the peak compressive strength remained largely unchanged regardless of the fiber content similar to the results reported by *Fanella and Naaman* (1985). However, the strain corresponding to peak stress ε'_c was slightly higher with an increase in the fiber content. This is similar to the results reported by *Soroushian and Bayasi* (1991). Also, the strain corresponding to the peak stress ε'_c was generally larger for LWC and HSC mixes in comparison to that obtained for NSC. For fiber content V_f =0% to 1%, ε'_c was between 0.002 and 0.0025 for NSC, 0.0024 and 0.0027 for LWC and 0.003 and 0.0035 for HSC. The modulus of elasticity E_c in Figure (4-1) was calculated using

a secant line between the origin and a point corresponding to the stress 0.4 f'_c on the compression stress–strain diagram. For a given type of concrete the modulus of elasticity E_c was found to be largely independent of the fiber content. Meanwhile, the average modulus of elasticity E_c of LWC was 24% lower than that of the NSC, which in turn was 21% lower than that of the HSC. The compressive toughness of different mixes is discussed in Section (4.4).

Table 4-1: Mechanical Response in Compression, Flexure and Direct Shear

		NSC			LWC			HSC		
V_f(%)		**0**	**0.5**	**1**	**0**	**0.5**	**1**	**0**	**0.5**	**1**
Compressive Strength f'_c	**Average(MPa)**	45	45	44	42	40	40	106	104	108
	COV (%)	3.1	1.3	5.7	1.4	2.3	1.2	1.6	12.8	5.4
Modulus of Elasticity E_c	**Average (10^3 MPa)**	24.7	24.9	24.1	19.3	18.9	17.7	32.3	30.8	30.9
	COV (%)	15.3	9.2	7.2	6.7	6.7	9.5	1.1	2.9	5.3
Compressive Toughness Factor T_c	**Average(MPa)**	0.12	0.20	0.26	0.10	0.17	0.2	0.15	0.33	0.38
	COV (%)	8.3	3.2	8.7	3.0	0.3	2.5	1.4	16.6	13.5
Modulus of Rupture f_r	**Average(MPa)**	3.53	4.18	5.27	2.6	3.64	6.21	5.2	6.2	9.41
	COV (%)	8.6	9.0	4.9	3.4	21.3	5.6	12	0.9	2.5
Flexural Toughness Factor T_f	**Average(MPa)**	0.17	3.78	4.84	0.04	3.08	4.97	0.12	3.98	8.01
	COV (%)	9.1	9	3.7	47.4	31.4	3.2	17.2	20.7	6.3
Shear Strength f_v	**Average(MPa)**	3.12	5.57	8.77	3.27	4.44	5.89	3.50	8.41	11.58
	COV (%)	20.3	14.2	13.3	11.6	22.5	5	6.2	17.3	16.0
Shear Toughness Factor(m=25) $T_{s,25}$	**Average(MPa)**	0.98	5.29	10.69	1.3	4.92	6.74	1.73	6.04	10.21
	COV (%)	23.3	5.3	17.8	19.1	37.6	8.8	2.5	13.5	9

NSC=Normal Strength Concrete; LWC=Lightweight Concrete; HSC=High Strength Concrete;
COV= Coefficient of Variation (for three test replicates)

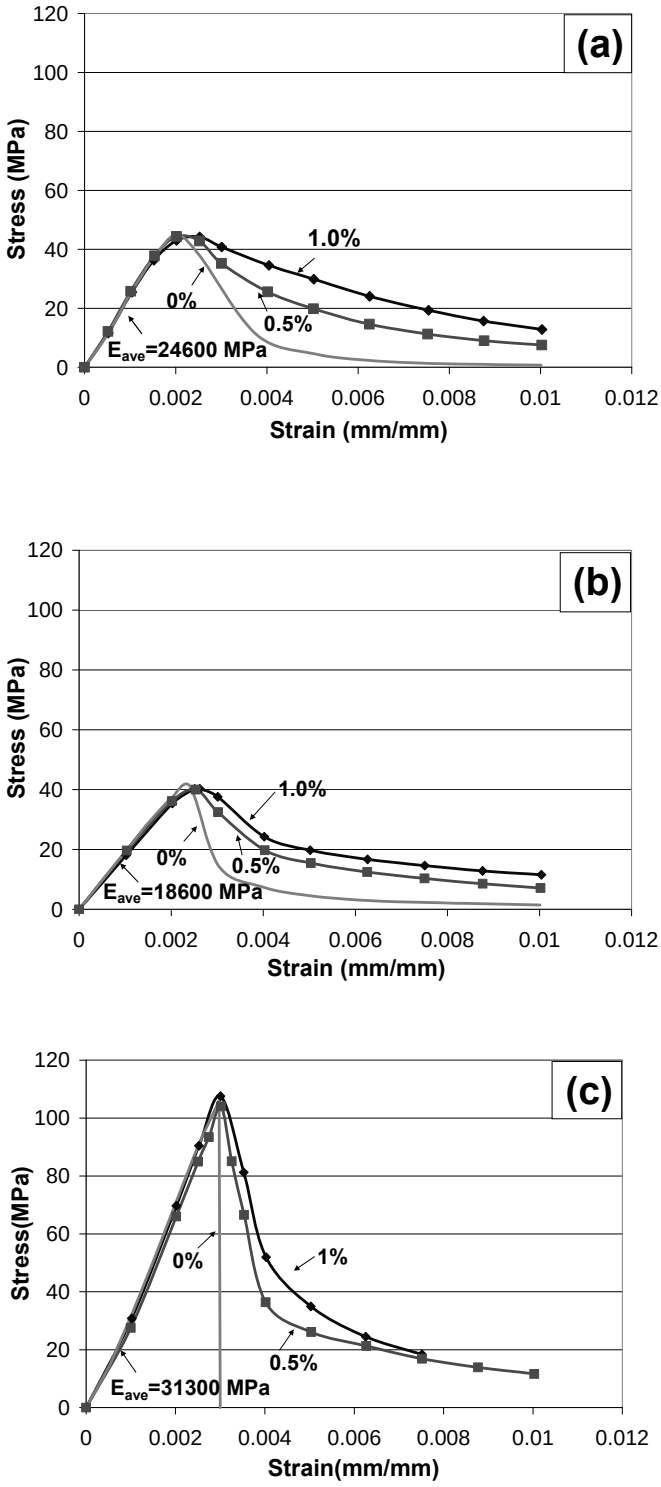

Figure 4-1: Representative Compressive Stress-Strain Response for a) Normal Strength Regular Concrete; b) Lightweight Concrete and c) High Strength Concrete

4.2 Flexural Strength

The load-deflection responses from representative flexural tests on the mixes evaluated in this study are shown in Figure (4-2). The modulus of rupture f_r was evaluated as the maximum tensile stress corresponding to the peak flexural load and is listed in Table (4-1). The height of prism section after accounting for the notch depth was used in the evaluation of f_r. Note that each graph in Figure (4-2) as well as strengths and toughness factors shown in Table (4-1) represent the average of three replicate tests performed for each mix. The detailed results of tests can be found in Appendix A.

For plain NSC and LWC mixes with average f'_c=45 MPa and f'_c=41 MPa, respectively, the values of f_r and corresponding deflection were similar. *Zhang et al.* (2004) have noted a similar trend. Whereas the addition of fibers resulted in an increase in the modulus of rupture for all three types of concrete, the steel fibers were most effective in the case of the LWC mixes (Figure 4-3), especially at the higher dosage rate. Adding steel fibers at 0.5% by volume improved the f_r by 18% for the NSC, 10% for the HSC mix and 12% in the LWC; however, the corresponding increase in f_r for 1% fiber volume fraction were 50%, 70% and 100%, respectively (Figure 4-3 and Table 4-1). Previous studies on the effect of steel fibers on the tensile response of structural LWC indicate a similar trend both in flexure and in splitting tension (*Balaguru and Foden* 1996).

The flexural toughness of different mixes is discussed in Section (4.4).

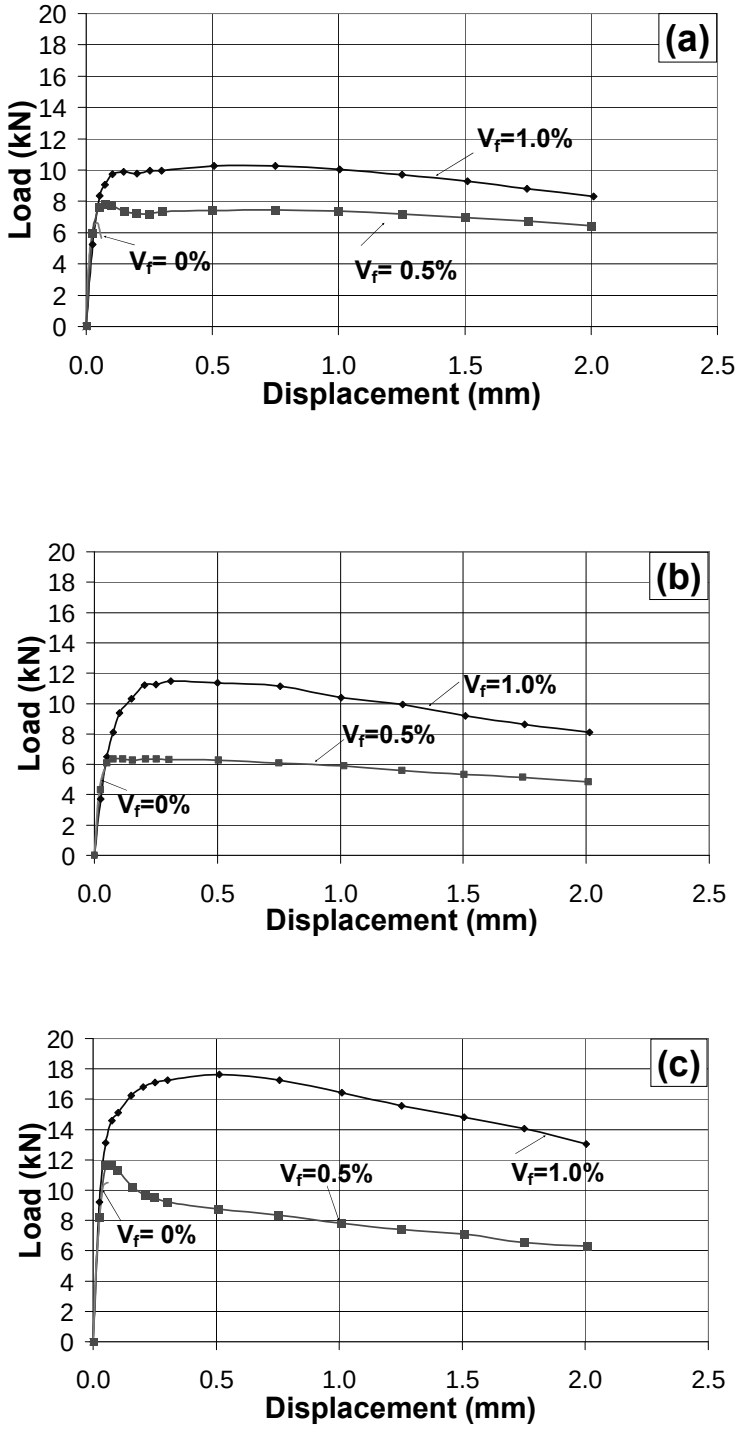

Figure 4-2: Representative Flexural Response of a) Normal Strength Regular Concrete; b) Lightweight concrete and c) High Strength Concrete.

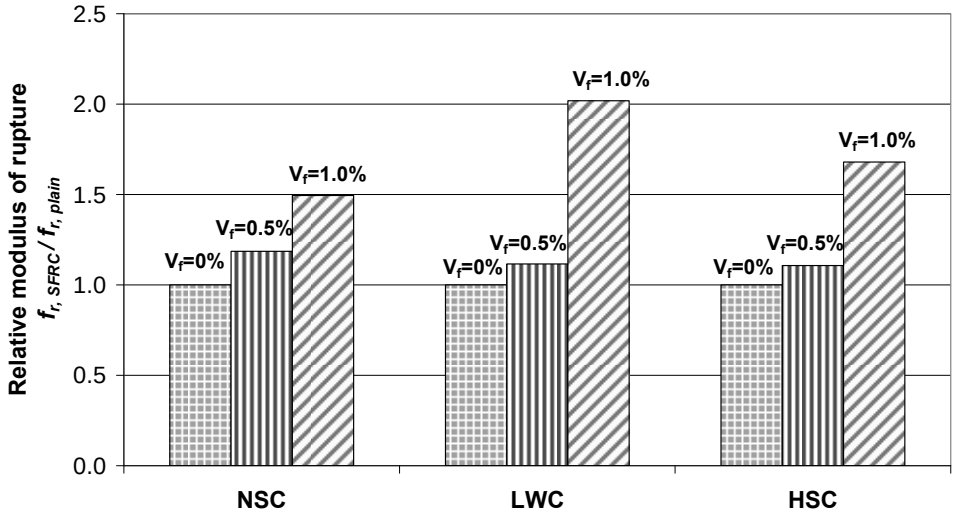

Figure 4-3: Modulus of rupture of SFRC expressed relative to that of the corresponding plain matrix.(NSC: Normal Strength Regular Concrete; LWC: Lightweight Concrete; HSC: High Strength Concrete)

4.3 Shear Strength

The load-displacement response in shear is shown in Figure (4-4). The maximum shear stress, f_v, was calculated as an average value of the stress over the loaded cross-section as follows:

$$f_v = P_{peak} / (2bh) \tag{4-1}$$

where P_{peak} refers to the peak load recorded during the direct shear test. The dimensions b and h are the width and height, respectively, of the prism section after accounting for the notch dimensions. Based on Equation (4-1), the average shear strengths of the nine mixes in this study are listed in Table (4-1). Note that each graph in Figure (4-4) as well as strengths and toughness factors shown in Table (4-1) represent the average of three replicate tests performed for each mix. The detailed results of tests can be found in Appendix A.

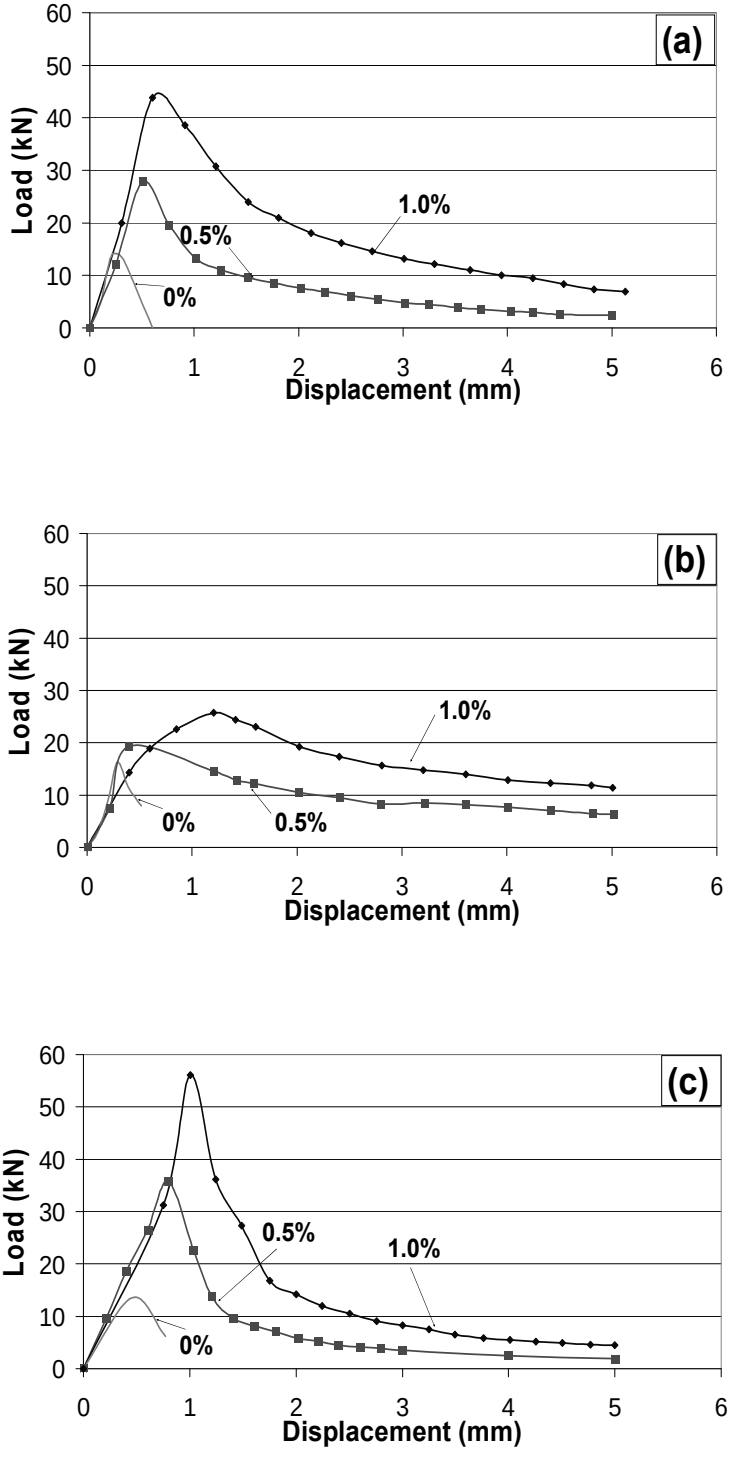

Figure 4-4: Representative Shear Test Results (a) Normal Strength Regular Concrete; b) Lightweight Concrete and c) High Strength Concrete.

Inclusion of steel fiber led to an increase in the direct shear strength for all the mixes evaluated in this study. To estimate the effect of the steel fiber content on the shear strength of different types of concrete, the following relationships derived and plotted in Figure (4-5) from the shear strength and the fiber volume fraction using a linear regression analysis:

$$f_{v,n} = f_{v0,n} + 5.65V_f \quad \text{(NSC)} \tag{4-2a}$$

$$f_{v,l} = f_{v0,l} + 2.62V_f \quad \text{(LWC)} \tag{4-2b}$$

$$f_{v,h} = f_{v0,h} + 8.74V_f \quad \text{(HSC)} \tag{4-2c}$$

Here, f_v is the shear strength (MPa) for SFRC, f_{v0} is the shear strength for plain concrete (MPa) and V_f is the volume fraction of steel fibers. Further, the subscripts *n*, *l* and *h* refer to the NSC, LWC and HSC mixes, respectively.

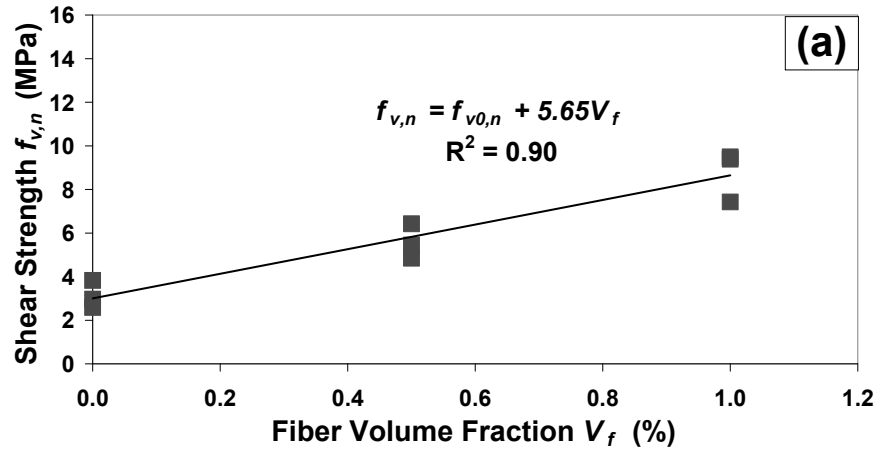

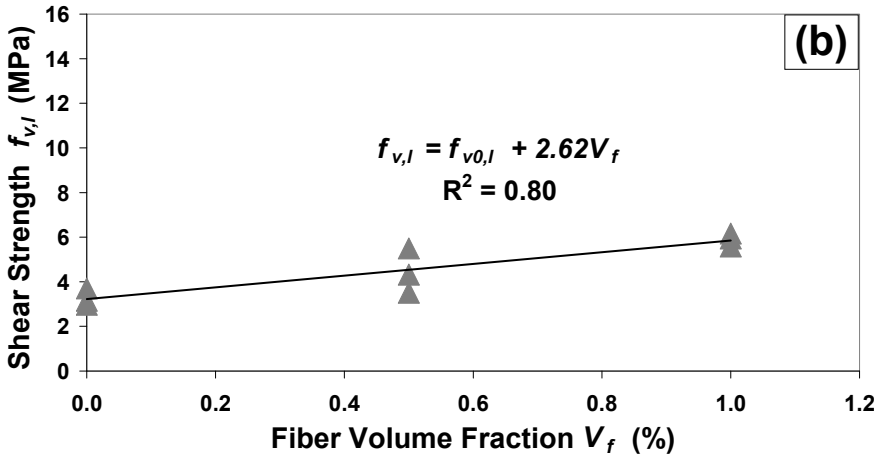

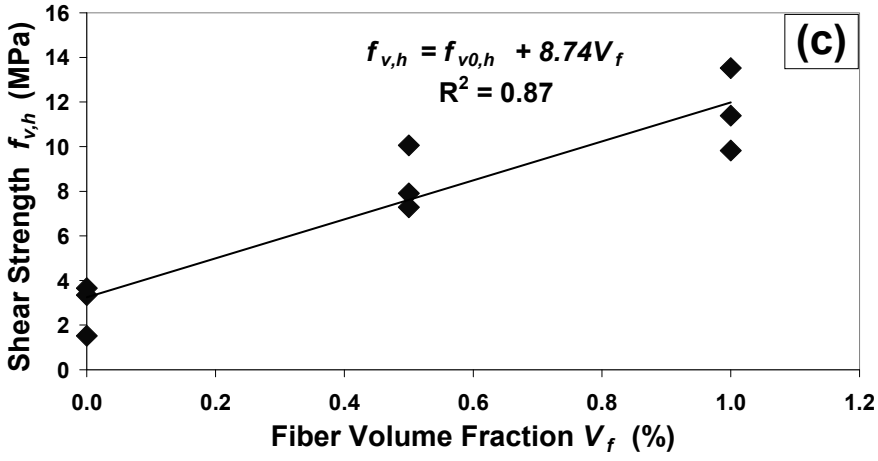

Figure 4-5: Relationship between shear strength and volume fraction of steel fibers for a) Normal Strength Regular Concrete; b) Lightweight concrete and c) High Strength Concrete.

Valle and Buyukozturk (1993) noted about 60% increase in shear resistance of HSC (f'_c =62~80 *MPa*) and 36% for NSC (f'_c =26~34 *MPa*) after including 1% by volume of steel fibers. This is similar to the results in the current study. As seen in Figure (4-6) the relative improvement in the shear strength due to fibers was highest for the HSC, which was followed closely by the NSC. It is well known that the fiber-matrix bond is superior in higher strength mortars (*Naaman and Najm* 1991). This was reflected in the stronger pre-peak shear response of the fiber reinforced high strength specimens. However, in the absence of steel fibers, the regular and high strength concrete mixes had similar shear strength (Table 4-1).

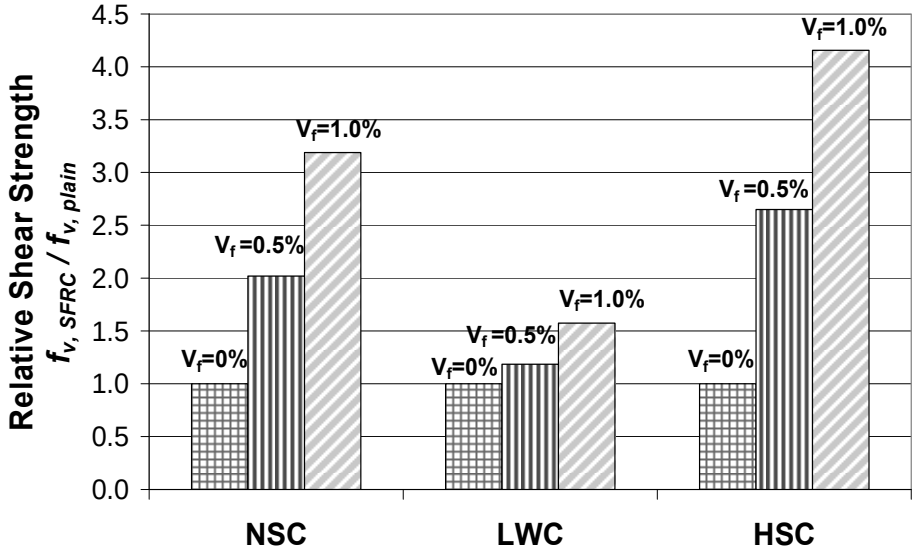

Figure 4-6: Shear strength of SFRC expressed relative to that of the corresponding plain matrix. (NSC: Normal Strength Regular Concrete; HSC: High Strength Concrete; LWC: Lightweight Concrete)

The lightweight matrix did not benefit as much from the presence of fibers in terms of peak shear strength enhancement. This was quite the opposite of the trend observed with their flexural response described in Section (4.2) and illustrated in Figure (4-3). However, between the NSC and the LWC, while the

compressive strength of the matrix remains the same, the mechanism of failure was distinctly different as seen in Figure (4-7). The normal weight aggregates in the NSC resisted shearing so that the path of the progressing crack through the mortar and around aggregates was longer. This provided additional keying action for the aggregate interlock mechanism and allowed the steel fibers to be more active in bridging the paste along the cracking path. On the other hand, in the LWC (Figure 4-7b), the weaker lightweight aggregates fractured and so reduced the length of the cracking path. Therefore, in the LWC, the aggregate interlock and the ability of fibers to bridge the paste were less than the NSC. Meanwhile, the sudden and early fracture of lightweight aggregates did not allow the fiber-paste bond to be sufficiently mobilized. A weaker fiber-paste bond along a shorter cracking path in LWC both resulted in smaller enhancement in the peak shear strength. Fracture in normal aggregates was also observed for the HSC mixes, likely due to the improvement in the strength of the paste compared to the strength of the aggregates. However, the aggregate resistance before fracture and the fiber-paste bond were both strong enough to offer adequate crack resistance even along a shorter cracking path. As a result, the fiber efficiency was highest for the shear strength of the HSC mixes.

The shear toughness of different mixes is discussed in Section (4.4).

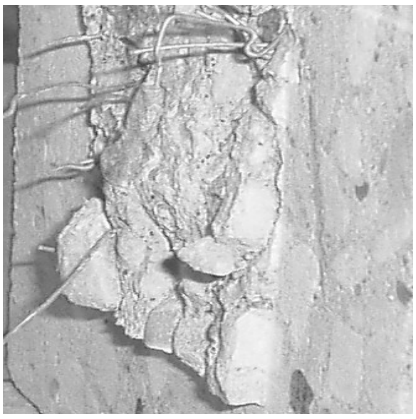

a) Normal Strength Concrete

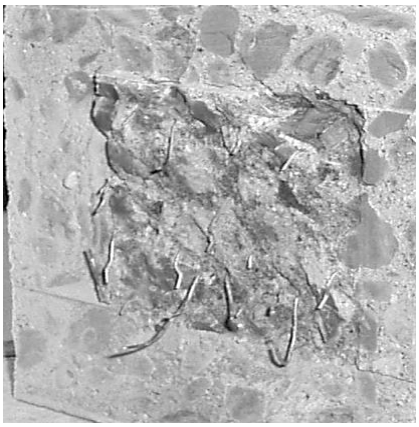

b) Lightweight Concrete

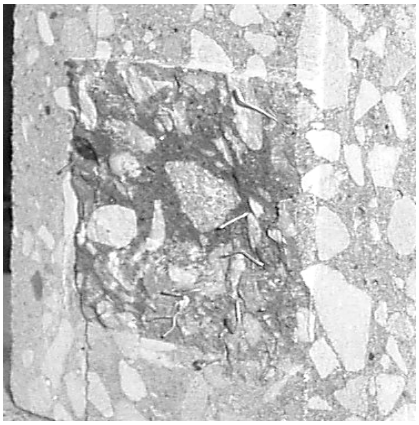

c) High Strength Concrete

Figure 4-7: Fracture Surface of SFRC Mixes with 0.5% Volume Fraction of Steel Fibers.

4.4 Toughness Factors (Post-Peak Response)

In this section, the compressive, flexural, and shear toughness of concrete with and without fibers is discussed. The correlation between flexural and shear toughness for different mixes is also studied.

4.4.1 Compressive Toughness Factor

While the introduction of steel macro-fibers to concrete has negligible effect on either the compressive strength or the pre-peak response, there is a significant influence on the post-peak energy dissipation (*Fanella and Naaman* 1985, *Ezeldin and Balaguru* 1992). The improvement in ductility in the post-peak phase can be captured by a parameter called the Compressive Toughness Factor (CTF) and a similar approach has been taken here. To this end, the load-deformation plots from the *ASTM C39-05* tests on 100 *mm* x 200 *mm* cylinders were analyzed to yield the stress-strain curves. The post peak response in compression was evaluated in previous research (e.g. *Fanella and Naaman* 1985, *Taerwe 1992*) by considering an area under the stress strain plot to a certain value of axial strain (0.7%~1.5%). Taking in to account the brittle nature of the HSC and LWC mixes during this study, the CTF was defined here as the area under the compressive stress-strain plot up to 1% axial strain (Table 4-1). The CTF from each type of concrete was normalized with respect to the corresponding plain mix without fibers ($T_{c,SFRC}$ /$T_{c,plain}$) and plotted in Figure (4-8). In compression, the fiber efficiency as given by the relative increase in CTF was the same in all three types of concrete.

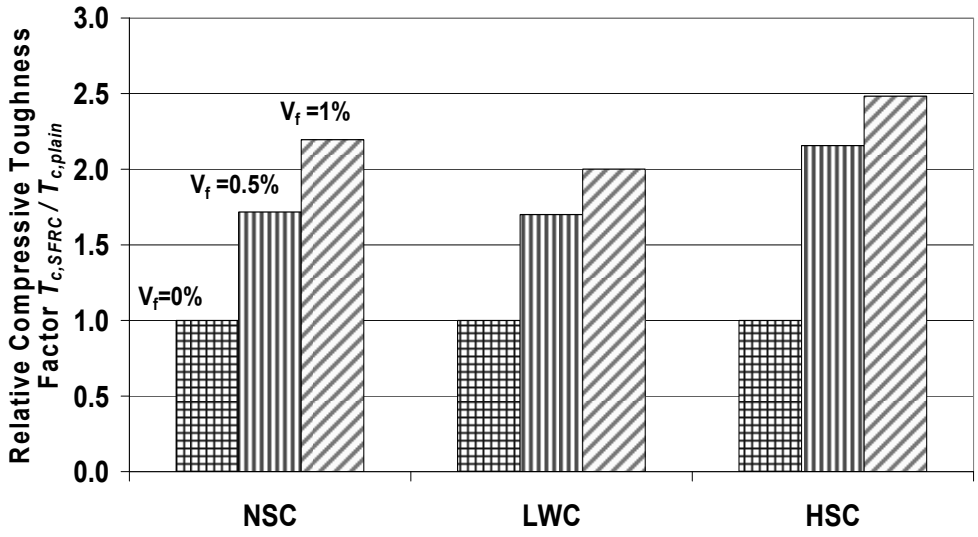

Figure 4-8: Compression toughness factor for steel fiber reinforced concrete normalized with respect to the corresponding plain mix.

4.4.2 Flexural Toughness Factor

As described in Section (2.1.2), steel macro-fibers introduce post-crack energy dissipation under flexural loading. In *ASTM C1609-05*, this change from a brittle failure to a ductile failure is captured by a parameter called the flexural toughness T_{150}^{D}. The flexural toughness T_{150}^{D} is measured as the area under flexural load-deflection curve up to a maximum deflection of 1/150 of the span. The *JSCE-G 552-1999* normalizes T_{150}^{D} by $bh^2/150$ to arrive at a size-independent parameter called Flexural Toughness Factor (FTF). The *JSCE-G 552-1999* expression has the following form:

$$T_f = \frac{A_f L}{\delta_{max} bh^2} \tag{4-3}$$

where:

T_f: flexural toughness factor (N/mm^2)

A_f: the area under load-deflection diagram from deflection 0 to L/150 (*N.mm*)

L: specimen span (*mm*)

δ_{max}: deflection of L/150 (*mm*)

b: width of the specimen (*mm*)

h: height of the specimen after accounting for the notch depth (*mm*)

The flexural toughness factors in this study were evaluated as per Equation (4-3) and shown in Table (4-1). The FTF from each type of concrete was normalized with respect to the corresponding plain mix without fibers ($T_{f,SFRC}$ /$T_{f,plain}$) and plotted in Figure (4-9). The LWC mixes gained the highest flexural toughness enhancement due to fibers. The superior fiber efficiency for the FTF in LWC mixes may in some measure be due to the relatively low absolute value in the plain LWC.

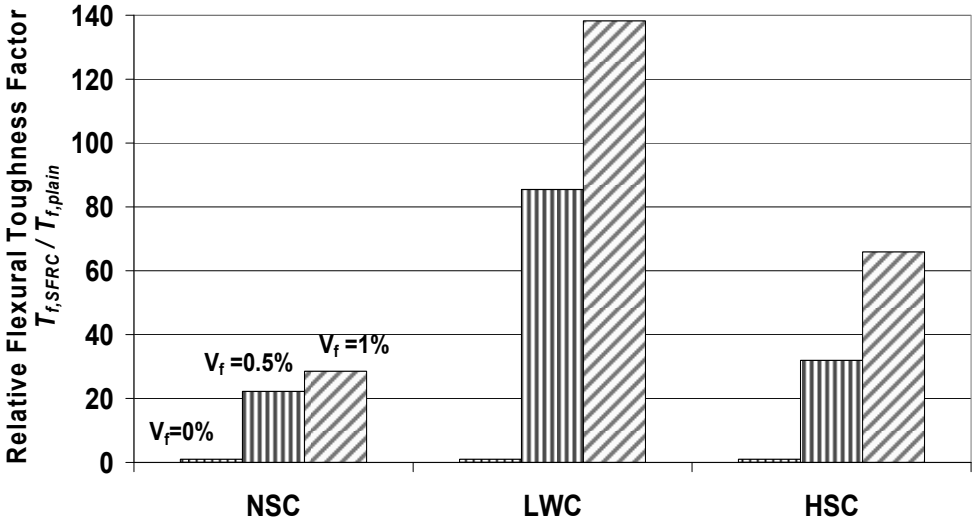

Figure 4-9: Flexural toughness factor for steel fiber reinforced concrete normalized with respect to the corresponding plain mix.

4.4.3 Shear Toughness Factor

An approach similar to the derivation of the flexural toughness factor described by Equation (4-3) in Section (4.4.2) was adopted by *Higashiyama and Banthia* (2008) to define a Shear Toughness Factor (STF) of SFRC beams tested as per the *JSCE-G 553-1999* method. In this study, a similar approach has been taken to evaluate the STF, $T_{s,m}$, by using the following equation:

$$T_{s,m} = \frac{A_v h}{\delta_s b h^2} = \frac{A_v}{\delta_s b h} \tag{4-4}$$

where:

$T_{s,m}$: shear toughness factor (N/mm^2)

A_v : the area under direct shear load-displacement curve from displacement 0 to $\delta_s = h/m$ ($N.mm$) (the parameter m is discussed below)

b: width of the specimen after accounting for the notch depth (mm)

h: height of the specimen after accounting for the notch depth (mm)

Given the relative familiarity with standardized flexural testing and absence of a standard direct shear test in the North America, *Higashiyama and Banthia* (2008) proposed use of a linear correlation between STF and FTF. They used different values of $\delta_s = h/m$, where m=80, 40, 20 and 10 to compare the FTF from Equation (4-3) versus STF from Equation (4-4) for 6 specimens of normal strength SFRC (41~47 *MPa*) and lightweight aggregates SFRC (21~45 *MPa*) including crimped steel fibers. A similar exercise was performed in the current study to compare the flexural and shear toughness factors for NSC, LWC and HSC mixes with hooked end steel fibers. However, in order to study the role of the aggregate type and concrete density on toughness of SFRC, the NSC and LWC mixes in the current study were cast to the same compressive strength (f'_c=41~45 *MPa*). Meanwhile, the HSC mix was cast to the same density as NSC mix but with much higher strength (f'_c=104~108 *MPa*), to also examine the effect of high matrix strength on

the toughness factors of SFRC. The maximum shear displacement δ_s was taken to be h/m, where m was variously chosen as 10, 20, 25, 40 and 50 and the results are plotted versus FTF in Figures (4-10) to (4-12). A value of m = 50 gave the best linear fit for NSC mixes (Figure 4-10), while the best fit was obtained for m = 10 in the cases of the LWC (Figure 4-11) and HSC mixes (Figure 4-12). Accordingly, the best linear correlation between STF and FTF for different type of mixes was obtained as:

$T_{sn,50} = 1.78T_{fn} + 1.33$ (MPa) for NSC (4-5a)

$T_{sl,10} = 0.66T_{fl} + 0.49$ (MPa) for LWC (4-5b)

$T_{sh,10} = 1.14T_{fh} + 0.44$ (MPa) for HSC (4-5c)

Where:

$T_{sn,50}$: shear toughness factor for NSC and $m=50$

T_{fn} : flexural toughness factor for NSC

$T_{sl,10}$: shear toughness factor for LWC and $m=10$

T_{fl} : flexural toughness factor for LWC

$T_{sh,10}$: shear toughness factor for HSC and $m=10$

T_{fh} : flexural toughness factor for HSC

Note that the FTF or STF value for each data point in Figures (4-10) to (4-12) represent average FTF or STF for three replicate specimens taken from the same mix batch. The coefficient of variation for FTF and STF ($m=25$) values are shown in Table (4-1). The FTF and STF values for all specimens in this study are given in Appendix A.

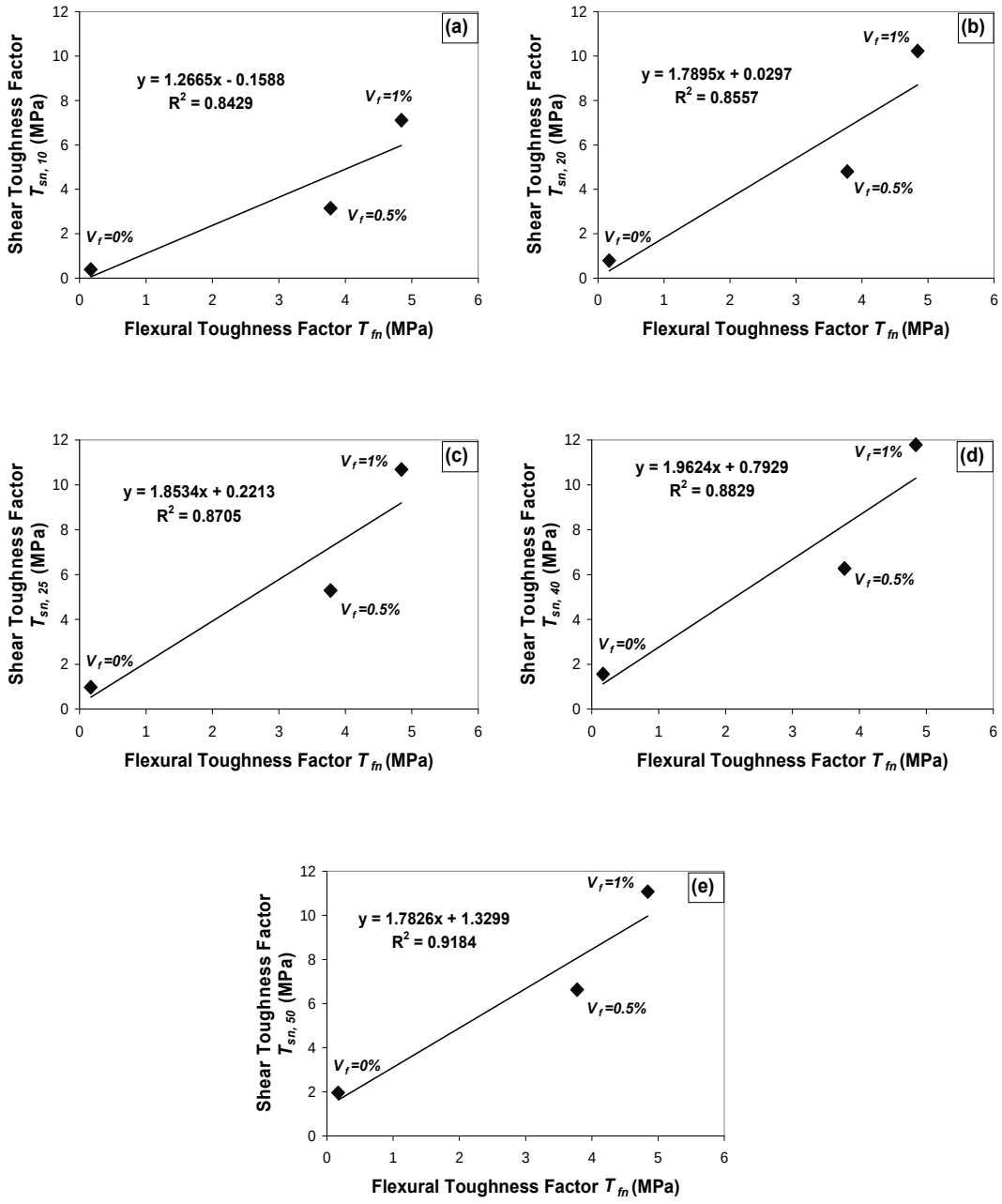

Figure 4-10: Correlation between the Flexural and Shear Toughness Factors of Normal Strength Concrete for a) $\delta_s = h/10$ b) $\delta_s = h/20$ c) $\delta_s = h/25$ d) $\delta_s = h/40$ e) $\delta_s = h/50$

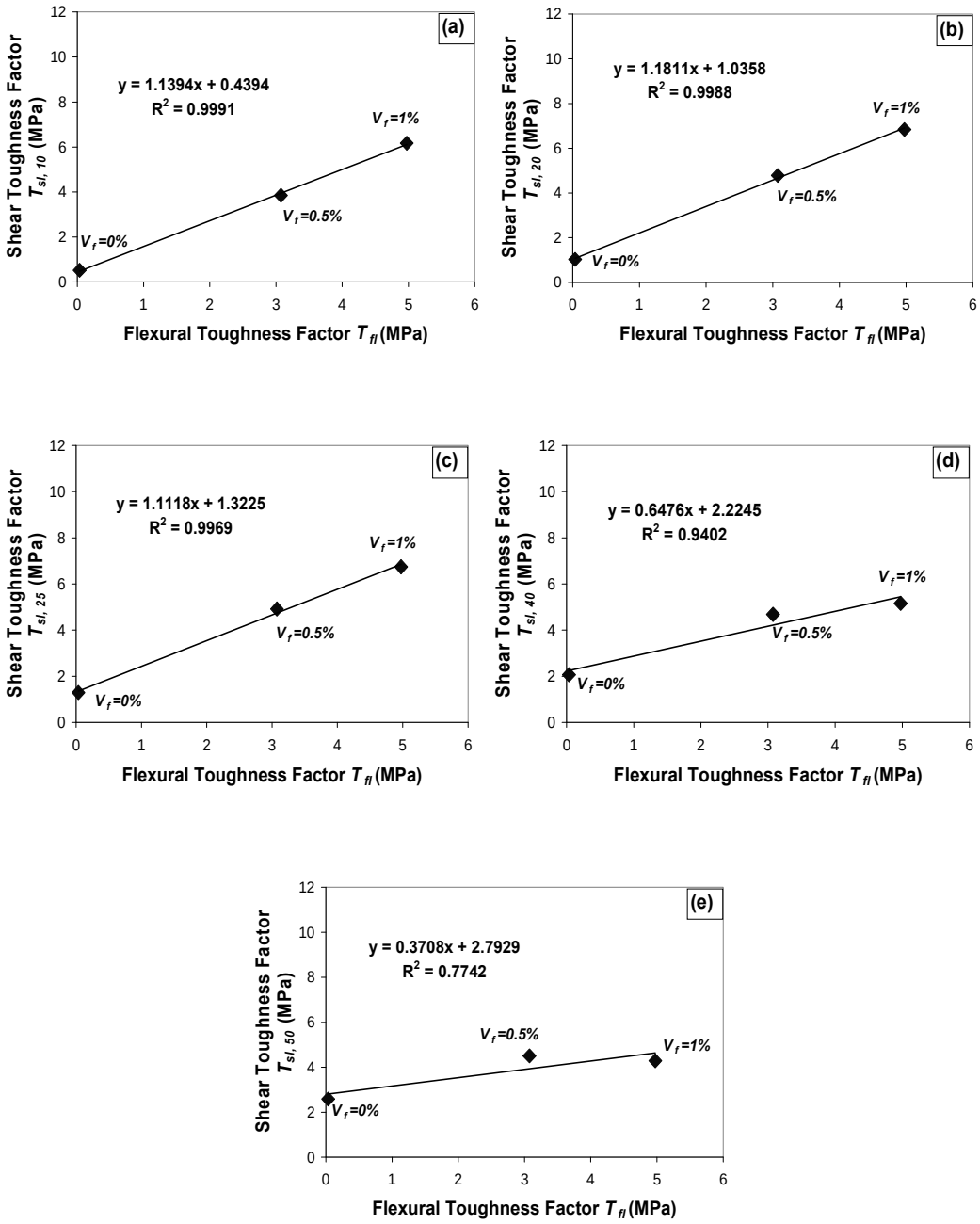

Figure 4-11: Correlation between the Flexural and Shear Toughness Factors of Lightweight Concrete for a) $\delta_s = h/10$ b) $\delta_s = h/20$ c) $\delta_s = h/25$ d) $\delta_s = h/40$ e) $\delta_s = h/50$

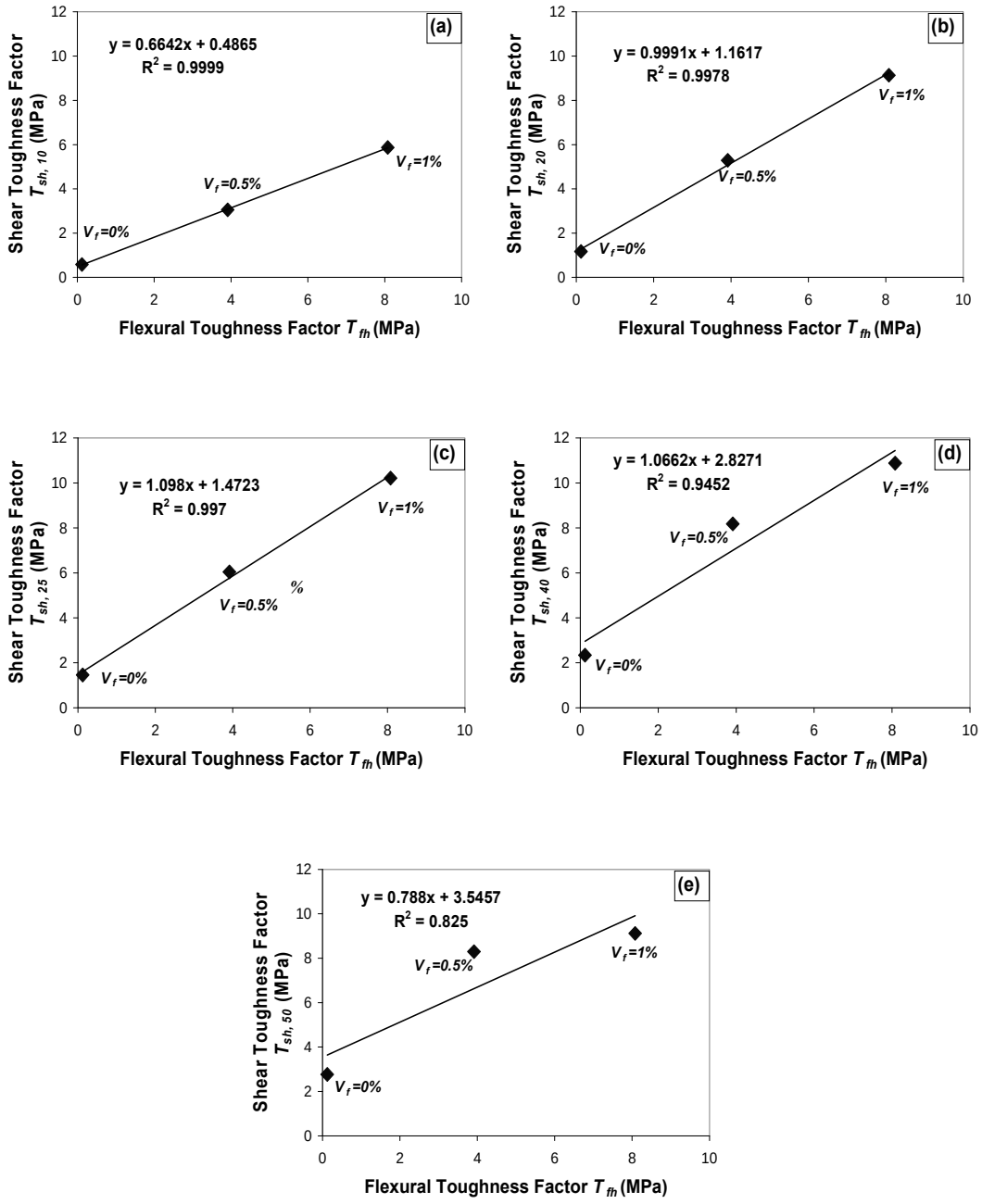

Figure 4-12: Correlation between the Flexural and Shear Toughness Factors of High Strength Concrete for a) $\delta_s = h/10$ b) $\delta_s = h/20$ c) $\delta_s = h/25$ d) $\delta_s = h/40$ e) $\delta_s = h/50$

Equations (4-5a) to (4-5c) indicate that the FTF of NSC, LWC and HSC can be used to estimate the corresponding STF up to a shear displacement of $\delta_s=h/50$, $\delta_s=h/10$, and $\delta_s=h/10$, respectively. However, with little loss of accuracy in the linear estimation, the correlation between FTF and STF for all mixes was examined in Figure (4-13). The best fit was obtained for $m=25$ or $\delta_s=h/25$:

$$T_{s,25} = 1.24T_f + 1.29 \quad \text{(MPa)} \tag{4-6}$$

where $T_{s,25}$ is the STF for $m=25$ or $\delta_s=h/25$.

In the current study the height of shear specimens after deducting the notch depth was about h=50 *mm*. This means that $\delta_s=h/25=2$ *mm*. *Higashiyama and Banthia* (2008) also used notched *100 mm* x *100 mm* x *350 mm* prisms for direct shear tests and the height of specimens after accounting for notch depth was h=80 *mm*. They obtained the best linear correlation between FTF and STF for the case $m=40$ or $\delta_s=h/40=2$ *mm* which is the same absolute displacement value obtained in this research for the best fit. Furthermore, this value of maximum direct shear displacement in STF (2 *mm*) is identical to the maximum flexural deflection used for FTF in both studies i.e. $\delta_{max}=L/150=2$ *mm*. However, further research is needed to understand the relation between the δ_s and δ_{max}.

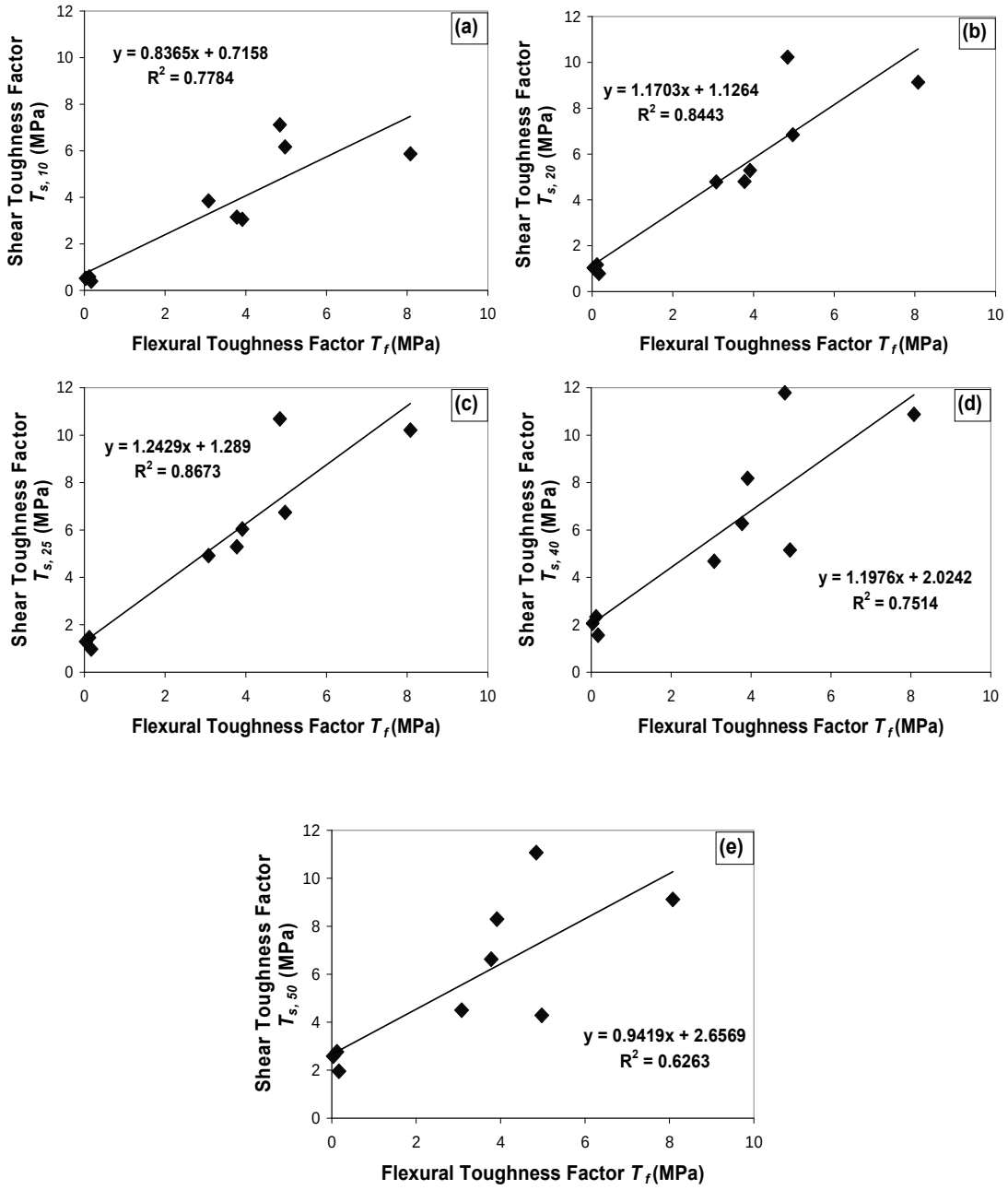

Figure 4-13: Correlation between the Flexural and Shear Toughness Factors of all mixes for a) $\delta_s = h/10$ b) $\delta_s = h/20$ c) $\delta_s = h/25$ d) $\delta_s = h/40$ e) $\delta_s = h/50$

To compare the influence of fibers on the shear toughness of all mixes in this study, the STF was evaluated based on m=25 and shown in Table (4-1). The STF (with $\delta_s = h/25$) from each type of concrete was normalized with respect to the corresponding plain concrete mix ($T_{s,SFRC} / T_{s,plain}$) and plotted in Figure (4-14). Under direct shear, the fiber efficiency on the post-peak response was highest in the NSC and not in the HSC mixes as may be expected from their pre-peak response. Recall that the improvement with fibers on the shear strength was highest for the HSC mixes (Figure 4-6). However, due to the fracture of aggregates in both LWC and HSC mixes, the post-peak phase was most promising with the NSC mixes, where the cracks traveled around the aggregate as illustrated in Figure (4-7). Clearly, while fibers can significantly enhance the shear strength of concrete, the nature of aggregates and their mode of failure can limit the improvement on the residual shear strength. As discussed in Section (2.1.4), *Higashiyama and Banthia* (2008) studied normal strength SFRC (f'_c=41~47 *MPa*) and lightweight SFRC (f'_c=21~25 *MPa*), and indicated that improvement in post-peak shear strength due to steel fibers (V_f =0.5~1%) was higher for normal strength concrete compared to lightweight concrete. However, they did not isolate the role of the aggregate type and matrix strength that may significantly affect the shear response of SFRC.

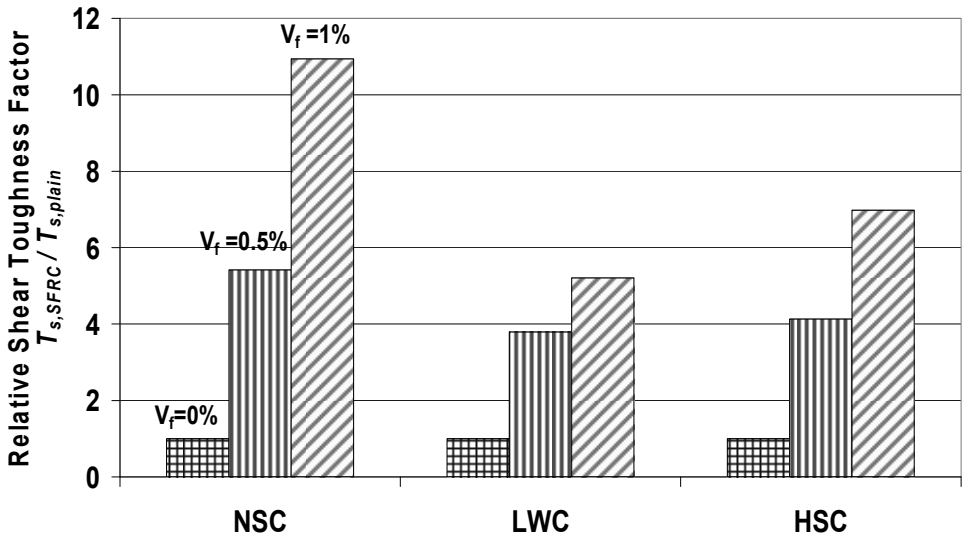

Figure 4-14: Shear toughness factor with δ_s= h/25 for steel fiber reinforced concrete normalized with respect to the corresponding plain mix.

4.5 Equivalent Uniform Tensile Stress σ_f

In this section, the contribution of steel fibers to the tension resistance across the flexural crack surfaces is quantified. An approach similar to that employed by *Dinh* (2009) (Section 2.1.2) is taken to determine the equivalent uniform tensile stress σ_f imparted by the steel fibers across a flexural crack. Figure (4-15) shows the details of a flexural test according to *ASTM C1609-05* and an idealized model for the deflection and rigid body rotation of the prism after cracking.

Figure (4-15) shows mid-span section of a flexural test prism. Since the SFRC flexural specimens in this study were notched at the mid-span, the height h is taken as specimen effective depth after deduction of notch depth. An equivalent uniform tensile stress σ_f representing the tension in the steel fibers is assumed and applied across the vertical flexural crack. Similar to the flexural model for RC members in *CSA A23.3-04*, a uniform compressive stress block with stress magnitude of $\alpha_1 f'_c$ and depth of $\beta_1 c$ is assumed here, where

$$\alpha_1 = 0.85 - 0.0015 f'_c \geq 0.67 \quad (4\text{-}7)$$

$$\beta_1 = 0.97 - 0.0025 f'_c \geq 0.67 \quad (4\text{-}8)$$

The assumption of concrete crushing at the extreme compression fiber might not be reasonable for all stages of the flexural test; however, the depth of compression zone c represents a very small percentage ($\leq 7\%$) of the total height of the prism, and the effect of this error on estimation of the equivalent tensile stress would be negligible (*Dinh* 2009).

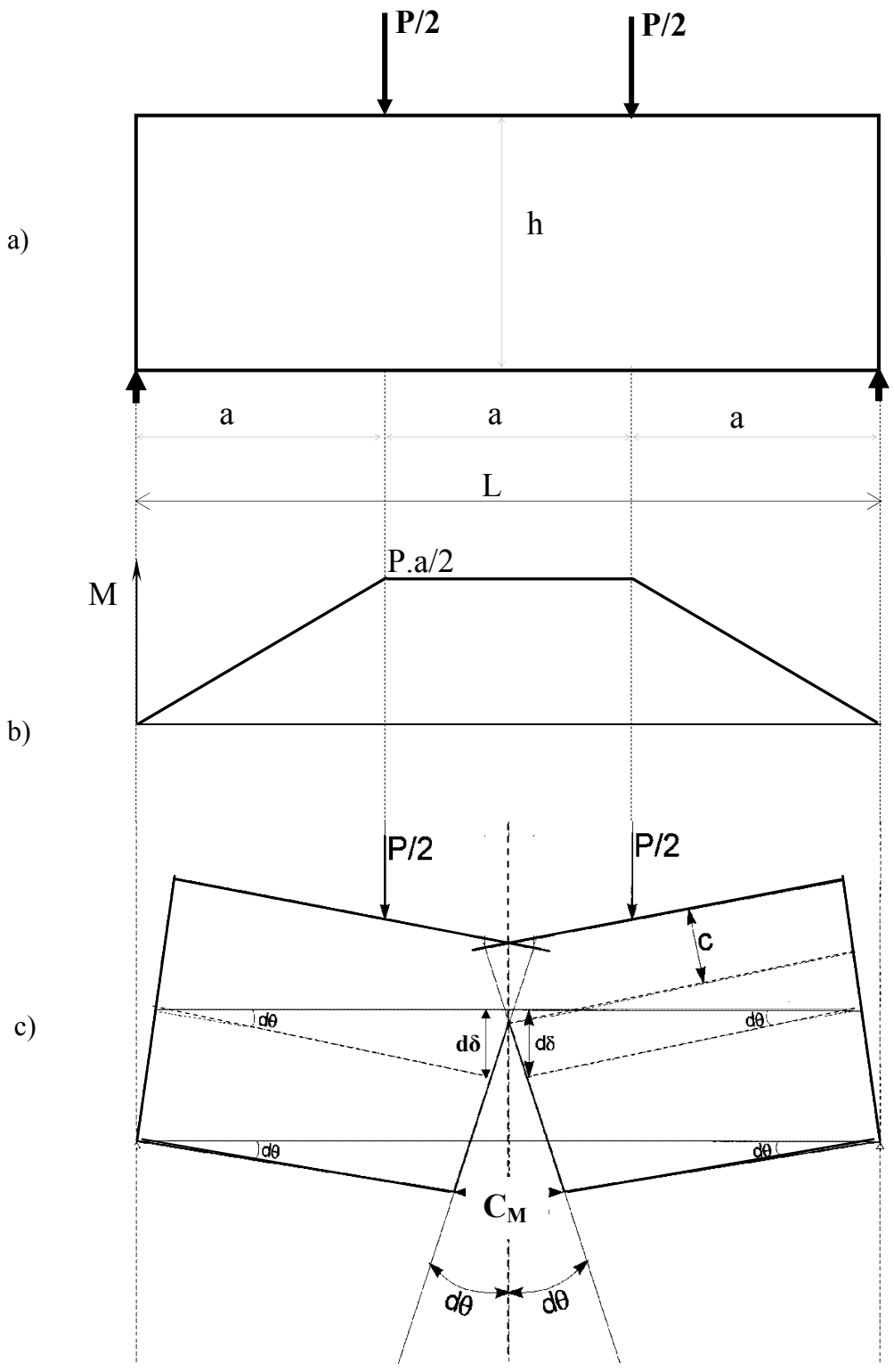

Figure 4-15: a) A typical four point flexural test for SFRC prism according to *ASTM C1609*, b) Bending moment diagram c) Idealized deflected and cracked SFRC prism (adapted from *Armelin and Banthia* 1997)

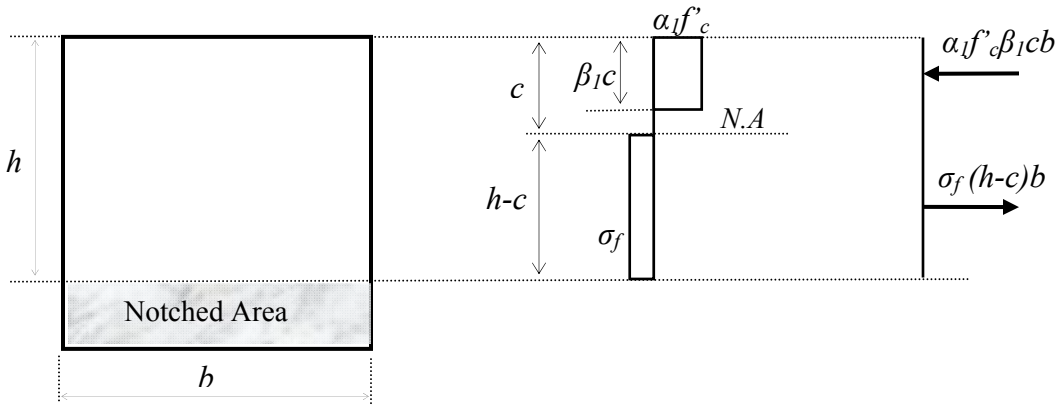

Figure 4-16: The equivalent uniform stress across the section of an SFRC prism in flexural test a) The notched section at mid-span b) Stress distribution c) Compression and Tension forces.

From flexural test at each stage of loading, the flexural moment at the notch location can be obtained as:

$$M = \frac{Pa}{2} \tag{4-9}$$

This moment must be equal to the calculated moment from the tensile and compressive forces in the section shown in Figure (4-16c):

$$M = \alpha_1 f_c' \beta_1 cb\left[\frac{h + (1-\beta_1)c}{2}\right] = \frac{Pa}{2} \tag{4-10}$$

The neutral axis depth from the compression face c for a given value of M can be obtained by solving Equation (4-10). Then, from equilibrium of the axial forces in the section, the equivalent uniform tensile stress can be calculated:

$$\alpha_1 f_c' \beta_1 cb - \sigma_f (h-c)b = 0 \tag{4-11a}$$

$$\longrightarrow \quad \sigma_f = \frac{\alpha_1 f_c' \beta_1 c}{h - c} \tag{4-11b}$$

The geometry shown in Figure (4-15c) is employed to calculate the corresponding crack mouth opening displacement (CMOD), C_M. At each stage of the flexural test with a deflection of $d\delta$, the following relation can be applied:

$$C_M = 2\, d\theta\, (h-c) = 2\,(h-c)\,\frac{d\delta}{0.5L} = 4(h-c)\frac{d\delta}{L} \tag{4-12}$$

Using the flexural test results from Section (4.2), the graph of σ_f versus C_M has been plotted for normal strength, lightweight and high strength SFRC containing V_f=0.5% and V_f=1% (Figure 4-17). Note that each graph in Figure (4-17) represents an average of three flexural test replicates.

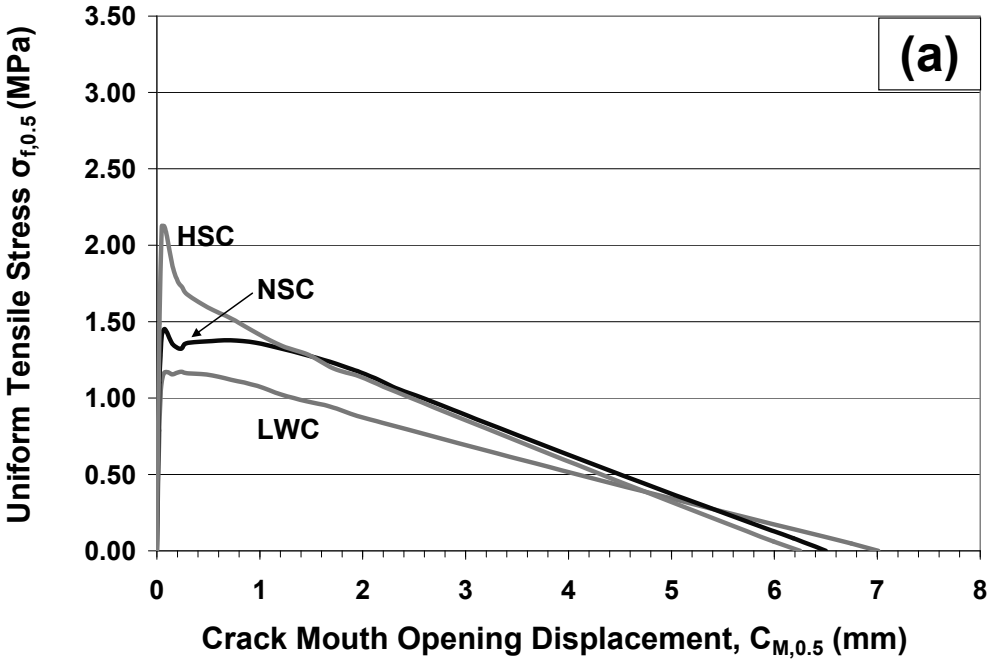

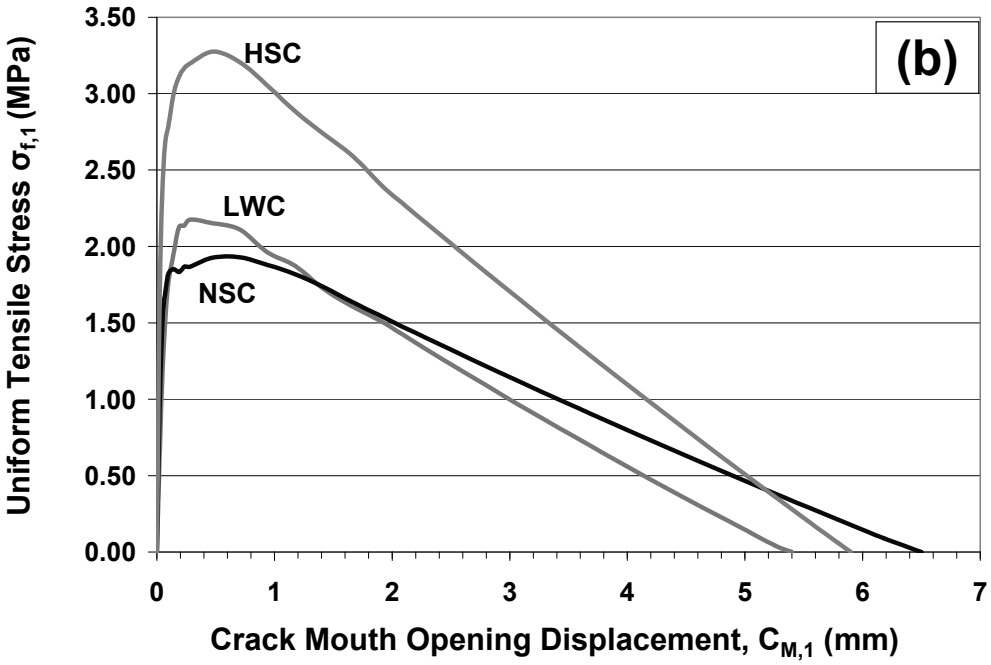

Figure 4-17: Equivalent uniform tensile stress versus CMOD for a) V_f=0.5% b) V_f=1%.

It is observed from Figure (4-17) that σ_f is higher for the case of high strength SFRC compared to the NSC and LWC. This is mainly attributed to the higher compressive strength f'_c and stronger bond between fibers and cement-based matrix (*Naaman and Najm* 1991). However, if σ_f is normalized by $\sqrt{V_f.f'_c}$, all six SFRC mixes give a similar relationship with respect to C_M (Figure 4-18).

To simplify the normalized σ_f versus C_M relationship, a bilinear model is proposed (Figure 4-18). According to this model a peak value of $\sigma_f = 2.9\sqrt{V_f.f'_c}$ occurs at C_M=0.2 *mm* and σ_f reaches zero at C_M= 6 *mm*, so:

$$\sigma_f \approx 2.9\sqrt{V_f.f'_c}\left(\frac{C_M}{0.2}\right) \qquad \text{For } C_M < 0.2 \text{ mm} \qquad (4\text{-}13a)$$

$$\sigma_f \approx 2.9\sqrt{V_f.f'_c}\left(1.03 - \frac{C_M}{5.8}\right) \qquad \text{For } C_M \geq 0.2 \text{ mm} \qquad (4\text{-}13b)$$

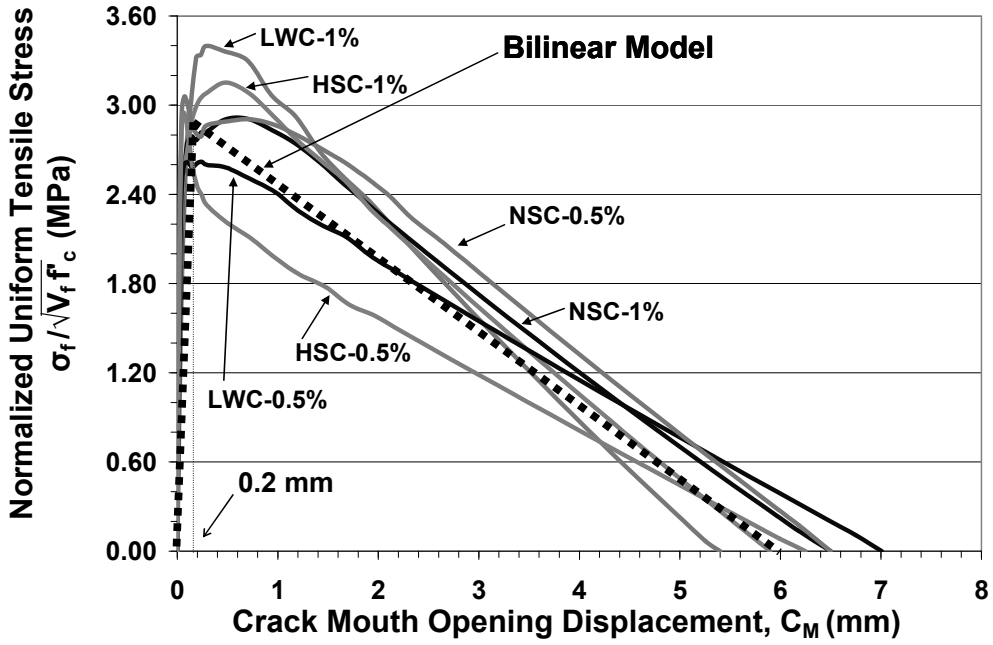

Figure 4-18: Normalized equivalent uniform tensile stress versus CMOD

5. Shear Strength of Structural SFRC Members: Experimental Program

A total of 18 steel fiber reinforced concrete (SFRC) structural specimens were designed, constructed, and tested to failure to improve the understanding of the behavior of shear-critical SFRC members. The specimens contained longitudinal reinforcement but no stirrups, and utilized different mix types selected from Chapters 3 & 4. All specimens had simple supports and were tested under single concentrated loading at mid-span (Figure 5-1). The following parameters were the main test variables considered in these 18 specimens:

- overall depth, h
- SFRC compressive strength, f'_c
- SFRC density, γ
- longitudinal reinforcement ratio, ρ

The constant parameters were:

- shear span to effective depth ratio, a/d
- steel fiber content and geometry, V_f, L_f, and D_f
- width of the specimens, b
- maximum aggregate size, a_g

In this chapter, the experimental program related to testing SFRC structural specimens is discussed. The specimen design procedure, specimen configurations, and test setup are provided. The construction of specimens and the mechanical properties of material used in the construction are also discussed. Meanwhile, the instrumentation and test procedure are explained.

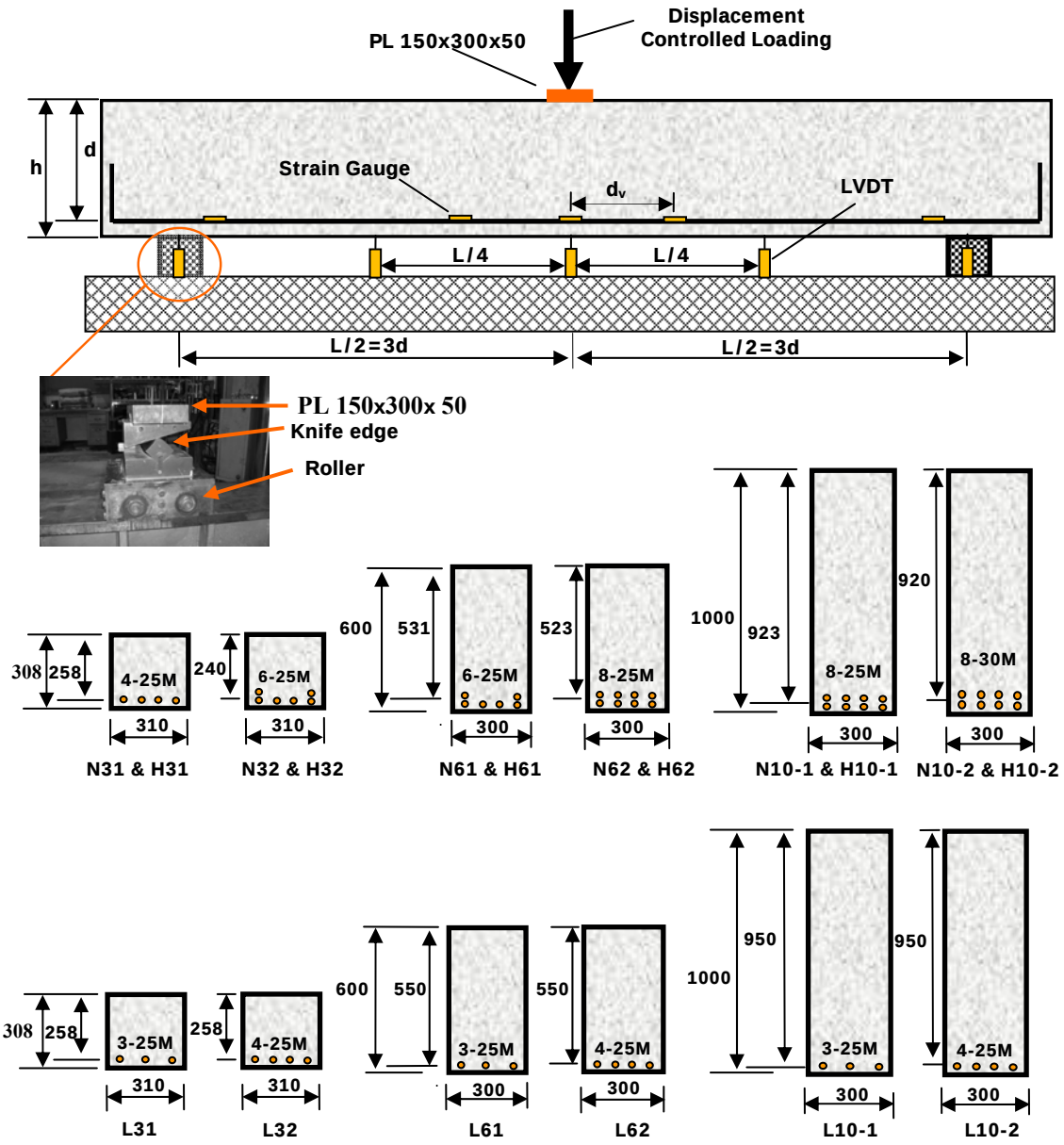

All dimensions in *mm*.

Figure 5-1: Schematic of test set-up and specimen configuration.

5.1 Test Set-up and Specimen Configuration

Specimens were tested under 3-point bending in a MTS-6000 loading frame as shown in Figure (5-1). Simple supports with knife-edges and rollers were used at each support location to allow horizontal translation and rotation. Bearing plates with dimensions 150 x 300 x 50 *mm* were used at the supports and at the loading point. To provide uniform contact between the plates and the concrete specimens, a thin layer of plaster was used at each location. Details of the specimen configurations and the test set-up are summarized in Table (5-1).

Table 5-1: Details of 18 SFRC specimens tested in this study

Specimen	b (mm)	h (mm)	d (mm)	L (mm)	f'_c (MPa)	γ (kg/m^3)	ρ %	a/d	V_f (%)	L_f/D_f	Age (days)	f_y (MPa)
N31	310	308	258	1548	23	2370	2.50	3.0	1.0	55	134	404
N61	300	600	531	3186	23	2370	1.88	3.0	1.0	55	118	404
N62	300	600	523	3138	23	2370	2.55	3.0	1.0	55	112	449
H31	310	308	258	1548	41	2410	2.50	3.0	1.0	55	119	404
N32	310	308	240	1440	41	2400	4.03	3.0	1.0	55	308	404
H61	300	600	531	3186	41	2410	1.88	3.0	1.0	55	106	404
H62	300	600	523	3138	41	2410	2.55	3.0	1.0	55	109	404
N10-1	300	1000	923	5538	41	2400	1.44	3.0	1.0	55	284	404
N10-2	300	1000	920	5520	41	2400	2.03	3.0	1.0	55	269	415
H32	310	308	240	1440	80	2450	4.03	3.0	1.0	55	300	404
H10-1	300	1000	923	5538	80	2450	1.44	3.0	1.0	55	283	404
H10-2	300	1000	920	5520	80	2450	2.03	3.0	1.0	55	279	415
L31	310	308	258	1548	22	1900	1.88	3.0	1.0	55	92	404
L32	310	308	258	1548	31	1930	2.50	3.0	1.0	55	287	404
L61	300	600	550	3300	30	1920	0.91	3.0	1.0	55	85	404
L62	300	600	550	3300	30	1920	1.21	3.0	1.0	55	81	404
L10-1	300	1000	950	5700	31	1930	0.53	3.0	1.0	55	279	404
L10-2	300	1000	950	5700	31	1930	0.7	3.0	1.0	55	275	404

5.2 Specimen Design

5.2.1 Selecting the SFRC Mixes for the Structural Stage

The results of the material tests presented in Chapter 4 showed that the compressive strength and density of concrete both play important roles in the shear and flexural performance of SFRC. Also, among the mixes studied in Chapters 3 and 4, the SFRC mixes containing V_f=1% of hooked end steel fibers showed higher improvement in the shear and flexural response compared to the mixes with V_f=*0.5%*. Furthermore, the SFRC mixes with 1% fiber content met the performance criteria for use of steel fibers in place of minimum shear reinforcement quantities based on Clause (5.6.6.2) of *ACI 318-08* (Table 5-2). According to these performance criteria the SFRC flexural strength at mid-span deflections of 1/300 and 1/150 of the span length must be greater than or equal to 90% and 75% of the first-peak flexural strength, respectively, using the *ASTM C1609-05* procedure. Therefore, three mix designs from Table (3-5) in Chapter 3 with V_f=*1%* were selected for regular normal strength, high strength and lightweight SFRC.

Table 5-2: Comparing flexural strength of SFRC mixes (V_f=*1%*) from Chapters 3 & 4 with *ACI 318-08* performance criteria

SFRC Mix	Flexural Strength (MPa)			Meeting the *ACI 318-08* Clause (5.6.6.2) Performance Criteria?
	First-Peak	L/300	L/150	
NSC	5.27	5.34	4.43	yes
LWC	6.12	5.55	4.56	yes
HSC	9.41	8.80	7.17	yes

The SFRC ready-mixes used for casting of structural specimens in Table (5-1) will be discussed in section (5.3).

5.2.2 Overall Member Geometry

To study the influence of the member effective depth *d* on the shear performance of SFRC members, a scaling factor of 3.7 has been considered in this project. Geometrically scaled specimens with total depth of *h*=308~1000 *mm* were constructed. As discussed in Section (2.2.7), *Kani et al.* (1979) showed that for shear-span to effective depth ratios of 3 and higher, the width of a member does not influence the shear stress at which shear failure occurs. Hence, a constant width of *b*=300 *mm* has been used for all specimens in this project.

A constant shear-span to effective depth ratio of *a/d=3* was adopted for all specimen sizes. This ratio was selected to obtain a constant ratio between bending moment and shear at the critical section in shear and to obtain a failure mode dominated by beam-action rather than arch action. As discussed in Section (2.2.2), previous research on the shear resistance of both RC members (e.g. *Zsutty* 1968, *Kani et al.* 1979) and SFRC members (e.g. *Mansur et al.* 1986; *Ashour et al.* 1992, *Kwak et al.* 2002) indicated that members with *a/d* > 2.5 can be predicted with sectional shear models.

5.2.3 Longitudinal Reinforcement Ratio

The SFRC members were designed so that they would reach their shear capacity before failing in flexure. To achieve this goal, the maximum shear capacity of the SFRC specimens was initially estimated. Then, the longitudinal reinforcement configuration was selected so that the predicted flexural capacity according to the *CSA A23.3-04* flexural model was at least 10% greater than that corresponding to the estimated shear resistance.

The critical section in shear for a simple span member subjected to a concentrated load (Figure 5-1) and its own weight is assumed to be at about $d_v=0.9d$ from the

mid-span, where the imposed bending moment and shear are both considerable. At this critical section, ½ of the strain in the longitudinal reinforcement (ε_x from Equation 2-7) reaches a high level and therefore Equations (2-6) & (2-5) give lower estimates of shear strength for V_{CSA}. For a given ratio of longitudinal reinforcement, the flexural capacity of a member cross-section can be calculated (*CSA A23.3-04*). The value of the concentrated load *P* can also be solved for the condition where the shear at the critical section reaches the estimated shear capacity of the SFRC specimen. In order to have a shear failure at this point, the maximum bending moment at the mid-span must remain less than the flexural capacity, otherwise the flexural failure will happen first. The longitudinal reinforcement configuration for each specimen was selected using a trial and error method.

Based on published research on the shear strength of SFRC members, the shear strength for each specimen size was estimated and expressed relative to the shear strength of geometrically similar RC members without fibers. *Dinh* (2009) observed that the shear strength of normal weight SFRC beams containing V_f *=0.75~1.5%* steel fibers reached about $2V_{ACI}$ to $3.6V_{ACI}$, where V_{ACI} represents the shear strength of similar RC beams without fibers according to *ACI 318-08*. Test results from several researchers summarized by *Parra-Montesinos* (2006) typically showed shear strengths between $1.8V_{ACI}$ and $3.8V_{ACI}$ for normal weight SFRC members with 1% steel fiber content and f'_c=18~104 *MPa*. The shear resistance mechanism of SFRC members is more complicated than direct shear resistance of SFRC prisms; however, the results of direct shear tests from Chapter 4 of this study show that the shear strength of normal and high strength SFRC specimens with V_f *=1%* can reach about 3.2 and 4.2 times, respectively, that of similar concrete prisms without fibers. This information provided useful data for estimating the shear strength of normal weight SFRC members in the current study.

As discussed in Section (2.2.1), *Kang & Kim* (2009) reported that addition of V_f =0.5% and V_f =0.75% hooked steel fibers increased the shear strength of plain lightweight concrete by about 25% and 45%, respectively. *Swamy et al.* (1993) tested lightweight SFRC beams with I-shaped cross-sections, and showed that for V_f =1% the ultimate shear strength increased by 60% to 210% compared to equivalent beams without steel fibers. The results of direct shear tests from Chapter 4 of current study indicate that the shear strength of lightweight SFRC specimens with V_f =1% can reach about 1.6 times of that of RC prisms without fibers.

The SFRC specimens with normal strength and normal density concrete (λ=1) in this project were initially estimated to fail at shear capacities equal to $2.5V_{CSA}$ or $3.2V_{CSA}$, where the V_{CSA} is the shear strength of a reinforced concrete member obtained from *CSA A23.3-04* (see Section 2.3.1). By using V_{CSA} according to the *CSA A23.3-04*, it is assumed that the size effect in shear still exists for SFRC members. Similarly, the shear strength of lightweight SFRC specimens (semi-low-density λ=0.85) were assumed to reach $1.85V_{CSA}$ or $2.5V_{CSA}$, while for high strength and normal density (λ=1) SFRC specimens the shear capacities of $2.5V_{CSA}$ or $4V_{CSA}$ were estimated. However, all of these shear capacities need to be investigated during the real tests on the SFRC specimens, toward development of a model that directly consider the influences of the longitudinal reinforcement ratio, the member depth, and the steel fibers on the shear strength.

Based on the procedure explained above and the selection of two shear capacity estimates per size, two different longitudinal reinforcement ratios were designed. Thus, the experimental results would also provide useful data to study the influence of the longitudinal reinforcement ratio ρ on the shear performance of SFRC members.

5.3 Materials

5.3.1 Concrete

As discussed in Section (5.2.1), the mix design for NSC, HSC and LWC with V_f=*1%* from Table (3-5) were provided to a ready-mix concrete local supplier. Concrete was supplied by trucks in batch sizes of 2.5 m^3 or 5.5 m^3; one concrete batch had a smaller volume of 1 m^3 (see Table 5-3). Hooked end steel fibers (type *Dramix ZP305* with L_f /D_f = 55, L_f =30 *mm*) were added and mixed with the concrete inside the truck. The maximum aggregate size for all mixes was 10 *mm*. In the concrete batches 1, 2 and 3b (Table 5-3), it was noticed that some unknown amount of extra water was added at the ready-mix plant compared to the original mix design provided to the supplier. The main source of this extra water was the remaining frozen water inside the truck mixer after washing the mixer in a cold weather during winter time. This extra water increased the water to cement ratio *w/c*, and therefore the compressive strength achieved was lower than the targeted strength (*Kosmatka et al.* 2002). A lower compressive strength could reduce the bond strength between fibers and the concrete matrix in SFRC (*Naaman and Najm* 1991). However, in Section (4.5), it was observed that for different SFRC mixes, regardless of difference in compressive strength and density, the relation between CMOD and normalized tensile stress of fibers $\sigma_f / \sqrt{V_f f_c'}$ was almost the same. Hence, the effect of a lower compressive strength on this trend was considered negligible, and the produced ready mixes were accepted. No flexural prism tests (*ASTM C1609-05*) were performed for the ready mixes, but the relationship between CMOD and normalized tensile stress of fibers $\sigma_f / \sqrt{V_f f_c'}$ was assumed to be the same as that observed for the mixes in Chapter 4. Table (5-3) shows the details of different concrete batches and corresponding constructed specimens. Compression tests according to *ASTM C39-05* were performed on 100 *mm* x 200 *mm* concrete cylinders prepared from each concrete batch and cured under the same conditions as the structural specimens (Table 5-3 & Figure 5-2).

Table 5-3: SFRC batches used for construction of specimens

Batch	Batch Volume (m^3)	Casting Date (mm/dd/yy)	Density (kg/m^3)	Constructed Specimens	f'_c at the Day of Test (MPa)				
					Cylinder Sample			Average	COV %
					(1)	(2)	(3)		
1	2.5	02/12/09	Normal weight (2370)	N31	21.7	22.5	22.4	22.2	2.0
				N61	23.2	21.9	22.7	22.6	2.9
				N62	22.5	23.3	22.8	22.9	1.8
2	2.5	02/26/09	Normal weight (2410)	H31	40.2	38.3	36.3	38.3	5.1
				H61	38.5	40.8	39.1	39.5	3.0
				H62	38.1	38.6	39.9	38.9	2.4
3a	2.5	03/23/09	Light weight (1920)	L61	30.5	31.9	29.7	30.7	3.6
				L62	30.9	32.1	29.5	30.8	4.2
3b	1	03/23/09	Light weight (1900)	L31	20.3	20.2	19.5	20.0	2.2
4	5.5	07/31/09	Normal weight (2400)	N32	43.5	42.5	44.2	43.4	2.0
				N10-1	41.5	43.9	43.9	43.1	3.2
				N10-2	44.1	42.6	43.0	43.2	1.8
5	5.5	08/11/09	Normal weight (2450)	H32	82.1	83.1	82.2	82.5	0.7
				H10-1	82.7	82.7	82.3	82.6	0.3
				H10-2	81.2	84.1	81.4	82.2	2.0
6	5.5	08/26/09	Light weight (1930)	L32	29.9	32.6	31.9	31.5	4.4
				L10-1	32.7	30.1	31.1	31.3	4.2
				L10-2	31.2	32.2	31.0	31.5	2.0

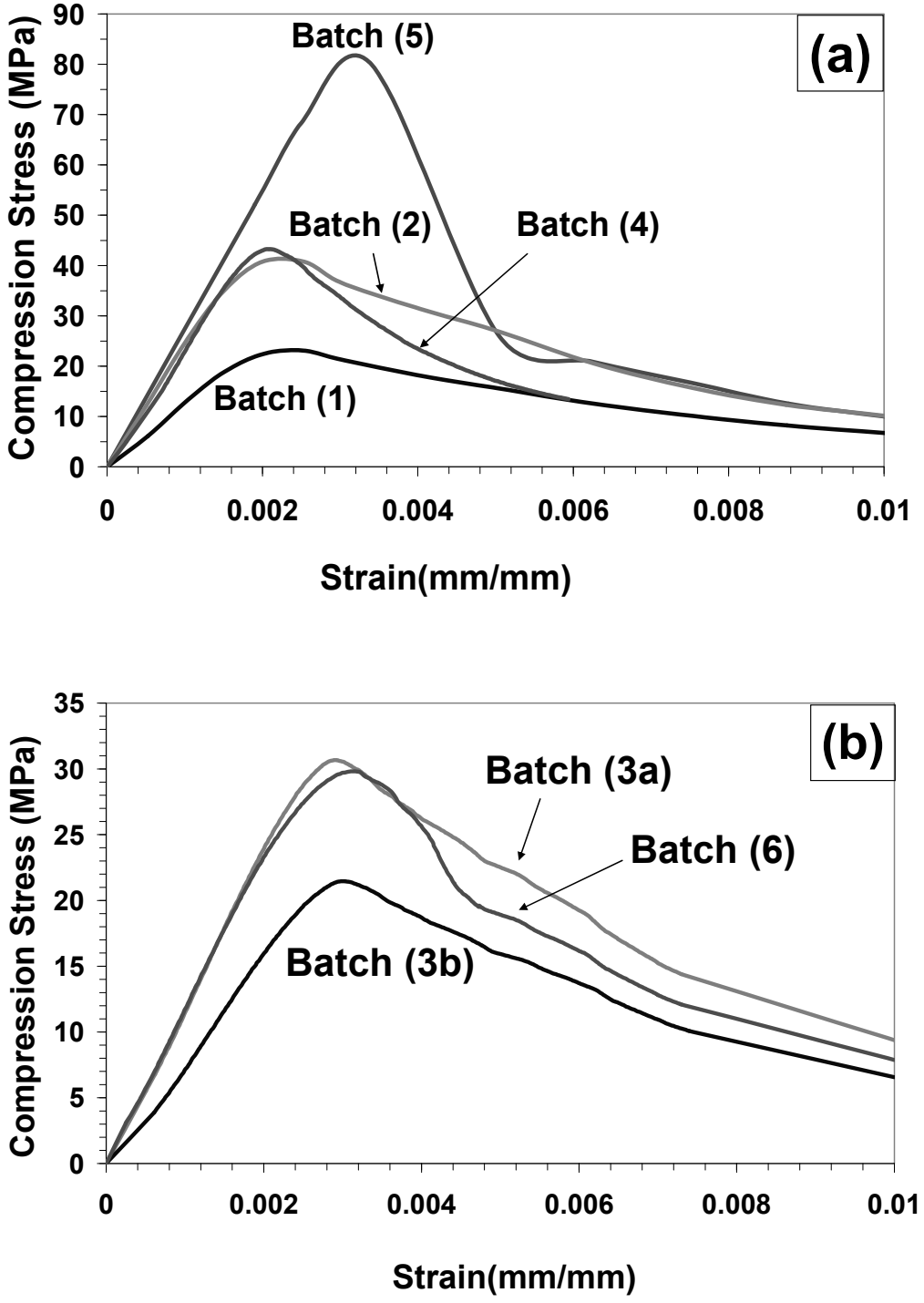

Figure 5-2: Representative compressive stress-strain response at the day of test for SFRC batches, a) normal weight SFRC, b) lightweight SFRC

5.3.2 Longitudinal Reinforcing Steel

All specimens except *N10-2* and *H10-2* contained *25M* deformed longitudinal reinforcement (Area=500 mm^2/bar). Specimens *N10-2* and *H10-2* contained *30M* deformed rebars (Area=700 mm^2/bar). Coupon tests were performed on random samples from the steel to obtain the yielding stress f_y and modulus of elasticity E_s (Table 5-4). For specimen *N62* only, a group of *25M (II)* deformed rebars with different f_y were utilized. Representative stress-strain responses for steel rebars are shown in Figure (5-3).

A standard 90^o hook as per *CSA A23.3-04* was used at the end of each bar in specimens with overall height *h*=600 and *h*=1000 mm, while bars in specimens with *h*=308 mm had a straight extension about 555 *mm* beyond the outer face of the support bearing plate. The details of reinforcing steel for each specimen are shown in Appendix B.

Table 5-4: Yielding stress f_y and modulus of elasticity E_s for steel rebars

Bar Size	f_y (MPa)					E_s (MPa)				
	Sample			Average (MPa)	COV (%)	Sample			Average (MPa)	COV (%)
	(1)	(2)	(3)			(1)	(2)	(3)		
25M(I)	401	407	405	404	0.8	185400	181800	184100	183800	1
25M(II)	455	445	448	449	1.1	206700	203500	205800	205300	0.8
30M	411	418	416	415	0.9	213400	210600	212800	212800	0.7

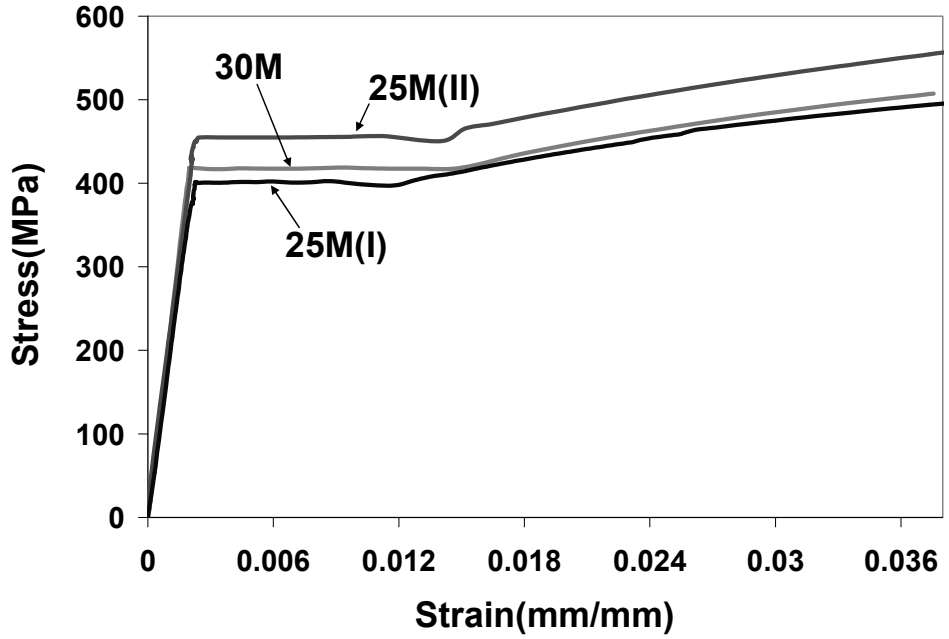

Figure 5-3: Representative tensile stress-strain response of Steel rebars

5.4 Formwork for Casting Structural Specimens

An existing metal formwork in the I. F. Morrison Structural Engineering Laboratory at the University of Alberta was used for casting the SFRC specimens with total height of *h=308 mm* (Figure 5-4). Specimens with *h=600 mm* were cast into a pair of available wooden formwork supported by a steel frame.

To cast the large size specimens with *h=1000 mm*, a new wooden formwork was built (Figure 5-5). This formwork had an overall length of 7.5 meters and was supported by an exterior steel-wooden frame for the bottom 600 *mm* of the height along the entire length. Additional bracing was provided by 2"x4" timber pieces and metal clamps at the top of the formwork. The stages of formwork construction and casting the large specimens are described and shown in Figure (5-5).

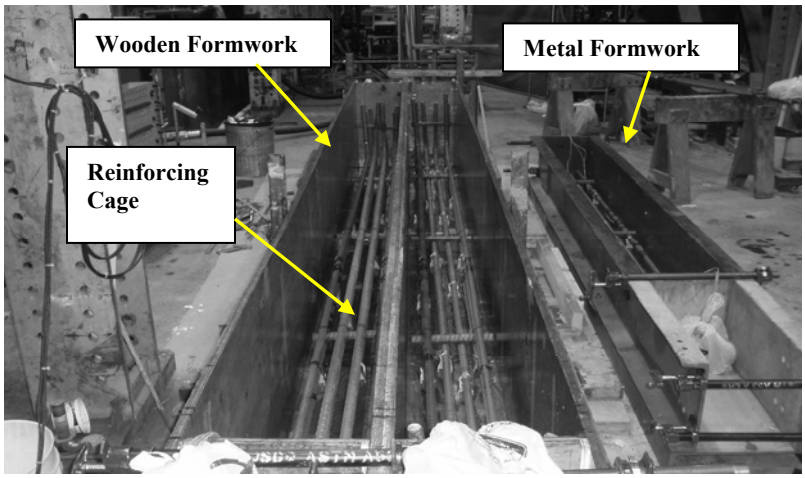

Figure 5-4: Formwork for specimens with *h=308 mm & h=600 mm*

For concrete batches 1, 2, 3a, and 3b (see Table 5-3), a concrete bucket was used to cast the concrete into the formwork for specimens with *h=308 mm* and *h=600 mm*. The truck chute was used to cast the concrete directly from the truck mixer into the formworks with *h=308 mm* and *h=1000 mm* for batches 4, 5, and 6 (see Figure 5-5e). The concrete was cast in layers of about 300 *mm* height into the formwork and then compacted by an internal vibrator.

(a)

(b)

(c)

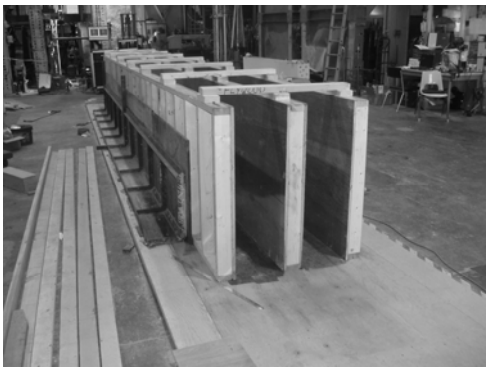

(d)

(e)

(f)

Figure 5-5: Formwork and casting for large size specimens with *h=1000 mm*; a) building the wooden walls of the formwork; b) erecting the wooden walls; c) bolting the walls to the wooden base; d) exterior supporting steel-wooden frame ; e) casting fresh SFRC mix; f) removing the SFRC large specimen from formwork by crane

5.5 Instrumentation

Different instruments were employed to measure the deflection and strain in the SFRC specimens. Electrical resistance strain gauges were mounted on the surface of the longitudinal reinforcing bars at certain locations as shown in Figure (5-1) and Appendix B. These locations were selected to obtain the steel strain at the flexural critical section (mid-span), at the estimated shear critical section ($d_v=0.9d$ from mid-span), and at a section adjacent to the support where the imposed shear is considerable. Five LVDTs were used to measure the vertical deflections at the mid-span, the quarter span points and at each support. For 9 specimens (N32, H32, L32, N10-1, N10-2, H10-1, H10-2, L10-1, L10-2), three pi (π) gauges at three levels of the height were mounted on the surface of the specimen at mid-span. The data from these pi gauges could be used to determine the distribution of surface longitudinal strain over the height of the specimens at mid-span. A cable potentiometer was used to measure the horizontal translation between the support bearing plates. The details of the instrumentation for each specimen including the position and designation of strain gauges and LVDTs are shown in Appendix B.

To facilitate photography of the crack pattern at each load stage, a 100 *mm* grid (200 *mm* grid for specimens with h=1000 *mm*) was drawn on the face of the specimens (Figure 5-6). Reflective target stickers were also used on the surface of the specimen at the cross points of the grid to collect the images required for future work based on a photogrammetric measurement system. In this system, the reflection of target stickers is employed to analyze the images and to capture the relative movement of points on the specimen surface during test.

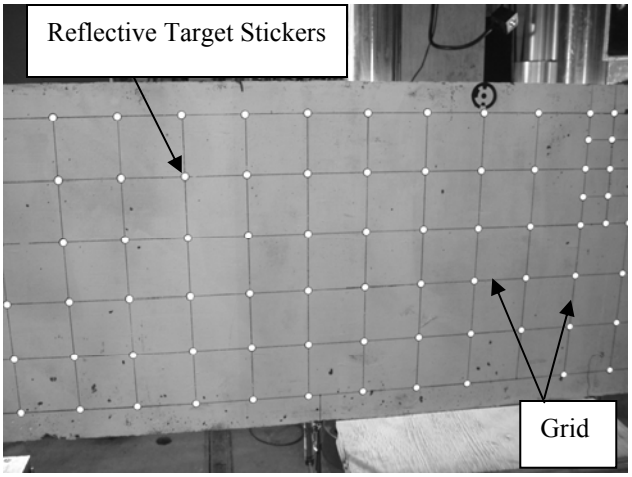

Figure 5-6: Reflective target stickers for photogrammetric system

A digital image correlation (DIC) system (Vic-3D 2009) was employed to continuously record and measure the strain and displacement on the surface of the specimens during each test (Figure 5-7). This system included three pairs of digital cameras with 12.5 *mm* or 35 *mm* focal length lenses to capture images at 10 second intervals during the test. Based on the camera lens sizes, their distance from the specimen, and their angular separation (15^{o}~45^{o}), each pair of cameras imaged a specific area of interest on the specimen surface. Accordingly, and by using a speckling spray gun, the specimen surface was speckled with dots. The dot diameter was about five pixels in size. Software (Vic-3D 2009) was used to process and analyze the images to calculate the strain and displacement at any point of the imaged area. The crack width or the relative movement of any two points on the specimen surface can be measured by using the data from the DIC. The crack width at each stage of loading during the test was measured by calculating the relative distance between two points on a line perpendicular to the crack path. At the service limit state (SLS), the comparator gauges were not able to measure the flexural cracks widths less than 0.08 *mm*, and the DIC system was employed for this purpose. For the diagonal shear cracks, the crack width was

projected from the relative horizontal and vertical distance between two points on a line perpendicular to the crack path.

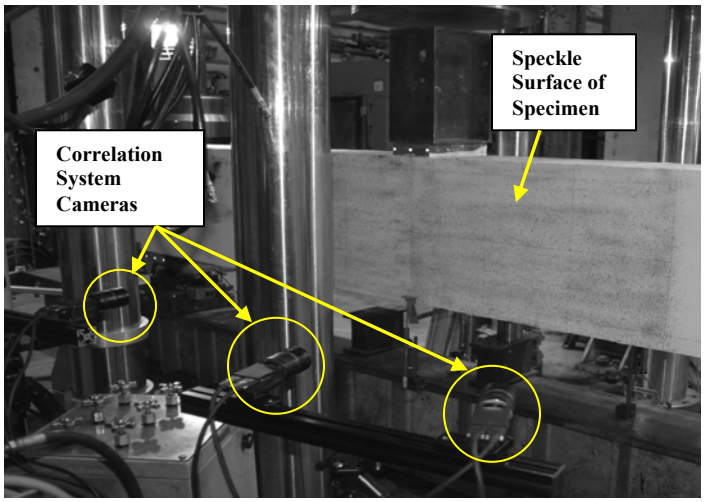

Figure 5-7: Digital image correlation system

5.6 Test Procedure

All structural tests reported in this study were performed using an MTS 6000 universal testing machine. Displacement-controlled loading was used to apply the quasi-static load at a rate of 0.15~0.25 *mm/minute* at mid-span (Figure 5-1 & Figure 5-8). During the test and up to failure, 6 to 8 load stages were used. At each load stage, the displacement was briefly held while the cracks were marked, measured by comparator gauges and photographed. Load, deflection, and strain gauge data were recorded continuously all the way up to failure. Digital images were continuously taken by the digital image correlation system cameras throughout the loading process of each test. The total duration of each test was 3 to 4 hours, depending on the reinforcement configuration of the specimen and the number of load stages. All the presented data for mid-span and quarter-point

deflections in Chapter 6 and Appendix B was corrected for the measured support settlement.

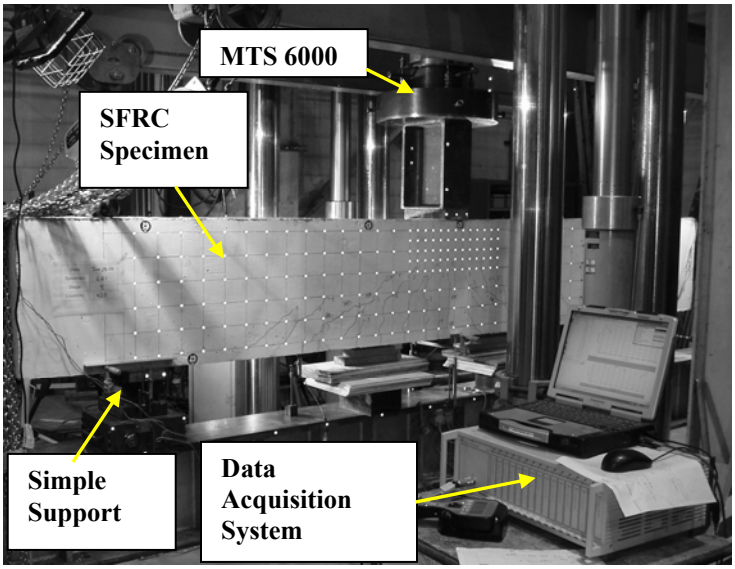

Figure 5-8: SFRC specimen *L61* under loading during test

6. Shear Strength of Structural Normal Weight SFRC Members: Results and Discussion

The ultimate shear capacity and failure mode of the 12 normal weight SFRC specimens are shown in Table (6-1). Eleven specimens failed in shear and only one specimen (*H61*) failed in flexure. In this chapter, the behavior of each group of specimens with the same depth is studied. Crack development, failure mode, load-deflection response, load-steel strain response and load-crack width response for each group of specimens are investigated. The deflection and crack width of SFRC specimens at service load are also examined. The influence of member depth and longitudinal reinforcement ratio on the shear strength of SFRC specimens are investigated. The observed shear capacity of SFRC members are also compared to *ACI 318-08* and *CSA A23.3-04* predictions for similar RC members without fibers. The detailed test results for each specimen can be found in Appendix *B*.

Table 6-1: Test results for normal weight SFRC specimens

Specimen	***b* (mm)**	***h* (mm)**	***d* (mm)**	***f'c* (MPa)**	***ρ* %**	**Failure Type**	***Pmax** (kN)**	***Vtest*** (kN)**	$\frac{V_{test}}{\sqrt{f'_c}\, b\, d}$ **(MPa)**
N31	310	308	258	23	2.50	Shear	420	211	0.55
N61	300	600	531	23	1.88	Shear	496	252	0.32
N62	300	600	523	23	2.55	Shear	476	242	0.32
H31	310	308	258	41	2.50	Shear++	554	278	0.54
N32	310	308	240	41	4.03	Shear	560	281	0.59
H61	300	600	531	41	1.88	Flexure	838	423	0.41
H62	300	600	523	41	2.55	Shear	880	444	0.44
N10-1	300	1000	923	41	1.44	Shear	958	492	0.27
N10-2	300	1000	920	41	2.03	Shear	968	497	0.27
H32	310	308	240	80	4.03	Shear++	915	458	0.55
H10-1	300	1000	923	80	1.44	Shear	1265	646	0.32
H10-2	300	1000	920	80	2.03	Shear	1261	644	0.32

* The maximum applied load at mid-span

**The maximum shear force during test including selfweight at a section *2d* from mid-span

++ These specimens approached their shear and flexural capacities simultaneously (see Section 6.1.1.2)

6.1 Behavior of SFRC Specimens without Stirrups

6.1.1 Specimens with *h=308 mm* (*N31*, *N32*, *H31*, *H32*)

6.1.1.1 Crack Development and Failure Mode

The crack patterns after failure of shear critical specimens with *h=308 mm* (*N31*, *N32*, *H31* and *H32*) are shown in Figure (6-1). For all four specimens, flexural cracks near mid-span were detected first during initial load stages. Then, new flexural cracks formed in the shear spans and curved diagonally towards the loading point. The diagonal crack widths gradually increased as the applied load at mid-span increased. At the last stages of loading before failure ($P > 0.9\ P_{max}$), an existing diagonal crack rapidly widened and extended upwards to the loading plate. The widening of the critical shear crack caused a relative rotation of the two pieces of the specimens around the compression zone at the top end of the shear crack. A combination of this rotation with the shear stress carried by the uncracked concrete caused a significant compression strain in the compressive zone. The shear failure occurred when the compressive concrete crushed in the region between the top end of the diagonal crack and the edge of the loading plate at mid-span (Figure 6-1).

During the shear failure and after occurrence of the crushing mechanism in the compressive concrete, cracking along the longitudinal reinforcement towards the support region was also observed in specimens *N31*, *H31* and *H32*. The curved shapes for the primary diagonal cracks intercepted the longitudinal reinforcement at considerable distances (*0.71 d ~ 1.12 d*) from the support plates, confirming that the shear failure was representative of "sectional" shear model behavior rather than arch action. *Dinh* (2009) observed that slender RC members without stirrups exhibit a single diagonal crack followed by a brittle shear failure; however, shear critical SFRC members with V_f =0.75% ~ 1.5% typically exhibit multiple inclined cracks followed by widening of at least one diagonal crack before shear failure. This was also observed in the current study.

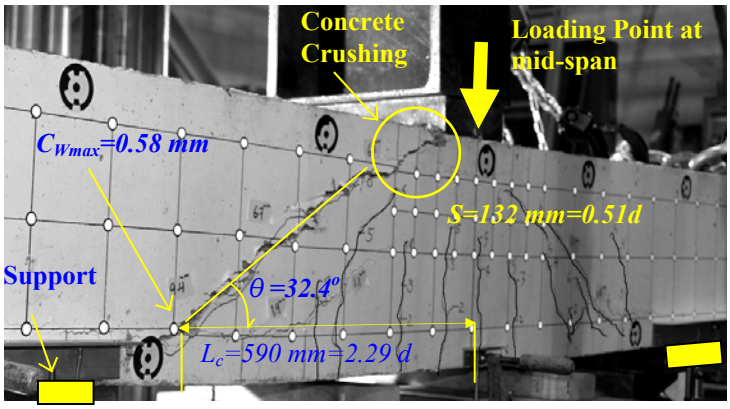

a) Specimen *N31*: f'_c=23 *MPa*, ρ=2.50 %

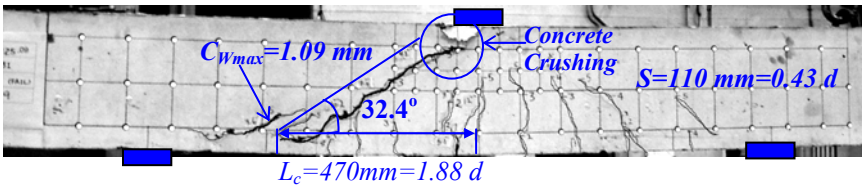

b) Specimen *H31*: f'_c=41 *MPa*, ρ=2.50 %

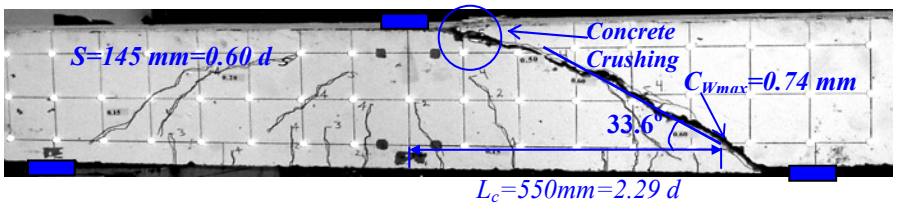

c) Specimen *N32*: f'_c=41 *MPa*, ρ=4.03 %

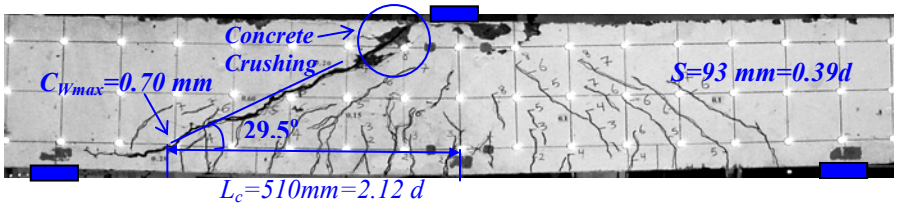

d) Specimen *H32*: f'_c=80 *MPa*, ρ=4.03 %

Figur 6-1: Crack pattern after shear failure for 4 specimens with *h=308 mm*. Size of grid on the specimen surface is 100 *mm*.

The average crack spacing (*S*) at the mid-depth level was determined by considering all the distinct inclined cracks which propagated beyond the specimen mid-depth level at angles between 0 and 75 degrees with respect to the longitudinal axis of the specimen. The average crack spacing (*S*) at mid-depth level are shown in Figure (6-1) and summarized in Table (6-2). For specimens *N31* and *H31* with similar configurations, the average crack spacing decreased by 17% with an increase in the compressive strength f_c' from *23 MPa* to *41 MPa*. For specimens *H31* and *N32* with similar compressive strength but with different ρ, the average crack spacing was 32% larger for specimen *N32* with higher longitudinal reinforcement ratio. As shown in Figure (6-1), the average crack spacing for specimens with *h=308 mm* ranged from *0.39d* to *0.6d*.

Dinh (2009) reported that the average horizontal crack spacing for SFRC members without stirrups was about *0.4d*. In other words, an increase in effective depth of SFRC members from *d*=375*mm* to *d*=610 *mm* resulted in larger crack spacing, but when represented based on effective depth *d*, the average horizontal crack spacing for all members were approximately the same. No clear trend was observed by *Dinh* (2009) for the relationship between the longitudinal reinforcement ratio and diagonal crack spacing, and between fiber content (V_f =0.75% ~ 1.5%) and inclined crack spacing. *Kwak et al.* (2002) reported that average crack spacing in SFRC members with V_f =0.5% ~ 0.75% was about 38% smaller compared to that of RC members without fibers. For RC members without stirrups, *Shioya et al.* (1989) showed that the spacing of cracks at the mid-height of the web is about *1/2* of the member depth.

For each specimen in Figure (6-1), the distance from mid-span L_c of interception point of critical shear crack with the longitudinal steel is shown. The measured values of L_c are also presented in Table (6-2). The results show that for specimens with similar longitudinal reinforcement ratio (*N31 & H31*), L_c decreases with an increase in the concrete compressive strength f_c'. For specimens *H31* and *N32* with similar compressive strength but with different ρ, the distance L_c increased

17% when ρ increased from 2.5% to 4.03%. As shown in Figure (6-1), for specimens with *h=308 mm*, L_c ranged between *1.88d* and *2.29d*. The exact values of L_c from previous research on SFRC members have rarely been reported; however, from the illustrated crack patterns by *Dinh* (2009) for both RC and SFRC specimens with *a/d=3.5*, one can estimate a range of L_c *=1.5d~2.5d*.

Table 6-2: Crack observations for SFRC specimens with *h=308 mm*

Specimen	***b (mm)***	***d (mm)***	***f'c (MPa)***	***ρ %***	***Failure Type***	***θ (degree)***	***C_{Wmax} (mm)***	***L_c (mm)***	***S (mm)***
N31	310	258	23	2.50	Shear	32.4	0.58	590	132
H31	310	258	41	2.50	Shear	32.4	1.09	470	110
N32	310	240	41	4.03	Shear	33.6	0.74	550	145
H32	310	240	80	4.03	Shear	29.5	0.70	510	93

The crack width C_{Wmax} of the critical shear crack at the level of longitudinal reinforcement just before failure at $P=P_{max}$ was determined by using the data obtained from the digital image correlation measurement system. The results for C_{Wmax} are shown in Figure (6-1) and summarized in Table (6-2). For specimens *H31* and *N32* with similar f_c' but with different ρ, the crack width C_{Wmax} decreased when ρ increased from 2.5% to 4.03%. Table (6-2) does not show a consistent trend in C_{Wmax} when the concrete compressive strength f_c' changes for the SFRC specimens with *h=308 mm*. *Minelli and Plizzari* (2006) reported that for shear-critical RC specimens with *d=435 mm*, the maximum value of the shear crack width at mid-depth before failure was equal to 0.1-0.2 *mm*, while for similar SFRC specimens, this value was about 1.5-3 *mm*. The load-crack width response for specimens *N31*, *N32*, *H31* and *H32* is discussed in Section (6.1.1.4).

The idealized angle of the critical shear crack θ, was determined using a secant line taken between the crack interception point at the level of the longitudinal reinforcement and a point about 80% of the total specimen height above the bottom. The results for θ are shown in Figure (6-1) and summarized in Table (6-

2). Regardless of the differences in f_c' and ρ, similar values for θ were obtained for specimens *N31*, *N32*, and *H31*. However, for specimen *H32* with $f_c'=80$ *MPa*, the idealized angle θ was slightly smaller than that of *N31*, *N32*, and *H31*. According to *Dinh* (2009), the average crack angle for the shear critical beams which failed due to compressive concrete crushing was about 37 degrees. However, for beams that failed due to sudden extension of diagonal shear crack without compressive concrete crushing, the average angle for the critical inclined crack was approximately 27 degrees.

6.1.1.2 Load-Deflection Response

The load-deflection response of specimens with total depth of *h=308 mm* is shown in Figure (6-2). In contrast to typical behaviour of RC members without steel fibers, the SFRC specimens in this group did not exhibit a sudden or large change of slope in the load-deflection plot at the initiation of flexural cracking. A non-linear relationship with gradually reducing slope was observed for specimens *N31* and *N32* up to shear failure. The load-deflection response for specimens *H31* and *H32* in Figure (6-2) started to exhibit a plateau after reaching the ultimate load, mainly due to non-linear behavior of the longitudinal reinforcement shown in Figure (6-3). After some additional deformation in specimen *H31* and *H32*, a significant diagonal crack formed leading to a shear failure. In all four specimens, a sudden and large drop in load was recorded at failure due to concrete crushing at the area between the top of the diagonal crack and the side edge of the loading plate at mid-span (Figure 6-1). In specimens *H31* and *H32*, no significant flexural crack or concrete crushing in the compression zone at mid-span was observed prior to the shear failure. However, exhibiting a plateau at ultimate load due to reinforcement yielding at mid-span indicates that specimens *H31* and *H32* were both approaching their flexural and shear capacities simultaneously. The maximum deflections at mid-span before shear failure for specimens *N31*, *N32*, *H31* and *H32* were 7.48 *mm*, 5.64 *mm*, 13.76 *mm* and 17.52 *mm*, respectively.

Note that for specimens *N32* and *H31* with similar f_c'*=41 MPa* but different longitudinal reinforcement ratios, the ultimate shear capacities were almost identical.

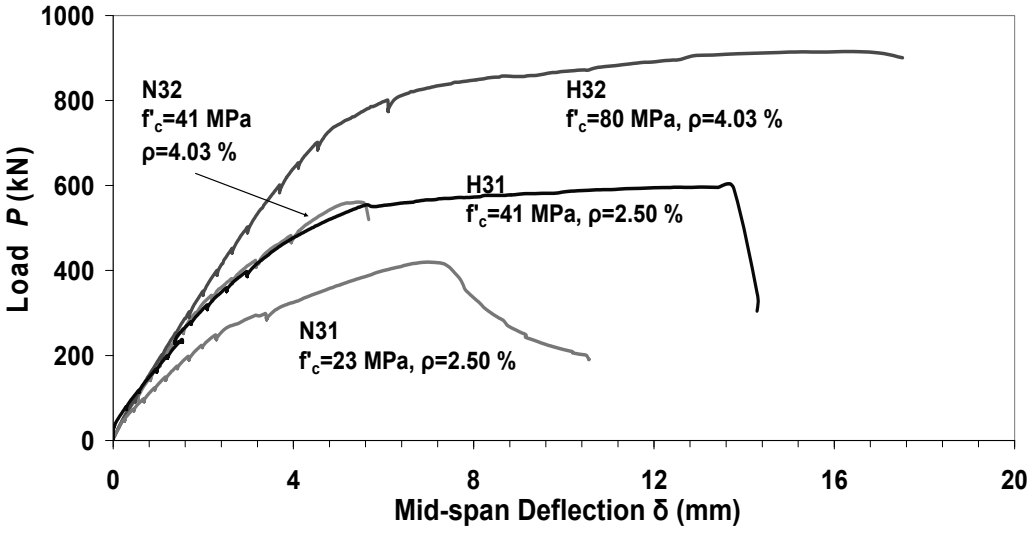

Figure 6-2: Load-Deflection response at mid-span for specimens with *h=308 mm*.

6.1.1.3 Load-Steel Strain Response

The load-steel strain response at mid-span for specimens with total depth of *h=308 mm* is shown in Figure (6-3). The mid-span load-strain response of the reinforcement remained linear for specimens *N31* and *N32* up to failure indicating that reinforcement yielding did not occur. However, the mid-span load-strain response for specimen *H3*1 in Figure (6-3) started to exhibit a plateau after reaching the ultimate load, due to yielding of the longitudinal reinforcement. For specimen *H32*, the strain gauges became unbonded since wide cracks intercepted the strain gauge locations on the longitudinal reinforcement at mid-span.

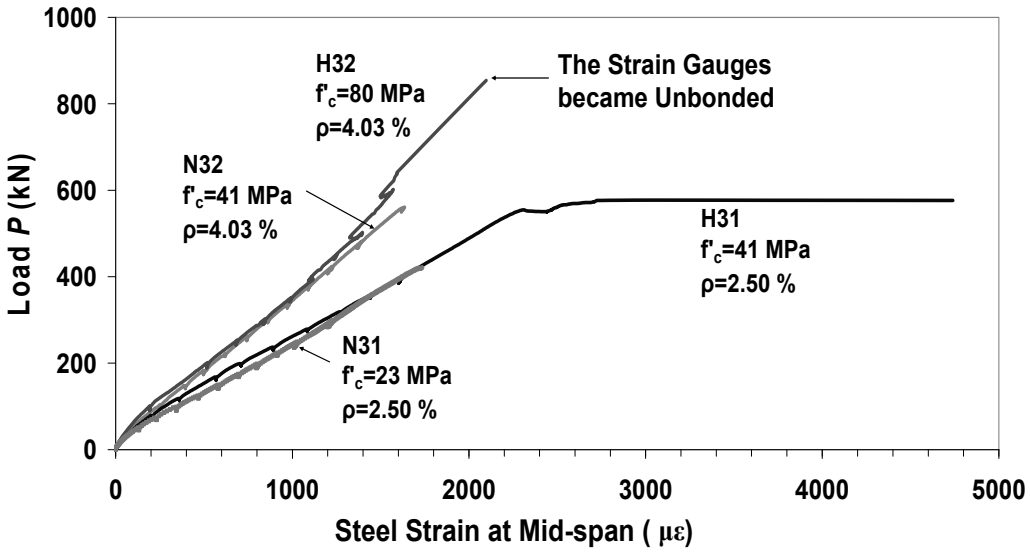

Figure 6-3: Load-steel strain response at mid-span for specimens with *h=308 mm*.

Specimens N31 and H31 were similar in configuration, but they were cast using two different SFRC mixes with $f_c'=23$ *MPa* and $f_c'=41$ *MPa*, respectively. As shown in Figure (6-3), specimen *N31* failed in a shear mode before reinforcement yielding at mid-span while specimen *H31* was observed to have steel yielding at mid-span before shear failure. A similar trend in reinforcement yielding and failure mode was identified for specimens *N32* and *H32*, both with similar ρ but different f_c'. Meanwhile, the difference in behaviour of *H31* compared to *N32*, both with $f_c'=41$ *MPa* can be attributed to the lower reinforcement ratio in *H31* which resulted in higher reinforcement strains at similar load levels compared to N32 (Figure 6-3).

6.1.1.4 Load-Crack Width Response of Shear Critical Specimens

The load-crack width response for specimens with total depth of *h=308 mm* is shown in Figure (6-4). The crack width C_W was measured for the critical shear crack at the level of the longitudinal reinforcement (see Figure 6-1) by using the data obtained from digital image correlation system and the crack comparator

gauges. A non-linear relationship with gradually reducing slope was observed for all four specimens (*N31*, *N32*, *H31*, and *H32*) up to 90% of the maximum applied load before shear failure. It was observed that in the last stage of loading just before shear failure, the crack widths increased rapidly and reached very large values relative to the crack widths recorded at 90% of P_{max} (see C_{Wmax} values in Table 6-2). A similar trend in crack width increase at mid-depth was reported by *Minelli and Plizzari* (2006) (see Section 2.2.1). Note that unlike the specimens *H31* and *H32*, reinforcement yielding at mid-span did not occur in specimens *N31* and *N32* (Section 6.1.1.3), but a similar increase in the crack widths at the last stage of loading before failure was observed. As a result of this large increase of the crack widths, the aggregate interlock is reduced significantly. Meanwhile, from a structural behavior point of view, the crack widening in SFRC members prior to shear failure can be important, since it provides warning about imminent shear failure. The large increase of crack widths before failure can be attributed to the pullout of fibers out of the concrete matrix due to the tension between the adjacent crack surfaces (also see Figure 6-14 in Section 6.1.3.4).

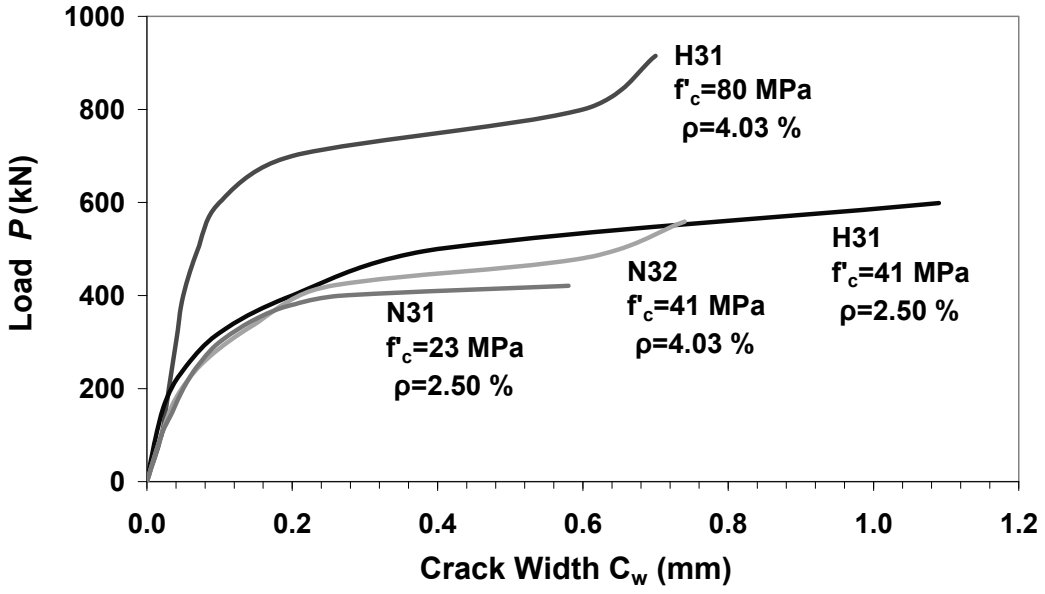

Figure 6-4: Load-crack width response for critical shear crack at level of longitudinal reinforcement in specimens with *h=308 mm*.

6.1.1.5 Deflection and Crack Width at Service Limit State (SLS)

In order to study the behavior of SFRC specimens at the equivalent service load, the ratio of service load to the ultimate capacity must be estimated. Considering the design procedure at the ultimate limit state in *ACI 318-08* or other similar codes, the relation between nominal ultimate capacity R, the capacity resistance factor φ, and the load combination of dead load D_L and live load L_L with load factors of f_1 and f_2, respectively, can be written as:

$$\varphi R \geq (f_1 D_L + f_2 L_L) \tag{6-1}$$

If the live-to-dead load ratio $L_L / D_L = \lambda_1$, then the service load S_L will be:

$$S_L = L_L + D_L = D_L (\lambda_1 + 1) \tag{6-2}$$

From Equations (6-1) and (6-2), the ratio of service load to nominal ultimate capacity can be expressed as:

$$\frac{S_L}{R} = \frac{D_L(\lambda_1 + 1)}{(f_1 D_L + f_2 \lambda_1 D_L) / \varphi} = \frac{\varphi(\lambda_1 + 1)}{f_1 + f_2 \lambda_1} \tag{6-3}$$

Assuming a typical ratio of $L_L / D_L = 1$, and applying the load factors $f_1 = 1.4$ and $f_2 = 1.7$ from *ACI 318-08*, one can observe:

i) For shear critical specimens with $\varphi = 0.75$:

$S_L / R = 0.75(1+1) / (1.4+1.7) = 0.48$

ii) For flexure critical specimens with $\varphi = 0.9$:

$S_L / R = 0.9(1+1) / (1.4+1.7) = 0.58$

From Equation (6-3), one can observe that S_L/R decreases with an increase in the ratio L_L / D_L. However, the ratio $S_L/R = 0.48$ was used in this study to establish the equivalent SLS deflection and crack widths reported in Table (6-3).

As shown in Table (6-3), all relative deflection values at service load δ/L are lower than the common deflection limit of $L/360$ for RC members under live load alone according to *ACI 318-08* or *CSA A23.3-04*.

Table 6-3: Deflection and crack width of SFRC specimens with $h=308$ *mm* at SLS

Specimen	Failure Type	$0.48P_{max}$ from test (kN)	Behavior at SLS		
			Mid-span Deflection δ (mm)	δ/L	Max. Flexural Crack Width (mm)
N31	Shear	202	1.76	0.0011	0.05
H31	Shear	266	1.60	0.0010	0.06
N32	Shear	269	1.63	0.0011	0.08
H32	Shear	439	2.56	0.0018	0.06

The detected cracks at SLS were all very narrow flexural cracks near the mid-span; however, the crack control factor z might also be checked according to *ACI 318-08* or *CSA A23-04* provisions for RC members without fibers, where:

$$z = f_s (d_c A)^{1/3} \tag{6-4}$$

The requirement is $z \leq 30000$ *N/mm* for RC members with interior exposure.
Consider specimen *N32* with the largest crack width reported in Table (6-3). According to *ACI 318-08* or *CSA A23-04*, 60% of yielding strength $f_y = 400$ *N/mm*^{2} can be used as tensile stress in reinforcement under service load:

$f_s = 0.6 f_y = 240$ *N/mm*^{2}

From Figure (5-1), the distance d_c from the centroid of the lowest row of tension steel to the bottom (tension) face of member is:

d_c=50 mm

The area A is calculated as twice the area enclosed between the centroid of the tension steel and the bottom (tension) face of the member, divided by the number of steel reinforcing bars:

$$A = \frac{2 \times 68 \times 310}{6} = 7027 mm^2$$

Therefore,

$$z = f_s (d_c A)^{1/3} = (240)(50 \times 7027)^{1/3} = 16928 N/mm \leq 30000 N/mm \qquad OK$$

These calculations for crack control factor z show that the maximum crack width for specimen *N32* was within the acceptable range for design of RC members with interior exposure.

6.1.2 Specimens with *h=600 mm* (*N61*, *N62*, *H61*, *H62*)

6.1.2.1 Crack Development and Failure Mode

The crack patterns after failure of specimens with *h=600 mm* are shown in Figures (6-5) and (6-6). The specimens *N61*, *N62*, and *H62* failed in shear (Figure 6-5), while specimen *H61* had a flexural failure mode (Figure 6-6). For all four specimens, flexural cracks near mid-span were detected first during initial load stages. Then, new flexural cracks formed in the shear spans and curved diagonally towards the loading point. The diagonal crack widths gradually increased as the applied load at mid-span increased.

For shear critical specimens *N61*, *N62*, and *H62*, the crack development before failure was similar to that observed for specimens with *h=308 mm* and described in Section (6.1.1.1). An existing diagonal crack rapidly widened and extended upwards to the loading plate at the last stages of loading before failure ($P > 0.9\ P_{max}$). After widening of the diagonal shear crack, a relative rotation of the two pieces of the specimens around the compressive zone at the top of the shear crack was observed. This rotation plus the shear stress carried by the uncracked concrete caused a significant compression strain in the compressive zone, followed by a shear failure due to concrete crushing in the region between the top of the diagonal crack and the edge of the loading plate at mid-span. At shear failure and after compressive concrete crushing, cracks also extended along the longitudinal reinforcement and stopped at the support region (Figure 6-5). The primary diagonal cracks intercepted the longitudinal reinforcement at considerable distances ($0.81\ d \sim 1.06\ d$) from the support plates, confirming that the shear failure was representative of "sectional" shear model behavior rather than arch action.

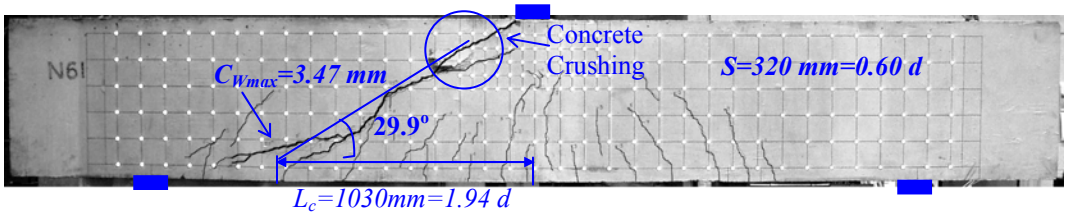

a) Specimen *N61: f'_c=23 MPa, ρ=1.88 %*

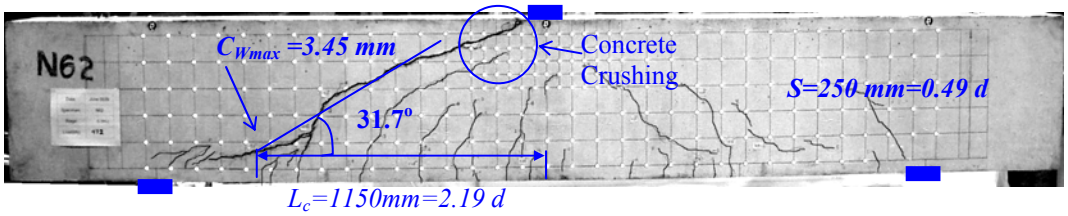

b) Specimen *N62: f'_c=23 MPa, ρ=2.55 %*

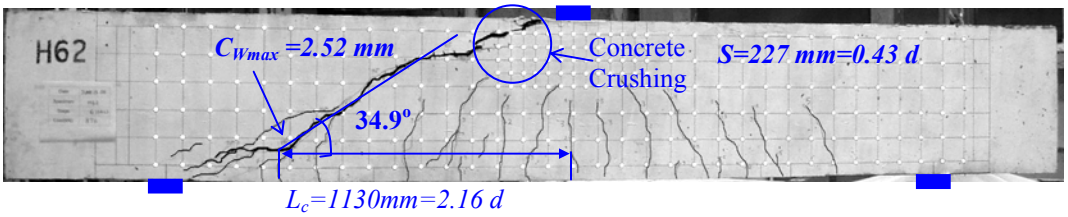

c) Specimen *H62: f'_c=41 MPa, ρ=2.55 %*

Figure 6-5: Crack patterns after shear failure for 3 specimens with *h = 600 mm*. Size of grid on the specimen surface is 100 *mm*.

Specimen *H61* was the only specimen out of 12 normal weight specimens that failed in flexure (Figure 6-6). For this specimen, no significant diagonal crack was observed before or during the failure. The flexural failure occurred when one of the existing flexural cracks near mid-span extended considerably upwards to the loading plate, and a large increase in crack widths, steel strains and specimen

deflection was observed, followed by concrete crushing in the compressive zone adjacent to the loading point at mid-span.

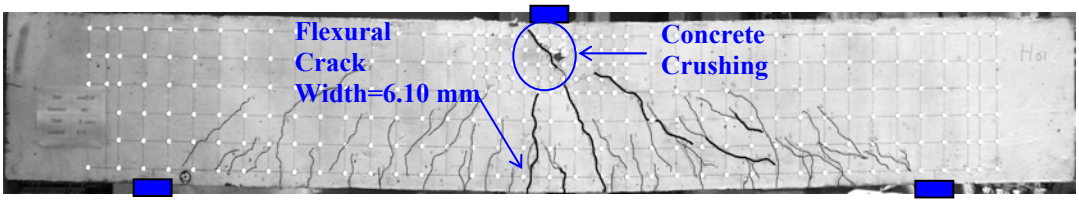

Figure 6-6: Crack pattern after flexural failure for specimen *H61* with *h=600mm*, f'_c*=41 MPa*, and ρ*= 1.88 %*. Size of grid on the specimen surface is 100 mm.

For shear critical specimens in Figure (6-5), the idealized angle of critical shear crack θ, the crack width C_{Wmax} of the critical shear crack at the level of the longitudinal reinforcement just before failure at $P=P_{max}$, and the distance from mid-span L_c of interception point of critical shear crack with the longitudinal steel are shown. The results for θ, C_w and L_c as well as average crack spacing S at the mid-depth level are summarized in Table (6-4).

Table 6-4: Crack observations for SFRC specimens with *h=600 mm*

Specimen	***b* (mm)**	***d* (mm)**	***f'c* (MPa)**	***ρ* %**	***Failure Type***	***θ* (degree)**	***C_{Wmax}* (mm)**	***L_c* (mm)**	***S* (mm)**
N61	300	531	23	1.88	Shear	29.9	3.47	1030	320
N62	300	523	23	2.55	Shear	31.7	3.45	1150	250
H61	300	531	41	1.88	Flexure	-	-	-	-
H62	300	523	41	2.55	Shear	34.9	2.52	1130	227

The results show that for specimens *N62* and *H62* with similar configuration, the average crack spacing decreased slightly (9%) with an increase in the compressive strength f_c' from *23 MPa* to *41 MPa*. For specimens *N61* and *N62* with similar compressive strength of $f_c'=23$ *MPa* but with different ρ, the average crack spacing was 22% smaller for specimen *N62* with higher longitudinal reinforcement ratio. This trend in the crack spacing of specimens *N61* and *N62* with $f_c'=23$ *MPa* was in contrast to that observed for *N31* and *H31* with $f_c'=41$ *MPa* and *h=308 mm* (Section 6.1.1.1). The range of average crack spacing for specimens with *h=600 mm* was $S=0.43d \sim 0.6d$ which is approximately the same range seen for specimens with *h=308 mm* ($S=0.39d \sim 0.6d$) in Figure (6-1).

The L_c values in Table (6-4) show that for specimens with similar longitudinal reinforcement ratios (*N62 & H62*) but with different f_c', L_c remained almost constant. For specimens *N61* and *N62* with similar concrete compressive strength but with different ρ, the distance L_c increased by 12% when ρ increased from 1.88% to 2.55%. As shown in Figure (6-5), for specimens with *h=600 mm*, L_c ranged between *1.94d* and *2.21d*, which is similar to the observed range $L_c=1.88d\sim2.29d$ for specimens with *h=308 mm* (Section 6.1.1.1).

For specimens *N61* and *N62* with similar compressive strength but with different ρ, the crack width C_{Wmax} remained almost the same when ρ increased from 2.5% to 4.03%. Also, the results for idealized angle of critical shear crack in Table (6-4) indicate a range of $\theta = 29.9^o \sim 34.9^o$ for *N61, N62* and *H62*, which is similar to the observed range $\theta = 29.5^o \sim 33.6^o$ for specimens with *h=308 mm* (Section 6.1.1.1).

6.1.2.2 Load-Deflection Response

The load-deflection response of specimens with total depth of *h=600 mm* is shown in Figure (6-7). Similar to SFRC specimens with *h=308 mm* and in

contrast to typical behaviour of RC members without steel fibers, the SFRC specimens with *h=600 mm* did not exhibit a sudden or large change of slope in the load-deflection plot at the initiation of flexural cracking. For specimens *N61*, *N62*, and *H62* a non-linear relationship with gradually reducing slope was observed up to shear failure. The maximum deflections at mid-span before shear failure for specimens *N61*, *N62*, and *H62* were 9.12 *mm*, 8.10 *mm* and 10.78 *mm*, respectively. In these three specimens, a sudden and large drop in load was recorded at failure due to concrete crushing at the area between the top end of diagonal crack and the edge of the loading plate at mid-span (Figure 6-5). Both specimens *N61* and *N62*, with similar $f_c'=23$ *MPa* but different longitudinal reinforcement ratio, failed in shear with less than 5% difference in the ultimate capacity, and about 11% difference in the maximum deflection before failure.

The load-deflection response for specimen *H61* started to exhibit a plateau after reaching the ultimate load, mainly due to non-linear behavior of the longitudinal reinforcement shown in Figure (6-8). In this specimen, no significant diagonal crack was observed. The flexural failure occurred when large increases in deflection at mid-span were observed (δ=33.25 *mm*), followed by a drop in the load due to concrete crushing in the compressive zone under the loading point at mid-span.

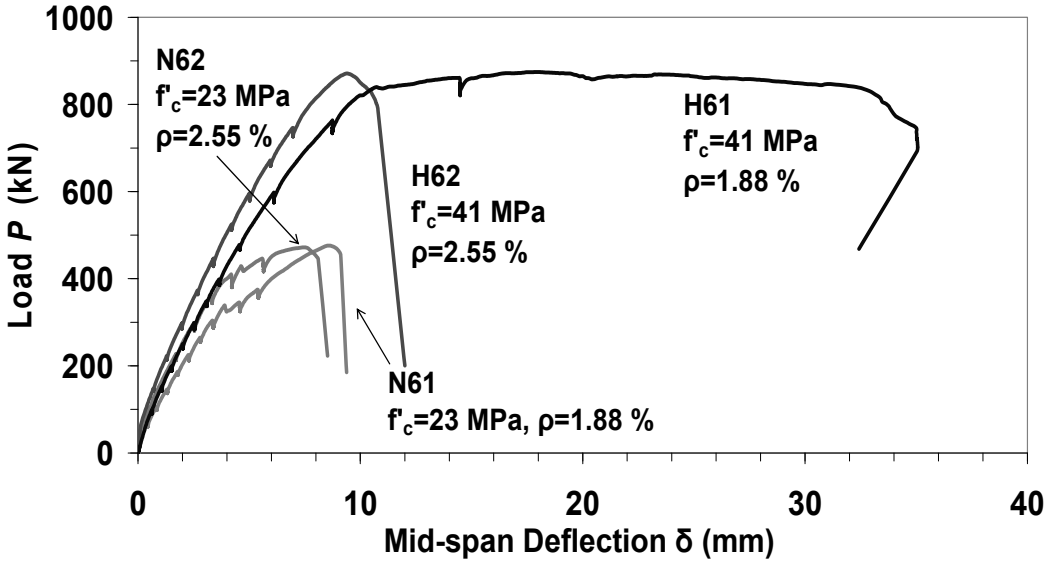

Figure 6-7: Load-Deflection response at mid-span for specimens with *h=600 mm*.

6.1.2.3 Load-Steel Strain Response

The load-steel strain response at mid-span for specimens with total depth of *h=600 mm* is shown in Figure (6-8). The mid-span load-strain response of the reinforcement remained almost linear for specimens *N61*, *N62* and *H62* up to shear failure indicating that reinforcement yielding did not occur. For specimen *H61*, however, the mid-span load-strain response started to exhibit a plateau after reaching the ultimate load, due to yielding of the longitudinal reinforcement.

Specimens *N61* and *H61* were similar in configuration, but they were cast using two different SFRC mixes with f_c'= 23 *MPa* and f_c'=41 *MPa*, respectively. As shown in Figure (6-8), specimen *N61* failed in a shear mode before reinforcement yielding while specimen *H61* was observed to have a flexural failure after steel yielding. However, for specimens *N62* and *H62*, a similar trend was not observed with reference to f_c', and both specimens failed in shear before steel yielding. Meanwhile, the differences in behavior and failure mode of *H61* compared to *H62*, both with f_c'*=41 MPa*, can be attributed to the lower reinforcement ratio in

H61 which resulted in higher reinforcement strains at similar load levels compared to *H62* (Figure 6-8).

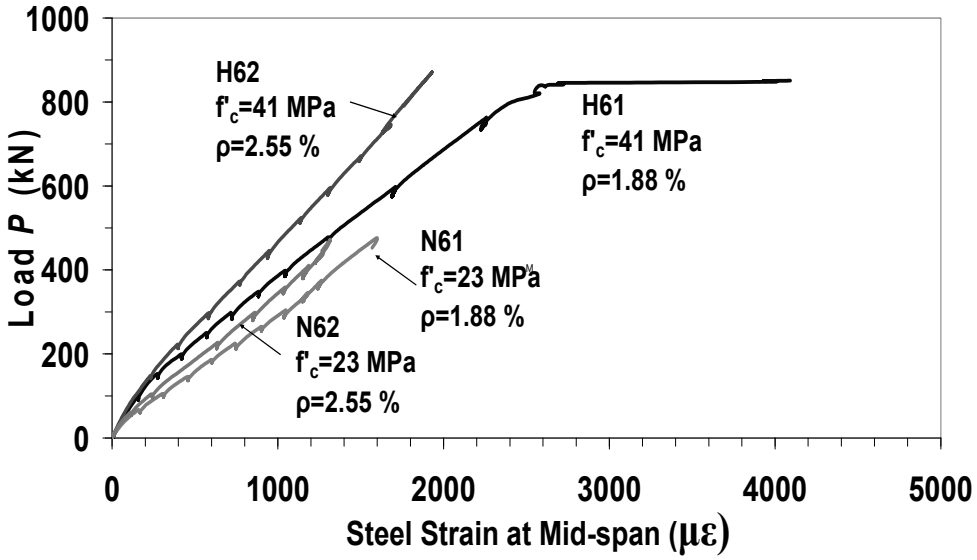

Figure 6-8: Load-steel strain response at mid-span for specimens with *h=600 mm*.

6.1.2.4 Load-Crack Width Response of Shear Critical Specimens

The load-crack width response for shear critical specimens with total depth of *h=600 mm* is shown in Figure (6-9). A non-linear relationship with gradually reducing slope was observed for specimens *N61*, *N62*, *and H62* up to about 90% of maximum applied load before shear failure. Similar to the behavior of specimens with *h=308 mm* studied in Section (6.1.1.4), in the last stages of loading just before shear failure, the crack widths increased dramatically, reaching large values relative to the crack widths recorded at $0.9P_{max}$ (see C_{Wmax} in Table 6-4). No reinforcement yielding at mid-span was observed for specimens *N61*, *N62* and *H62* before this large increase in the crack widths (Section 6.1.2.3). The crack widening in SFRC members prior to shear failure reduces the aggregate interlock significantly. By comparing the values of C_{Wmax} in Tables (6-4) and (6-2), one can observe that C_{Wmax} increases with an increase in the height of specimens from

h=308 mm to *h=600 mm*. As explained in Section (6.1.1.4), the large increase of crack widths before failure can be attributed to the pullout of fibers out of the concrete matrix due to the tension between the adjacent crack surfaces (also see Figure 6-14 in Section 6.1.3.4).

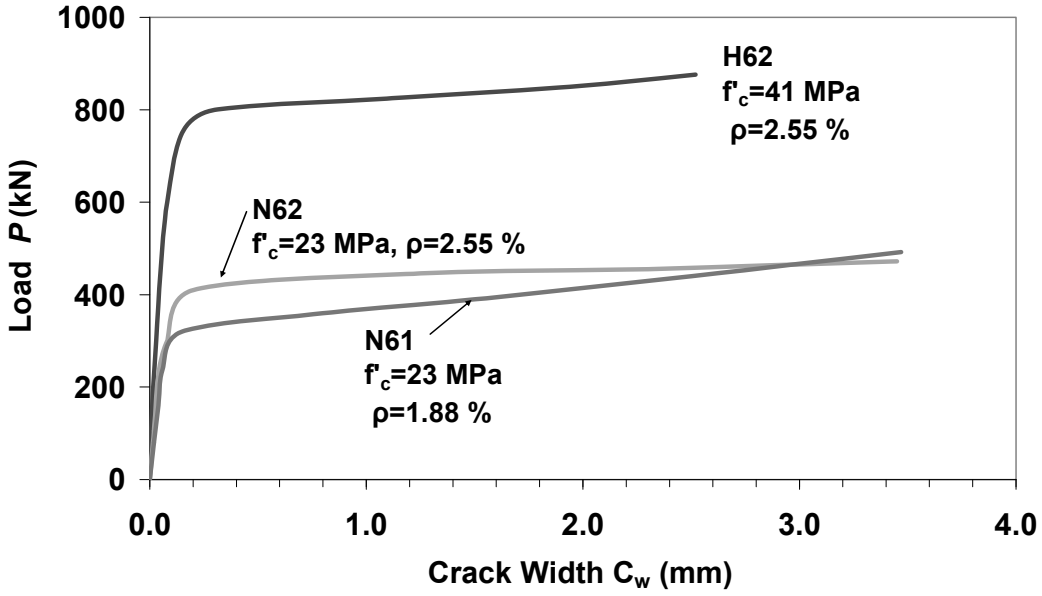

Figure 6-9: Load-crack width response for critical shear crack at level of longitudinal reinforcement in specimens with *h=600 mm*.

6.1.2.5 Deflection and Crack Width at SLS

According to the procedure explained in Section (6.1.1.5), an equivalent service load $S_L = 0.48\ P_{max}$ was used to determine the SLS deflection and crack widths for specimens with *h=600 mm* in Table (6-5). All relative deflection values at service load δ/L are lower than the common deflection limit of $L/360$ for RC members under live load alone (*ACI 318-08*).

Table 6-5: Deflection and crack width of SFRC specimens with *h=600 mm* at SLS

Specimen	0.48 P_{max} from test (kN)	Failure Type	Behavior at SLS		
			Mid-span Deflection δ (mm)	δ/L	Max. Flexural Crack Width (mm)
N61	238	Shear	2.47	0.0008	0.06
N62	228	Shear	1.79	0.0006	0.04
H61	402	Flexure	4.71	0.0015	0.05
H62	422	Shear	3.16	0.0010	0.06

The detected cracks at SLS were all very narrow flexural cracks near the mid-span. The crack control factor *z* (see Section 6.1.1.5) indicated that the crack widths for specimens *N61* and *H61* (*z=16825 N/mm*) as well as specimens *N62* and *H62* (*z=15856 N/mm*) are expected to be within the acceptable range for design of RC members with interior exposure ($z \leq 30000$ *N/mm*).

6.1.3 Specimens with *h=1000 mm* (*N10-1*, *N10-2*, *H10-1*, *H10-2*)

6.1.3.1 Crack Development and Failure Mode

The crack patterns after failure of shear critical specimens with *h=1000 mm* (*N10-1*, *N10-2*, *H10-1* and *H10-2*) are shown in Figure (6-10). For all four specimens, flexural cracks near mid-span were detected first during initial load stages. Then, new flexural cracks formed in the shear spans and curved diagonally towards the loading point. The diagonal crack widths gradually increased as the applied load at mid-span increased. At the last stages of loading before failure ($P > 0.9\ P_{max}$), an existing diagonal crack rapidly widened and extended upwards to the loading plate. For specimen *N10-2*, the depth of the uncracked compression zone above the tip of the diagonal crack before failure was smaller (about *1/2*) compared to that of the other three specimens with *h=1000 mm*. Shear failure for *N10-2* occurred when the critical shear crack extended through the remaining compression zone between top end of shear crack and side edge of loading plate at mid-span without causing crushing in the concrete (Figure 6-10b). For specimens *N10-1*, *H10-1* and *H10-2* the widening of the critical shear crack caused a relative rotation of the two pieces of the specimens around the compressive zone at the top of the shear crack. A combination of this rotation with the shear stress carried by the uncracked concrete caused a significant compression strain in the compressive zone. The shear failure occurred when the compressive concrete crushed at the area between the top of the diagonal crack and the edge of the loading plate at mid-span (Figure 6-10).

During the shear failure, cracking along the longitudinal reinforcement towards the support region was also observed in specimens *N10-1*, *H10-1* and *H10-2* after compressive concrete crushing. The curved shapes for the primary diagonal cracks intercepted the longitudinal reinforcement at considerable distances (*0.61 d ~ 1.16 d*) from the support plates, confirming that the shear failure was representative of "sectional" shear model behavior rather than arch action.

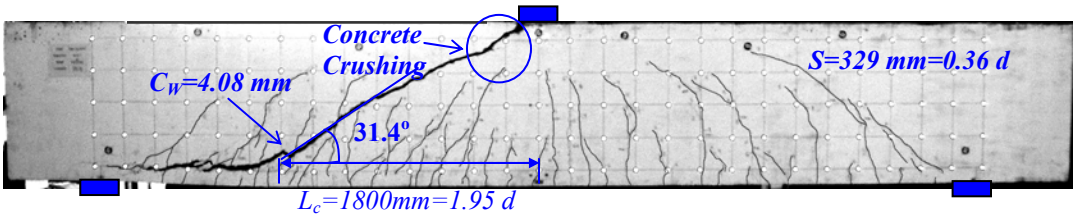

a) Specimen *N10-1: f'_c=41 MPa, ρ=1.44 %*

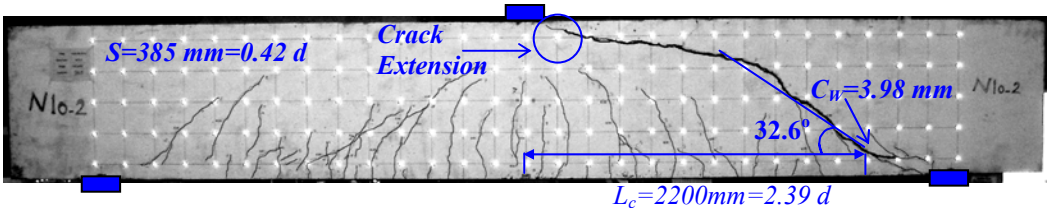

b) Specimen *N10-2: f'_c=41 MPa, ρ=2.03 %*

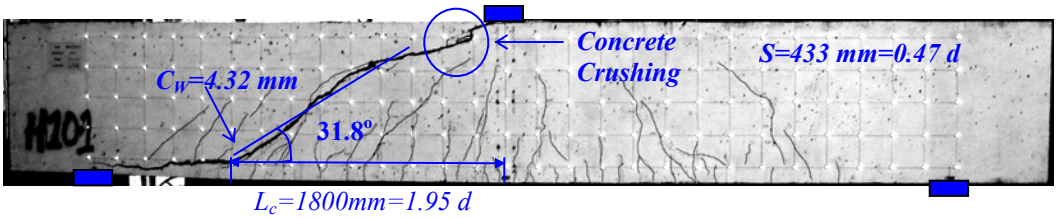

c) Specimen *H10-1: f'_c=80 MPa, ρ=1.44 %*

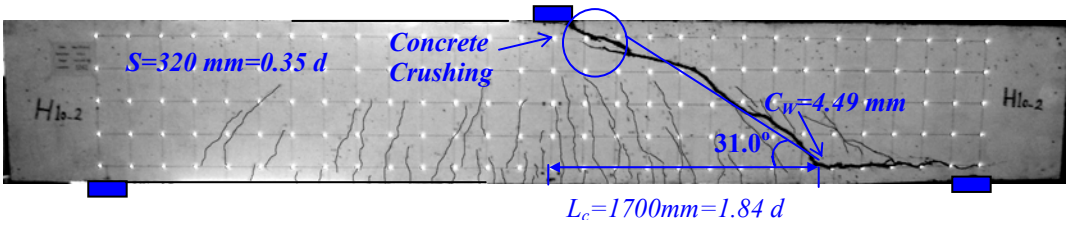

d) Specimen *H10-2: f'_c=80 MPa, ρ=2.03 %*

Figure 6-10: Crack patterns after shear failure for specimens with *h = 1000 mm*. Size of grid on the specimen surface is 200 *mm*.

For shear critical specimens in Figure (6-10), the idealized angle of the critical shear crack θ, the crack width C_{Wmax} of the critical shear crack at the level of the longitudinal reinforcement just before failure at $P=P_{max}$, and the distance from mid-span L_c of interception point of critical shear crack with the longitudinal steel are shown. The results for θ, C_w and L_c as well as average crack spacing S at the mid-depth level are summarized in Table (6-6).

Table 6-6: Crack observations for SFRC specimens with *h=1000 mm*

Specimen	***b (mm)***	***d (mm)***	***f'c (MPa)***	***ρ %***	***Failure Type***	***θ (degree)***	***C_{Wmax} (mm)***	***L_c (mm)***	***S (mm)***
N10-1	300	923	41	1.44	Shear	31.4	4.08	1800	329
N10-2	300	920	41	2.03	Shear	32.6	3.98	2200	385
H10-1	300	923	80	1.44	Shear	31.8	4.32	1800	433
H10-2	300	920	80	2.03	Shear	31.0	4.49	1700	320

No clear trend was observed for the relationship between average crack spacing and the reinforcement ratio ρ or compressive strength f_c'. As shown in Figure (6-10), the range of average crack spacing for specimens with *h=1000 mm* was *S=0.35d ~ 0.47d*. This range of *S* normalized by the effective depth *d*, is smaller than the ranges seen for specimens with *h=600 mm* (*S=0.43d ~ 0.6d*) and *h=308 mm* (*S=0.39d ~ 0.6d*) in Figures (6-5) and (6-1).

The values of L_c in Table (6-6) do not show a clear trend in reference to ρ or f_c'. Figure (6-10) shows that L_c for specimens with *h=1000 mm*, ranged between *1.84d* and *1.95d* for *N10-1*, *H10-1* and *H10-2*. For specimen *N10-2*, which failed as a result of diagonal crack extension into the compression zone without concrete crushing, the interception point of the critical shear crack with the longitudinal reinforcement was closer to the support compared to the other three specimens (L_c *=2.39d*). However, the total range of L_c*=1.84d~2.39d* for specimens with *h=1000 mm* is comparable to the ranges L_c*=1.94d~2.21d* for specimens with *h=600 mm* and L_c*=1.88d~2.29d* for specimens with *h=308 mm* (Sections 6.1.2.1 & 6.1.1.1).

Table (6-6) shows that for specimens with *h=1000 mm*, regardless of differences in ρ and f_c', the maximum crack width C_{Wmax} did not vary considerably. Also, the results for the idealized angle of the critical shear crack indicate a range of θ = 31.0°~32.6° for *N10-1*, *N10-2*, *H10-1* and *H10-2*, which is close to the observed ranges θ = 29.5°~33.6° for specimens with *h=308 mm* (Table 6-2) and θ = 29.9°~34.9° for specimens with *h=600 mm* (Table 6-4).

6.1.3.2 Load-Deflection Response

The load-deflection response of specimens with total depth of *h=1000 mm* is shown in Figure (6-11). Similar to SFRC specimens with *h=308 mm* and *h=600 mm*, the SFRC specimens with *h=1000 mm* did not exhibit a sudden or large change of slope in the load-deflection plot at the initiation of flexural cracking. For all four specimens, a non-linear behaviour with gradually reducing slope was observed up to shear failure. The maximum deflections at mid-span before shear failure for specimens *N10-1*, *N10-2*, *H10-1* and *H10-2* were 19.24 *mm*, 9.99 *mm*, 18.35 *mm* and 16.80 *mm*, respectively. In specimens *N10-1*, *H10-1* and *H10-2*, a sudden and large drop in load was recorded at failure due to concrete crushing in the region between the top end of the diagonal crack and the edge of the loading plate at mid-span (Figure 6-10). For specimen *H10-2*, a large drop in load was observed when the critical shear crack extended upwards to the edge of the loading plate at mid-span without causing concrete crushing. As shown in Figure (6-11), for each pair of specimens with similar f_c' but with different ρ, the ultimate load capacity was almost identical. However, for specimens *N10-1* and *N10-2*, with similar f_c'*=41 MPa* but different longitudinal reinforcement ratio, the maximum deflection before failure in *N10-1* was almost twice that observed in *N10-2*.

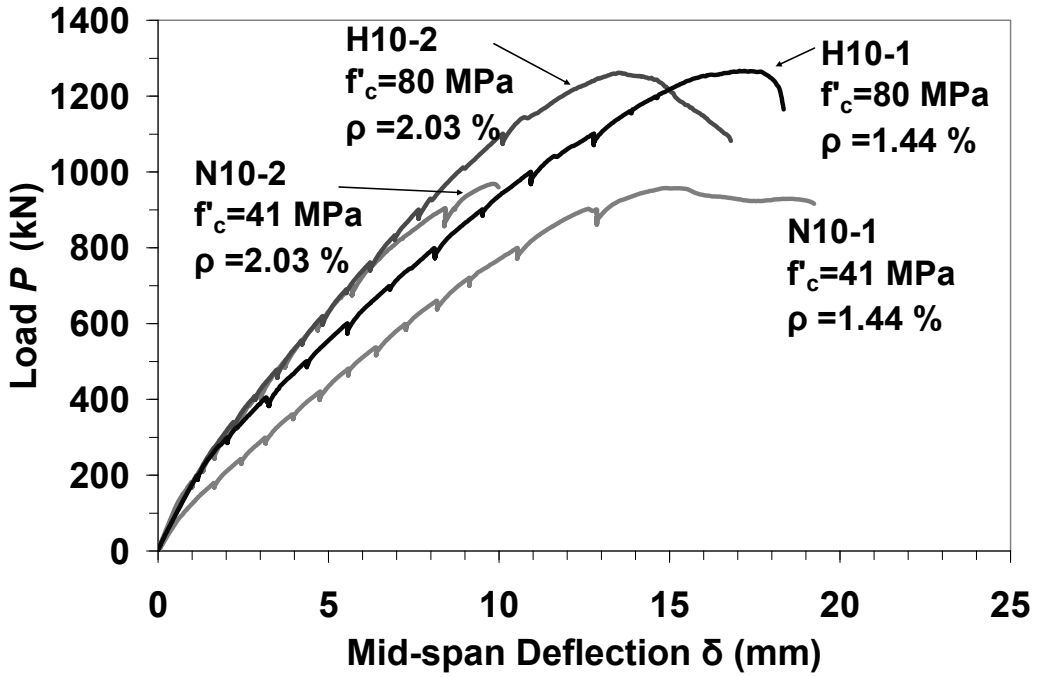

Figure 6-11: Load-Deflection response at mid-span for specimens with *h=1000 mm*.

6.1.3.3 Load-Steel Strain Response

The load-steel strain response at mid-span for specimens with total depth of *h=1000 mm* is shown in Figure (6-12). The mid-span load-strain response of the reinforcement remained almost linear up to shear failure indicating that reinforcement yielding did not occur for any of the specimens. However, for specimen *H10-2*, the strain gauges became unbonded mainly due to interception of wide cracks with the strain gauge locations on the longitudinal reinforcement at mid-span.

The difference in steel strain for *H10-1* compared to *H10-2*, both with $f_c'=80$ *MPa*, might be attributed to the lower reinforcement ratio in *H10-1* which resulted in higher reinforcement strains at similar load levels compared to *H10-2* (Figure

6-12). However, for specimens *N10-1* and *N10-2*, both with f_c'=41 MPa, a similar trend in steel strain was not observed with reference to ρ.

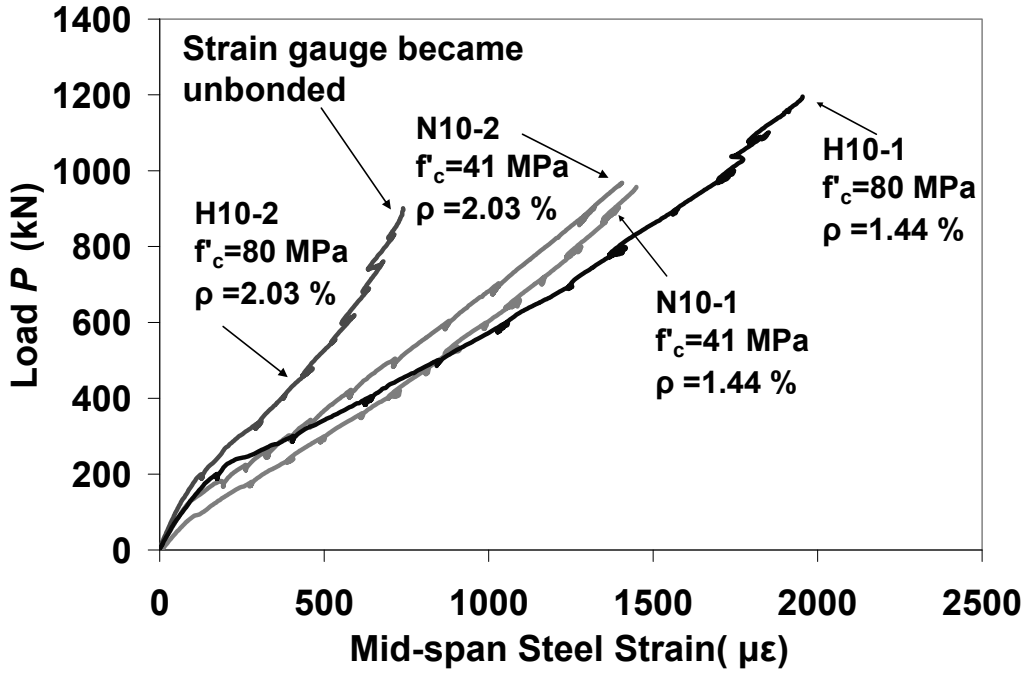

Figure 6-12: Load-steel strain response at mid-span for specimens with *h=1000 mm*.

6.1.3.4 Load-Crack Width Response of Shear Critical Specimens

The load-crack width response for shear critical specimens with total depth of *h=1000 mm* is shown in Figure (6-13). A non-linear relationship with gradually reducing slope was observed for all four specimens up to about 90% of maximum applied load before shear failure. Similar to the behavior of specimens with *h=308 mm* and *h=600 mm* discussed in Sections (6.1.1.4) and (6.1.2.4), in the last stages of loading just before shear failure, the crack widths increased dramatically, reaching relatively large values compared to the crack widths recorded at $0.9P_{max}$ (see C_{Wmax} in Table 6-6). Before this large increase in the crack widths, no reinforcement yielding at mid-span was observed for specimens

N10-1, *N10-2, H10-1* and *H10-2* (Section 6.1.3.3). This crack widening in SFRC members prior to shear failure reduces the aggregate interlock significantly. As shown in Tables (6-6), (6-4) and (6-2), C_{Wmax} increases with an increase in the height of specimens from *h=308 mm* to *h=1000 mm*. The large increase of crack widths before failure can be attributed to the pullout of fibers from the concrete matrix due to the tension between the adjacent crack surfaces. As a sample, the critical shear crack after failure and the pullout of fibers out of the matrix are shown in Figure (6-14) for the specimen *H10-2*. Note that in contrast to the fracture of the normal aggregates in direct shear test for the high strength SFRC prisms (Figure 4-7 in Section 4.3) no extensive fracture in aggregates was indicated in Figure (6-14) for the high strength specimen *H10-2* with $f_c'=80\ MPa$. This confirms that before shear failure, the fiber pullout due to tension between crack surfaces was the dominant mode rather than pure shear dislocation.

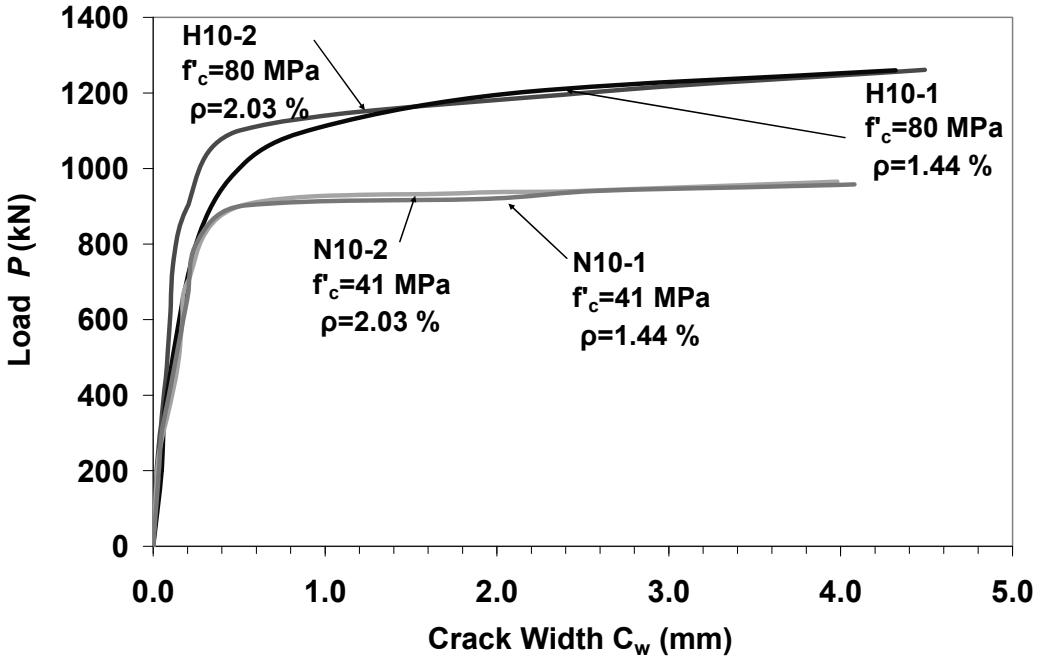

Figure 6-13: Load-crack width response for critical shear crack at level of longitudinal reinforcement in specimens with *h=1000 mm*.

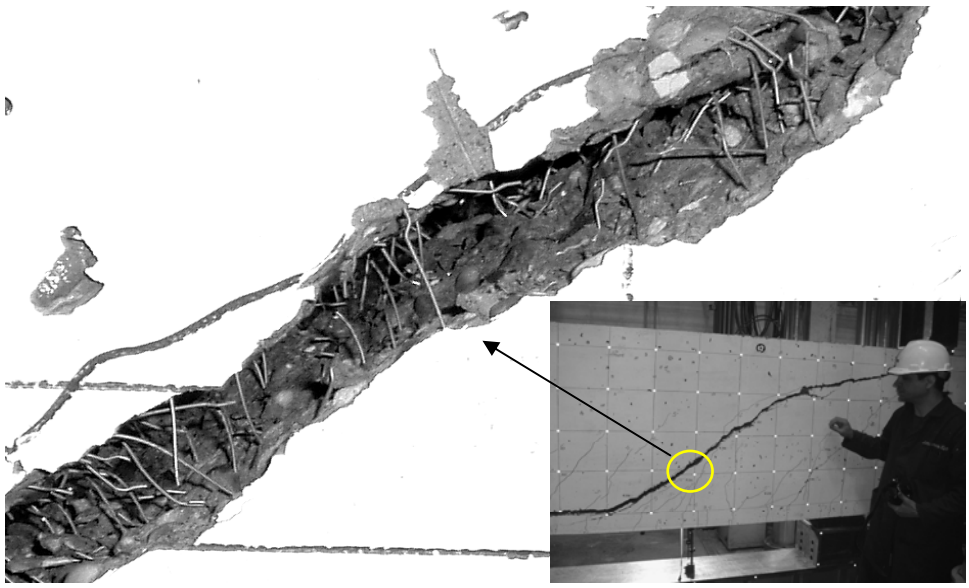

Figure 6-14: Critical shear crack after failure for a typical normal weight SFRC specimen.

6.1.3.5 Deflection and Crack Width at SLS

Considering an equivalent service load $S_L = 0.48\ P_{max}$ (see Section 6.1.1.5), the SLS deflection and crack widths for specimens with $h=1000\ mm$ were determined (Table 6-7). All relative deflection values at service load δ/L were lower than the common deflection limit of $L/360$ for RC members under live load alone (ACI 318-08).

Table 6-7: Deflection and crack width of SFRC specimens with $h=1000\ mm$ at SLS

Specimen	0.48 P_{max} from test (kN)	Failure Type	Behavior at SLS		
			Mid-span Deflection δ (mm)	δ/L	Max. Flexural Crack Width (mm)
N10-1	466	Shear	5.58	0.0010	0.10
N10-2	468	Shear	3.42	0.0006	0.15
H10-1	613	Shear	5.78	0.0010	0.10
H10-2	612	Shear	4.90	0.0009	0.10

The detected cracks at SLS were all very narrow flexural cracks near the mid-span. The crack control factor z (see Section 6.1.1.5) indicated that the crack widths for specimens *N10-1* and *H10-1* ($z=15856\ N/mm$) as well as specimens *N10-2* and *H10-2* ($z=16060\ N/mm$) are expected to be within the acceptable range for design of RC members with interior exposure ($z \leq 30000\ N/mm$).

6.2 Size Effect in the Shear Strength of Normal Weight SFRC Specimens

6.2.1 Normalized Shear Stress versus Effective Depth

The test results of 11 specimens which failed in shear are used to evaluate the influence of effective depth d on the shear capacity of SFRC specimens without stirrups. Based on the L_c values (i.e. the distance from mid-span of interception point of critical shear crack with the longitudinal steel) in Figures (6-1), (6-6), and (6-11), the critical section was taken at about *2d* from mid-span. Using the maximum shear force at the critical section including member self weight, the normalized shear stress $V_{test}/(b\,d\,\sqrt{f_c'})$ from Table (6-1) versus the effective depth d is plotted in Figure (6-15). Note that for specimens *H31* and *H32* which approached their shear and flexural capacities simultaneously (see Section 6.1.1.2), different symbols are shown in Figure (6-15). The normalized shear stress is observed to decrease as d increases. The average normalized shear stress for specimens with *h=1000 mm* was only about 53% of that observed in specimens with *h=308 mm*. This trend clearly indicates that a size effect in shear is present in the case of SFRC members.

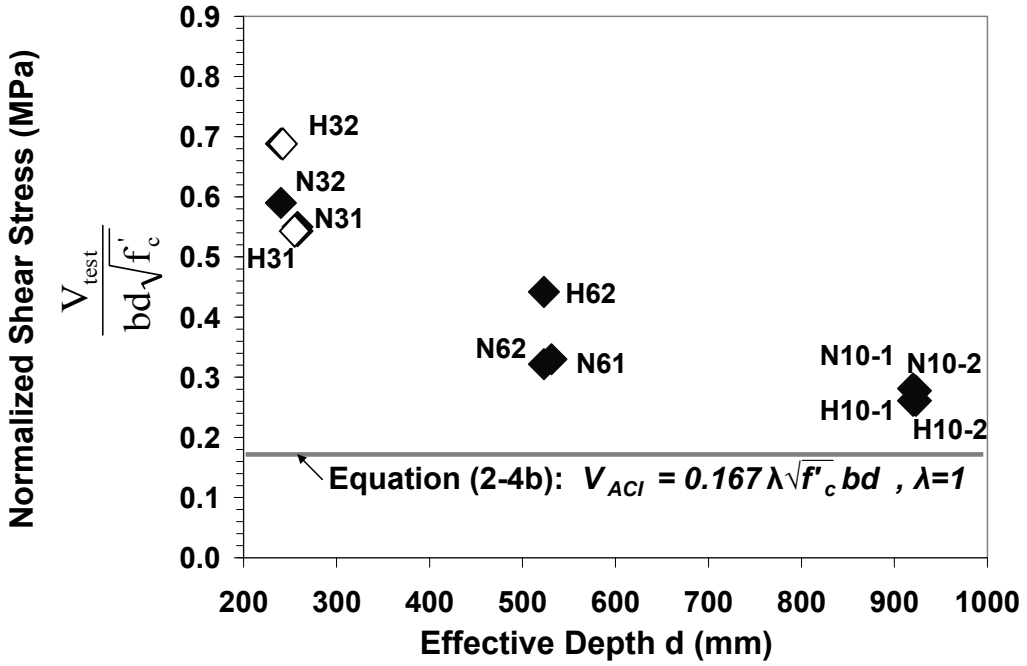

Figure 6-15: Normalized shear stress versus effective depth for shear critical SFRC specimens (Note: *H31* and *H32* approached their shear and flexural capacities simultaneously).

Shioya et al. (1989) observed a similar size effect for RC members without stirrups, where the shear stress at failure decreased by about 49% when the effective depth increased from *d=250 mm* to *d=975 mm*. *Kwak et al.* (2002) compared the shear strength of small size SFRC members from different researchers, mostly with $d \leq 300$ *mm*, and did not observe a significant size effect on the shear strength. However, *Rosenbusch and Teutsch* (2002) reported that an increase in effective depth from *260 mm* to *540 mm*, while other parameters were kept mostly constant, resulted in a 26% decrease in the average shear strength.

As discussed in Section (2.2.3), the size effect in shear for RC members without stirrups and without fibers can be captured by considering the decreased ability of wide cracks to transmit shear stress (*Vecchio* and *Collins* 1986, *Walraven* 1981). When the crack widths increase, the aggregate interlock decreases. *Shioya et al.* (1989) have shown that doubling the member depth will double the crack width at

mid-depth, if the strain in the longitudinal steel is kept the same. Hence, the shear stress at failure in large members is lower than in small members, and this has been experimentally verified in many studies (e.g. *Kani* 1967, *Shioya et al.* 1989, *Collins and Kuchma* 1999).

However, the new test results from this study (Section 6.1) as well as previous research by *Minelli and Plizzari* (2006) have both shown that the width of the critical shear crack in SFRC members increases considerably at the last stages of loading before failure. The results in Section (6.1) indicate that the maximum crack width before shear failure C_{Wmax} increases with an increase in the member depth from $h=308\ mm$ to $h=1000\ mm$. Even for small SFRC members with $h=308\ mm$ the crack widths before shear failure C_{Wmax} (Table 6-2) were large enough (0.58 *mm*~1.09 *mm*) to cause a considerable reduction in the aggregate interlock. Thus, decrease of shear stress at failure with increase in SFRC member depth (Figure 6-15) can not be attributed mainly to a decrease in the aggregate interlock. Instead, the bridging action of fibers across the adjacent surfaces of a diagonal crack in SFRC members can be considered analogous to the aggregate interlock action on the crack surfaces of RC members. As discussed in Section (4.5), for the steel fiber type used in this study ($L_f/D_f=55$, $L_f=30\ mm$) and crack widths larger than about $0.5\ mm$, the equivalent fiber tensile stress across adjacent surfaces of a crack σ_f decreases with an increase in the crack width. Hence, the shear stress at failure in large SFRC members with larger crack widths is lower than that in small SFRC members.

6.2.2 Size Effect in Shear Strength: Comparing Test Results with *ACI 318-08* and *CSA A23.3-04* Approaches

6.2.2.1 Test Results from Current Study

Even though size effect still exists for SFRC specimens (Section 6.2.1), a large increase in shear capacity was observed for SFRC specimens in comparison to the *ACI 318-08* shear model for conventional RC members without web reinforcement and without fibers (Figure 6-15). For all cases, the normalized shear stress was above the equivalent *ACI 318-08* shear capacity prediction V_{ACI} for plain concrete (Equation 2-4b). For SFRC specimens with *h=308 mm* (or *d* =240 *mm* ~ 258 *mm*), the average enhancement in shear capacity was 263% compared to the *ACI 318* model. The average enhancement in shear capacity for specimens with *h=600 mm* (or *d* =523 *mm* ~ 531 *mm*) and specimens with *h=1000 mm* (or *d* =920 *mm* ~ 923 *mm*) were 126% and 67%, respectively. The effectiveness of steel fibers in shear capacity enhancement relative to the *ACI 318* prediction, decreases with an increase in the total depth of specimens from *h=308 mm* to *h=1000 mm*.

Figure (6-16) compares the maximum shear capacity at failure for the 11 shear critical SFRC specimens in this study against the *CSA A23.3-04* prediction for similar RC members without steel fibers. Adding steel fibers into the concrete matrix gave considerable enhancement to the shear capacity of RC members relative to the *CSA A23.3-04* shear prediction for members without fibers. As illustrated in Figure (6-16), for specimens with *h=308 mm*, *h=600 mm* and *h=1000 mm*, the average increases in shear capacity were 134%, 71% and 88%, respectively, compared to the *CSA A23.3-04* model. The ratio V_{test}/V_{CSA} in Figure (6-16) does not show a clear trend as *d* increases from 240 *mm* to 923 *mm*. The average ratio V_{test}/V_{CSA} decreases when total depth of specimens increases from *h=308 mm* to *h=600 mm*, but then increases slightly with an increase in *h* from 600 *mm* to 1000 *mm*.

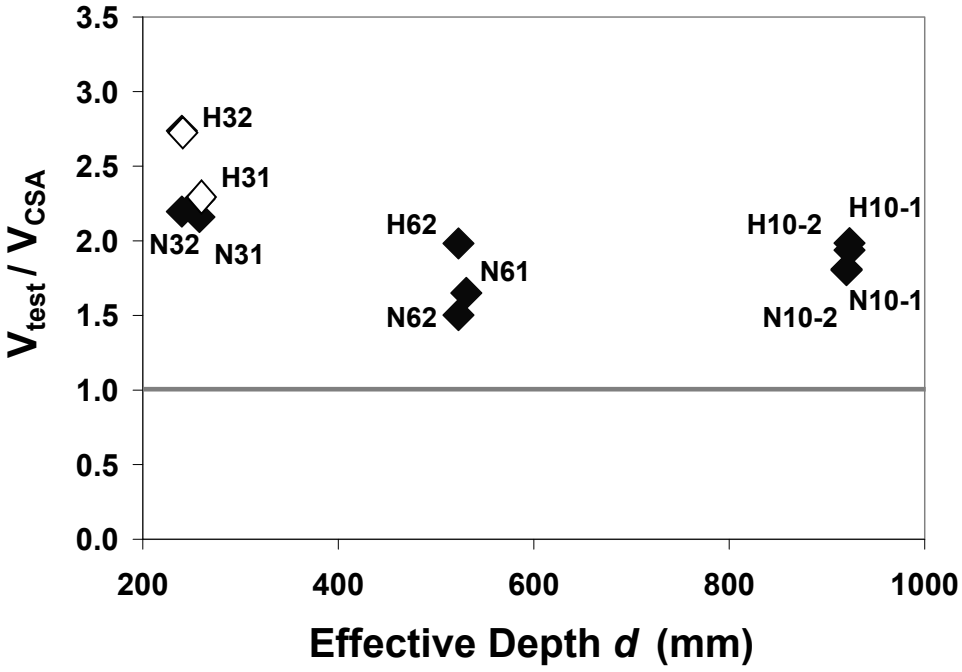

Figure 6-16: Comparing the shear capacity from current study against *CSA A23.3-04* model

6.2.2.2 Test Results from Previous Research and Current Study

A data base including 56 shear critical SFRC members from previous research and the current study was used to compare the maximum shear capacity at failure against the *ACI 318-08* and *CSA A23.3-04* predictions for similar RC members without steel fibers (Figures 6-17 & 6-18). These 56 SFRC members satisfy the following criteria (also see Table 7-3 in Chapter 7):

- Rectangular sections with $180\ mm \le h \le 1000\ mm$ and $b \ge 100\ mm$
- $a/d \ge 2.5$
- $0.75\% \le V_f \le 1.5\%$, $45 \le L_f/D_f \le 100$, and $25mm \le L_f \le 60\ mm$ (hooked end steel fibers)
- $20\ MPa \le f'_c \le 90\ MPa$

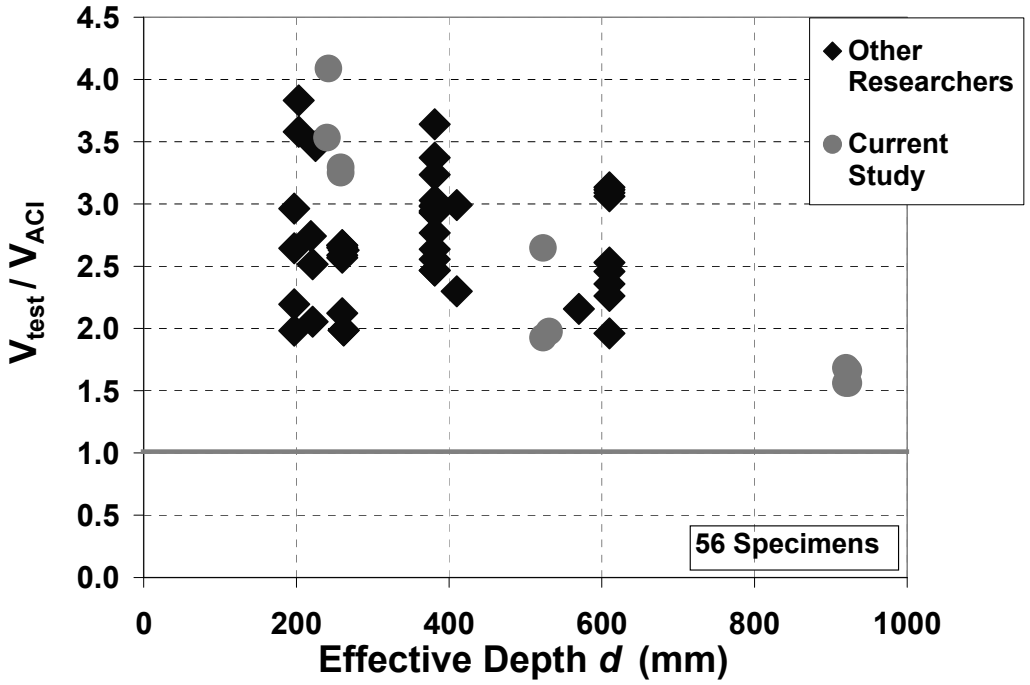

Figure 6-17: Comparing the shear capacity from previous research and current study against *ACI 318-08* model.

While Figure (6-17) does not indicate a size effect for specimens with $d \leq 400mm$, it clearly shows that shear capacity at failure decreases with an increase in the effective depth d from 400 *mm* to 923 *mm*. Note that the specimens in Figure (6-17) have a large range of ρ=1.15%~4.03% which is not accounted for in the *ACI 318-08* prediction, and this may influence the V_{test}/V_{ACI} ratio, too. However, for all specimens, the normalized shear stress was above the equivalent *ACI 318-08* prediction V_{ACI} for plain concrete. The minimum enhancement in shear capacity of SFRC members compared to V_c from the *ACI 318-08* model was 53% for the case of $d=923mm$ ($h=1000$ *mm*). These results validate the approach in *ACI 318-08* for using steel fibers instead of minimum stirrups to enhance the useable shear capacity from $0.5\varphi V_c$ up to φV_c in members with $h \leq 600\ mm$, $f'_c \leq 41\ MPa$ and without transverse reinforcement. The current study indicates that this approach

can also be extended for members with larger depths $h \leq 1000\ mm$ or higher compressive strengths $f_c' \leq 80\ MPa$.

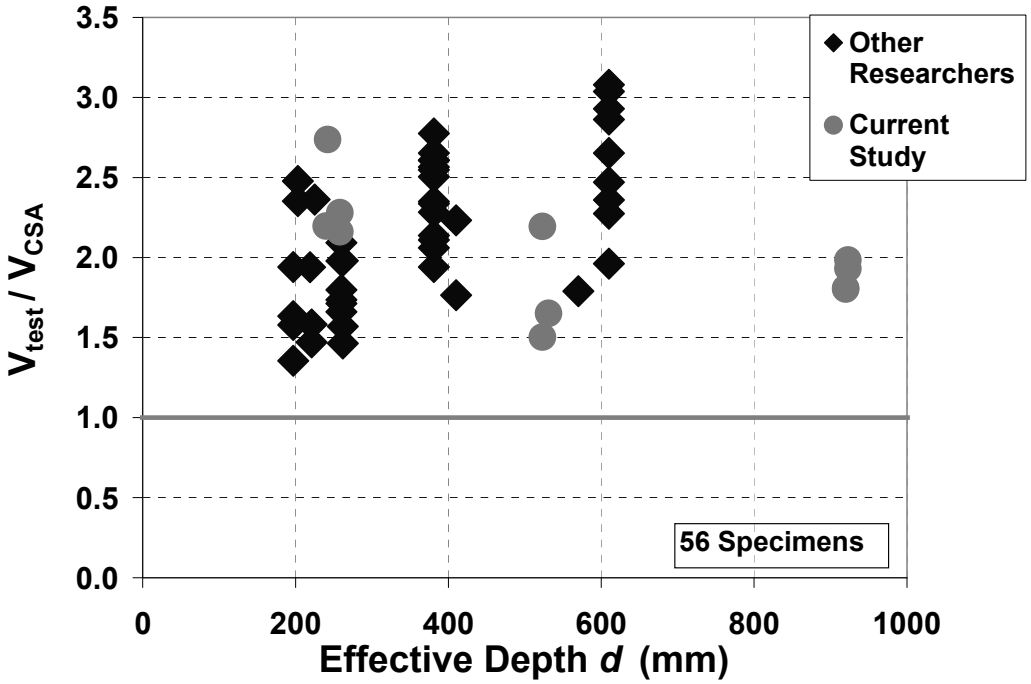

Figure 6-18: Comparing the shear capacity from previous research and current study against *CSA A23.3-04* model.

Figure (6-18) shows that shear capacity of SFRC members was at least 35% higher than the *CSA A23.3-04* shear capacity prediction for similar RC members without fibers. In Section (2.3.1), it was noted that the *CSA A23.3-04* model accounts for size effect related to the aggregate interlock at the cracks for plain concrete. The ratio V_{test}/V_{CSA} in Figure (6-18) does not show a decreasing trend as h increases from 180 *mm* to 1000 *mm*. As explained in Section (6.2.1), the size effect mechanism in SFRC members is different from that of RC members without fibers. However, the trend of V_{test}/V_{CSA} in Figure (6-18) indicates that there is no additional size effect for SFRC members beyond that considered in *CSA A23.3-04* model for RC members. Note that *CSA A23.3-04* model for RC

members also accounts for the steel strain effect (Section 2.3.1). Hence, the differences in longitudinal reinforcement ratio among the specimens are reflected in the calculation of shear capacity V_{CSA} for similar RC members without fibers. The effect of longitudinal reinforcement ratio on the shear strength of SFRC specimens is discussed in Section (6.3).

According to *Collins et al.* (1996), the size and strain effects on shear capacity are not independent. However, in deriving the *CSA A23.3-04* provisions (*Bentz et al.* 2006) based on simplifications to the MCFT (*Vecchio and Collins* 1986), the interdependence of the two effects is ignored. It is assumed that the parameter β, used in establishing the shear stress at failure, can be taken as the product of a strain effect term and a size effect term for RC members (Section 2.3.1). However, validity of a similar approach for separation and formulation of strain and size effect terms in SFRC members needs to be investigated through further research.

Based on the results in Figure (6-18) and the discussions in this section, the *CSA A23.3-04* shear model (Equation 2-5) can be modified to account for the shear capacity enhancement due to use of steel fibers. For normal weight SFRC members (λ=1) which satisfy the same criteria indicated earlier for the 56 members in Figure (6-18), a fiber contribution factor η may be proposed as follows:

$$V_{CSA,f} = \lambda \eta \beta \sqrt{f_c'}\, b\, d_v \qquad (6\text{-}5)$$

where $\eta = 1.33$ representing a lower bound for the shear capacity enhancement due to the contribution of hooked end steel fibers (see Figure 6-18). All other parameters for Equation (2-5) remain unchanged.

6.3 Influence of Longitudinal Reinforcement on the Shear Behavior of SFRC

6.3.1 Relationship between Normalized Shear Stress and Reinforcement Ratio

Figures (6-19), (6-20) and (6-21) summarize the influence of the longitudinal reinforcement ratio ρ on the shear capacity of SFRC specimens with *h=308 mm*, *h=600 mm* and *h=1000 mm*, respectively. These results indicate that for the range of ρ used in this study, the influence of the longitudinal reinforcement ratio on the normalized shear stress at failure was very small. For specimens with *h=308 mm* and f'_c*=41 MPa* in Figure (6-19), there was a 9% increase in the shear capacity as ρ varied from 2.50% to 4.03%. In specimens with *h=600 mm*, when ρ increased by 36%, the increase in shear capacity of specimens with f'_c*=41 MPa* and f'_c*=23 MPa* was about 7% and 0%, respectively. Meanwhile, for specimens with *h=1000 mm*, as the longitudinal reinforcement ratio varied from 1.44% to 2.03%, there was 4% and 0% variation in normalized shear stress at failure for cases with f'_c*=41 MPa* and f'_c*=80 MPa*, respectively. Test results reported by *Dinh (2009)* showed that the shear capacity of SFRC specimens with V_f *=1%*, f'_c*=38 MPa*, and *h=457 mm* did not change considerably (1.4%) when the reinforcement ratio varied from 1.96% to 2.67%.

This study and research by *Dinh (2009)* both have shown that changes in the longitudinal reinforcement ratio (36% ~ 61%) do not lead to a significant change in the shear capacity of SFRC members with V_f *=1%*.

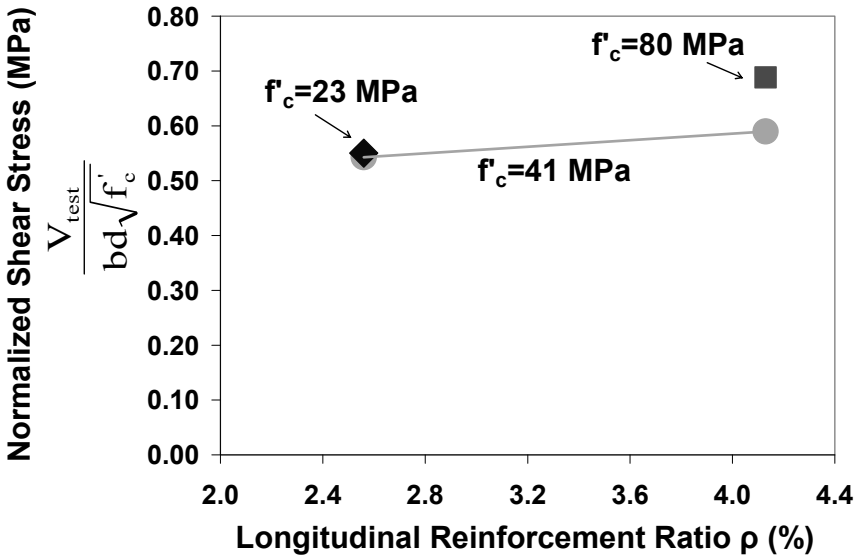

Figure 6-19: Effect of longitudinal reinforcement ratio on the shear capacity of SFRC specimens with *h=308 mm.*

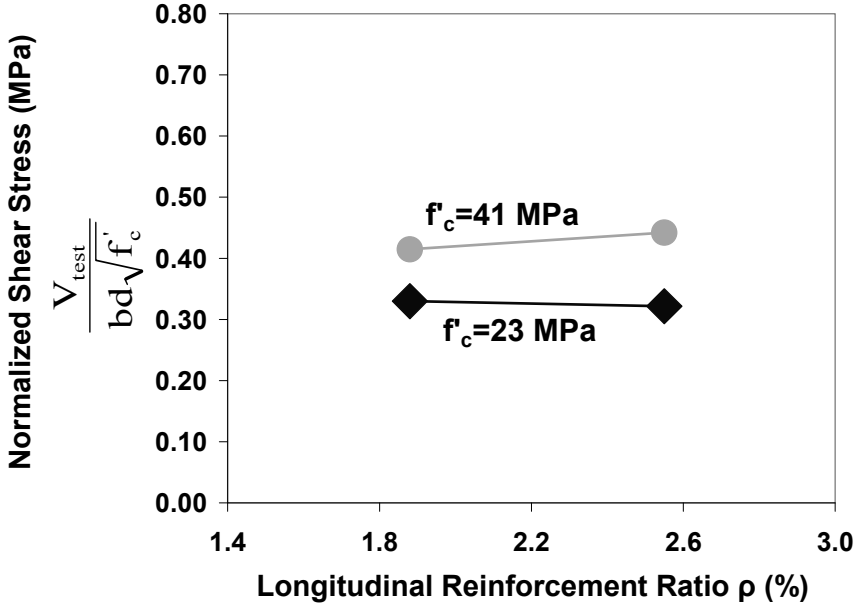

Figure 6-20: Effect of longitudinal reinforcement ratio on the shear capacity of SFRC specimens with *h=600 mm*.

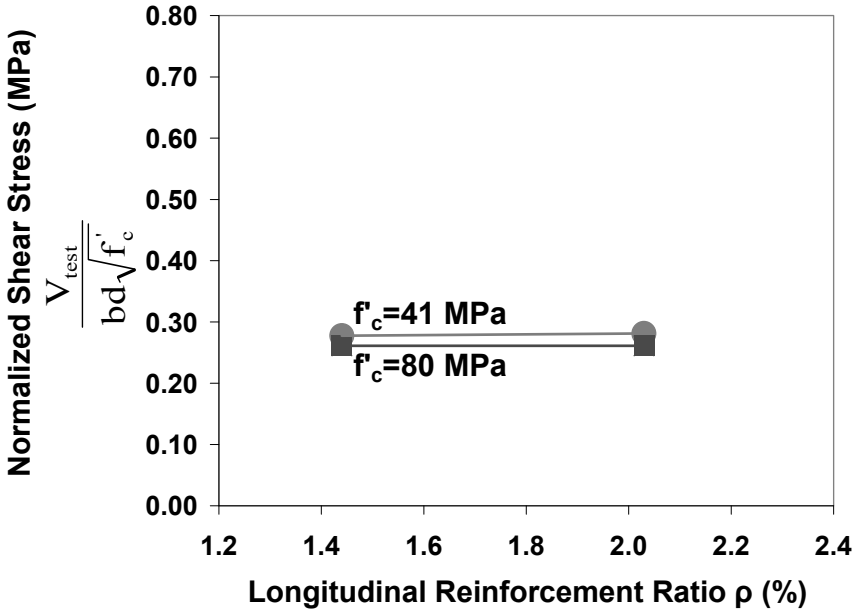

Figure 6-21: Effect of longitudinal reinforcement ratio on the shear capacity of SFRC specimens with *h=1000 mm.*

6.3.2 Estimation of Tensile Steel Strains in SFRC Members

As discussed in Section (2.3.1), the *CSA A23.3-04* shear model for RC members accounts for the decrease in shear stress at failure due to increases in the member longitudinal strain. According to *CSA A23.3-04*, this strain effect is considered through parameter ε_x which is taken as 1/2 of the strain in the longitudinal tensile steel at the critical section for RC members, and can be estimated from:

$$\varepsilon_x = \frac{M/d_v + V}{2E_s A_s} \tag{2-7}$$

In this section, the validity of this formula for SFRC members will be examined. Note that the shear term in Equation (2-7) for RC members, represents the shear force transferred through the aggregate interlock; however, for the specimens in

the current study the aggregate interlock is negligible due to the large crack widths observed before failure (Section 6.1). For these specimens the bridging action of steel fibers is assumed to replace the aggregate interlock across the shear crack. As shown in Equation (2-7), tensile strain in the longitudinal reinforcement changes when A_s, V and M change. Since the ratio between M and V is related to the shear-span to effective depth ratio a/d, this formula also includes the effect of a/d implicitly.

For the SFRC members in the current study, two strain gauges were installed at the distance $d_v = 0.9d$ from mid-span (one at each side), where the bending moment and shear force are both considerable. The steel strain ε_s estimated from the *CSA A23.3-04* shear model (i.e. double ε_x from Equation 2-7) and the average measured strain gauge magnitudes have been compared in Table (6-8) for 8 shear critical specimens at the ultimate condition before failure ($P=P_{max}$). The strain gauges at distance of $d_v = 0.9d$ from mid-span in specimens *H32*, *H10-1*, and *H10-2* became unbonded before shear failure, so these specimens were not included in Table (6-8). The bending moment M and the shear force V for Equation (2-7), were calculated from the applied load at the ultimate condition before shear failure ($P=P_{max}$) at a section $d_v = 0.9d$ from mid-span.

Table 6-8: Comparing the measured strain from test with the strain from Equation (2-7) at the ultimate condition before failure ($P=P_{max}$)

Specimen Name	$\varepsilon_{s,test}$ ***(με)***	$\varepsilon_s = 2\varepsilon_x$ ***from CSA (με)***	$\varepsilon_s / \varepsilon_{s,test}$
N31	1682	1860	1.11
N32	1358	1660	1.2
H31	2077	2000	0.96
N61	1290	1460	1.13
N62	952	1060	1.11
H62	1803	1940	1.08
N10-1	2220	2000	0.90
N10-2	1551	1400	0.90
Average			$1.05 \approx 1$

The calculated $\varepsilon_s=2\varepsilon_x$ using Equation (2-7) shows a good agreement with the results obtained from strain gauges during test (*i.e.* $\varepsilon_s \approx \varepsilon_{s,test}$) at the ultimate load before failure ($P=P_{max}$). This demonstrates that Equation (2-7) is still applicable to SFRC members and therefore it can also be used to estimate the steel strain at the distance L_c from mid-span where the critical shear crack intercepts the longitudinal reinforcement (Section 6.1). The Equation (2-7) was employed to estimate the tensile steel strain for shear critical SFRC specimens at a typical distance $L_c \approx 2d$ from mid-span at the ultimate load ($P=P_{max}$) before failure (Table 6-9). The estimated values of tensile strain in Table (6-9) indicate that no yielding occurred in longitudinal reinforcement at *2d* from mid-span, and the steel stress values were between $f_s=0.35f_y$ and $f_s=0.91f_y$.

Table 6-9: Tensile Steel strain at *2d* from mid-span at the ultimate load ($P=P_{max}$)

Specimen	***ρ (%)***	***ε_s at 2d from mid-span (με)***
N31	2.56	1180
N32	4.13	1040
N61	1.88	880
N62	2.56	660
H31	2.56	1540
H32	4.13	1700
H62	2.56	1220
N10-1	1.44	1340
N10-2	2.03	860
H10-1	1.44	1760
H10-2	2.03	1140

6.4 Flexural Capacity Enhancement in Comparison to *ACI 318-08* Flexural Model

In this section, the flexural capacity enhancement due to the contribution of the steel fibers is studied for the normal weight concrete specimens *H31*, *H32*, and *H62* in comparison to the *ACI 318-08* flexural model for similar RC members without fibers (Table 6-10). In Section (6.1), it was observed that specimen *H61* failed in flexure before reaching its shear capacity. Meanwhile, it was noted that specimens *H31* and *H32* both approached their flexural and shear capacities simultaneously, with reinforcement yielding at mid-span.

Table 6-10: Flexural capacity of specimens *H31*, *H32*, and *H62*

Specimen	b (mm)	d (mm)	f'_c (MPa)	ρ %	Failure Type	P_{max}* (kN)	M_{test}** (kN.m)	M_{ACI} (kN.m)	M_{test}/M_{ACI}
H31	310	258	41	2.50	Shear++	554	215	177	1.22
H61	300	531	41	1.88	Flexure	838	673	568	1.19
H32	310	240	80	4.03	Shear++	915	333	258	1.29

* The maximum applied load at mid-span
*The maximum moment at mid-span during test including selfweight
++ These specimens approached their shear and flexural capacities simultaneously (see Section 6.1.1.2)

According to *ACI 318-08*, the nominal flexural capacity of tension controlled RC members without fibers can be calculated from:

$$M_{ACI} = A_s f_y (d - \frac{\beta_1 c}{2}) = \rho b d^2 f_y (1 - \rho \frac{f_y}{2\alpha_1 f'_c}) \quad (6\text{-}6)$$

where, the parameter $\alpha_1 = 0.85$ and β_1 can be obtained from:

$$\beta_1 = \begin{cases} 0.85 & \text{for } f'_c \leq 28\ MPa \\ 1.05 - 0.007\, f'_c \geq 0.65 & \text{for } f'_c > 28\ \text{MPa} \end{cases} \quad (2\text{-}28)$$

Figure (6-22) compares the maximum flexural capacity at failure for SFRC specimens *H31*, *H32*, and *H61* against the *ACI 318-08* prediction for similar RC members without steel fibers. Adding steel fibers into the concrete matrix gave considerable enhancement to the flexural capacity of RC members relative to the *ACI 318-08* flexure prediction for members without fibers. As illustrated in Figure (6-22), for specimens *H31*, *H32*, and *H61* the increases in flexural capacity were 22%, 29% and 19%, respectively, compared to the *ACI 318-08* model.

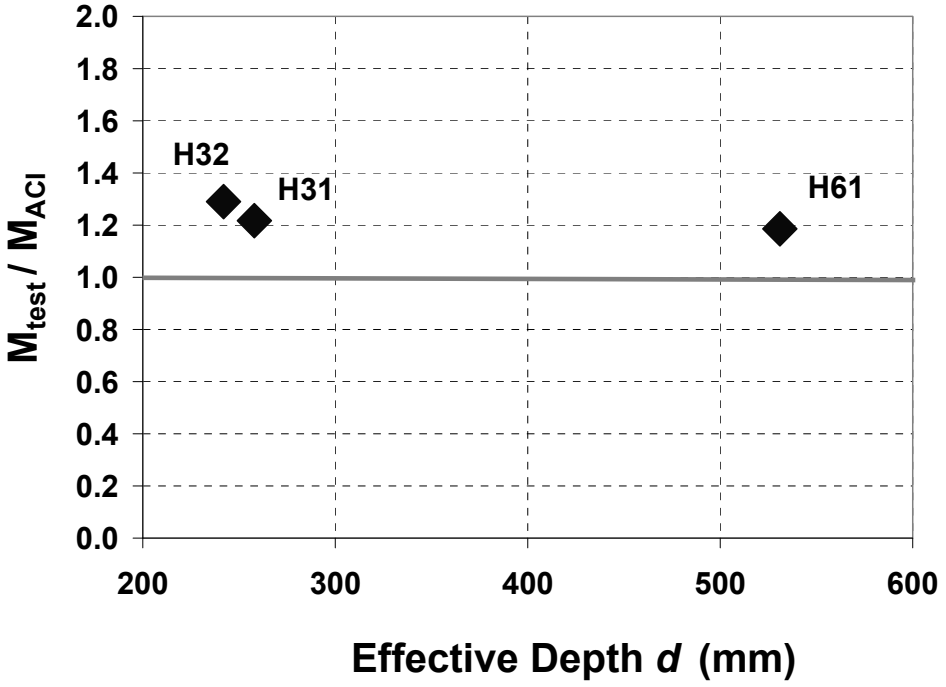

Figure 6-22: Comparing the flexural capacity of specimens *H31*, *H32*, and *H6*1 against *ACI 318-08* flexural model

7. Shear Modeling for Slender SFRC Members without Stirrups

In this chapter, two shear capacity models for slender SFRC members without stirrups are developed. First, an analytical model is developed based on mechanical principles and empirical measurements of crack geometry reported in Section (6.1). Then, the analytical model is further simplified to be suitable for use in design. For validation, capacity predictions for both models are examined for a filtered database. Furthermore, the prediction quality of the simplified design model is compared against results using seven published SFRC shear models from other researchers as well as *ACI 318-08* and *CSA A23.3-04* shear models for RC members without fibers.

The scope of the models developed in this chapter is limited to structural members which satisfy the following criteria:

- Rectangular cross section with $180\ mm \le h \le 1000\ mm$ and $b \ge 100\ mm$
- $a/d \ge 2.5$
- $0.75\% \le V_f \le 1.5\%$, $45 \le L_f/D_f \le 100$, and $25mm \le L_f \le 60\ mm$ (hooked end steel fibers)
- $20\ MPa \le f'_c \le 90\ MPa$

The range of overall member depth values ($180\ mm \le h \le 1000\ mm$) reflects the typical size of concrete members without stirrups in buildings and bridges, including slabs, foundations and walls. Some of the empirical measurements of crack geometry used to develop the models, were extracted from structural tests on specimens with a maximum depth $h=1000\ mm$ in the current study. A minimum section width of $b \ge 100\ mm$ was considered to reflect SFRC members with reasonable space for placing the reinforcement in the section with adequate concrete cover. Note that a small section width b relative to the steel fiber length

can also influence the alignment of fibers in the concrete matrix. The shear-span to effective depth $a/d \geq 2.5$ was selected to represent slender SFRC members with a sectional shear behavior. As discussed in Section (2.2.2), this limiting value of a/d is comparable to the $a/d=2.5$ limit for RC members without fibers reported by *Zsutty* (1968) and *Kani* (1979) as a transition point between the beam action and arch action. Commercially available hooked end steel fibers with an aspect ratio between 45 and 100 and a length of $25mm \leq L_f \leq 60\ mm$ were considered. The range of fiber content $0.75\% \leq V_f \leq 1.5\%$ represents a moderate and practical volume fraction of fibers which can also satisfy the performance requirements in *ACI 318-08* for use of steel fibers as a replacement for minimum shear reinforcement. Also, the range of $20\ MPa \leq f'_c \leq 90\ MPa$ was selected to reflect the typical and practical range of compressive strengths used in most concrete structures.

7.1 Analytical Model

7.1.1 Overview of the Approach

Consider a critical shear crack at the ultimate limit state for a slender SFRC member without stirrups just before shear failure (Figure 7-1a). The shape of the critical shear crack is typically curved, and at the shear failure it usually extends rapidly toward the farthest compressive fiber of the member (Section 6.1). As discussed in Section (6.1), this extension of the critical shear crack at shear failure may occur with or without concrete crushing in the compression zone.

Similar to prior research (e.g. *Narayanan and Darwish* 1987, *Dinh* 2009), an idealized model for the crack shape was assumed in which the crack starts vertically as a flexural crack from the tension face of the member up to the centroid of the longitudinal reinforcement (Figure 7-1b). Then, the crack extends along an inclined line until it reaches the neutral axis occurring at depth c below the extreme compression face. The inclined line is assumed to be straight and

forms an angle of θ with the longitudinal axis of member. The cross section through the uncracked compressive region is shown as a vertical straight line.

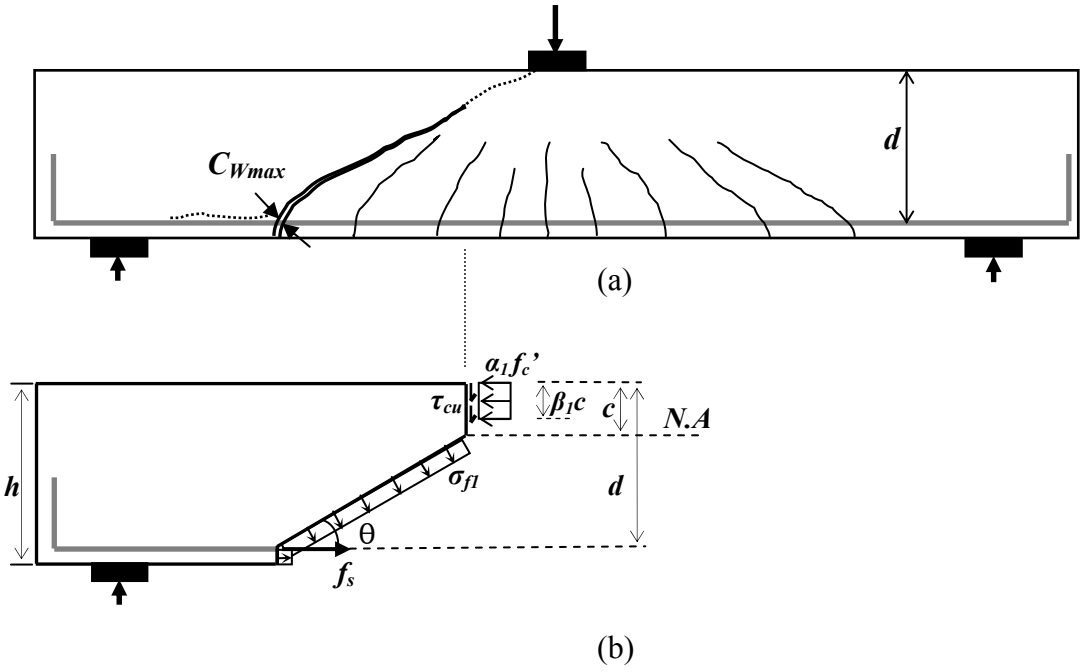

Figure 7-1: a) A critical shear crack before shear failure b) Distribution of stress along diagonal crack and compression zone for proposed model

At the ultimate state, the critical shear section of a slender SFRC member without stirrups resists the shear force through four possible components: 1) shearing in the uncracked compression region 2) fiber bridging forces across the inclined shear crack 3) aggregate interlock across the inclined shear crack and 4) dowel action of longitudinal reinforcement. These mechanisms have been previously described by several researchers (e.g. *Mansur et al.* 1986, *Ashour et al.* 1992, *Khuntia et al.* 1999). Most of these researchers assumed that the components 1, 3 and 4 are reflected in the shear resistance V_c of an RC member without stirrups and without fibers. Accordingly, the contribution of fibers to the shear capacity of SFRC members was added as an additional, independent component to the V_c prediction for RC members. However, in the current model, components 3 and 4

are neglected for some reasons which are discussed in the following lines, and the contribution from components 1 and 2 are directly considered.

According to the empirical crack width measurements for the SFRC members in this study (Section 6.1) as well as test results reported by *Minelli and Plizzari* (2006) the critical shear crack width increases considerably at the ultimate condition just prior to shear failure (see C_{Wmax} in Table 7-1). The observed range of crack widths is large enough to diminish any contribution of aggregate interlock to the shear resistance of SFRC members. Also, the component of dowel action is believed to be small (*Bresler and Pister* 1958) and is therefore neglected here.

Table 7-1: C_{Wmax} and R_1 for shear critical specimens

Specimen	***h* *(mm)***	C_{Wmax} ***(mm)***	$R_1 = \frac{\sigma_{f1}}{\sqrt{V_f \cdot f_c'}}$ **(*MPa*)**
N31	308	0.58	2.70
N32	308	0.74	2.62
H31	308	1.09	2.44
H32	308	0.7	2.64
N61	600	3.47	1.25
N62	600	3.45	1.26
H62	600	2.52	1.73
N10-1	1000	4.08	0.95
N10-2	1000	3.98	1.00
H10-1	1000	4.32	0.83
H10-2	1000	4.49	0.74

The shear model developed in this study assumes that the shear force capacity of SFRC members without stirrups V_{frc1} can be approximated by considering two components, expressed as:

$$V_{frc1} = V_{cc} + V_{ft} \tag{7-1}$$

where,

V_{cc} : Shear force resistance from the uncracked compressive concrete zone

V_{ft} : Shear force resistance from the vertical component of the fiber crack bridging force

The procedure and details for calculation of V_{cc} and V_{ft} are described in Sections (7.1.3) and (7.1.4), respectively.

As discussed in section (2.3.2), a similar concept was also proposed by *Dinh* (2009). However, in the current study, the model formulations for the resistance components as well as the scope of model are different. After explaining the procedure for development of current model, the efficiency of the proposed shear strength model is compared against *Dinh* (2009) and other published models in Section (7.2.2).

7.1.2 Geometry

7.1.2.1 Angle of Diagonal Shear Crack and Critical Section Location

In Section (6.1), the diagonal shear crack angle θ and the distance of interception point with longitudinal reinforcement from mid-span L_c were calculated for the shear critical specimens. The values of θ and L_c for all normal weight concrete shear critical specimens are shown in Table (7-2). As shown in Table (7-2), no relationship between θ or L_c/d and ρ could be established for SFRC specimens with similar d and f'_c. Parameters θ and L_c/d were treated as independent of ρ in the model development.

Table 7-2: θ and L_c/d for normal weight shear critical specimens in the current study

Shear critical Specimen	d(mm)	f'_c (MPa)	ρ (%)	L_c (mm)	L_c/d	θ (degree)
N31	258	23	2.50	590	2.29	32.4
N32	240	41	4.03	550	2.29	33.6
H31	258	41	2.50	470	1.82	32.0
H32	240	80	4.03	510	2.12	29.5
N61	531	23	1.88	1030	1.94	29.9
N62	523	23	2.55	1150	2.19	31.7
H62	523	41	2.55	1130	2.16	34.9
N10-1	923	41	1.44	1800	1.95	31.4
N10-2	920	41	2.03	2200	2.39	32.6
H10-1	923	80	1.44	1800	1.95	31.8
H10-2	920	80	2.03	1700	1.84	31.0
Average					2.09 ≈ 2	31.9 ≈ 32°
COV					9.4%	4.8%

From Table (7-2), the average values for θ and L_c are approximately 32° and *2d*, respectively, with Coefficients of Variation of 4.8% and 9.4%. Thus, constant values of $\theta=32^o$ and $L_c=2d$ are assumed for the proposed analytical model (Figure 7-2).

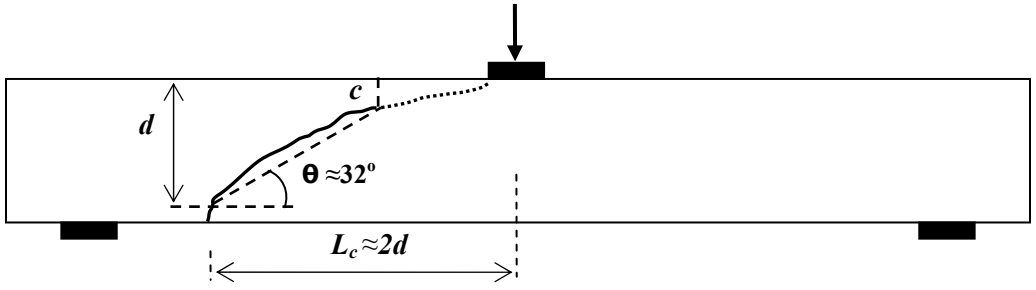

Figure 7-2: The assumed values of θ and L_c for the proposed analytical model

7.1.2.2 Depth of Compression Zone *c*

As discussed in Section (6.1), for most of the SFRC members in the current study, the compression strain in the compressive zone increased dramatically at the ultimate load before shear failure. The shear failure occurred when the compressive concrete crushed at the region between the top of the diagonal crack and the edge of the loading plate at mid-span. Thus, it is assumed that the strain in the extreme concrete compressive fiber reaches the value of 0.0035 *mm/mm* according to the *CSA A23.3-04* flexural design model for RC members without fibers. The results of compression tests on SFRC cylinders from the current study (Section 4.1) and previous research (e.g. *Fanella and Naaman* 1985, *Soroushian and Bayasi* 1991, *Ezeldin and Balaguru* 1992) have shown that addition of a moderate volume fraction of steel fibers has insignificant influence on the pre-peak compressive strength of SFRC. However, there was considerable improvement in ductility in the post-peak phase for SFRC compared to the plain concrete. The strain corresponding to the peak stress was slightly higher in SFRC compared to that in plain concrete. In the current model, a uniform compressive stress block with stress magnitude of $\alpha_1 f'_c$ and depth of $\beta_1 c$ was assumed in the compression zone, similar to flexural model for RC members (Figure 7-1b). While the post-peak response of SFRC cylinders may allow some adjustment to α_1 and β_1, for simplicity these two parameters were taken in accordance with *CSA A23.3-04*:

$$\alpha_1 = 0.85 - 0.0015 f'_c \geq 0.67 \quad (4\text{-}7)$$

$$\beta_1 = 0.97 - 0.0025 f'_c \geq 0.67 \quad (4\text{-}8)$$

From the critical shear section shown in Figure (7-1b), the axial forces for static equilibrium can be written as:

$$\sum F_x = 0 \rightarrow \alpha_1 f_c^{'} \beta_1 cb - \sigma_{f1} b(\frac{d-c}{\sin\theta})\sin\theta - \sigma_{f1}(h-d)b - A_s f_s = 0 \qquad (7\text{-}2a)$$

$$\rightarrow \alpha_1 f_c^{'} \beta_1 cb - \sigma_{f1}(h-c)b - A_s f_s = 0 \qquad (7\text{-}2b)$$

$$\rightarrow c = \frac{A_s f_s + \sigma_{f1} bh}{(\alpha_1 f_c^{'} \beta_1 + \sigma_{f1})b} \qquad (7\text{-}2c)$$

As discussed in Section (6.3.2), the tensile steel strain ε_s can be estimated as double ε_x determined from Equation (2-7). Therefore, the steel stress at *2d* from mid-span can be calculated as:

$$f_s = E_s \varepsilon_s = \frac{M\ /(0.9d) + V}{A_s} \le f_y \qquad \text{(MPa)} \qquad (7\text{-}3)$$

For a simple span member with shear-span to effective depth ratio $a/d \ge 2.5$ and negligible selfweight, the moment M at $L_c \approx 2d$ from mid-span can be calculated as:

$$M = V(a-2d) = Vd(\frac{a}{d} - 2) \qquad (7\text{-}4)$$

Therefore, the Equation (7-3) can be expressed as:

$$f_s = \frac{V}{0.9A_s}(\frac{a}{d} - 1.1) \le f_y \qquad \textit{(MPa)} \qquad (7\text{-}5)$$

For Equation (7-5), the shear force V at the critical section needs to initially be estimated and then checked against the shear capacity V_{frc1} obtained from the current model at the end. Iterations can be performed as needed until convergence ($V \approx V_{frc1}$) happens. The procedure for calculation of the equivalent tensile stress of fibers σ_{f1} for structural SFRC members will be discussed in Section (7.1.4).

7.1.3 Calculation of V_{cc}

From Figure (7-1b), resistance from shearing action of the concrete compressive block V_{cc} can be calculated as:

$$V_{cc} = \tau_{cu}\beta_1 cb \tag{7-6}$$

where, τ_{cu} is the ultimate shear stress in the compressive block which is subjected to a uniform compression stress of $\alpha_1 f'_c$. To calculate τ_{cu}, the failure criterion proposed by *Bresler and Pister* (1958) for plain concrete subjected to combined normal compressive stress and shear stress was adopted (see Section 2.3.1):

$$\frac{\tau_{cu}}{f'_c} = 0.1\sqrt{0.62 + 7.86(\frac{\sigma_{cu}}{f'_c}) - 8.46(\frac{\sigma_{cu}}{f'_c})^2} \tag{2- 9}$$

where σ_{cu} and τ_{cu} are the ultimate uniform compressive stress and shear stress, respectively. As discussed above and shown in Figure (7-1a), for the current model $\sigma_{cu}/f'_c=\alpha_1$. By substituting $\sigma_{cu}/f'_c=\alpha_1$ from Equation (4-7) into Equation (2-9), the ultimate shear stress in the compressive block τ_{cu} can be calculated as:

$$\tau_{cu} = 0.1 f'_c\sqrt{0.62 + 7.86\alpha_1 - 8.46(\alpha_1)^2} \tag{7-7}$$

Bresler and Pister (1958) did not indicate an upper limit of f'_c in Equation (2-9) for prediction of shear strength of RC members without stirrups. However, they observed that the calculated shear strength from Equation (2-9) correlates well with the test data for 21 RC specimens which had 21 $MPa \le f'_c \le 41$ MPa (Section 2.3.1). *Dinh* (2009) used the *Bresler and Pister* (1958) failure criterion in his model to estimate the shearing stress in compression zone of SFRC members with $f'_c \le 55$ MPa. For the current study, it is assumed that Equation (2-9) is

applicable for higher f'_c up to 90 MPa, and model validation for SFRC specimens with 20 $MPa \leq f'_c \leq 90\ MPa$ is studied in Section (7.1.6).

7.1.4 Calculation of V_{ft}

The fiber tension across the critical shear crack before failure depends on the crack width which varies along the crack length (see Sections 6.1 & 4.5). The number of fibers bridging the crack, fibers alignment and the distribution of fibers can also affect the fiber tension across the shear crack (*Swamy and Al-Taan* 1981). However, similar to the previous research (e.g. *Narayanan and Darwish* 1987, *Khuntia et al.* 1999, *Dinh* 2009) an equivalent uniform stress distribution σ_{f1} is proposed here to simplify the calculation procedure (Figure 7-1b). Accordingly, the vertical component of the steel fiber tensile force can be calculated from:

$$V_{ft} = \sigma_{f1} b \frac{d-c}{\sin\theta}.\cos\theta = \sigma_{f1} b \frac{d-c}{\tan\theta} \tag{7-8}$$

From Section (7.1.2), the shear crack angle was specified as a constant value of $\theta=32^o$ based on the tests in this study. The equivalent uniform tensile stress σ_{f1} can be obtained from an analogy between the diagonal shear crack and the vertical flexural crack in the material bending test according to *ASTM C1609-05* (see Section 4.5). The observations in Section (6.1), about widening of the critical shear crack just before shear failure and the relative rotation of the two pieces of the specimens around the compressive zone at the top of the shear crack support this analogy. Based on this analogy, shear crack width at the level of tensile reinforcement C_{Wmax} can be considered as similar to the crack mouth opening in the material bending test C_M. For a given $C_{Wmax} \geq 0.2\ mm$, an equivalent uniform tensile stress σ_{f1} can be determined from Equation (4-13b) in Section (4.5) and then applied along the diagonal shear crack in Figure (7-1b):

$$\sigma_{f1} = 2.9\sqrt{V_f \cdot f_c'}\,(1.03 - \frac{C_{W\,max}}{5.8}) \qquad \text{for } C_{Wmax} \geq 0.2\ mm \qquad (7\text{-}9)$$

Note that for shear critical specimens with normal weight concrete in the current study having total height of $308\ mm \leq h \leq 1000mm$, the measured C_{Wmax} from Section (6.1) are all larger than 0.2 *mm* (Table 7-1). From Equation (7-9), the normalized fiber tensile stress R_1 can be calculated as:

$$R_1 = \frac{\sigma_{f1}}{\sqrt{V_f \cdot f_c'}} = 2.99 - \frac{C_{W\,max}}{2} \qquad (7\text{-}10)$$

The values of R_1 were determined for the 11 specimens in Table (7-1) using Equation (7-10). Based on the test results in Section (6.1), for specimens with similar total depth h and different longitudinal reinforcement ratio ρ, no relationship between C_{Wmax} or R_1 and the longitudinal reinforcement strain could be established. However, C_{Wmax} increased with an increase in the total depth of specimens from $h=308\ mm$ to $h=1000\ mm$. For the 11 shear critical specimens in Table (7-1), the relationship between R_1 and h is plotted in Figure (7-3). It is observed that R_1 decreases with an increase in h. This means that R_1 can represent a size effect term in the proposed model.

In Figure (7-3), an empirical linear formula was selected as a simple fit to facilitate calculation of R_1 from total depth and without the need for using C_{Wmax} directly:

$$R_1 = 3.2 - \frac{h}{431} \qquad (7\text{-}11)$$

Note that additional refinement of the empirical Equation (7-11) may be warranted as additional test data for the relationship between C_{Wmax} or R_1 and the member depth in shear critical SFRC members becomes available.

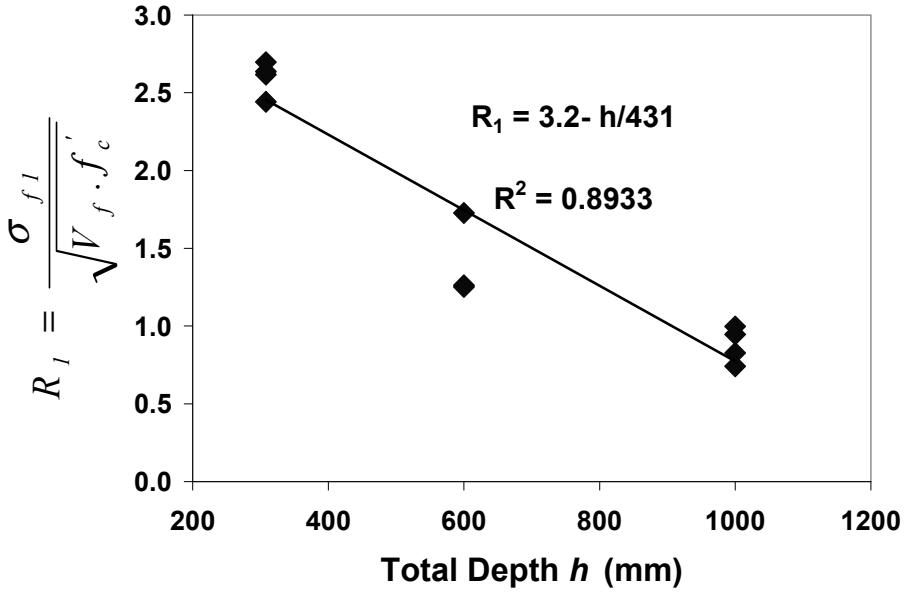

Figure 7-3: Factor R_1 versus the total depth for shear critical specimens

By using the empirical Equation (7-11) for the normalized fiber tensile stress R_1, Equation (7-9) for $C_{Wmax} \geq 0.2\ mm$ can be rewritten as:

$$\sigma_{f2} = \sqrt{V_f . f_c'}\,(3.2 - \frac{h}{431}) \qquad \text{For } L_f/D_f=55, \text{ and } 300mm < h \leq 1000mm \qquad (7\text{-}12)$$

For structural members with smaller height, i.e. $180\ mm \leq h \leq 300mm$, it is assumed that $C_{Wmax} > 0.2\ mm$, and therefore the Equation (7-9) is also applicable. Note that the crack width $C_{Wmax}=0.20\ mm$ is still large enough to reduce the aggregate interlock considerably.

According to the previous shear models for SFRC members (e.g. *Narayanan and Darwish* 1987, *Ashour et al.* 1992, *Khuntia et al.* 1999), the equivalent tensile stress σ_{f2} for hooked steel fibers increases with an increase in the aspect ratio of fibers L_f/D_f. *Dinh* (2009) adapted an empirical formula for σ_{f2} in which an increase in L_f/D_f results in a higher value of σ_{f2}. Similar to *Dinh* (2009) approach, the Equation (7-12) for $L_f/D_f=55$ can be expanded as:

$$\sigma_{f3} = \sqrt{V_f \cdot f_c'}\,(3.2 - \frac{h}{431})\frac{L_f}{D_f}\cdot\frac{1}{55} \qquad (7\text{-}13)$$

Commercially available hooked end steel fibers usually have an aspect ratio between 45 and 100. However, the reported test data by some researchers like *Li et al.*(1992) show a limited effect of aspect ratio on the shear strength when it exceeds $L_f/D_f=60$. *Balaguru et al.* (1992) investigated the flexural toughness of SFRC containing hooked end steel fibers with $60 \le L_f/D_f \le 100$ and concluded that post-crack strength was not significantly affected by the change in the fiber aspect ratio. *Naaman and Najm* (1991) observed that increasing the embedment length of hooked end steel fibers did not significantly affect the load-slip response of fibers because the bond strength for hooked end steel fibers was mainly provided by the end hooks. Thus, in order to have a safe and simple estimation for σ_{f3}, the constant aspect ratio of $L_f/D_f=60$ is assumed and applied to Equation (7-13). The formula for the equivalent uniform tensile stress is then expressed as below:

$$\sigma_{f4} = \sqrt{V_f \cdot f_c'}\,(3.49 - \frac{h}{395}) \qquad (7\text{-}14)$$

Accordingly, the equivalent uniform tensile stress σ_{f4} should replace σ_{f1} in Equations (7-2c) and (7-8). By replacing V_{cc} from Equation (7-6) and V_{ft} from Equation (7-8) with $\theta=32^o$ into Equation (7-1), the shear force capacity of an SFRC member without stirrups V_{frc1} can be estimated as:

$$V_{frc1} = [\tau_{cu}\beta_1 c + 1.6\sigma_{f4}(d-c)]b \qquad (7\text{-}15)$$

7.1.5 Summary of the Proposed Analytical Model

Shear capacity predictions based on the analytical model are summarized in the following flowchart:

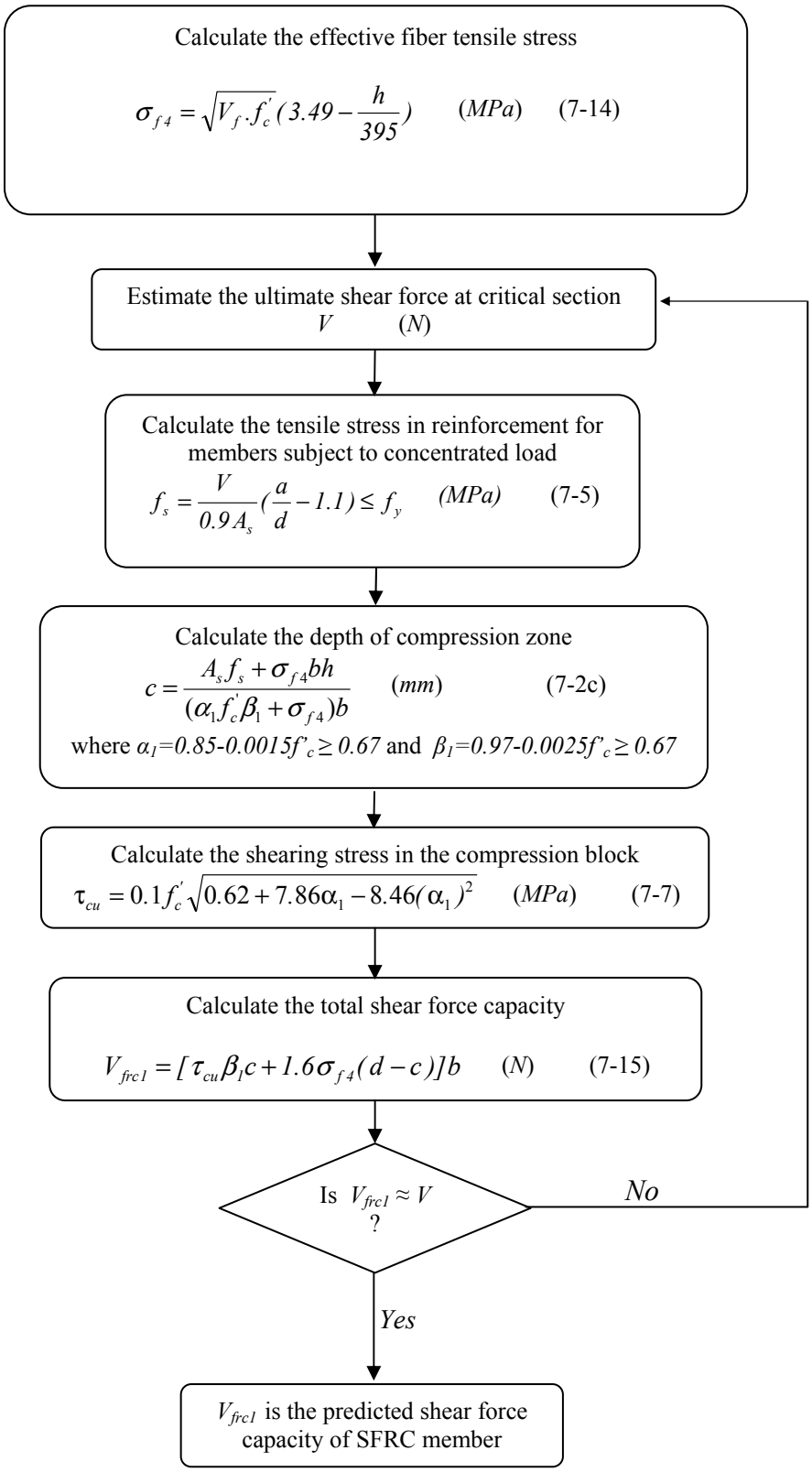

Figure 7-4: The steps of shear capacity prediction based on proposed analytical model

7.1.6 Validation of Analytical Model for Database of SFRC Members without Stirrups

In addition to SFRC specimens tested in the current study, a large database of shear critical SFRC specimens without stirrups was assembled for use in validation of the proposed analytical model. For this purpose, reported shear critical specimens by several researchers (*Dinh* 2009, *Cucchiara et al.* 2004, *Rosenbusch and Teutsch* 2002a, *Rosenbusch and Teutsch* 2002b, *Dupont and Vandewalle* 2003, *Noghabai* 2000, *Casanova and Rossi* 1999, *Lim et al.* 1987) were reviewed. Many of these tests were also summarized by *Yakoub* (2011). The analytical model was validated against a total of 56 specimens which satisfied the criteria of the proposed analytical model (Table 7-3). As stated in the introduction of this chapter, the scope of the proposed model is for members with the following limits:

- Rectangular cross section with $180\ mm \le h \le 1000\ mm$ and $b \ge 100\ mm$
- $a/d \ge 2.5$
- $0.75\% \le V_f \le 1.5\%$, $45 \le L_f/D_f \le 100$, and $25mm \le L_f \le 60\ mm$ (hooked end steel fibers)
- $20\ MPa \le f'_c \le 90\ MPa$

As shown in Table (7-3), the analytical shear model gives good predictions for the shear capacity of slender SFRC members without stirrups with an average test to predicted capacity ratio $V_{test}/V_{frc1} = 1.03$ and $COV = 18\%$.

Table 7-3: Validation of proposed analytical model for the available database

Researcher	Specimen	b (mm)	h (mm)	d (mm)	f'_c (MPa)	ρ %	a/d	L_f/D_f	V_f (%)	V_{test} (kN)	V_{frc1} Eq.(7-15) (kN)	V_{test}/V_{frc1}
Current study	N31	310	308	258	23	2.50	3	55	1	211	177	1.19
	N61	300	600	531	23	1.88	3	55	1	252	281	0.90
	N62	300	600	523	23	2.55	3	55	1	242	277	0.87
	H31	310	308	258	41	2.50	3	55	1	278	262	1.06
	N32	310	308	240	41	4.03	3	55	1	281	244	1.15
	H62	300	600	523	41	2.55	3	55	1	444	405	1.10
	N10-1	300	1000	923	41	1.44	3	55	1	492	391	1.26
	N10-2	300	1000	920	41	2.03	3	55	1	497	390	1.27
	H32	310	308	242	80	4.03	3	55	1	458	390	1.17
	H10-1	300	1000	923	80	1.44	3	55	1	646	614	1.05
	H10-2	300	1000	920	80	2.03	3	55	1	644	612	1.05
Dinh (2009)	B18-1a	152	457	381	45	1.96	3.43	55	0.75	171	163	1.05
	B18-1b	152	457	381	45	1.96	3.43	55	0.75	160	171	0.93
	B18-2a	152	457	381	38	1.96	3.50	55	1	175	169	1.04
	B18-2b	152	457	381	38	1.96	3.50	55	1	178	169	1.05
	B18-2c	152	457	381	38	2.67	3.50	55	1	201	169	1.19
	B18-2d	152	457	381	38	2.67	3.50	55	1	147	169	0.87
	B27-1a	203	686	610	51	2.00	3.50	55	0.75	363	326	1.11
	B27-1b	203	686	610	51	2.00	3.50	55	0.75	334	326	1.03
	B27-3b	203	686	610	42	1.56	3.50	55	0.75	339	284	1.19
	B18-3a	152	457	381	31	2.67	3.43	55	1.5	149	165	0.90
	B18-3b	152	457	381	31	2.67	3.43	55	1.5	196	165	1.18
	B18-3c	152	457	381	45	2.67	3.43	55	1.5	191	216	0.88
	B18-3d	152	457	381	45	2.67	3.43	55	1.5	190	216	0.88
	B18-5a	152	457	381	49	2.67	3.43	80	1	173	201	0.86
	B18-5b	152	457	381	49	2.67	3.43	80	1	219	201	1.09
	B18-7a	152	457	381	43	1.96	3.43	80	0.75	192	166	1.16
	B18-7b	152	457	381	43	1.96	3.43	80	0.75	189	166	1.14
	B27-2a	203	686	610	29	2	3.5	80	0.75	349	220	1.58
	B27-2b	203	686	610	29	2	3.5	80	0.75	341	220	1.55
	B27-4a	203	686	610	30	1.56	3.50	80	0.75	267	225	1.18
	B27-4b	203	686	610	30	1.56	3.50	80	0.75	222	225	0.99
	B27-5	203	686	610	45	2.00	3.50	55	1.5	432	383	1.13
	B27-6	203	686	610	43	2.00	3.50	80	1.5	419	371	1.13
Rosenbusch &Teutsch (2002)	1.2/4	200	300	260	48.3	3.56	3.5	67	0.76	155	182	0.85
	2.3/3	200	300	262	38.7	1.15	2.5	67	0.76	108	144	0.75
	2.4/3	200	300	260	38.7	1.81	2.5	67	0.76	144	143	1.01
	2.6/3	200	300	260	40.3	1.81	4	67	0.76	117	168	0.70
Noghabai (2000)	9 Type C	200	500	410	68.4	3	2.9	86	0.75	339	291	1.17
	10 Type C	200	500	410	86	3	2.9	86	0.75	292	341	0.86
	4 Type D	300	700	570	68.4	2.9	3	86	0.75	510	501	1.02
Li et al. (1992)	1	127	229	203	22.7	2.2	3	60	1	79	59	1.33
	2	127	229	203	26	2.2	3	100	1	79	65	1.21
Mansur (1986)	C2	152	229	197	29.9	1.34	2.8	60	0.75	60	74	0.81
	E2	152	229	197	20.6	1.34	2.8	60	0.75	45	58	0.77
	E3	152	229	197	20.6	2	2.8	60	0.75	60	58	1.03
	F3	152	229	197	33.4	2	2.8	60	0.75	86	80	1.07
Lim et al. (1987)	4/1.0/2.5	152	254	221	34	2.39	2.5	60	1	82	98	0.84
	4/1.0/3.5	152	254	221	34	2.39	3.5	60	1	67	103	0.66
Cucchiara et al. (2004)	A10	150	250	219	40.9	1.92	2.79	60	1	96	110	0.88
Casanova& Rossi(1999)	HSFRC1	125	250	225	90	3.57	2.9	60	1.3	154	177	0.87
Dupont & Rossi (2003)	18	200	300	262	38.6	1.15	2.5	65	0.75	108	143	0.76
	27	200	300	262	27.2	1.15	2.5	45	0.75	120	115	1.05
	30	200	300	260	27.2	1.18	2.5	45	0.75	120	114	1.05
	21	200	300	260	38.6	1.18	2.5	65	0.75	144	142	1.01
	4	200	300	260	47.6	3.55	3.5	65	0.75	155	179	0.86
Average												**1.03**
COV												**18%**

7.2 Simplified Shear Design Model

In this section the proposed analytical model from section (7.1) is simplified to be more suitable for design purposes and to eliminate the iteration in the flowchart in Figure (7-4). The scope of this design model is for structural members which satisfy the same criteria indicated for the analytical model. The process of simplification includes different stages which are explained below. The simplified design model is validated against the database of collected test results in Table (4-3) and compared with design models proposed by other researchers.

7.2.1 Simplification of Analytical Shear Model

For the compressive strength range indicated for the current model $f'_c=20\sim90$ *MPa*, the α_1 from Equation (4-7) is between 0.82 and 0.72. Applying this range of α_1 into Equation (7-7) gives an ultimate shear stress capacity of compression block of τ_{cu} =0.117 f'_c ~0.137 f'_c. However, for a simple estimation of V_{cc}, an ultimate shear stress at the lower limit of τ_{cu} =0.117f'_c is adopted for the current design model. For high strength concrete with $f'_c \geq 70$ *MPa* ($\alpha_1 \leq 0.75$), the τ_{cu} from Equation (2-9) will be slightly higher than $0.117f'_c$, but due to the cleavage of aggregates in the high strength concrete under direct shear (Section 4.3), the same τ_{cu} =0.117f'_c is used here.

For the analytical model in Section (7.1), Equation (7-2c) was developed to calculate the compression zone depth *c*. From the calculations of *c* performed for the 56 SFRC specimens in Table (7-3), it was observed that with a slight error (*COV=5%*), Equation (7-2c) yields *c* values which are an average of 1.20 times those obtained from the same equation taking $\sigma_{f4}=0$:

$$c = \frac{A_s f_s + \sigma_{f4} bh}{(\alpha_1 f'_c \beta_1 + \sigma_{f4})b} \approx (1.20)\frac{A_s f_s}{\alpha_1 f'_c \beta_1 b} \qquad (7\text{-}16)$$

According to Equation (7-5), in all 56 SFRC specimens in Table (7-3) the tensile reinforcement at the critical shear section did not yield. Steel stress values were calculated between $f_s=0.35f_y$ and $f_s=0.97f_y$. Most specimens included commercially available steel reinforcing bars with $400\ MPa \leq f_y \leq 450\ MPa$. For simplicity and in order to avoid the iteration process due to estimation of V in Equation (7-5) (see Figure 7-4), an average $f_s=0.67f_y$ and a typical reinforcement steel with $f_y = 400\ MP$ has been assumed at the critical shear section for the current design model. As discussed in Section (7.1.2), the critical shear section was assumed to occur at a distance of $2d$ from the section with maximum flexural moment.

When the tensile reinforcement stress f_s changes, the compression zone depth will be affected. For instance, a decrease in f_s in Equation (7-16) will decrease the compression zone depth c. A smaller c will decrease V_{cc} (Equation 7-6) and increase V_{ft} (Equation 7-8), but the total shear capacity V_{frc1} (Equation 7-15) will not be affected considerably. By applying $f_s=0.67(400)=268\ MPa$ into Equation (7-16), the compression zone depth c can be calculated as:

$$c = \frac{320 A_s}{\alpha_1 f_c' \beta_1 b} \tag{7-17}$$

Using τ_{cu} =0.117 f'_c and compression zone depth c from Equation (7-17) in Equation (7-6) will result in:

$$V_{cc} = \frac{37.44 \rho b d}{\alpha_1} \tag{7-18}$$

Substituting c and σ_{f4} from Equations (7-17) and (7-14), respectively, into Equation (7-8) yields:

$$V_{ft} = \sqrt{V_f . f_c^{'}}(5.58 - \frac{h}{247})(1 - \frac{320\rho}{\alpha_1 f_c^{'} \beta_1})bd \quad (7\text{-}19)$$

The total shear capacity for the design model V_{frc2} can be obtained by adding V_{ft} (Equation 7-19) to V_{cc} (Equation 7-18):

$$V_{frc2} = \left[\frac{37.44\rho}{\alpha_1} + \sqrt{V_f . f_c^{'}}(5.58 - \frac{h}{247})(1 - \frac{320\rho}{\alpha_1 f_c^{'} \beta_1})\right]bd \quad (7\text{-}20)$$

Equation (7-20) is relatively simple and can be easily used without iteration to estimate the shear capacity of slender SFRC members without stirrups.

7.2.2 Validation of Proposed Design model

The simplified design Equation (7-20) was used to predict the shear capacity of the 56 specimens previously reported in Table (7-3). The V_{test}/V_{frc2} ratios are shown in Table (7-4). While the proposed design model is simple and easy to use, it yields $V_{test}/V_{frc2} = 1.07$ and a coefficient of variation of $COV = 17\%$, which are comparable to $V_{test}/V_{frc1} = 1.03$ and $COV = 18\%$ for the general analytical model in Section (7.1). Meanwhile, these statistics are comparable to the available statistics of widely accepted models such as *ACI 318-08* model for RC members without stirrups and without fibers. Reineck et al. (2003) showed that for a database of 361 slender RC specimens without stirrups and without fibers, *ACI 318-08* Equation (2-4b) yields an average $V_{test}/V_{model} = 1.43$ and $COV = 32\%$.

The accuracy of the proposed design model (Equation 7-20), was also compared to seven SFRC shear models proposed by other researchers. The V_{test}/V_{model} results are shown in Table (7-4). These seven models include:

- *Yakoub* (2011) (the modified *CSA A23.3-04* model for SFRC members)

- *Dinh* (2009)
- *Kwak et al.* (2002)
- *Khuntia et al.* (1999)
- *Ashour et al.* (1992)(using a modified *Zsutty* 1968 model for SFRC members)
- *Narayanan and Darwish* (1987)
- *Sharma* (1987)

The details and the locations of the critical section in shear for these models are described in Section (2.3). Furthermore, the shear predictions of *ACI 318-08* and *CSA A23.3-04* models for RC members without fibers are shown in Table (7-4). The ratio V_{test}/V_{model} for *ACI 318-08* and *CSA A23.3-04* were already discussed in Section (6.2.2) to show the shear capacity enhancement due to the addition of steel fibers to RC members.

Table 7-4: Comparing the accuracy of proposed design model with other published models

Researcher	Specimen	V_{test}/V_{model}									V_{test}/V_{frc2}
		Yakoub (2011)	Dinh (2009)	Kwak et al. (2002)	Khuntia et al. (1999)	Ashour et al. (1992)	Narayanan & Darwish (1987)	Sharma (1986)	ACI 318-08	CSA A23.3-04	
Current study	N31	1.40	1.41	1.06	1.81	1.32	1.14	1.37	3.29	2.16	1.17
	N61	1.07	0.85	0.68	1.08	0.87	0.74	0.82	1.98	1.65	0.86
	N62	0.98	0.82	0.62	1.06	0.77	0.67	0.80	1.93	1.50	0.79
	H31	1.48	1.64	1.19	1.78	1.54	1.34	1.36	3.25	2.28	1.10
	N32	1.43	1.78	1.14	1.94	1.43	1.26	1.47	3.53	2.20	1.11
	H62	1.43	1.33	0.96	1.45	1.25	1.09	1.10	2.65	2.19	1.07
	N10-1	1.25	0.90	0.69	0.91	0.95	0.77	0.69	1.66	1.93	1.19
	N10-2	1.17	0.85	0.65	0.92	0.85	0.73	0.70	1.68	1.80	1.05
	H32	1.78	2.76	1.43	2.24	1.98	1.69	1.70	4.09	2.74	1.27
	H10-1	1.29	1.15	0.72	0.86	1.07	0.80	0.65	1.56	1.98	1.19
	H10-2	1.18	1.06	0.66	0.86	0.95	0.76	0.65	1.56	1.81	1.06
Dinh (2009)	B18-1a	1.59	1.49	1.29	1.63	1.59	1.36	1.14	2.64	2.28	1.11
	B18-1b	1.49	1.39	1.21	1.52	1.49	1.27	1.06	2.47	2.14	1.04
	B18-2a	1.63	1.45	1.29	1.61	1.55	1.30	1.27	2.94	2.50	1.13
	B18-2b	1.66	1.47	1.32	1.64	1.58	1.32	1.29	2.99	2.55	1.15
	B18-2c	1.72	1.65	1.38	1.85	1.61	1.40	1.46	3.37	2.65	1.24
	B18-2d	1.26	1.21	1.01	1.35	1.18	1.02	1.07	2.47	1.94	0.90
	B27-1a	1.73	1.45	1.25	1.52	1.53	1.29	1.07	2.46	2.47	1.24
	B27-1b	1.59	1.33	1.15	1.40	1.41	1.19	0.98	2.26	2.27	1.14
	B27-3b	1.85	1.48	1.32	1.56	1.63	1.35	1.10	2.53	2.65	1.35
	B18-3a	1.20	1.14	0.90	1.24	1.05	0.89	1.19	2.77	2.11	0.92
	B18-3b	1.58	1.51	1.19	1.63	1.38	1.17	1.57	3.64	2.77	1.21
	B18-3c	1.34	1.37	1.06	1.32	1.25	1.06	1.27	2.94	2.35	0.95
	B18-3d	1.33	1.37	1.05	1.31	1.25	1.05	1.26	2.93	2.34	0.95
	B18-5a	1.19	1.11	0.95	1.16	1.13	0.95	1.10	2.56	2.06	0.93
	B18-5b	1.51	1.41	1.20	1.47	1.43	1.21	1.40	3.23	2.61	1.18
	B18-7a	1.65	1.37	1.30	1.59	1.60	1.33	1.31	3.03	2.61	1.28
	B18-7b	1.63	1.35	1.28	1.57	1.57	1.30	1.29	2.98	2.57	1.26
	B27-2a	1.86	1.25	1.25	1.65	1.47	1.23	1.36	3.13	2.93	1.54
	B27-2b	1.81	1.23	1.22	1.61	1.44	1.21	1.33	3.06	2.86	1.50
	B27-4a	1.50	0.98	1.00	1.24	1.22	0.98	1.02	2.36	2.36	1.24
	B27-4b	1.24	0.81	0.83	1.03	1.01	0.82	0.85	1.96	1.96	1.03
	B27-5	1.76	1.45	1.21	1.39	1.47	1.18	1.35	3.11	3.08	1.26
	B27-6	1.49	1.13	0.99	1.10	1.20	0.94	1.34	3.09	3.04	1.25
Rosenbusch &Teutsch (2002)	1.2/4	1.10	1.33	1.05	1.46	1.22	1.08	1.11	2.57	1.66	0.87
	2.3/3	0.97	1.05	0.74	1.13	1.16	0.95	0.79	1.98	1.46	0.80
	2.4/3	1.15	1.30	0.89	1.51	1.34	1.16	1.06	2.67	1.74	1.02
	2.6/3	1.14	1.05	1.12	1.20	1.26	1.03	0.95	2.12	1.71	0.81
Noghabai (2000)	9 Type C	1.38	1.57	1.04	1.52	1.44	1.23	1.24	2.99	2.23	1.20
	10 Type C	1.09	1.36	0.81	1.17	1.18	0.98	0.95	2.30	1.76	0.93
	4 Type D	1.11	1.13	0.78	1.10	1.06	0.90	0.90	2.16	1.79	1.00
Li et al. (1992)	1	1.57	1.57	1.22	2.02	1.54	1.32	1.60	3.83	2.48	1.33
	2	1.25	1.13	0.95	1.43	1.18	0.98	1.49	3.58	2.35	1.22
Mansur (1986)	C2	1.08	1.11	0.87	1.31	1.22	1.03	0.90	2.19	1.58	0.84
	E2	0.93	0.90	0.72	1.18	1.00	0.84	0.81	1.98	1.35	0.78
	E3	1.12	1.14	0.87	1.58	1.16	1.01	1.08	2.64	1.63	1.01
	F3	1.33	1.43	1.09	1.77	1.49	1.31	1.21	2.96	1.94	1.09
Lim et al. (1987)	4/1.0/2.5	1.00	1.14	0.73	1.33	1.05	0.92	1.00	2.52	1.58	0.84
	4/1.0/3.5	0.93	0.93	0.82	1.08	0.95	0.82	0.89	2.05	1.47	0.68
Cucchiara2004	A10	1.23	1.33	0.97	1.44	1.34	1.14	1.12	2.74	1.94	0.92
Casanova1999	HSFRC1	1.38	2.22	1.12	1.60	1.59	1.34	1.43	3.47	2.36	0.98
Dupont & Rossi (2003)	18	1.05	1.08	0.75	1.15	1.17	0.97	0.79	1.99	1.57	0.80
	27	1.44	1.58	1.03	1.75	1.58	1.37	1.05	2.63	1.98	1.07
	30	1.44	1.59	1.03	1.76	1.58	1.37	1.06	2.65	1.98	1.08
	21	1.40	1.45	1.00	1.54	1.56	1.29	1.06	2.67	2.09	1.08
	4	1.21	1.36	1.07	1.50	1.24	1.10	1.12	2.59	1.80	0.88
Average		**1.36**	**1.32**	**1.02**	**1.43**	**1.31**	**1.11**	**1.13**	**2.67**	**2.14**	**1.07**
COV		**19%**	**25%**	**21%**	**21%**	**19%**	**20%**	**22%**	**22%**	**20%**	**17%**

As shown in Table (7-4), the models from *Khuntia et al.* (1999), *Yakoub* (2011), *Dinh* (2009), and *Ashour et al.* (1992) give conservative predictions of shear capacity with average V_{test}/V_{model} ratios equal to 1.43, 1.36, 1.32 and 1.31, respectively. The *Dinh* (2009) model shows a relatively high scatter *COV=25%* in shear estimation for the 56 SFRC specimens in Table (7-4). However, some of the specimens in Table (7-4) do not fit into the limitation of $f'_c \leq 55$ *MPa* that apply to the *Dinh* (2009) model. By excluding the specimens with $f'_c > 55$ *MPa* from the database, the *Dinh* (2009) model still gives relatively conservative estimations with an average $V_{test}/V_{model} = 1.27$ and *COV=19%*. The *Kwak et al.* (2002) and *Sharma* (1986) models show good results for the average V_{test}/V_{model} ratios but with relatively large scatter (*COV>20%*). The results in Table (7-4) indicate that about 1/4 of the *Kwak et al.* (2002) predictions over-estimate the shear capacity considerably with $0.62 \leq V_{test}/V_{model} \leq 0.85$ and therefore give non-conservative estimations for shear strength of SFRC members in the database. Among the SFRC models from previous research in Table (7-4), the *Narayanan and Darwish* (1987) model with $V_{test}/V_{model} = 1.11$ and *COV=20%* gives relatively more accurate predictions; however, the shear predictions according to the *Narayanan and Darwish* (1987) model show a larger scatter compared to the proposed design model with $V_{test}/V_{frc2} = 1.07$ and *COV=17%*. About 15% of *Narayanan and Darwish* (1987) predictions over-estimated the shear capacity considerably with $0.67 \leq V_{test}/V_{model} \leq 0.85$, while 12% of the proposed design model (Equation 7-20) predictions had $0.68 \leq V_{test}/V_{frc2} \leq 0.85$ (Table 7-4).

To further compare the accuracy of the proposed design model (Equation 7-20) and the *Narayanan and Darwish* (1987) model, as well as their sensitivity to different variables, Figures (7-5), (7-6), (7-7), and (7-8) plot the ratio V_{test}/V_{model} versus effective depth d, tensile reinforcement ratio ρ, concrete compressive strength f'_c, and fiber volume fraction V_f, respectively. The symbols with light color in Figures (7-5) to (7-8) represent the normal weight shear critical specimens tested in the current study. For the test database in Table (7-4), the parameters d, ρ, f'_c, and V_f had relatively wider ranges compared to other

parameters such as *a/d*. According to *Kang and Kim (2010)*, the slope (steepness) of a linear regression between V_{test}/V_{model} and an independent variable can be used as a statistical indicator for evaluation of V_{test}/V_{model} sensitivity to that variable. Note that the proposed analytical model (Equation 7-15) and design model (Equation 7-20) in this study yield similar results in term of V_{test}/V_{model} for the test database in Tables (7-3) and (7-4). Therefore, only one of them, i.e. the design model (Equation 7-20) was considered for comparison against the *Narayanan and Darwish* (1987) model in Figures (7-5) to (7-8).

Figure (7-5) indicates that the ratio V_{test}/V_{model} for the *Narayanan and Darwish* (1987) model is sensitive to the changes in the effective depth *d.* As shown in Figure (7-5a), this model gives non-conservative estimations for the shear capacity of large size members especially those with $h=1000\ mm$ ($0.73< V_{test}/V_{model} < 0.80$). However, Figure (7-5b) shows that the proposed design model (Equation 7-20) is less sensitive to the changes in *d* and with a different trend compared to the *Narayanan and Darwish* (1987) model. With a decrease in *h*, especially when $h \leq 300\ mm$, the average ratio V_{test}/V_{model} decreases for the proposed design Equation (7-20).

According to Figure (7-6), the ratio V_{test}/V_{model} for the *Narayanan and Darwish* (1987) model shows some level of sensitivity to the changes in the tensile reinforcement ratio ρ. With an increase in ρ, the average ratio V_{test}/V_{model} increases for the *Narayanan and Darwish* (1987) model, while very low sensitivity is shown for the proposed design model. For both models in Figure (7-7), no significant sensitivity in V_{test}/V_{model} is observed due to the changes in concrete compressive strength f'_c=20~90 *MPa*. However, for the *Narayanan and Darwish* (1987) model, the average V_{test}/V_{model} decreases slightly with a decrease in f'_c. Furthermore, the slope of the regression lines in Figure (7-8) indicate that the ratio V_{test}/V_{model} for the *Narayanan and Darwish* (1987) model is slightly sensitive to the changes in fiber content V_f =0.75~1.5%. For the proposed design

model in Figure (7-8a), very low sensitivity in V_{test}/V_{model} is observed due to the changes in fiber content.

The discussions in this section indicate that among the SFRC shear models shown in Table (7-4), the proposed design model (Equation 7-20) is the most accurate model with a relatively low sensitivity to different variables.

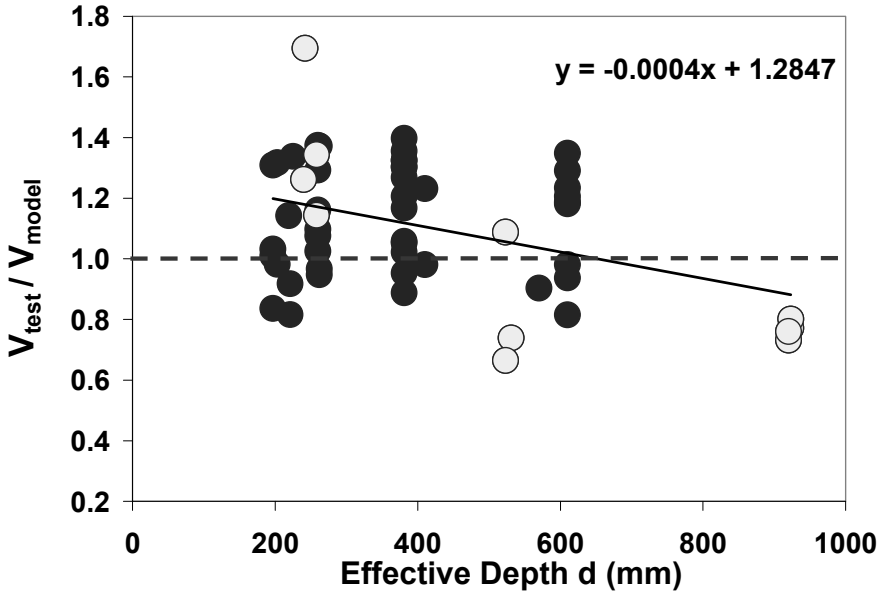

a) *Narayanan and Darwish* (1987)

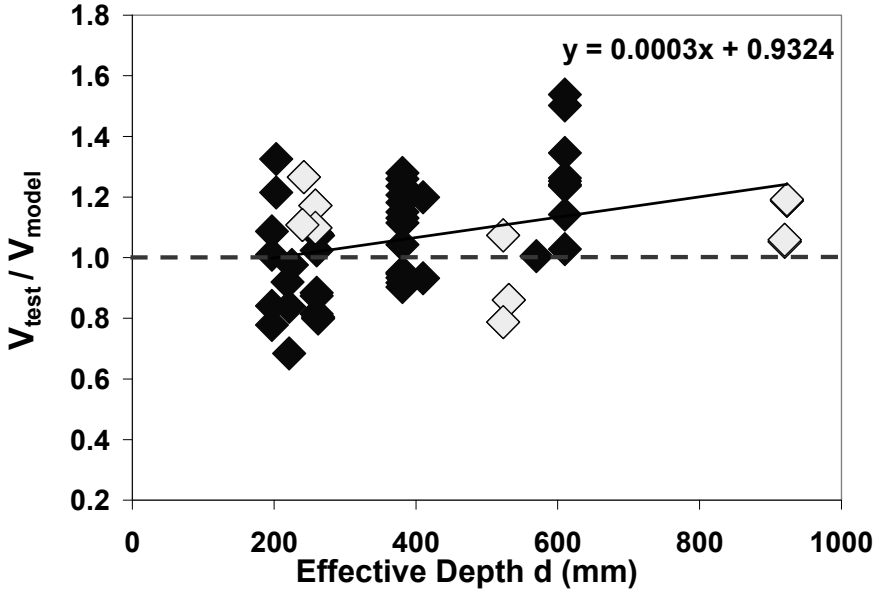

b) Proposed Design Model (Equation 7-20)

Figure 7-5: The ratio V_{test} / V_{model} versus d for the proposed design Equation (7-20) and *Narayanan and Darwish* (1987) model (Note: the symbols with lighter color indicate the specimens from the current study).

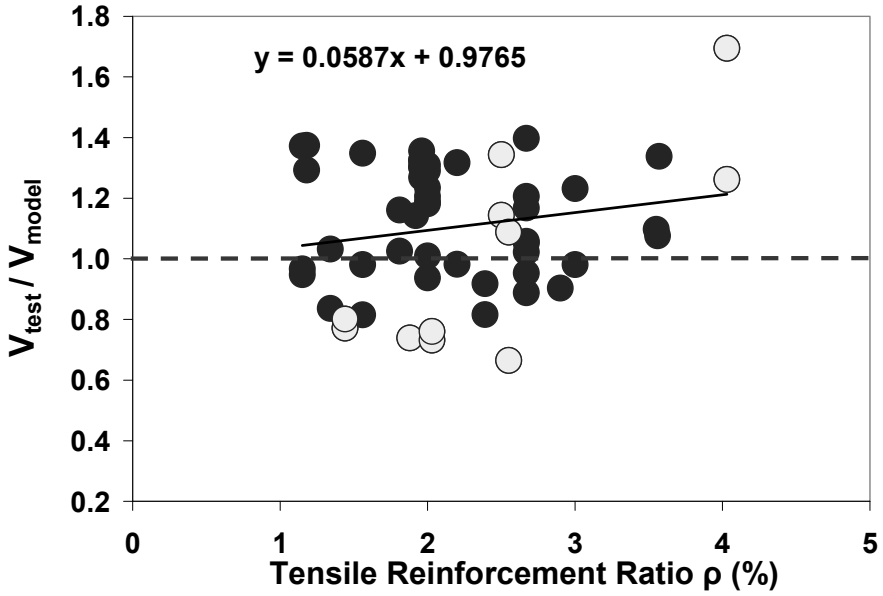

a) *Narayanan and Darwish* (1987)

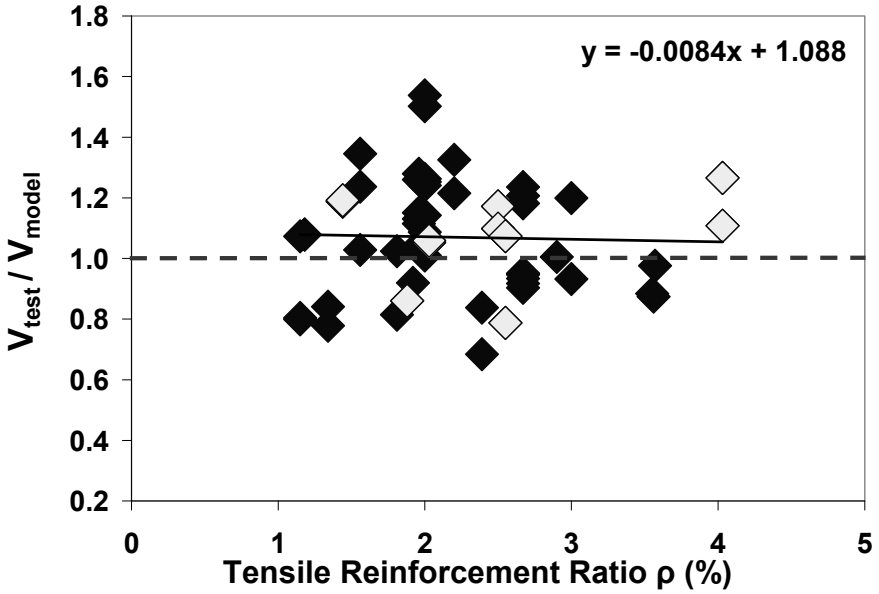

b) Proposed Design Model (Equation 7-20)

Figure 7-6: The ratio V_{test} /V_{model} versus ρ for the proposed design Equation (7-20) and *Narayanan and Darwish* (1987) model (Note: the symbols with lighter color indicate the specimens from the current study).

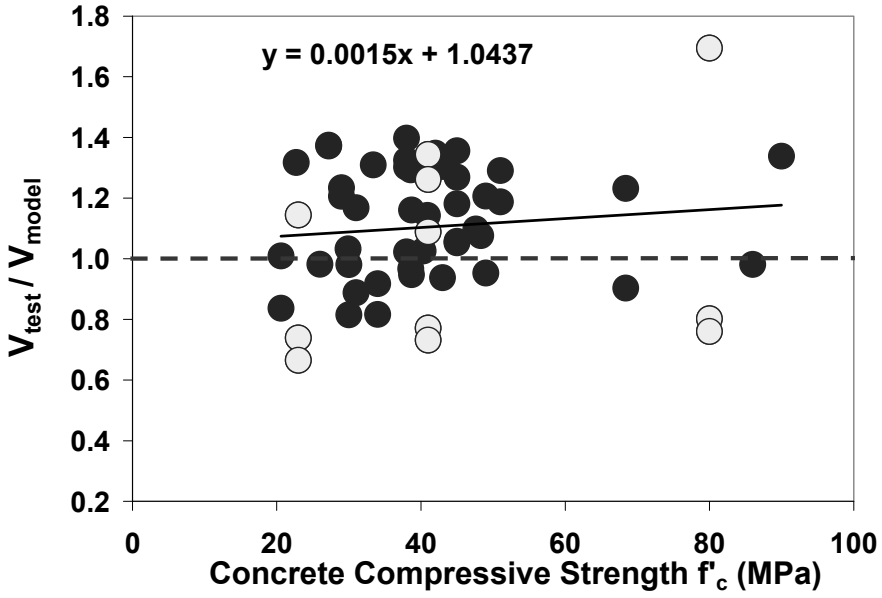

a) *Narayanan and Darwish* (1987)

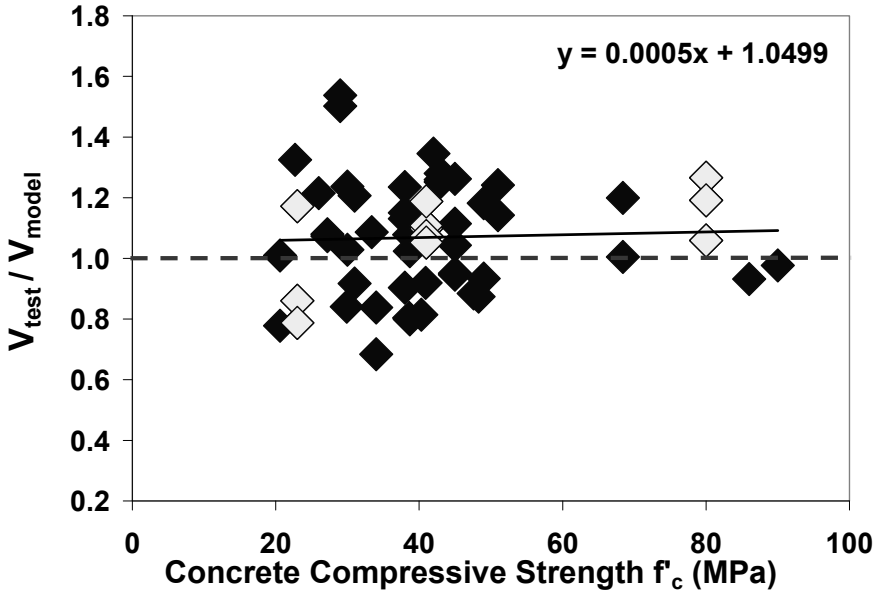

b) Proposed Design Model (Equation 7-20)

Figure 7-7: The ratio V_{test} / V_{model} versus f'_c for the proposed design Equation (7-20) and *Narayanan and Darwish* (1987) model (Note: the symbols with lighter color indicate the specimens from the current study).

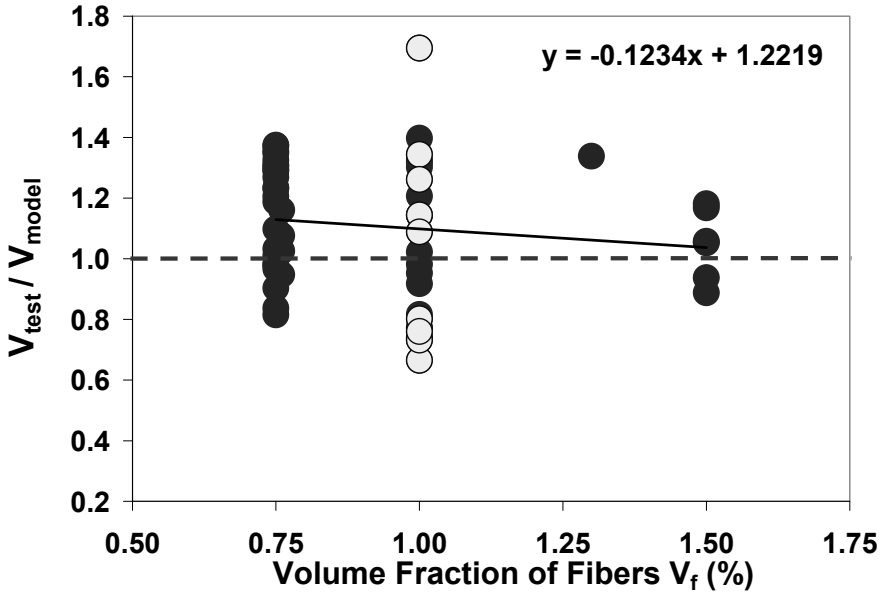

a) *Narayanan and Darwish* (1987)

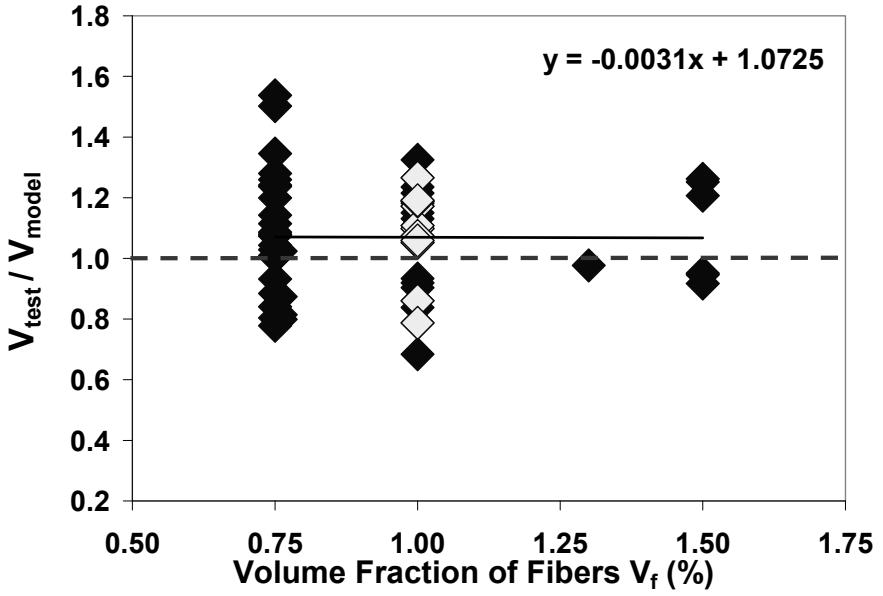

b) Proposed Design Model (Equation 7-20)

Figure 7-8: The ratio V_{test} /V_{model} versus V_f for the proposed design Equation (7-20) and *Narayanan and Darwish* (1987) model (Note: the symbols with lighter color indicate the specimens from the current study).

8. Shear Strength of Structural Lightweight SFRC Members: Results, Discussion, and Shear Modeling

The ultimate shear capacity and failure mode of the 6 lightweight SFRC specimens are shown in Table (8-1). This table shows that 3 specimens failed in shear while the other 3 specimens had flexural failures. In this chapter, the behavior of each group of tested specimens with the same depth is studied. The crack development, failure mode, load-deflection response, load-steel strain response and load-crack width response for each group of specimens are investigated. The deflection and maximum crack width of the specimens at the service load are established. The influences of member depth and longitudinal reinforcement ratio on the shear strength of lightweight SFRC specimens are also investigated. The observed shear capacities of lightweight SFRC members are compared to *ACI-318-08* and *CSA A23.3-04* predictions for similar RC members without fibers. Based on the test results for lightweight SFRC members, the shear models from Chapter 7 are modified to account for the concrete density. The details of test results for each lightweight SFRC specimen can be found in Appendix *B*.

Table 8-1: Test results for lightweight SFRC specimens

Specimen	b (mm)	h (mm)	d (mm)	f'_c (MPa)	γ (kg/m^3)	ρ %	Failure Type	P_{max} * (kN)	V_{test}** (kN)	$\frac{V_{test}}{\sqrt{f'_c}bd}$ (MPa)
L31	310	308	258	22	1900	1.88	Shear^{++}	405	203	0.54
L32	310	308	258	31	1930	2.50	Shear^{++}	595	298	0.67
L61	300	600	550	30	1920	0.91	Flexure	497	252	0.28
L62	300	600	550	30	1920	1.21	Shear^{++}	612	310	0.34
L10-1	300	1000	950	31	1930	0.53	Flexure	532	277	0.17
L10-2	300	1000	950	31	1930	0.7	Flexure	692	357	0.22

* The maximum applied load at mid-span

**The maximum shear force during test including selfweight at a section *2d* from mid-span

++ These specimens approached their shear and flexural capacities simultaneously (see Section 8.1)

8.1 Behavior of Lightweight SFRC Specimens without Stirrups

8.1.1 Specimens with *h=308 mm* (*L31*, *L32*)

8.1.1.1 Crack Development and Failure Mode

The crack patterns after failure of the shear critical specimens with *h=308 mm* (*L31*, *L32*) are shown in Figure (8-1). For both specimens, flexural cracks near mid-span were detected first during initial load stages. Then, new flexural cracks formed in the shear spans and curved diagonally towards the loading point. The diagonal crack widths gradually increased as the applied load at mid-span increased. At the last stages of loading before failure ($P > 0.9\ P_{max}$), an existing diagonal crack rapidly widened and extended upwards to the loading plate. The widening of the critical shear crack caused a relative rotation of the two pieces of the specimens around the compressive zone at the top end of shear crack. A combination of this rotation with the shear stress carried by the uncracked concrete caused a significant compression strain in the compressive zone. The shear failure occurred when the compressive concrete crushed at the area between the top of the diagonal crack and the edge of the loading plate at mid-span (Figure 8-1). No significant flexural cracks or concrete crushing in the compression zone at the top of the flexural cracks at mid-span was observed prior to the shear failure.

The curved shapes for the primary diagonal cracks intercepted the longitudinal reinforcement at considerable distances (*~0.95 d*) from the support plates, confirming that the shear failure was representative of "sectional" shear model behavior rather than arch action. During the shear failure, cracking along the longitudinal reinforcement towards the support region was also observed in specimens *L31* after compressive concrete crushing.

Swamy et al. (1993) observed that lightweight RC members without stirrups experience a single diagonal crack followed by a brittle shear failure and tensile splitting along the longitudinal reinforcement; Similar to the crack patterns seen in the specimens *L31* and *L32* in the current study (Figure 8-1), *Swamy et al. (1993)* observed multiple inclined cracks in lightweight SFRC members with V_f =1% followed by development of an existing inclined crack at shear failure. However, *Swamy et al. (1993)* reported that the final critical shear crack in their specimens cut across several other diagonal cracks that had formed earlier in the loading history. They also reported that steel fibers appeared to reduce the bond cracking along the tensile steel and the amount of concrete spalling in the vicinity of the support.

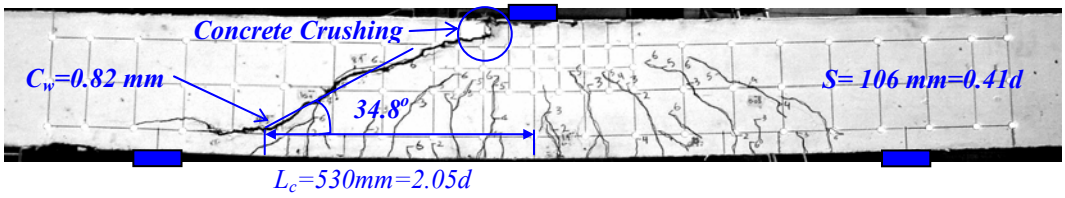

a) Specimen *L31: h=308 mm, f'_c=22 MPa, ρ=1.88 %*

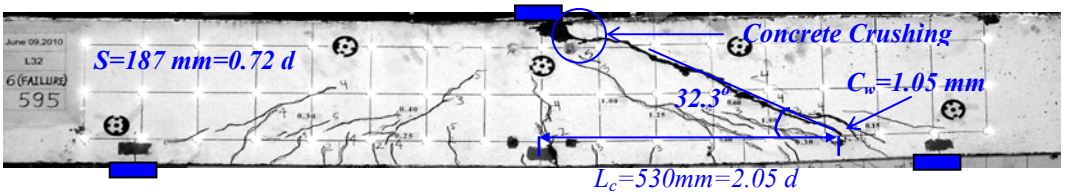

b) Specimen *L32: h=308 mm, f'_c=31 MPa, ρ=2.50 %*

Figure 8-1: Crack pattern after shear failure for lightweight SFRC specimens with *h=308 mm*. Size of grid on the specimen surface is 100 *mm*.

As explained in Section (6.1.1.1), the average crack spacing *S* at the mid-depth level was determined by considering all the distinct inclined cracks at the shear failure which propagated beyond the specimen mid-depth level at an angle

between 0 and 75 degrees with respect to the longitudinal axis of the specimen. The average crack spacing *S* at the mid-depth level are shown in Figure (8-1) and summarized in Table (8-2). As shown in Figure (8-1), the number of inclined cracks in specimen *L32* which extended beyond the specimen mid-depth at the shear failure were fewer than in specimen *L31*, and therefore the average crack spacing for *L32* (*S=0.72d*) was larger than that of *L31* (*S=0.41d*). *Swamy et al. (1993)* reported that lightweight SFRC specimens exhibited an increased number of both flexural and shear cracks at closer spacing compared to the similar lightweight RC specimens without fibers. A similar trend was also observed for the crack spacing in the normal weight SFRC specimens in the current study (Section 6.1).

Table 8-2: Crack observations for lightweight SFRC specimens with *h=308 mm*

Specimen	***b (mm)***	***d (mm)***	***f'c (MPa)***	***ρ %***	***Failure Type***	***θ (degree)***	***C_{Wmax} (mm)***	***L_c (mm)***	***S (mm)***
L31	310	258	22	1.88	Shear	34.8	1.15	530	106
L32	310	258	31	2.50	Shear	32.3	0.90	530	187

For each specimen in Figure (8-1), the distance from mid-span L_c of interception point of critical shear crack with the longitudinal steel is shown. The results for L_c are also summarized in Table (8-2). For both specimens, regardless of differences in f_c' and ρ, a similar $L_c = 2.05d$ was observed. The crack width C_{Wmax} of the critical shear crack at the level of longitudinal reinforcement just before failure was determined by using the data obtained from the digital image correlation measurement system. The results for C_{Wmax} are shown in Figure (8-1) and summarized in Table (8-2). The values of C_{Wmax} for lightweight specimens *L31* and *L32* are comparable to the observed crack widths for normal weight SFRC specimens with *h=308 mm* in Table (6-2). The load-crack width response for specimens *L31* and *L32* is discussed in Section (8.1.1.4).

The idealized critical shear crack angle θ is shown in Figure (8-1) and summarized in Table (8-2). Regardless of the differences in f_c' or ρ, a similar θ was observed for specimens *L31* and *L32*. Note that the range of θ for lightweight concrete specimens *L31* and *L32* was similar to that observed for the normal weight SFRC specimens with *h=308 mm* in Table (6-2).

8.1.1.2 Load-Deflection Response

The load-deflection response of the lightweight SFRC specimens with total depth of *h=308 mm* is shown in Figure (8-2). The lightweight SFRC specimens in this group did not exhibit a sudden or large change of slope in the load-deflection plot at the initiation of flexural cracking. A non-linear relationship with gradually reducing slope was observed for specimens *L31* and *L32* up to the ultimate load where the load-deflection response started to exhibit a plateau, mainly due to yielding of the longitudinal reinforcement shown in Figure (8-3). After some additional deformation in specimen *L31* and *L32*, a significant diagonal crack formed leading to a shear failure. In both specimens, a sudden and large drop in load was recorded at failure due to concrete crushing in the region between the top of the diagonal crack and the edge of the loading plate at mid-span (Figure 8-1). No wide flexural cracks or concrete crushing in the compression zone at mid-span was observed prior to the shear failure. However, the load-deflection plateau at ultimate load due to reinforcement yielding at mid-span indicates that specimens *L31* and *L32* were both approaching their flexural and shear capacities simultaneously. The maximum deflections at mid-span before shear failure for specimens *L31* and *L32* were 16.1 *mm* and 16.3 *mm*, respectively.

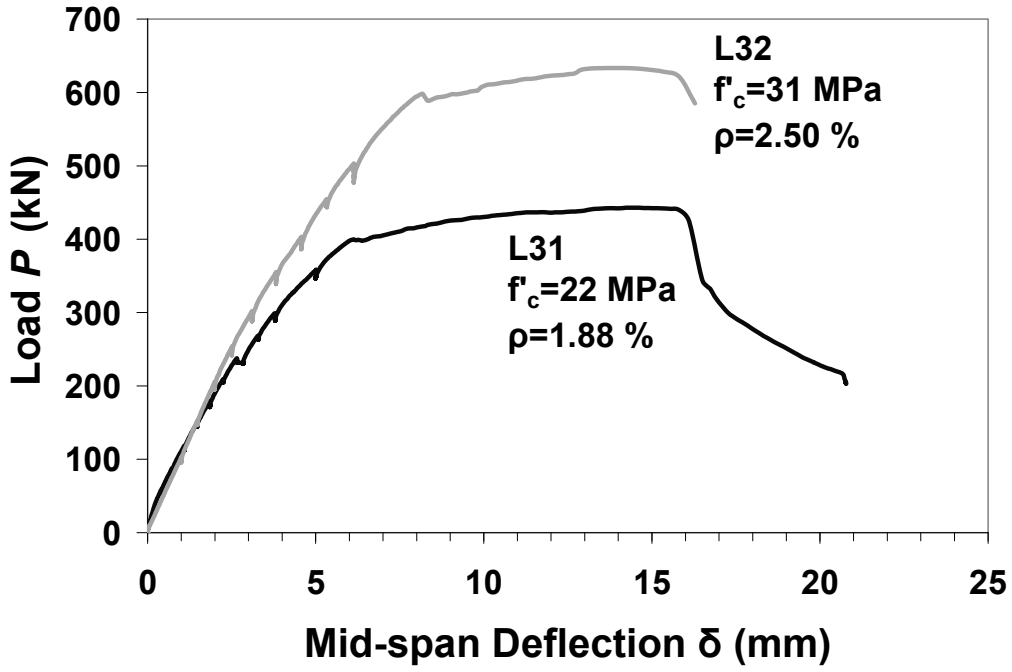

Figure 8-2: Load-deflection response at mid-span for lightweight SFRC specimens with *h=308 mm*.

8.1.1.3 Load-Steel Strain Response

The load-steel strain response at mid-span for the lightweight SFRC specimens with *h=308 mm* is shown in Figure (8-3). An almost linear relationship was observed for specimens *L31* and *L32* up to the ultimate load, where the load-steel strain response started to exhibit a plateau due to yielding of the longitudinal reinforcement. As shown in Figure (8-3), for specimen *L32* with both higher f_c' and ρ compared to specimen *L31*, a larger slope in the load-steel strain response at failure was observed.

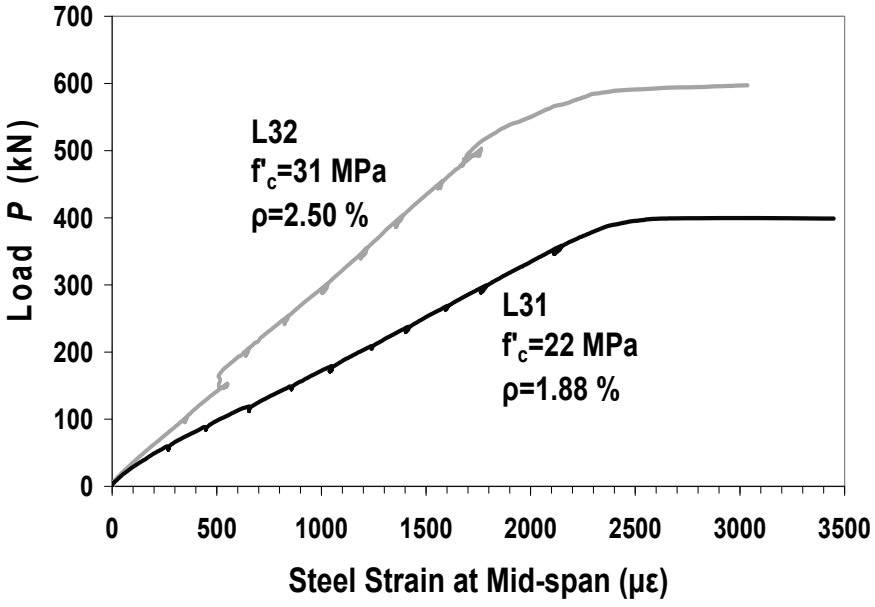

Figure 8-3: Load-steel strain response at mid-span for lightweight SFRC specimens with *h=308 mm*.

8.1.1.4 Load-Crack Width Response of Shear Critical Specimens

The load-crack width response for shear critical specimens *L31* and *L32* is shown in Figure (8-4). As explained in Section (6.1.1.4), the crack width C_W was measured for the critical shear crack at the level of the longitudinal reinforcement (see Figure 8-1) by using the data obtained from digital image correlation system and the comparator gauges. A non-linear relationship with gradually reducing slope was observed in both specimens up to 90% of maximum applied load before shear failure. It was observed that in the last stage of loading just before shear failure, the crack widths increased suddenly and reached large values compared to the crack widths recorded at 90% of P_{max} (see C_{Wmax} values in Table 8-2). As a result of this large increase of the crack widths, the aggregate interlock is reduced significantly. Meanwhile, from a structural behavior point of view, the crack widening in lightweight SFRC members prior to shear failure can be important, since it provides warning about imminent shear failure. The large increase of

crack widths before failure can be attributed to the pullout of fibers from the concrete matrix due to the tension between the adjacent crack surfaces. Note that the pullout of fibers out of the lightweight matrix was evident after shear failure (Figure 8-5). In contrast to the fracture of aggregates in the direct shear test (Figure 4-7 in Section 4.3) no extensive fracture in lightweight aggregates was indicated. This confirms that before shear failure, the fiber pullout due to tension between crack surfaces was the dominant mode rather than pure shear dislocation.

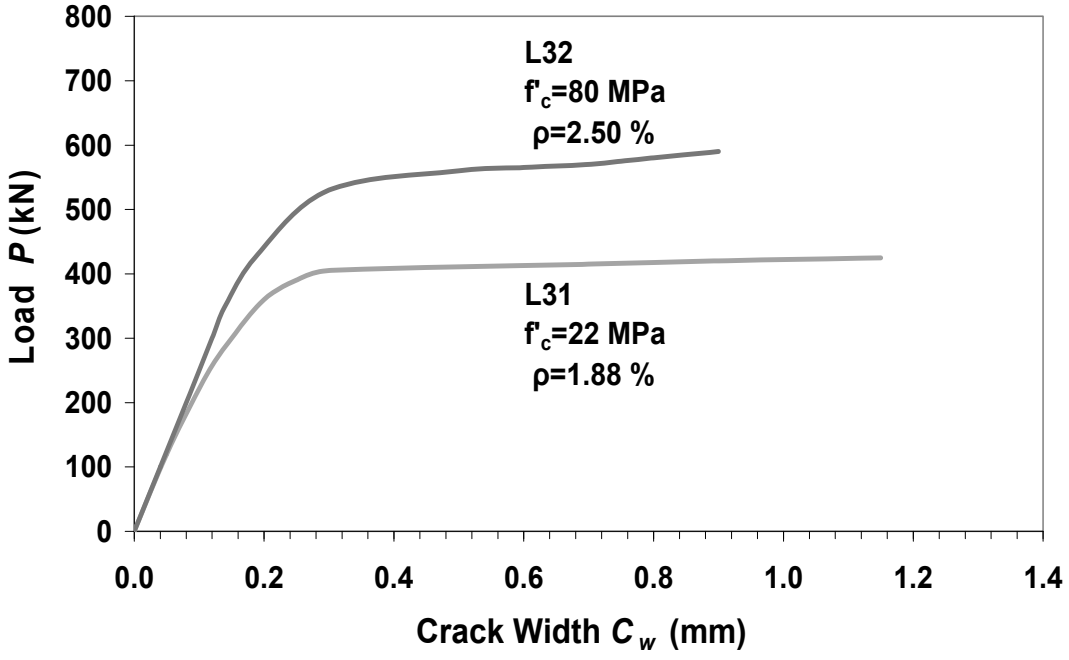

Figure 8-4: Load-crack width response for critical shear crack at level of longitudinal reinforcement in lightweight SFRC specimens with *h=308 mm*.

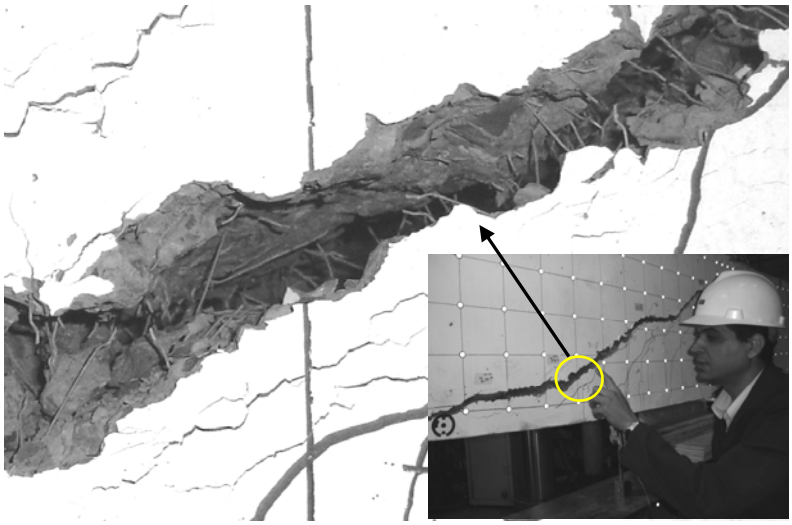

Figure 8-5: Critical shear crack after failure for a typical lightweight SFRC specimen.

8.1.1.5 Deflection and Crack Width at SLS

According to the procedure explained in Section (6.1.1.5), an equivalent service load $S_L = 0.48\ P_{max}$ was used to determine the SLS deflection and crack widths for the specimens *L31* and *L32* in Table (8-3). All relative deflection values at service load δ/L were lower than the common deflection limit of $L/360$ for RC members under live load alone (*ACI 318-08*).

Table 8-3: Deflection and crack width of lightweight SFRC specimens with *h=308 mm* at SLS

Specimen	**Failure Type**	**$0.48P_{max}$ from test (kN)**	**Behavior at SLS**		
			Mid-span Deflection δ (mm)	**δ/L**	**Max. Crack Width (mm)**
L31	Shear	194	2.31	0.0015	0.06 (flexural)
L32	Shear	286	2.90	0.0019	0.13 (shear)

The detected cracks at SLS for specimen *L31* were all very narrow flexural cracks near the mid-span. However, for specimen *L32*, both flexural and diagonal shear cracks were observed at SLS. The crack control factor *z* (see Section 6.1.1.5) indicated that the crack widths for specimens *L31* (*z=19250 N/mm*) and *L32* (*z=17490 N/mm*) are expected to be within the acceptable range for design of RC members with interior exposure ($z \leq 30000$ *N/mm*).

8.1.2 Specimens with *h=600 mm* (*L61, L62*)

8.1.2.1 Crack Development and Failure Mode

The crack patterns after failure of the lightweight SFRC specimens with *h=600 mm* are shown in Figures (8-6) and (8-7). Specimen *L62* with $\rho = 1.21\%$ failed in shear (Figure 8-6), while specimen *L61* with $\rho = 0.91\%$ failed in flexure (Figure 8-7). For both specimens, flexural cracks near mid-span were detected first during initial load stages. Then, new flexural cracks formed in the shear spans and curved diagonally towards the loading point. The diagonal crack widths gradually increased as the applied load at mid-span increased.

For shear critical specimen *L62*, the crack development before failure was similar to that observed for specimens with *h=308 mm* in Section (8.1.1.1). An existing diagonal crack rapidly widened and extended upwards to the loading plate at the last stages of loading before failure ($P > 0.9\ P_{max}$). After widening of the diagonal shear crack, a relative rotation of the two pieces of the specimen around the compressive zone at the top end of shear crack was observed. This rotation and the shear stress carried by the uncracked concrete caused a significant compression strain in the compressive zone, followed by a shear failure due to concrete crushing in the region between the top of the diagonal crack and the edge of the loading plate at mid-span. At shear failure and after compressive concrete crushing, cracks also extended along the longitudinal reinforcement and stopped

at the support region (Figure 8-6). No concrete crushing in the compression zone at the top of flexural cracks at mid-span was observed prior to the shear failure. The primary diagonal crack intercepted the longitudinal reinforcement at considerable distance (*0.91 d*) from the support plates, confirming that the shear failure was representative of "sectional" shear model behavior rather than arch action.

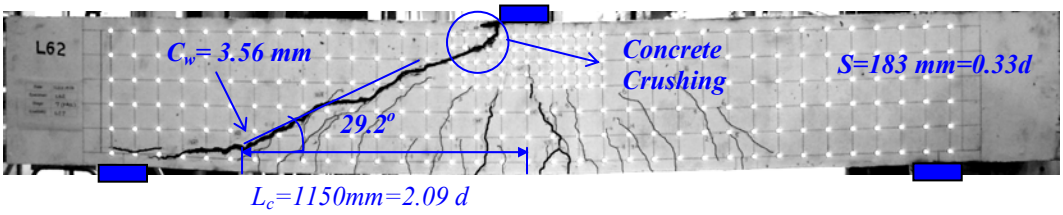

Figure 8-6: Crack patterns after shear failure for specimen *L62* with h = *600 mm*, f'_c=*30 MPa*, and ρ= *1.21 %*. Size of grid on the specimen surface is 100 *mm*.

For specimen *L61* (Figure 8-7), no significant diagonal crack was observed before or during the failure. The flexural failure occurred when the existing flexural cracks near mid-span extended upwards to the loading plate, and a large increase in crack widths, steel strains and specimen deflection was observed, followed by concrete crushing in the compressive zone under the loading point at mid-span.

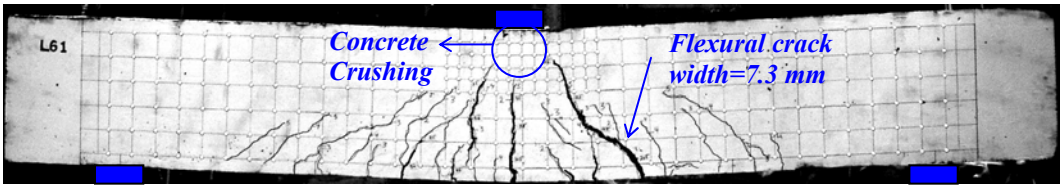

Figure 8-7: Crack pattern after flexural failure for specimen *L61* with h=*600mm*, f'_c=*30 MPa*, and ρ= *0.91 %*. Size of grid on the specimen surface is 100 mm.

For shear critical specimen *L62* in Figure (8-6), the idealized critical shear crack angle θ, the crack width C_{Wmax} of the critical shear crack at level of the longitudinal reinforcement just before failure, average crack spacing *S* at the mid-depth level, and the distance from mid-span L_c of interception point of critical shear crack with the longitudinal steel are shown.

The average crack spacing for specimen *L62* was *S=0.33d* which is lower than the range seen for lightweight SFRC specimens with *h=308 mm* (*S=0.41d ~ 0.72d*) in Figure (8-1). As shown in Figure (8-6), for specimen *L62*, the L_c*=2.09d* was similar to the observed L_c*=2.05d* for specimens with *h=308 mm* (Section 8.1.1.1). Also, the idealized critical shear crack angle $\theta = 29.2^o$ is comparable to the range $\theta = 32.3^o$~34.8^o for lightweight SFRC specimens with *h=308 mm*.

8.1.2.2 Load-Deflection Response

The load-deflection response of lightweight SFRC specimens with total depth of *h=600 mm* is shown in Figure (8-8). Similar to SFRC specimens with *h=308 mm*, the SFRC specimens with *h=600 mm* did not exhibit a sudden or large change of slope in the load-deflection plot at the initiation of flexural cracking. A non-linear relationship with gradually reducing slope was observed for specimen *L62* up to the ultimate load where the load-deflection response started to exhibit a plateau, mainly due to non-linear behavior of the longitudinal reinforcement shown in Figure (8-9). After some additional deformation in specimen *L62*, a significant diagonal crack formed leading to a shear failure. The maximum deflection at mid-span before shear failure was 36.0 *mm*. In this specimen, a sudden and large drop in load was recorded at failure due to concrete crushing in the region between the top of diagonal crack and the edge of the loading plate at mid-span (Figure 8-6). No significant flexural crack or concrete crushing in the compression zone at mid-span was observed prior to the shear failure. However, the load-deflection plateau at the ultimate load due to reinforcement yielding at mid-span indicates that

specimen *L62* was approaching both its flexural and shear capacities simultaneously.

The load-deflection response for specimen *L61* started to exhibit a plateau after reaching the ultimate load, mainly due to yielding of the longitudinal reinforcement shown in Figure (8-9). In this specimen, no significant diagonal crack was observed. The flexural failure occurred when large increases in deflection at mid-span were observed (δ=53.2 *mm*), followed by a drop in the load due to concrete crushing in the compressive zone under the loading point at mid-span.

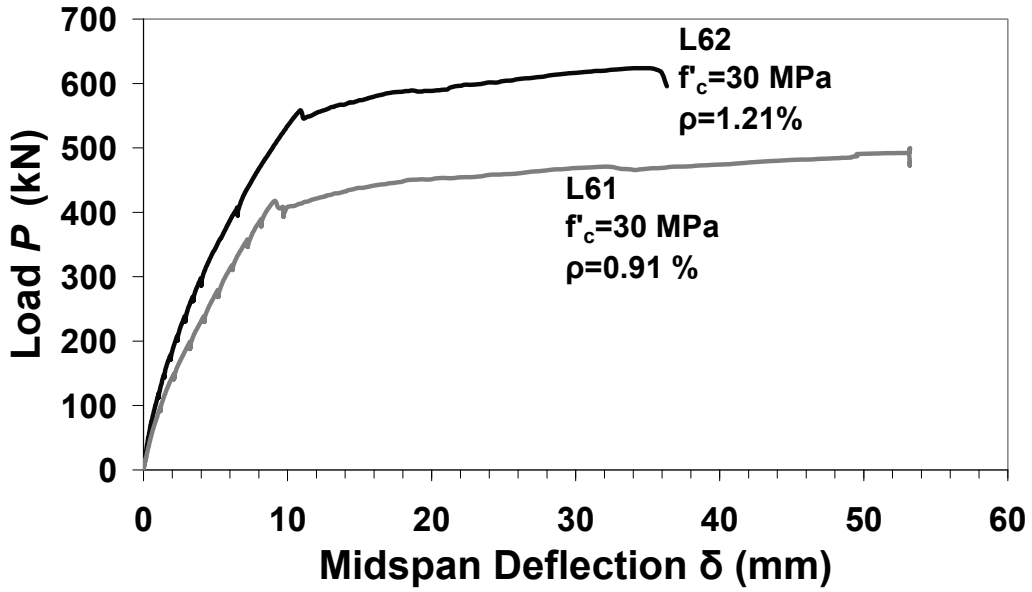

Figure 8-8: Load-Deflection response at mid-span for lightweight SFRC specimens with *h=600 mm*.

8.1.2.3 Load-Steel Strain Response

The load-steel strain response at mid-span for specimens with total depth of *h=600 mm* is shown in Figure (8-9). The mid-span load-strain responses of the

reinforcement for specimens *L61* and *L62* both started to exhibit a plateau after reaching the ultimate load, due to yielding of the longitudinal reinforcement. The differences in behavior and failure mode of *L61* compared to *L62*, both with f_c'*=30 MPa*, can be attributed to the lower reinforcement ratio in *L61* which resulted in higher reinforcement strains at similar load levels compared to *L62*.

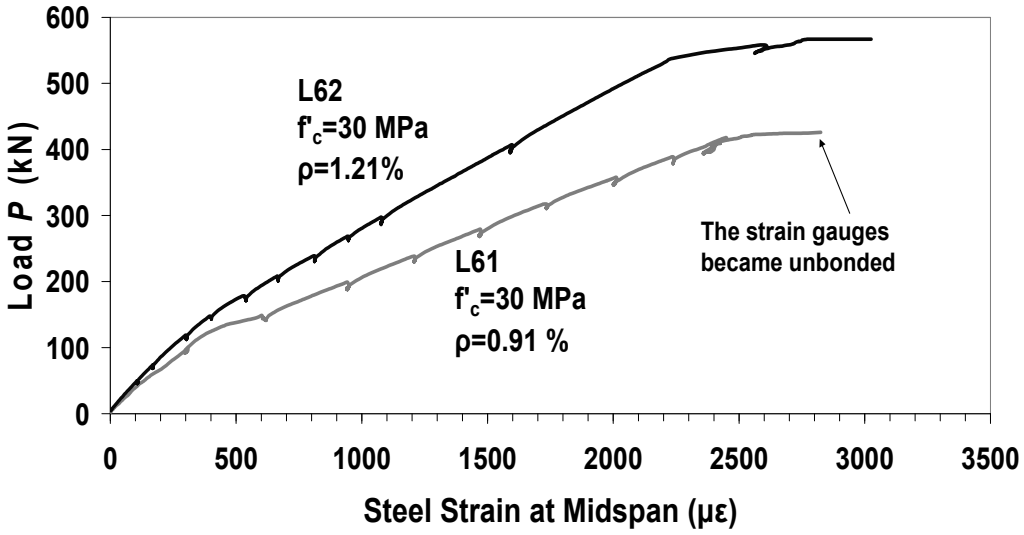

Figure 8-9: Load-steel strain response at mid-span for lightweight SFRC specimens with *h=600 mm*.

8.1.2.4 Load-Crack Width Response of Shear Critical Specimen *L62*

The load-crack width response for shear critical specimen *L62* is shown in Figure (8-10). The crack width C_{Wmax} increased gradually up to about 90% of the maximum applied load before shear failure. Similar to the behavior of lightweight SFRC specimens with *h=308 mm* studied in Section (8.1.1.4), in the last stages of loading just before shear failure the crack widths increased dramatically, reaching large values compared to the crack widths recorded at $0.9P_{max}$ (see C_{Wmax} in Figure 8-6). As a result of this large increase of the crack widths, the aggregate interlock is reduced significantly. By comparing the values of C_{Wmax} in Figures (8-

6) and (8-1), one can observe that C_{Wmax} increases with an increase in specimen height from *h=308 mm* to *h=600 mm*. As explained in Section (8.1.1.4), the large increase of crack widths before failure can be attributed to the pullout of fibers out of the concrete matrix due to the tension between the adjacent crack surfaces. For specimen *L62*, the pullout of fibers out of the lightweight matrix was also evident after shear failure, and no extensive fracture of the lightweight aggregates was observed (Figure 8-5).

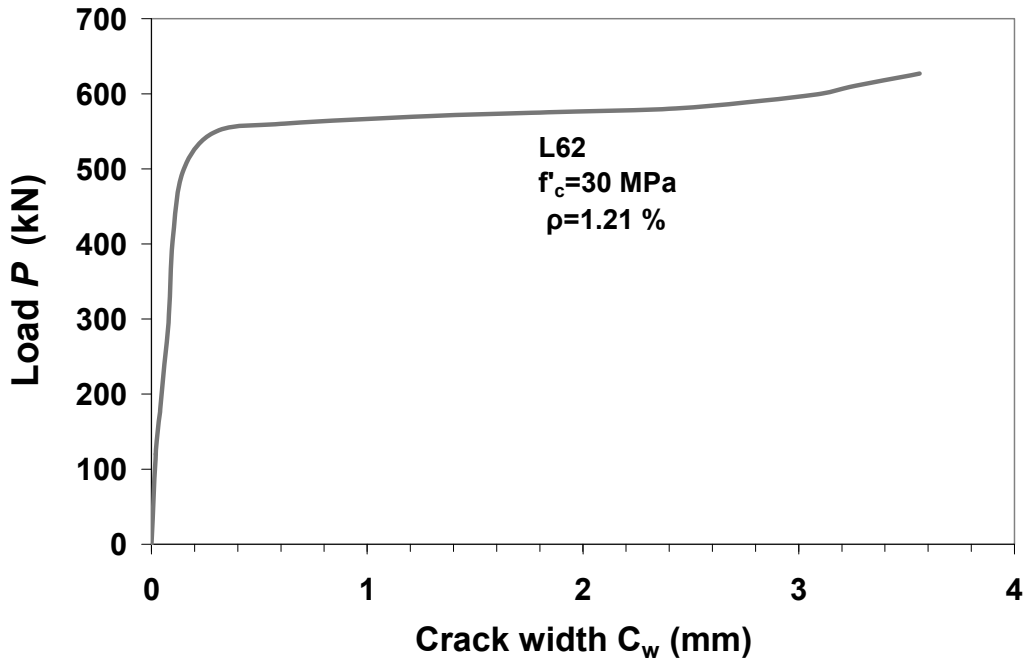

Figure 8-10: Load-crack width response for critical shear crack at level of longitudinal reinforcement in specimen *L62*.

8.1.2.5 Deflection and Crack Width at SLS

According to the procedure explained in Section (6.1.1.5), an equivalent service load $S_L = 0.48\ P_{max}$ was used to determine the SLS deflection and crack widths for the specimens *L61* and *L62* in Table (8-4). All relative deflection values at service

load δ/L were lower than the common deflection limit of $L/360$ for RC members under live load alone (*ACI 318-08*).

Table 8-4: Deflection and crack width of lightweight SFRC specimens with $h=600\ mm$ at SLS

Specimen	Failure Type	$0.48P_{max}$ from test (kN)	Behavior at SLS		
			Mid-span Deflection δ (mm)	δ/L	Max. Flexural Crack Width (mm)
L61	Flexure	240	4.32	0.0013	0.05
L62	Shear	296	4.11	0.0012	0.06

The detected cracks at SLS were all very narrow flexural cracks near the mid-span. The crack control factor z (see Section 6.1.1.5) indicated that the crack widths for specimens *L61* ($z=19040\ N/mm$) and *L62* ($z=17300\ N/mm$) are expected to be within the acceptable range for design of RC members with interior exposure ($z \leq 30000\ N/mm$).

8.1.3 Specimens with *h=1000 mm* (*L10-1, L10-2*)

8.1.3.1 Crack Development and Failure Mode

The crack patterns after failure of the lightweight SFRC specimens with *h=1000 mm* are shown in Figures (8-11). Both specimens *L10-1* and *L10-2* failed in flexure. Flexural cracks near mid-span were detected first during initial load stages. Then, new flexural cracks formed in the shear spans and curved diagonally towards the loading point. The diagonal and vertical crack widths gradually increased as the applied load at mid-span increased.

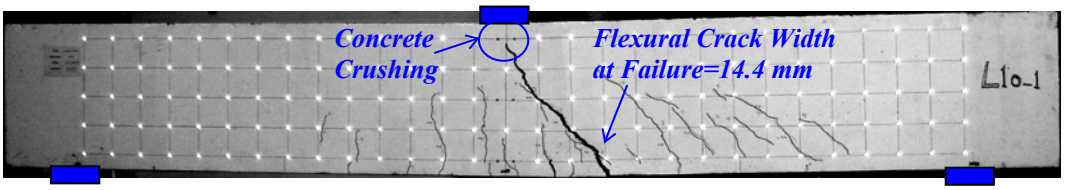

a) Specimen *L10-1: f'_c=31 MPa, ρ=0.53%*

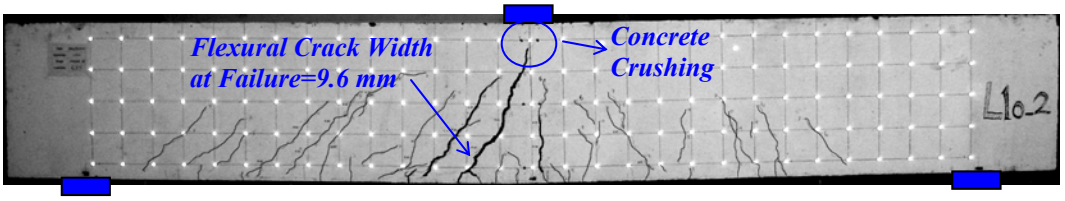

b) Specimen *L10-2: f'_c=31 MPa, ρ=0.70 %*

Figure 8-11: Crack patterns after flexural failure for specimens with *h = 1000 mm*. Size of grid on the specimen surface is 200 *mm*.

For both specimens (Figure 8-11), no significant diagonal cracks were observed before or during the failure. The flexural failure started when the existing flexural cracks near mid-span extended upwards to the loading plate, and a large increase in crack widths, steel strain and specimen deflection was observed followed by concrete crushing in the compressive zone adjacent to the loading point at mid-span.

8.1.3.2 Load-Deflection Response

The load-deflection responses of the lightweight SFRC specimens with total depth of *h=1000 mm* are shown in Figure (8-12). A non-linear relationship with gradually reducing slope was observed up to the ultimate load where the load-deflection response for specimens *L10-1* and *L10-2* started to exhibit a plateau, mainly due to yielding of the longitudinal reinforcement shown in Figure (8-13). In these specimens, no significant diagonal crack was observed. The flexural failure occurred when large increases in deflection at mid-span were observed for specimens *L10-1* and *L10-2* (δ=53.80 *mm* and δ=54.70 *mm*, respectively), followed by a drop in the load due to concrete crushing in the compressive zone under the loading point at mid-span.

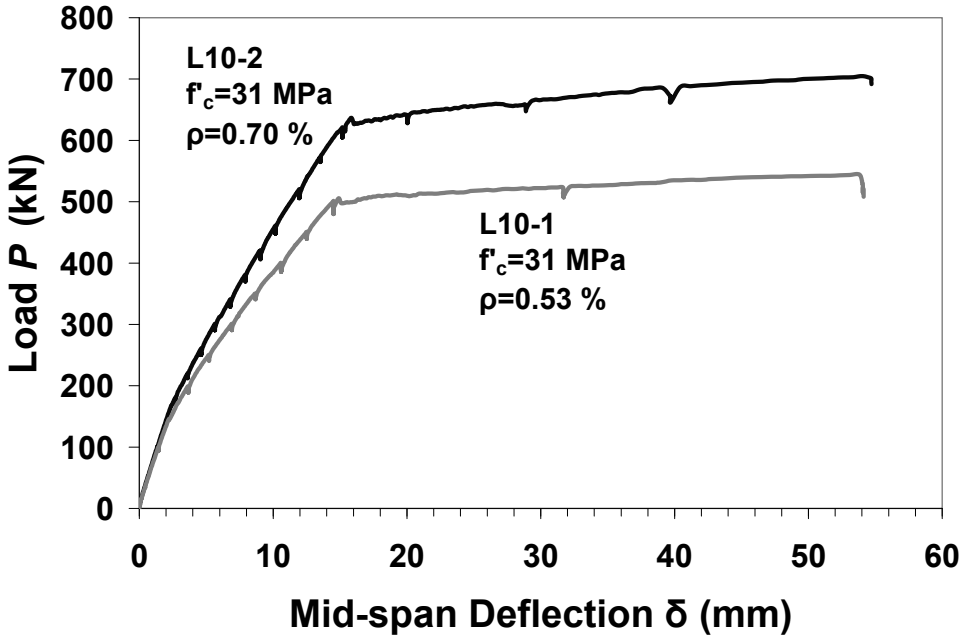

Figure 8-12: Load-Deflection response at mid-span for lightweight SFRC specimens with *h=1000 mm*.

8.1.3.3 Load-Steel Strain Response

The load-steel strain responses at mid-span for the lightweight SFRC specimens with total depth of *h=1000 mm* are shown in Figure (8-13). The mid-span load-strain response of the reinforcement for specimens *L10-1* and *L10-2* started to exhibit a plateau after reaching the ultimate load, due to yielding of the longitudinal reinforcement. For both specimens, a clear change in the slope of load-steel strain response was observed at about *P=170 kN* due to first flexural cracking at mid-span. The difference in behavior of *L10-1* compared to *L10-2*, both with f_c*'=31 MPa*, can be attributed to the lower reinforcement ratio in *L10-1* which resulted in higher reinforcement strains at similar load levels compared to *L10-2*. For specimen *L10-1*, the strain gauges on the longitudinal reinforcement became unbonded once the crack widths at the mid-span increased significantly.

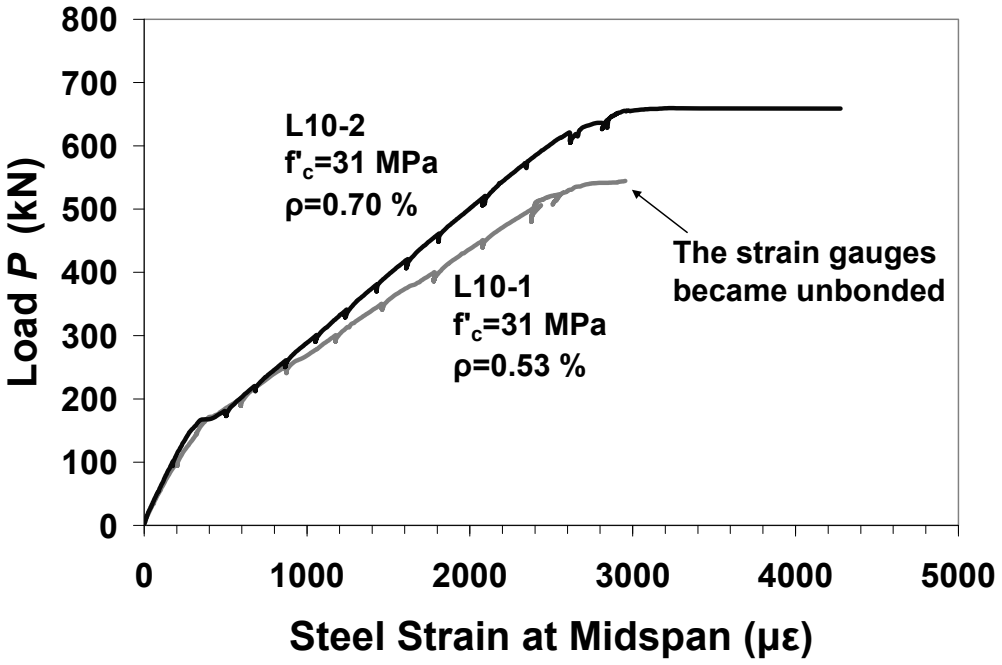

Figure 8-13: Load-steel strain response at mid-span for lightweight SFRC specimens with *h=1000 mm*.

8.1.3.4 Deflection and Crack Width at SLS

According to the procedure explained in Section (6.1.1.5), an equivalent service load $S_L = 0.48\ P_{max}$ was used to determine the SLS deflection and crack widths for the specimens *L10-1* and *L10-2* in Table (8-5). All relative deflection values at service load δ/L are lower than the typical deflection limit of $L/360$ for RC members under live load alone (*ACI 318-08*).

Table 8-5: Deflection and crack width of lightweight SFRC specimens with $h=1000\ mm$ at SLS

Specimen	Failure Type	$0.48P_{max}$ from test (kN)	Behavior at SLS		
			Mid-span Deflection δ (mm)	δ/L	Max. Flexural Crack Width (mm)
L10-1	Flexure	262	5.27	0.0009	0.08
L10-2	Flexure	338	5.92	0.0010	0.07

The detected cracks at SLS were all very narrow flexural cracks near the mid-span. The crack control factor z (see Section 6.1.1.5) indicated that the crack widths for specimens *L10-1* ($z=19040\ N/mm$) and *L10-2* ($z=17300\ N/mm$) are expected to be within the acceptable range for design of RC members with interior exposure ($z \leq 30000\ N/mm$).

8.2 Size Effect in the Shear Strength of Lightweight SFRC Specimens

8.2.1 Normalized Shear Stress versus Effective Depth

The test results of the 6 lightweight SFRC specimens reported in Section (8.1) were used to evaluate the influence of effective depth d on the shear stress at failure. Note that 3 out of 6 specimens (*L61*, *L10-1*, and *L10-2*) in the current study failed in flexure before they reached the ultimate shear strength. The reported shear capacities for these specimens represent the shear strength calculated based on the maximum applied load reached in the test and are lower bound estimates of the actual shear capacity.

Based on the L_c values (i.e. the distance from mid-span of interception point of critical shear crack with the longitudinal steel) in Figures (8-1) and (8-6) as well as L_c values in Section (6.1), the critical section was taken at about *2d* from mid-span. Using the maximum shear force at the critical section, the normalized shear stress $V_{test}/(b\ d\ \sqrt{f_c'})$ from Table (8-1) versus the effective depth d is plotted in Figure (8-14). Note that for specimens *L61*, *L10-1* and *L10-2* which failed in flexure, open symbols are shown in Figure (8-14). The normalized shear stress is observed to decrease as d increases. As shown in Figure (8-14), the average normalized shear stress for specimens with *h=1000 mm* was approximately 32% of that observed in specimens with *h=308 mm*. This trend clearly indicates a size effect in shear for lightweight SFRC members. For the lightweight SFRC members in Figure (8-14), the decrease in normalized shear stress at failure due to increase in the effective depth is larger than that observed for the normal weight SFRC specimens in Section (6.2). However, it should be noted that the real shear capacity of specimens *L61*, *L10-1* and *L10-2* which failed in flexure could be higher than what shown in Figure (8-14).

The test results from previous research on size effect in shear was discussed in Sections (2.2.3) and (6.2) for normal weight RC and SFRC members without stirrups. However, available data on the shear strength of lightweight SFRC structural members are scarce, especially for members with large effective depths. *Swamy et al. (1993)* tested lightweight SFRC specimens with *I-section* and similar depth *h=300 mm*. *Kang & Kim* (2009) reported test data of small size lightweight SFRC specimens, all with similar depth *h=250 mm*. The limited specimen size ranges tested by these researchers (*h=250 mm~300 mm*) prevented prior identification of a size effect in the shear strength of lightweight SFRC members without stirrups.

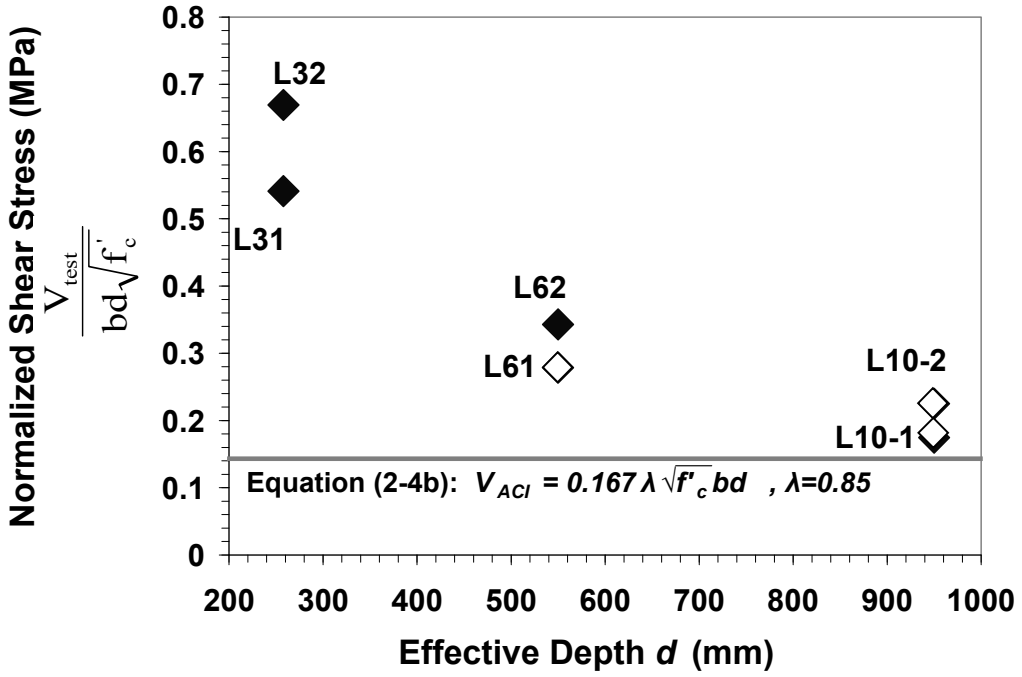

Figure 8-14: Normalized shear stress versus effective depth for lightweight SFRC specimens (Note: the open symbols indicate the specimens with a flexural failure).

As discussed in Section (8.1), the width of shear critical cracks in lightweight SFRC specimens (*L31*, *L32*, *L62*) increased considerably at the last stages of

loading before failure. Also, the results indicated that the maximum shear crack width before shear failure C_{Wmax} increases with an increase in the member depth from *h=308 mm* to *h=600 mm*. Even for small lightweight SFRC members with *h=308 mm* the crack widths before shear failure C_{Wmax} (Table 8-2) were large enough to cause a considerable reduction in the aggregate interlock. As discussed for normal weight SFRC specimens in Section (6.2), the decrease of shear stress at failure in the larger lightweight SFRC members (Figure 8-14) can be attributed to the reduced ability of fibers in bridging the adjacent surfaces of a diagonal crack in SFRC members. As shown in Section (4.5), for the steel fiber type used in this study ($L_f/D_f=55$, $L_f=30$ *mm*) and crack widths larger than about *0.5 mm*, the equivalent fiber tensile stress across adjacent surfaces of a crack σ_f decreases with an increase in the crack width. Hence, the shear stress at failure in large SFRC members with larger crack widths is lower than that in small SFRC members.

8.2.2 Size Effect in Shear Strength: Comparing Test Results with *ACI 318-08* and *CSA A23.3-04* Approaches

Even though size effect still exists for lightweight SFRC specimens (Section 8.2.1), a large increase in shear capacity was observed for SFRC specimens in comparison to the *ACI 318-08* shear model for lightweight RC members without web reinforcement (Figure 8-14). Note that the *ACI 318-08* shear model does not account for the size effect in shear for RC members without web reinforcement and without fibers. For all cases, the normalized shear stress was above the equivalent *ACI 318-08* shear capacity prediction for plain semi-low-density concrete (Equation 2-4b) with $\lambda=0.85$. The semi-low-density factor $\lambda=0.85$ was selected since the density of lightweight SFRC used for casting of specimens in the current study was $\gamma=1900\sim1930$ *kg/m*^{3}. For lightweight SFRC specimens with *h=308 mm* (or *d*=258 *mm*), the average enhancement in shear capacity was 326% compared to the *ACI 318* model. The average enhancement in shear capacity for

specimens with *h=600 mm* (or *d* =550 *mm*) and specimens with *h=1000 mm* (or *d* =950 *mm*) were at least 118% and 37%, respectively. The test results of normal weight SFRC specimens in Section (6.2.2) validated the approach in *ACI 318-08* for using steel fibers instead of minimum stirrups to enhance the useable shear capacity from $0.5\varphi V_c$ up to φV_c in members with $h \leq 600\ mm$, $f'_c \leq 41\ MPa$ and without transverse reinforcement. The current study indicates that this approach can be also extended for lightweight SFRC members with $h \leq 1000\ mm$.

Figure (8-15) compares the maximum shear at failure for the 6 lightweight SFRC specimens in this study against the *CSA A23.3-04* shear capacity predictions for similar lightweight RC members without steel fibers. In section (2.3.1), it was noted that the *CSA A23.3-04* model accounts for size effect in shear related to the aggregate interlock at the cracks for lightweight plain concrete. As illustrated in Figure (8-15), adding steel fibers into the concrete matrix gave considerable enhancement to the shear capacity of lightweight RC members relative to the *CSA A23.3-04* shear prediction for members without fibers. For specimens with *h=308 mm*, *h=600 mm* and *h=1000 mm*, the average increases in shear capacity were 218%, 153% and 140%, respectively, compared to the *CSA A23.3-04* model. The *CSA A23.3-04* model for RC members also accounts for the steel strain effect on shear capacity of RC without fibers (Section 2.3.1), so differences in longitudinal reinforcement ratio among the specimens are reflected in the shear capacity prediction V_{CSA}. The effect of longitudinal reinforcement ratio on the shear strength of lightweight SFRC specimens is discussed in Section (8.3).

The V_{test}/V_{CSA} ratios in Figure (8-15) do not show a clear trend as *d* increases from 258 *mm* to 950 *mm*. The average V_{test}/V_{CSA} ratio decreases when the total depth of specimens increases from *h=308 mm* to *h=600 mm*, but remains almost the same when *h* increases from 600 *mm* to 1000 *mm*. Note that for specimens *L61*, *L10-1* and *L10-2* which failed in flexure, the real shear capacity and therefore V_{test}/V_{CSA} could be higher than what is shown in Figure (8-15). However, a larger sample of

results from an extended testing program is required to better define this trend experimentally. The issue is also examined analytically in Section (8.4).

The proposed modified *CSA A23.3-04* shear model for normal weight SFRC members (Equation 6-5) in Section (6.2.2) may also be used for the lightweight SFRC members with a semi-low-density factor of $\lambda=0.85$. Note that the lower bound for V_{test}/V_{CSA} ratios in Figure (8-15) (also see Table 8-8) is larger than the $\eta=1.33$ considered in Equation (6-5) for the normal weight SFRC members.

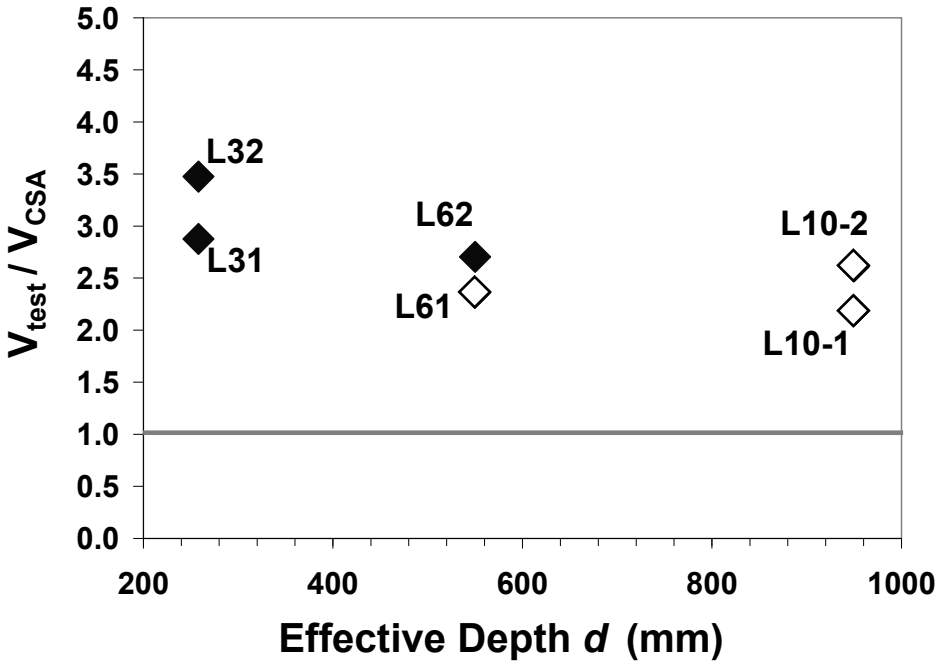

Figure 8-15: Comparing the shear capacity of lightweight SFRC specimens from current study against *CSA A23.3-04* model.

8.3 Effect of Longitudinal Reinforcement Ratio on the Shear Strength

Figure (8-16) summarizes the influence of longitudinal reinforcement ratio on the shear stress at failure of lightweight SFRC specimens with *h=308 mm*, *h=600 mm* and *h=1000 mm*. Note that for specimens *L61*, *L10-1* and *L10-2* which failed in flexure, open symbols are shown in Figure (8-16). These results indicate that for the 33% increase in ρ within each specimen group with similar depth, the normalized shear stress at failure increased by 21% to 29%. For specimens with *h=308 mm*, there was a 24% increase in the shear capacity as ρ varied from 1.88% to 2.50%. In specimens with *h=600 mm* and *h=1000 mm*, when ρ increased by 33%, the increase in shear capacity was about 21% and 29%, respectively. Test results reported by *Swamy et al. (1993)* showed that the shear stress capacity of both lightweight RC and lightweight SFRC (V_f*=1%*) specimens with *a/d=3.43~4.91* did not change considerably when the reinforcement ratio varied from 1.55% to 4.31%.

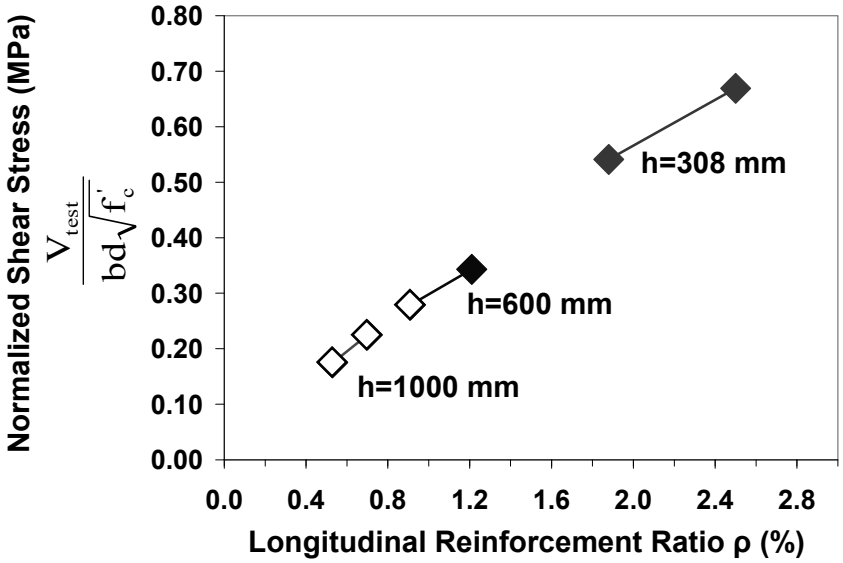

Figure 8-16: Effect of longitudinal reinforcement ratio on the shear capacity of lightweight SFRC specimens (Note: the open symbols indicate the specimens with a flexural failure).

8.4 Flexural Capacity Enhancement in Comparison to *ACI 318-08* Flexural Model

The focus of this study is on the shear performance of the SFRC members without stirrups. However, in this section, the flexural capacity enhancement for all 6 lightweight specimens in this study due to the contribution of steel fibers is examined. Comparisons are made to the *ACI 318-08* flexural model for similar RC members without fibers (Table 8-6). In section (8.1), it was observed that specimens *L61*, *L10-1*, and *L10-2* failed in flexure before reaching their shear capacity. It was also noted that specimens *L31*, *L32*, and *L62* approached their flexural and shear capacities simultaneously.

Table 8-6: Flexural capacity of lightweight specimens in this study

Specimen	b (mm)	d (mm)	f'_c (MPa)	ρ %	Failure Type	P_{max} * (kN)	M_{test}** (kN.m)	M_{ACI} (kN.m)	M_{test}/M_{ACI}
L31	310	258	22	1.88	Shear++	405	157	124	1.27
L32	310	258	31	2.50	Shear++	595	231	167	1.38
L61	300	550	30	0.91	Flexure	497	415	307	1.35
L62	300	550	30	1.21	Shear++	612	510	398	1.28
L10-1	300	950	31	0.53	Flexure	532	781	551	1.42
L10-2	300	950	31	0.7	Flexure	692	1009	718	1.41
Average									1.35
COV									5%

***** The maximum applied load at mid-span
*****The maximum moment at mid-span during test including selfweight
++ These specimens approached their shear and flexural capacities simultaneously (see Section 8.1)

According to *ACI 318-08*, the nominal flexural capacity of tension-controlled RC members can be calculated from:

$$M_{ACI} = A_s f_y (d - \frac{\beta_1 c}{2}) = \rho b d^2 f_y (1 - \rho \frac{f_y}{2\alpha_1 f_c'}) \quad (6\text{-}6)$$

where, parameter α_1 =0.85, and β_1 can be obtained from:

$$\beta_1 = \begin{cases} 0.85 & \text{for } f'_c \leq 28\ MPa \\ 1.05 - 0.007 f'_c \geq 0.65 & \text{for } f'_c > 28\ MPa \end{cases} \quad (2\text{-}28)$$

Figure (8-17) and Table (8-6) compare the maximum flexural capacity at failure for lightweight SFRC specimens in this study against the *ACI 318-08* prediction for similar RC members without steel fibers. Adding steel fibers into the concrete matrix gave considerable enhancement to the flexural capacity of lightweight RC members relative to the *ACI 318-08* flexure predictions. As shown in Table (8-6) and Figure (8-17), for the six lightweight SFRC specimens with relatively wide range of depths and reinforcement ratios, the average M_{test} / M_{ACI} ratio was 1.35 with a *COV=5%*. These results are comparable to those obtained for normal weight specimens in Section (6.4) with an average M_{test} / M_{ACI} ratio of 1.23 and a *COV=4%*.

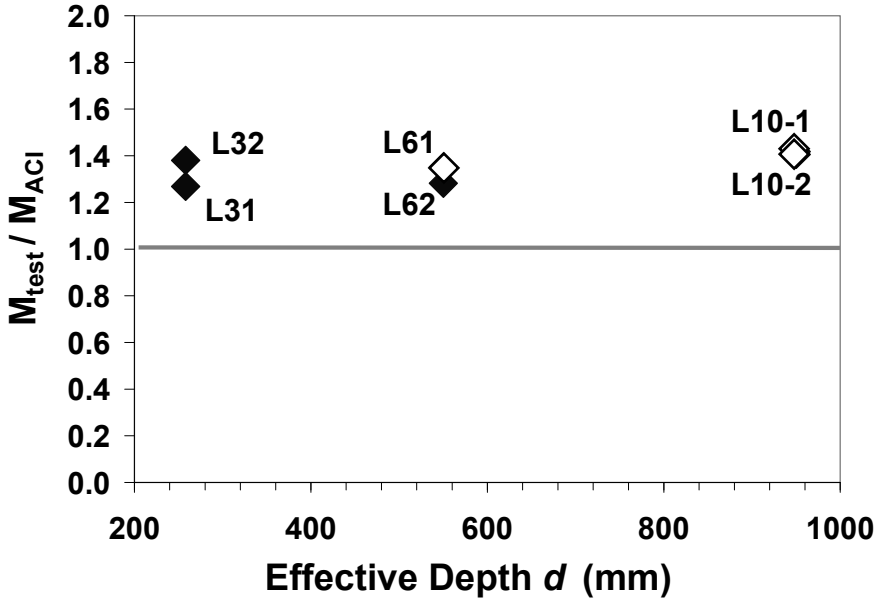

Figure 8-17: Comparing the flexural capacity of lightweight SFRC specimens in this study against *ACI 318-08* flexural model.

8.5 Shear Modeling for Lightweight SFRC Members without Stirrups

In this section, it is assumed that the same approach for development of analytical and design shear models in Chapter 7 is applicable to lightweight SFRC members. In Section (4.5), it was observed that the normalized fiber tensile stress $\sigma_f / \sqrt{V_f . f_c'}$ shows a similar relationship with respect to the crack width for both normal weight and lightweight SFRC. The maximum crack widths C_{Wmax} for lightweight SFRC members which failed in shear (Section 8.1) were also comparable to those observed for the normal weight specimens in Section (6.1). The ultimate shear stress capacity in the compression zone τ_{cu} for the analytical model in Section (7.1.3) was assumed to be a function of $\sigma_{cu} / f'_c = \alpha_1$. According to *CSA A23.3-04*, the parameter α_1 can be calculated identically from Equation (4-7) for both normal weight and lightweight concrete. Therefore, Equations (7-6) and (7-8) for calculation of V_{cc} and V_{ft}, respectively, may also be used for lightweight SFRC members:

$$V_{cc} = \tau_{cu} \beta_1 c b \tag{7-6}$$

$$V_{ft} = \sigma_{f1} b \frac{d-c}{\sin\theta} . \cos\theta = \sigma_{f1} b \frac{d-c}{\tan\theta} \tag{7-8}$$

To account for the weakness of aggregates in lightweight SFRC and in accordance with the *CSA A23.3-04* model, a density factor λ is multiplied in the calculated shear strengths V_{cc} and V_{ft} determined from Equations (7-6) and (7-8), respectively. In Clause (8.6.5) of *CSA A23.3-04*, a semi-low-density concrete is defined as a concrete which may include natural sand and lightweight coarse aggregates; however, the density ranges for low-density ($\lambda=0.75$) and semi-low-density ($\lambda=0.85$) concretes are not indicated. Based on *MacGregor et al. (2006)*, concretes with $\gamma \leq 1850\ kg/m^3$ and $1850\ kg/m^3 < \gamma \leq 2150\ kg/m^3$ can be considered as low-density and semi-low-density concretes, respectively. Meanwhile, in *Kang*

and Kim (2010) shear model (see Section 2.3) a low-density factor of $\lambda=0.75$ was used for lightweight SFRC with $\gamma = 1800\ kg/m^3$. As noted in Chapter 5, for the lightweight SFRC mix in the current study, bottom ash and expanded clay were used as fine and coarse aggregates, respectively. However, due to the range of density for the lightweight SFRC specimens in the current study ($\gamma=1900\sim1930\ kg/m^3$), a semi-low-density factor of $\lambda=0.85$ is selected according to Clause (8.6.5) of *CSA A23.3-04*. For lightweight SFRC with low-density $\gamma \leq 1850\ kg/m^3$ (*MacGregor et al. 2006)* a factor of $\lambda=0.75$ is chosen.

The scope of the proposed shear models in this section is for lightweight structural members which satisfy the same criteria indicated for the analytical and design shear models in Chapter 7, with the following limits:

- Rectangular cross section with $180\ mm \leq h \leq 1000\ mm$ and $b \geq 100\ mm$
- $a/d \geq 2.5$
- $0.75\% \leq V_f \leq 1.5\%$, $45 \leq L_f/D_f \leq 100$, and $25mm \leq L_f \leq 60\ mm$ (hooked end steel fibers)
- $20\ MPa \leq f'_c \leq 90\ MPa$

8.5.1 Analytical Shear Model for Lightweight SFRC Members

The flowchart for the analytical shear model in Figure (7-4) is updated to account for the lightweight factor λ. All other steps for the analytical model remain unchanged. The proposed analytical model for lightweight SFRC members is summarized as Figure (8-18):

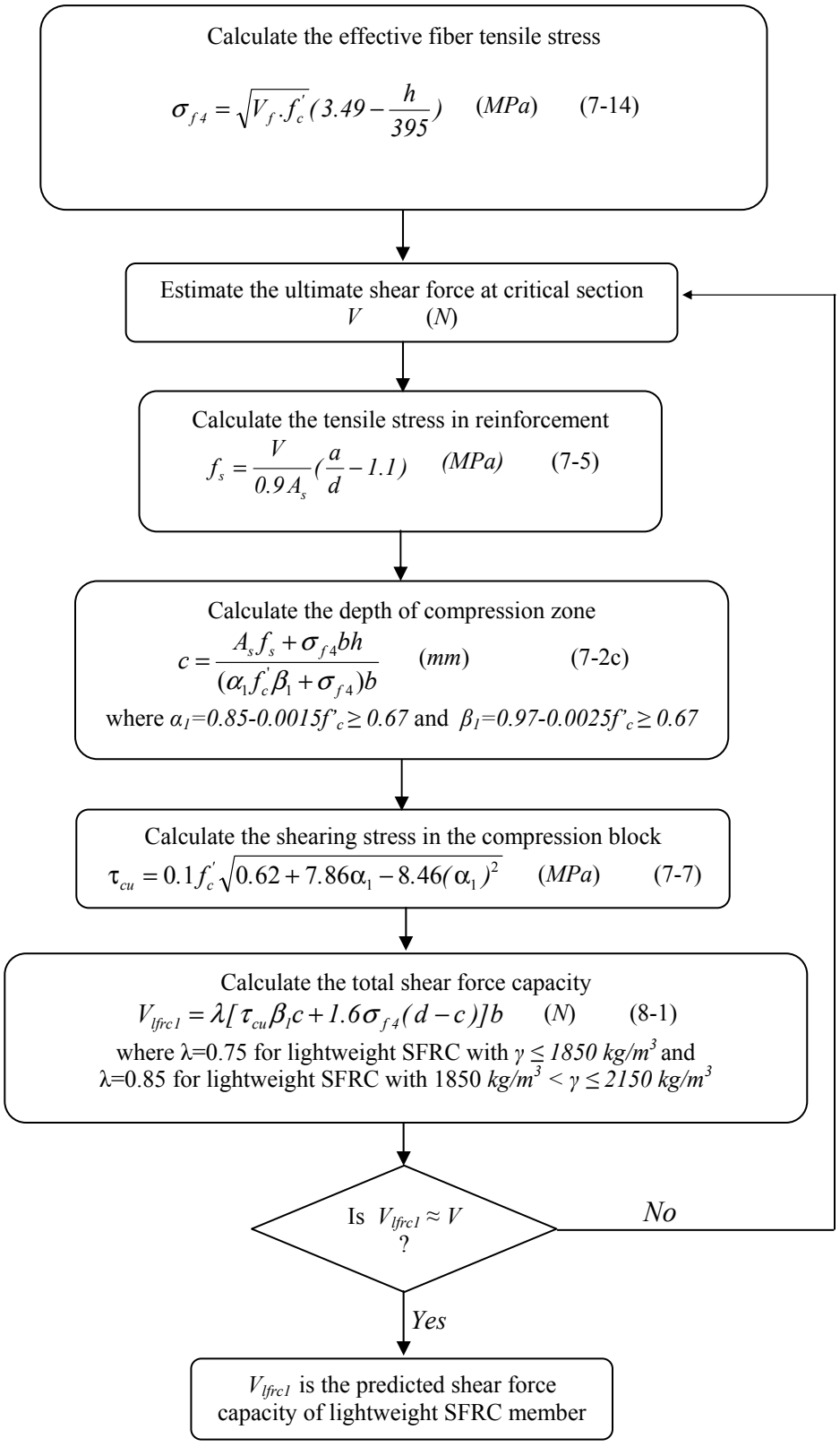

Figure 8-18: The steps of shear capacity prediction for lightweight SFRC members based on proposed analytical model

The test results of the 6 lightweight SFRC specimens in this study were used to validate the proposed analytical model (Table 8-7). Note that three out of 6 specimens in the current study failed in flexure before they reach the ultimate shear strength, so the reported V_{test} for these specimens is the shear capacity calculated based on the maximum applied load in the test. In contrast to the large number of existing test data on normal weight SFRC structural members, available studies on the shear strength of lightweight SFRC structural members are scarce. *Swamy et al.* (1993) tested nine lightweight SFRC structural specimens with I-section and very thin web (b_w=*55 mm*). *Kang & Kim* (2009) reported test data of nine lightweight SFRC specimens (γ=*1800 kg/m*^{3}) with *a/d=2, 3* and *4* and steel fiber volume fraction V_f =*0.5%~ 0.75%*. Only two of the *Kang & Kim* (2009) specimens had $a/d \geq 2.5$ and fiber content $V_f \geq 0.75\%$, but both of them failed in flexure before reaching their shear capacity.

Table 8-7: Validation of proposed analytical model for the available database

Researcher	Specimen	*b* (mm)	*h* (mm)	*d* (mm)	f'_c (MPa)	γ (kg/m^3)	ρ %	*a/d*	L_f/D_f	V_f (%)	V_{lfrc1} (kN)	V_{test}/V_{lfrc1}
Current Study	*L31*	310	308	258	22	1900	1.88	3	55	1	145	1.40
	L32	310	308	258	31	1930	2.50	3	55	1	182	1.64
	*L61**	300	600	550	30	1920	0.91	3	55	1	287	0.88
	L62	300	600	550	30	1920	1.21	3	55	1	287	1.08
	*L10-1**	300	1000	950	31	1930	0.53	3	55	1	274	1.01
	*L10-2**	300	1000	950	31	1930	0.7	3	55	1	274	1.30
Kang & Kim (2009)	FLB*-0.75-3	125	250	210	48	1800	1.5	3	62	0.75	64	0.75
	FLB*-0.75-4	125	250	210	48	1800	1.5	4	62	0.75	69	0.61
Average												**1.08**
COV												**32%**

*Flexural failure

As shown in Table (8-7), the analytical shear model for the shear capacity of lightweight SFRC members without stirrups gives an average V_{test}/V_{lfrc1} =*1.08* and a relatively large scatter of *COV=32%*. The observed large scatter in Table

(8-7) is mainly due to the low V_{test} /V_{lfrc1} ratios for the two flexural critical specimens reported by *Kang & Kim* (2009), compared to the other 6 specimens from the current study. The analytical shear model gives an average V_{test} /V_{lfrc1} *=1.22* and a *COV=23%* for the 6 specimens tested in the current study. These results are reasonable but less accurate compared to those obtained for normal weight SFRC specimens in Table (7-3). However, due to flexural failure of some specimens in Table (8-7) and lack of extensive data from previous research, additional refinement of the model may be warranted as additional data for shear failures become available.

8.5.2 Simplified Shear Design Model for Lightweight SFRC Members

The simplified design model from Chapter 7 (Equation 7-20) was modified to account for the lightweight factor λ as below:

$$V_{lfrc2} = \lambda\left[\frac{37.44\rho}{\alpha_1} + \sqrt{V_f . f_c^{'}}\,(5.58 - \frac{h}{247})(1 - \frac{320\rho}{\alpha_1 f_c^{'} \beta_1})\right] bd \qquad (8\text{-}2)$$

where λ is equal to 0.75 and 0.85 for low-density SFRC ($\gamma \leq 1850\ kg/m^3$) and semi-low-density SFRC ($1850\ kg/m^3 < \gamma \leq 2150\ kg/m^3$), respectively, in accordance with Clause (8.6.5) of *CSA A23.3-04*. The Equation (8-2) was applied to the 8 specimens in Table (8-7) and the V_{test}/V_{lfrc2} ratios have been shown in Table (8-8). The proposed design model yields reasonable predictions with V_{test} /V_{lfrc2} *=1.13* and a coefficient of variance of *COV=28%*. For the 6 specimens tested in the current study, the design shear model gives an average V_{test} /V_{lfrc2} *=1.26* and a *COV=19%*.

To verify and compare the accuracy of the proposed design model (Equation 8-2), the ratio V_{test}/V_{model} for four existing models are also calculated and shown in Table (8-8). These four models include:

- *Kang and Kim* (2010)-1 (modified *Ashour et al.* 1992 model for lightweight SFRC members)
- *Kang and Kim* (2010)-2 (modified *Kwak et al.* 2002 model for lightweight SFRC members)
- *ACI 318-08* shear model for RC members without fibers
- *CSA A23.3-04* shear model for RC members without fibers

The details of these models are described in Section (2.3). The V_{test}/V_{model} ratios for the *ACI 318-08* and *CSA A23.3-04* models were previously discussed in Section (8.2.2) to examine the shear capacity enhancement due to the addition of steel fibers to lightweight RC members.

Table 8-8: Comparing the accuracy of proposed design model with other published models

Researcher	Specimen	V_{test}/V_{model}				***Proposed Design Model Equation (8-2)*** V_{test}/V_{lfrc2}
		***Kang and Kim* (2010)-1**	***Kang and Kim* (2010)-2**	***ACI 318-08***	***CSA A23.3-04***	
Current Study	***L31***	1.57	1.23	3.81	2.88	1.39
	L32	1.97	1.60	4.71	3.47	1.62
	L61*	1.14	0.82	1.96	2.36	0.94
	L62	1.27	0.95	2.42	2.70	1.12
	L10-1*	0.86	0.57	1.23	2.19	1.11
	L10-2*	1.01	0.70	1.58	2.61	1.36
Kang & Kim (2009)	**FLB-0.75-3***	1.12	0.85	2.11	1.70	0.80
	FLB-0.75-4*	1.07	0.96	1.85	1.68	0.70
Average		**1.25**	**0.96**	**2.46**	**2.45**	**1.13**
COV		**29%**	**34%**	**48%**	**25%**	**28%**

*Flexural failure

As shown in Table (8-8), the *Kang and Kim* (2010)-1 model gives conservative predictions of shear capacity with relatively large scatter. However, the *Kang and Kim* (2010)-2 model yields non-conservative and highly scattered estimations (average $V_{test}/V_{model}=0.96$ and $COV=34\%$). Note that the *Kang and Kim* (2010)-2 model over-estimated the shear capacity of 75% of the specimens in Table (8-8) with $0.57 \leq V_{test}/V_{model} \leq 0.96$. Among the shear models in Table (8-8), the proposed design model (Equation 8-2) with $V_{test}/V_{lfrc2}=1.13$ and $COV=28\%$ gives more accurate predictions for shear capacity of lightweight SFRC members without stirrups.

To study the sensitivity of the proposed design model (Equation 8-2) and the *Kang and Kim* (2010)-1 model to different variables, the ratio V_{test}/V_{model} versus effective depth d, tensile reinforcement ratio ρ, and concrete compressive strength f'_c is plotted in Figures (8-18), (8-19), and (8-20), respectively. The symbols with light color represent the lightweight specimens from the current study and the letter *F* indicates a flexural failure. For the test database in Table (8-7), the parameters d, ρ, and f'_c had relatively wider ranges compared to other parameters such as a/d and V_f. According to *Kang and Kim (2010)*, the slope (steepness) of a linear regression between V_{test}/V_{model} and an independent variable can be used as a statistical indicator for evaluation of V_{test}/V_{model} sensitivity to that variable.

Figure (8-18) indicates that the ratio V_{test}/V_{model} for *Kang and Kim* (2010)-1 model is highly sensitive to the changes in the effective depth d. As shown in Figure (8-18a), the average ratio V_{test}/V_{model} for this model decrease considerably with an increase in d. However, Figure (18-8b) shows that V_{test}/V_{model} for the proposed design model (Equation 8-2) is not sensitive to the changes in d, and therefore Equation (8-2) better accounts for the depth related size effect in shear.

According to Figure (8-19), the ratio V_{test}/V_{model} for the proposed design model and *Kang and Kim* (2010)-1 show sensitivity to the changes in the tensile reinforcement ratio ρ. However, the slope (steepness) of the regression line for

Kang and Kim (2010)-1 is considerably higher compared to the proposed design model. Both models in Figure (8-20) show sensitivity in V_{test}/V_{model} due to the changes in the concrete compressive strength f'_c=22~48 *MPa*. This sensitivity to f'_c for the proposed design model is slightly higher than that for the *Kang and Kim* (2010)-1 model.

The discussions in this section indicate that among the lightweight SFRC shear models shown in Table (8-8), the proposed design model (Equation 8-2) is the most accurate model with a relatively low sensitivity to different variables.

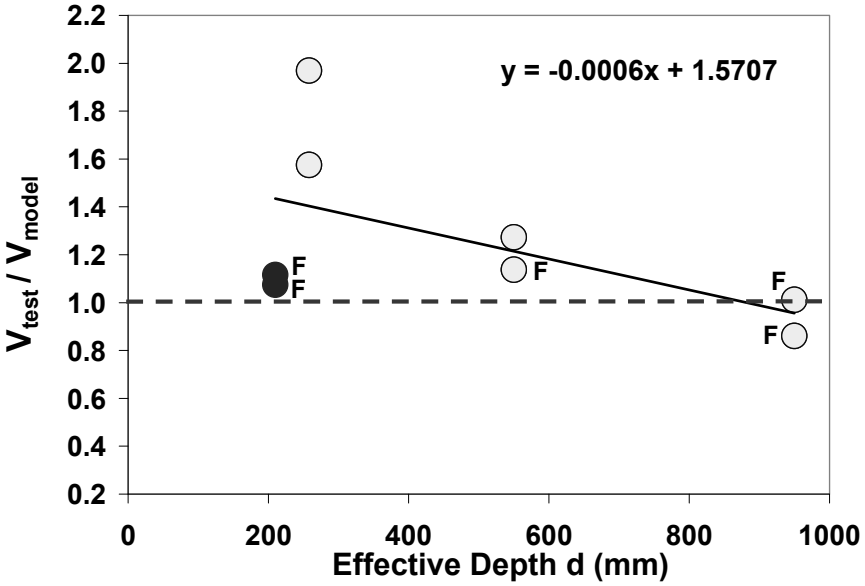

a) *Kang and Kim* (2010)-1 model

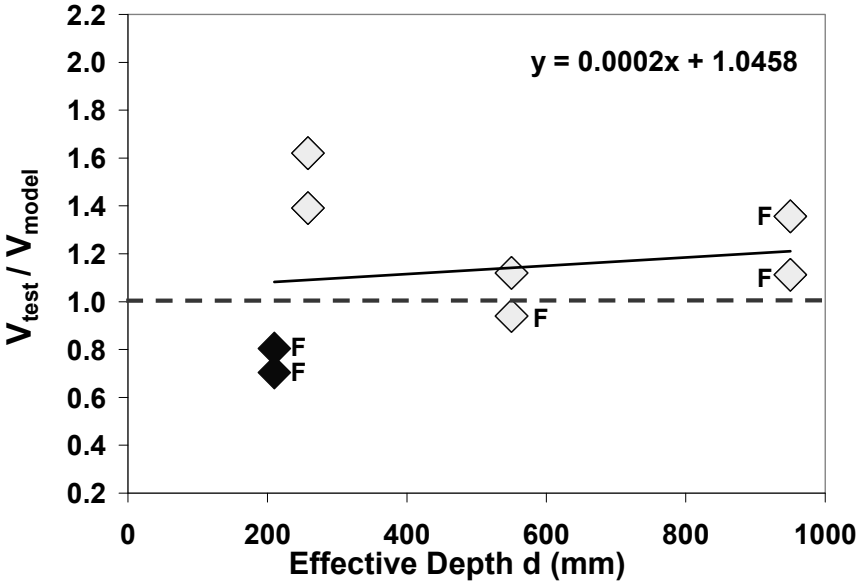

b) Proposed Design Model (Equation 8-2)

Figure 8-18: The ratio V_{test} /V_{model} versus d for the proposed design Equation (8-2) and *Kang and Kim* (2010)-1 model (Note: the symbols with lighter color indicate the specimens from the current study, F: flexural failure).

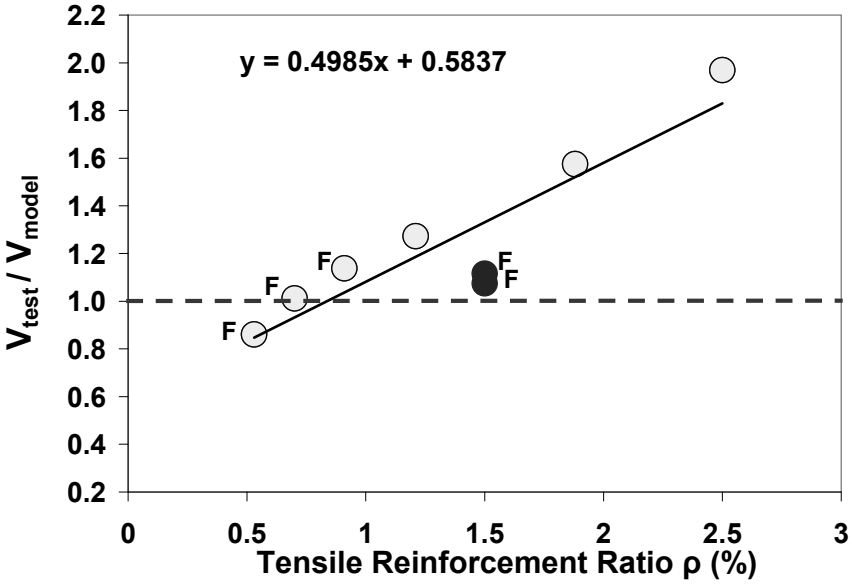

a) *Kang and Kim* (2010)-1 model

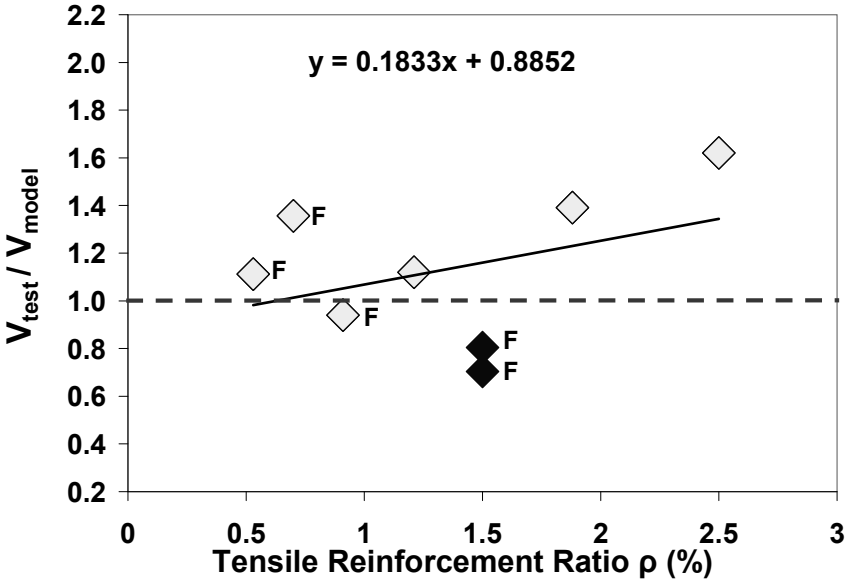

b) Proposed Design Model (Equation 8-2)

Figure 8-19: The ratio V_{test}/V_{model} versus ρ for the proposed design Equation (8-2) and *Kang and Kim* (2010)-1 model (Note: the symbols with lighter color indicate the specimens from the current study, F: flexural failure).

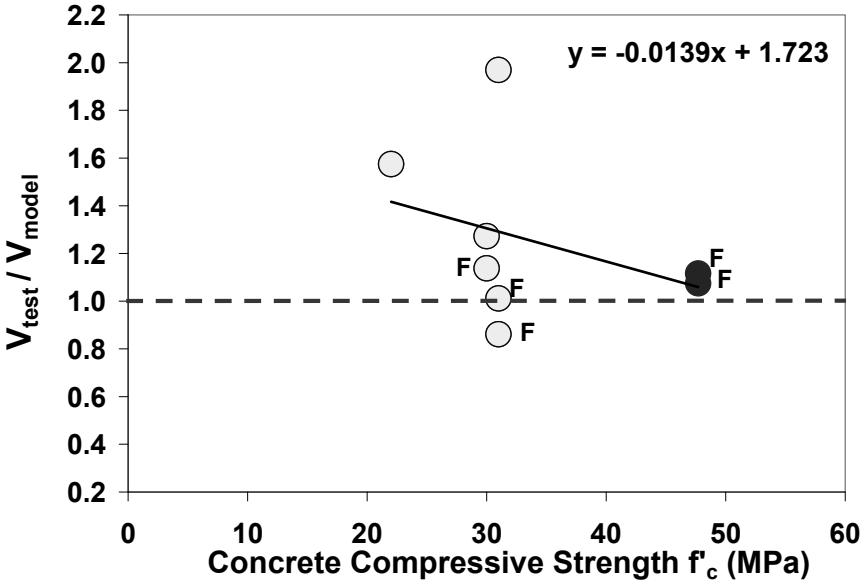

a) *Kang and Kim* (2010)-1 model

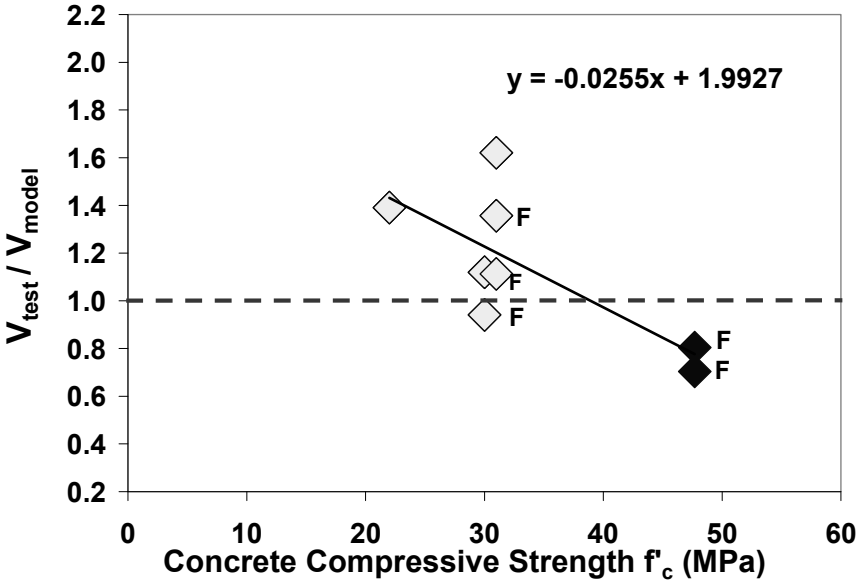

b) Proposed Design Model (Equation 8-2)

Figure 8-20: The ratio V_{test} /V_{model} versus f'_c for the proposed design Equation (8-2) and *Kang and Kim* (2010)-1 model (Note: the symbols with lighter color indicate the specimens from the current study, F: flexural failure).

9. Summary

9.1 Conclusions

9.1.1 Mechanical Properties of SFRC

This research highlighted the following significant aspects regarding the mechanical properties of steel fiber reinforced concrete (SFRC), with particular emphasis on the presence of lightweight aggregates on the one hand and a high strength matrix on the other:

a) The strain corresponding to the peak stress in compression increases with an increase in the fiber content. This increase in the strain-at-peak stress was most pronounced for high strength concrete (HSC). The addition of steel fibers into lightweight concrete (LWC) and HSC at practical dosage (up to 1% by volume) had very little effect on their ultimate compressive strength or the modulus of elasticity, which conforms to the previously known trend for normal weight concrete (NSC). There was a significant improvement in the post-peak energy dissipation due to the addition of steel fibers.

b) While the addition of steel fibers resulted in an increase in the modulus of rupture for all mix types, it was most pronounced for LWC. Similarly, the steel fibers were most effective in imparting superior flexural toughness factors to the LWC mixes.

c) The addition of steel fibers enhanced the direct shear strength in all three types of concrete examined in this study. However, it was least effective in the LWC. A linear correlation was obtained to express the shear strength as a function of the fiber content.

d) The steel fibers were most effective in imparting post-crack shear resistance to the NSC mixes with regular aggregates. This may be attributed to the more tortuous path around the aggregate taken by cracks in the NSC mixes as opposed to the LWC and HSC mixes, where cleavage was through the coarse aggregates.

e) All of the toughness factors for compression, flexure, and shear increased with an increase in the fiber content; however, among the three toughness factors, the flexural toughness factor saw higher increase due to presence of steel fibers.

f) The shear toughness factor and the flexural toughness factor bear a linear relationship. However, in order to obtain the most accurate linear relationship between these two factors, the maximum deflection up to which the shear toughness is evaluated must be suitably selected for each type of concrete.

g) An approach similar to that employed by *Dinh* (2009) was taken to determine the equivalent uniform tensile stress σ_f imparted by the steel fibers across a flexural crack for NSC, HSC and LWC with V_f=*0.5%* and V_f=*1%*. When σ_f was normalized by $\sqrt{V_f.f_c^{'}}$, all of the SFRC mixes had similar relationship with respect to the crack mouth opening displacement C_M.

9.1.2 Shear Strength of Structural SFRC Members without Stirrups

This study established the following significant points regarding the shear strength of both normal weight and lightweight structural SFRC members without stirrups including V_f=*1%*:

i) In contrast to typical behaviour of reinforced concrete (RC) members, no sudden or large change of slope in the load-deflection relationship was observed at the initiation of flexural cracks for the SFRC specimens in this study.

j) In shear critical specimens, non-linear load-deflection relationships with gradually reducing slopes were observed up to the failure at the formation of significant diagonal cracking. In these specimens, a sudden and large drop in load was recorded at failure due to concrete crushing in the region between the top of the diagonal crack and the edge of the loading plate at mid-span.

k) In one-third of the shear critical specimens, the load-deflection response at the mid-span started to exhibit a plateau after reaching the ultimate load, mainly due to yielding of the longitudinal reinforcement. After yielding of the longitudinal steel and some additional deformation, a significant diagonal crack formed leading to shear failure.

l) For all specimens, flexural cracks near mid-span were detected first during initial load stages. Then, new flexural cracks formed in the shear spans and curved diagonally towards the loading point.

m) In shear critical specimens, the critical diagonal cracks intercepted the longitudinal reinforcement at considerable distances from the support plates, representing a "sectional" shear model behavior rather than arch action.

n) The critical diagonal crack for shear had an angle of $\theta=29.5^{o} \sim 34.9^{o}$ with respect to the longitudinal axis of member, and intercepted the longitudinal reinforcement in a distance of $L_c=1.84d \sim 2.39d$ from mid-span.

o) The normalized shear stress at failure $\frac{V_{test}}{\sqrt{f_c'}\, b\ d}$ decreased with an increase in the specimen total depth from 308 *mm* to 1000 *mm*. This clearly indicates that the size effect in shear still exists for SFRC specimens without stirrups.

p) Even though size effect in shear still exists for SFRC specimens, adding steel fibers into the concrete matrix enhanced the shear capacity considerably compared to the *ACI 318-08* and *CSA A23.3-04* predictions for RC members without steel fibers.

q) The test results for shear critical specimens indicated that for the range of ρ used in this project, the influence of longitudinal reinforcement ratio on the normalized shear stress at failure was very small. The longitudinal reinforcement ratio ρ varied by about 33% to 61% in each group of specimens with the same total height.

9.1.3 Analytical Shear Modeling for SFRC members without Stirrups

r) An analytical model was developed based on mechanical principles and empirical measurements of crack geometry observed in the current study for both normal weight and lightweight SFRC members without stirrups which satisfy the following limits:

- Rectangular sections with $180\ mm \le h \le 1000\ mm$ and $b \ge 100\ mm$
- $a/d \ge 2.5$
- $0.75\% \le V_f \le 1.5\%$, $45 \le L_f/D_f \le 100$, and $25mm \le L_f \le 60\ mm$ (hooked end steel fibers)
- $20\ MPa \le f'_c \le 90\ MPa$

The analytical model was further simplified to be suitable for use in design. For validation, shear capacity predictions were examined for a large database and gave reliable and accurate predictions.

s) The prediction quality of the simplified design model for both normal and lightweight SFRC members was compared against results using several published SFRC shear models from other researchers as well as the *ACI 318-08* and *CSA A23.3-04* shear capacity models for RC members without stirrups. Among the SFRC shear models studied, the proposed design model was the most accurate model with a relatively low sensitivity to different variables.

9.2 Recommendations

Based on test results, discussions and conclusions in this study, the following recommendations are given:

i) The application of *ACI 318-08* Clause (11.4.6) for replacing minimum web reinforcement with steel fibers when $0.5\varphi V_c < V_u \leq \varphi V_c$, can be extended to include members with larger depths up to $h \leq 1000\ mm$, higher compressive strengths up to $f_c' \leq 80\ MPa$ containing normal weight or lightweight SFRC.

ii) In *CSA A23.3-04* shear model for slender members without stirrups and with $a/d \geq 2.5$, $20\ MPa \leq fc' \leq 90\ MPa$ and $180\ mm \leq h \leq 1000\ mm$, a 'fiber contribution factor' η is proposed as follows:

$$V_{CSA,f} = \lambda\, \eta\, \beta \sqrt{f_c'}\, b\, d_v \qquad (6\text{-}5)$$

where $\eta = 1.33$ for SFRC members with $V_f \geq 0.75\%$, representing a lower bound for the shear capacity enhancement due to the contribution of hooked end steel fibers.

iii) The proposed simplified design model in this study is recommended for prediction of shear capacity of SFRC members without stirrups which satisfy the limitations described in Section (9.1.3):

$$V_{frc} = \lambda \left[\frac{37.44\rho}{\alpha_1} + \sqrt{V_f . f_c'} \left(5.58 - \frac{h}{247}\right)\left(1 - \frac{320\rho}{\alpha_1 f_c' \beta_1}\right) \right] bd \qquad (9\text{-}1)$$

where λ is equal to 0.75, 0.85, and 1 for low-density SFRC ($\gamma \leq 1850\ kg/m^3$), semi-low-density SFRC ($1850\ kg/m^3 < \gamma \leq 2150\ kg/m^3$), and normal density SFRC, respectively, in accordance with Clause (8.6.5) of *CSA A23.3-04*.

9.3 Future work

1) The focus of this project was on the shear strength of slender SFRC members without stirrups. However, the recorded data under service load for deflection, crack width, and strain on the surface of the specimens from this study and from other researchers can be used to model the deformation of SFRC members without stirrups under service load.

2) Beyond the test data obtained in this study, available data on the shear strength of large size lightweight SFRC members are scarce. Meanwhile, in this project expanded clay and bottom ash were used as lightweight aggregates. There is a need for more studies on the shear strength of large size lightweight SFRC members, especially those utilizing different types of lightweight aggregates.

3) The proposed shear models in this study were only applicable to slender SFRC members with $a/d \geq 2.5$ containing hooked end steel fibers. More experimental data and analytical work are needed to extend the application of these models to short members with $a/d<2.5$ as well as members containing different types of fibers.

4) The material and structural test data from this project and previous research may be used to develop nonlinear finite elements models for prediction of shear strength in SFRC members.

References

ACI Committee 318 (2008), "Building Code Requirements for Structural Concrete and Commentary," American Concrete Institute, Farmington Hills, MI, 473 pp.

ACI-ASCE Committee 326 (1962), "Shear and Diagonal Tension," *ACI Journal Proceedings*, 59(1), 59(2), and 59(3), 1-30, 277-334, and 352-396.

ACI-ASCE Committee 426 (1973), "The Shear Strength of Reinforced Concrete Members," *ACI Journal Proceedings*, 70(7), 471-473.

ACI-ASCE Committee 544 (1988), "Design Considerations for Steel Fiber Reinforced Concrete," *ACI Journal Proceedings*, 85(5), 563-579.

Angelakos, D., Bentz, E. C., and Collins, M. P. (2001), "Effect of Concrete Strength and Minimum Stirrups on Shear Strength of Large Members,"*ACI Structural Journal*, 98(3), 290-300.

Armelin, H. S. and Banthia, N. (1997), "Predicting the Flexural Post cracking Performance of Steel Fiber Reinforced Concrete from the Pullout of Single Fibers," *ACI Materials Journal*, 94 (1), 18-31.

Ashour, S. A., Hasanain, G. S. and Wafa, F. F. (1992), "Shear Behavior of High-Strength Fiber Reinforced Concrete Beams," *ACI Structural Journal*, 89(2), 176-184.

ASTM C39/C39M (2005), "Standard Test Method for Compressive Strength of Cylindrical Concrete Specimens", ASTM International, West Conshohocken, PA, 7 pp.

ASTM C1609/C1609M (2005), "Standard Test Method for Flexural Performance of Fiber-Reinforced concrete (Using Beam with Third-Point Loading)," ASTM International, West Conshohocken, PA, 8 pp.

Balaguru, P. and Foden, A. (1996), "Properties of Fiber Reinforced Structural Lightweight Concrete", *ACI Materials Journal*, 93(1), 63-78.

Balaguru, P., Narahari, R., Patel, M. (1992), "Flexural Toughness of Steel Fiber Reinforced Concrete", *ACI Materials Journal*, 89(6), 541-546.

Banthia, N., and Trottier, J. (1994), "Concrete Reinforced with Deformed Steel Fibers, Part I: Bond-Slip Mechanisms," *ACI Materials Journal*, 91(5), 435-446.

Banthia, N. and Trottier, J. (1995), "Test Methods for Flexural Toughness Characterization of Fiber Reinforced Concrete: Some Concerns and a Proposition" *ACI Materials Journal*, 92(1), 48-57.

Barragan, B., Gettu, R., Agullo, L., and Zerbino, R. (2006), "Shear Failure of Steel Fiber-Reinforced Concrete Based on Push-Off Tests", *ACI Materials Journal*, 103(4), 251-257.

Batson, G., Jenkins, E., and Spatney, R. (1972), "Steel Fibers as Shear Reinforcement in Beams," *ACI Journal Proceedings*, 69(10), 640-644.

Bazant, Z. P. and Sun, H. H. (1987), "Size Effect in Diagonal Shear Failure: Influence of Aggregate Size and Stirrups," *ACI Material Journal*, 84(27), 259-272.

Bentz, E. C., Vecchio, F. J., and Collins, M. P. (2006), "The Simplified MCFT for Calculating the Shear Strength of Reinforced Concrete Elements," *ACI Structural Journal*, 103(4), 614-624.

Bresler, B., and K.S., Pister (1958). "Strength of Concrete under Combined Stresses," *ACI Journal Proceedings*, 55(9), 321-345.

Casanova, P., and Rossi, P. (1999), "High-Strength Concrete Beams Submitted to Shear: Steel Fibers versus Stirrups," Structural Applications of Fiber Reinforced Concrete*,* ACI SP-182, American Concrete Institute, 53-68.

Chern, J. C., Yang, H. J., and Chen, H. W. (1992), "Behavior of Steel Fiber Reinforced Concrete in Multiaxial Loading," *ACI Material Journal*, 89(1), 32-40.

Collins, M. P., and Kuchma, D. (1999), "How Safe Are Our Large, Lightly-Reinforced Concrete Beams, Slabs and Footings?" *ACI Structural Journal*, 96(4), 482-490.

Collins, M. P., Mitchell, D., Adebar, P. and Vecchio, F. J. (1996), "A General Shear Design Method," *ACI Structural Journal,* 93 (1), 36-45.

CSA Committee A23.2 (2000), "Methods of Test for Concrete," Canadian Standards Association, Mississauga, ON.

CSA Committee A23.3 (2004), "Design of Concrete Structures," Canadian Standards Association, Mississauga, ON, 214 pp.

CSA S6-06 (2006), "Canadian Highway Bridge Design Code," Canadian Standard Association, Rexdale, ON, 733 pp.

Cucchiara, C., Mendola, L.L., and Papia, M. (2004), "Effectiveness of Stirrups and Steel Fibers as Shear Reinforcement," *Cement and Concrete Composites*, 26(7), 777-786.

Dinh, H.H. (2009), " Shear Behavior of Steel Fiber Reinforced Concrete Beams without Stirrup Reinforcement," Doctoral Dissertation, Department of Civil and Environmental Engineering, University of Michigan, Ann Arbor, MI, 285 pp.

Dinh, H. H., Parra-Montesinos, G. J. and Wight, J. K. (2010), " Shear Behavior of Steel Fiber-Reinforced Concrete Beams without Stirrup Reinforcement," *ACI Structural Journal*, 107(5), 597-606.

Dupont D. and Vandewalle L. (2003), "Shear Capacity of Concrete Beams Containing Longitudinal Reinforcement and Steel Fibers", ACI SP-216, American Concrete Institution, 79-94.

Ezeldin, A.S. and Balaguru, P.N. (1992), "Normal and High Strength Fiber Reinforced Concrete under Compression", *ASCE Journal of Materials in Civil Engineering*, 4(4), 415-427.

Fanella, D. A., and Naaman, A. E. (1985), "Stress-Strain Properties of Fiber Reinforced Mortar in Compression," *ACI Journal Proceedings*, 82(4), 475-483.

Fenwick, R. C., and Paulay, T. (1968), "Mechanisms of Shear Resistance of Concrete Beams," *Journal of the Structural Division*, ASCE, V. 94, No. ST10, pp. 2235-2350.

Gray, R. J., and Johnston, C. D. (1984), "The Effect of Matrix Composition on Fiber/Matrix Interfacial Bond Shear Strength in Fiber Reinforced Mortar," *Cement and Concrete Research*, Vol. 14, 285-296.

Higashiyama, H. and Banthia, N. (2008), "Correlating Flexural and Shear Toughness of Lightweight Fiber-Reinforced Concrete," *ACI Materials Journal*, 105(3), 251-257.

Hognestad, E., Hanson, N. W., and McHenry, D. (1955), "Concrete Stress Distribution in Ultimate Strength Design," *ACI Journal Proceedings*, 52(12), 455-480.

Hughes, B.P. and Fattuhi, N. I. (1975), "Fiber Bond Strengths in Cement and Concrete", *Magazine of Concrete Research*, 27(92), 161-166.

Johnston, C.D. (1982), "Definition and Measurement of Flexural Toughness Parameters for Fiber Reinforced Concrete," *Cement and Concrete Aggregates*, 4(2), 53-60.

Johnston, C.D. (1974), "Steel Fiber Reinforced Mortar and Concrete: A Review of Mechanical Properties", ACI SP-44, American Concrete Institution, 127-142.

JSCE-G 552-1999 (2005), "Test Method for Bending Strength and Bending Toughness of Steel Fiber Reinforced Concrete," Standard Specification for Concrete Structures, Test Methods and Specifications, *JSCE*, 362 pp.

JSCE-G 553-1999 (2005),"Test Method for Shear Strength of Steel Fiber Reinforced concrete," Standard Specifications for Concrete Structures, Test Methods and Specifications," *JSCE*, 362 pp.

Kang, T.H.-K. and Kim, W. (2009), "Lightweight Concrete Beams with Steel Fiber Shear Reinforcement," Presented at: Research in Progress Session, ACI Fall Convention, New Orleans, LA.

Kang, T.H.-K. and Kim, W. (2010), "Shear Strength of Steel Fiber-Reinforced Lightweight Concrete Beams," Proceedings of Fracture Mechanics of Concrete and Concrete Structures Conference, Framcos-7, Jeju, South Korea, 1386-1392.

Kani, G. N. J., (1967), "How Safe Are Our Large Concrete Beams?," *ACI Journal Proceedings*, 64(3), 128-141.

Kani, M. W., Huggins, M. W., and Wittkopp, R. R. (1979), "Kani on Shear in Reinforced Concrete," University of Toronto Press, Toronto, Canada, 225 pp.

Khaloo, A. R. and Kim, N. (1997), "Influence of Concrete and Fiber Characteristics on Behavior of Steel Fiber Reinforced Concrete under Direct Shear," *ACI Materials Journal*, 94(6), 592-601.

Khuntia, M., Stojadinovic, B., and Goel, S. C. (1999), "Shear Strength of Normal and High-Strength Fiber Reinforced Concrete Beams without Stirrups," *ACI Structural Journal*, 96(2), 282-289.

Kosmatka, S., Kerkhoff, B., and Panarese, W. (2002, Rev. 2008), "Design and Control of Concrete Mixture", 14th Edition, Portland Cement Association, 372 pp.

Kwak, Y.-K., Eberhard, M.O., Kim, W.-S., and Kim, J. (2002), "Shear Strength of Steel Fiber-Reinforced Concrete Beams Without Stirrups,"*ACI Structural Journal*, 99(4), 530-538.

Li, V. C., Ward, R., and Hamza, A. M. (1992), "Steel and Synthetic Fibers as Shear Reinforcement," *ACI Materials Journal*, 89(5), 499-508.

Lim, T.Y., Paramasivam, P., and Lee, S.L. (1987), "Shear and Moment Capacity of Reinforced Steel-Fiber-Concrete Beams," *Magazine of Concrete Research*, 39(140), 148-160.

Lubell, A., Sherwood, T., Bentz, E. C., and Collins, M. P. (2004), "Safe Shear Design of Large, Wide Beams," *Concrete International*, 26(1), 66-78.

MacGregor, J. G., Saatcioglu, M., Cumming, S., and McGrath, R. J. (2006), "Chapter 1- General Concrete Design Information," Concrete Design Handbook, Part II, Third Edition, Cement Association of Canada, 76 pp.

Malhotra, V. M. and Zoldners, N. G. (1969), "Some Field Experience in the Use of an Accelerated Method of Estimating 28-day Strength of Concrete," *ACI Journal Proceedings*, 66(11), 894-897.

Mansur, M.A., Ong, K.C.G., and Paramasivam, P. (1986), "Shear Strength of Fibrous Concrete Beams Without Stirrups," *Journal of Structural Engineering*, 112(9), 2066-2079.

Minelli, F. and Plizzari, G.A. (2006), "Steel Fibers as Shear Reinforcement for Beams," *Proceedings of the 2nd International fib congress,* Naples, Italy, ID: 3-60, 12 pp.

Mirsayah, A. A. and Banthia, N. (2002), "Shear Strength of Steel Fiber-Reinforced Concrete," *ACI Materials Journal*, 99(5), 473-479.

Naaman, A. E. and Najm, H. (1991), "Bond-Slip Mechanisms of Steel Fibers in Concrete, *ACI Materials Journal*, 88(2), 135-145.

Narayanan, R. and Darwish, I. Y. S. (1987), "Use of Steel Fibers as Shear Reinforcement," *ACI Structural Journal*, 84(3), 216-227.

Noghabai, K. (2000), "Beams of Fibrous Concrete in Shear and Bending: Experiment and Model," *Journal of Structural Engineering*, 126(2), 243-251.

Parra-Montesinos, G. (2006), "Shear Strength of Beams with Deformed Steel Fibers," *Concrete International*, 28(11), 57-66.

Reineck, K. H., Kuchma, D. A., Kim, K. S., and Marx, S. (2003), "Shear Database for Reinforced Concrete Members without Shear Reinforcement," *ACI Structural Journal*, 100 (2), 240-249.

Rosenbusch, J. and Teutsch, M. (2002), "Trial Beams in Shear," Brite/Euram Project 97-4163, Final Report, Sub Task 4.2, Technical University of Braunschweig, Germany.

Schantz, B. A. (1993), "The Effect of Shear Stress on Full Scale Steel Fiber Reinforced Concrete Beams," M.Sc Thesis, Clarkson University, Potsdam, NY.

Sharma, A. K. (1986), "Shear Strength of Steel Fiber Reinforced Concrete Beams," *ACI Journal Proceedings*, 83(4), 624-628.

Sherwood, E. G., Bentz, E. C., and Collins, M. P. (2007), "Effect of Aggregate Size on Beam-Shear Strength of Thick Slabs," *ACI Structural Journal*, 104 (2), 180-190.

Shioya, T., Iguro, M., Nojiri, Y., Akiyama, H., and Okada, T. (1989), "Shear Strength of Large Reinforced Concrete Beams," Fracture Mechanics: Application to Concrete, ACI SP-118, American Concrete Institution, 259-279.

Soroushian, P. and Bayasi, Z. (1991), "Fiber Type Effects on the Performance of Steel Fiber Reinforced Concrete," *ACI Materials Journal*, 88(2), 129-134.

Susetyo, J., Gauvreau, P. & Vecchio, F. J. (2011), "Effectiveness of Steel Fiber as Minimum Shear Reinforcement," *ACI Structural Journal*, 108 (4), 488-496.

Swamy, R. N. and Al-Ta'an, S. A. (1981), "Deformation and Ultimate Strength in Flexure of Reinforced Concrete Beams Made with Steel Fiber Concrete," *ACI Journal Proceedings*, 78(5), 395-405.

Swamy, R. N., Jones, R. & Chiam, A.T.P. (1993), "Influence of Steel Fibers on the Shear Resistance of Lightweight Concrete I-Beams," *ACI Structural Journal*, 90 (1), 103-114.

Taerwe, L.R. (1992), "Influence of steel fibers on strain-softening of high strength concrete", *ACI Materials Journal*, 88 (6), 54-60.

Valle, M. and Buyukozturk, O. (1993), "Behaviour of Fiber Reinforced High-Strength Concrete under Direct Shear", *ACI Materials Journal*, 90(2), 122-133.

Vecchio, F. J. and Collins, M. P. (1986), "The Modified Compression-Field Theory for Reinforced Concrete Elements Subjected to Shear," *ACI Journal Proceedings*, 83(2), 219-231.

Wafa, F. F. and Ashour, S. A. (1992), "Mechanical Properties of High-Strength Fiber Reinforced Concrete," *ACI Materials Journal*, 89(5), 449-455.

Walraven, J. C. (1981), "Fundamental Analysis of Aggregate Interlock," *ASCE Journal of Structural Engineering*, 107(11), 2245-2270.

Xu, S. and Reinhardt, H.W. (2005), "Shear Fracture on the Basis of Fracture Mechanics," *Otto-Graf-Journal*, Vol. 16, 21-78.

Yakoub, H. E. (2011), "Shear Stress Prediction: Steel Fiber-Reinforced Concrete Beams without Stirrups,"*ACI Structural Journal*, 108(3), 304-314.

Zhang, MH, Li, L. and Paramasivam, P. (2004), "Flexural Toughness and Impact Resistance of Steel Fiber Reinforced Lightweight Concrete", *Magazine of Concrete Research*, 56(5), 251-262.

Zsutty, T. C. (1968), "Beam Shear Strength Prediction by Analysis of Existing Data,"*ACI Journal Proceedings*, 65(11), 943-951.

Appendix A: Material Tests Details

A.1 Normal Strength Concrete (NSC)

A.1.1 Compression

Table A-1: Mechanical Response in Compression for NSC

Normal Strength Mix		**V_f=0%**			**V_f=0.5%**			**V_f=1%**		
Cylinder Specimen		**C1***	**C11**	**C111**	**C2**	**C22**	**C222**	**C3**	**C33**	**C333**
Compressive Strength f'_c	**f'_c (MPa)**	25	44	46	44	44	45	47	42	44
	Average(MPa)	45			44			44		
	COV (%)	3.1			1.3			5.7		
Modulus of Elasticity E_c	**E_c(10^3 MPa)**	12.4	22.0	27.4	22.6	27.2	24.9	22.4	24.1	25.8
	Average (10^3 MPa)	24.7			24.9			24.1		
	COV (%)	15.3			9.2			7.2		
Compressive Toughness Factor T_c	**T_c (MPa)**	0.06	0.11	0.13	0.21	0.20	0.20	0.29	0.24	0.25
	Average(MPa)	0.12			0.20			0.26		
	COV (%)	8.3			3.2			8.7		

* This specimen was neglected due to the large difference in the results between this specimen and the other two specimens from the same mix.

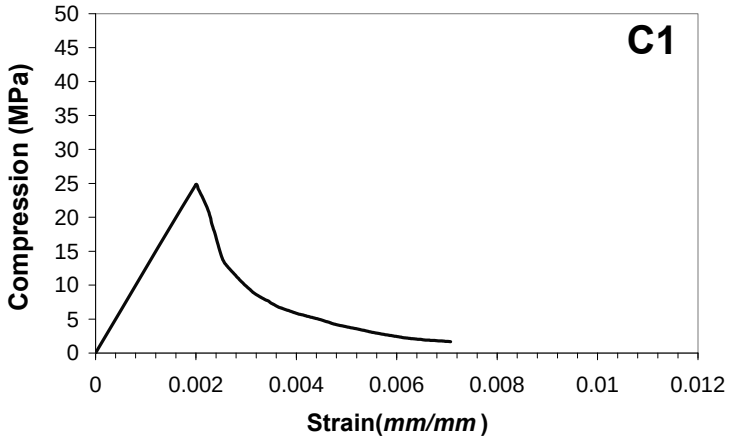

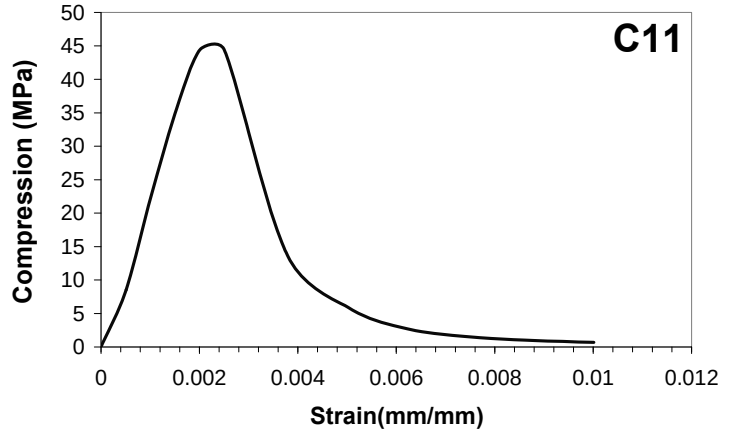

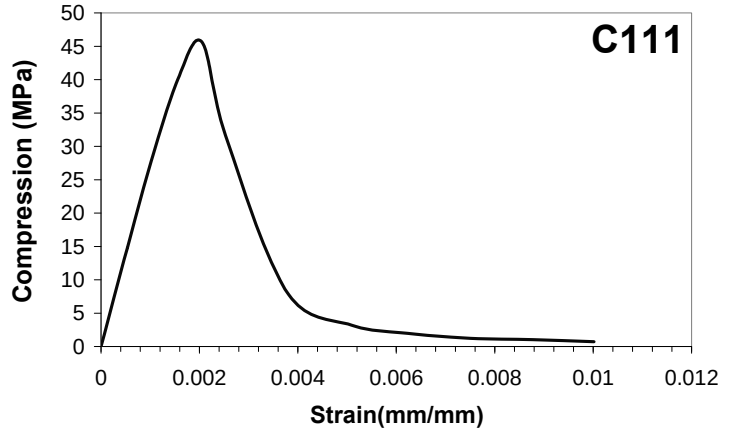

Figure A-1: Compressive Stress-Strain Response for Normal Strength Concrete Cylinders with V_f=0%.

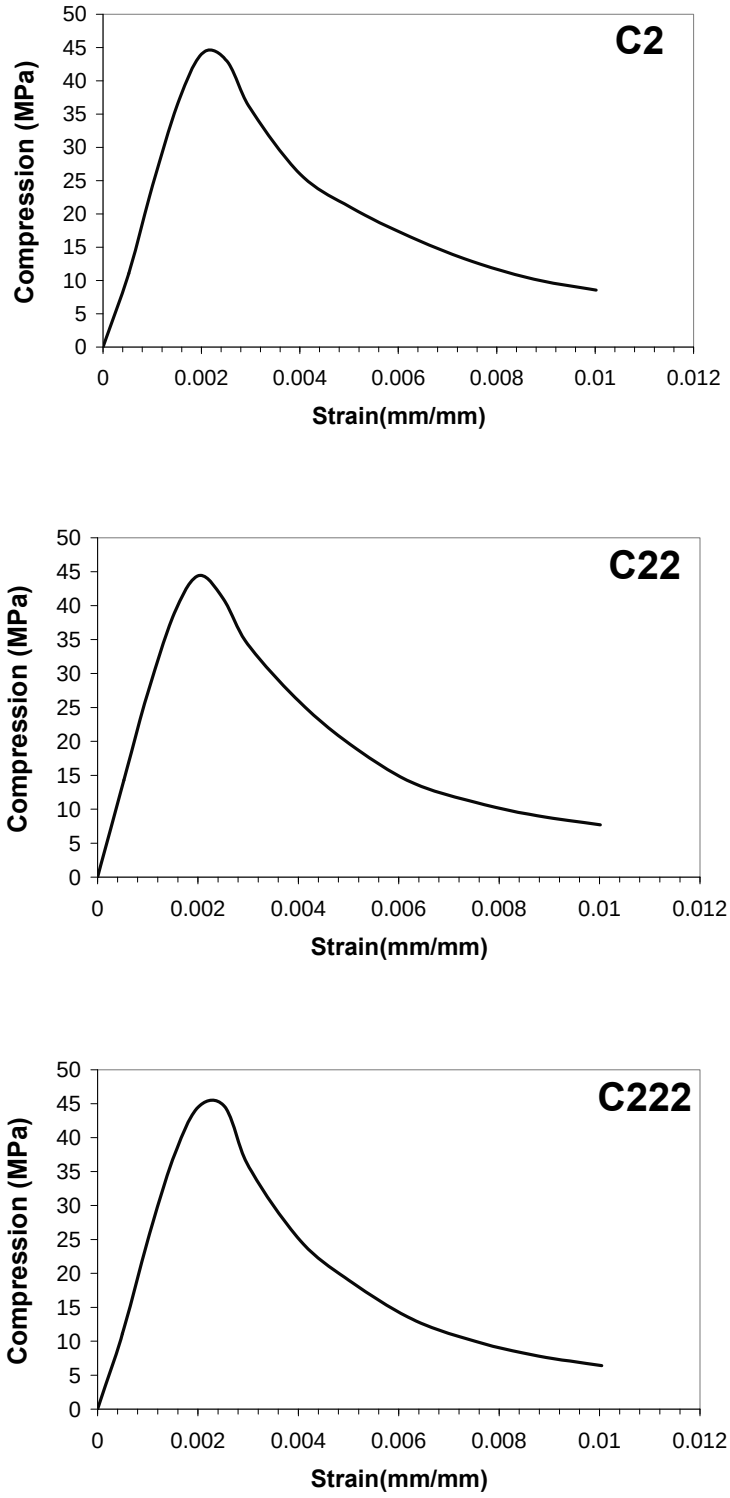

Figure A-2: Compressive Stress-Strain Response for Normal Strength Concrete Cylinders with V_f=0.5%.

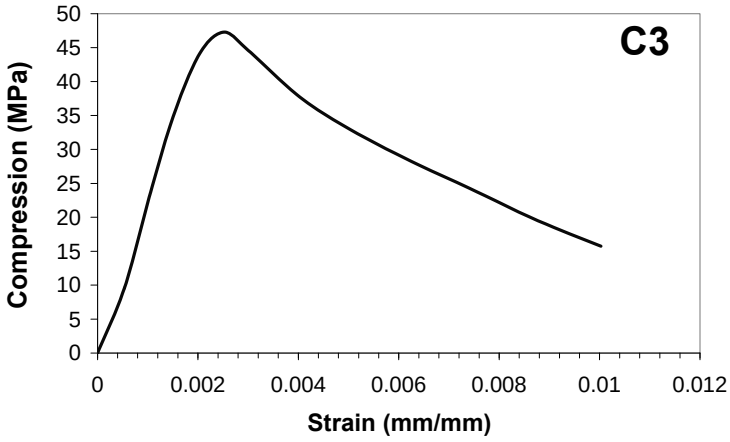

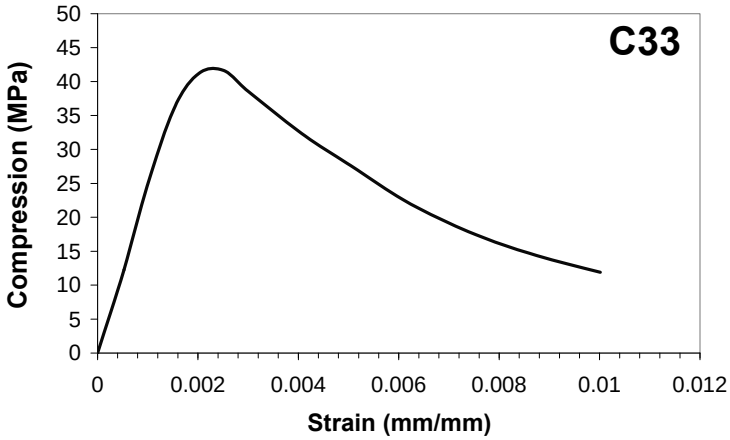

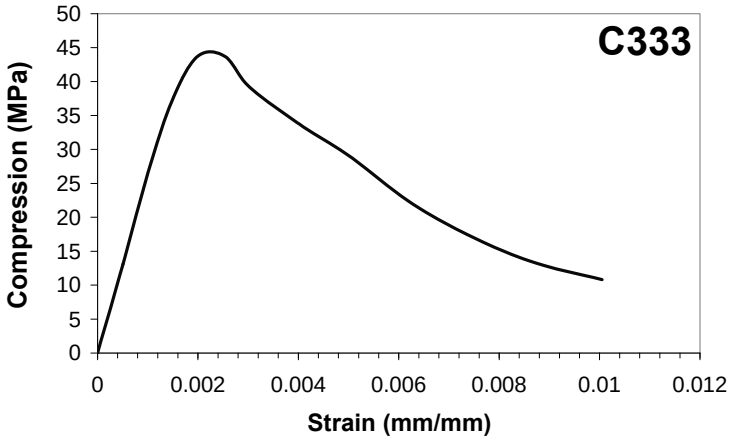

Figure A-3: Compressive Stress-Strain Response for Normal Strength Concrete Cylinders with V_f=1%.

A.1.2 Flexure

Table A-2: Mechanical Response in Flexure for NSC

Normal Strength Mix		**V_f=0%**			**V_f=0.5%**			**V_f=1%**		
Prism Specimen		**A1**	**A11**	**A111**	**A2**	**A22**	**A222**	**A3**	**A33**	**A333**
Modulus of Rupture f_r	**f_r (MPa)**	3.48	3.86	3.26	4.30	3.76	4.48	5.54	5.03	5.24
	Average(MPa)	3.53			4.18			5.27		
	COV (%)	8.6			9.0			4.9		
Flexural Toughness Factor T_f	**T_f (MPa)**	0.17	0.18	0.15	3.81	3.42	4.09	4.97	4.64	4.93
	Average(MPa)	0.17			3.78			4.84		
	COV (%)	9.1			9.0			3.7		

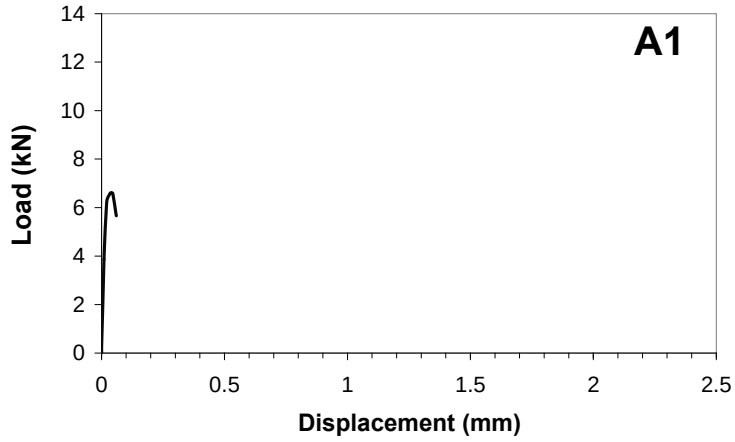

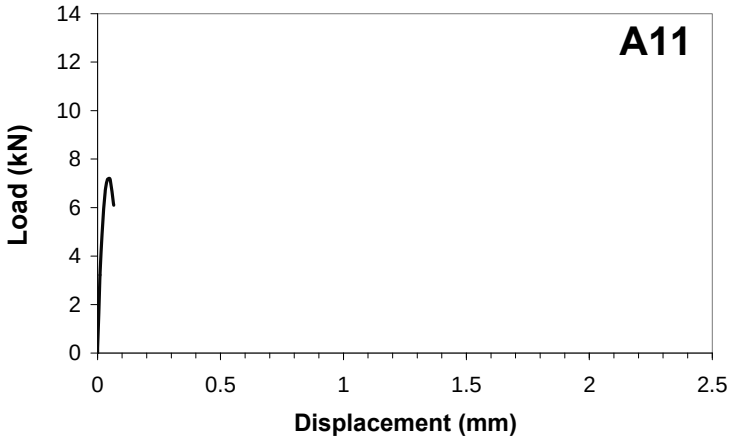

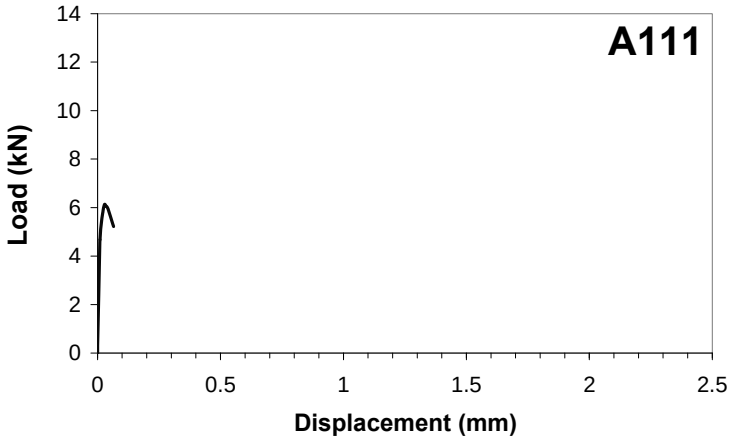

Figure A-4: Flexural Response for Normal Strength Concrete Prisms with V_f=0%.

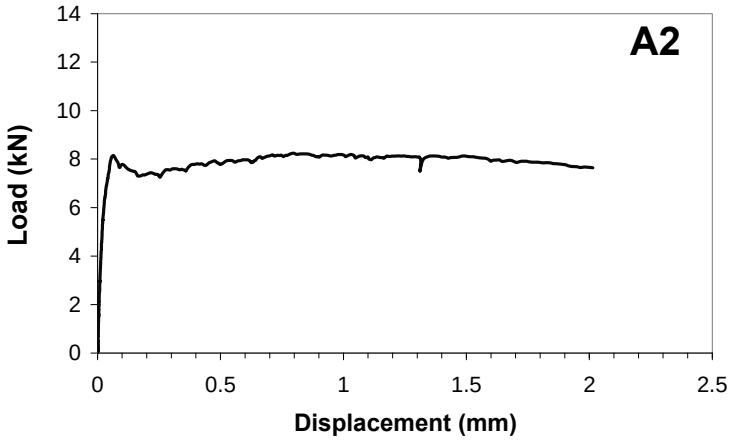

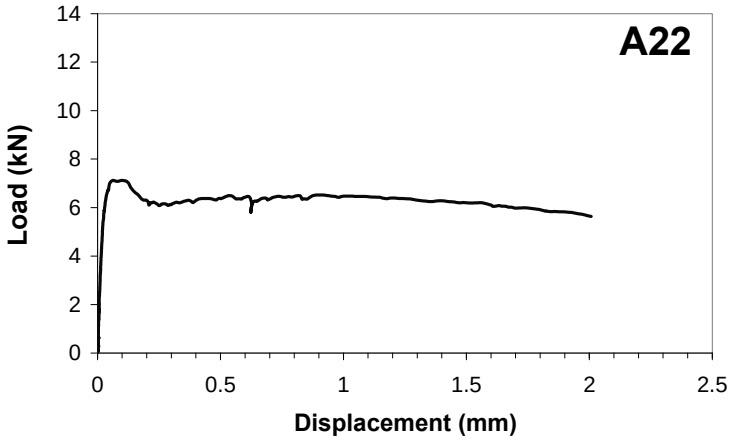

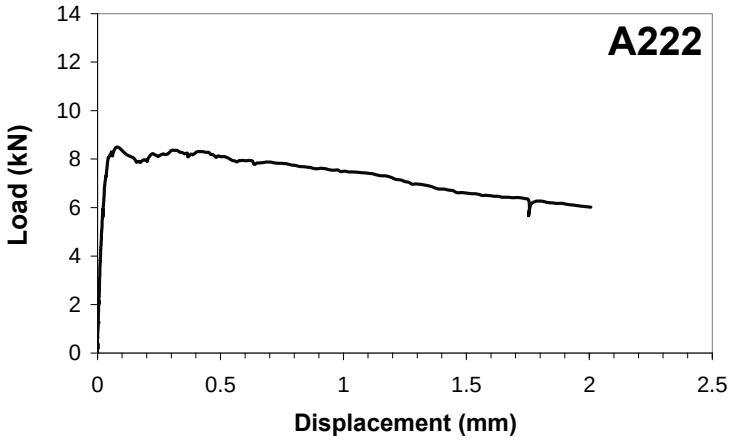

Figure A-5: Flexural Response for Normal Strength Concrete Prisms with V_f=0.5%.

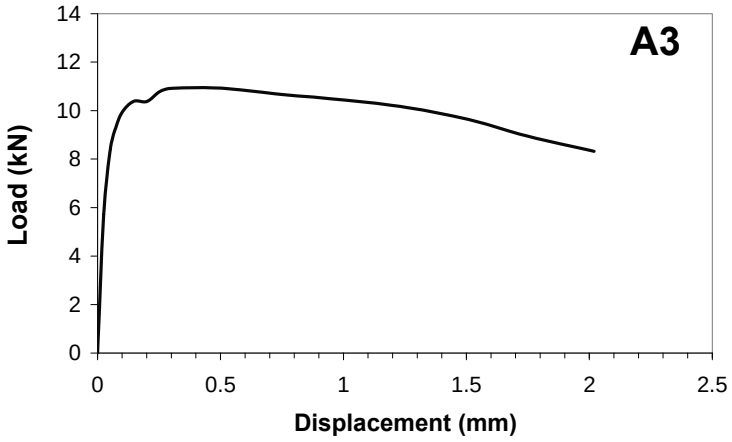

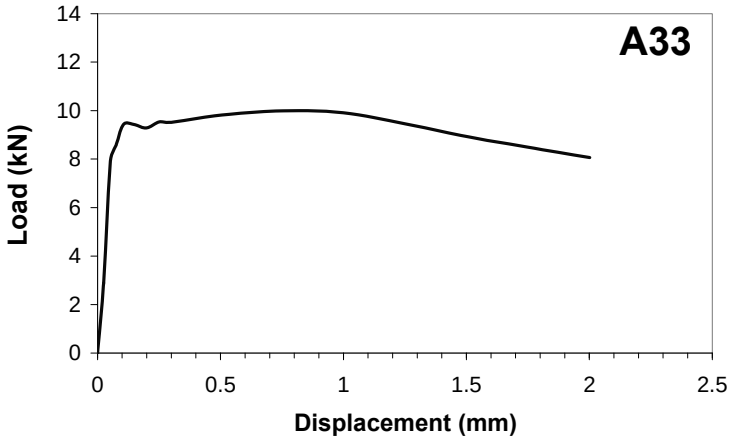

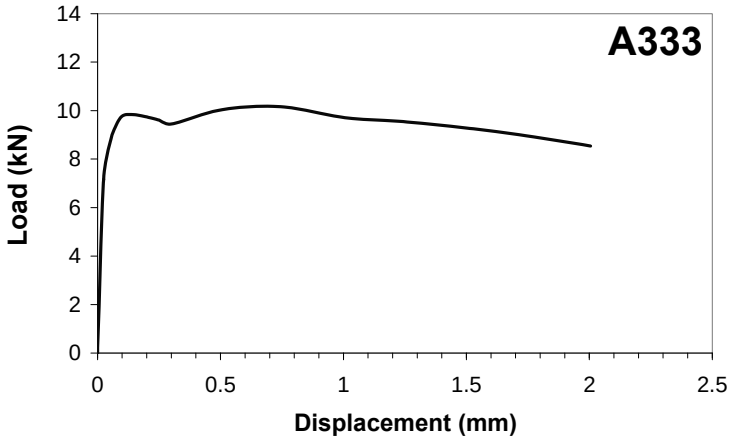

Figure A-6: Flexural Response for Normal Strength Concrete Prisms with V_f=1%.

A.1.3 Direct Shear

Table A-3: Mechanical Response in Direct Shear for NSC

Normal Strength Mix		**V_f=0%**			**V_f=0.5%**			**V_f=1%**		
Prism Specimen		**B1**	**B11**	**B111**	**B2**	**B22**	**B222**	**B3**	**B33**	**B333**
Shear Strength f_v	**f_v (MPa)**	3.82	2.59	2.96	6.42	5.45	4.85	9.49	7.43	9.39
	Average(MPa)	2.76			5.57			8.8		
	COV (%)	20.3			7.6			0.6		
Shear Toughness Factor(m=25) $T_{s,25}$	**T_s (MPa)**	1.24	0.84	0.85	5.61	5.18	5.08	12.05	8.51	11.51
	Average(MPa)	0.98			5.29			10.69		
	COV (%)	23.3			5.3			17.8		

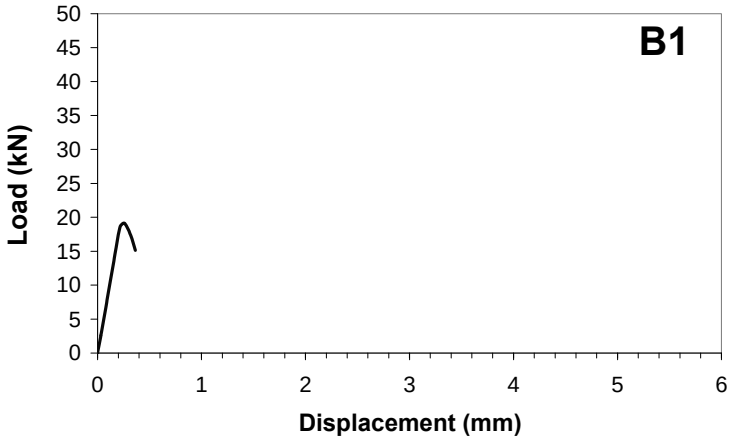

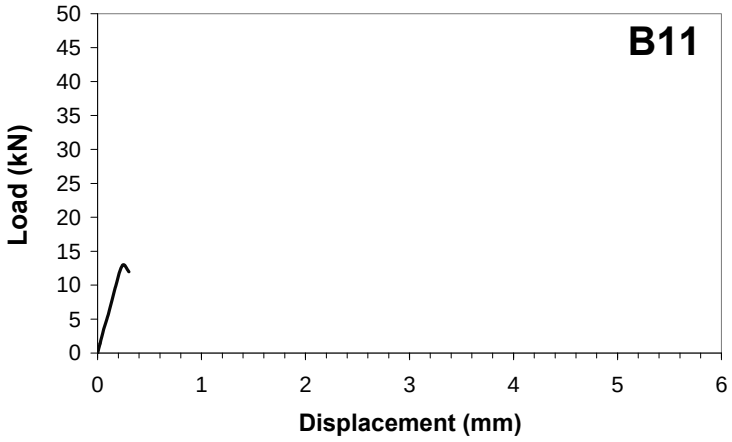

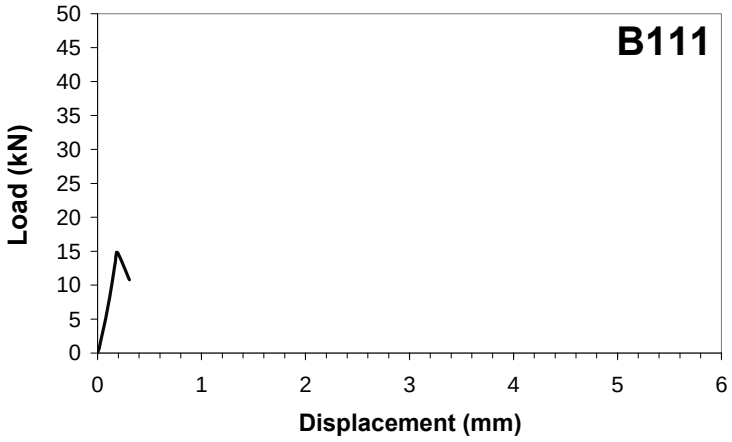

Figure A-7: Shear Test Results for Normal Strength Concrete with V_f=0%.

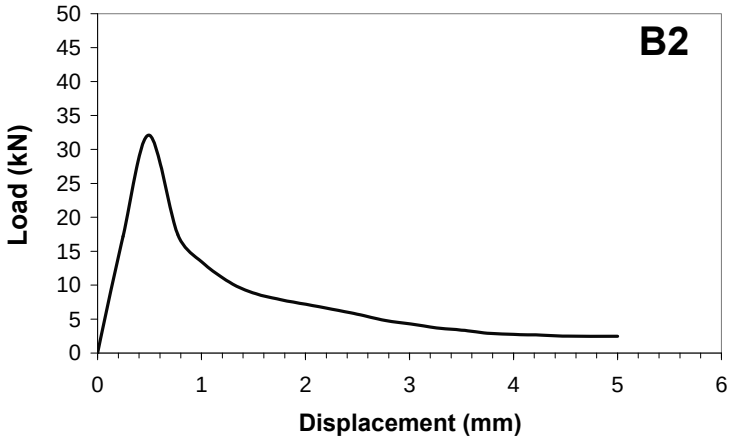

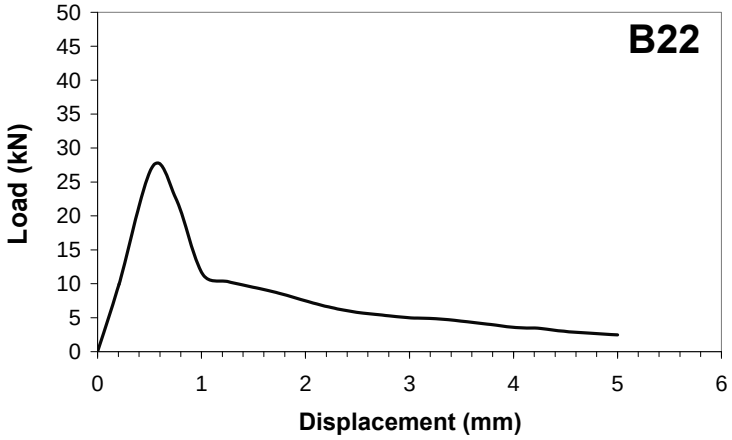

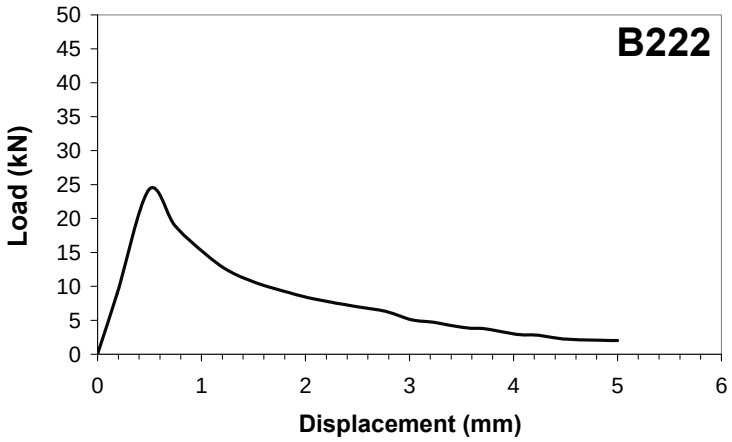

Figure A-8: Shear Test Results for Normal Strength Concrete with V_f=0.5%.

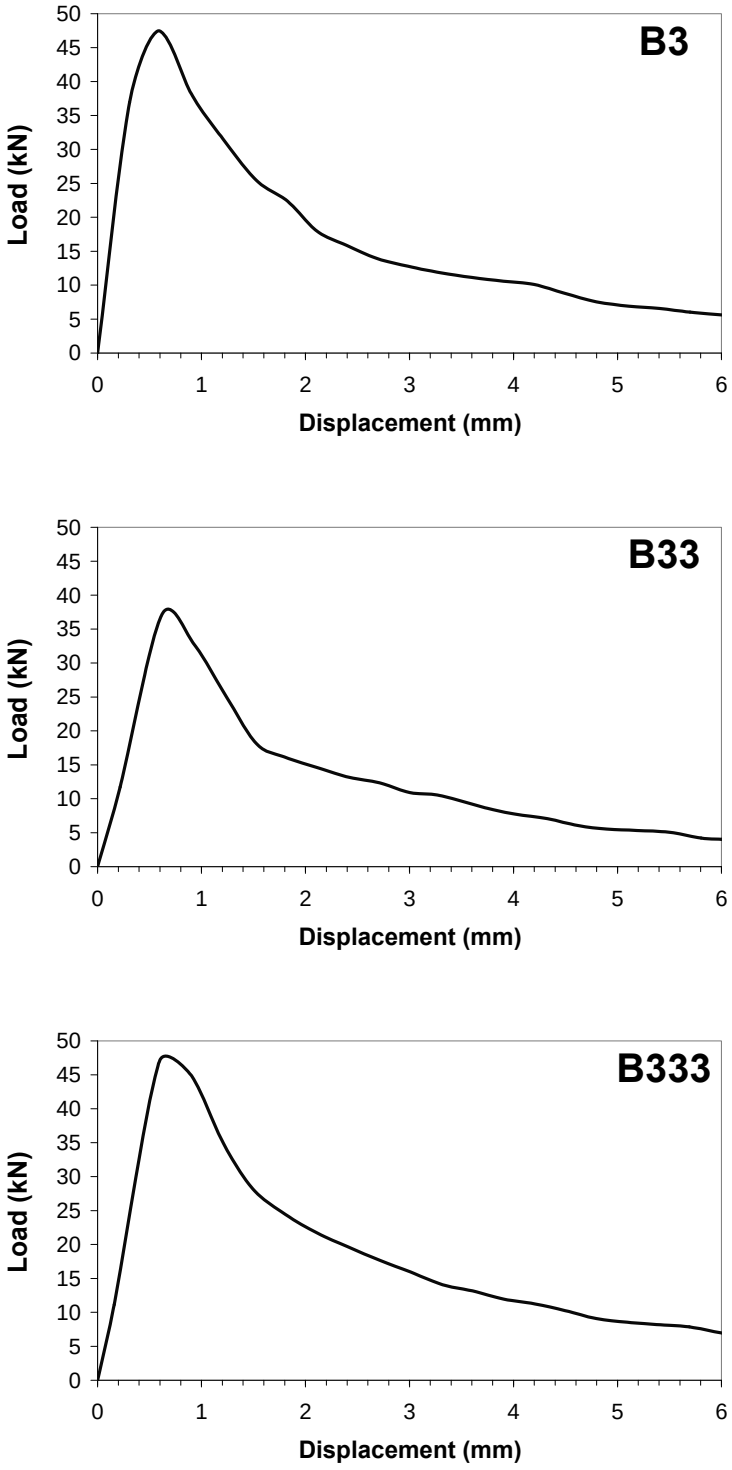

Figure A-9: Shear Test Results for Normal Strength Concrete with V_f=1%.

A.2 High Strength Concrete (HSC)

A.2.1 Compression

Table A-4: Mechanical Response in Compression for HSC

High Strength Mix		**V_f=0%**			**V_f=0.5%**			**V_f=1%**		
Cylinder Specimen		**C4**	**C44**	**C444**	**C5**	**C55**	**C555**	**C6**	**C66**	**C666**
Compressive Strength f'_c	**f'_c (MPa)**	107	107	104	96	119	96	111	111	101
	Average(MPa)	106			104			108		
	COV (%)	1.6			12.8			5.4		
Modulus of Elasticity E_c	**E_c(10^3 MPa)**	32.0	32.4	32.6	31.4	31.4	29.8	29.7	32.8	30.1
	Average (10^3 MPa)	32.3			30.8			30.9		
	COV (%)	1.1			2.9			5.3		
Compressive Toughness Factor T_c	**T_c (MPa)**	0.15	0.15	0.15	0.30	0.40	0.30	0.41	0.40	0.32
	Average(MPa)	0.15			0.33			0.38		
	COV (%)	1.4			16.6			13.5		

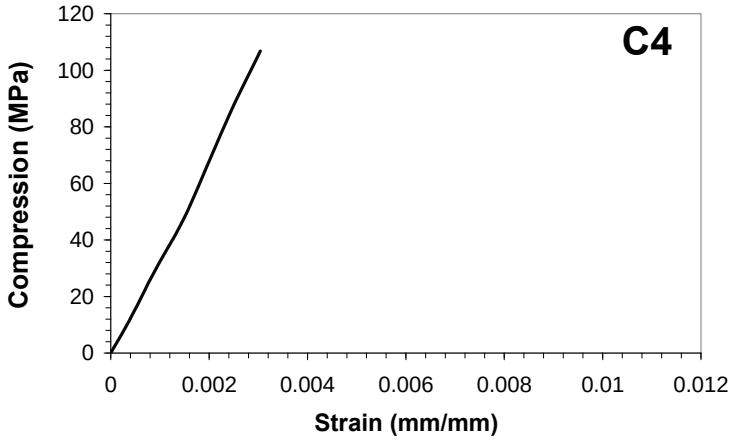

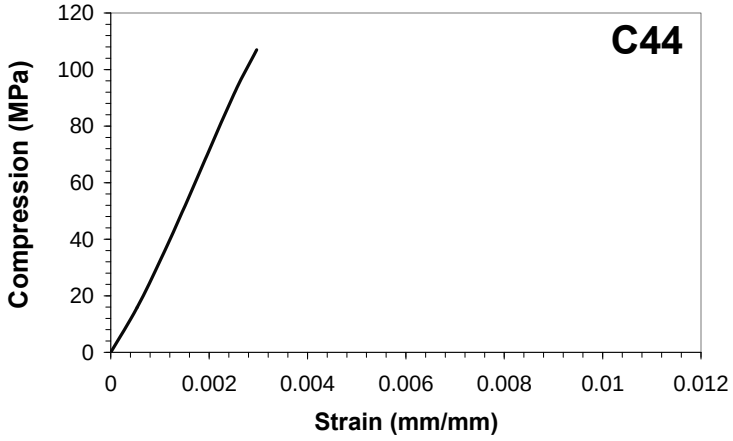

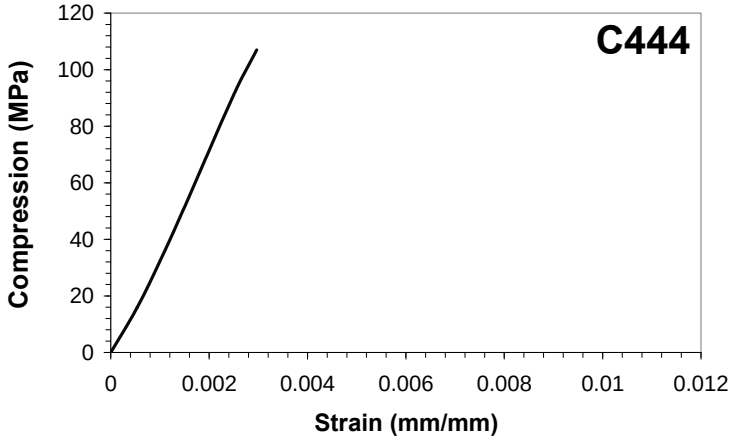

Figure A-10: Compressive Stress-Strain Response for High Strength Concrete Cylinders with V_f=0%.

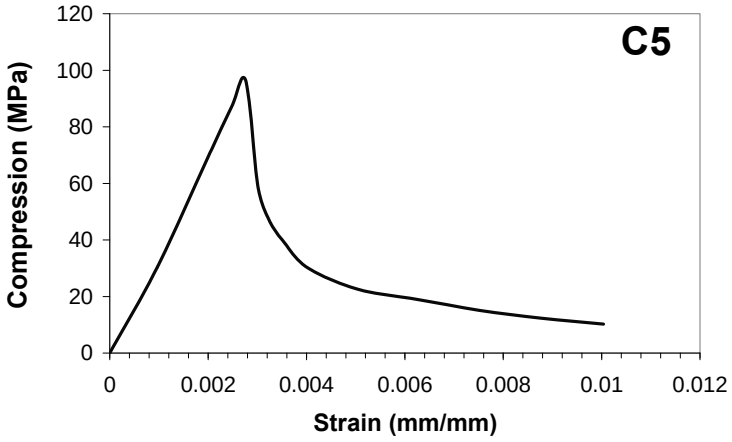

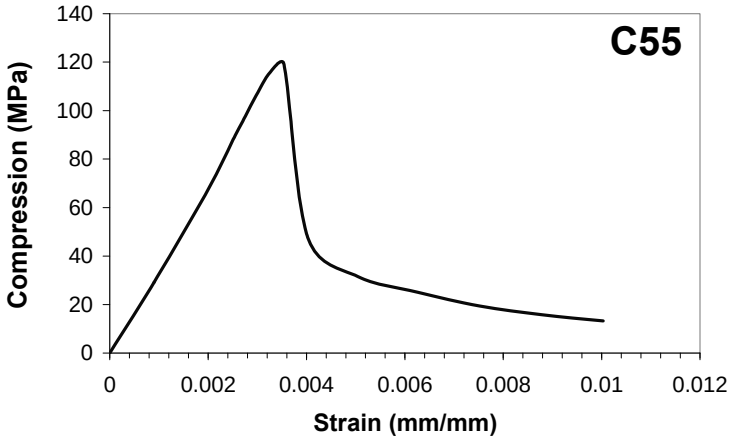

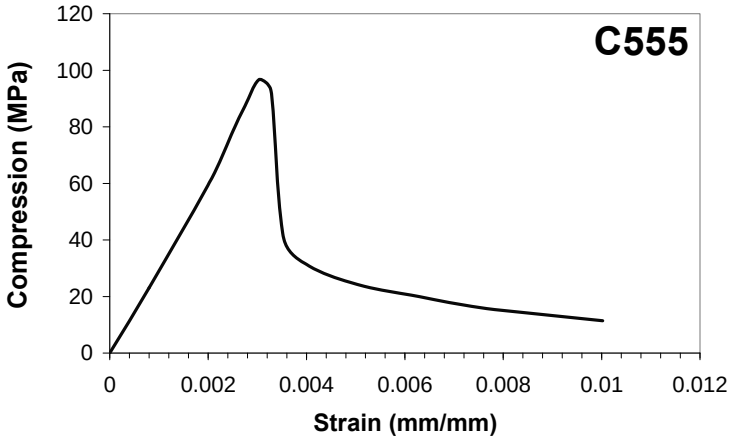

Figure A-11: Compressive Stress-Strain Response for High Strength Concrete Cylinders with V_f=0.5%.

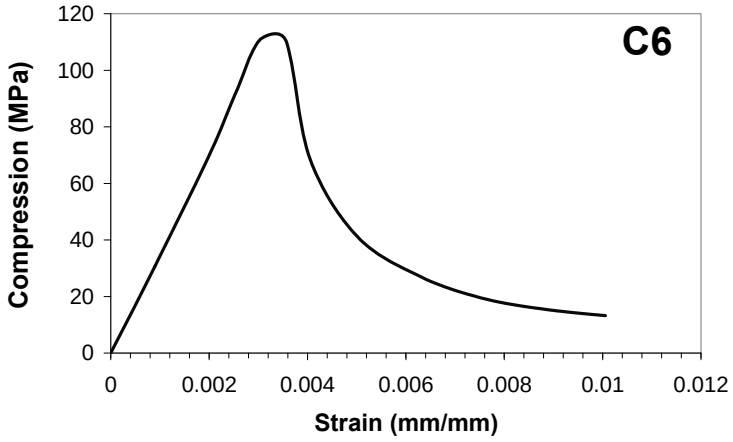

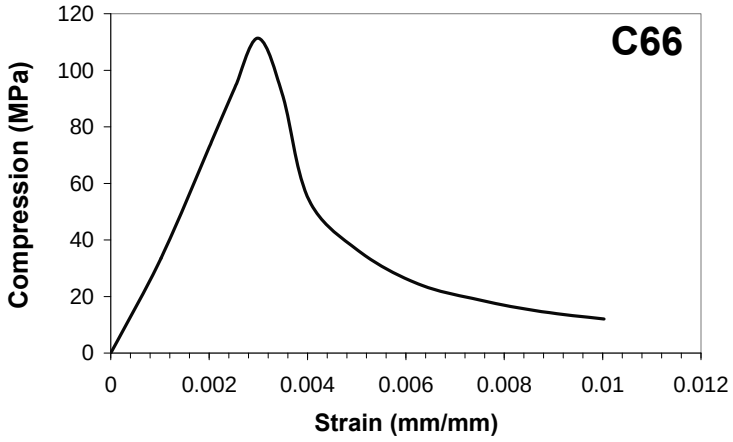

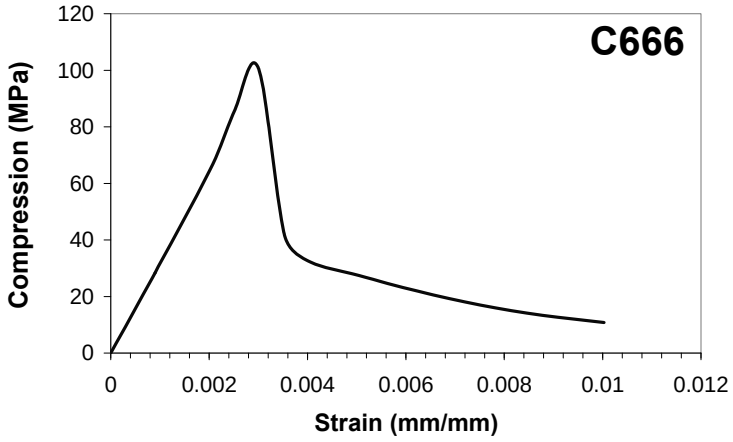

Figure A-12: Compressive Stress-Strain Response for High Strength Concrete Cylinders with V_f=1%.

A.2.2 Flexure

Table A-5: Mechanical Response in Flexure for HSC

High Strength Mix		**V_f=0%**			**V_f=0.5%**			**V_f=1%**		
Prism Specimen		**A4**	**A44**	**A444**	**A5**	**A55**	**A555**	**A6**	**A66**	**A666**
Modulus of Rupture f_r	**f_r (MPa)**	4.72	4.96	5.9	6.24	6.15	6.13	9.25	9.68	9.32
	Average(MPa)	5.19			6.18			9.42		
	COV (%)	12.0			0.9			2.4		
Flexural Toughness Factor T_f	**T_f (MPa)**	0.15	0.12	0.10	3.33	4.90	3.71	7.78	8.69	7.79
	Average(MPa)	0.12			3.98			8.01		
	COV (%)	17.2			20.7			6.3		

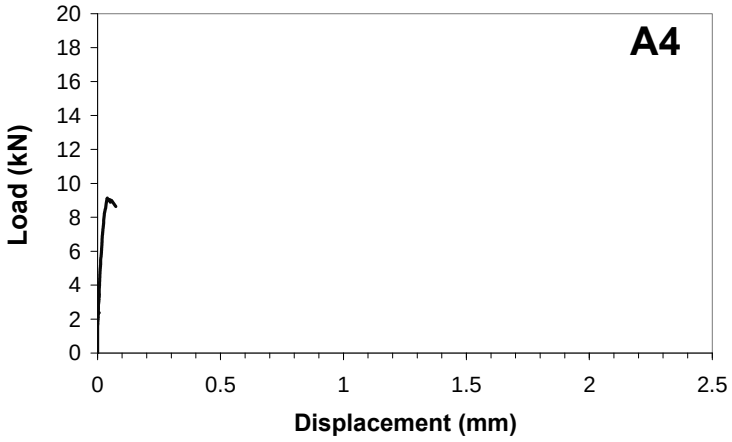

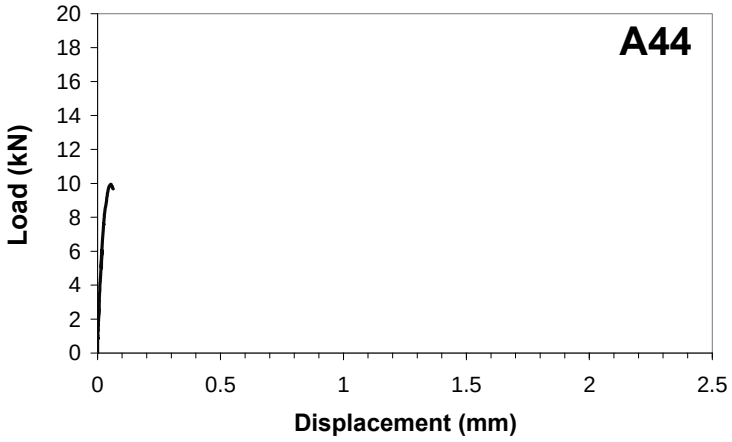

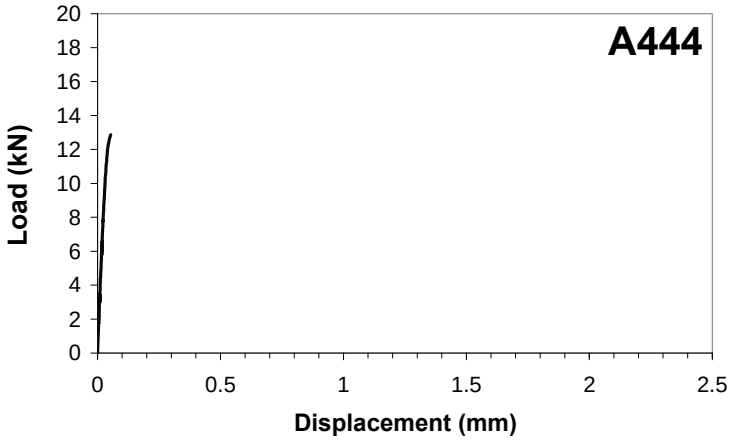

Figure A-13: Flexural Response for High Strength Concrete Prisms with V_f=0%.

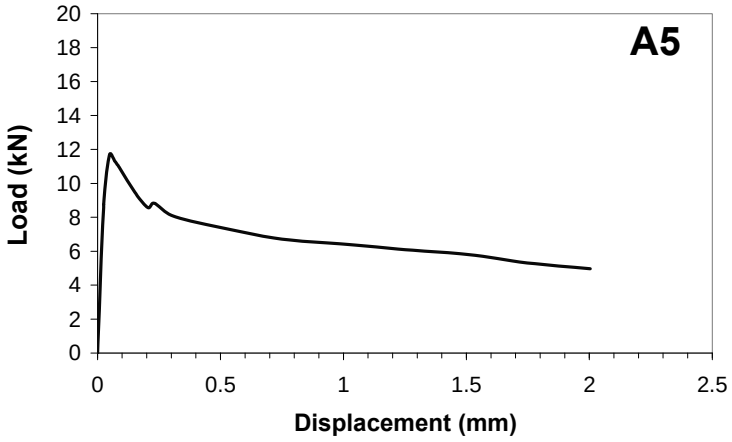

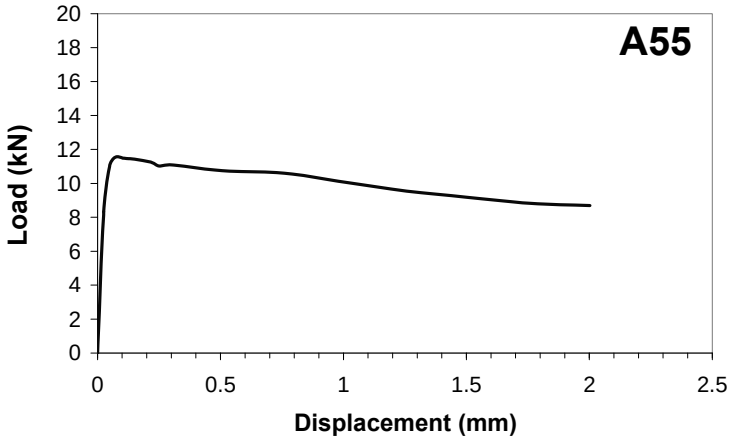

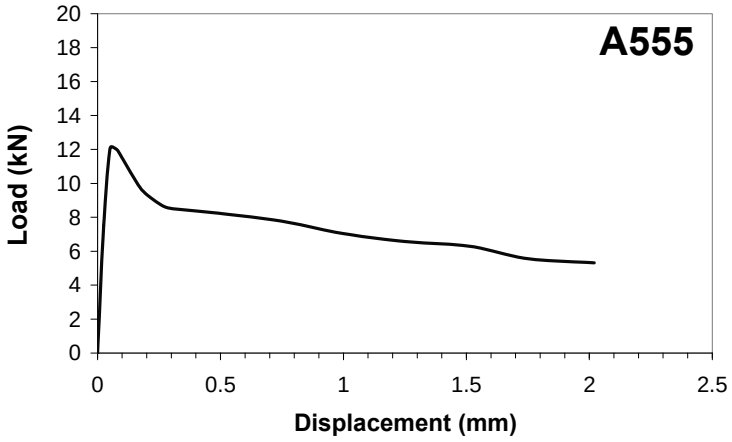

Figure A-14: Flexural Response for High Strength Concrete Prisms with V_f=0.5%.

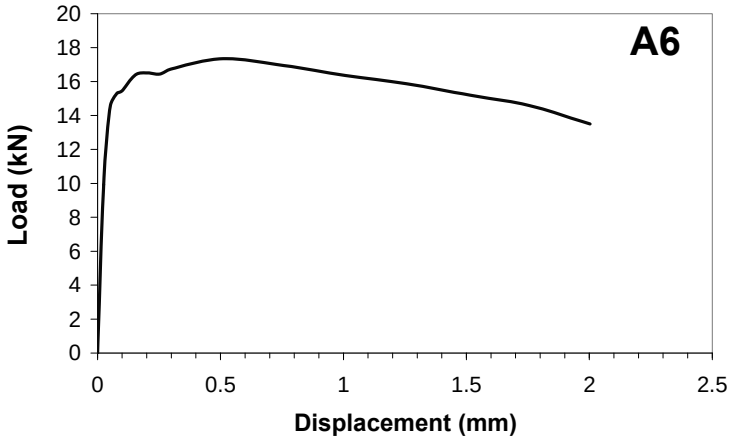

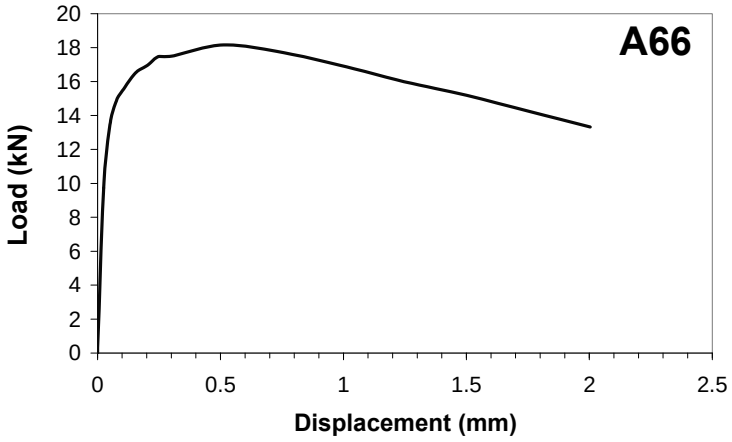

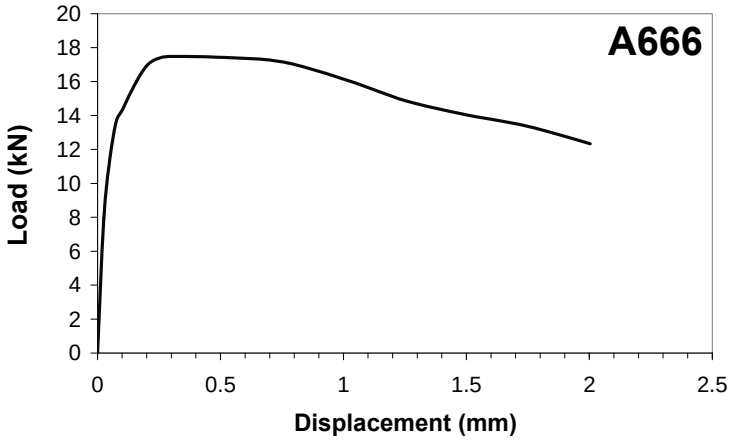

Figure A-15: Flexural Response for High Strength Concrete Prisms with V_f=1%.

A.2.3 Direct Shear

Table A-6: Mechanical Response in Direct Shear for HSC

High Strength Mix		**V_f=0%**			**V_f=0.5%**			**V_f=1%**		
Prism Specimen		**B4**	**B44***	**B444**	**B5**	**B55**	**B555**	**B6**	**B66**	**B666**
Shear Strength f_v	**f_v (MPa)**	3.35	1.52	3.66	7.91	10.05	7.28	11.39	9.82	13.52
	Average(MPa)	3.50			8.41			11.58		
	COV (%)	6.2			17.3			16.0		
Shear Toughness Factor(m=25) $T_{s,25}$	**T_s (MPa)**	1.70	0.92	1.76	5.67	6.98	5.49	10.65	9.15	10.84
	Average(MPa)	1.73			6.04			10.21		
	COV (%)	2.5			13.5			9.0		

***** This specimen was neglected due to the large difference in the results between this specimen and the other two specimens from the same mix.

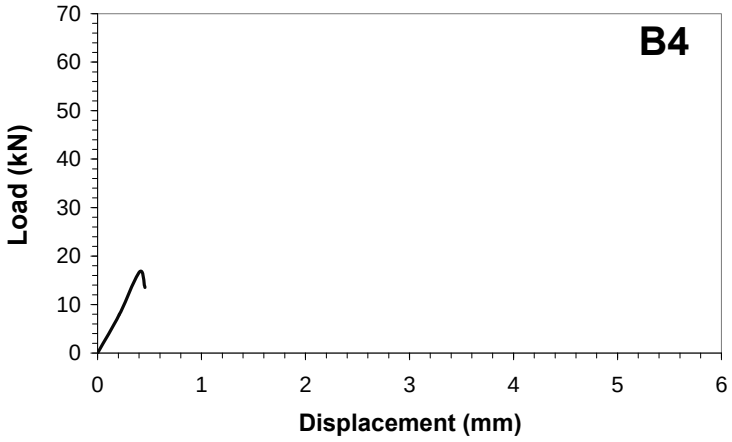

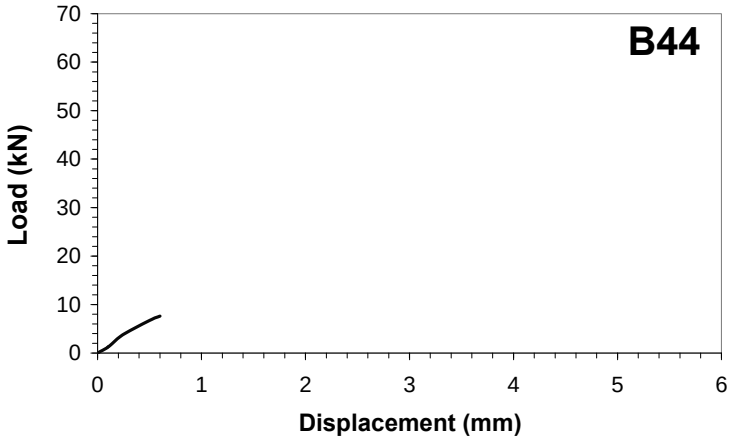

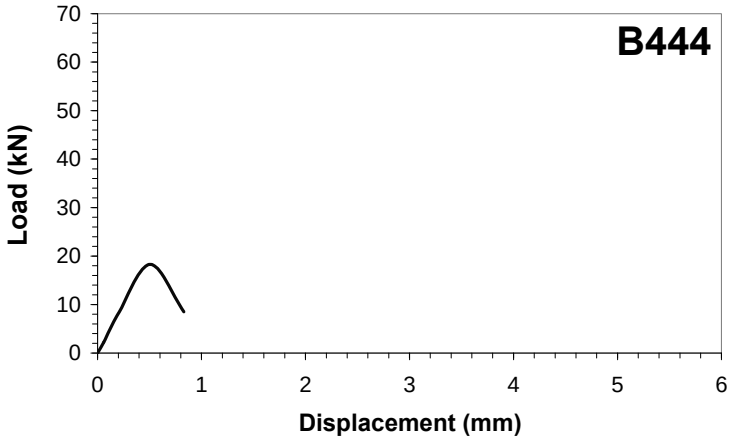

Figure A-16: Shear Test Results for High Strength Concrete with V_f=0%.

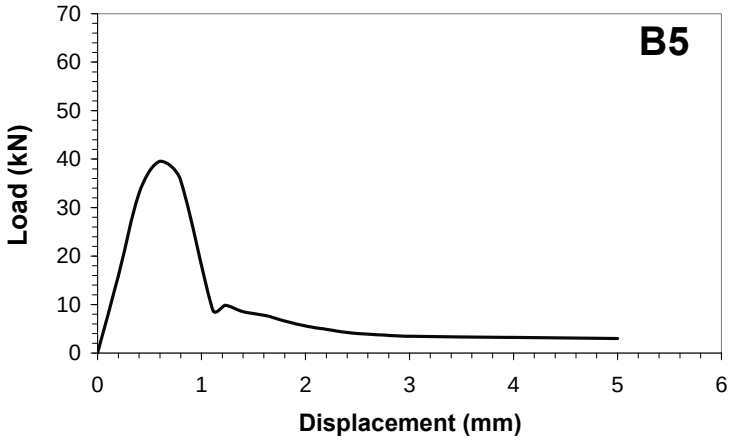

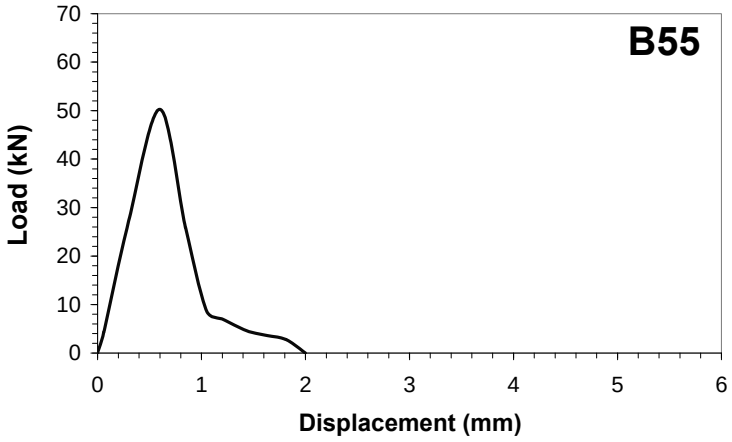

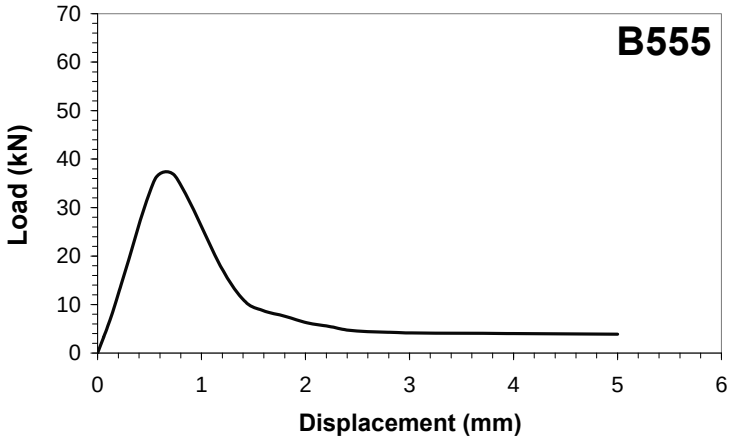

Figure A-17: Shear Test Results for High Strength Concrete with V_f=0.5%.

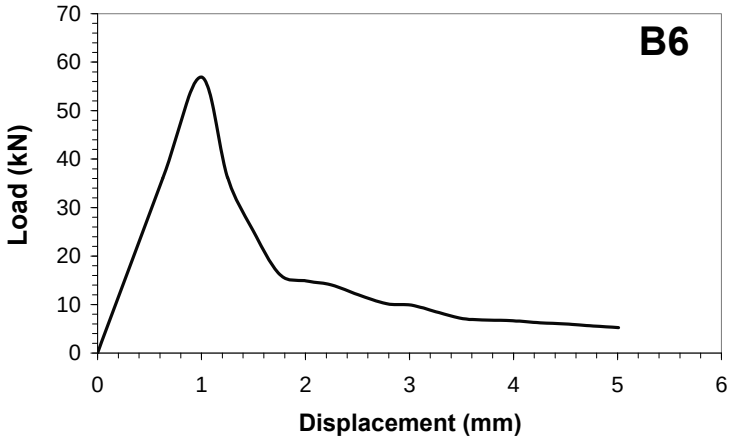

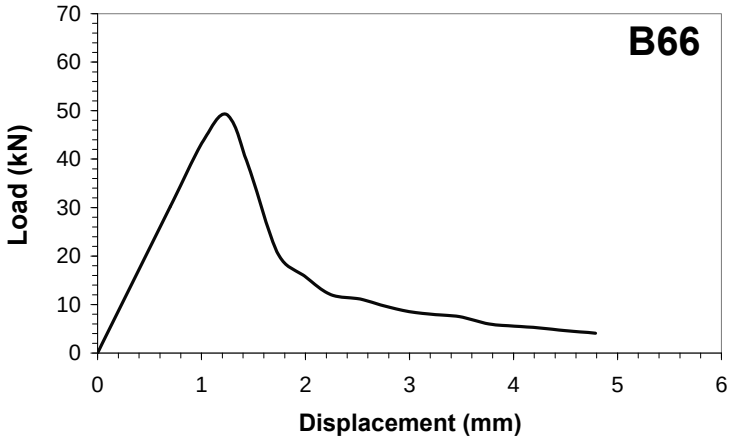

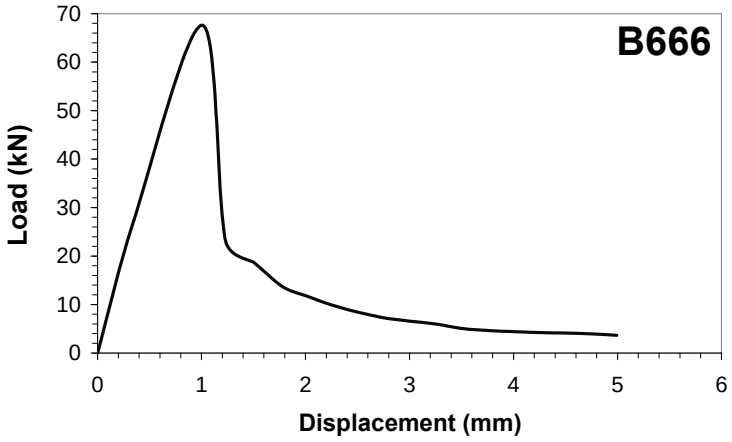

Figure A-18: Shear Test Results for High Strength Concrete with V_f=1%.

A.3 Lightweight Concrete (LWC)

A.3.1 Compression

Table A-7: Mechanical Response in Compression for LWC

Lightweight Mix		**V_f=0%**			**V_f=0.5%**			**V_f=1%**		
Cylinder Specimen		**C7**	**C77**	**C777**	**C8**	**C88**	**C888**	**C9**	**C99**	**C999**
Compressive Strength f'_c	**f'_c (MPa)**	42	41	42	39	41	40	41	40.1	40.2
	Average(MPa)	42			40			40		
	COV (%)	1.4			2.3			1.2		
Modulus of Elasticity E_c	**E_c(10^3 MPa)**	20.1	17.8	19.9	18.5	20.4	18.0	18.3	15.7	18.9
	Average (10^3 MPa)	19.3			18.9			17.7		
	COV (%)	6.7			6.7			9.5		
Compressive Toughness Factor T_c	**T_c (MPa)**	0.10	0.10	0.1	0.17	0.17	0.17	0.21	0.20	0.20
	Average(MPa)	0.10			0.17			0.2		
	COV (%)	3.0			0.3			2.5		

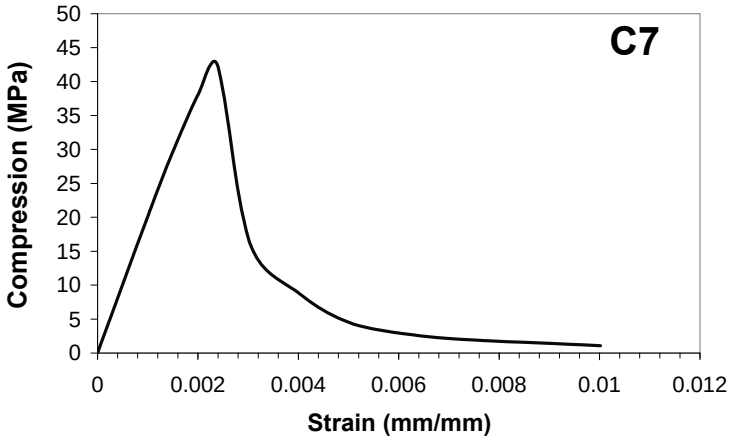

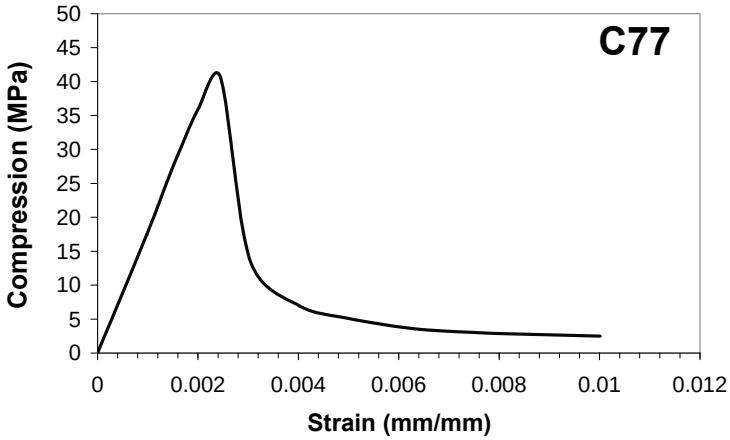

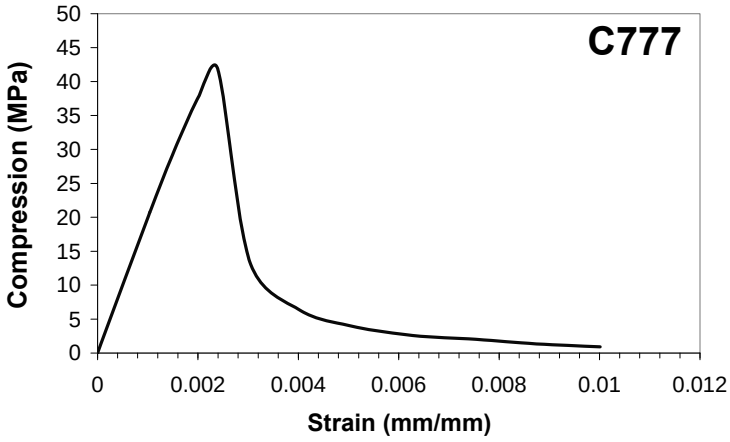

Figure A-19: Compressive Stress-Strain Response for Lightweight Concrete Cylinders with V_f=0%.

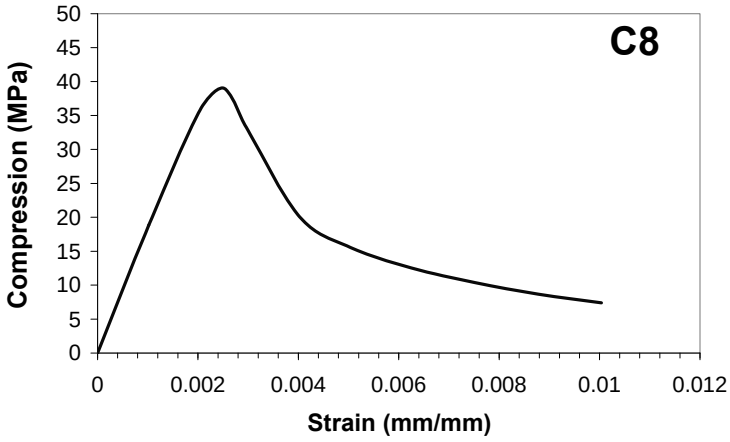

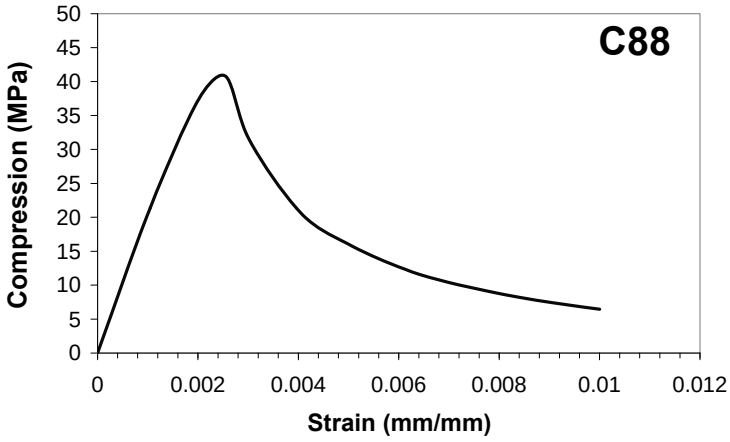

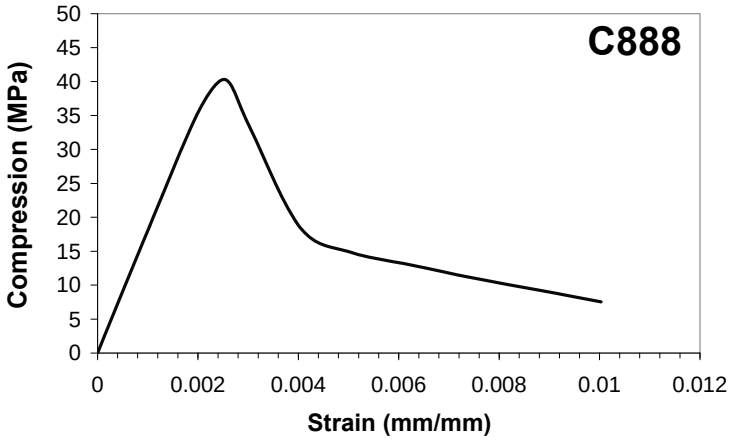

Figure A-20: Compressive Stress-Strain Response for Lightweight Concrete Cylinders with V_f=0.5%.

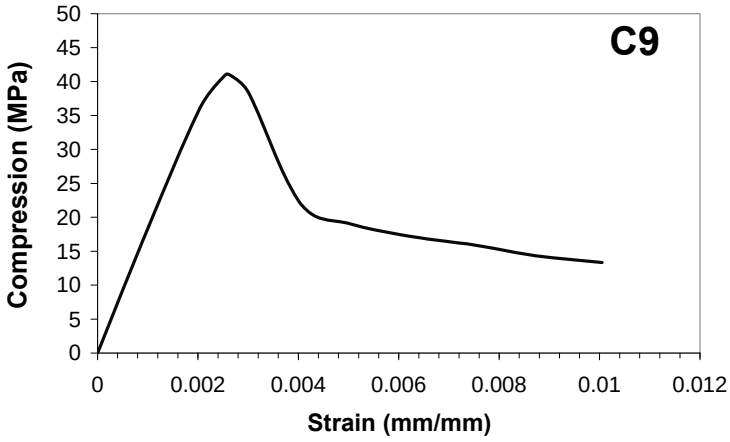

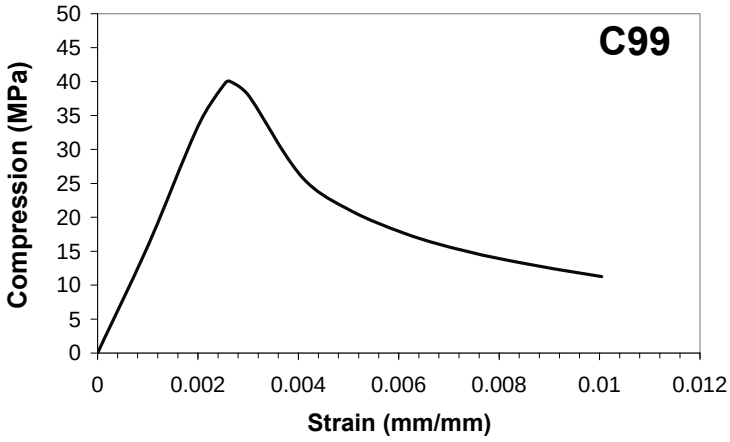

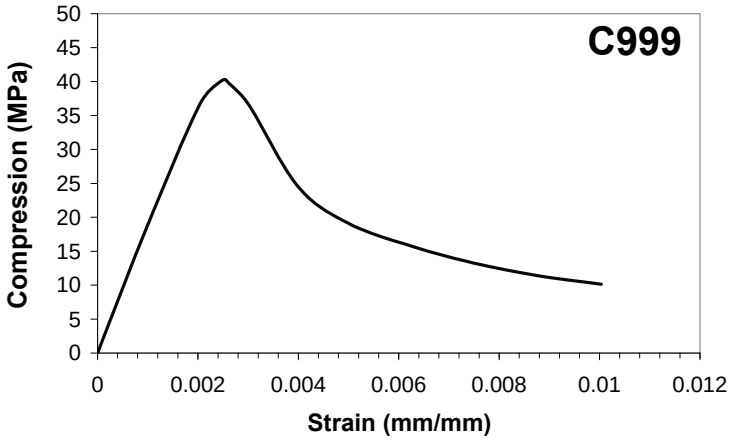

Figure A-21: Compressive Stress-Strain Response for Lightweight Concrete Cylinders with V_f=1%.

A.3.2 Flexure

Table A-8: Mechanical Response in Flexure for LWC

Lightweight Mix		**V_f=0%**			**V_f=0.5%**			**V_f=1%**		
Prism Specimen		**A8**	**A88**	**A888**	**A9**	**A99**	**A999**	**A101**	**A102**	**A103**
Modulus of Rupture f_r	**f_r (MPa)**	2.64	2.50	2.66	4.31	2.79	3.82	5.88	6.19	6.57
	Average(MPa)	2.60			3.64			6.21		
	COV (%)	3.4			21.3			5.6		
Flexural Toughness Factor T_f	**T_f (MPa)**	0.02	0.04	0.05	3.94	2.03	3.25	4.90	5.16	4.86
	Average(MPa)	0.04			3.08			4.97		
	COV (%)	47.4			31.4			3.2		

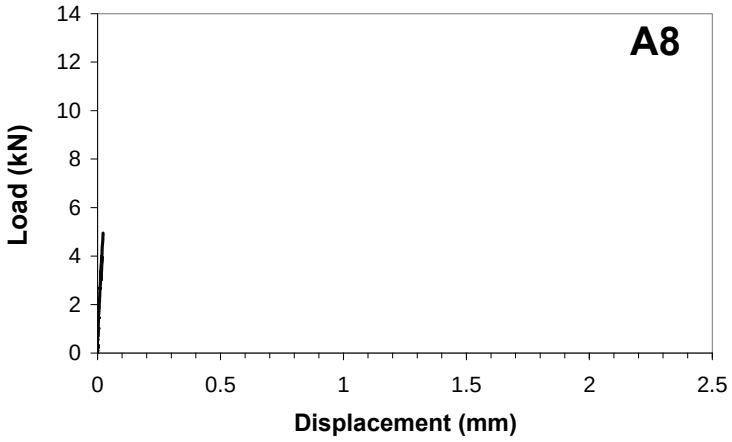

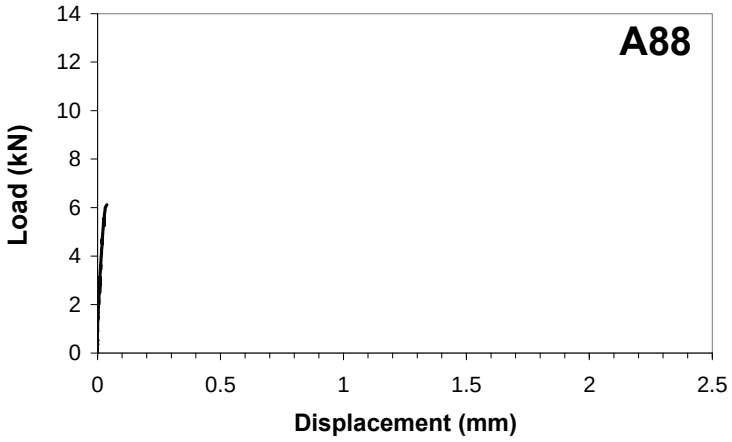

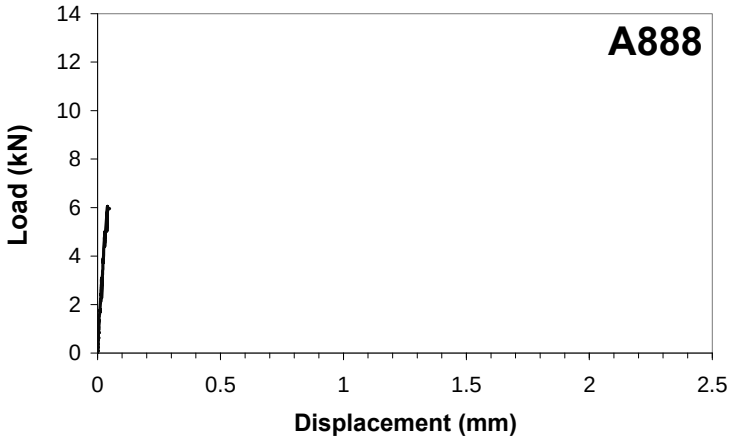

Figure A-22: Flexural Response for Lightweight Concrete Prisms with V_f=0%.

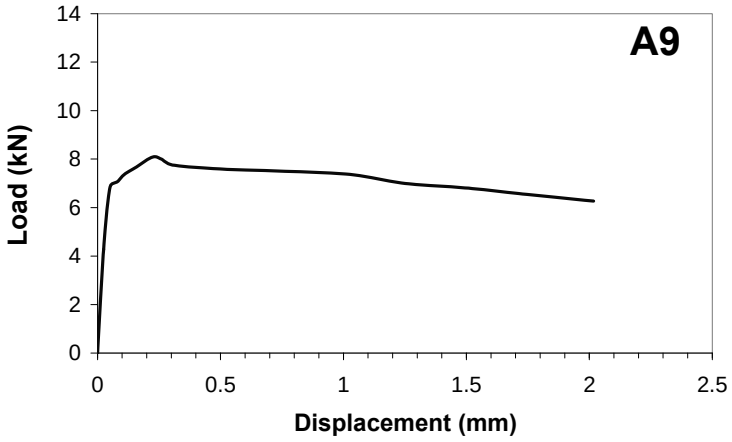

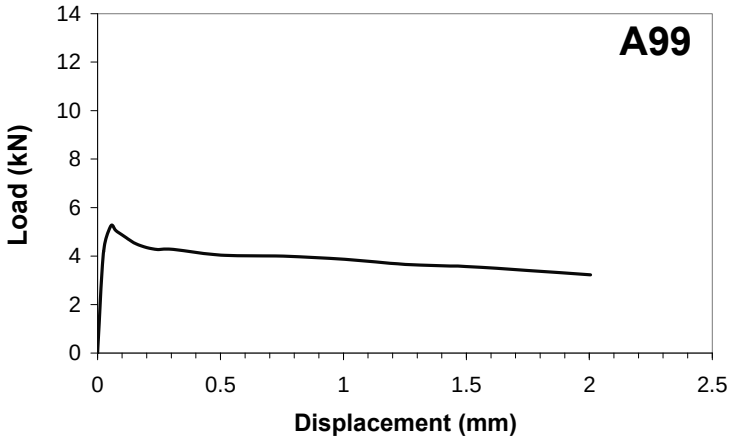

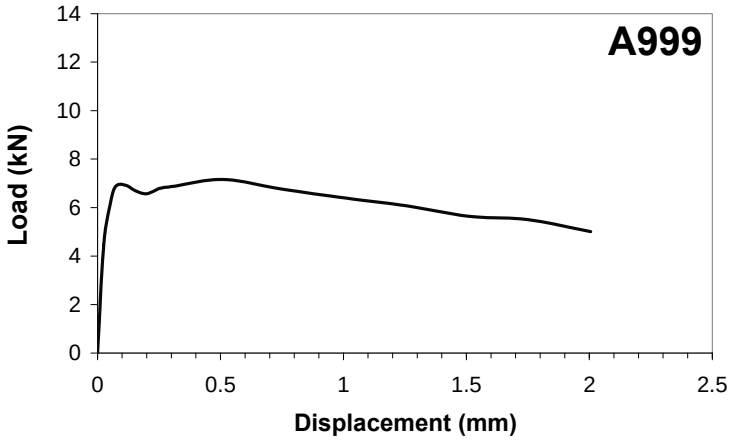

Figure A-23: Flexural Response for Lightweight Concrete Prisms with V_f=0.5%.

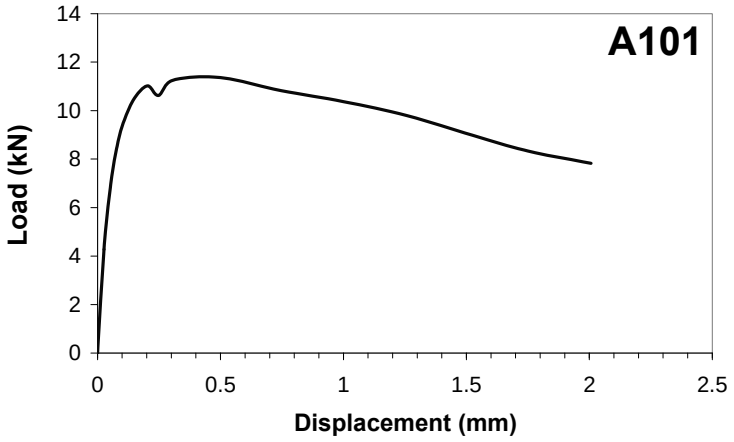

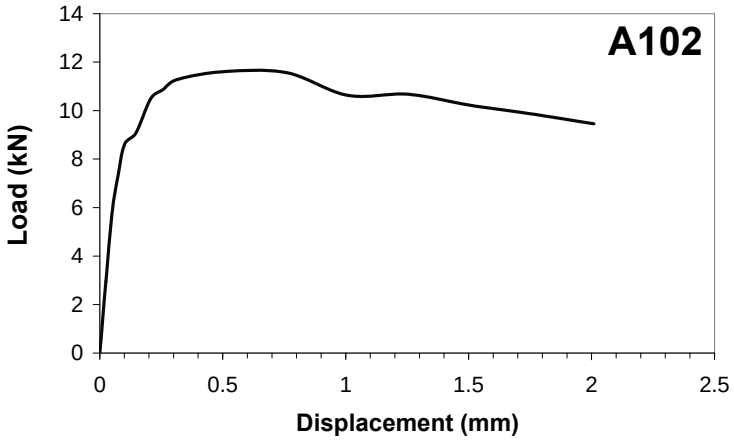

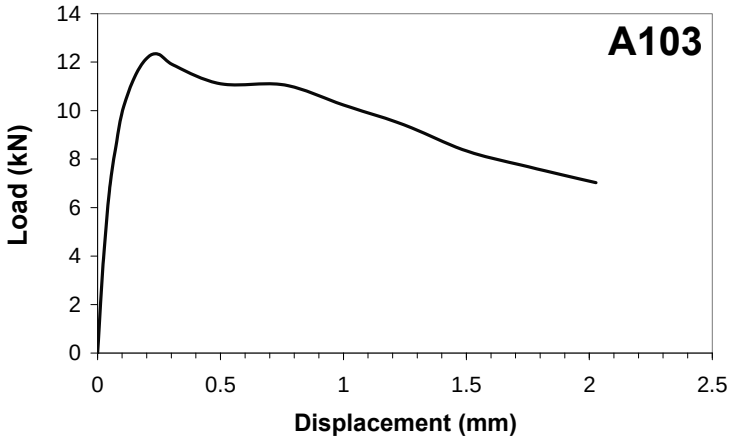

Figure A-24: Flexural Response for Lightweight Concrete Prisms with V_f=1%.

A.3.3 Direct Shear

Table A-9: Mechanical Response in Direct Shear for LWC

Lightweight Mix		**V_f=0%**			**V_f=0.5%**			**V_f=1%**		
Prism Specimen		**B7**	**B77**	**B777**	**B8**	**B88**	**B888**	**B9**	**B99**	**B999**
Shear Strength f_v	**f_v (MPa)**	3.70	3.15	2.97	5.49	3.51	4.32	5.58	6.16	5.94
	Average(MPa)	3.27			4.44			5.89		
	COV (%)	11.6			22.5			5.0		
Shear Toughness Factor(m=25) $T_{s,25}$	**T_s (MPa)**	1.57	1.23	1.09	6.88	3.21	4.66	6.27	7.41	6.55
	Average(MPa)	1.3			4.92			6.74		
	COV (%)	19.1			37.6			8.8		

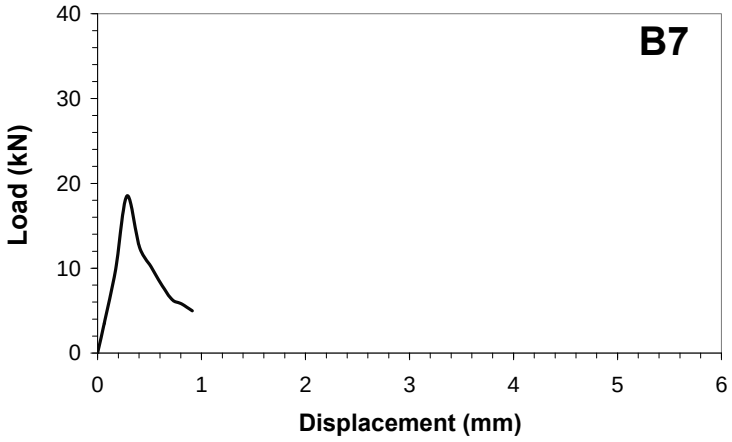

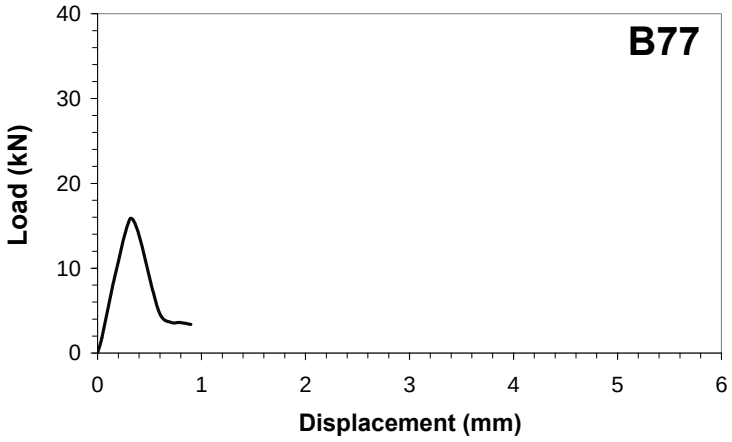

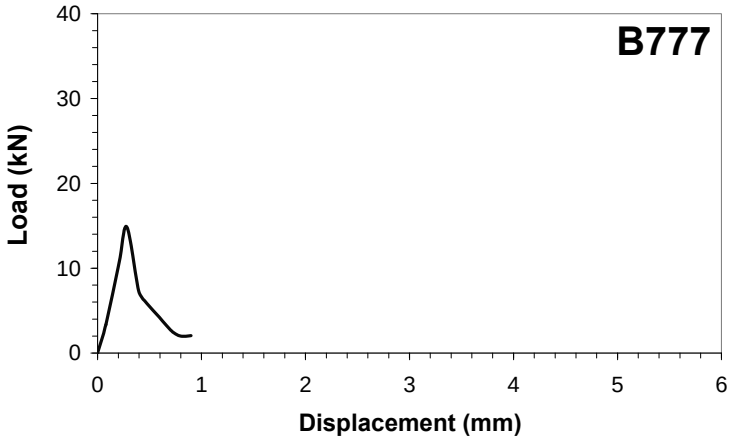

Figure A-25: Shear Test Results for Lightweight Concrete with V_f=0%.

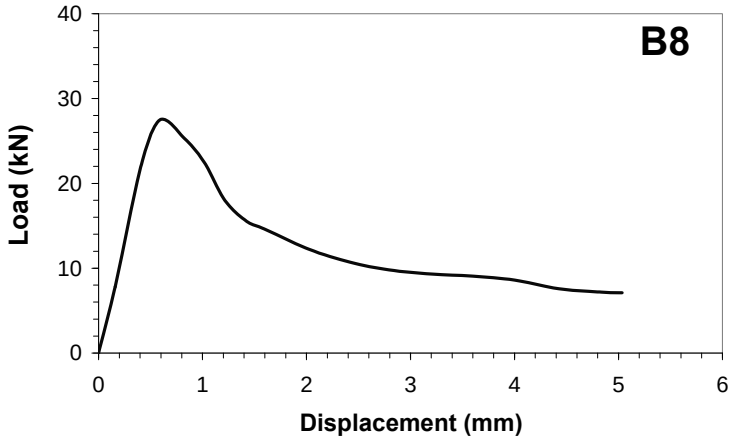

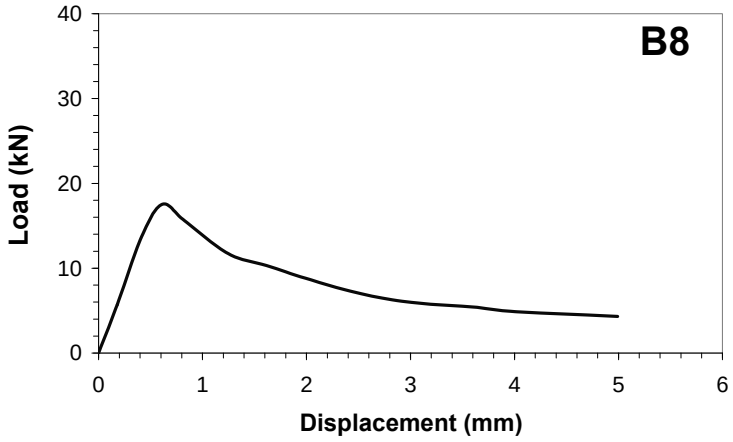

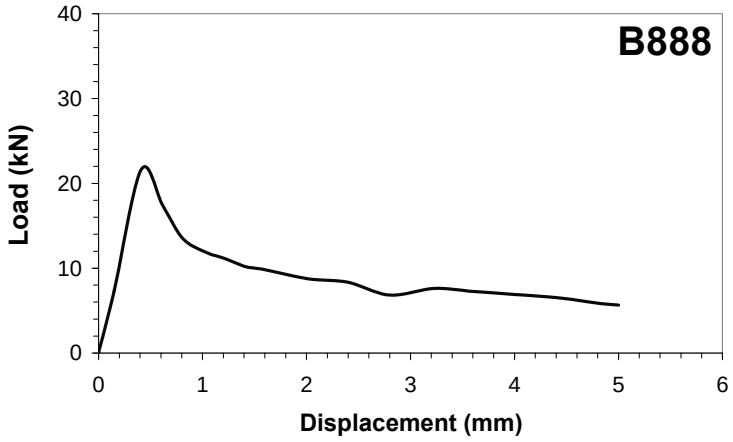

Figure A-26: Shear Test Results for Lightweight Concrete with V_f=0.5%.

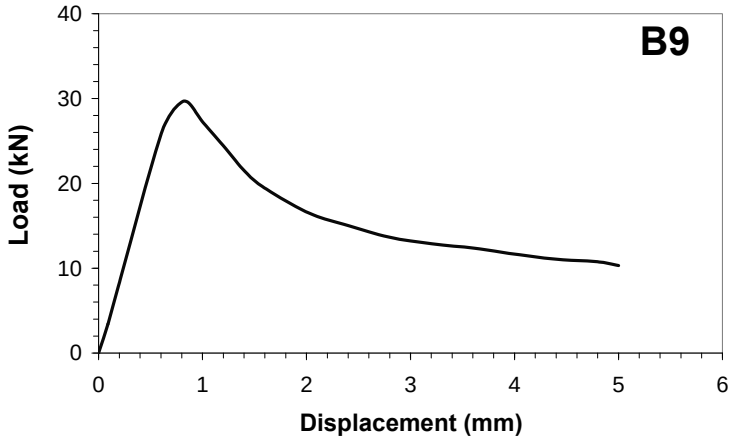

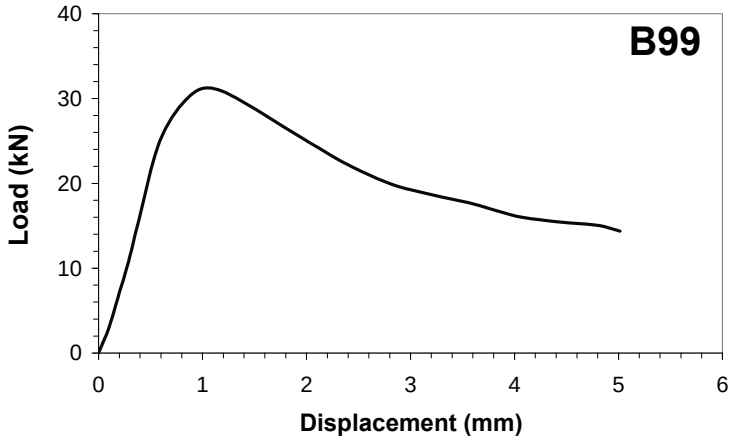

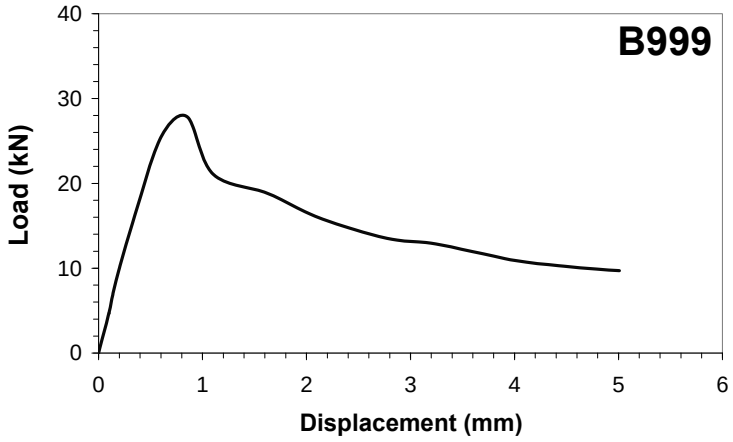

Figure A-27: Shear Test Results for Lightweight Concrete with V_f=1%.

Appendix B: Structural Tests Details

B.1 Specimens with *h=308 mm*

B.1.1 Specimen *N31*

B.1.1.1 Instrumentation (Strain Gauges and LVDTs)

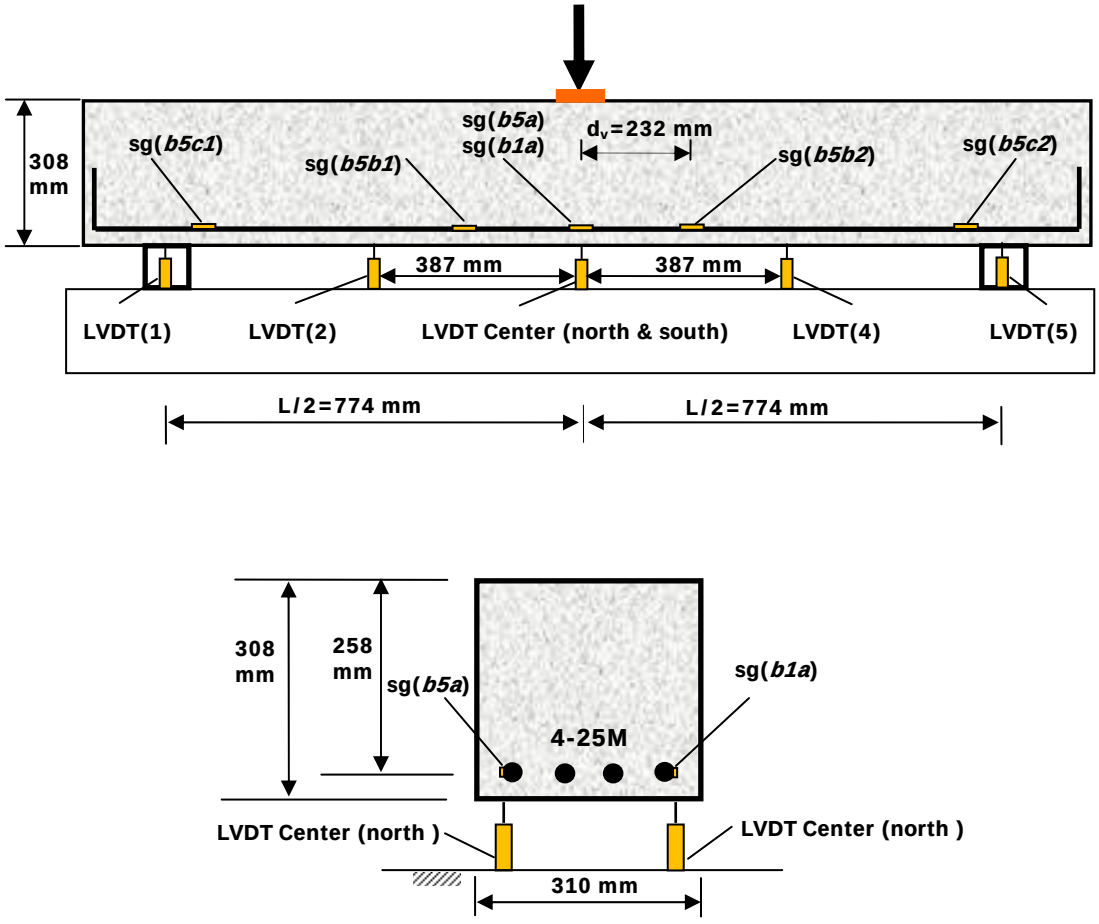

Mid-span Section

Figure B-1: Instrumentation for specimen *N31* (sg: strain gauge).

B.1.1.2 Load-Deflection Response

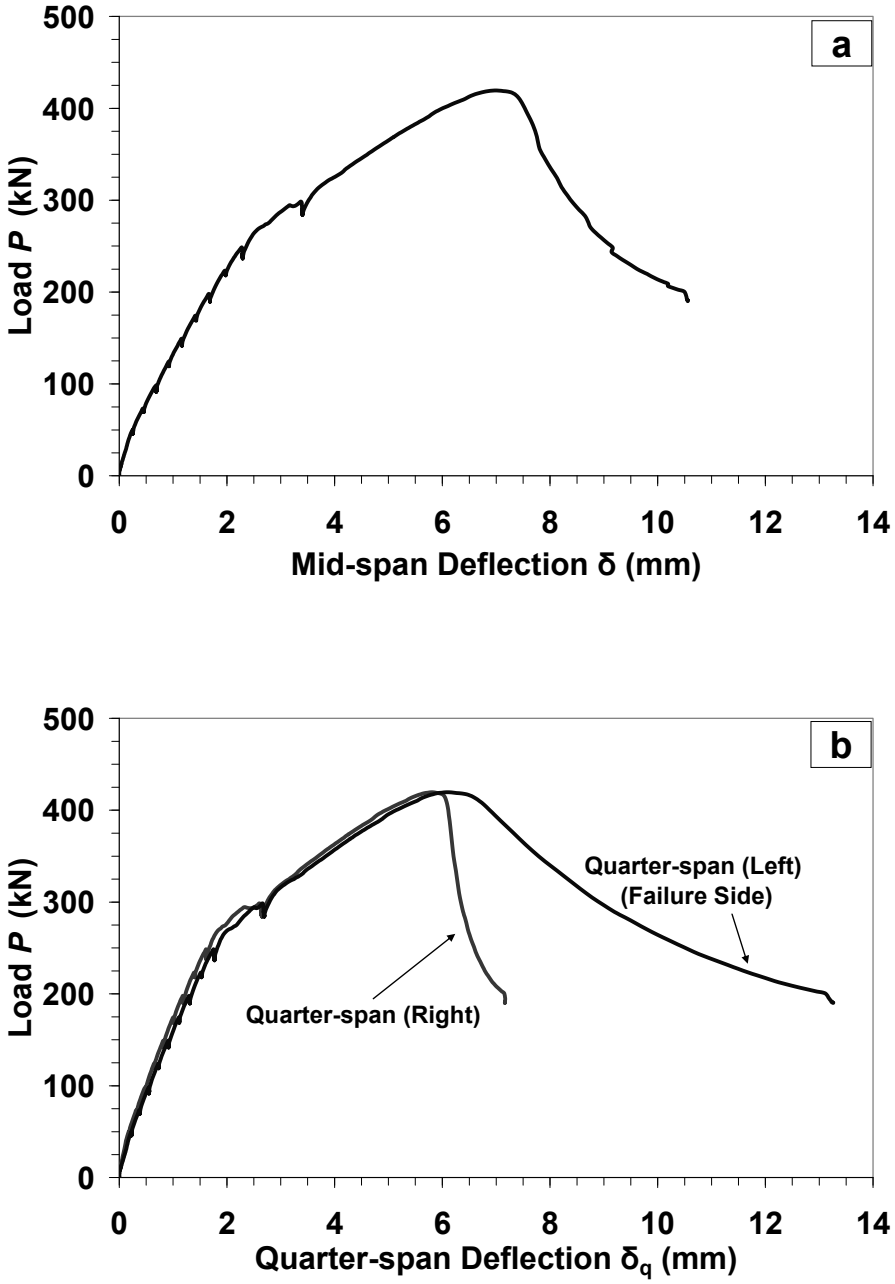

Figure B-2: Load-Deflection response for specimen *N31* at (a) mid-span; (b) quarter-span. (Note: all presented deflection data were corrected for the measured support settlement)

B.1.1.3 Load-Steel Strain Response

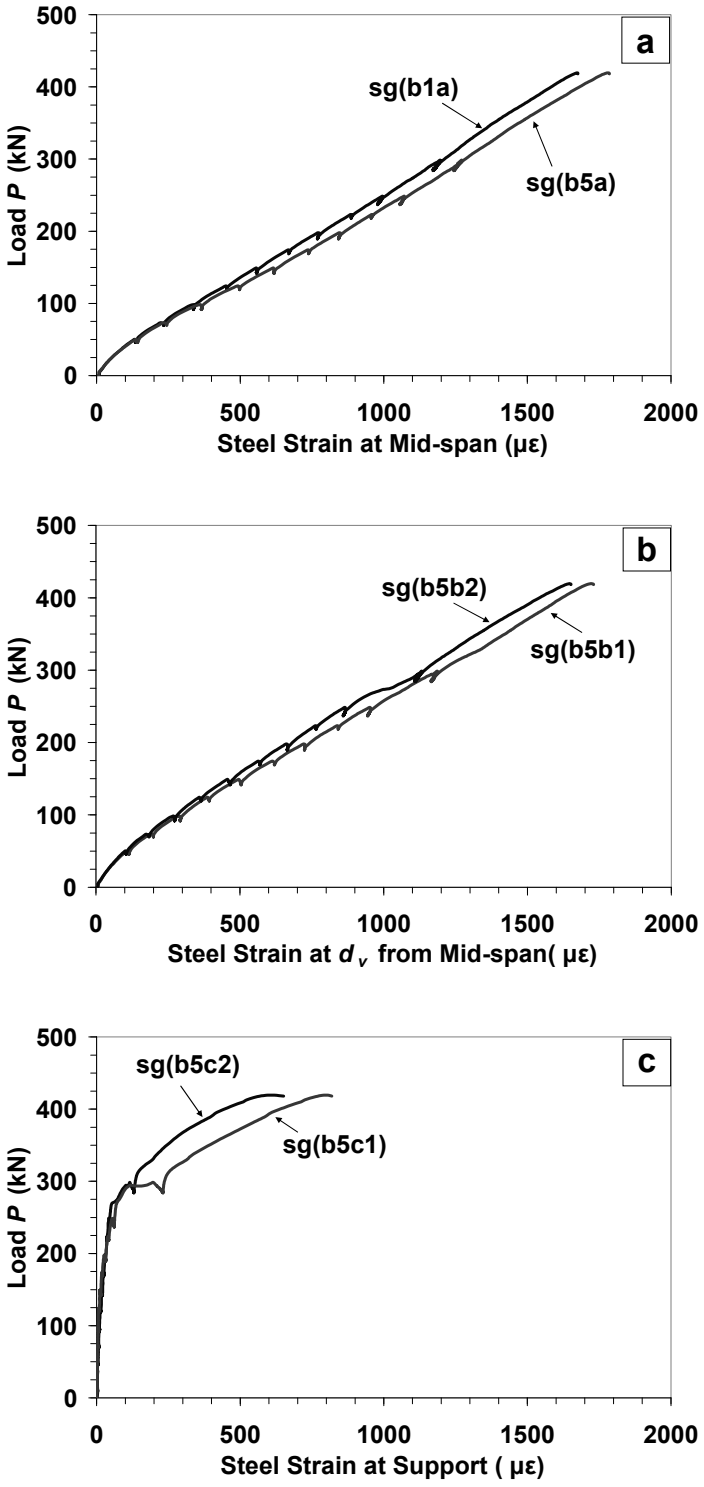

Figure B-3: Load-steel strain response for specimen *N31* at (a) mid-span; (b) d_v from mid-span; (c) support.

B.1.1.4 Crack Development

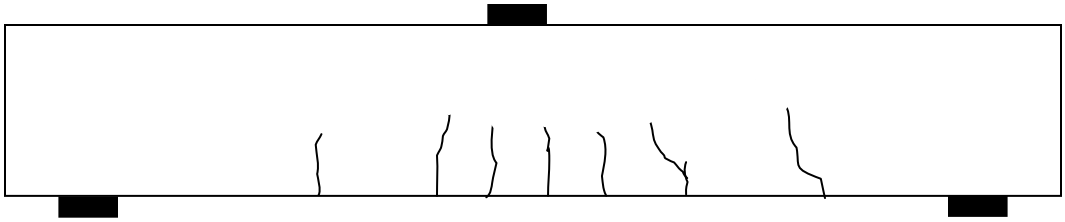

(a) At $P=200\ kN=0.48\ P_{max}$
(maximum flexural crack width < 0.08 *mm*)

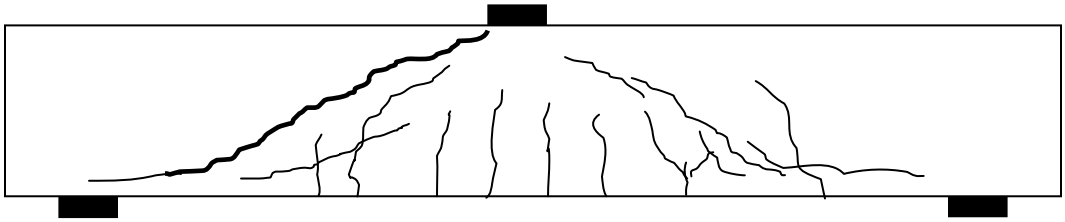

(b) After shear failure ($P_{max}=420\ kN$)

Figur B-4: Crack pattern for specimen *N31*.

B.1.2 Specimen *N32*

B.1.2.1 Instrumentation (Strain Gauges and LVDTs)

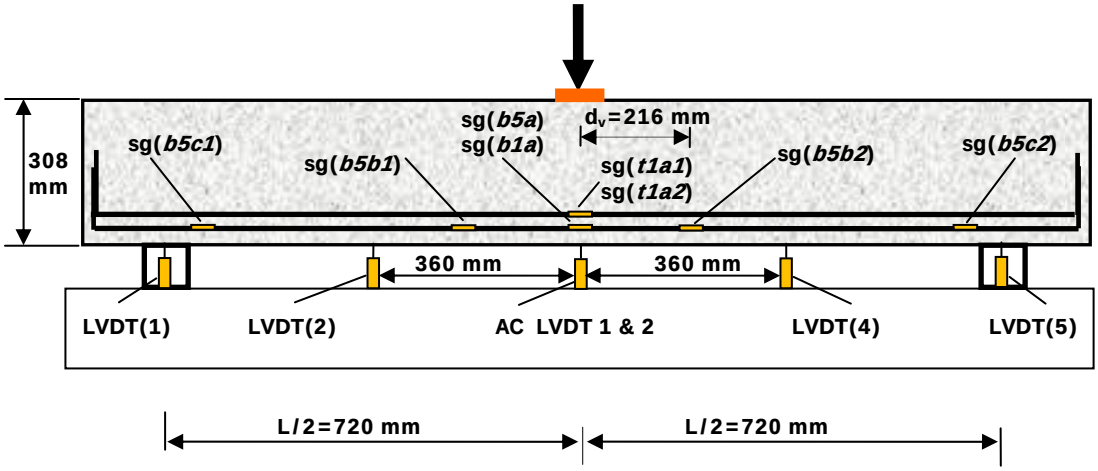

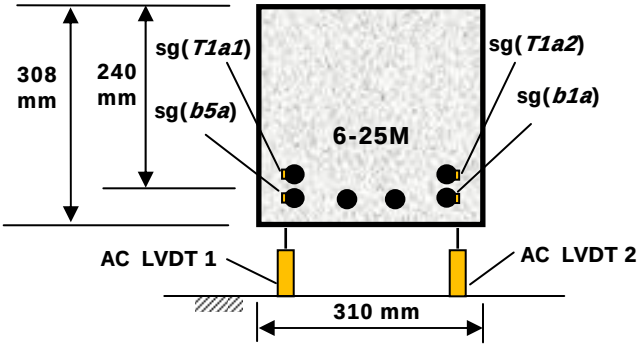

Mid-span Section

Figure B-5: Instrumentation for specimen *N32* (sg: strain gauge).

B.1.2.2 Load-Deflection Response

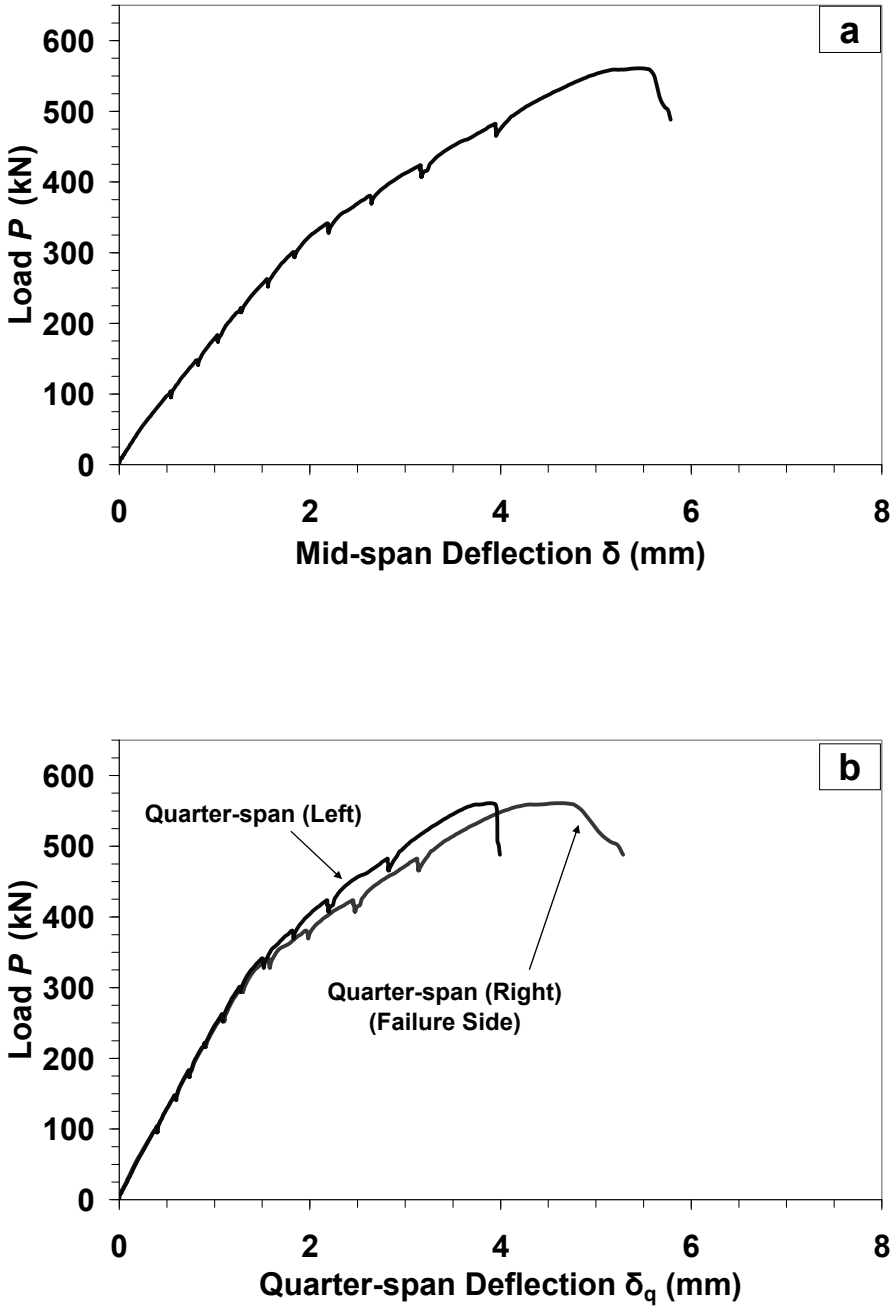

Figure B-6: Load-Deflection response for specimen *N32* at (a) mid-span; (b) quarter-span. (Note: all presented deflection data were corrected for the measured support settlement)

.

B.1.2.3 Load-Steel Strain Response

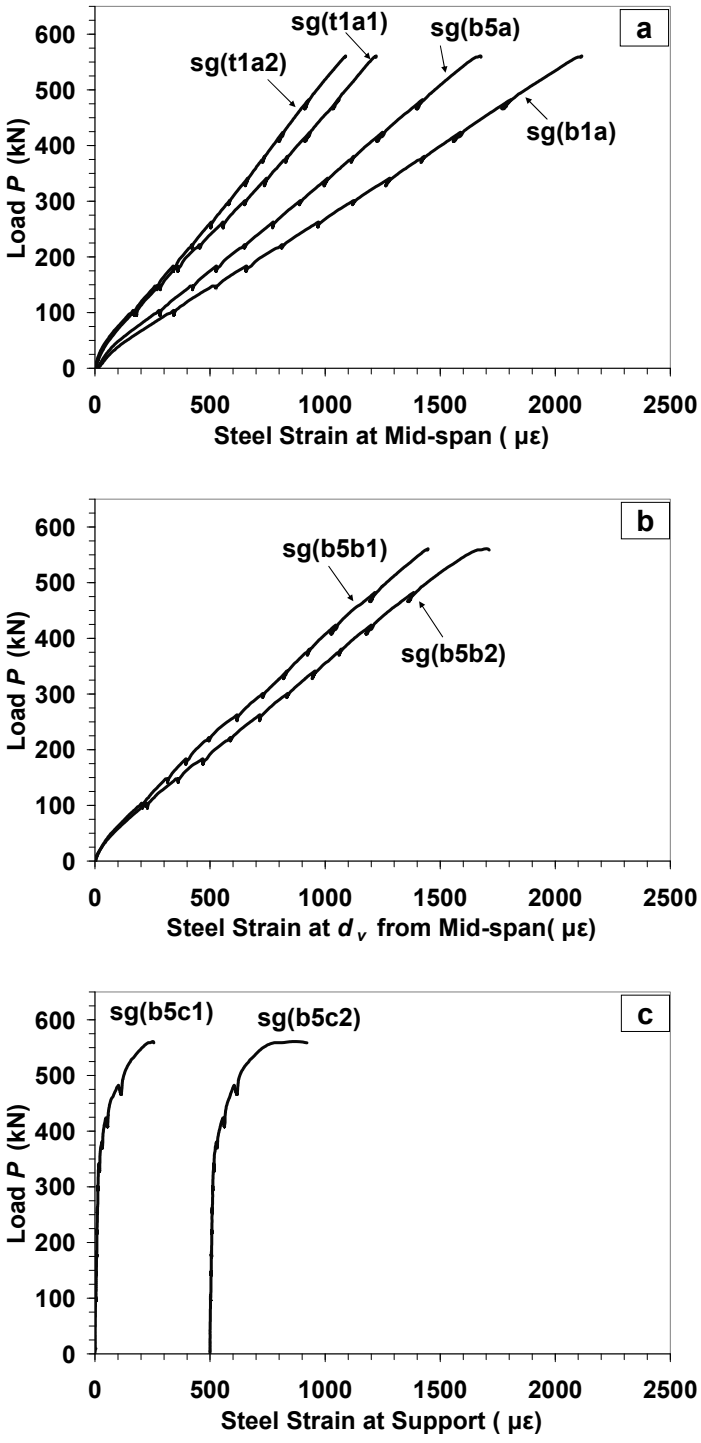

Figure B-7: Load-steel strain response for specimen *N32* at (a) mid-span; (b) d_v from mid-span; (c) support.

B.1.2.4 Crack Development

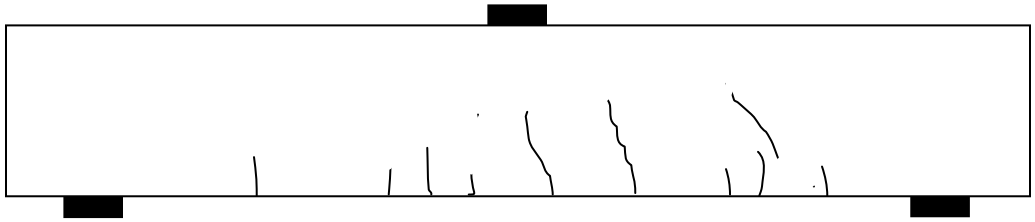

(a) At $P=260\ kN=0.46\ P_{max}$
(maximum flexural crack width = 0.08 *mm*)

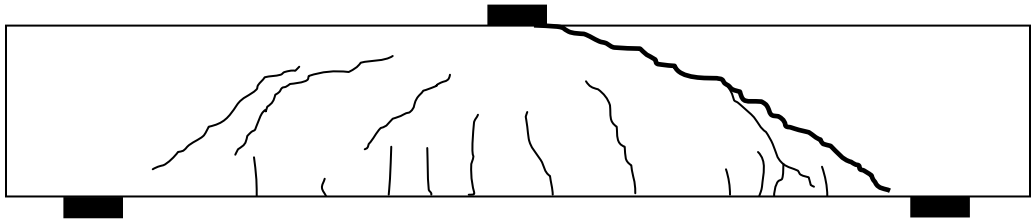

(b) After shear failure ($P_{max}=560\ kN$)

Figur B-8: Crack pattern for specimen *N32*.

B.1.3 Specimen *H31*

B.1.3.1 Instrumentation (Strain Gauges and LVDTs)

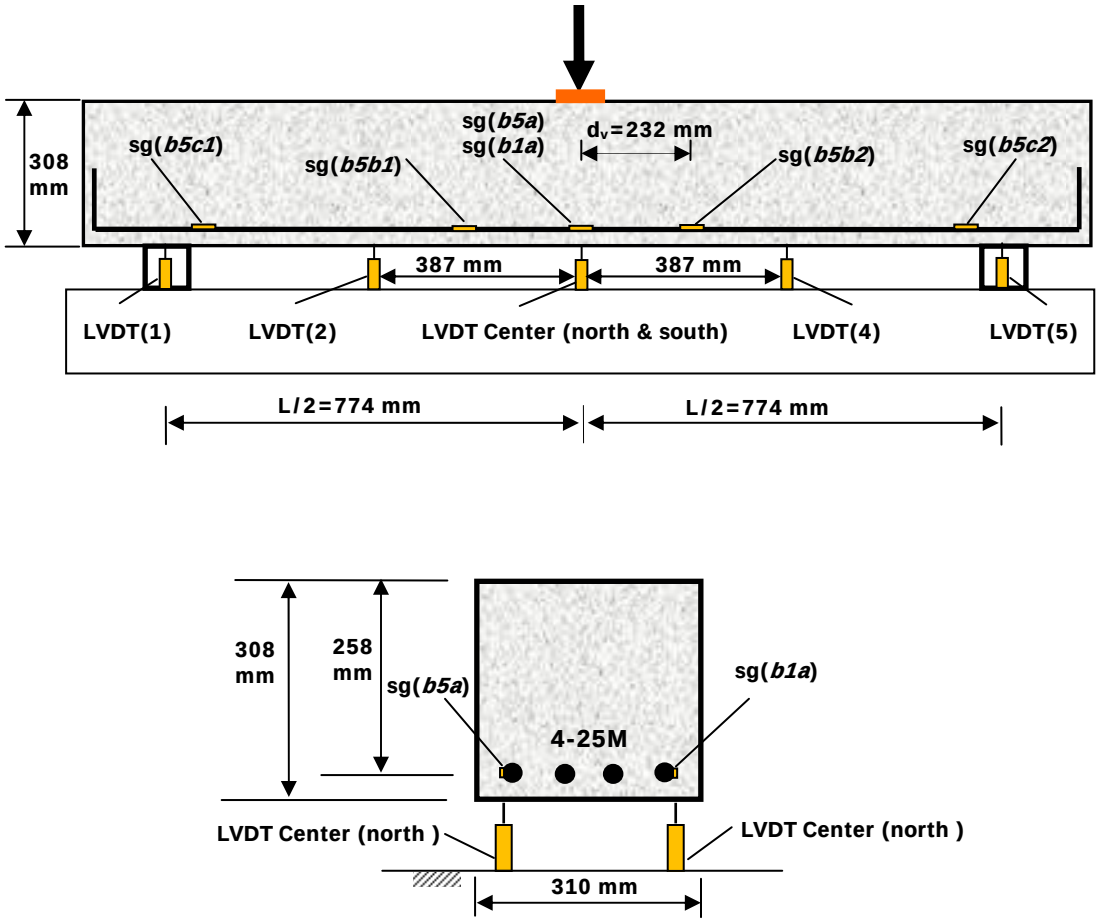

Mid-span Section

Figure B-9: Instrumentation for specimen *H31* (sg: strain gauge).

B.1.3.2 Load-Deflection Response

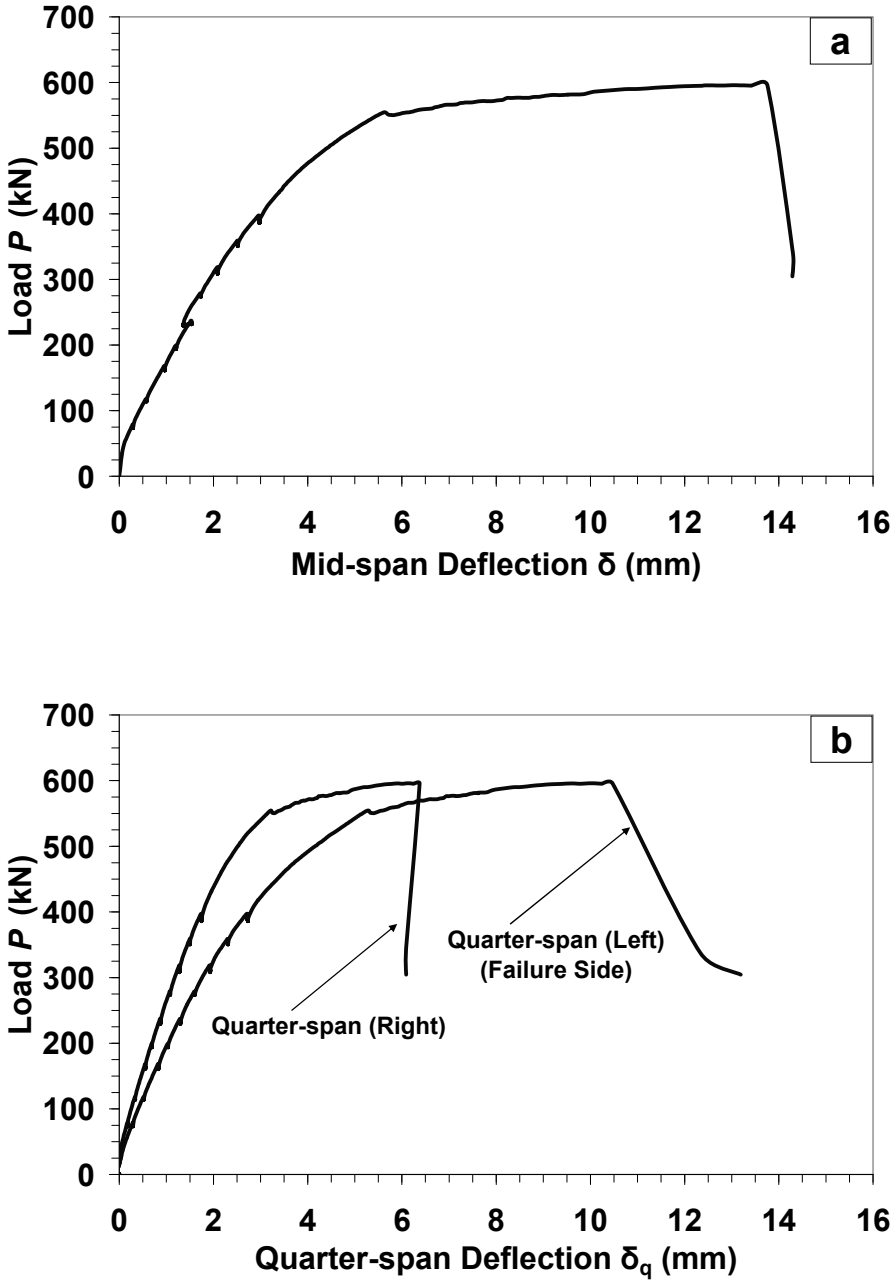

Figure B-10: Load-Deflection response for specimen *H31* at (a) mid-span; (b) quarter-span. (Note: all presented deflection data were corrected for the measured support settlement)

B.1.3.3 Load-Steel Strain Response

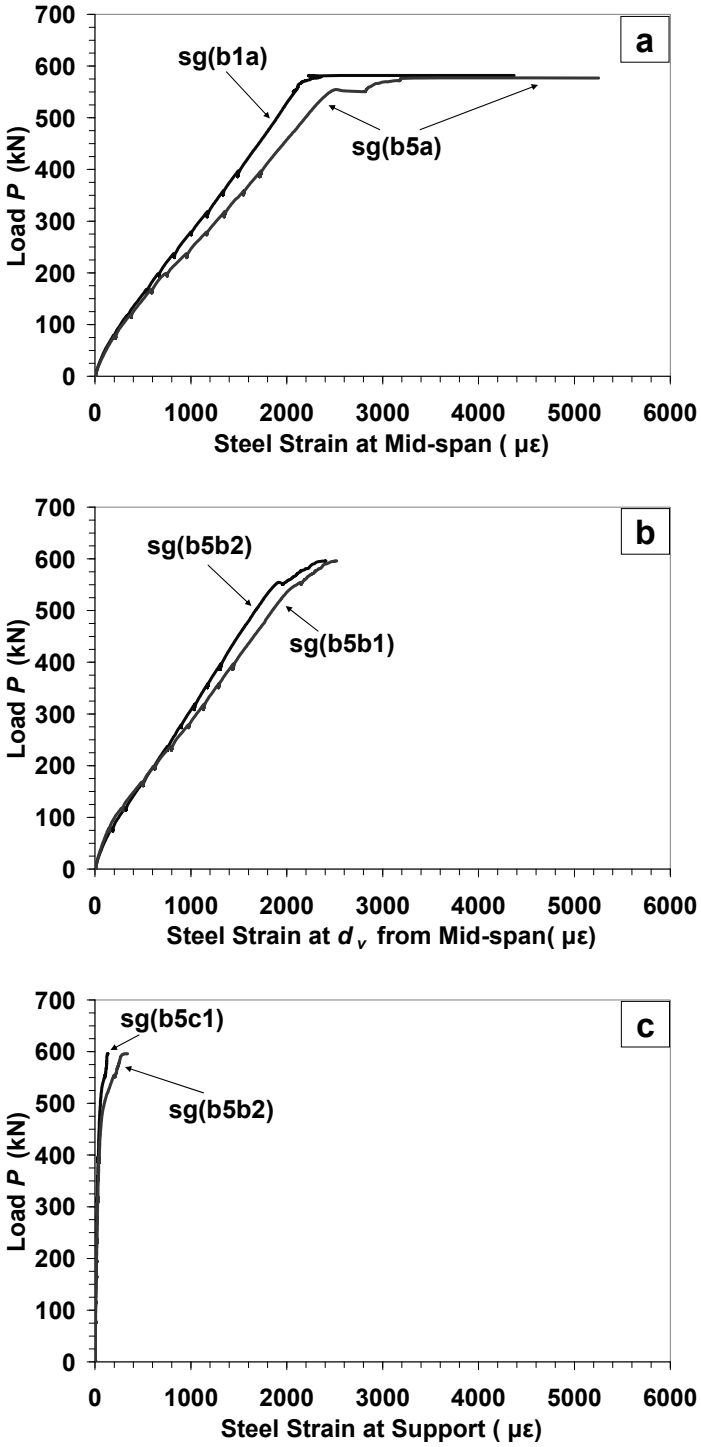

Figure B-11: Load-steel strain response for specimen *H31* at (a) mid-span; (b) d_v from mid-span; (c) support.

B.1.3.4 Crack Development

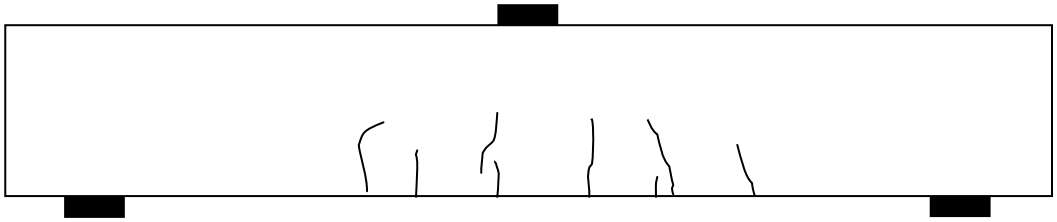

(a) At $P=240\ kN=0.43\ P_{max}$
(maximum flexural crack width < 0.08 *mm*)

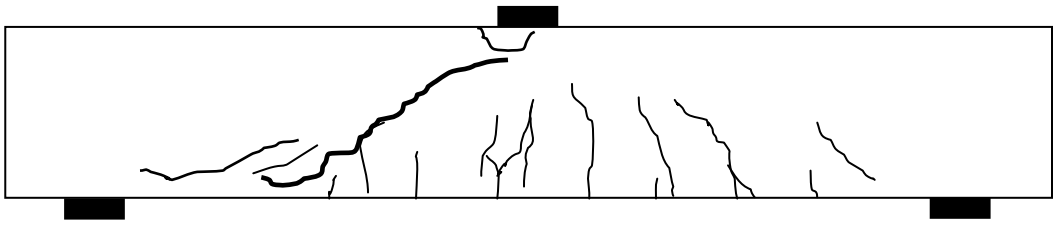

(b) After shear failure ($P_{max}=554\ kN$)

Figur B-12: Crack pattern for specimen *H31*.

B.1.4 Specimen *H32*

B.1.4.1 Instrumentation (Strain Gauges and LVDTs)

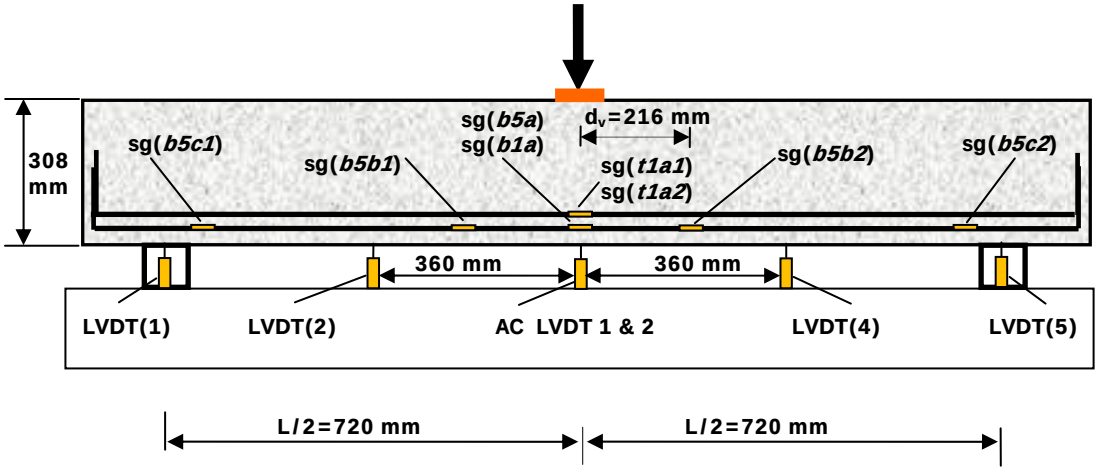

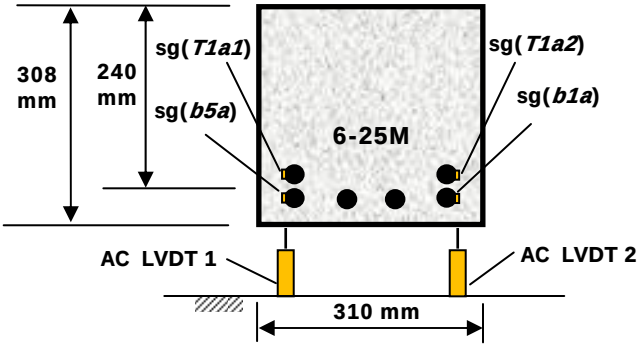

Mid-span Section

Figure B-13: Instrumentation for specimen *H32* (sg: strain gauge).

B.1.4.2 Load-Deflection Response

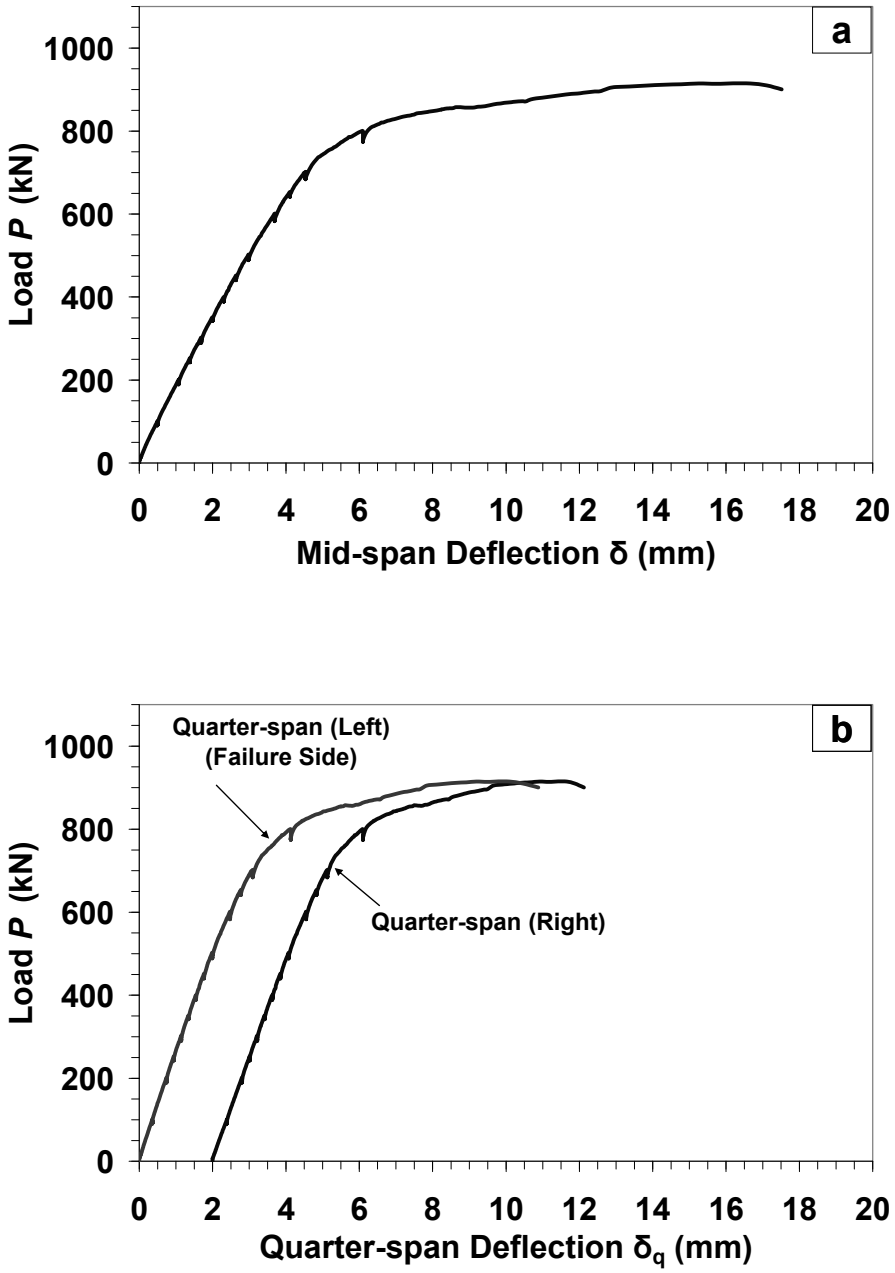

Figure B-14: Load-Deflection response for specimen *H32* at (a) mid-span; (b) quarter-span. (Note: all presented deflection data were corrected for the measured support settlement)

B.1.4.3 Load-Steel Strain Response

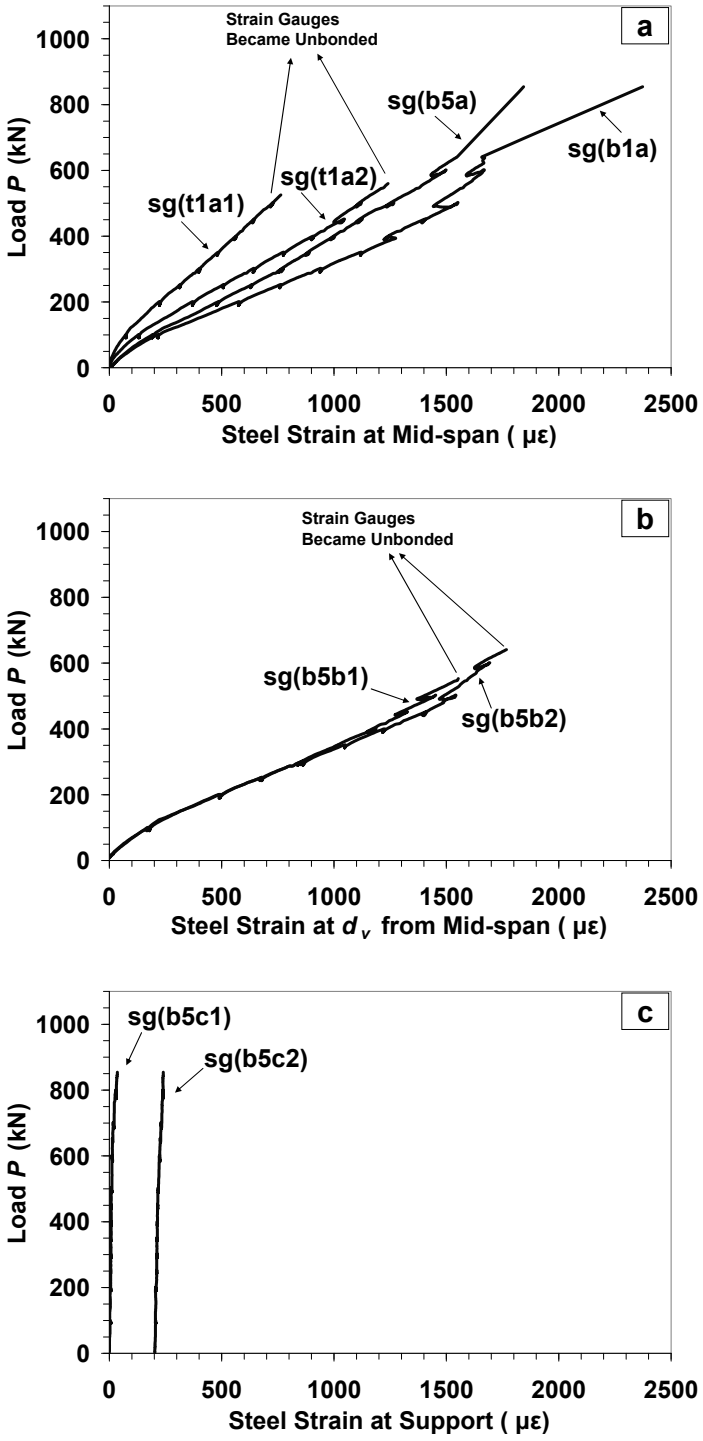

Figure B-15: Load-steel strain response for specimen *H32* at (a) mid-span; (b) d_v from mid-span; (c) support.

B.1.4.4 Crack Development

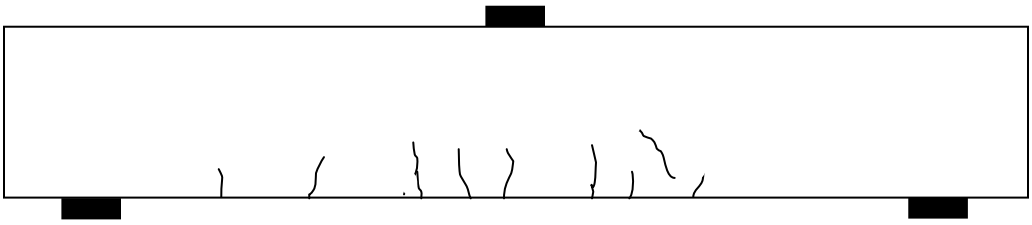

(a) At $P=400\ kN=0.44\ P_{max}$
(maximum flexural crack width < 0.08 *mm*)

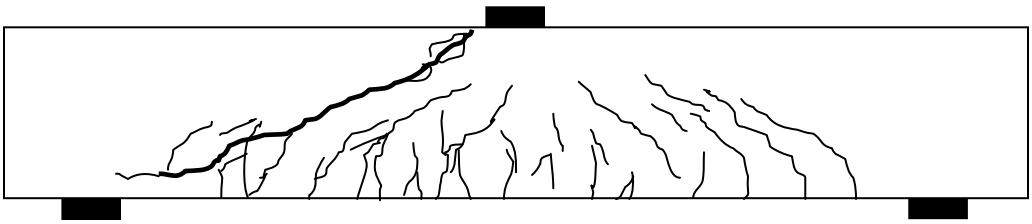

(b) After shear failure ($P_{max}=915\ kN$)

Figur B-16: Crack pattern for specimen *H32*.

B.1.5 Specimen *L31*

B.1.5.1 Instrumentation (Strain Gauges and LVDTs)

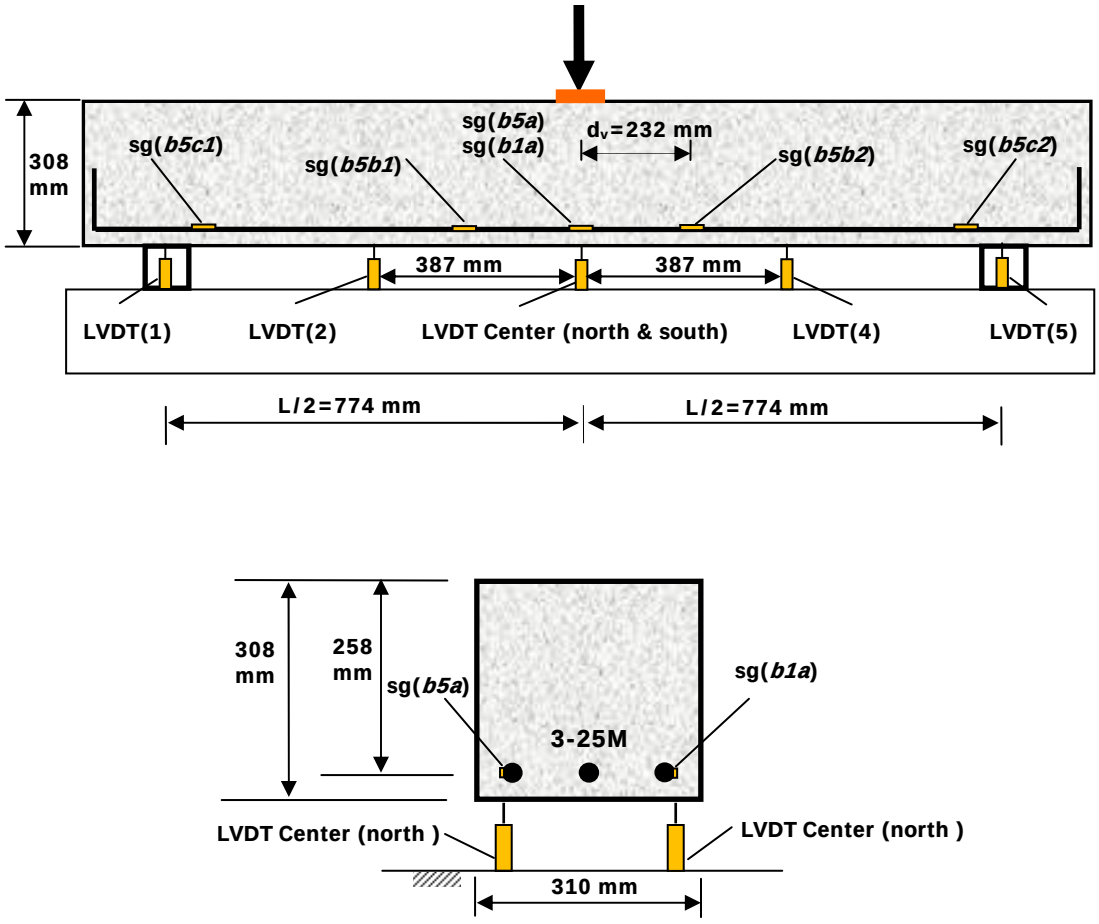

Mid-span Section

Figure B-17: Instrumentation for specimen *L31* (sg: strain gauge).

B.1.5.2 Load-Deflection Response

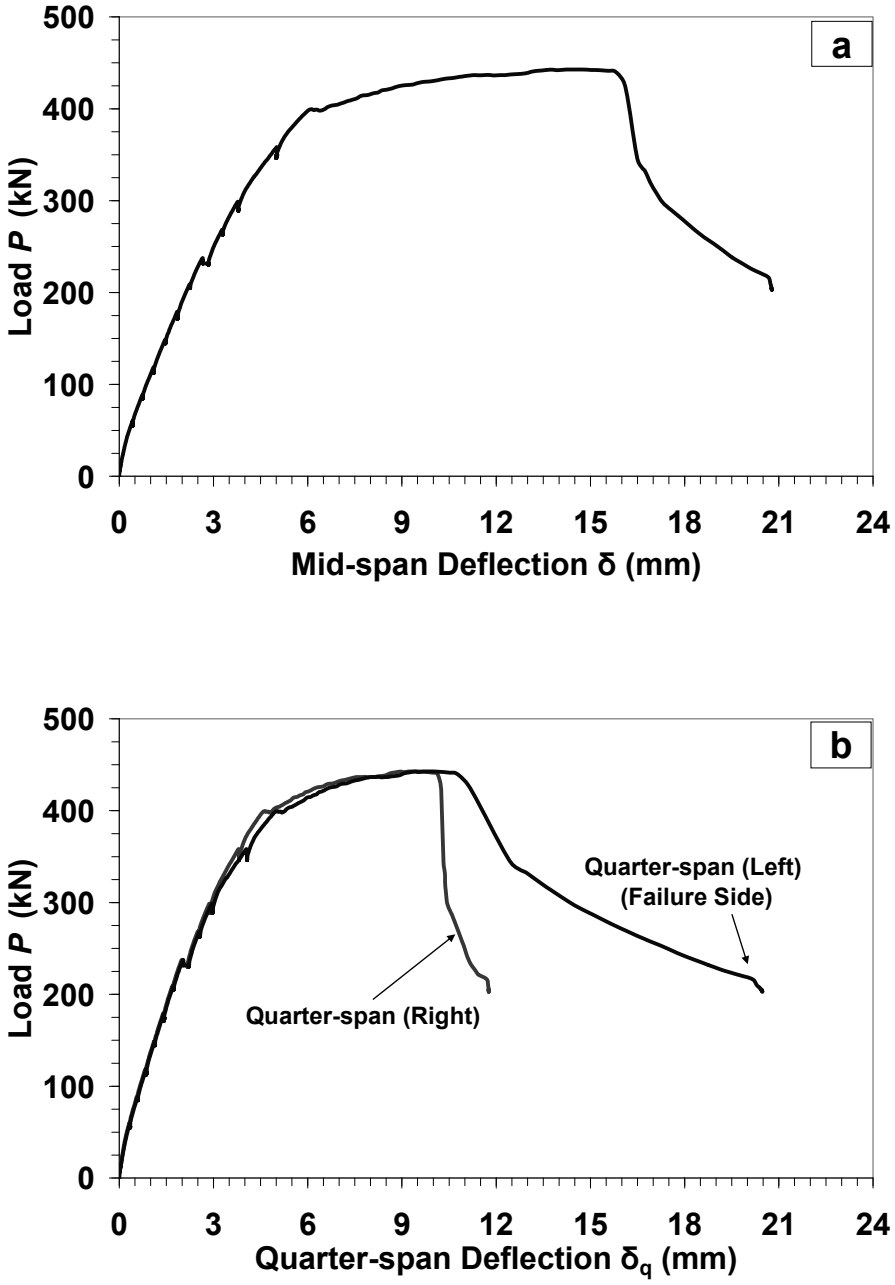

Figure B-18: Load-Deflection response for specimen *L31* at (a) mid-span; (b) quarter-span. (Note: all presented deflection data were corrected for the measured support settlement)

B.1.5.3 Load-Steel Strain Response

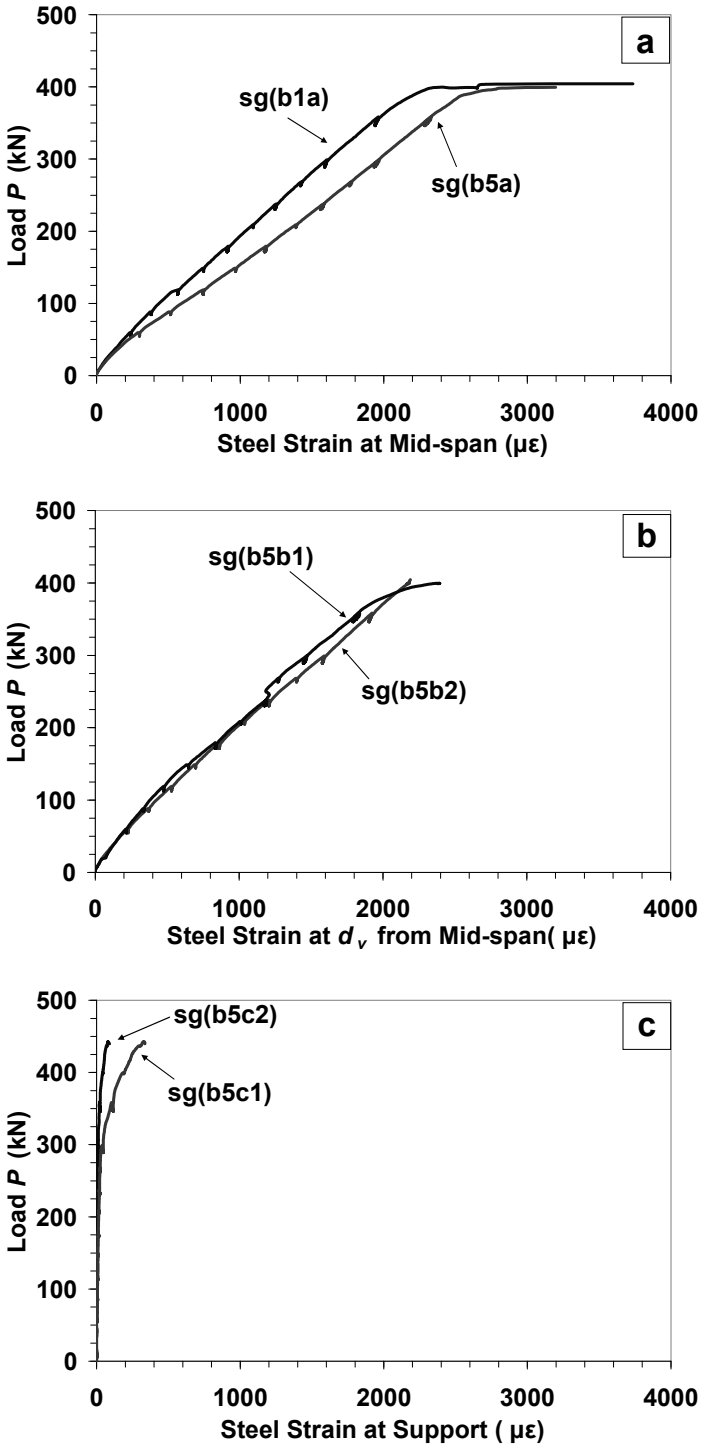

Figure B-19: Load-steel strain response for specimen *L31* at (a) mid-span; (b) d_v from mid-span; (c) support.

B.1.5.4 Crack Development

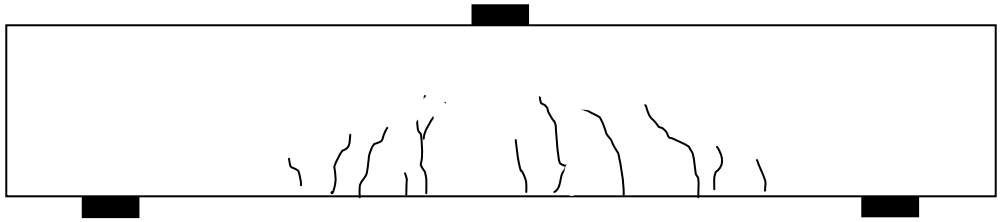

(a) At $P=180\ kN=0.44\ P_{max}$
(maximum flexural crack width < 0.08 *mm*)

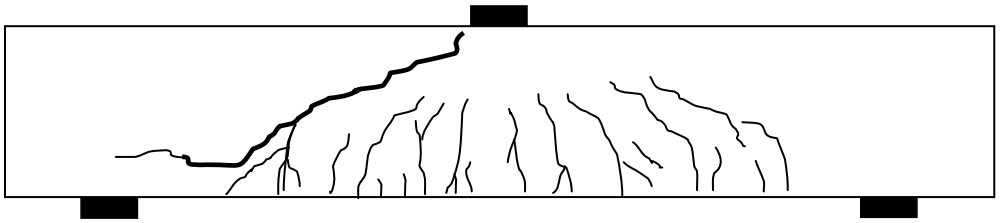

(b) After shear failure ($P_{max}=405\ kN$)

Figur B-20: Crack pattern for specimen *L31*.

B.1.6 Specimen *L32*

B.1.6.1 Instrumentation (Strain Gauges and LVDTs)

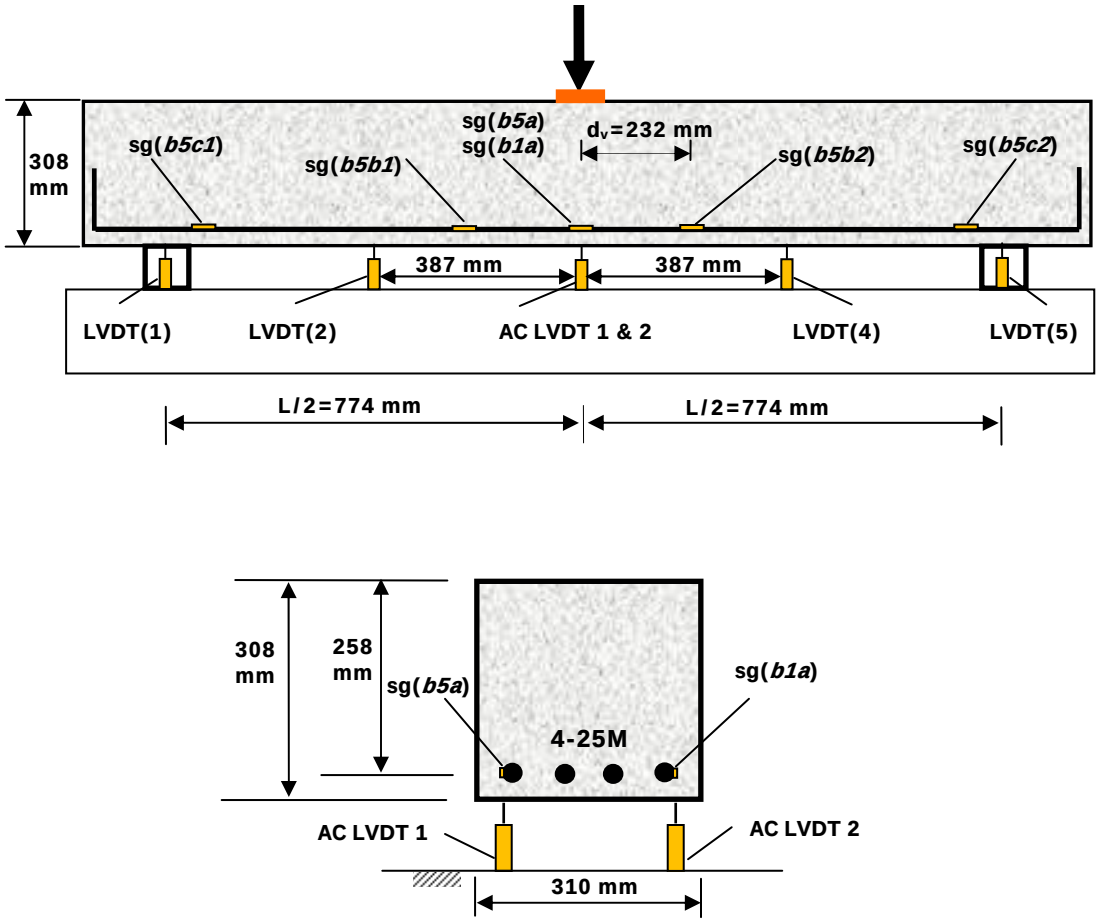

Mid-span Section

Figure B-21: Instrumentation for specimen *L32* (sg: strain gauge).

B.1.6.2 Load-Deflection Response

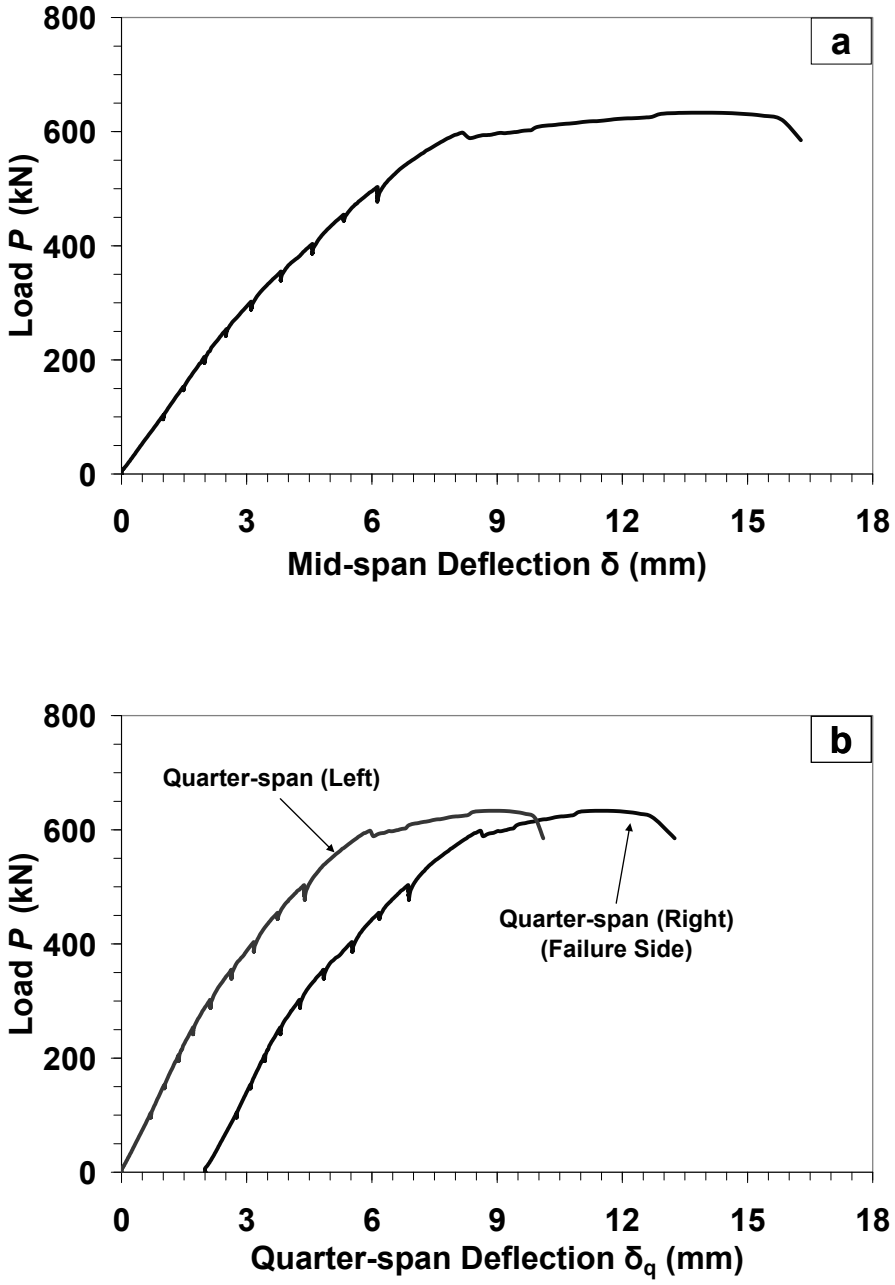

Figure B-22: Load-Deflection response for specimen *L32* at (a) mid-span; (b) quarter-span. (Note: all presented deflection data were corrected for the measured support settlement)

B.1.6.3 Load-Steel Strain Response

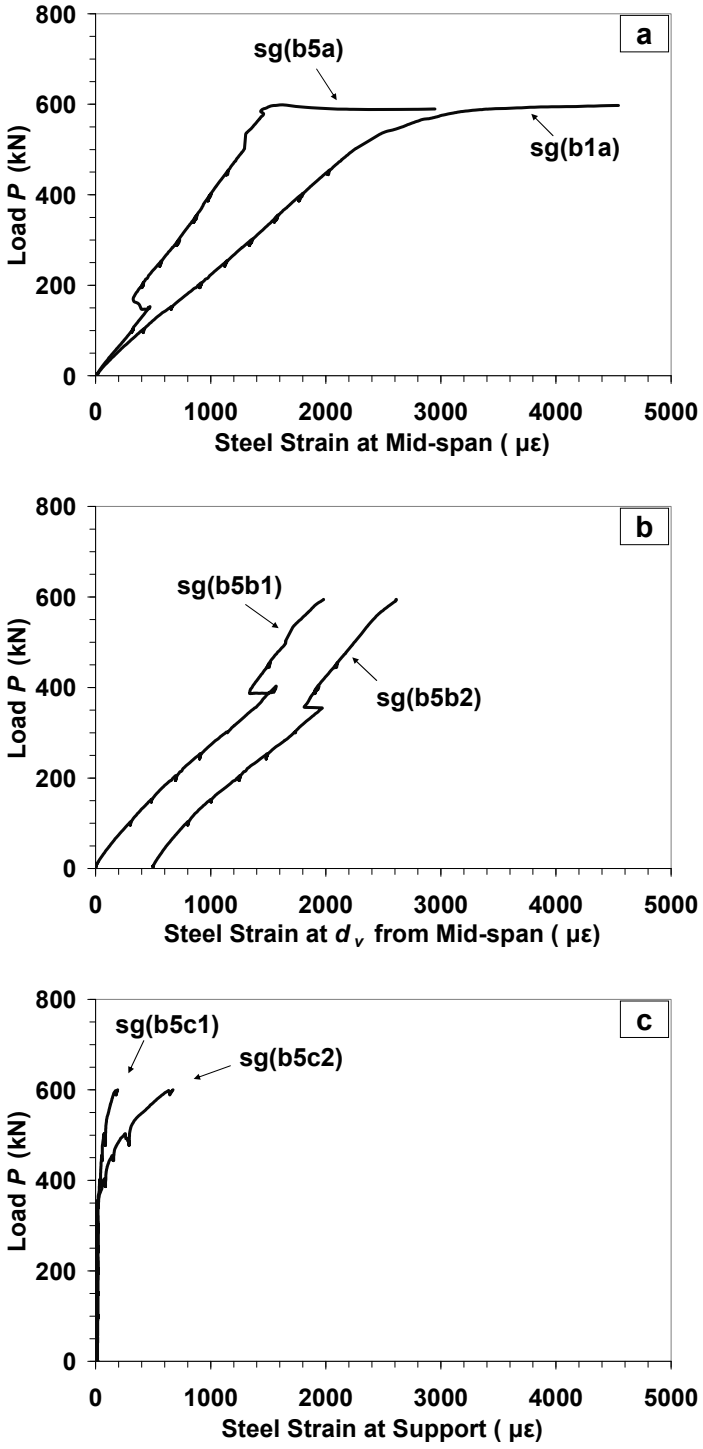

Figure B-23: Load-steel strain response for specimen *L32* at (a) mid-span; (b) d_v from mid-span; (c) support.

B.1.6.4 Crack Development

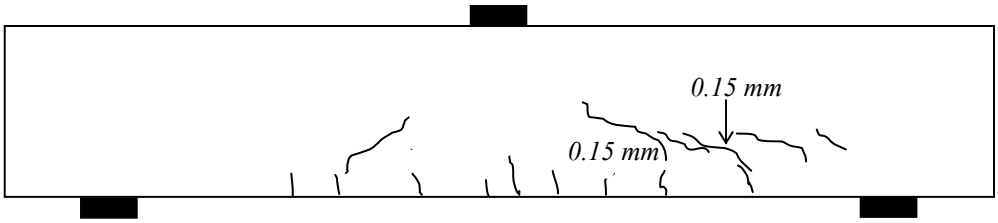

(a) At P= *300 kN=0.50* P_{max}
(maximum shear crack width = 0.15 *mm*)

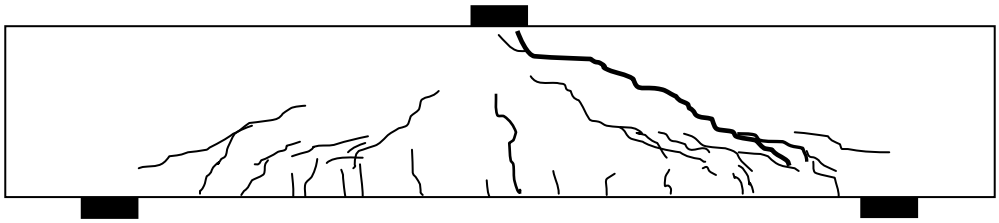

(b) After shear failure (P_{max}=*595 kN)*

Figur B-24: Crack pattern for specimen *L32*.

B.2 Specimens with *h=600 mm*

B.2.1 Specimen *N61*

B.2.1.1 Instrumentation (Strain Gauges and LVDTs)

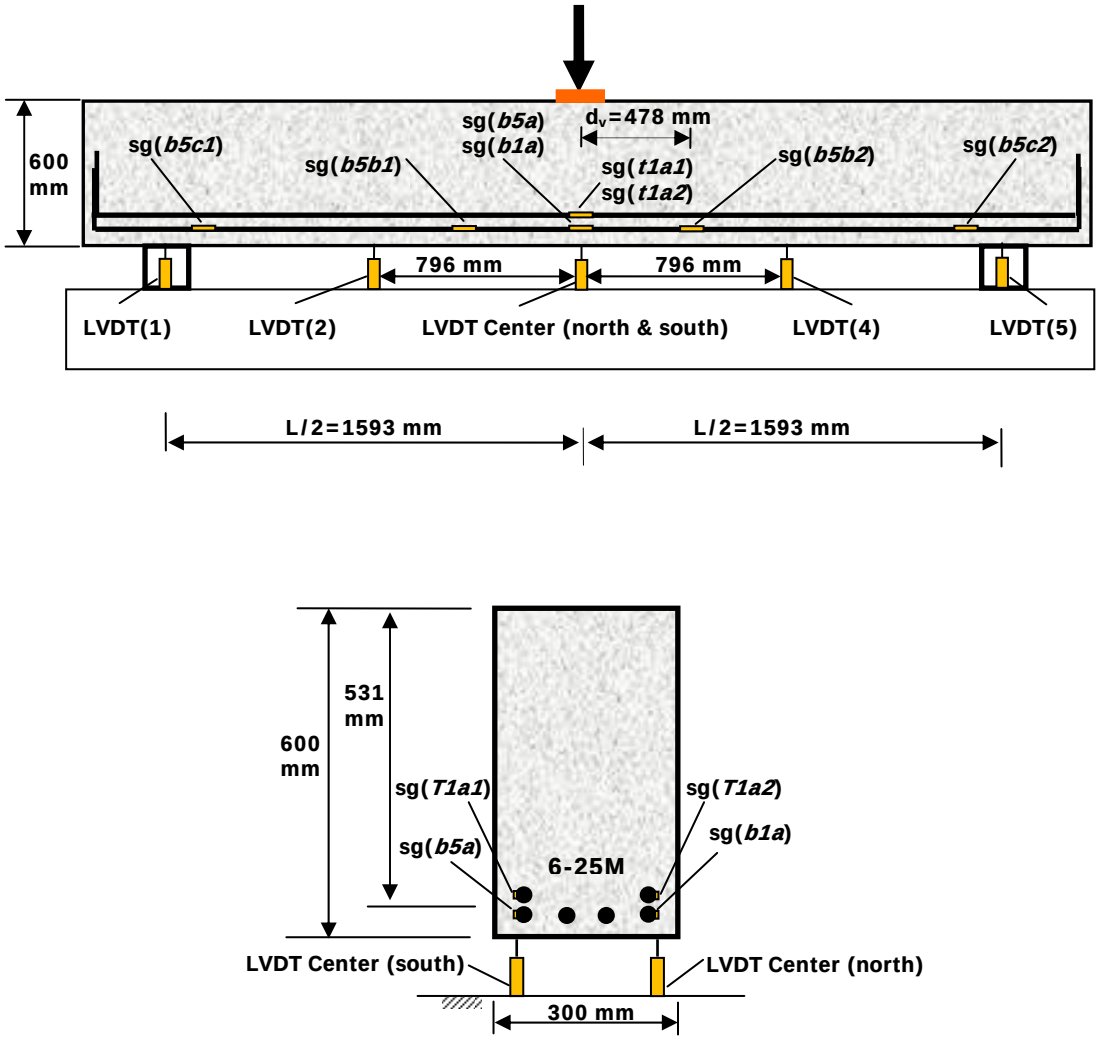

Mid-span Section

Figure B-25: Instrumentation for specimen *N61* (sg: strain gauge).

B.2.1.2 Load-Deflection Response

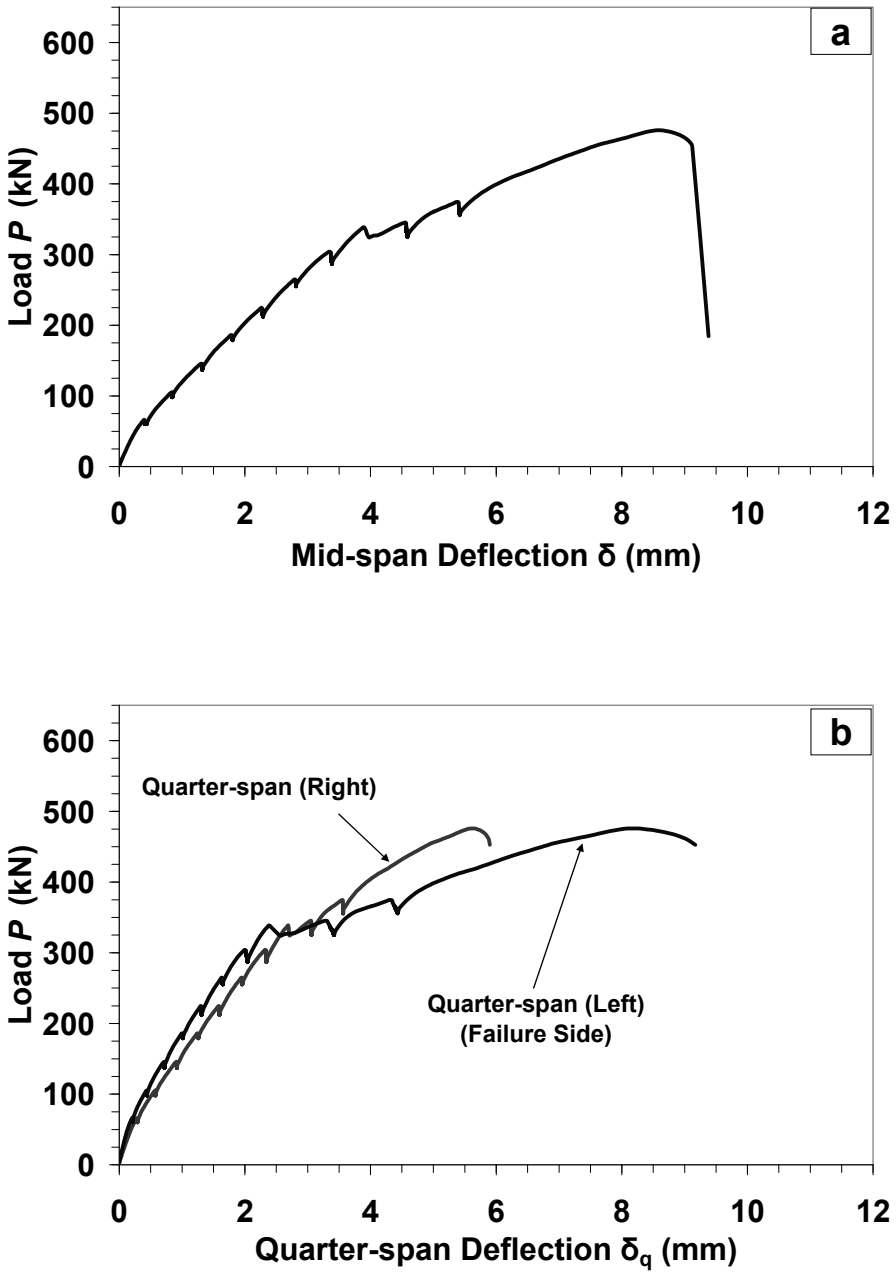

Figure B-26: Load-Deflection response for specimen *N61* at (a) mid-span; (b) quarter-span. (Note: all presented deflection data were corrected for the measured support settlement)

B.2.1.3 Load-Steel Strain Response

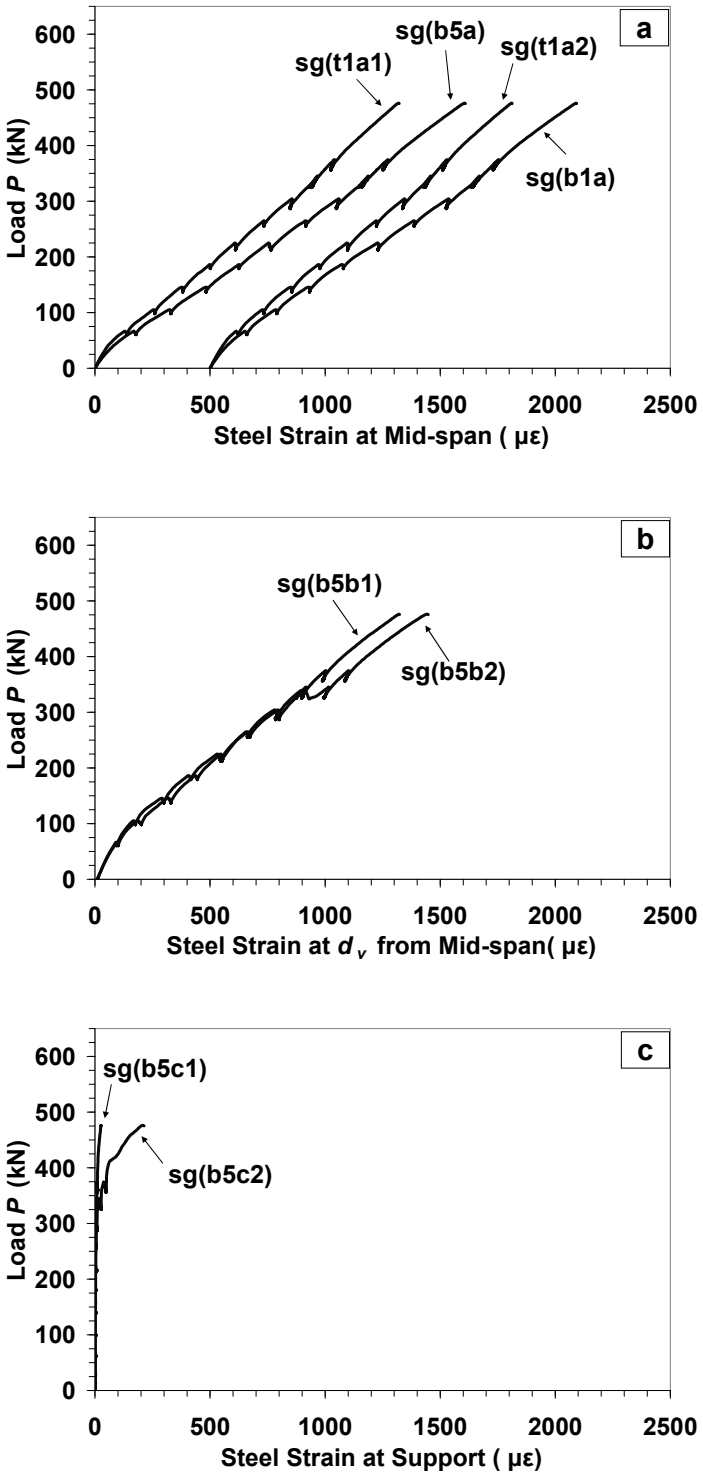

Figure B-27: Load-steel strain response for specimen *N61* at (a) mid-span; (b) d_v from mid-span; (c) support.

B.2.1.4 Crack Development

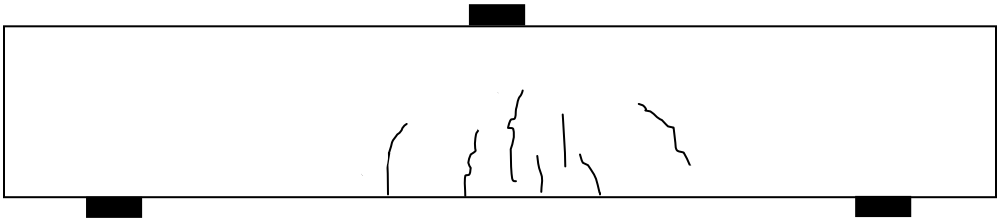

(a) At $P=240\ kN=0.48\ P_{max}$
(maximum flexural crack width < 0.08 *mm*)

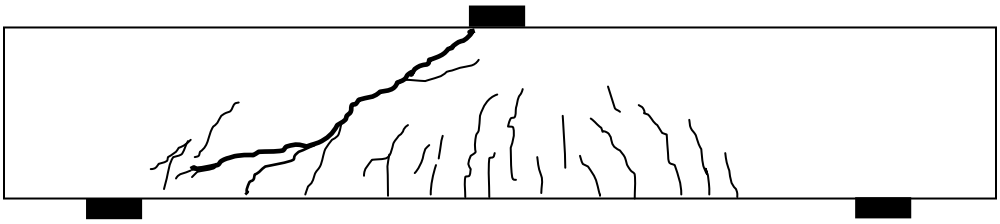

(b) After shear failure ($P_{max}=496\ kN$)

Figur B-28: Crack pattern for specimen *N61*.

B.2.2 Specimen *N62*

B.2.2.1 Instrumentation (Strain Gauges and LVDTs)

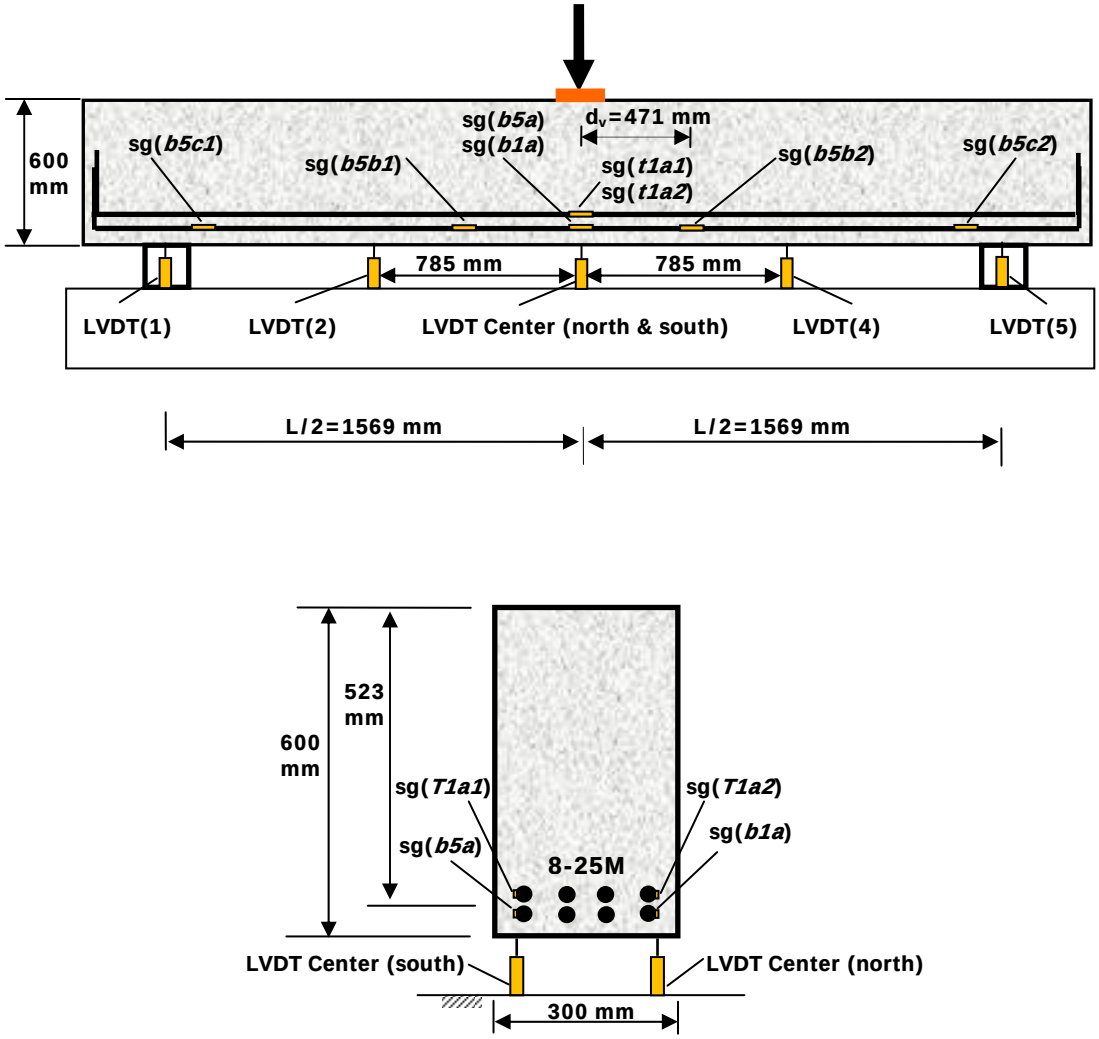

Mid-span Section

Figure B-29: Instrumentation for specimen *N62* (sg: strain gauge).

B.2.2.2 Load-Deflection Response

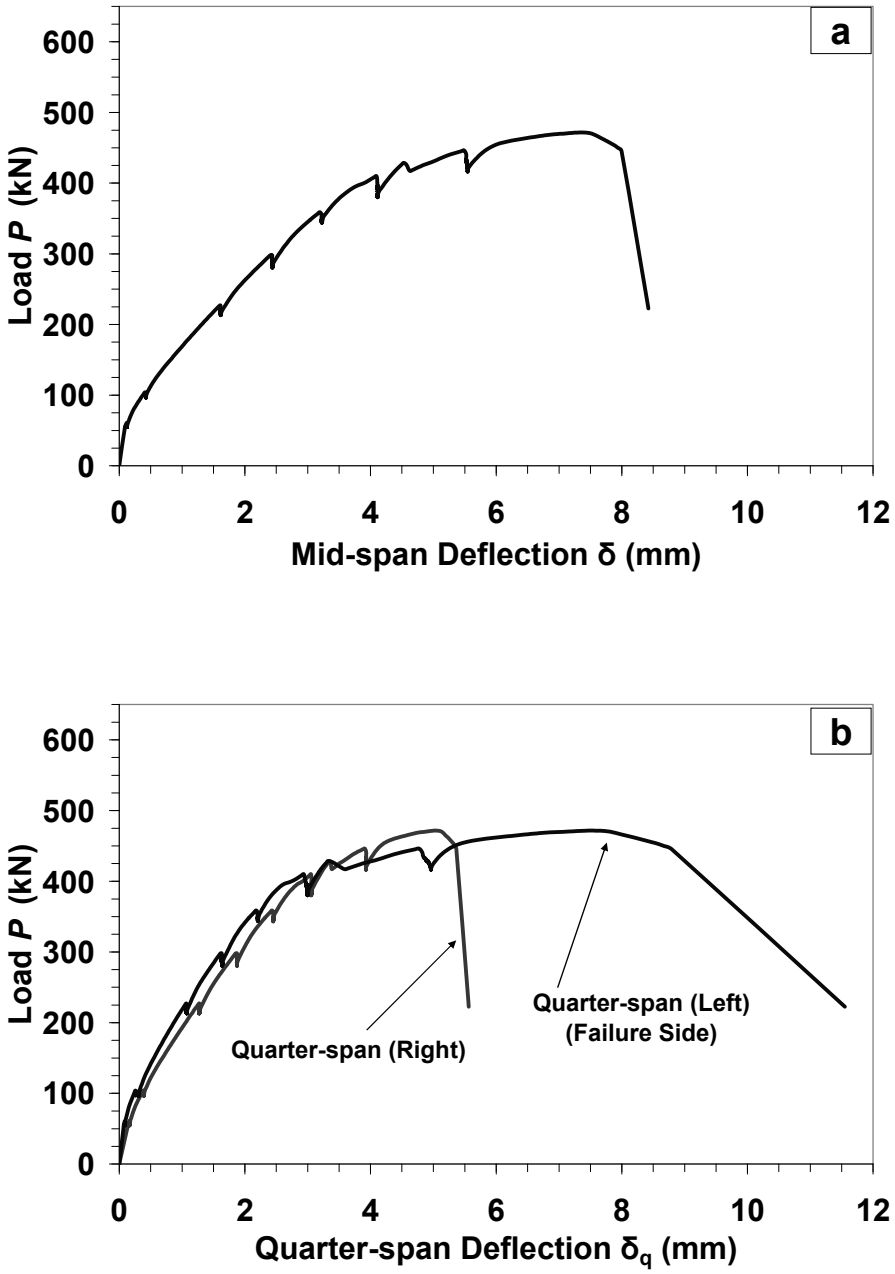

Figure B-30: Load-Deflection response for specimen *N62* at (a) mid-span; (b) quarter-span. (Note: all presented deflection data were corrected for the measured support settlement)

B.2.2.3 Load-Steel Strain Response

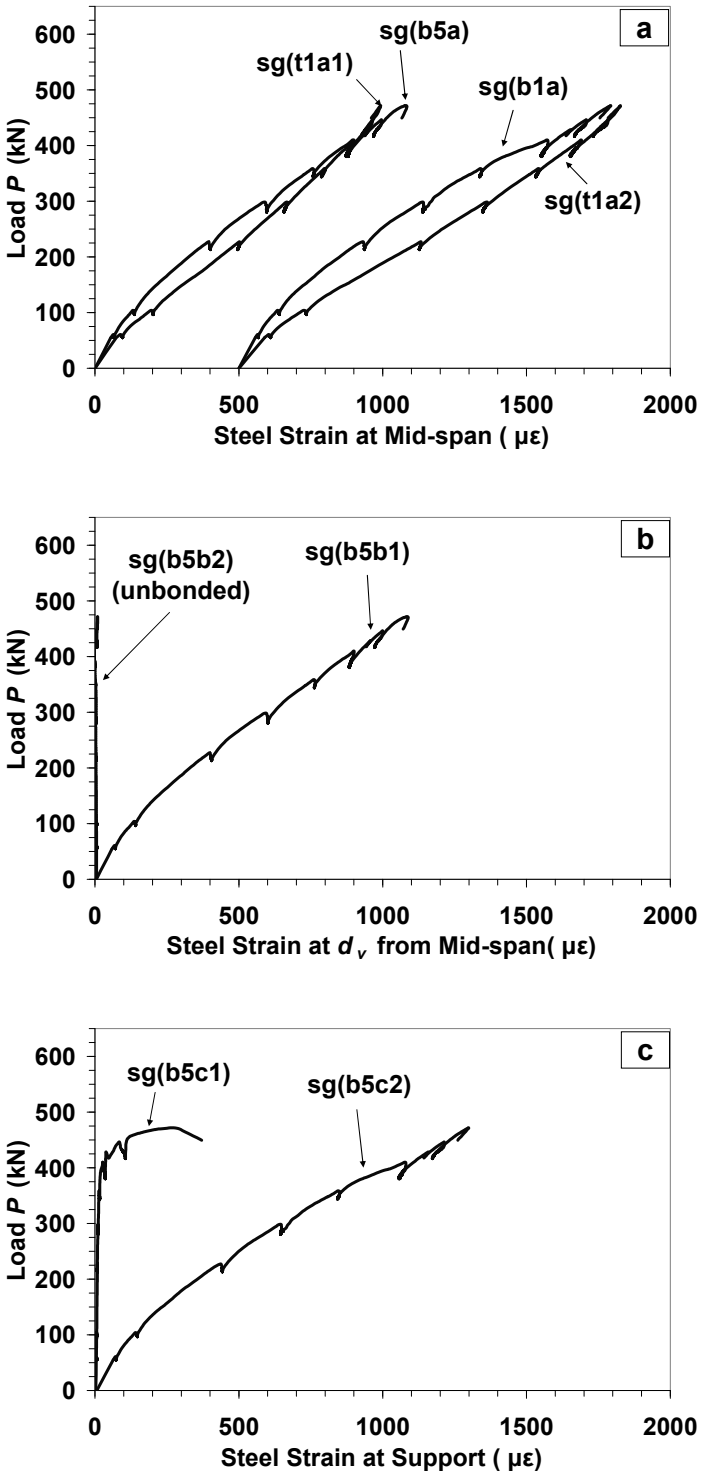

Figure B-31: Load-steel strain response for specimen *N62* at (a) mid-span; (b) d_v from mid-span; (c) support.

B.2.2.4 Crack Development

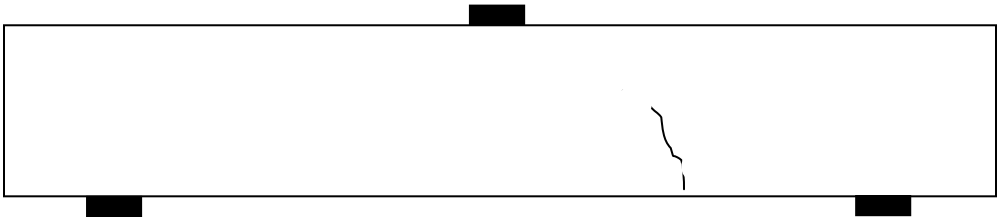

(a) At $P=227\ kN=0.48P_{max}$
(maximum flexural crack width < 0.08 *mm*)

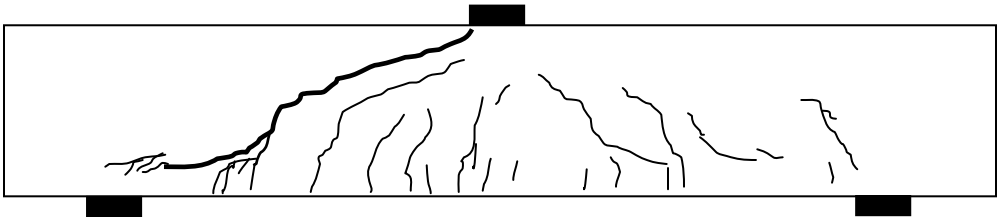

(b) After shear failure ($P_{max}=476\ kN$)

Figur B-32: Crack pattern for specimen *N62*.

B.2.3 Specimen *H61*

B.2.3.1 Instrumentation (Strain Gauges and LVDTs)

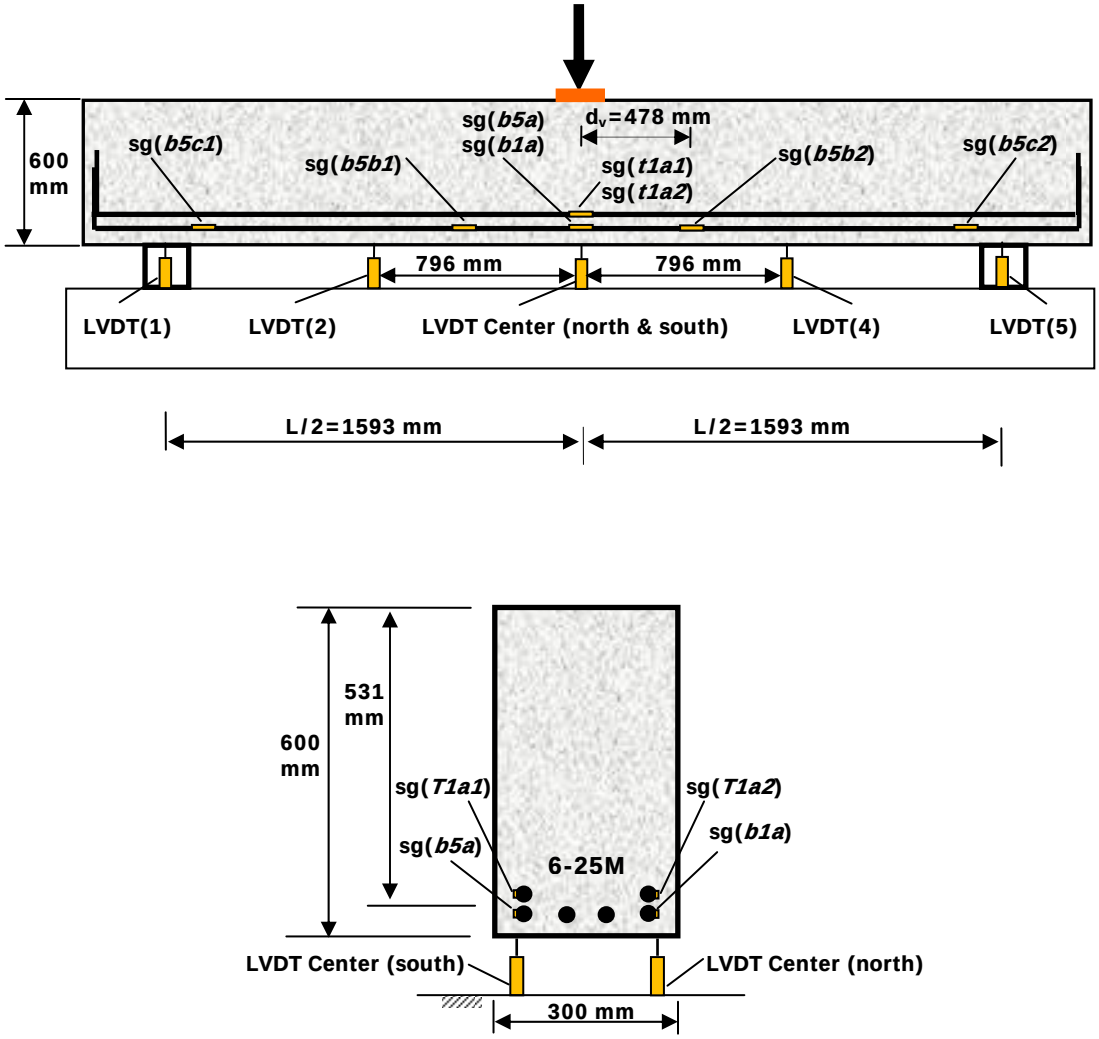

Mid-span Section

Figure B-33: Instrumentation for specimen *H61* (sg: strain gauge).

B.2.3.2 Load-Deflection Response

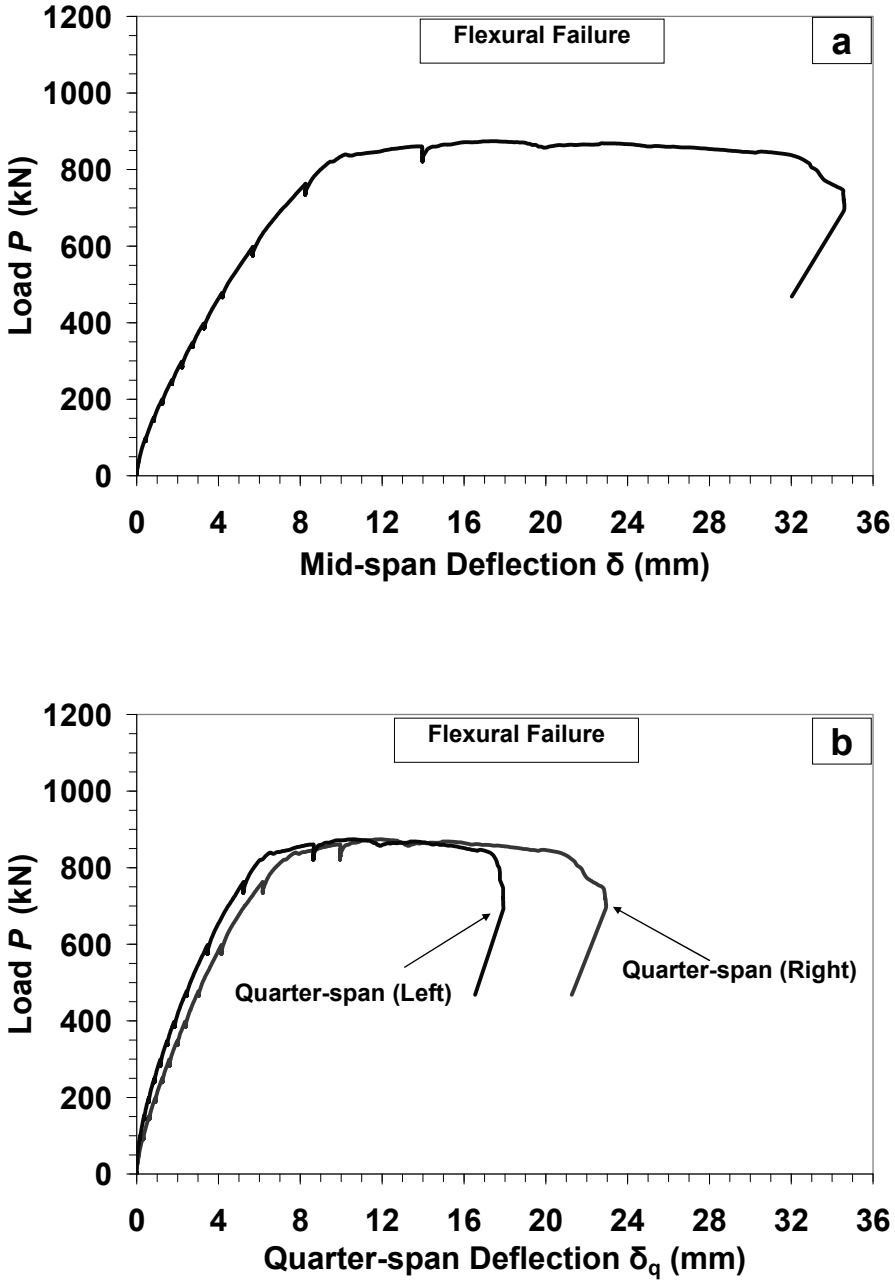

Figure B-34: Load-Deflection response for specimen *H61* at (a) mid-span; (b) quarter-span. (Note: all presented deflection data were corrected for the measured support settlement)

B.2.3.3 Load-Steel Strain Response

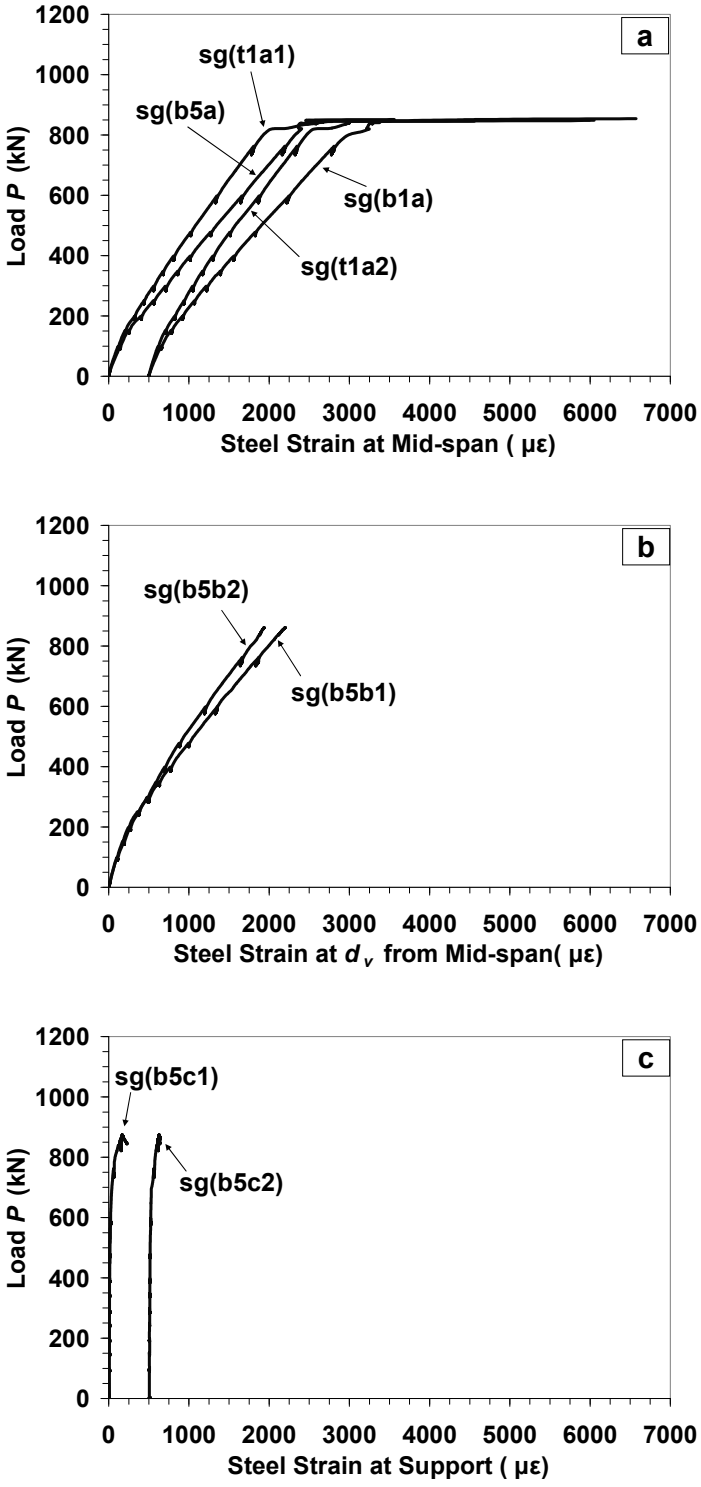

Figure B-35: Load-steel strain response for specimen *H61* at (a) mid-span; (b) d_v from mid-span; (c) support.

B.2.3.4 Crack Development

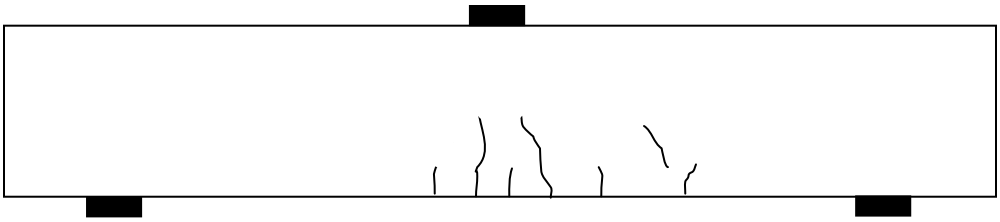

(a) At $P=400\ kN=0.48P_{max}$
(maximum flexural crack width < 0.08 *mm*)

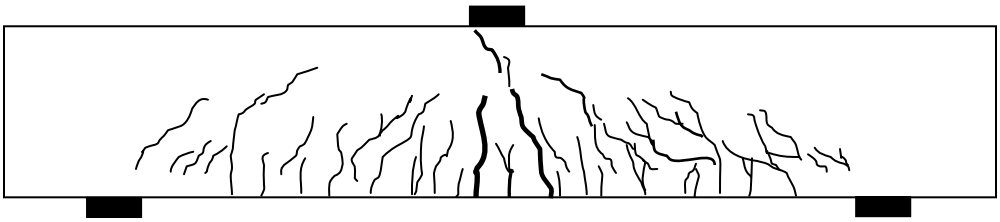

(b) After flexural failure ($P_{max}=838\ kN$)

Figur B-36: Crack pattern for specimen *H61*.

B.2.4 Specimen *H62*

B.2.4.1 Instrumentation (Strain Gauges and LVDTs)

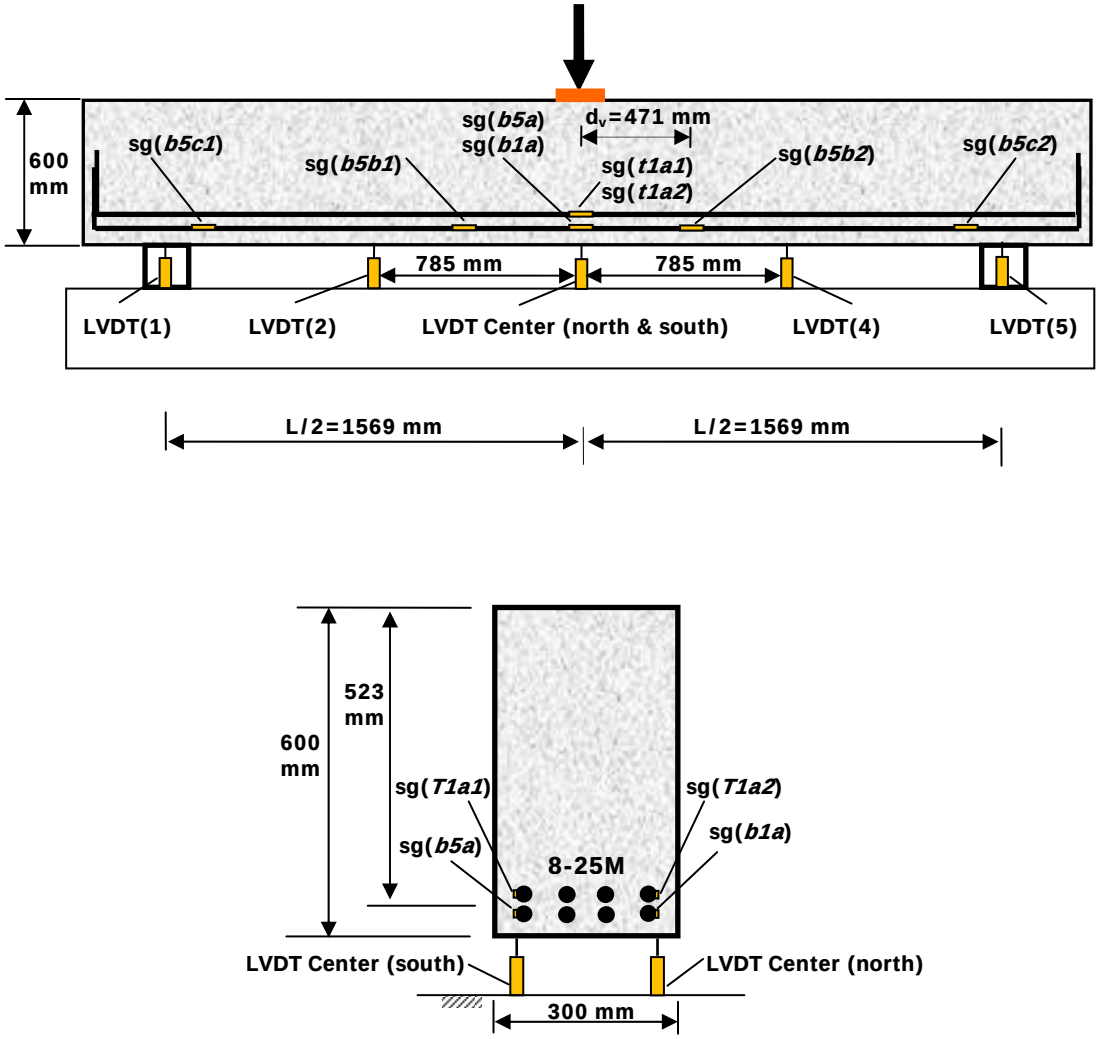

Mid-span Section

Figure B-37: Instrumentation for specimen *H62* (sg: strain gauge).

B.2.4.2 Load-Deflection Response

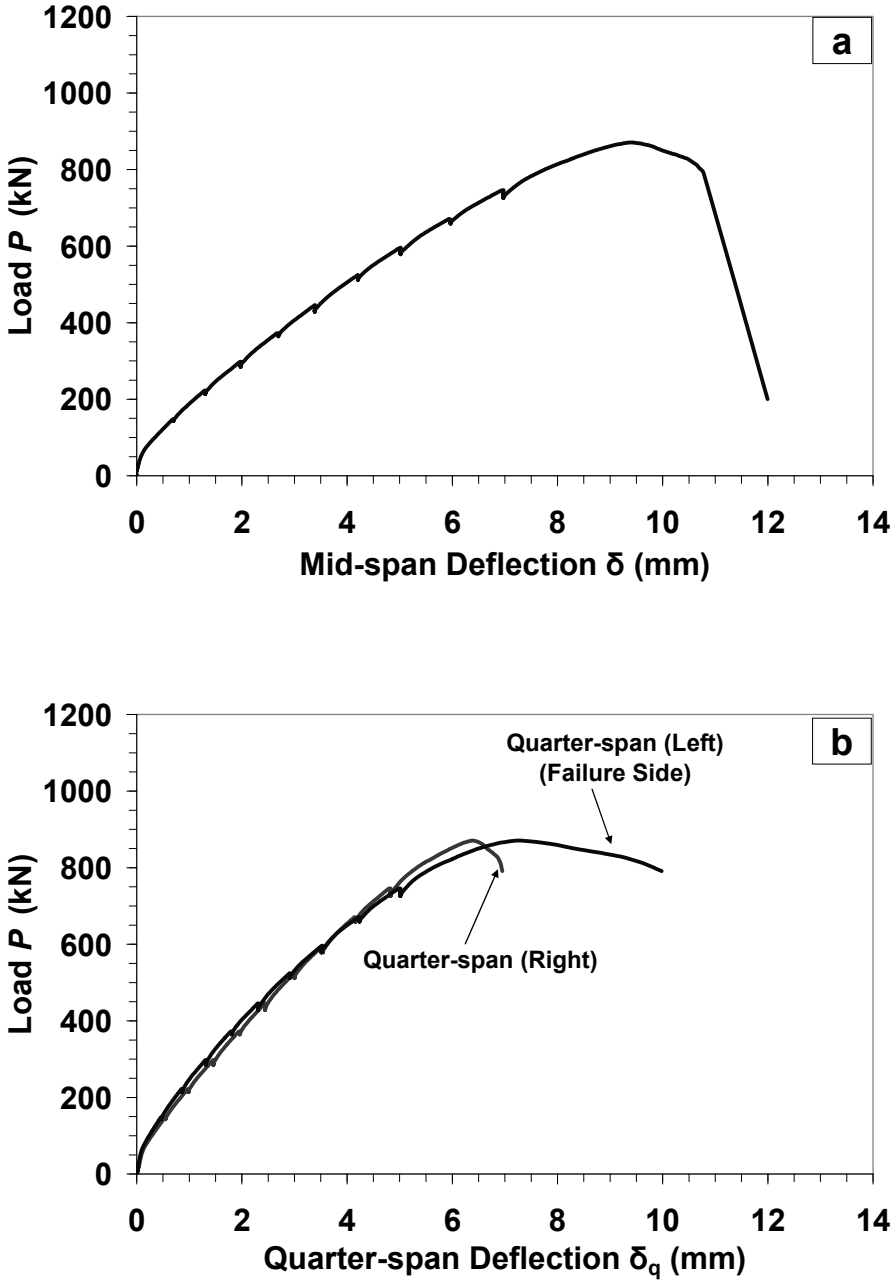

Figure B-38: Load-Deflection response for specimen *H62* at (a) mid-span; (b) quarter-span. (Note: all presented deflection data were corrected for the measured support settlement)

B.2.4.3 Load-Steel Strain Response

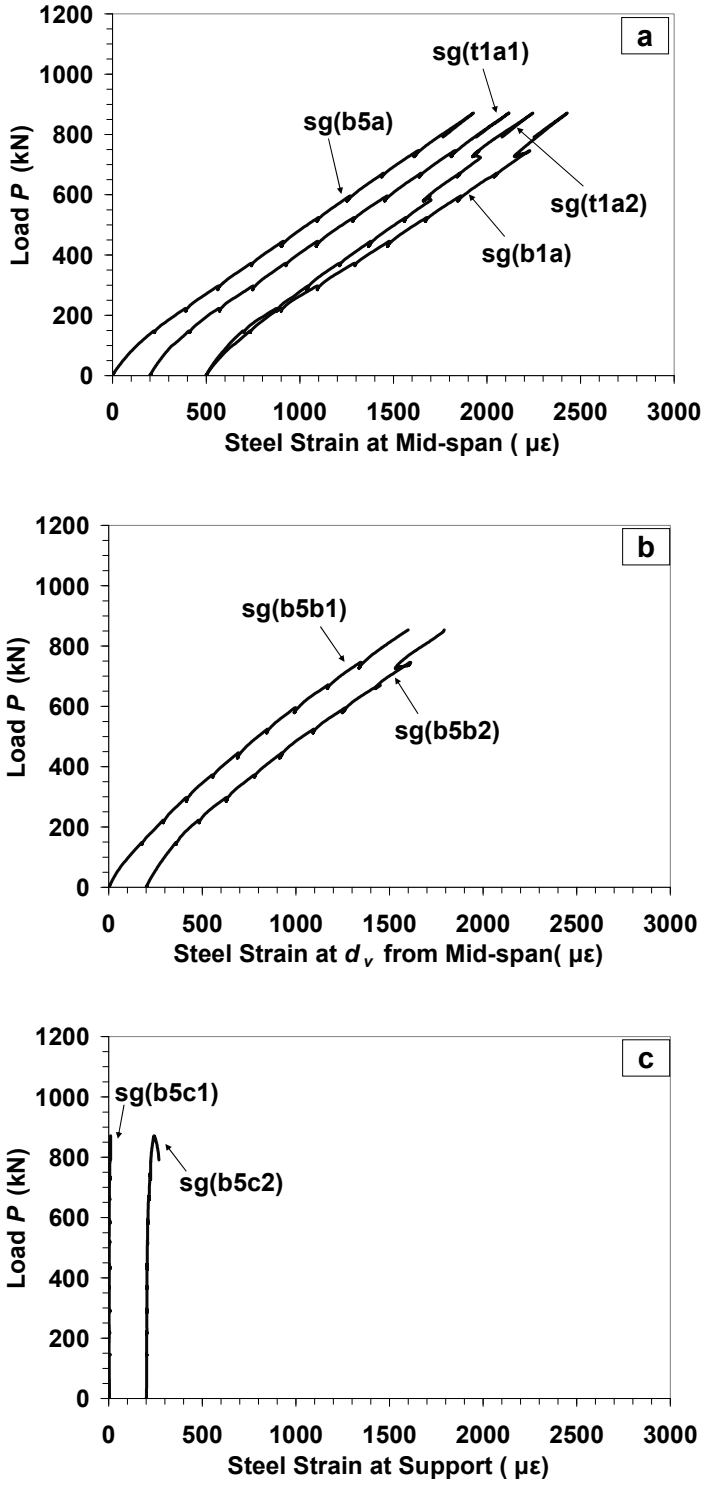

Figure B-39: Load-steel strain response for specimen *H62* at (a) mid-span; (b) d_v from mid-span; (c) support.

B.2.4.4 Crack Development

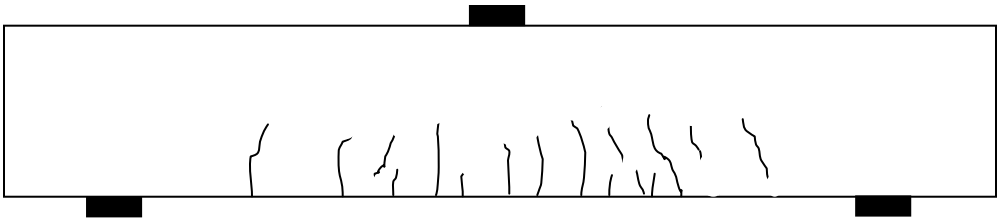

(a) At $P=450\ kN=0.51P_{max}$
(maximum flexural crack width < 0.08 *mm*)

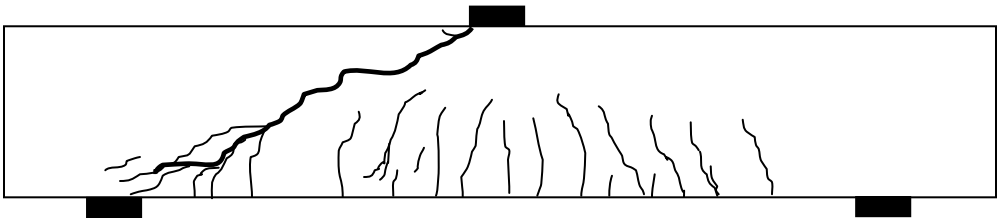

(b) After shear failure ($P_{max}=880\ kN$)

Figur B-40: Crack pattern for specimen *H62*.

B.2.5 Specimen *L61*

B.2.5.1 Instrumentation (Strain Gauges and LVDTs)

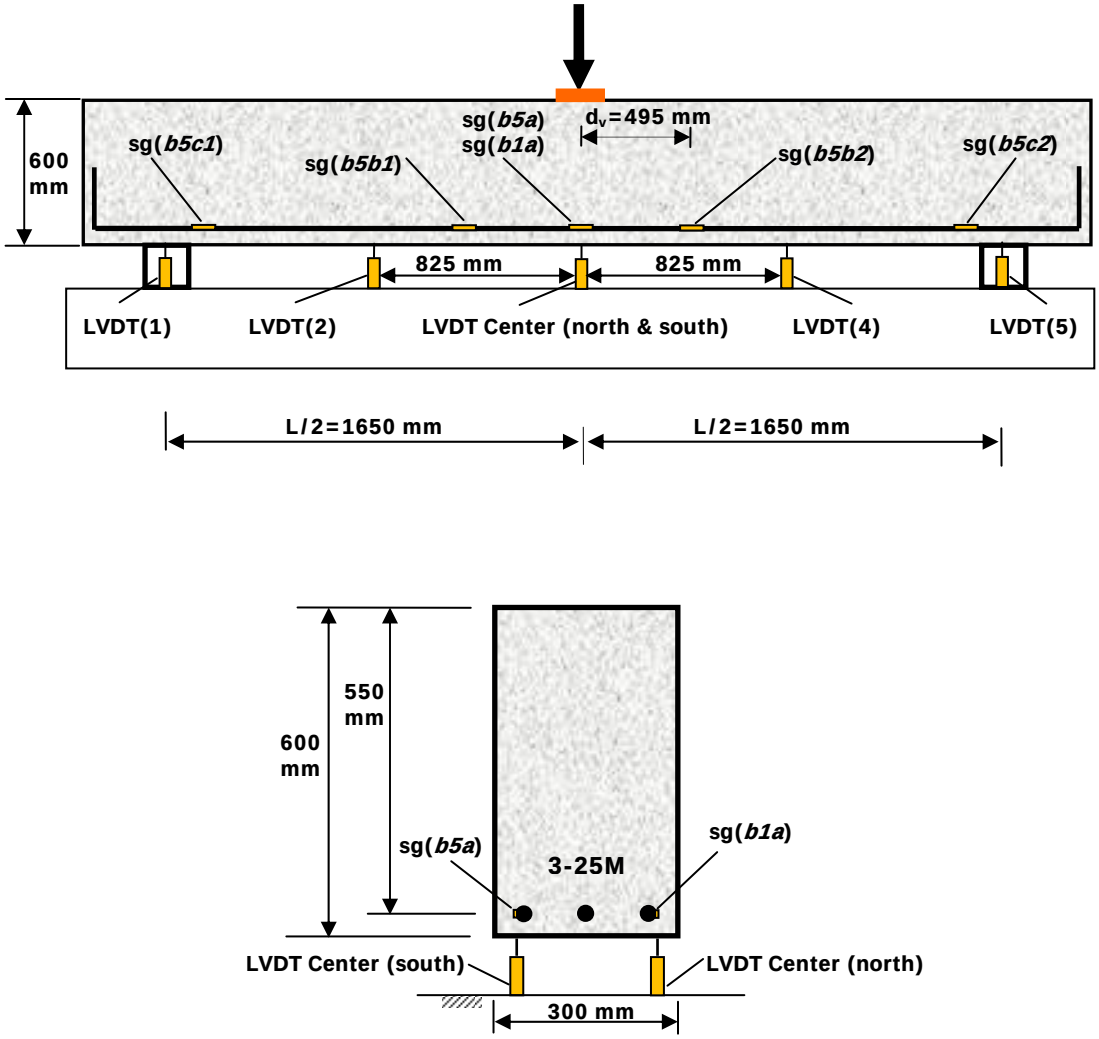

Mid-span Section

Figure B-41: Instrumentation for specimen *L61* (sg: strain gauge).

B.2.5.2 Load-Deflection Response

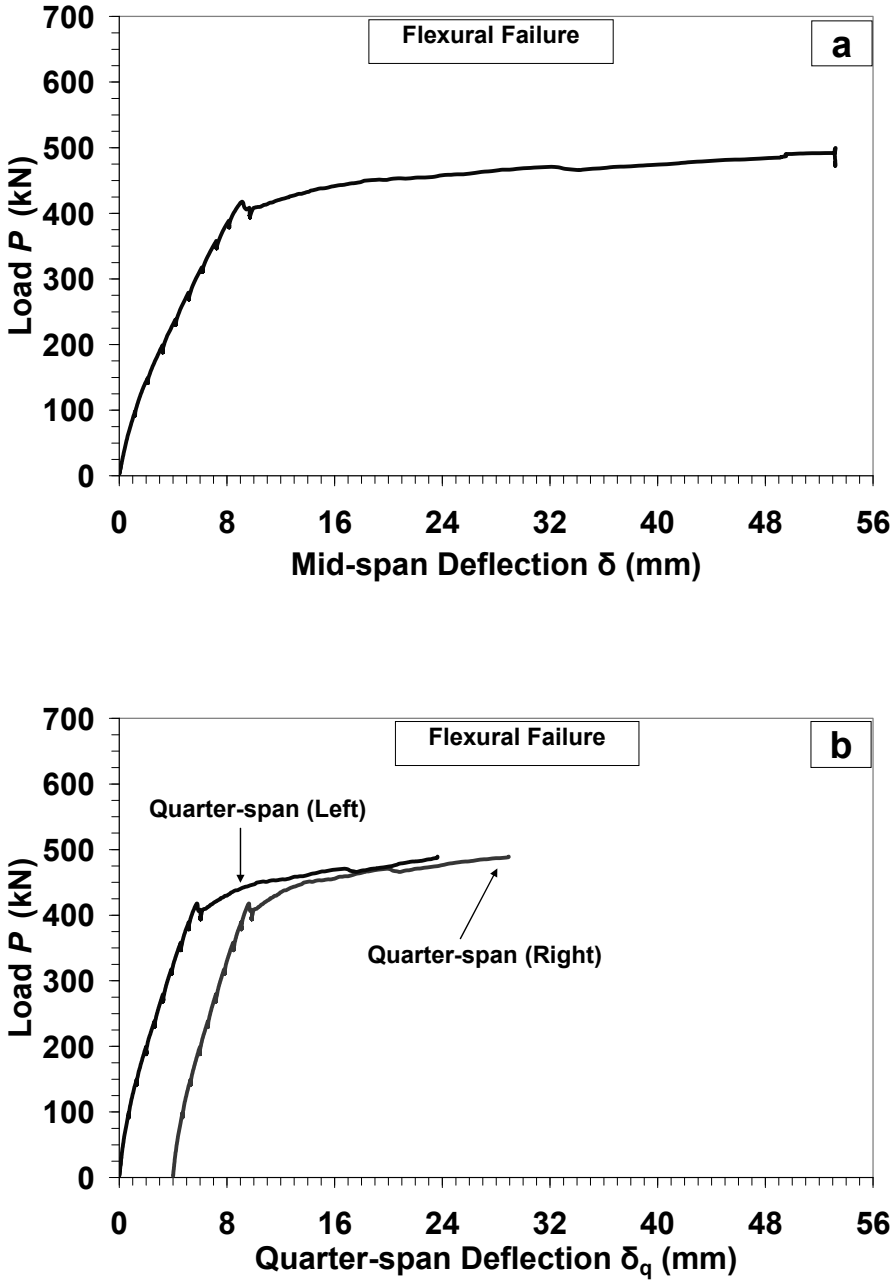

Figure B-42: Load-Deflection response for specimen *L61* at (a) mid-span; (b) quarter-span. (Note: all presented deflection data were corrected for the measured support settlement)

B.2.5.3 Load-Steel Strain Response

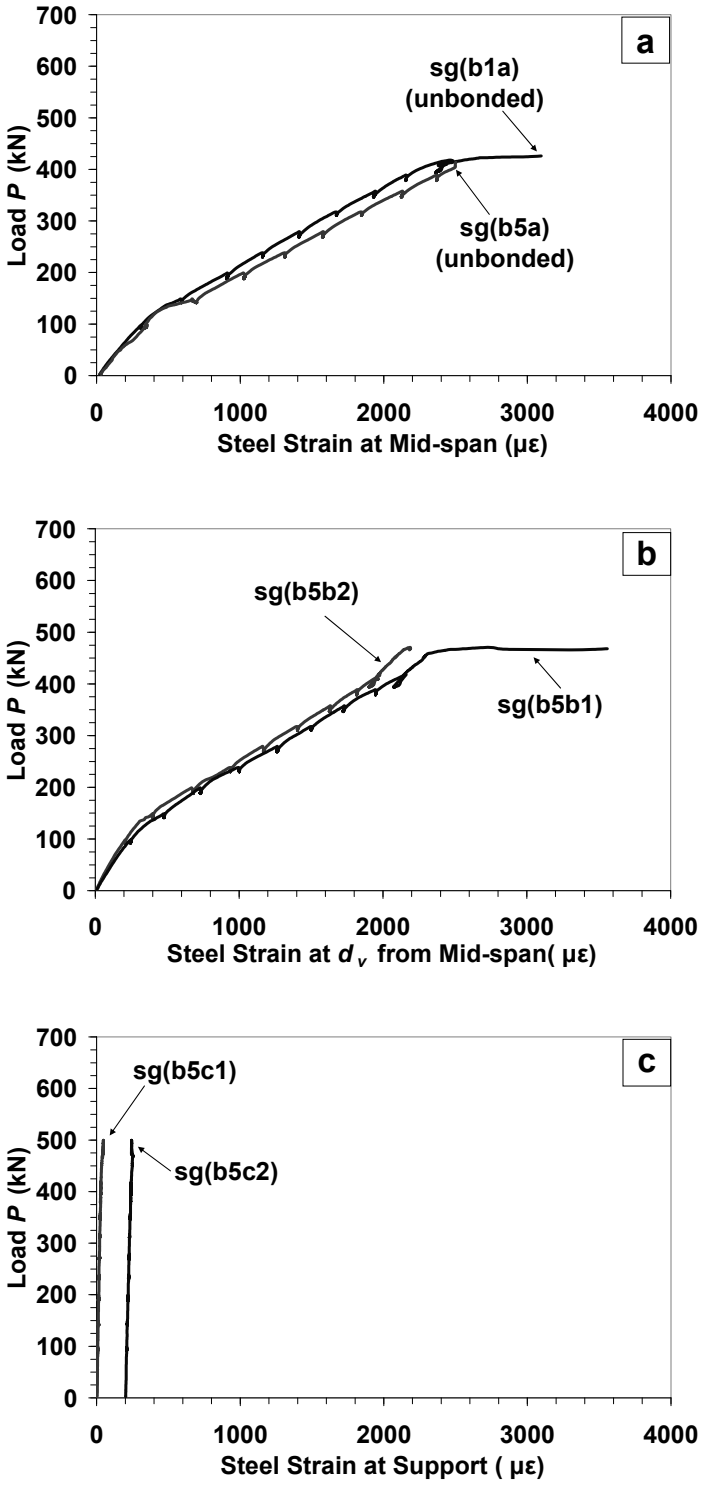

Figure B-43: Load-steel strain response for specimen *L61* at (a) mid-span; (b) d_v from mid-span; (c) support.

B.2.5.4 Crack Development

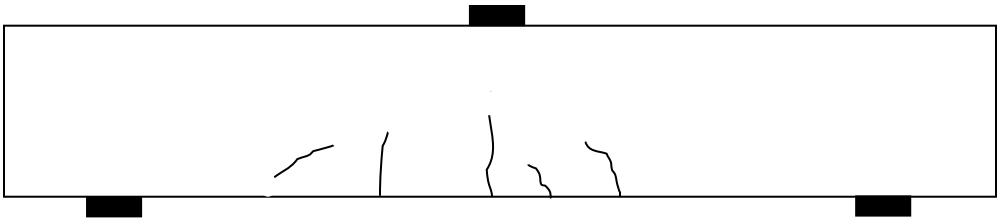

(a) At $P=240\ kN=0.48P_{max}$
(maximum flexural crack width < 0.08 *mm*)

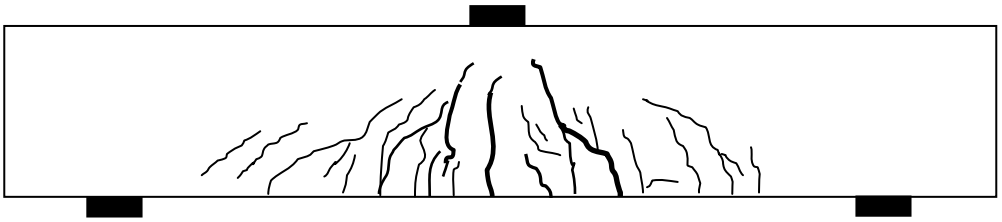

(b) After flexural failure ($P_{max}=497\ kN$)

Figur B-44: Crack pattern for specimen *L61*.

B.2.6 Specimen *L62*

B.2.6.1 Instrumentation (Strain Gauges and LVDTs)

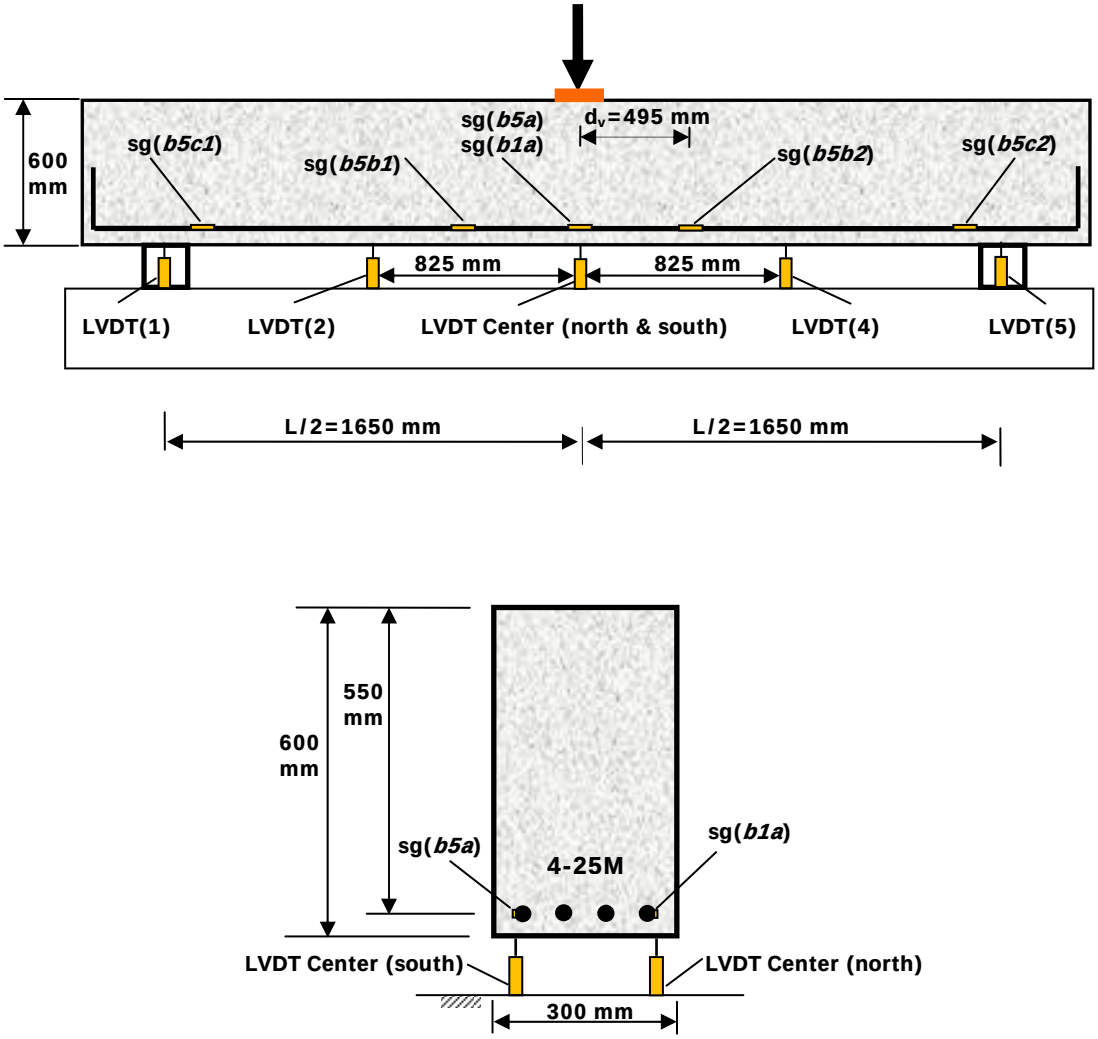

Mid-span Section

Figure B-45: Instrumentation for specimen *L62* (sg: strain gauge).

B.2.6.2 Load-Deflection Response

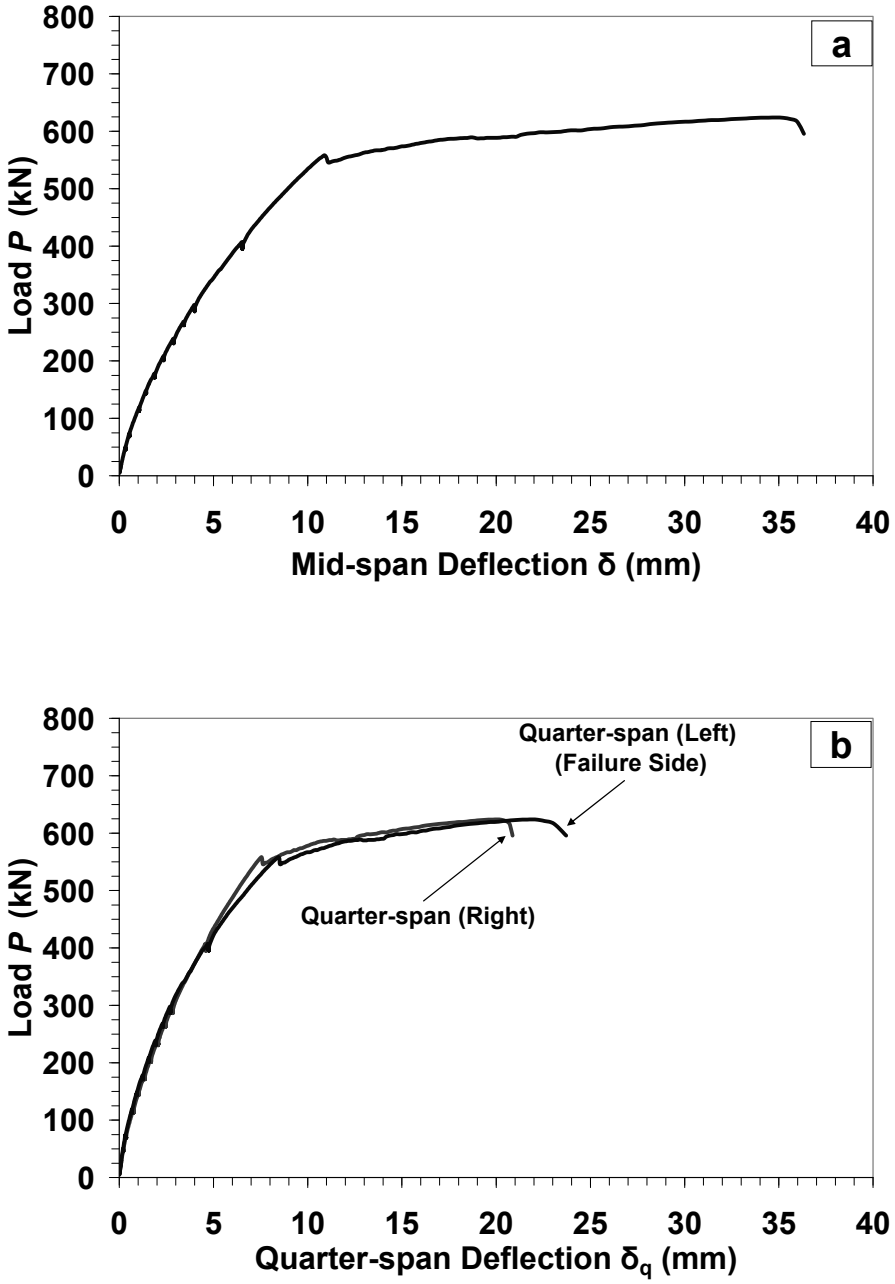

Figure B-46: Load-Deflection response for specimen *L62* at (a) mid-span; (b) quarter-span. (Note: all presented deflection data were corrected for the measured support settlement)

B.2.6.3 Load-Steel Strain Response

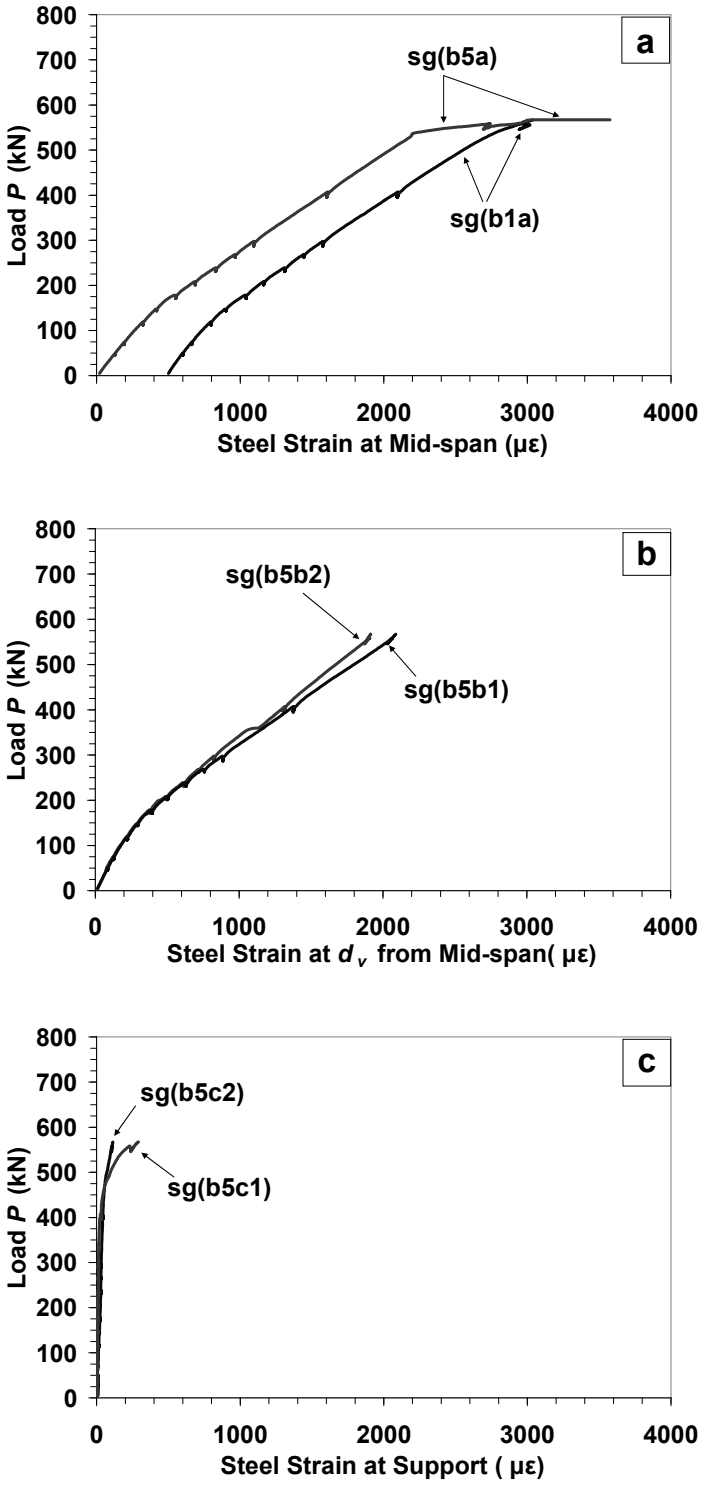

Figure B-47: Load-steel strain response for specimen *L62* at (a) mid-span; (b) d_v from mid-span; (c) support.

B.2.6.4 Crack Development

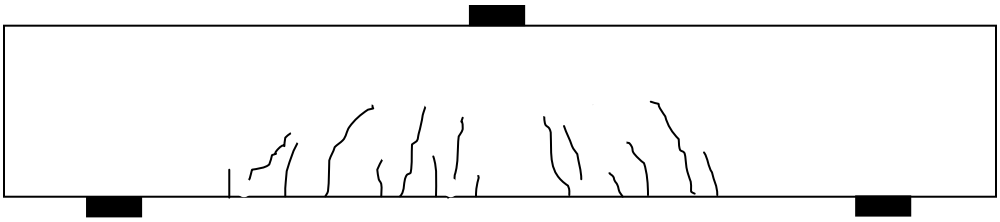

(a) At $P=300\ kN=0.49P_{max}$
(maximum flexural crack width < 0.08 *mm*)

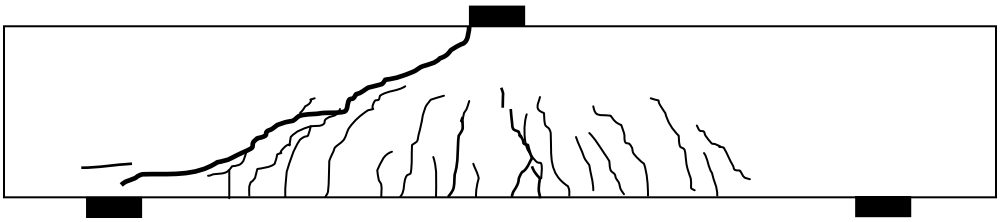

(b) After shear failure ($P_{max}=612\ kN$)

Figur B-48: Crack pattern for specimen *L62*.

B.3 Specimens with *h=1000 mm*

B.3.1 Specimen *N10-1*

B.3.1.1 Instrumentation (Strain Gauges and LVDTs)

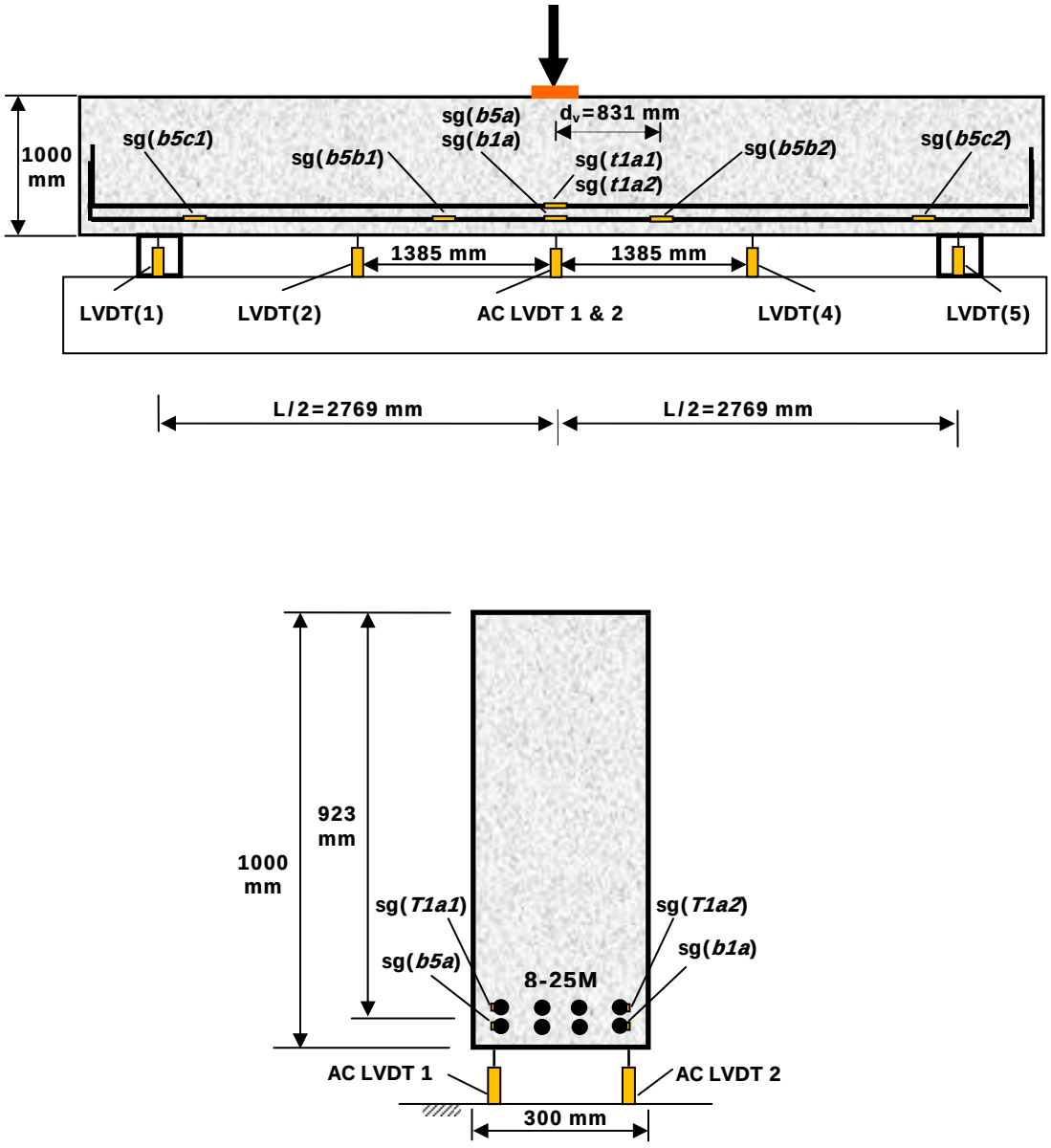

Mid-span Section

Figure B-49: Instrumentation for specimen *N10-1* (sg: strain gauge).

B.3.1.2 Load-Deflection Response

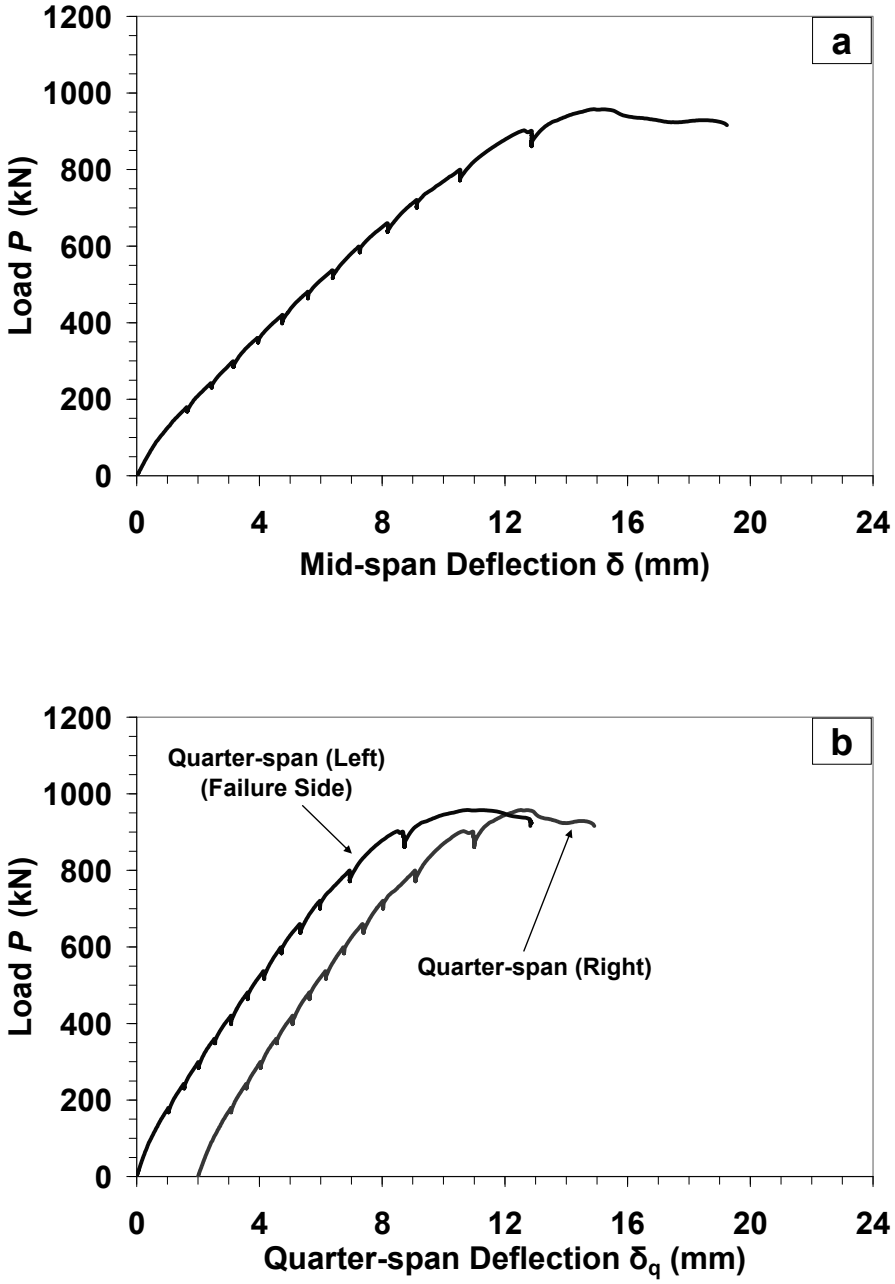

Figure B-50: Load-Deflection response for specimen *N10-1* at (a) mid-span; (b) quarter-span. (Note: all presented deflection data were corrected for the measured support settlement)

B.3.1.3 Load-Steel Strain Response

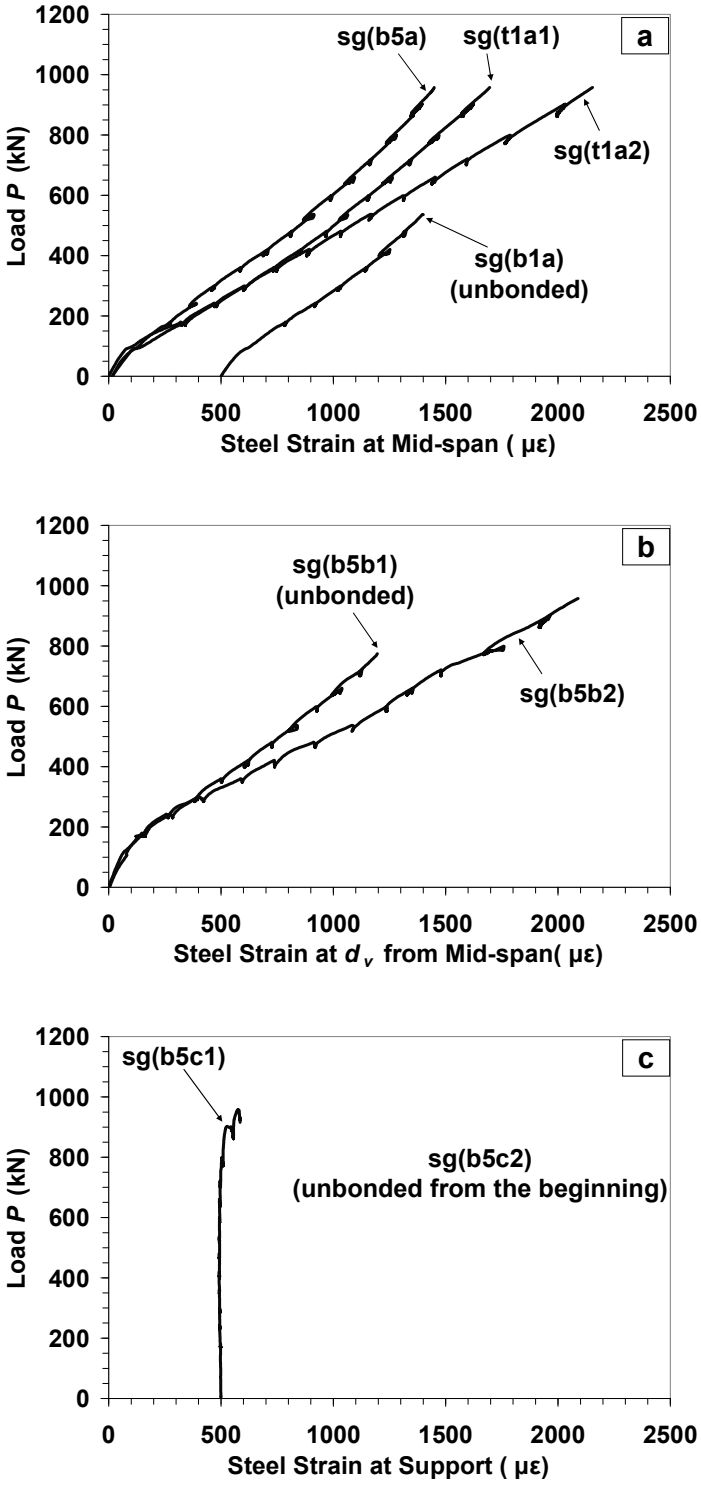

Figure B-51: Load-steel strain response for specimen *N10-1* at (a) mid-span; (b) d_v from mid-span; (c) support.

B.3.1.4 Crack Development

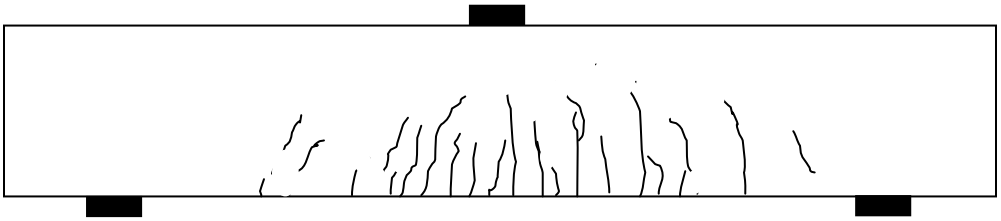

(a) At $P=420\ kN=0.44P_{max}$
(maximum flexural crack width = 0.08 *mm*)

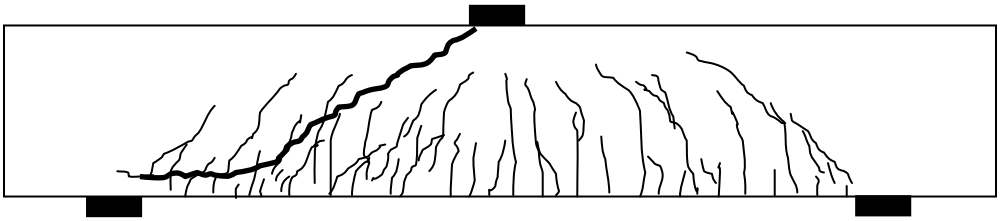

(b) After shear failure ($P_{max}=958\ kN$)

Figur B-52: Crack pattern for specimen *N10-1*.

B.3.2 Specimen *N10-2*

B.3.2.1 Instrumentation (Strain Gauges and LVDTs)

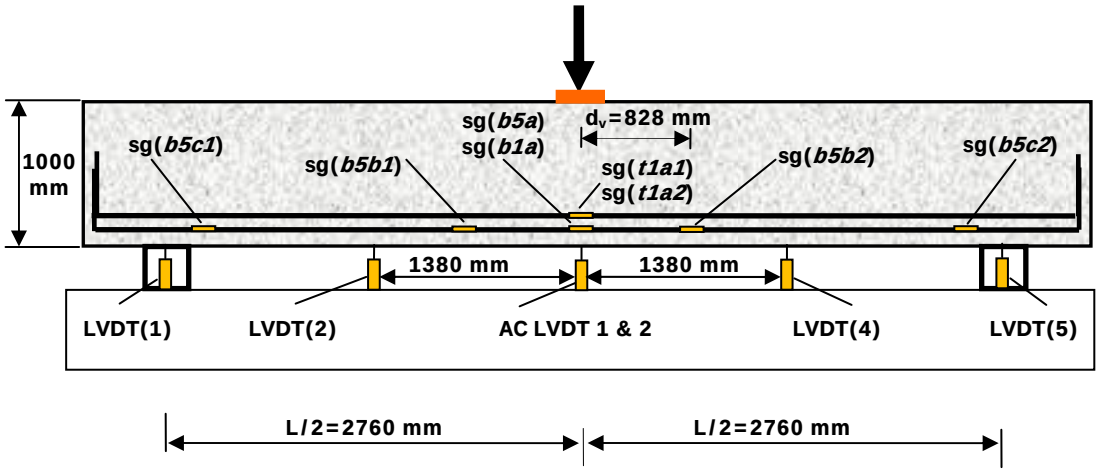

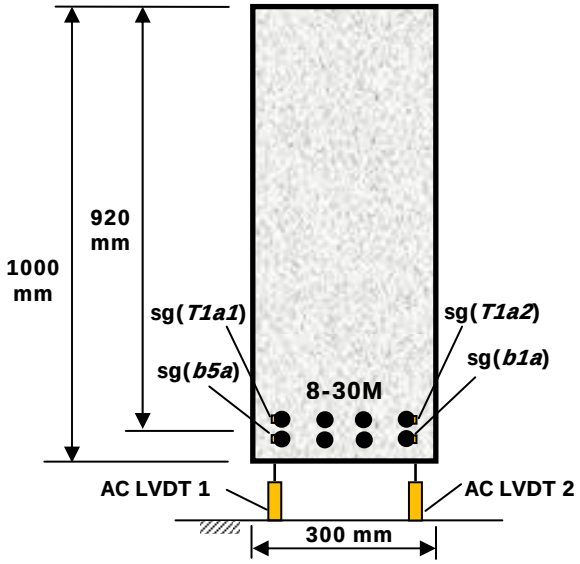

Mid-span Section

Figure B-53: Instrumentation for specimen *N10-2* (sg: strain gauge).

B.3.2.2 Load-Deflection Response

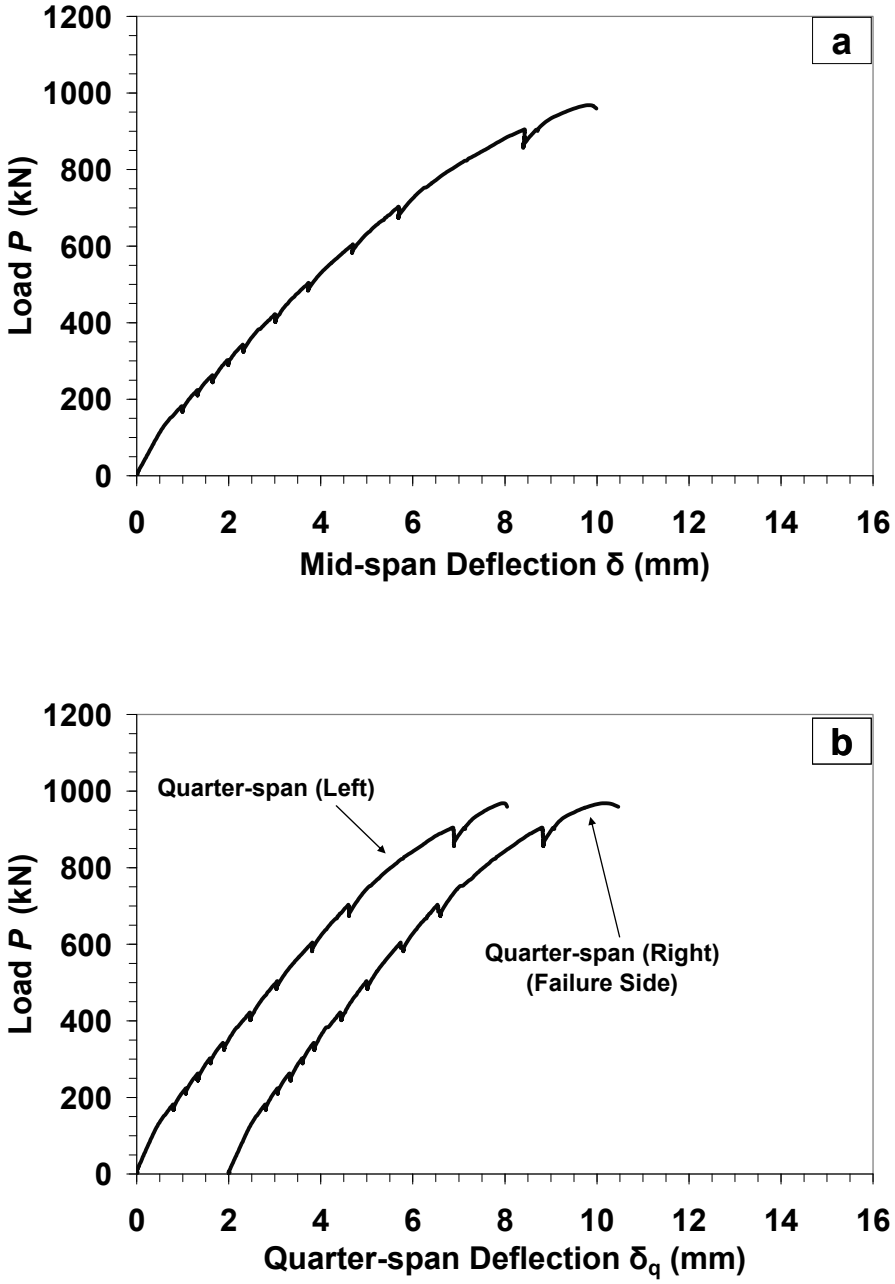

Figure B-54: Load-Deflection response for specimen *N10-2* at (a) mid-span; (b) quarter-span. (Note: all presented deflection data were corrected for the measured support settlement)

B.3.2.3 Load-Steel Strain Response

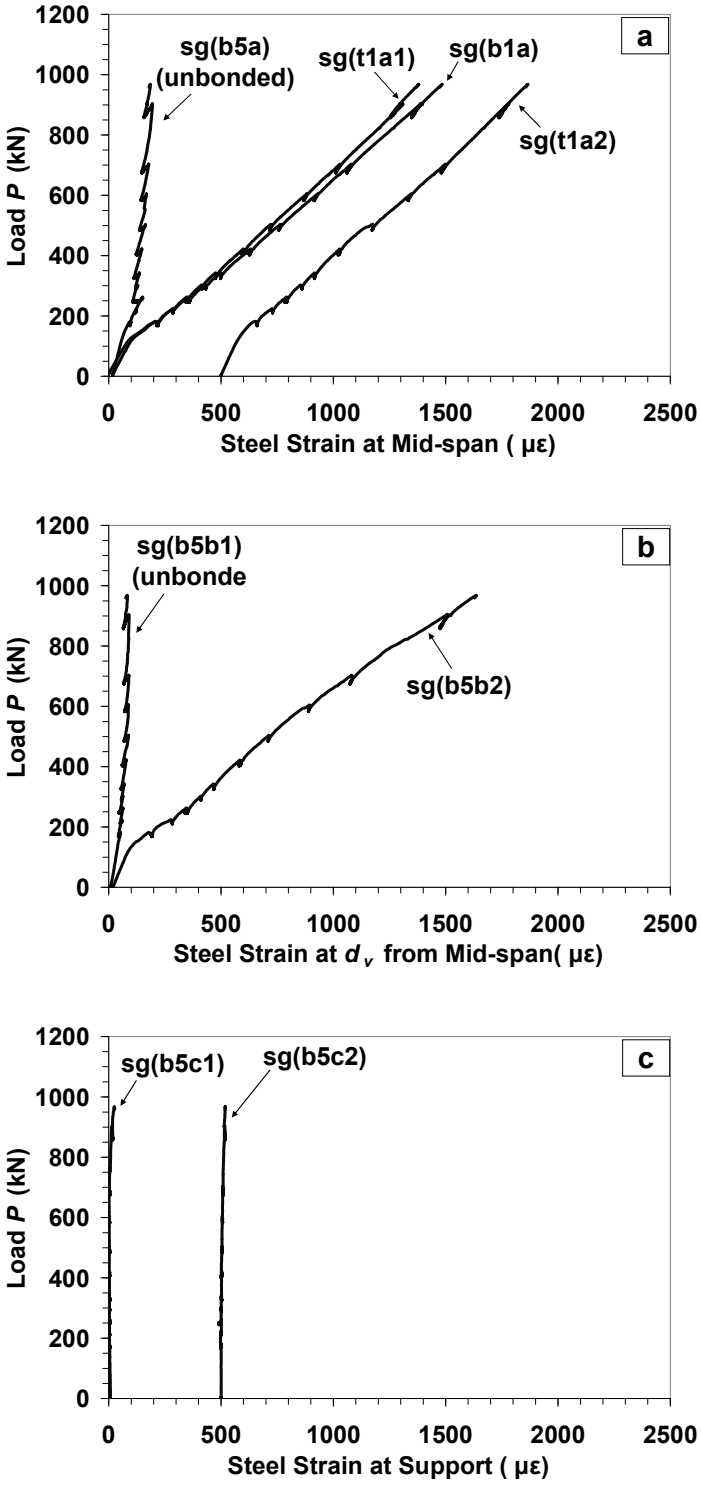

Figure B-55: Load-steel strain response for specimen *N10-2* at (a) mid-span; (b) d_v from mid-span; (c) support.

B.3.2.4 Crack Development

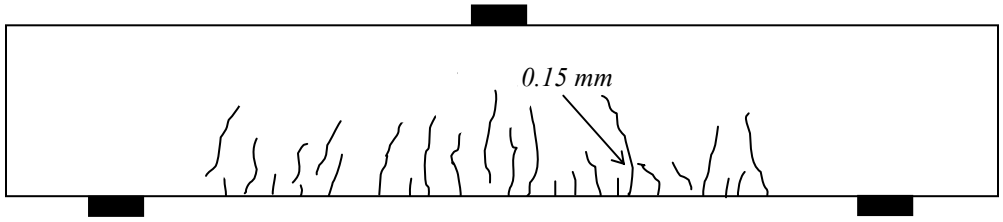

(a) At $P=420\ kN=0.43P_{max}$
(maximum flexural crack width = 0.15 *mm*)

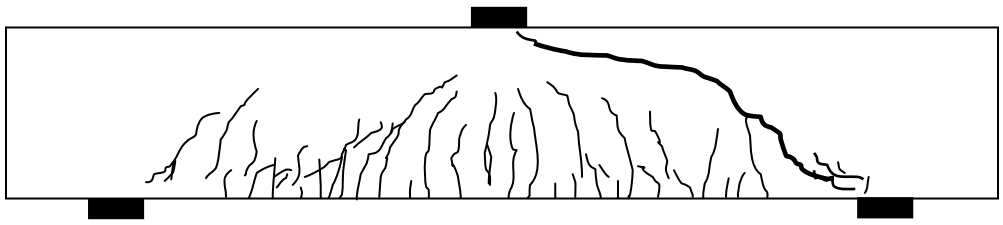

(b) After shear failure ($P_{max}=968\ kN$)

Figur B-56: Crack pattern for specimen *N10-2*.

B.3.3 Specimen *H10-1*

B.3.3.1 Instrumentation (Strain Gauges and LVDTs)

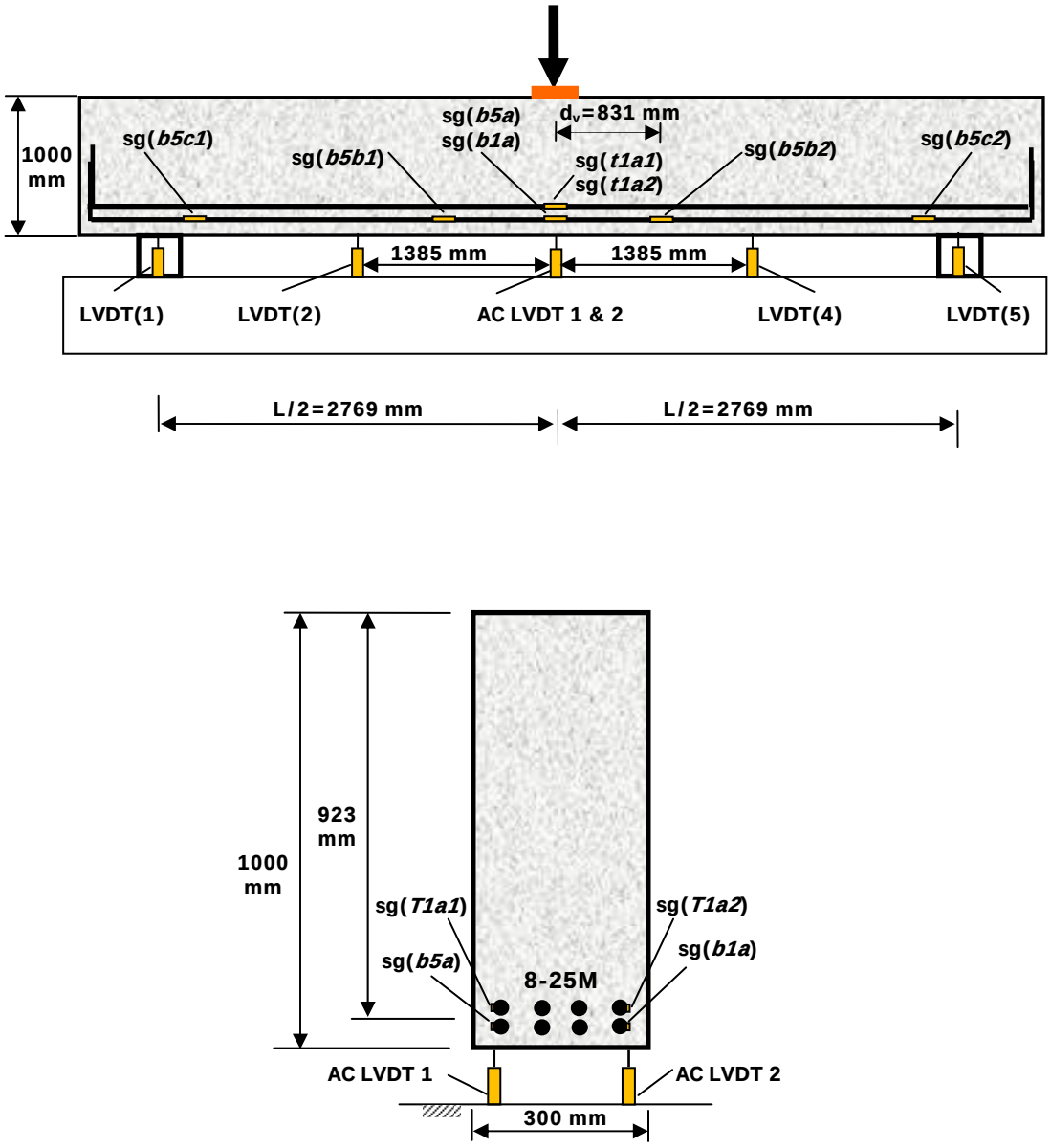

Mid-span Section

Figure B-57: Instrumentation for specimen *H10-1* (sg: strain gauge).

B.3.3.2 Load-Deflection Response

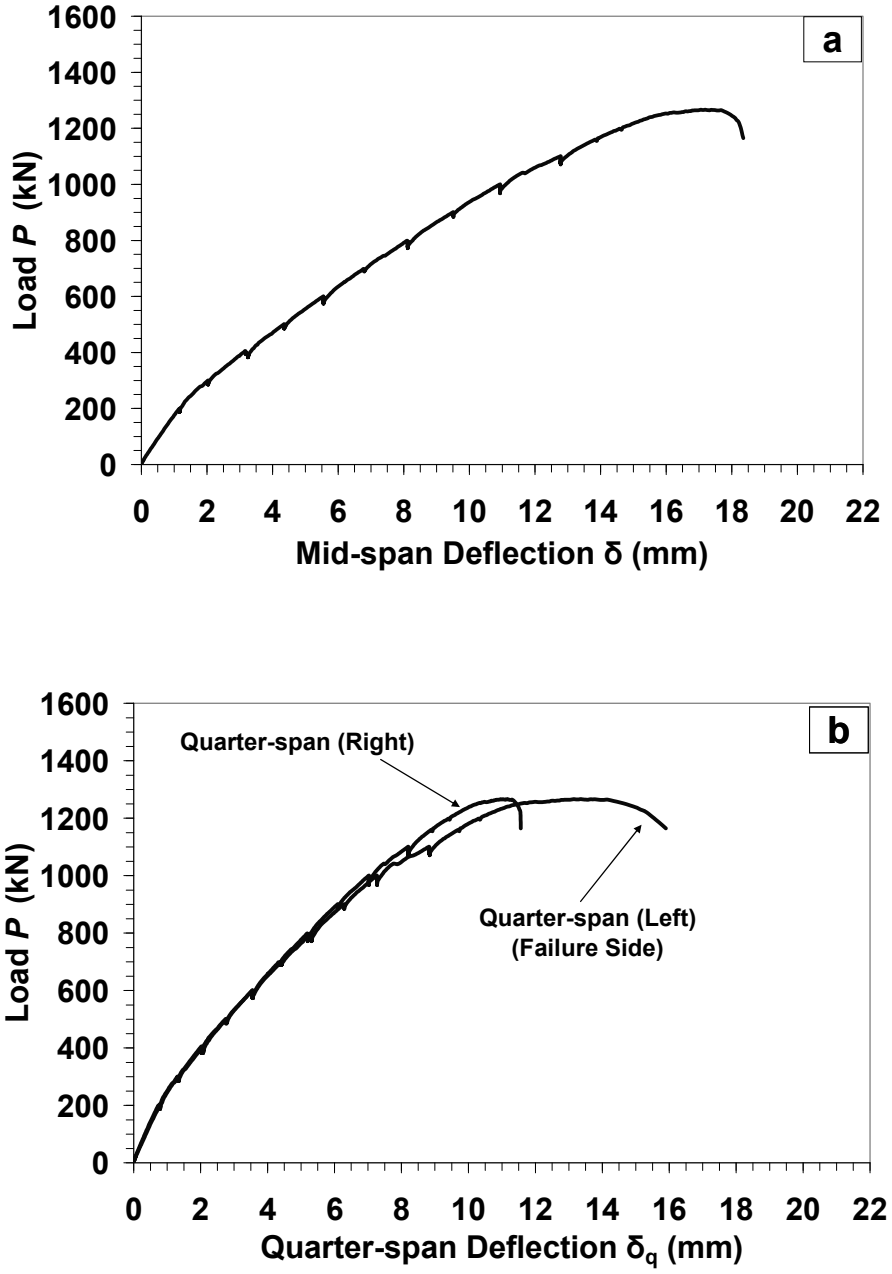

Figure B-58: Load-Deflection response for specimen *H10-1* at (a) mid-span; (b) quarter-span. (Note: all presented deflection data were corrected for the measured support settlement)

B.3.3.3 Load-Steel Strain Response

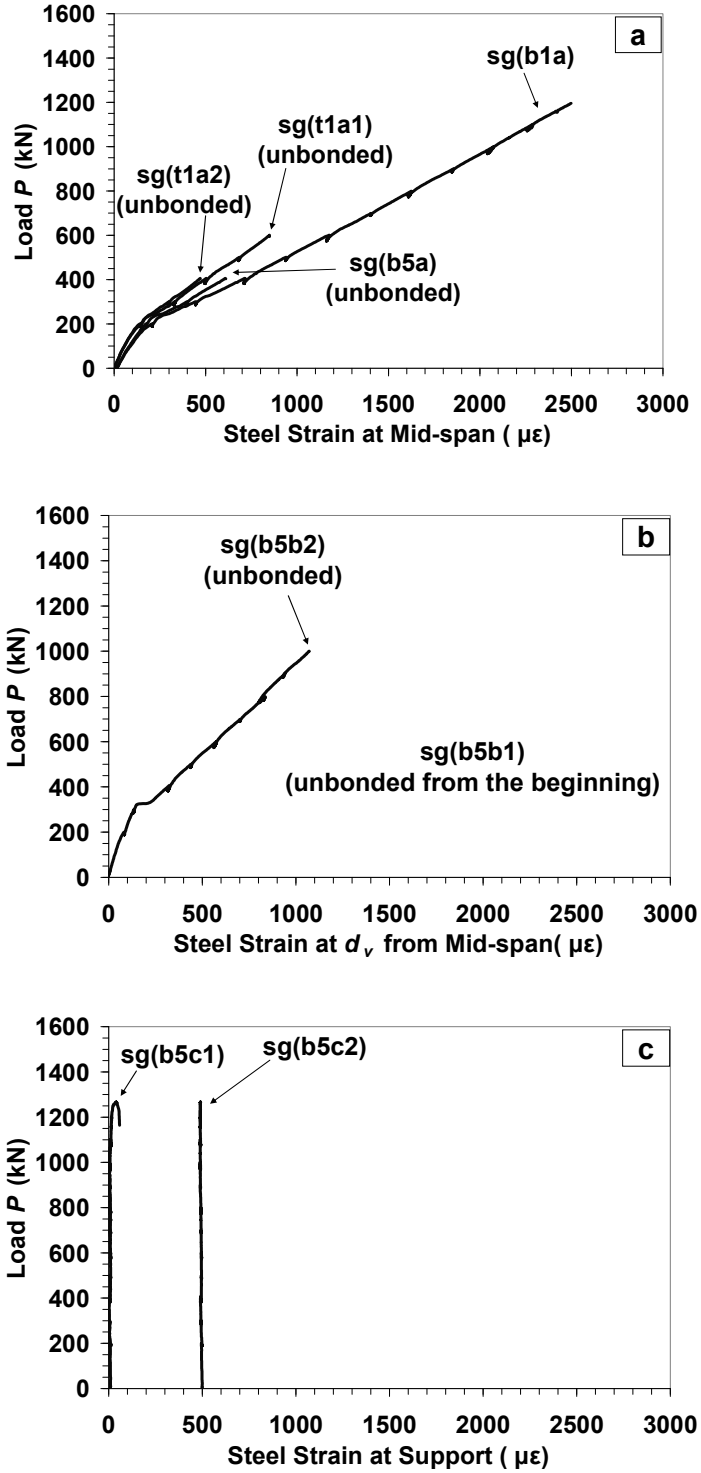

Figure B-59: Load-steel strain response for specimen *H10-1* at (a) mid-span; (b) d_v from mid-span; (c) support.

B.3.3.4 Crack Development

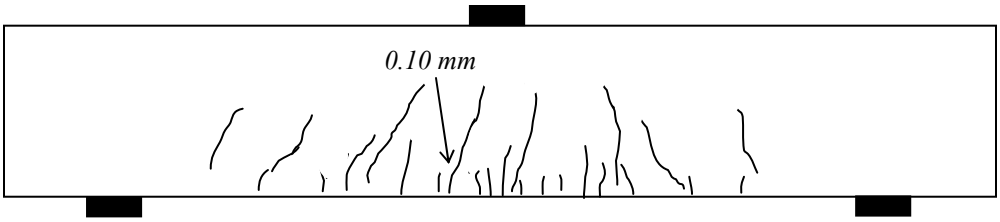

(a) At $P=600\ kN=0.47P_{max}$
(maximum flexural crack width = 0.10 *mm*)

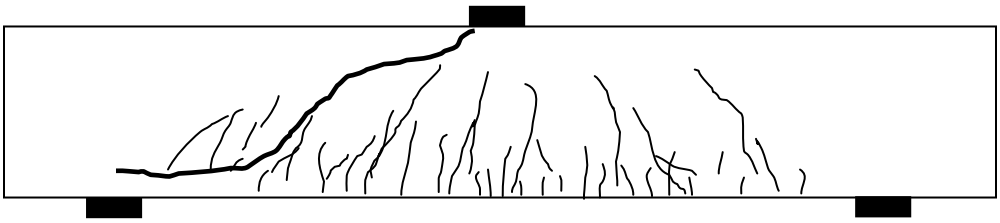

(b) After shear failure ($P_{max}=1265\ kN$)

Figur B-60: Crack pattern for specimen *H10-1*.

B.3.4 Specimen *H10-2*

B.3.4.1 Instrumentation (Strain Gauges and LVDTs)

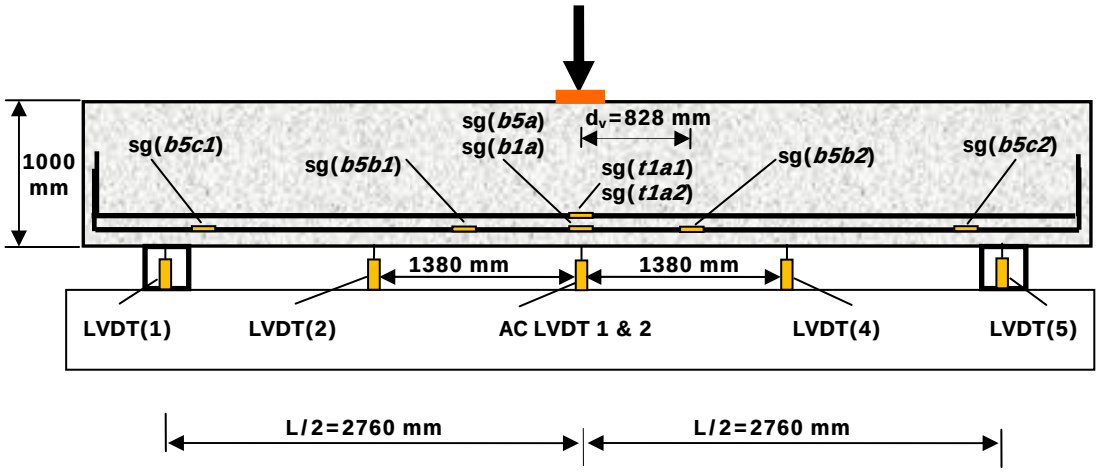

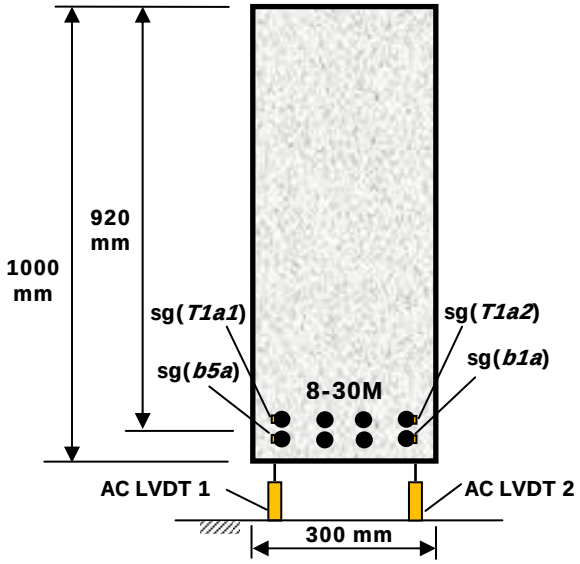

Mid-span Section

Figure B-61: Instrumentation for specimen *H10-2* (sg: strain gauge).

B.3.4.2 Load-Deflection Response

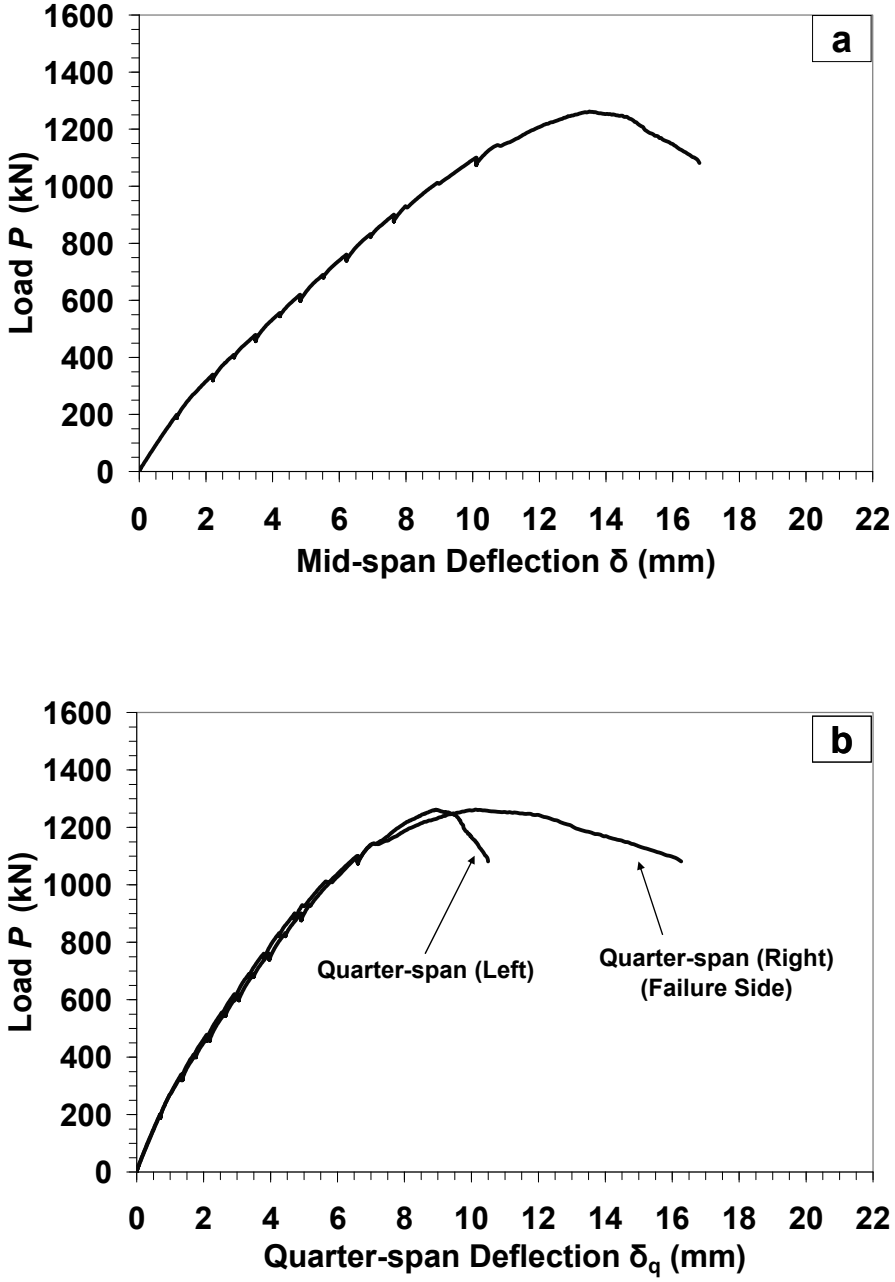

Figure B-62: Load-Deflection response for specimen *H10-2* at (a) mid-span; (b) quarter-span. (Note: all presented deflection data were corrected for the measured support settlement)

B.3.4.3 Load-Steel Strain Response

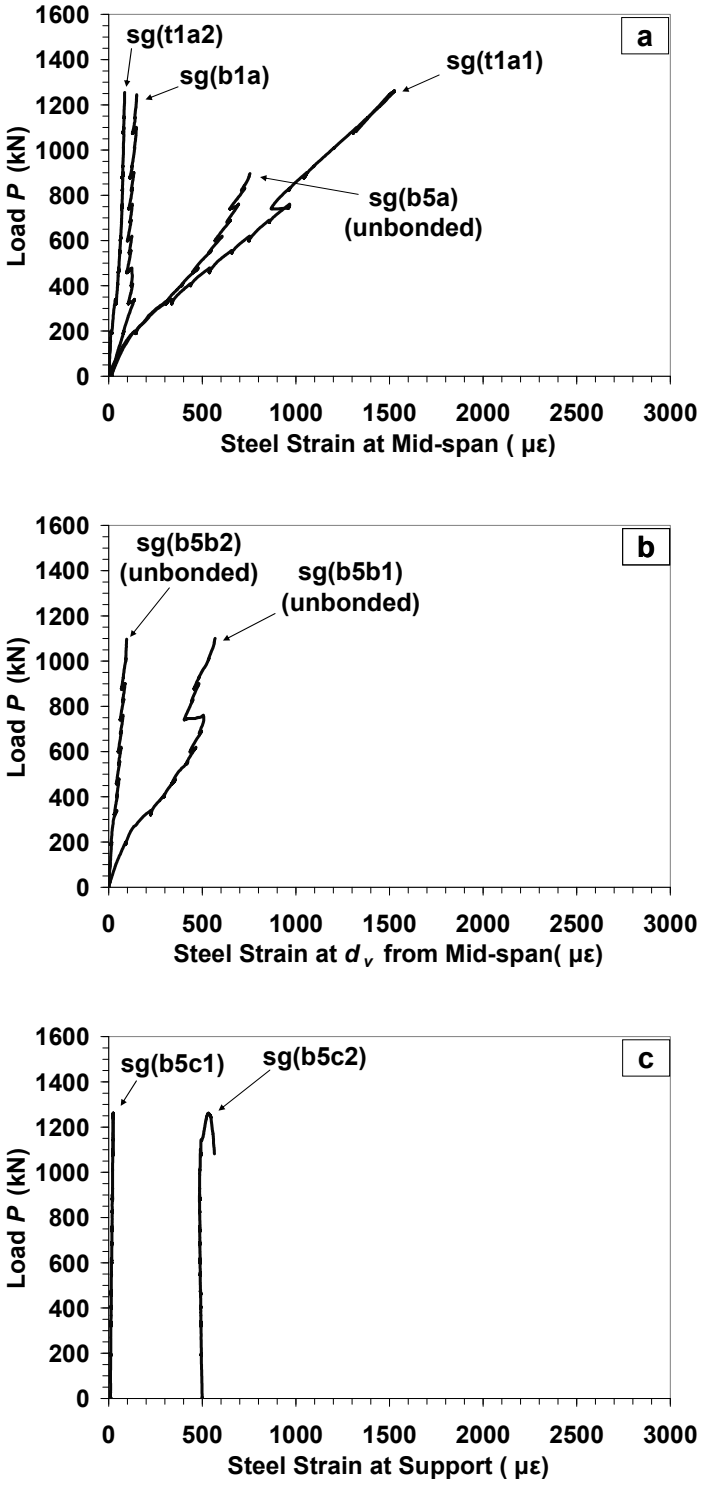

Figure B-63: Load-steel strain response for specimen *H10-2* at (a) mid-span; (b) d_v from mid-span; (c) support.

B.3.4.4 Crack Development

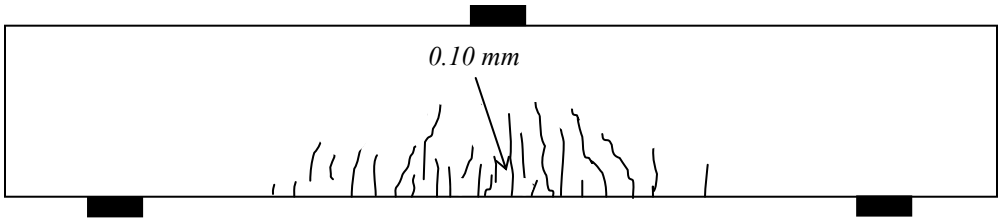

(a) At $P=620\ kN=0.49P_{max}$
(maximum flexural crack width = 0.10 *mm*)

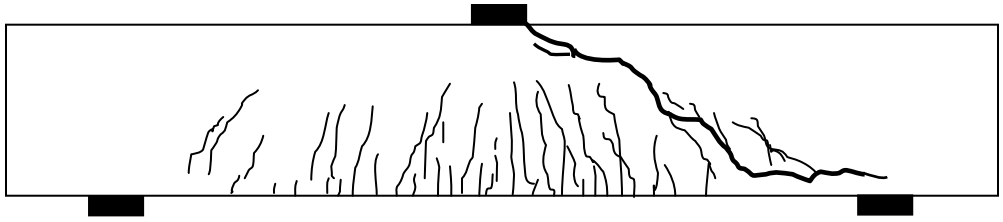

(b) After shear failure ($P_{max}=1261\ kN$)

Figur B-64: Crack pattern for specimen *H10-2*.

B.3.5 Specimen *L10-1*

B.3.5.1 Instrumentation (Strain Gauges and LVDTs)

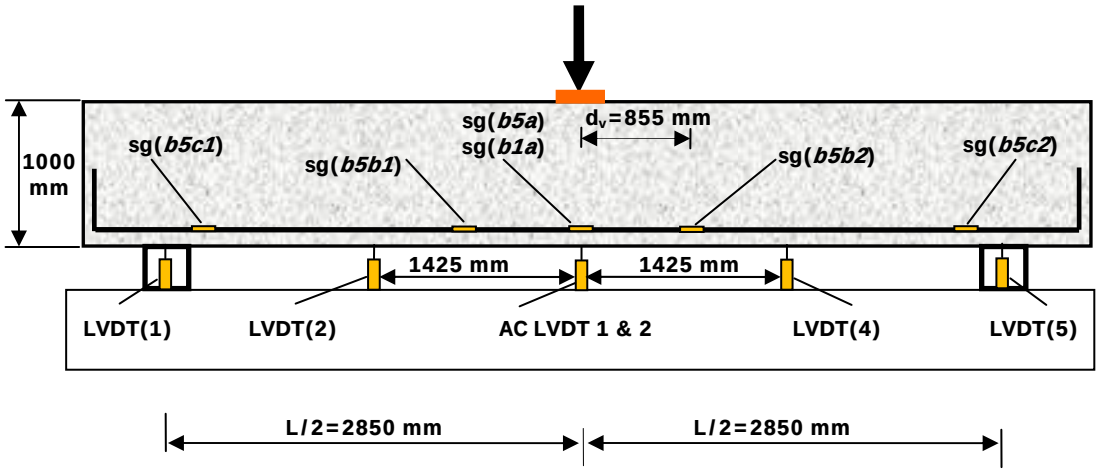

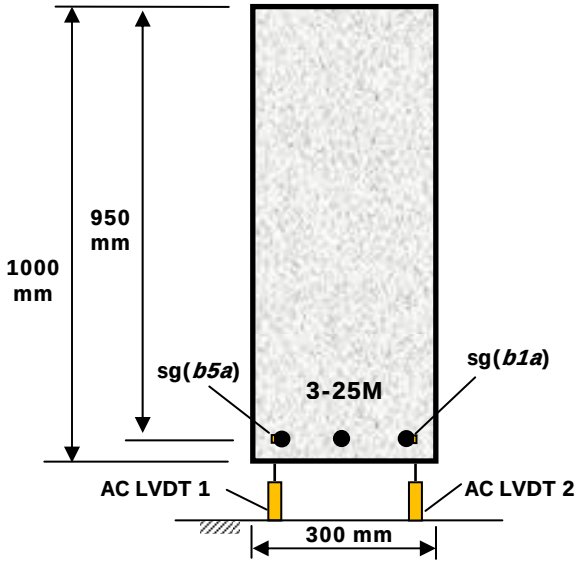

Mid-span Section

Figure B-65: Instrumentation for specimen *L10-1* (sg: strain gauge).

B.3.5.2 Load-Deflection Response

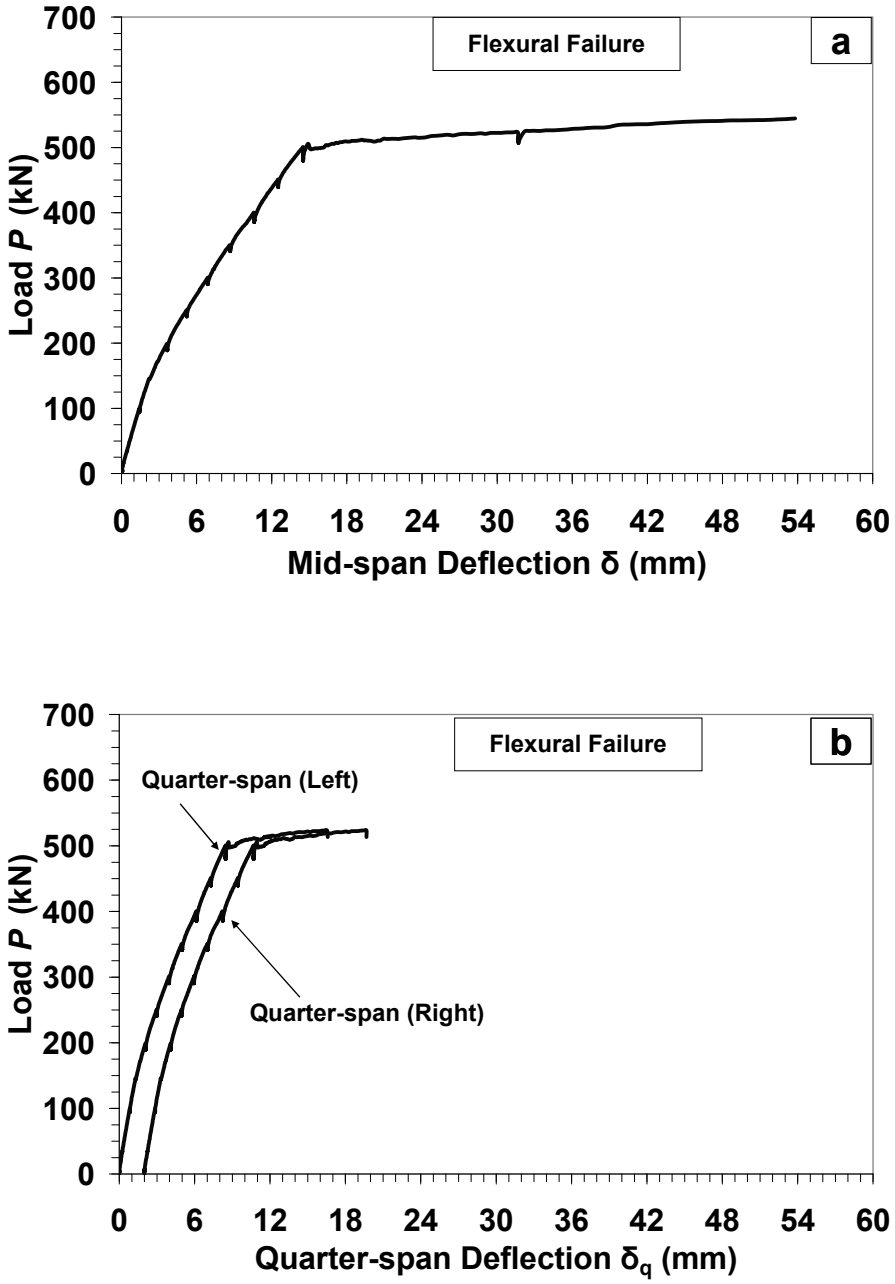

Figure B-66: Load-Deflection response for specimen *L10-1* at (a) mid-span; (b) quarter-span. (Note: all presented deflection data were corrected for the measured support settlement)

B.3.5.3 Load-Steel Strain Response

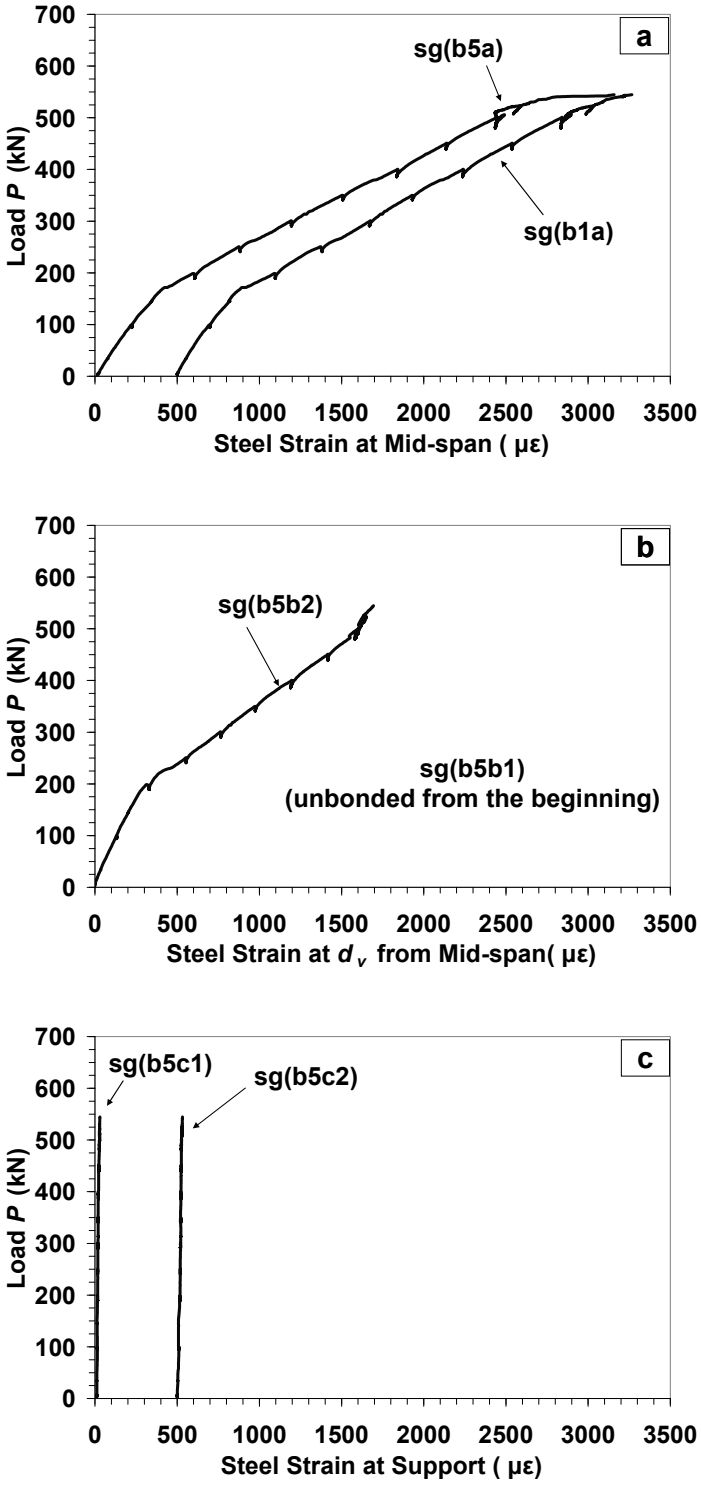

Figure B-67: Load-steel strain response for specimen *L10-1* at (a) mid-span; (b) d_v from mid-span; (c) support.

B.3.5.4 Crack Development

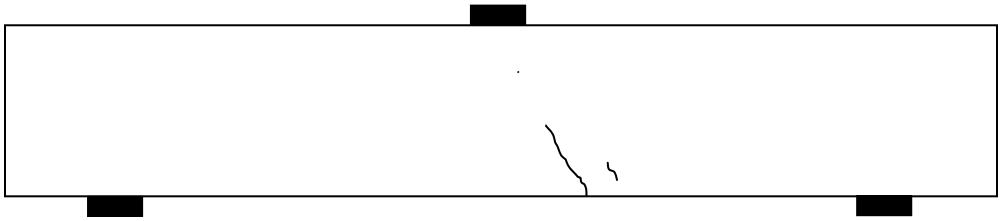

(a) At $P=250\ kN=0.47P_{max}$
(maximum flexural crack width = 0.08 *mm*)

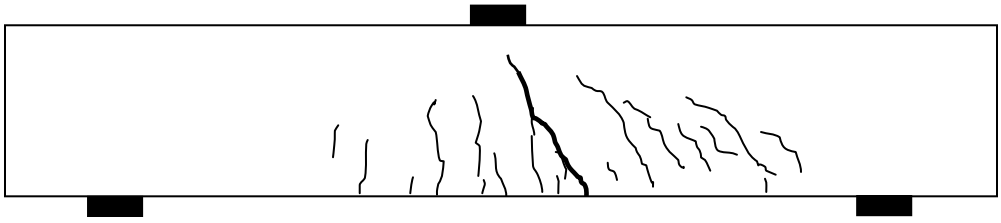

(b) After flexural failure ($P_{max}=532\ kN$)

Figur B-68: Crack pattern for specimen *L10-1*.

B.3.6 Specimen *L10-2*

B.3.6.1 Instrumentation (Strain Gauges and LVDTs)

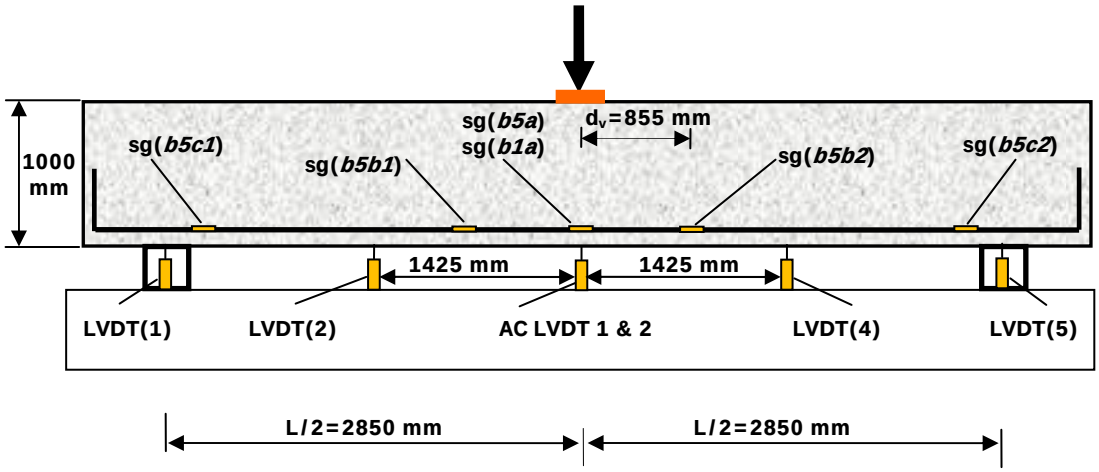

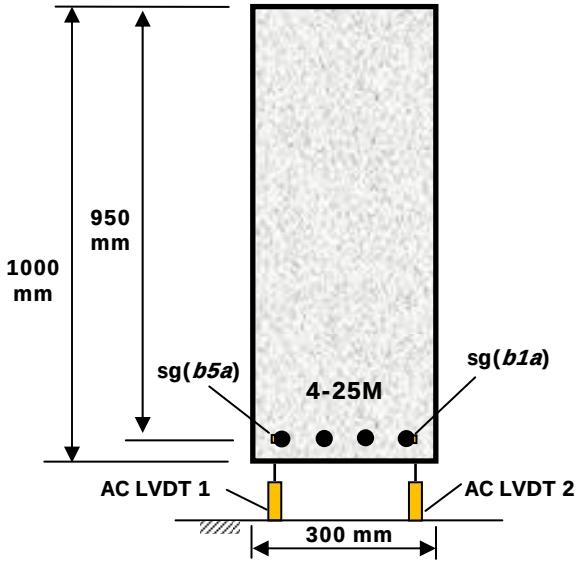

Mid-span Section

Figure B-69: Instrumentation for specimen *L10-2* (sg: strain gauge).

B.3.6.2 Load-Deflection Response

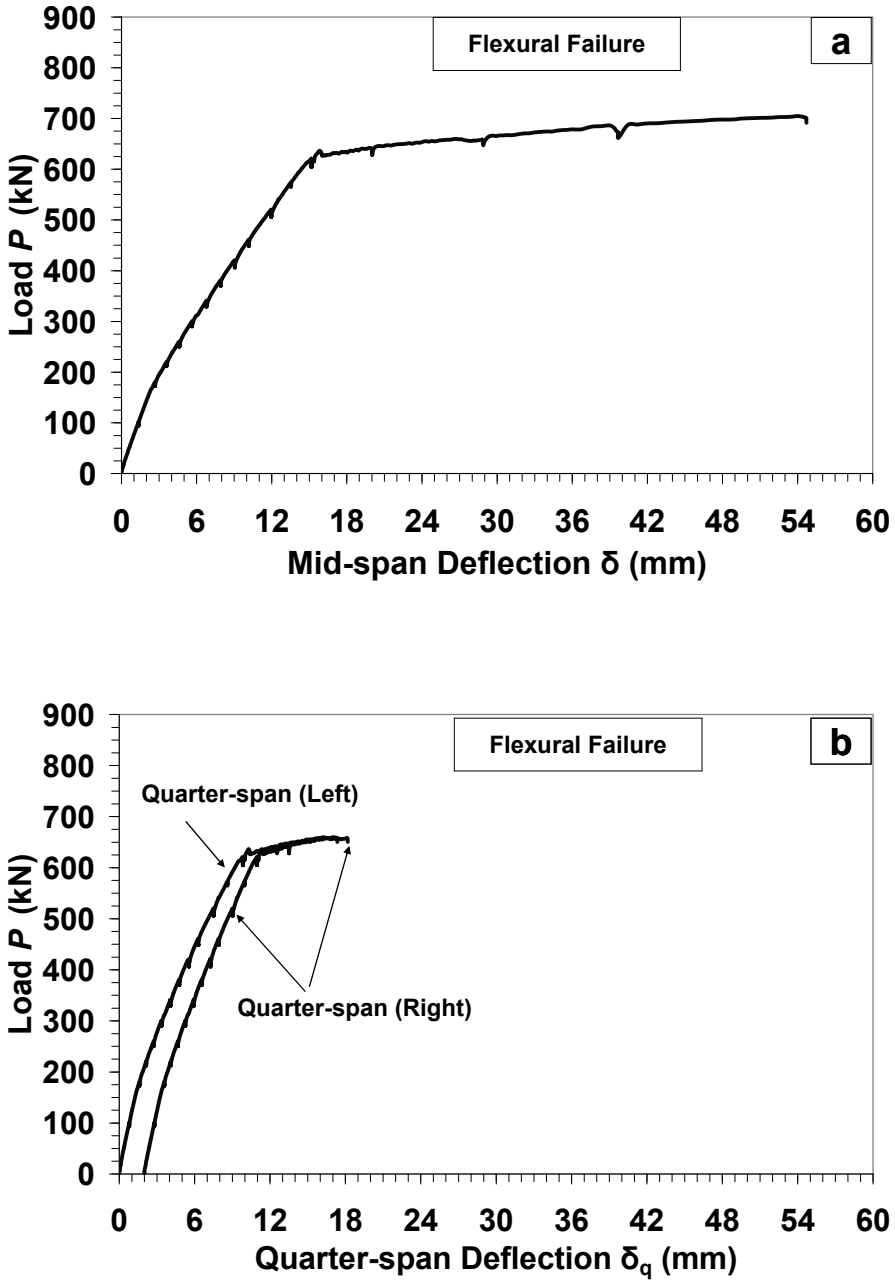

Figure B-70: Load-Deflection response for specimen *L10-2* at (a) mid-span; (b) quarter-span. (Note: all presented deflection data were corrected for the measured support settlement)

B.3.6.3 Load-Steel Strain Response

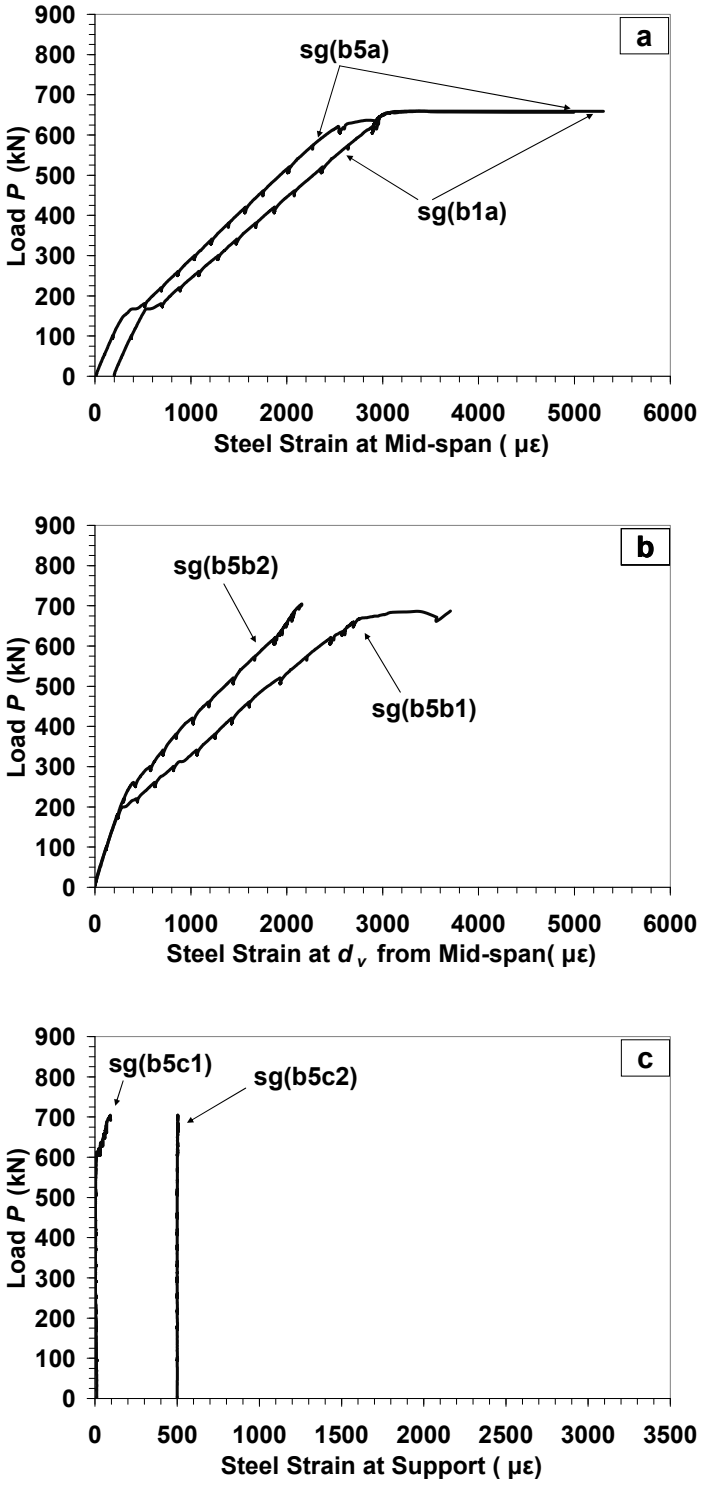

Figure B-71: Load-steel strain response for specimen *L10-2* at (a) mid-span; (b) d_v from mid-span; (c) support.

B.3.6.4 Crack Development

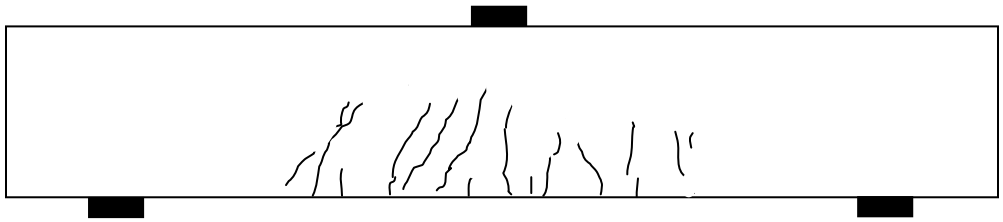

(a) At $P=340\ kN=0.49P_{max}$
(maximum flexural crack width < 0.08 *mm*)

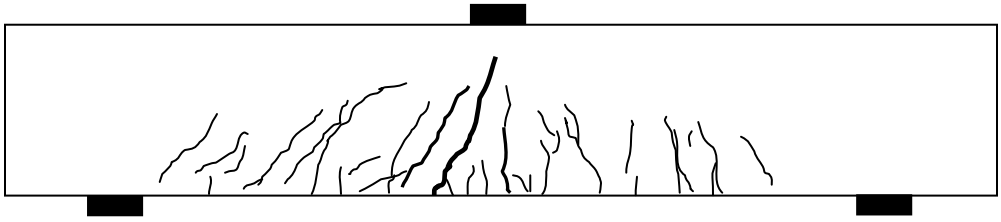

(b) After flexural failure ($P_{max}=692\ kN$)

Figur B-72: Crack pattern for specimen *L10-2*.